

AWARD NUMBER: W81XWH-14-1-0050

TITLE: Depleting Glycine and Sarcosine in Prostate cancer Cells as a New Treatment for Advanced Prostate Cancer

PRINCIPAL INVESTIGATOR: Zongbing You

CONTRACTING ORGANIZATION: The Administrators of the Tulane Educational Fund
New Orleans, LA 70118

REPORT DATE: April 2015

TYPE OF REPORT: Final Report

PREPARED FOR: U.S. Army Medical Research and Materiel Command
Fort Detrick, Maryland 21702-5012

DISTRIBUTION STATEMENT: Approved for Public Release;
Distribution Unlimited

The views, opinions and/or findings contained in this report are those of the author(s) and should not be construed as an official Department of the Army position, policy or decision unless so designated by other documentation.

| REPORT DOCUMENTATION PAGE | | | | Form Approved OMB No. 0704-0188 | |
|---|--------------|-----------------------|----------------------------|--|---|
| Public reporting burden for this collection of information is estimated to average 1 hour per response, including the time for reviewing instructions, searching existing data sources, gathering and maintaining the data needed, and completing and reviewing this collection of information. Send comments regarding this burden estimate or any other aspect of this collection of information, including suggestions for reducing this burden to Department of Defense, Washington Headquarters Services, Directorate for Information Operations and Reports (0704-0188), 1215 Jefferson Davis Highway, Suite 1204, Arlington, VA 22202-4302. Respondents should be aware that notwithstanding any other provision of law, no person shall be subject to any penalty for failing to comply with a collection of information if it does not display a currently valid OMB control number. PLEASE DO NOT RETURN YOUR FORM TO THE ABOVE ADDRESS. | | | | | |
| 1. REPORT DATE : April 2015 | | 2. REPORT TYPE: Final | | 3. DATES COVERED 1 Feb 2014 - 31 Jan 2015 | |
| 4. TITLE AND SUBTITLE Depleting Glycine and Sarcosine in Prostate cancer Cells as a New Treatment for Advanced Prostate Cancer | | | | 5a. CONTRACT NUMBER | |
| | | | | 5b. GRANT NUMBER W81XWH-14-1-0050 | |
| | | | | 5c. PROGRAM ELEMENT NUMBER | |
| 6. AUTHOR(S) Zongbing You email: zyou@tulane.edu | | | | 5d. PROJECT NUMBER | |
| | | | | 5e. TASK NUMBER | |
| | | | | 5f. WORK UNIT NUMBER | |
| 7. PERFORMING ORGANIZATION NAME(S) AND ADDRESS(ES) The Administrators of the Tulane Educational Fund 6823 SAINT CHARLES AVE NEW ORLEANS, LA 70118-5665 | | | | 8. PERFORMING ORGANIZATION REPORT NUMBER | |
| 9. SPONSORING / MONITORING AGENCY NAME(S) AND ADDRESS(ES) U.S. Army Medical Research and Materiel Command Fort Detrick, Maryland 21702-5012 | | | | 10. SPONSOR/MONITOR'S ACRONYM(S) | |
| | | | | 11. SPONSOR/MONITOR'S REPORT NUMBER(S) | |
| 12. DISTRIBUTION / AVAILABILITY STATEMENT Approved for Public Release; Distribution Unlimited | | | | | |
| 13. SUPPLEMENTARY NOTES | | | | | |
| 14. ABSTRACT Glycine is consumed by rapidly proliferating cancer cells but not rapidly proliferating normal cells, which offers an opportunity to deplete glycine and inhibit cancer cells without affecting normal cells. The major source of intracellular glycine is a reversible conversion of serine through serine hydroxymethyltransferases (SHMT). Glycine is required for synthesis of purines, proteins, glutathione, and sarcosine. Sarcosine is associated with invasion, migration, and metastasis of prostate cancer. Aminomethylphosphonic acid (AMPA) is an analog of glycine that can inhibit SHMT's enzyme activities, thus being able to block conversion of serine into glycine and subsequently to decrease sarcosine. We hypothesize that AMPA may inhibit proliferation, invasion, migration, and metastasis of prostate cancer through depleting glycine and sarcosine. In the one-year performance period, we found that AMPA indeed inhibited proliferation, invasion, migration, and metastasis of prostate cancer in the in vitro and in vivo experiments. | | | | | |
| 15. SUBJECT TERMS Prostate cancer, metabolism, glycine, sarcosine, serine, serine hydroxymethyltransferase, aminomethylphosphonic acid, proliferation, invasion, migration, metastasis | | | | | |
| 16. SECURITY CLASSIFICATION OF: | | | 17. LIMITATION OF ABSTRACT | 18. NUMBER OF PAGES | 19a. NAME OF RESPONSIBLE PERSON |
| a. REPORT | b. ABSTRACT | c. THIS PAGE | | | USAMRMC |
| Unclassified | Unclassified | Unclassified | Unclassified | 198 | 19b. TELEPHONE NUMBER (include area code) |

Table of Contents

| | <u>Page</u> |
|---|---------------|
| 1. Introduction..... | 4 |
| 2. Keywords..... | 5 |
| 3. Accomplishments..... | 6-23 |
| 4. Impact..... | 23 |
| 5. Changes/Problems..... | 23-24 |
| 6. Products..... | 24-27 |
| 7. Participants & Other Collaborating Organizations..... | 27 |
| 8. Special Reporting Requirements..... | 27 |
| 9. Appendices..... | 27-198 |

1. INTRODUCTION

Glycine is consumed by rapidly proliferating cancer cells but not rapidly proliferating normal cells [1], which offers an opportunity to deplete glycine and inhibit cancer cells without affecting normal cells. The major source of intracellular glycine is a reversible conversion of serine through serine hydroxymethyltransferases (SHMT). Glycine is required for synthesis of purines, proteins, glutathione, and sarcosine. Sarcosine is associated with invasion, migration, and metastasis of prostate cancer [2]. Aminomethylphosphonic acid (AMPA) is an analog of glycine that can inhibit SHMT's enzyme activities [3], thus being able to block conversion of serine into glycine and subsequently to decrease sarcosine. We hypothesize that AMPA may inhibit proliferation, invasion, migration, and metastasis of prostate cancer through depleting glycine and sarcosine. The objectives of this project are to complete two specific aims: Aim 1. To determine AMPA's effects on cellular proliferation, migration, and invasion of prostate cancer cells in vitro; and Aim 2. To determine AMPA's efficacy on growth, local invasion, and metastasis of prostate cancer in vivo.

2. KEYWORDS:

Prostate cancer, metabolism, glycine, sarcosine, serine, serine hydroxymethyltransferase, aminomethylphosphonic acid, proliferation, invasion, migration, metastasis

3. ACCOMPLISHMENTS:

- **What were the major goals of the project: see Table 1.**

Table 1. List of major goals, milestones/target dates, and actual completion dates

| Specific Aim 1(specified in proposal) | Timeline | Actual completion date |
|---|----------|--|
| Major Task 1: To determine AMPA's effects on cellular proliferation, migration, and invasion of prostate cancer cells in vitro | Months | |
| Milestone(s) Achieved: a meeting abstract and/or manuscript reporting the results. | 6 | <i>submitted a meeting abstract on 8/18/2014</i> |
| Local IACUC Approval | 2 | 1/31/2014 |
| Milestone Achieved: ACURO Approval | 2 | 3/13/2014 |
| Specific Aim 2 | | |
| Major Task 2: To determine AMPA's efficacy on growth, local invasion, and metastasis of prostate cancer in vivo | | |
| Milestone(s) Achieved: Publish a meeting abstract and/or manuscript reporting the results | 12 | Submitted a manuscript on 4/13/2015 |

- **What was accomplished under these goals:**

1) Major activities:

First, we performed in vitro studies on two immortalized human normal prostate epithelial cell lines (pRNS-1-1 and RWPE-1) and 4 prostate cancer cell lines (LNCaP, C4-2B, PC-3, and DU-145). The studies assessed: a) if AMPA can reduce the intracellular levels of glycine and sarcosine; b) if AMPA can inhibit cellular proliferation and induce cell cycle arrest and apoptosis; c) if AMPA can inhibit migration; d) if AMPA can inhibit invasion.

Second, we performed in vivo studies using PC-3-*LacZ-luc* cell line and orthotopic mouse models of prostate cancer by surgical orthotopic implantation in the ventral lateral lobes of mouse prostate gland according to the procedures described by Hoffman [4]. Animals were treated with phosphate-buffered saline (control group), a low dose AMPA of 400 mg/kg/day, or a high dose AMPA of 800 mg/kg/day injected intraperitoneally once a day, starting one week after tumor implantation and ending upon animal death. Prior to treatment and once a week after treatment, D-luciferin was injected subcutaneously into the animals and prostate tumor size and any metastases were recorded quantitatively using the IVIS[®] Lumina XRMS in vivo imaging system. After death, prostate tumor weight and metastases were examined and analyzed.

2) Specific objectives:

Our specific objectives were to complete two specific aims:

Aim 1. To determine AMPA's effects on cellular proliferation, migration, and invasion of prostate cancer cells in vitro.

Aim 2. To determine AMPA's efficacy on growth, local invasion, and metastasis of prostate cancer in vivo.

3) Significant results:

- a) We found that AMPA inhibits cell growth in cancer cell lines but not in normal cell lines. Because AMPA is a degraded form of glyphosate (a broad-spectrum herbicide that is used worldwide in weed control) and both AMPA and glyphosate are glycine analogs (Figure 1), we also tested glyphosate and found that glyphosate had similar effects. In addition to prostate cancer cell lines, we also studied human ovarian cancer cell lines (SKOV-3 and OVCAR-3), cervical cancer cell line (HeLa), and lung cancer cell line (A549). We found that both AMP and glyphosate inhibit cell growth in these human cancer cell lines (Figures 2 and 3). Details of the results are reported in our publication [5] (enclosed in Appendices).
- b) We found that AMPA inhibits entry into the S phase of cell cycle and increases apoptosis (Figure 4). Details of the results are reported in our publication [5] (enclosed in Appendices).
- c) We found that AMPA induces changes in expression levels of genes involved in cell cycle and apoptosis. AMPA at a concentration of 50 mM increased the levels of cleaved PARP in C4-2B cells in a time-dependent manner (Figure 5A). AMPA transiently increased the levels of p53 and its downstream gene p21 at 12 hours after treatment (Figure 5B). It also decreased cyclin D3 protein levels starting from 12 hours after treatment (Figure 5B). Further, AMPA increased the levels of pro-caspase 9 starting from 24 hours after treatment (Figure 5B). In contrast, AMPA decreased the levels of pro-caspase 3 starting from 24 hours after treatment (Figure 5B). Details of the results are reported in our publication [5] (enclosed in Appendices).
- d) We found that AMPA inhibits prostate cancer cell migration (Figure 6A and B).
- e) We found that AMPA inhibits prostate cancer cell invasion (Figure 6C and D).

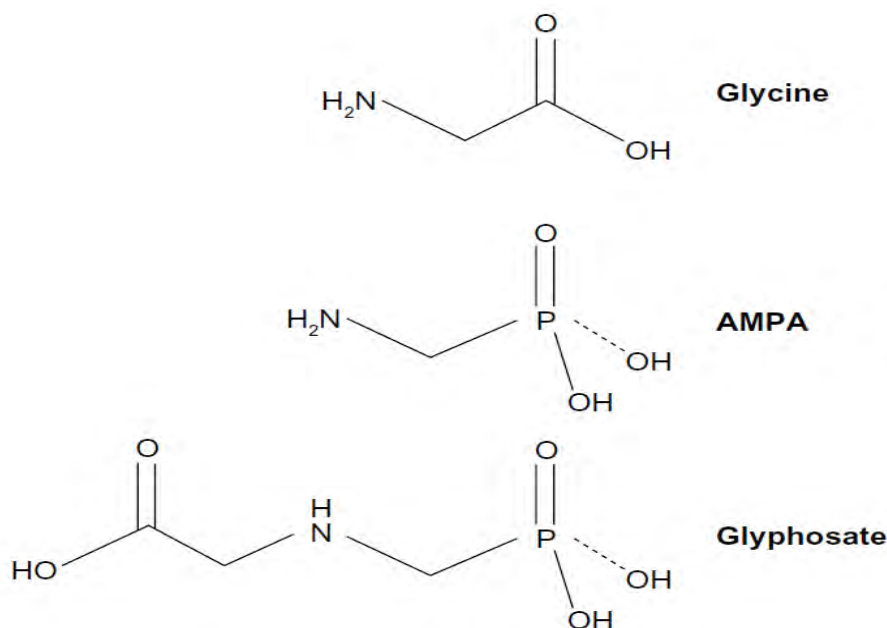


Figure 1 Chemical structure of glycine, AMPA, and glyphosate.
Abbreviation: AMPA, aminomethylphosphonic acid.

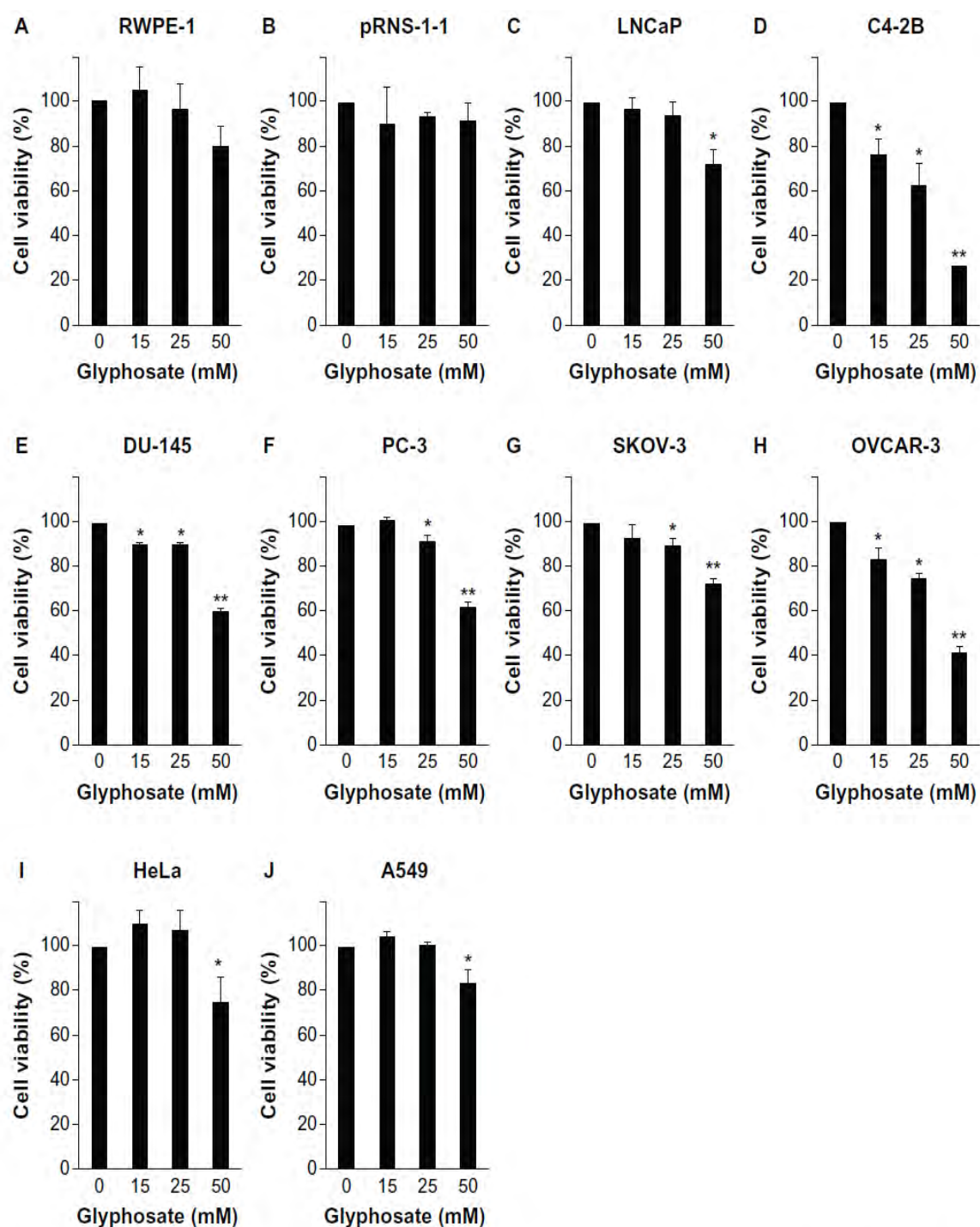


Figure 2 Glyphosate inhibits cell growth in cancer cell lines but not in normal cell lines.

Notes: (A–J) The cells were treated with 0, 15, 25, and 50 mM of glyphosate for 72 hours. Cell viability was determined using CellTiter-Glo® Luminescent Cell Viability Assay. Data represent the mean \pm SEM obtained from three independent experiments. * $P < 0.05$ and ** $P < 0.01$, compared with the untreated control group.

Abbreviation: SEM, standard error of the mean.

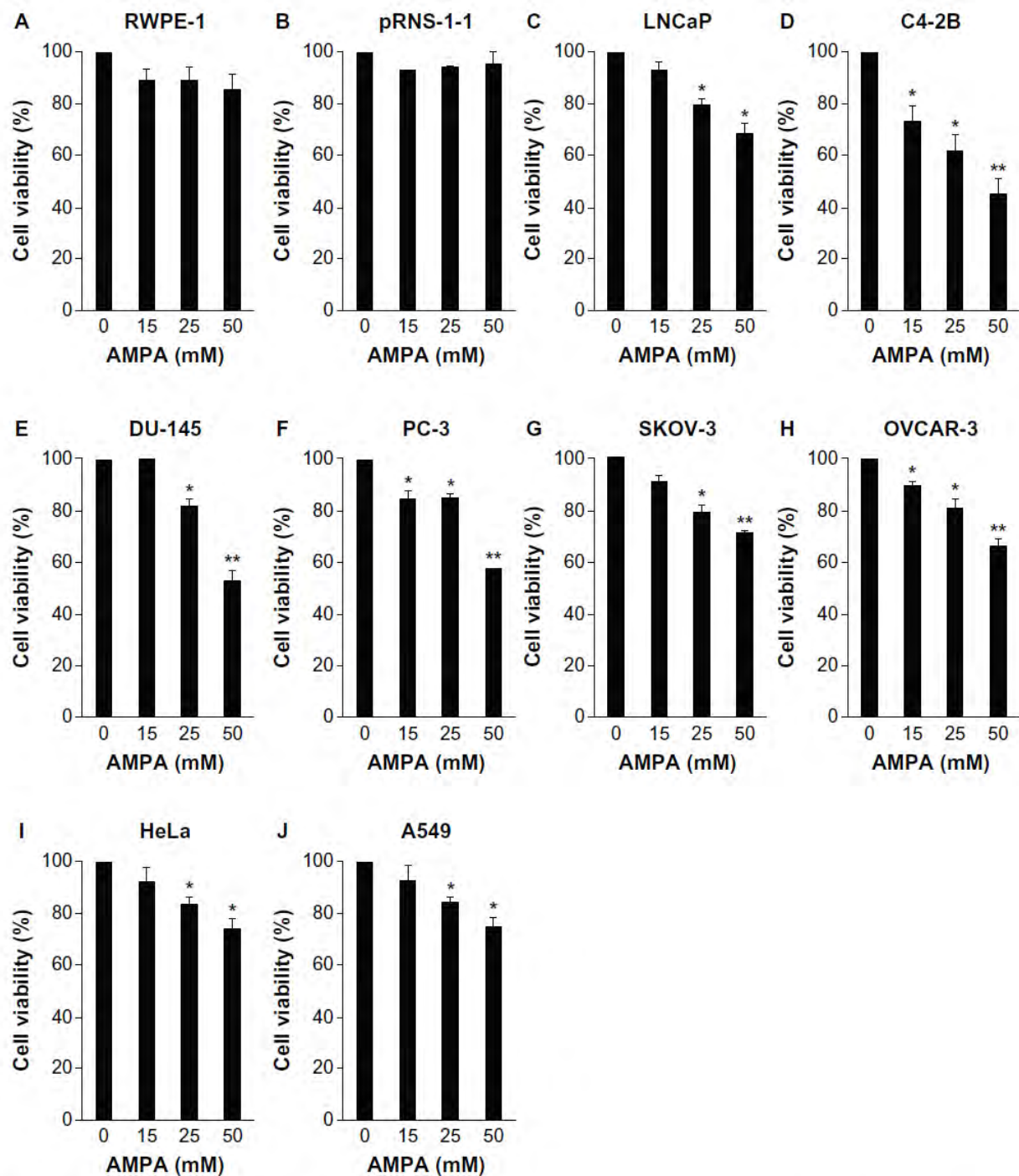


Figure 3 AMPA inhibits cell growth in cancer cell lines but not in normal cell lines.

Notes: (A-J) The cells were treated with 0, 15, 25, and 50 mM of AMPA for 72 hours. Cell viability was determined using CellTiter-Glo® Luminescent Cell Viability Assay. Data represent the mean \pm SEM obtained from three independent experiments. * $P < 0.05$ and ** $P < 0.01$, compared with the untreated control group.

Abbreviations: AMPA, aminomethylphosphonic acid; SEM, standard error of the mean.

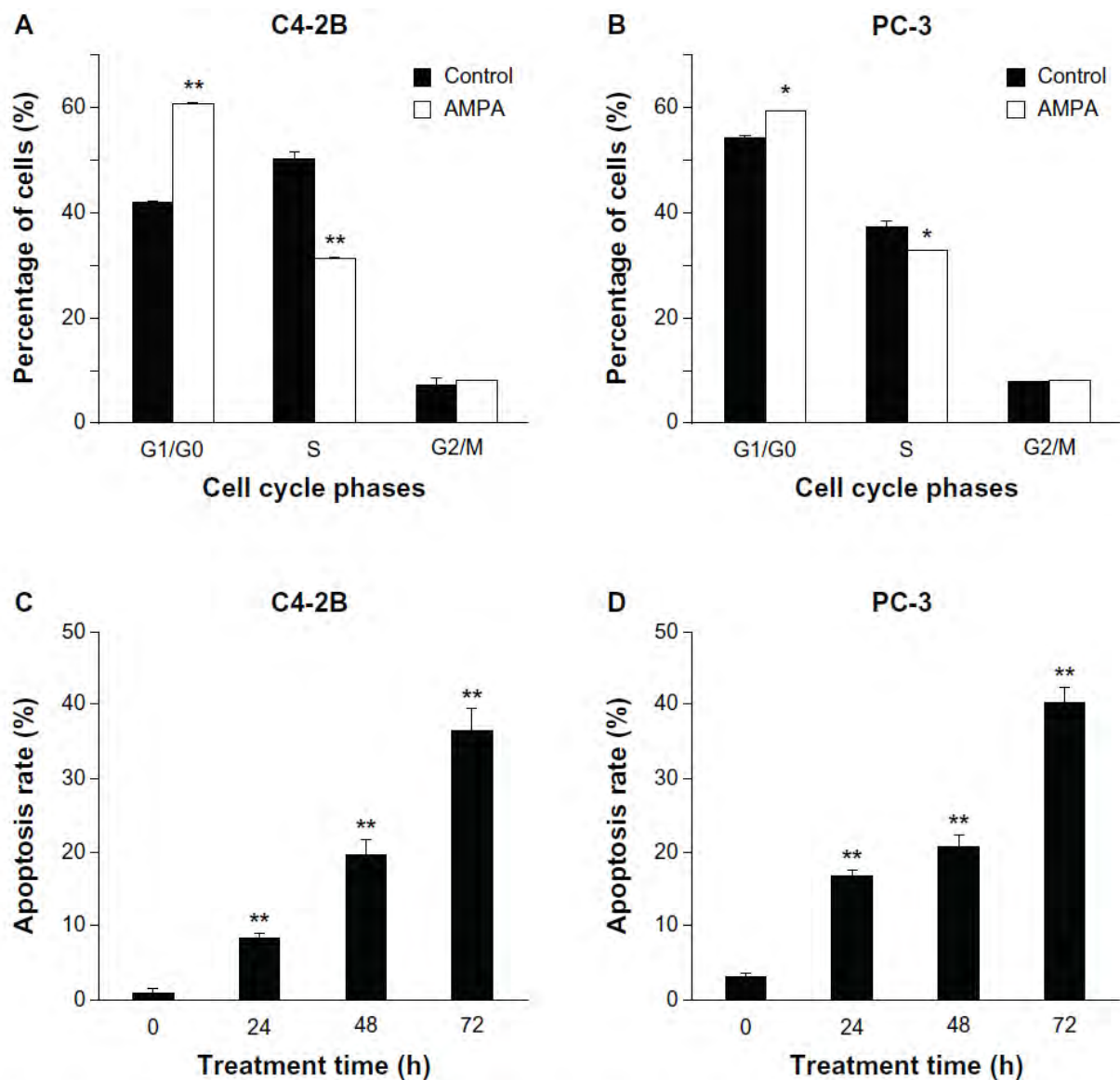


Figure 4 AMPA inhibits entry into the S phase of cell cycle and increases apoptosis.

Notes: C4-2B and PC-3 cells were treated with or without 50 mM AMPA for 24 hours (A and B) or 0, 24, 48, and 72 hours (h) (C and D). Percentages of the cells in G1/G0, S, and G2/M phases of cell cycle were determined using propidium iodide staining and flow cytometry analysis (A and B). Apoptosis rates were determined using Annexin-V FITC Conjugate and propidium iodide double staining and flow cytometry analysis (C and D). Data represent the mean \pm SEM obtained from three independent experiments.

* $P < 0.05$ and ** $P < 0.01$, compared with the control group.

Abbreviations: AMPA, aminomethylphosphonic acid; FITC, Fluorescein isothiocyanate; SEM, standard error of the mean.

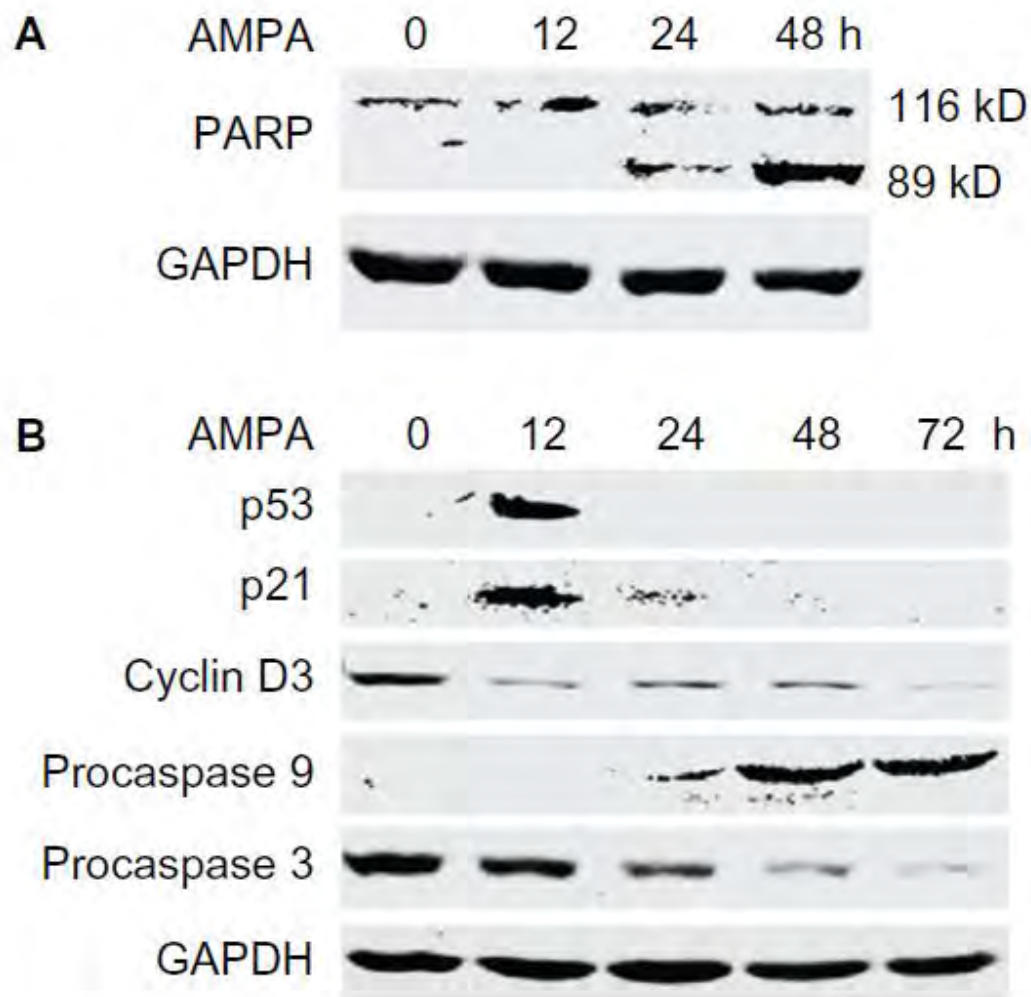


Figure 5 AMPA induces changes in expression levels of genes involved in cell cycle and apoptosis.

Notes: (A–B) C4-2B cells were treated with 50 mM AMPA for the indicated time. Western blot analysis was performed to determine the protein levels. For loading control, the blots were stripped and probed for GAPDH. For PARP, the 116-kD band is the full length, and the 89-kD band is the cleaved form.

Abbreviations: AMPA, aminomethylphosphonic acid; GAPDH, glyceraldehyde-3-phosphate dehydrogenase; h, hours; PARP, poly(ADP-ribose) polymerase; ADP, adenosine diphosphate.

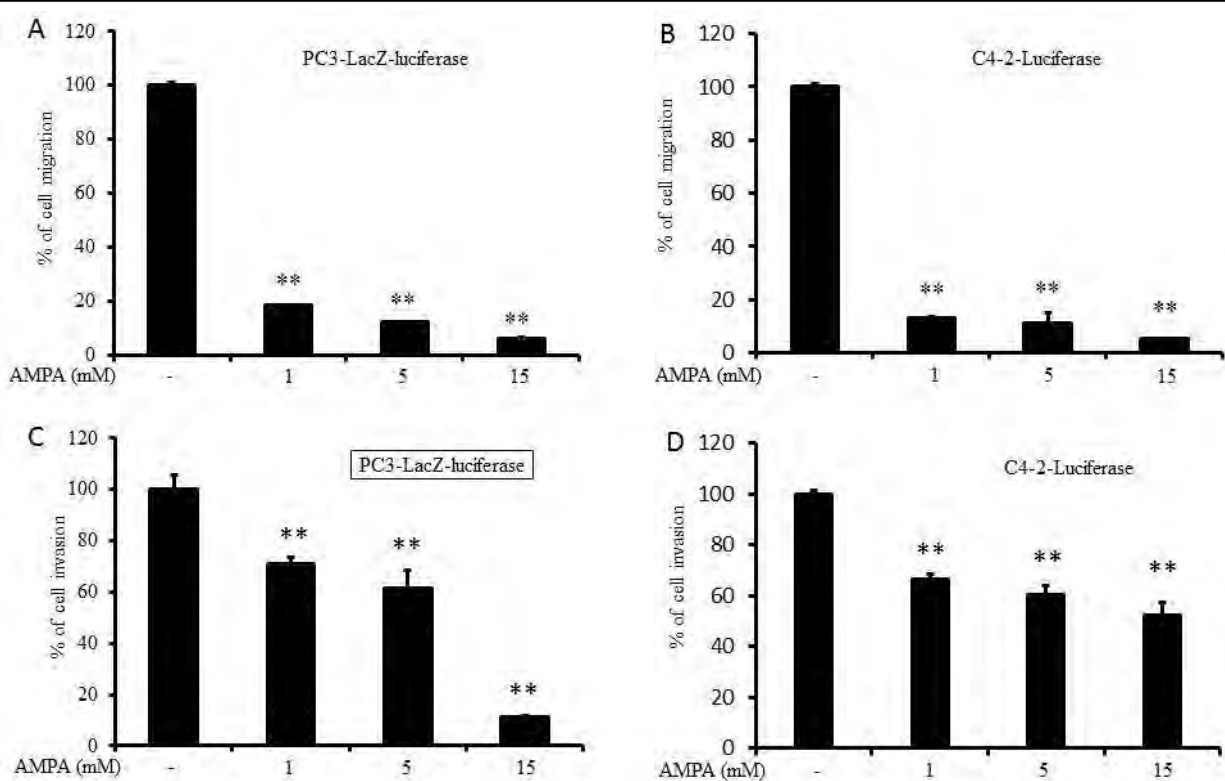


Figure 6 AMPA inhibits prostate cancer cell migration and invasion.

Note: (A-B) Cell migration assays. Briefly, 2×10^5 cells (PC3-LacZ-luciferase and C4-2-luciferase, both stably expressing luciferase gene for cell number quantification using luciferase assays) per well in serum-free medium were plated in the upper chamber of Transwell® plates (Product# 3422, Corning Life Sciences); AMPA at concentrations of 1, 5, and 15 mM were added to the upper chamber; the control group was treated with phosphate-buffered saline (PBS); each group had triplicate wells; the lower chamber was filled with medium containing 10% fetal bovine serum as chemoattractant; 24 hours later, the cells remained in the upper chamber were removed, and the cells that migrated to the lower chamber (on the under surface of the chamber insert) were lysed with protein lysis buffer; the cell number was determined using a luciferase assay kit (Promega), because the luciferase signals were proportional to the cell number; cell migration was normalized to the control group; ** $P < 0.01$, compared to the control group using Student's t test. (C-D) Cell invasion assay. Similar to cell migration assay, except that Transwell® inserts with 8.0- μ m pore polycarbonate membrane were coated with Cultrex® basement membrane (Product #3458, Corning Life Sciences), and that the cells were allowed to invade for 48 hours. Cell invasion was normalized to the control group; ** $P < 0.01$, compared to the control group using Student's t test. Each experiment was independently performed twice. Data from one representative experiment are shown.

f) We found that AMPA inhibits prostate tumor growth and metastasis.

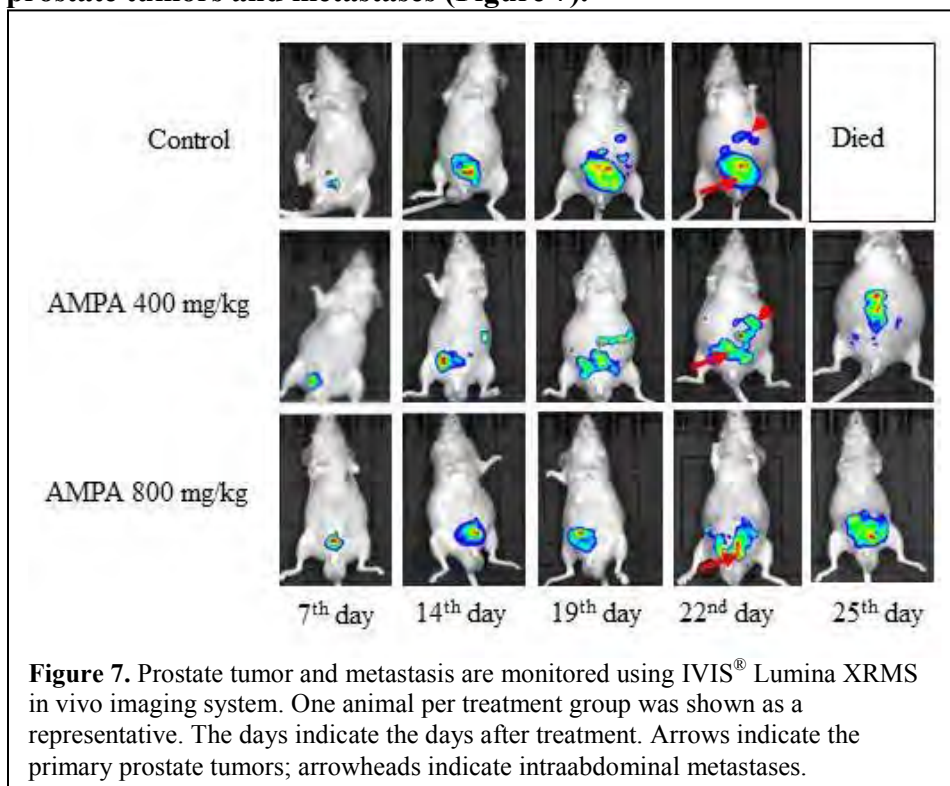
The methodology of animal studies is succinctly described herein. One million PC3-LacZ-luc cells in 50 μ l of PBS were mixed with 50 μ l of Matrigel[®], and then injected subcutaneously into 10 nude male mice. 7-8 week old Ncr-nu/nu mice were purchased from NCI Animal Production Program. Each mouse had two injection sites, one on each flank. After about 3 weeks, the subcutaneous tumors were harvested for orthotopic implantation in the prostate of 45 nude male mice at 7-8 week of age, so that orthotopic prostate cancer models are generated. Tumor tissues from the periphery of the tumors were cut into small cubes of 1 mm³ in standard tissue culture medium under sterile conditions. The tumor pieces were mixed and randomly selected to be implanted in the mouse prostates as described by Dr. Hoffman (Orthotopic metastatic mouse models of prostate cancer, in R.J. Ablin and M.D. Mason (eds), Cancer Metastasis - Biology and Treatment: Metastasis of Prostate Cancer, Springer Science+Business Media B.V., 2008, pp143-169, <http://www.springerlink.com/content/r876618788201762/fulltext.pdf>). Animals were anesthetized by 2-4% isoflurane inhalation. The skin over the lower abdomen was gently cleansed prior to disinfection by 70% ethanol, and then followed by Betadine solution. A 0.5-cm incision was made right above the pubis symphysis to expose the prostate gland; the fascia surrounding the ventral portion of the prostate was carefully isolated and the two ventral lateral lobes of the gland were separated by a small incision using a pair of fine surgical scissors; 5 tumor pieces were sutured into the incision using an 8-0 nylon suture; the two parts of the separated lobes were then sutured together with 5 tumor pieces wrapped within; the surrounding fascia was then used to wrap this portion of the gland to consolidate the incision; the testes were exposed by pulling the epididymal adipose tissue; a hemostat was applied to curtail blood flow followed by 6-0 suture ligation of blood vessels; the testes were excised; the abdomen was closed in 2 layers using a 6-0 suture. All instruments used were sterile. Buprenex 0.1 mg/kg, s.c., was given at the end of surgical procedure, and then every 12 hours up to 48 hrs. All animals were fed a standard maintenance diet/drinking and observed daily for any decreased activity levels for 7 days. Sutures were removed on the 7th day.

One week later, the tumor sizes were evaluated by non-invasive bioluminescent imaging, using the IVIS[®] Lumina XRMS in vivo imaging system (PerkinElmer, Inc). Animals were anesthetized by 2-4% isoflurane in oxygen. D-luciferin (80 μ l of 40 mg/ml sodium salt, Gold Biotechnology, St Louis, MO) was injected subcutaneously in the neck region. Image acquisition was started immediately with a series of images taken once every two minutes within 30-minutes period to determine the peak light emission. The peak light emission intensity (photon/second or photon/sec) represents the tumor size. Then, animals were treated with intraperitoneal injection of phosphate-buffered saline (PBS, control group), low dose AMPA (400 mg/kg/day in PBS), and high dose AMPA (800 mg/kg/day in PBS), once a day until endpoint (animal death). Animal body weight was recorded once a week.

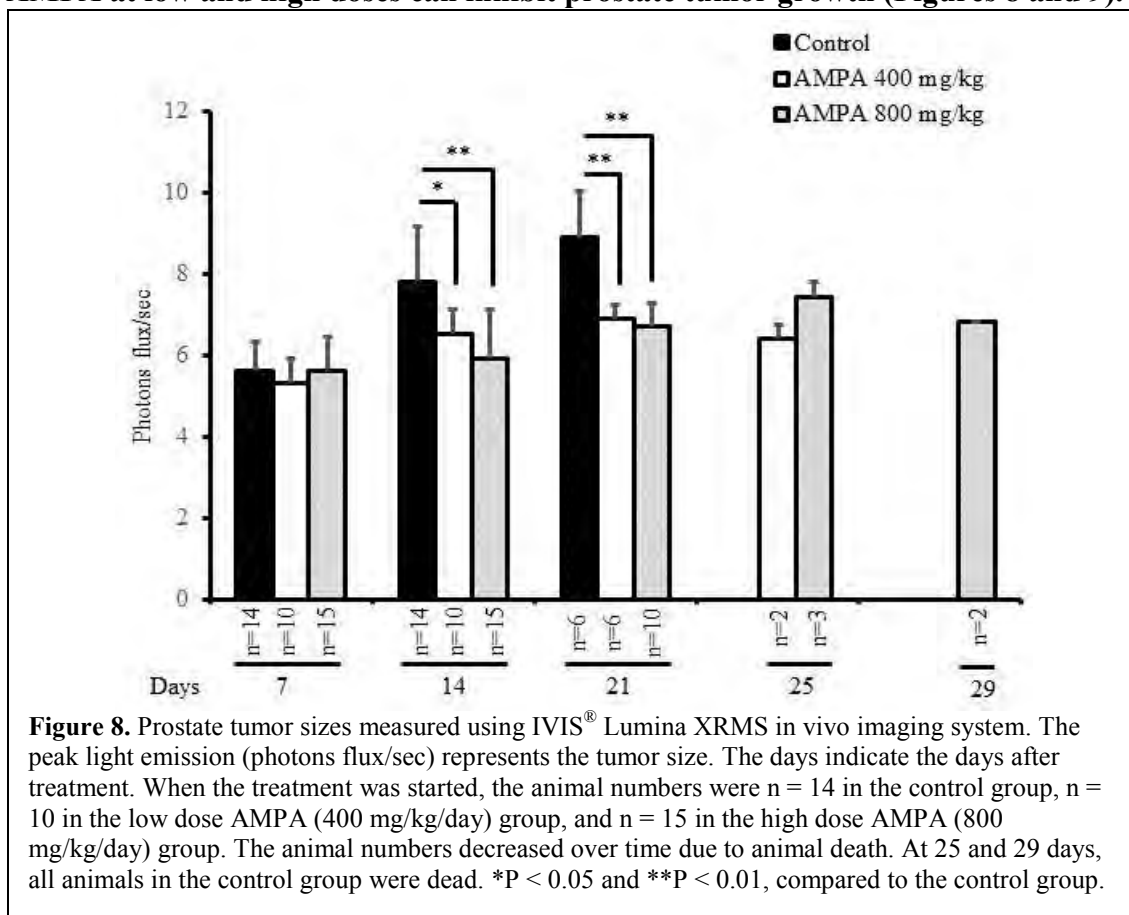
Animals were autopsied upon death. The tumors were dissected out and weighed. The tumor tissues were used for pathologic examination and protein isolation. Tissue sections were stained with hematoxylin and eosin (H&E), anti-Ki-67 antibody for cell proliferation, terminal deoxynucleotidyl transferase dUTP nick end labeling (TUNEL) for apoptosis, and anti-CD31 antibody for microvessels. The proteins were used for Western blot analysis. The detailed methods were described in our previous publications [6,7].

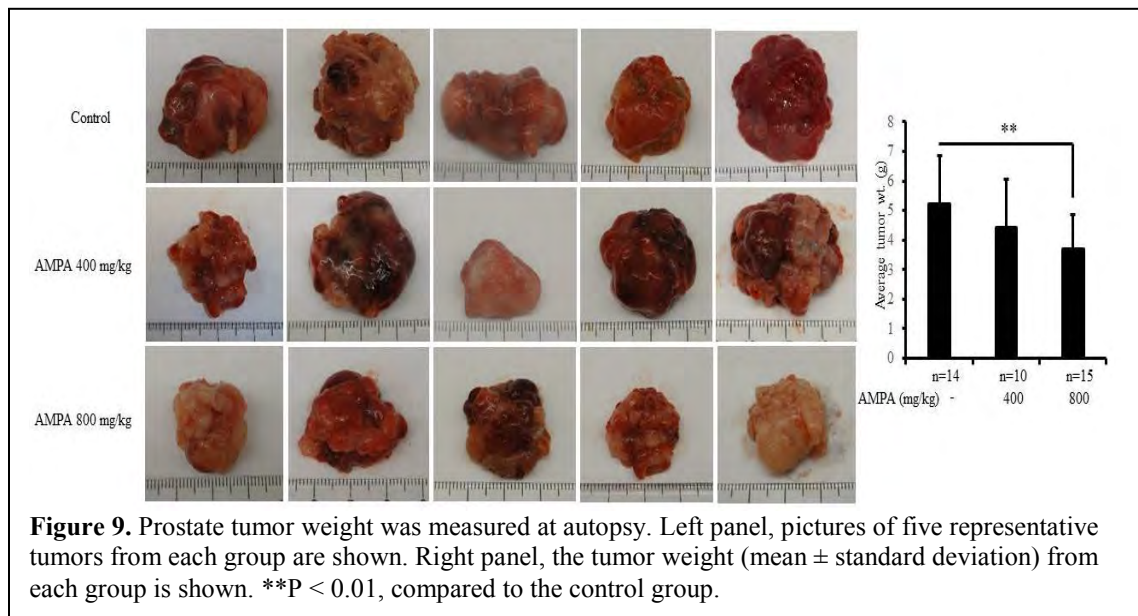
The significant results from animal studies are presented below:

- **IVIS® Lumina XRMS in vivo imaging system is able to monitor the growth of primary prostate tumors and metastases (Figure 7).**



- **AMPA at low and high doses can inhibit prostate tumor growth (Figures 8 and 9).**





➤ **AMPA at low and high doses can prolong the survival of animals with prostate tumors (Figure 10).**

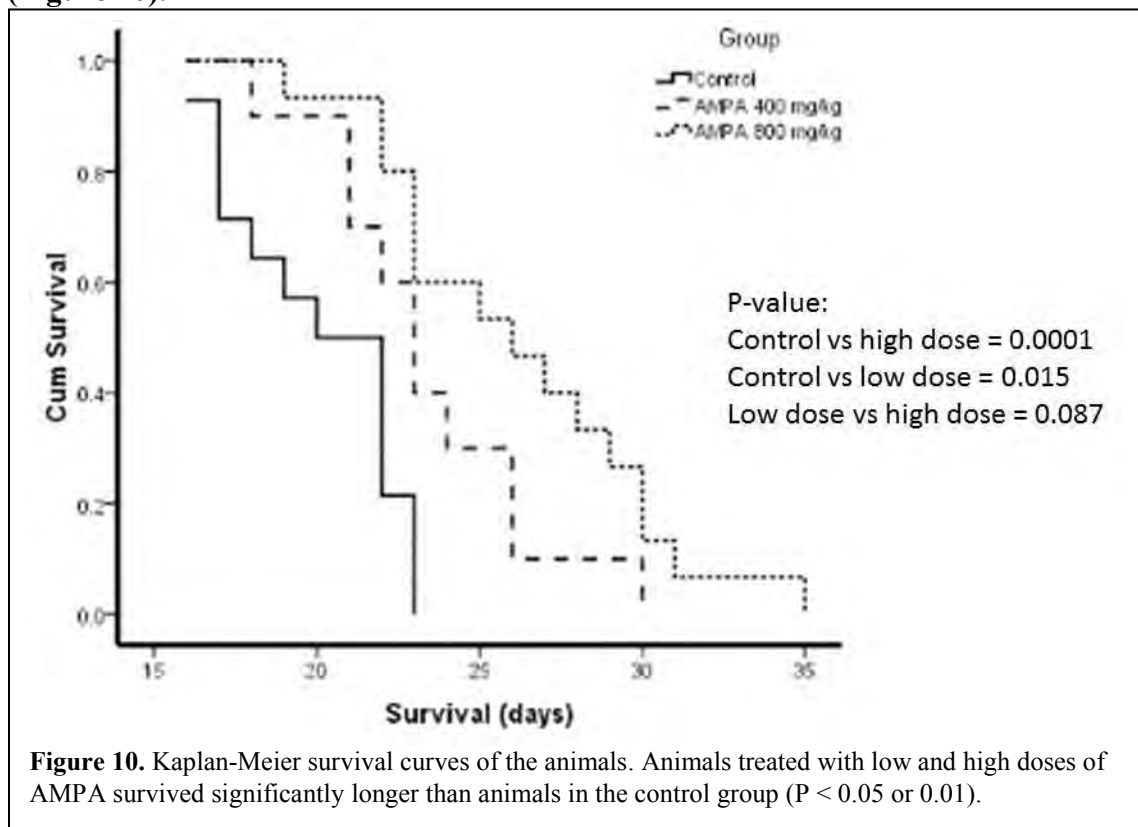
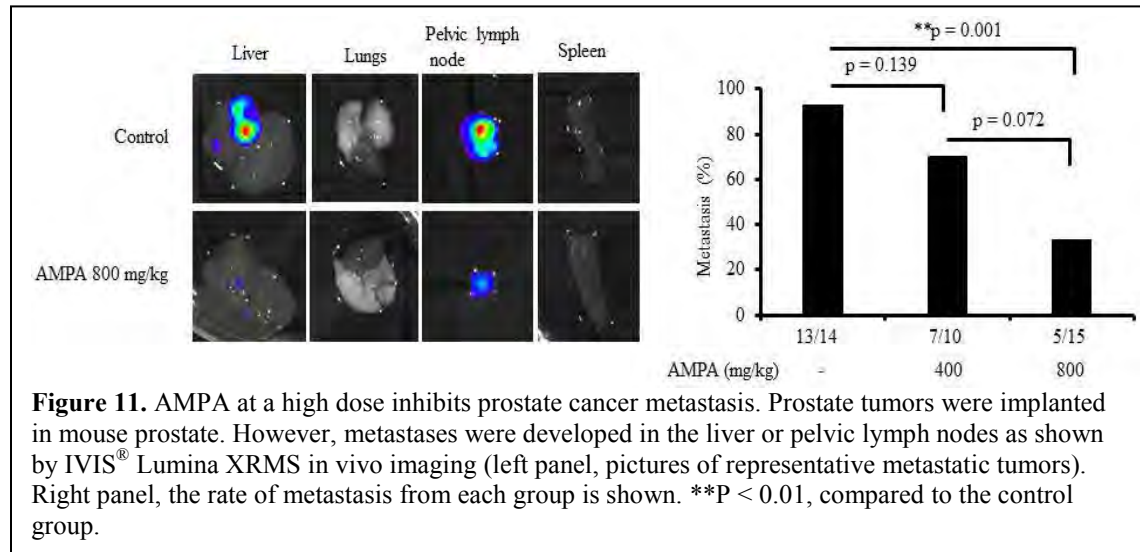
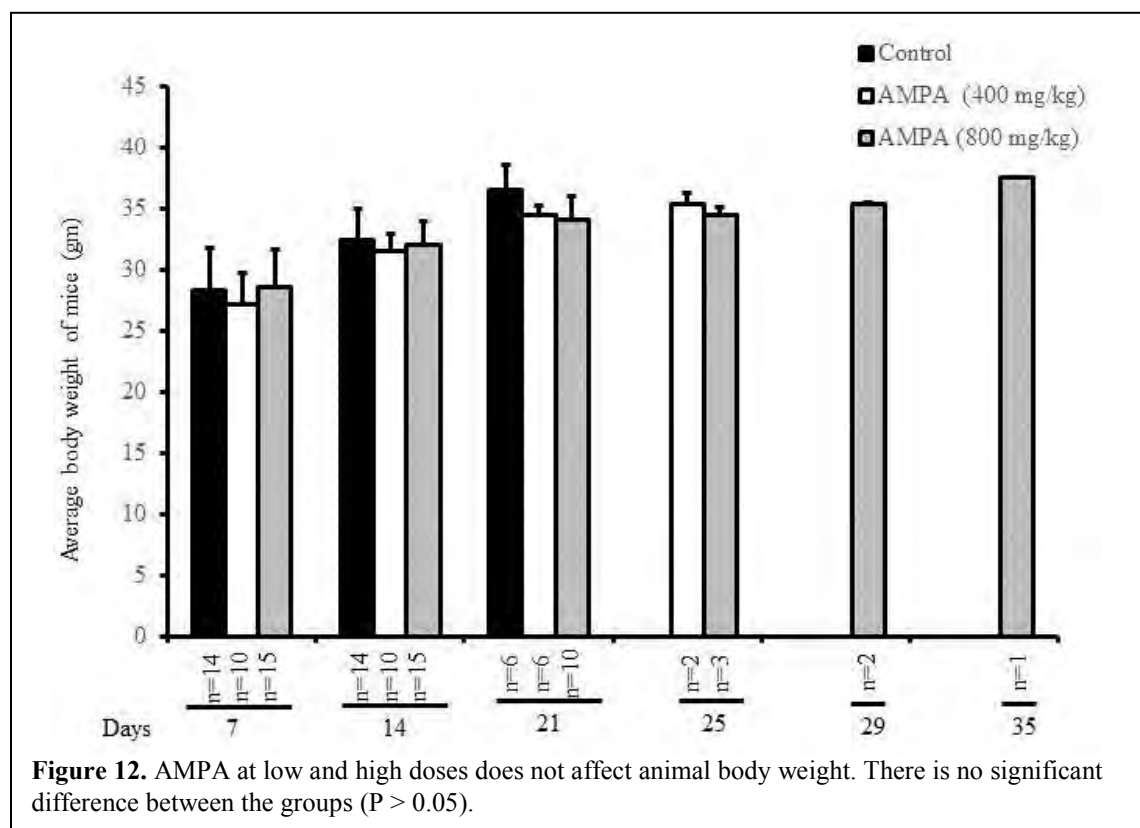


Figure 10. Kaplan-Meier survival curves of the animals. Animals treated with low and high doses of AMPA survived significantly longer than animals in the control group ($P < 0.05$ or 0.01).

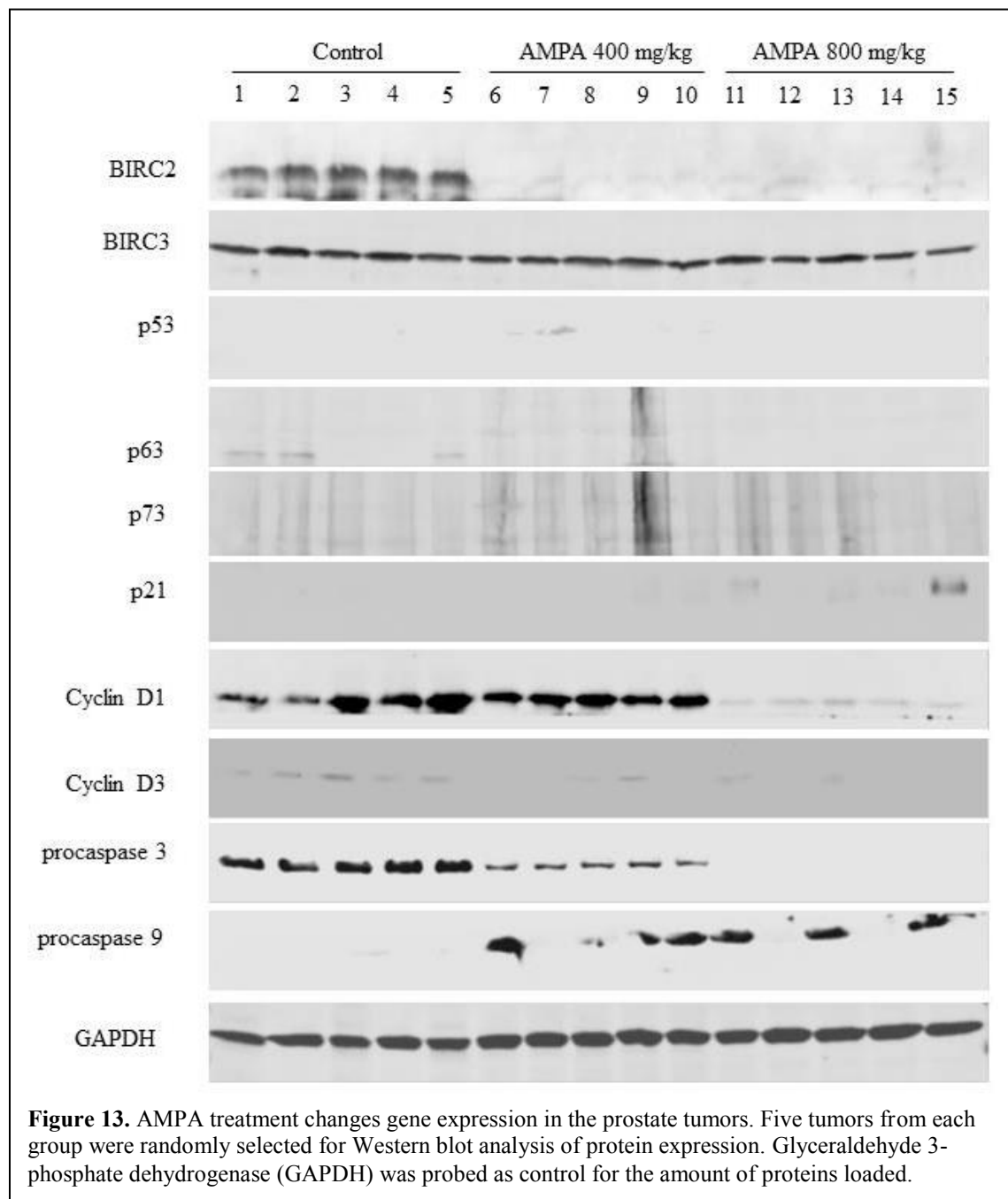
- **AMPA at a high dose can inhibit prostate cancer metastasis (Figure 11).**



- **AMPA at low and high doses does not affect animal body weight (Figure 12).**



- AMPA at low and high doses decreases expression of baculoviral inhibitor of apoptosis protein repeat containing 2 (BIRC2, also called cIAP1), but did not affect expression of BIRC2 (also called cIAP2), p53, p63, p73, or p21. AMPA at a high dose decreases expression of cyclin D1. AMPA at low and high doses decreases procaspase 3, but increases procaspase 9 levels (Figure 13).



➤ **AMPA at low and high doses increases caspase 3 activity (Figure 14).**

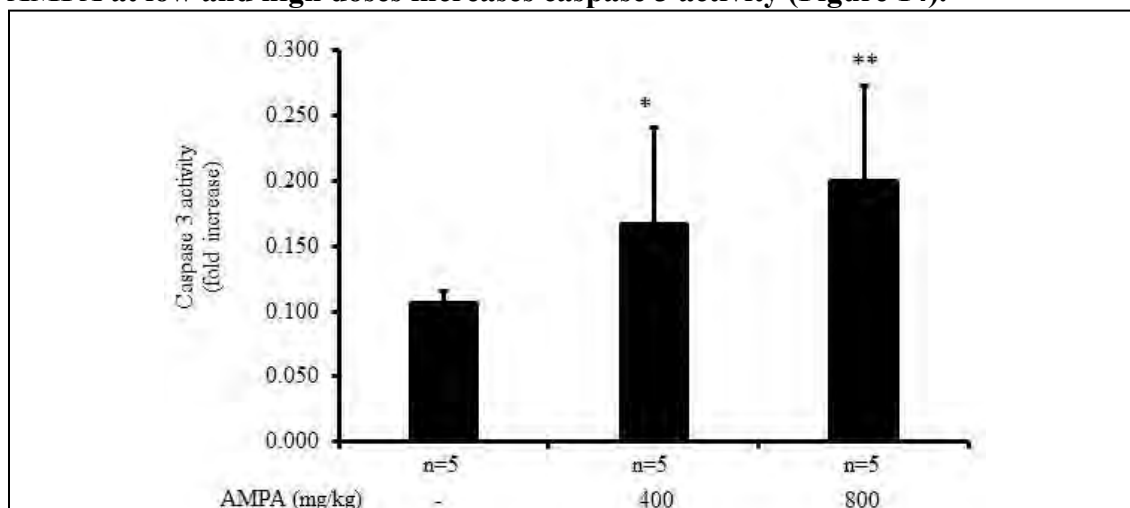


Figure 14. AMPA at low and high doses increases caspase 3 activity in the prostate tumors, indicating activation of caspase 3-mediated apoptotic pathway. Five tumors were randomly selected from each group. Proteins were isolated from the tumors and assessed for caspase 3 activity using ApoAlert™ Caspase-3 Colorimetric Assay Kit (Clontech Laboratories, Inc.). * $P < 0.05$ and ** $P < 0.01$, compared to the control group.

➤ **Animal prostate tumors were confirmed by pathologic examination (Figure 15).**

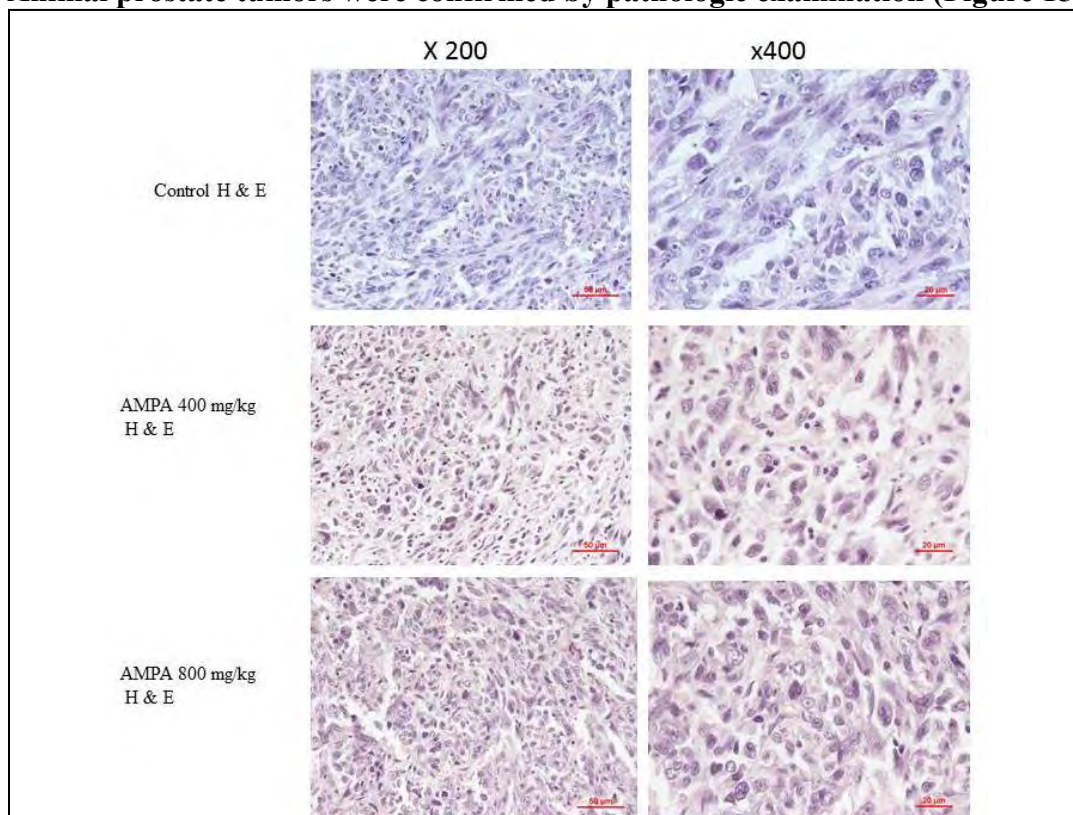
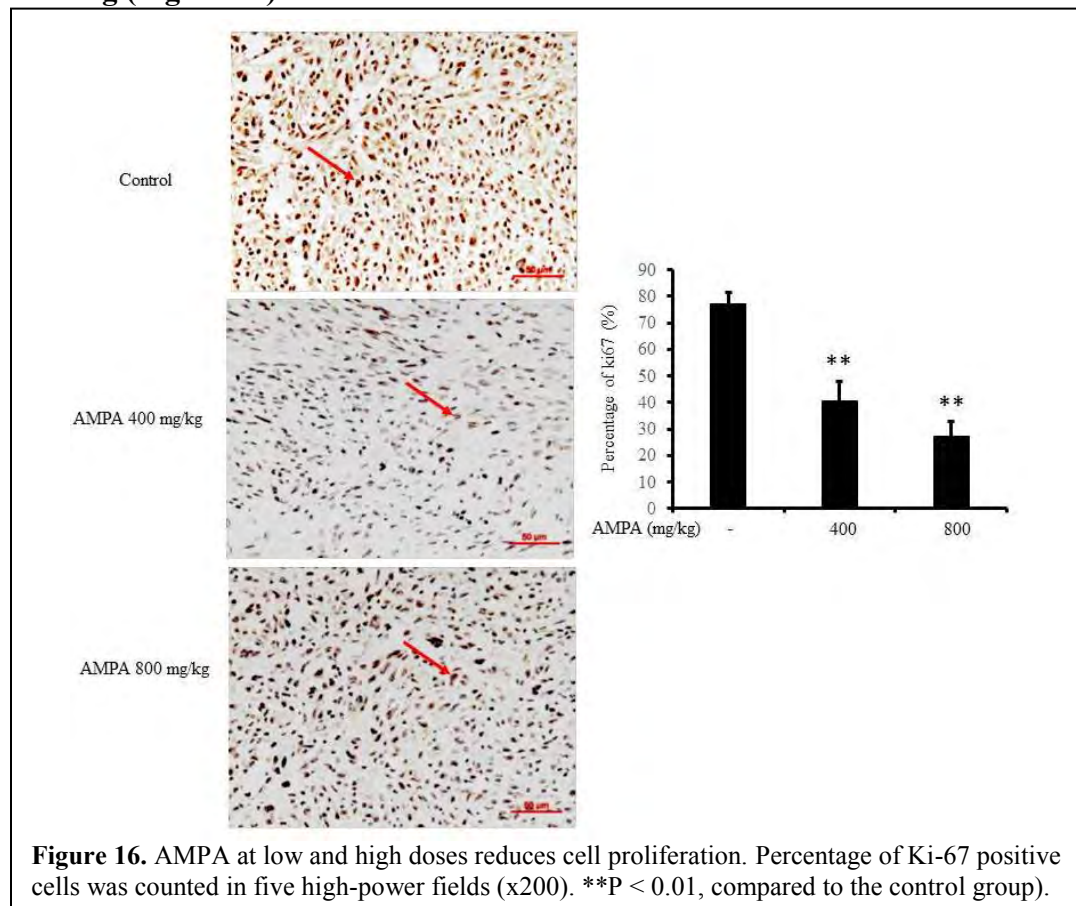
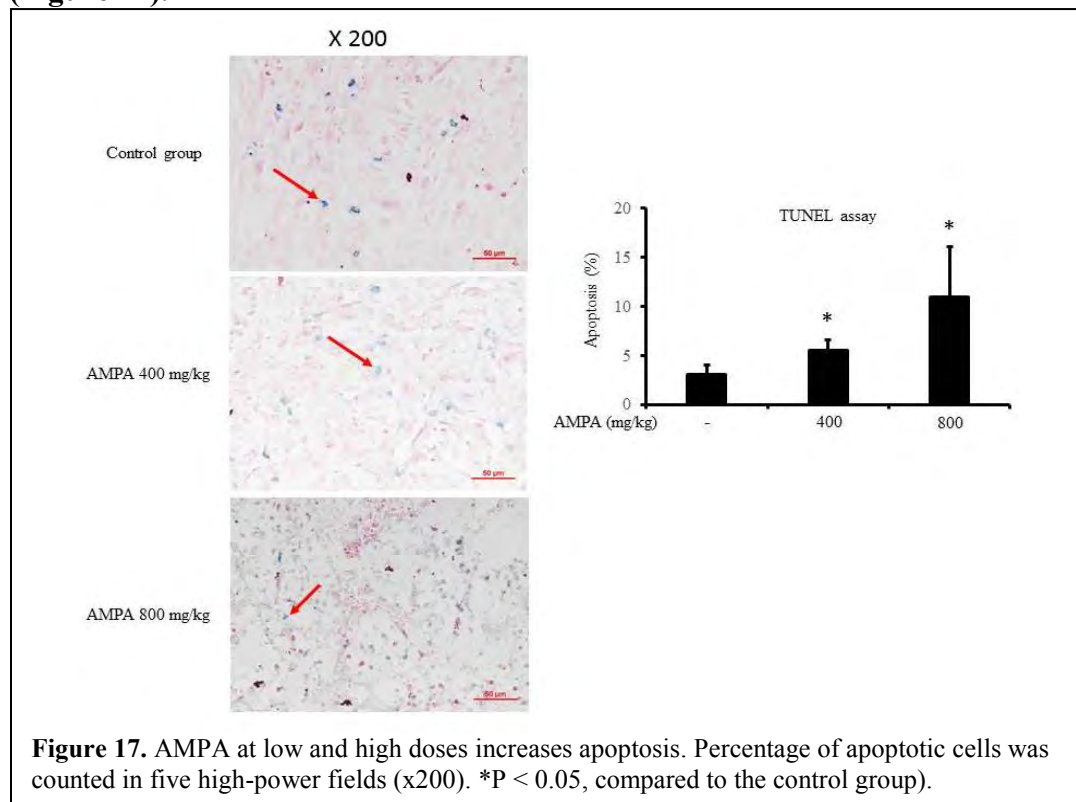


Figure 15. All prostate tumors were examined for pathology. A representative H&E stained tumor section from each group is shown. Original magnification, x200 (left column) and x400 (right column).

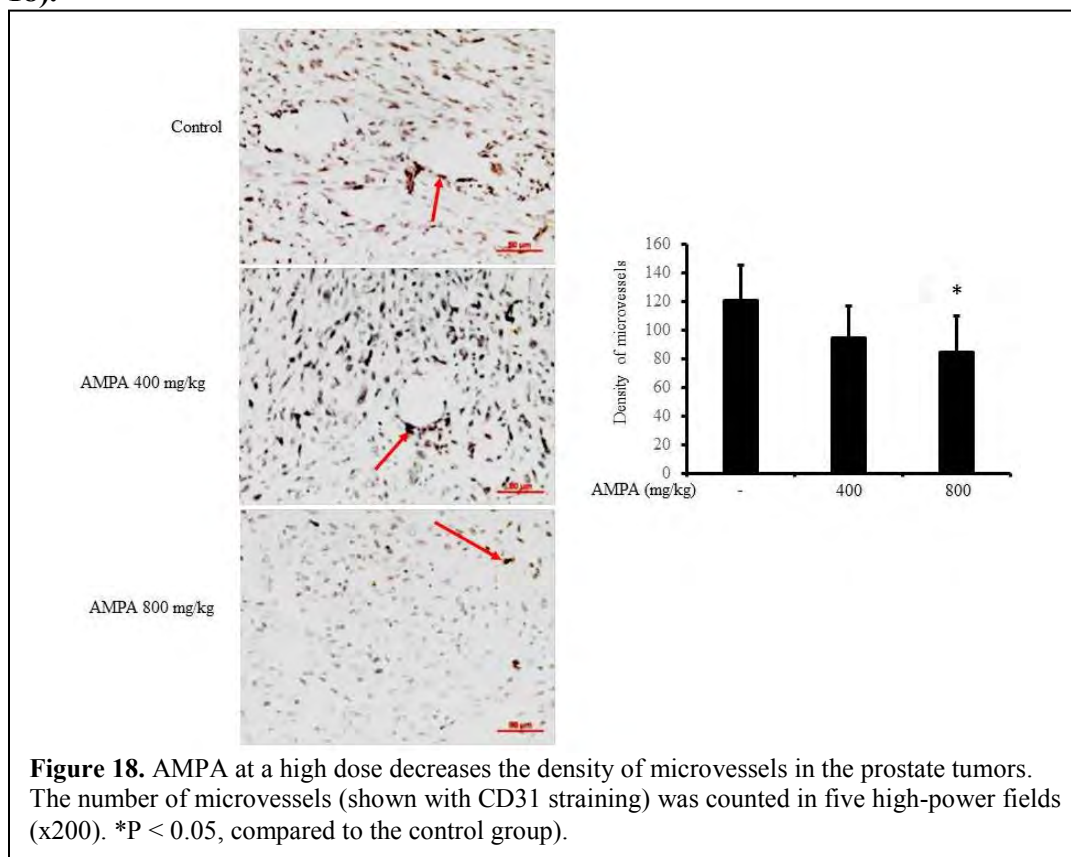
- **AMPA at low and high doses decreases tumor cell proliferation as shown by Ki-67 staining (Figure 16).**



- **AMPA at low and high doses increases tumor cell apoptosis as shown by TUNEL assay (Figure 17).**



- **AMPA at a high dose reduces the density of microvessels in the prostate tumors (Figure 18).**

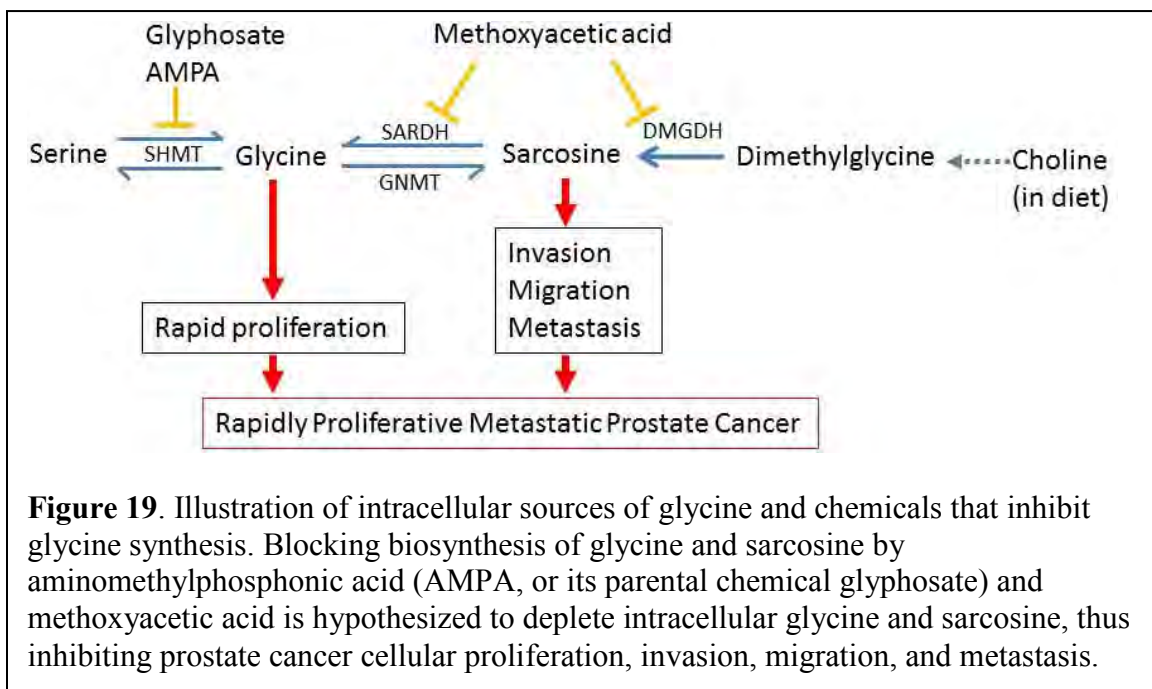


- **Interpretation and Discussion of the findings in animal studies:** we found that AMPA inhibits prostate tumor growth (Figures 8 and 9), which may be due to that AMPA inhibits cell proliferation (Figure 16) and increases apoptosis (Figure 17) as well as reduces angiogenesis (Figure 18). AMPA-mediated inhibition of cell proliferation is likely due to down-regulation of cyclin D1 expression. AMPA-mediated promotion of apoptosis is possibly due to down-regulation of expression of the anti-apoptotic gene BIRC2, thus activating caspase-3 (Figures 13 and 14). It is unlikely that p53/p63/p73, p21, and cyclin D3 are involved, as AMPA does not affect their expression levels (Figure 13). AMPA also inhibits prostate cancer metastasis in vivo (Figure 11), which may be due to that AMPA inhibits prostate cancer migration and invasion (Figure 6).

4) Other achievements:

- While working on AMPA, we searched literature and found that, besides conversion from serine, glycine has a second source of intracellular synthesis from a reversible conversion from sarcosine. Sarcosine dehydrogenase (SARDH) catalyzes the oxidative demethylation of sarcosine to become glycine. Glycine N-methyltransferase (GNMT) transfers a methyl group from S-adenosylmethionine to glycine, thus forming sarcosine. Sarcosine is also derived from dimethylglycine (an intermediate product derived from dietary choline), catalyzed by dimethylglycine dehydrogenase (DMGDH) [8] (see Figure 19). A sarcosine analog, methoxyacetic acid (MAA), inhibits both DMGDH and SARDH (inhibitor constant $K_i = 0.19$ to 0.26 mM) [9], thus can inhibit conversion of sarcosine into glycine (Figure 19). Therefore, we formulated a hypothesis that AMPA and MAA may have synergistic effects in inhibiting prostate cancer growth. We tested this hypothesis through a series of in vitro studies. We found that

AMPA and MAA synergistically induce apoptosis in prostate cancer cells. The detailed methods and results are described in a manuscript submitted to International Journal of Molecular Sciences (under review, enclosed in the Appendices).



- Keshab R. Parajuli, Qiuyang Zhang, Sen Liu, and Zongbing You. Aminomethylphosphonic Acid and Methoxyacetic Acid Synergistically Induce Apoptosis in Prostate Cancer Cells. International Journal of Molecular Sciences (enclosed in the Appendices). Status of publication: under review; acknowledgement of federal support: Yes.
- b) Further literature analysis revealed that MAA can inhibit histone deacetylases (HDAC1, HDAC2, and HDAC3), thus increasing the levels of acetylated histone H4, like the other well-known HDAC inhibitors such as trichostatin, valproic acid, and butyric acid [10]. In fact, it has been reported that MAA-induced hyperacetylation of histones H3 and H4 is associated with rapid spermatocyte death following MAA exposure [11]. Therefore, we studied the effects of MAA on prostate cancer cells. The detailed methods and results are described in our publication.
 - Parajuli KR, Zhang Q, Liu S, Patel NK, Lu H, Zeng SX, Wang G, Zhang C, You Z. Methoxyacetic acid suppresses prostate cancer cell growth by inducing growth arrest and apoptosis. Am J Clin Exp Urol 2014;2(4):300-312. PMID: PMC4297326 Status of publication: published; acknowledgement of federal support: Yes.
- c) Besides the above work that is directly related to the funded project, we have performed other studies. Because the PI's effort was partially funded by this award, we acknowledged this award in our following publications based on these studies:
 - (1) Ge D, Dauchy RT, Liu S, Zhang Q, Mao L, Dauchy EM, Blask DE, Hill SM, Rowan BG, Brainard GC, Hanifin JP, Cecil KS, Xiong Z, Myers L, **You Z ***. Insulin and IGF1 enhance IL-17-induced chemokine expression through a GSK3B-dependent mechanism: a new target for melatonin's anti-inflammatory action. J Pineal Res. 2013 Nov;55(4):377-87. doi: 10.1111/jpi.12084. Epub 2013 Aug 20 (***Corresponding author**). PMID: 24033914; PMID: PMC3797167

- (2) Mark Lambrechts, Michael J. O'Brien, Felix H. Savoie, and **Zongbing You***. Liposomal extended-release bupivacaine for postsurgical analgesia. Patient Preference and Adherence, September 5, 2013;7 885–890 (invited review article, peer-reviewed) (***Corresponding author**). PMID:24043932, PMCID:PMC3772762
- (3) Li Q, Liu L*, Zhang Q, Liu S, Ge D, and **You Z***. Interleukin-17 Indirectly Promotes M2 Macrophage Differentiation through Stimulation of COX-2/PGE2 Pathway in the Cancer Cells. Cancer Res Treat. 2014;46:297-306 (***Corresponding author**) PMID: 25038765; PMCID: PMC4132449
- (4) Qiuyang Zhang, Sen Liu, Qingsong Zhang, Zhenggang Xiong, Alun R. Wang, Leann Myers, Jonathan Melamed, Wendell W. Tang, and **Zongbing You***. Interleukin-17 promotes development of castration-resistant prostate cancer potentially through creating an immunotolerant and pro-angiogenic tumor microenvironment. The Prostate 2014 Jun;74(8):869-79. doi: 10.1002/pros.22805. PMID: 24691769; PMCID: PMC4063299 (***Corresponding author**).
- (5) Ge D, Zhang QS, Zabaleta J, Zhang Q, Liu S, Reiser B, Bunnell BA, Braun SE, O'Brien MJ, Savoie FH, **You Z***. Doublecortin may play a role in defining chondrocyte phenotype. Int J Mol Sci. 2014 Apr 22;15(4):6941-60. doi: 10.3390/ijms15046941. PMID: 24758934; PMCID: PMC4013671 (***Corresponding author**).
- (6) Xu B, Guenther JF, Pociask DA, Wang Y, Kolls JK, **You Z**, Chandrasekar B, Shan B, Sullivan DE, Morris GF. Promotion of lung tumor growth by interleukin-17. Am J Physiol Lung Cell Mol Physiol 2014;307(6):L497-508. PMID: 25038189; PMCID: PMC4166785
- (7) Fuqiang Ren, Mingyu Fan, Jiandong Mei, Yongqiang Wu, Chengwu Liu, Qiang Pu, **Zongbing You***, and Lunxu Liu*. Interferon- γ and celecoxib inhibit lung tumor growth through modulating M2/M1 macrophage ratio in the tumor microenvironment. Drug Design, Development and Therapy. 2014 Sep 23;8:1527-38. doi: 10.2147/DDDT.S66302. eCollection 2014. (***Correspondence author**) PMID: 25284985; PMCID: PMC4181549.
- (8) Mark Lambrechts, Behrooz Nazari, Arash Dini, Michael J. O'Brien, Wendell M. R. Heard, Felix H. Savoie, **Zongbing You***. Comparison of the cheese-wiring effects among three sutures used in rotator cuff repair. International Journal of Shoulder Surgery 2014, 8:81-5 PMID: 25258499; PMCID: PMC4168657 (***Correspondence author**)
- (9) Chong Chen, Qiuyang Zhang, Sen Liu, Mark Lambrechts, Yine Qu, and **Zongbing You***. AZD5363 inhibits inflammatory synergy between interleukin-17 and insulin/insulin-like growth factor 1. Front Oncol. 2014 Dec 1;4:343. doi: 10.3389/fonc.2014.00343. eCollection 2014. PMID: 25520943 [PubMed] PMCID: PMC4249256 (***Correspondence author**)
- (10) Chen C, Zhang Q, Liu S, Parajuli KR, Qu Y, Mei J, Chen Z, Zhang H, Khismatullin DB, **You Z***. IL-17 and insulin/IGF1 enhance adhesion of prostate cancer cells to vascular endothelial cells through CD44-VCAM-1 interaction. Prostate. 2015 Feb 14. 75(8):883-95. doi: 10.1002/pros.22971. PMID: 25683512; NIHMSID: 653942 (***Corresponding author**).
- (11) Chen RY, Fan YM*, Zhang Q, Liu S, Li Q, Ke GL, Li C, You Z*. Estradiol Inhibits Th17 Cell Differentiation through Inhibition of RORgammaT Transcription by Recruiting the ERalpha/REA Complex to Estrogen Response Elements of the RORgammaT Promoter. J

Summary and Discussion of the Accomplishments:

We have performed almost all research work that was originally proposed in our application. We have achieved the two major goals and determined that 1) AMPA can inhibit cellular proliferation, migration, and invasion of prostate cancer cells in vitro; and 2) AMPA can inhibit growth, local invasion and metastasis of prostate cancer in vivo. The positive outcome of this project may lead to further studies of AMPA and/or its derivatives in the future. Given to AMPA's low toxicity profile, it is possible that AMPA and/or its derivatives may be developed into potential drugs for the treatment of human prostate cancer. Our accomplishments are highlighted with two published articles and one submitted manuscript, and a fourth manuscript in preparation based on Figures 6 to 18, in addition to 3 meeting abstracts, all of which are directly funded by this award or closed related to this award. Furthermore, we have published other 11 articles that are not directly funded by this award, but this award was acknowledged due to the fact that the PI's effort was partially funded by this award (see the list under item 6. Products). We did meet some problems such as unable to measure intracellular glycine/sarcosine concentrations, unable to make DU-145-LacZ-luc cell line, and unable to generate tumors using C4-2B-LacZ-luc cells (see more details under item 5. Changes/Problems). However, we believe that we have sufficiently compensated for these deficiencies by studying more cancer cell lines (e.g., SKOV-3, OVCAR-3, HeLa, and A549), studying the combined effects of AMPA and MAA, and studying MAA's effects on prostate cancer cell lines. Overall, we believe that we have successfully completed the proposed research work.

➤ **What opportunities for training and professional development has the project provided:**

Nothing to Report.

➤ **How were the results disseminated to communities of interest:**

Nothing to Report.

➤ **What do you plan to do during the next reporting period to accomplish the goals:**

Nothing to Report.

4. IMPACT:

➤ **What was the impact on the development of the principal discipline(s) of the project?**

The findings from this project demonstrate that AMPA and MAA have potentials to be developed into anti-cancer drugs. Publication of these findings may stimulate the cancer research field to perform studies to further verify and improve the anti-cancer actions of AMPA and MAA. Thus, the results of this project advance our knowledge in targeting glycine metabolism as a new approach in the treatment of cancer including prostate cancer, which opens a new window in the cancer research field. In theory, the results demonstrate that glycine metabolism can become a new target in developing cancer therapeutics.

➤ **What was the impact on other disciplines**

Nothing to Report.

➤ **What was the impact on technology transfer?**

Nothing to Report.

➤ **What was the impact on society beyond science and technology?**

Nothing to Report.

5. CHANGES/PROBLEMS:

➤ **Changes in approach and reasons for change:**

Nothing to Report.

➤ **Actual or anticipated problems or delays and actions or plans to resolve them:**

Three problems were encountered: 1) We were not able to measure intracellular levels of glycine and sarcosine using liquid chromatography-tandem mass spectrometry (LC-MS/MS). We treated C4-2B cells with AMPA for 2, 4, 8 and 12 hours, and sent cell lysates to the Proteomics Core Facility for LC-MS/MS analysis. However, we were not able to accurately measure the levels of glycine and sarcosine. We speculate that one reason may be the similarity between AMPA and glycine, which confounded the analysis, and another reason may be the sensitivity of the assay was not sufficient to detect the changes. 2) We were unable to establish a DU-145 cell line that stably expresses LacZ and luciferase genes. We used the same protocol and were able to establish PC3-LacZ-luc and C4-2B-LacZ-luc cell lines. We speculate that DU-145 cells may be more difficult to transfect. We tried multiple rounds and used different transfection reagents, but still could not make it work. 3) We were unable to grow tumors in nude mice using C4-2B-LacZ-luc cell line. We injected one million cells with Matrigel[®] subcutaneously in 5 animals, which could be sufficient to grow tumors. However, after two to three months there was not any tumors formed. We speculate that maybe transfection of the LacZ and luciferase gene made C4-2B cell lines less aggressive or viable in animals.

➤ **Changes that had a significant impact on expenditures:**

Nothing to Report.

➤ **Significant changes in use or care of human subjects:**

Nothing to Report.

➤ **Significant changes in use or care of vertebrate animals.**

We used fewer animals than proposed, because we were only able to use one cell line PC3-LacZ-luc, instead of three cell lines. We were unable to generate DU-145-LacZ-luc cell line, and the C4-2B-LacZ-luc cell line was not able to form tumors in animals.

➤ **Significant changes in use of biohazards and/or select agents:**

Nothing to Report.

6. PRODUCTS:

➤ **Publications, conference papers, and presentations:**

- **Journal publications:**

The following publications are directly funded by this award or closely related:

- 1) Qingli Li, Mark J. Lambrechts, Qiuyang Zhang, Sen Liu, Dongxia Ge, Rutie Yin, Mingrong Xi, Zongbing You*. Glyphosate and AMPA inhibit cancer cell growth through inhibiting intracellular glycine synthesis. Drug Design, Development and Therapy, July 24, 2013, 7: 635-643. PMID: 23983455, PMCID:PMC3749059 (*Corresponding author). Status of publication: published; acknowledgement of federal support: Yes.
- 2) Parajuli KR, Zhang Q, Liu S, Patel NK, Lu H, Zeng SX, Wang G, Zhang C, You Z. Methoxyacetic acid suppresses prostate cancer cell growth by inducing growth arrest and

apoptosis. *Am J Clin Exp Urol* 2014;2(4):300-312. PMCID: PMC4297326. Status of publication: published; acknowledgement of federal support: Yes.

- 3) Keshab R. Parajuli, Qiuyang Zhang, Sen Liu, and Zongbing You. Aminomethylphosphonic Acid and Methoxyacetic Acid Synergistically Induce Apoptosis in Prostate Cancer Cells. *International Journal of Molecular Sciences* (enclosed in the Appendices). Status of publication: Submitted, under review; acknowledgement of federal support: Yes.

The following publications are not directly funded by this award, but this award was acknowledged because the PI's effort was partially supported by this award:

- 4) Ge D, Dauchy RT, Liu S, Zhang Q, Mao L, Dauchy EM, Blask DE, Hill SM, Rowan BG, Brainard GC, Hanifin JP, Cecil KS, Xiong Z, Myers L, You Z *. Insulin and IGF1 enhance IL-17-induced chemokine expression through a GSK3B-dependent mechanism: a new target for melatonin's anti-inflammatory action. *J Pineal Res.* 2013 Nov;55(4):377-87. doi: 10.1111/jpi.12084. Epub 2013 Aug 20 (*Corresponding author). PMID: 24033914; PMCID: PMC3797167. Status of publication: published; acknowledgement of federal support: Yes.
- 5) Mark Lambrechts, Michael J. O'Brien, Felix H. Savoie, and Zongbing You*. Liposomal extended-release bupivacaine for postsurgical analgesia. *Patient Preference and Adherence*, September 5, 2013;7 885–890 (invited review article, peer-reviewed) (*Corresponding author). PMID:24043932, PMCID:PMC3772762. Status of publication: published; acknowledgement of federal support: Yes.
- 6) Li Q, Liu L*, Zhang Q, Liu S, Ge D, and You Z*. Interleukin-17 Indirectly Promotes M2 Macrophage Differentiation through Stimulation of COX-2/PGE2 Pathway in the Cancer Cells. *Cancer Res Treat.* 2014;46:297-306 (*Corresponding author) PMID: 25038765; PMCID: PMC4132449. Status of publication: published; acknowledgement of federal support: Yes.
- 7) Qiuyang Zhang, Sen Liu, Qingsong Zhang, Zhenggang Xiong, Alun R. Wang, Leann Myers, Jonathan Melamed, Wendell W. Tang, and Zongbing You*. Interleukin-17 promotes development of castration-resistant prostate cancer potentially through creating an immunotolerant and pro-angiogenic tumor microenvironment. *The Prostate* 2014 Jun;74(8):869-79. doi: 10.1002/pros.22805. PMID: 24691769; PMCID: PMC4063299 (*Corresponding author). Status of publication: published; acknowledgement of federal support: Yes.
- 8) Ge D, Zhang QS, Zabaleta J, Zhang Q, Liu S, Reiser B, Bunnell BA, Braun SE, O'Brien MJ, Savoie FH, You Z*. Doublecortin may play a role in defining chondrocyte phenotype. *Int J Mol Sci.* 2014 Apr 22;15(4):6941-60. doi: 10.3390/ijms15046941. PMID: 24758934; PMCID: PMC4013671 (*Corresponding author). Status of publication: published; acknowledgement of federal support: Yes.
- 9) Xu B, Guenther JF, Pociask DA, Wang Y, Kolls JK, You Z, Chandrasekar B, Shan B, Sullivan DE, Morris GF. Promotion of lung tumor growth by interleukin-17. *Am J Physiol Lung Cell Mol Physiol* 2014;307(6):L497-508. PMID: 25038189; PMCID: PMC4166785. Status of publication: published; acknowledgement of federal support: Yes.
- 10) Fuqiang Ren, Mingyu Fan, Jiandong Mei, Yongqiang Wu, Chengwu Liu, Qiang Pu, Zongbing You*, and Lunxu Liu*. Interferon- γ and celecoxib inhibit lung tumor growth through modulating M2/M1 macrophage ratio in the tumor microenvironment. *Drug Design, Development and Therapy.* 2014 Sep 23;8:1527-38. doi: 10.2147/DDDT.S66302. eCollection 2014.

(*Correspondence author) PMID: 25284985; PMCID: PMC4181549. Status of publication: published; acknowledgement of federal support: Yes.

- 11) Mark Lambrechts, Behrooz Nazari, Arash Dini, Michael J. O'Brien, Wendell M. R. Heard, Felix H. Savoie, Zongbing You*. Comparison of the cheese-wiring effects among three sutures used in rotator cuff repair. *International Journal of Shoulder Surgery* 2014, 8:81-5 PMID: 25258499; PMCID: PMC4168657 (*Correspondence author). Status of publication: published; acknowledgement of federal support: Yes.
- 12) Chong Chen, Qiuyang Zhang, Sen Liu, Mark Lambrechts, Yine Qu, and Zongbing You*. AZD5363 inhibits inflammatory synergy between interleukin-17 and insulin/insulin-like growth factor 1. *Front Oncol.* 2014 Dec 1;4:343. doi: 10.3389/fonc.2014.00343. eCollection 2014. PMID: 25520943 [PubMed] PMCID: PMC4249256 (*Correspondence author). Status of publication: published; acknowledgement of federal support: Yes.
- 13) Chen C, Zhang Q, Liu S, Parajuli KR, Qu Y, Mei J, Chen Z, Zhang H, Khismatullin DB, You Z*. IL-17 and insulin/IGF1 enhance adhesion of prostate cancer cells to vascular endothelial cells through CD44-VCAM-1 interaction. *Prostate.* 2015 Feb 14. 75(8):883-95. doi: 10.1002/pros.22971. PMID: 25683512; NIHMSID: 653942 (*Corresponding author). Status of publication: published; acknowledgement of federal support: Yes.
- 14) Chen RY, Fan YM*, Zhang Q, Liu S, Li Q, Ke GL, Li C, You Z*. Estradiol Inhibits Th17 Cell Differentiation through Inhibition of RORgammaT Transcription by Recruiting the ERalpha/REA Complex to Estrogen Response Elements of the RORgammaT Promoter. *J Immunol.* 2015 Apr 15;194(8):4019-28. doi: 10.4049/jimmunol.1400806. PMID: 25769926; PMCID: PMC4390502 (*Corresponding author). Status of publication: published; acknowledgement of federal support: Yes.
- **Books or other non-periodical, one-time publications:**
Nothing to Report.
- **Other publications, conference papers, and presentations:**
 - 15) Keshab R. Parajuli, Qiuyang Zhang, Sen Liu, Neil K. Patel, Zongbing You. Methoxyacetic acid inhibits prostate cancer cell growth. 2014 SBUR Fall Symposium, Nov 13-16, 2014, Dallas, TX. Status of publication: published; acknowledgement of federal support: Yes.
 - 16) Parajuli KR, Zhang Q, Liu S, Patel NK, You Z. METHOXYACETIC ACID SUPPRESSES PROSTATE CANCER CELL GROWTH BY INDUCING GROWTH ARREST AND APOPTOSIS. The Tulane University Health Sciences Research Days, March 25-26, 2015, New Orleans, LA. Status of publication: published; acknowledgement of federal support: Yes.
 - 17) Keshab R. Parajuli, Qiuyang Zhang, Sen Liu, and Zongbing You. Aminomethylphosphonic acid inhibits human prostate xenograft tumor growth through interfering glycine synthesis in the cancer cells. 2015 Metabolism and Cancer, American Association of Cancer Research, June 7-10, 2015, Hyatt Regency Bellevue, Bellevue, WA. Status of publication: accepted, awaiting publication; acknowledgement of federal support: Yes.

➤ **Website(s) or other Internet site(s):**
Nothing to Report.

➤ **Technologies or techniques:**

Nothing to Report.

➤ **Inventions, patent applications, and/or licenses:**

Nothing to Report.

➤ **Other Products:**

Models: PC3-LacZ-luc cell line, which is a good cell model for prostate cancer research, especially for in vivo animal studies.

7. PARTICIPANTS & OTHER COLLABORATING ORGANIZATIONS

➤ **What individuals have worked on the project?**

| | |
|---|--|
| Name: | <i>Zongbing You</i> |
| Project Role: | <i>PD/PI</i> |
| Researcher Identifier (e.g. ORCID ID): | <i>0000-0001-5048-2229</i> |
| Nearest person month worked: | <i>1</i> |
| Contribution to Project: | <i>Dr. You was responsible for the overall direction, administration, supervision of laboratory staff, coordination and completion of the project, preparation of publications and annual report/final report. Dr. You performed in vitro studies and assisted Dr. Keshab Parajuli in performing in vitro and in vivo studies.</i> |
| Funding Support: | <i>Not Applicable</i> |
| Name: | <i>Keshab Parajuli</i> |
| Project Role: | <i>Postdoctoral Fellow</i> |
| Researcher Identifier (e.g. ORCID ID): | <i>0000-0003-3799-6991</i> |
| Nearest person month worked: | <i>11</i> |
| Contribution to Project: | <i>Dr. Parajuli performed the in-vitro and in-vivo studies with Dr. You's assistance.</i> |
| Funding Support: | <i>Not Applicable</i> |

➤ **What other organizations were involved as partners?**

Nothing to Report.

8. SPECIAL REPORTING REQUIREMENTS

Nothing to Report (not applicable).

9. APPENDICES:

The 14 articles and 3 meeting abstracts are enclosed in Appendices in the order shown under 6. Products.

References Cited in this report:

1. Jain M, Nilsson R, Sharma S, Madhusudhan N, Kitami T, Souza AL, Kafri R, Kirschner MW, Clish CB, Mootha VK. Metabolite profiling identifies a key role for glycine in rapid cancer cell proliferation. *Science* 2012;336(6084):1040-1044.
2. Sreekumar A, Poisson LM, Rajendiran TM, Khan AP, Cao Q, Yu J, Laxman B, Mehra R, Lonigro RJ, Li Y, Nyati MK, Ahsan A, Kalyana-Sundaram S, Han B, Cao X, Byun J, Omenn GS, Ghosh D, Pennathur S, Alexander DC, Berger A, Shuster JR, Wei JT, Varambally S, Beecher C, Chinnaiyan AM. Metabolomic profiles delineate potential role for sarcosine in prostate cancer progression. *Nature* 2009;457(7231):910-914.
3. Anderson DD, Stover PJ. SHMT1 and SHMT2 are functionally redundant in nuclear de novo thymidylate biosynthesis. *PLoS One* 2009;4(6):e5839.
4. Hoffman RM. Orthotopic metastatic mouse models of prostate cancer, in R.J. Ablin and M.D. Mason (eds), *Cancer Metastasis - Biology and Treatment: Metastasis of Prostate Cancer*. Ablin RJ, Mason MD, editors: Springer Science+Business Media B.V., 2008, pp143-169, <http://www.springerlink.com/content/r876618788201762/fulltext.pdf>
5. Li Q, Lambrechts MJ, Zhang Q, Liu S, Ge D, Yin R, Xi M, You Z. Glyphosate and AMPA inhibit cancer cell growth through inhibiting intracellular glycine synthesis. *Drug Des Devel Ther* 2013;7:635-643.
6. Zhang Q, Liu S, Xiong Z, Wang AR, Myers L, Melamed J, Tang WW, You Z. Interleukin-17 promotes development of castration-resistant prostate cancer potentially through creating an immunotolerant and pro-angiogenic tumor microenvironment. *Prostate* 2014;74(8):869-879.
7. Zhang Q, Liu S, Ge D, Xue Y, Xiong Z, Abdel-Mageed AB, Myers L, Hill SM, Rowan BG, Sartor O, Melamed J, Chen Z, You Z. Interleukin-17 promotes formation and growth of prostate adenocarcinoma in mouse models. *Cancer Res* 2012;72(10):2589-2599.
8. Murray RK, Bender DA, Botham KM, Kennelly PJ, Rodwell VW, Weil PA. Harper's illustrated biochemistry, 29th ed. New York: McGraw-Hill Companies, Inc.; 2012.
9. Porter DH, Cook RJ, Wagner C. Enzymatic properties of dimethylglycine dehydrogenase and sarcosine dehydrogenase from rat liver. *Arch Biochem Biophys* 1985;243(2):396-407.
10. Jansen MS, Nagel SC, Miranda PJ, Lobenhofer EK, Afshari CA, McDonnell DP. Short-chain fatty acids enhance nuclear receptor activity through mitogen-activated protein kinase activation and histone deacetylase inhibition. *Proc Natl Acad Sci U S A* 2004;101(18):7199-7204.
11. Wade MG, Kawata A, Williams A, Yauk C. Methoxyacetic acid-induced spermatocyte death is associated with histone hyperacetylation in rats. *Biol Reprod* 2008;78(5):822-831.

Glyphosate and AMPA inhibit cancer cell growth through inhibiting intracellular glycine synthesis

Qingli Li^{1,2}
Mark J Lambrechts¹
Qiuyang Zhang¹
Sen Liu¹
Dongxia Ge¹
Rutie Yin²
Mingrong Xi²
Zongbing You¹

¹Departments of Structural and Cellular Biology and Orthopaedic Surgery, Tulane Cancer Center and Louisiana Cancer Research Consortium, Tulane Center for Stem Cell Research and Regenerative Medicine, and Tulane Center for Aging, Tulane University Health Sciences Center, New Orleans, LA, USA; ²Department of Obstetrics and Gynecology, West China Second University Hospital, Sichuan University, Chengdu, People's Republic of China

Correspondence: Zongbing You, Department of Structural and Cellular Biology, Tulane University, 1430 Tulane Ave SL 49, New Orleans, LA 70112, USA
Tel +1 504 988 0467
Fax +1 504 988 1687
Email zyou@tulane.edu

Abstract: Glycine is a nonessential amino acid that is reversibly converted from serine intracellularly by serine hydroxymethyltransferase. Glyphosate and its degradation product, aminomethylphosphonic acid (AMPA), are analogs to glycine, thus they may inhibit serine hydroxymethyltransferase to decrease intracellular glycine synthesis. In this study, we found that glyphosate and AMPA inhibited cell growth in eight human cancer cell lines but not in two immortalized human normal prostatic epithelial cell lines. AMPA arrested C4-2B and PC-3 cancer cells in the G1/G0 phase and inhibited entry into the S phase of the cell cycle. AMPA also promoted apoptosis in C4-2B and PC-3 cancer cell lines. AMPA upregulated p53 and p21 protein levels as well as procaspase 9 protein levels in C4-2B cells, whereas it downregulated cyclin D3 protein levels. AMPA also activated caspase 3 and induced cleavage of poly (adenosine diphosphate [ADP]-ribose) polymerase. This study provides the first evidence that glyphosate and AMPA can inhibit proliferation and promote apoptosis of cancer cells but not normal cells, suggesting that they have potentials to be developed into a new anticancer therapy.

Keywords: serine hydroxymethyltransferase, prostate cancer, apoptosis

Introduction

Glycine is a nonessential amino acid that can be converted directly from serine in mammalian cells. Serine is derived from 3-phosphoglycerate. Serine hydroxymethyltransferase (SHMT) reversibly catalyzes the conversion of serine to glycine and vice versa. In the liver of vertebrates, glycine can be synthesized from N5,N10-methylene tetrahydrofolate by glycine synthase.¹ Glycine is the precursor material for biosynthesis of protein, purine, and glutathione. In addition, glycine is converted into sarcosine (N-methylglycine) by glycine N-methyltransferase,² and reversely, sarcosine can be converted into glycine by sarcosine dehydrogenase.³ The serum half-life of intravenously administered glycine varies from 1/2 hour to 4 hours.⁴ Recently, the importance of glycine in cancer cell biology has been revealed.⁵ In a human melanoma LOX IMVI cell line, about two-thirds of intracellular glycine is synthesized intracellularly, while one-third of intracellular glycine is taken from extracellular glycine sources. In a panel of 60 human cancer cell lines that the National Cancer Institute uses for anticancer drug screening, rapidly proliferating cancer cells consumed extracellular glycine due to increased demand for glycine. In contrast, rapidly proliferating human normal cell lines released glycine.⁵ These findings suggest that targeting glycine consumption may become a new strategy in killing rapidly proliferating cancer cells, while not harming rapidly proliferating normal cells. Indeed, the use of short hairpin RNA (shRNA) to knockdown expression of *SHMT2*, thus blocking endogenous glycine synthesis,

effectively halted proliferation of LOX IMVI cells in the absence of extracellular glycine. In contrast, slowly proliferating cells were not affected by *SHMT2* knockdown and deprivation of extracellular glycine.⁵

There are two isozymes of SHMT. *SHMT1* encodes for the cytoplasmic and *SHMT2* encodes for the mitochondrial isozyme.^{6–8} In mammalian cells, *SHMT2* gene has an alternative promoter within intron 1, thus *SHMT2* encodes for two transcripts, *SHMT2* and *SHMT2α*.⁹ *SHMT2* protein containing exon 1 (with mitochondrial-targeting sequence) is localized in mitochondria. *SHMT2α* protein without exon 1 is not imported into mitochondria efficiently and is localized predominantly in the cytoplasm and nucleus. *SHMT1* protein, like *SHMT2α*, is also localized in the cytoplasm and nucleus, and both *SHMT1* and *SHMT2α* catalyze production of one-carbon units from serine for nuclear de novo thymidylate biosynthesis.⁹ Interestingly, a glycine analog, aminomethylphosphonate (aminomethylphosphonic acid [AMPA]) (molecular formula $\text{CH}_6\text{NO}_3\text{P}$ [Figure 1]), inhibits more than 95% of nuclear thymidylate biosynthesis that requires *SHMT1* and *SHMT2α*, suggesting that AMPA is an effective inhibitor of *SHMT1* and *SHMT2α*, as well as *SHMT2*.⁹

AMPA is the primary degradation product of glyphosate (N-(phosphonomethyl)glycine; molecular formula $\text{C}_3\text{H}_3\text{NO}_3\text{P}$ [Figure 1]). Glyphosate is water soluble and chemically stable and is degraded by microbes to produce AMPA.¹⁰ Glyphosate is a weak organic acid consisting of a glycine moiety and a phosphonomethyl moiety. Glyphosate is a broad-spectrum herbicide that is used worldwide in

agriculture, forestry, and aquatic weed control. It is applied to many crops in various commercial formulations. The major formulation is Roundup® (Monsanto Co, St Louis, MO, USA), in which glyphosate is formulated as the isopropylamine salt,¹¹ whereas AMPA has no commercial use.¹⁰ In animal studies using [¹⁴C]glyphosate in rats, rabbits, and goats, approximately 30% of the oral dose was absorbed through the gastrointestinal tract. On day 7 after the oral dose of [¹⁴C]glyphosate in rats, the isotope was distributed throughout the animal body, with the highest concentration found in the bones. Almost all of the isotope was eliminated in urine and feces, with a very low level exhaled in air. The only metabolite was AMPA, which accounted for about 0.2% to 0.3% of the administered dose of glyphosate.¹⁰ In a study in rats, approximately 20% of the oral dose of AMPA was absorbed, which was excreted almost exclusively through the urine, with less than 0.1% of the dose expired as CO_2 .¹⁰ Glyphosate and AMPA have been found to present no significant toxicity in acute, subchronic, and chronic animal studies, nor any genotoxicity, teratogenicity, or carcinogenicity.^{10,12} In this study, we assessed the effects of glyphosate and AMPA on cancer cell growth. Our results suggest that glyphosate and AMPA inhibit cell growth in eight cancer cell lines but not in two immortalized human normal prostatic epithelial cell lines, at concentrations up to 50 mM.

Materials and methods

Cell culture

The immortalized human normal prostatic epithelial cell lines RWPE-1 and pRNS-1-1 were obtained from John S Rhim (Uniformed Services University of the Health Sciences, Bethesda, MD, USA).¹³ Human castration-resistant prostate cancer cell line C4-2B was obtained from Leland WK Chung (Cedars-Sinai Medical Center, Los Angeles, CA, USA).¹⁴ Human prostate cancer cell lines (LNCaP, DU-145, and PC-3), human ovarian cancer cell lines (SKOV-3 and OVCAR-3), human cervical cancer HeLa cell line, and human lung cancer A549 cell line were purchased from the American Type Culture Collection (Manassas, VA, USA). RWPE-1 and pRNS-1-1 cells were cultured in Dulbecco's Modified Eagle's medium (DMEM) (Mediatech, Inc, Manassas, VA, USA) containing 10% fetal bovine serum (FBS) (HyClone Standard Fetal Bovine Serum; Thermo Fisher Scientific Inc, Waltham, MA, USA), 100 IU/mL penicillin/streptomycin, 5 µg/mL bovine insulin, 25 µg/mL bovine pituitary extract, and 6 ng/mL recombinant human epidermal growth factor (Sigma-Aldrich Corp, St Louis, MO, USA). LNCaP cells were cultured in

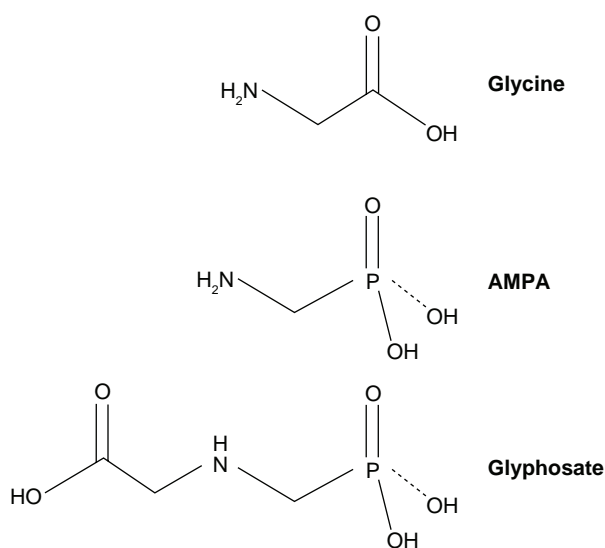


Figure 1 Chemical structure of glycine, AMPA, and glyphosate.
Abbreviation: AMPA, aminomethylphosphonic acid.

T-Medium (Life Technologies Corp, Carlsbad, CA, USA) containing 5% FBS and 100 IU/mL penicillin/streptomycin. C4-2B and SKOV-3 cells were cultured in Roswell Park Memorial Institute (RPMI)-1640 medium (Thermo Fisher Scientific) containing 10% FBS and 100 IU/mL penicillin/streptomycin. OVCAR-3 cells were cultured in RPMI-1640 medium containing 20% FBS, 100 IU/mL penicillin/streptomycin, 5 µg/mL bovine insulin, and 1 mM sodium pyruvate. DU-145, PC-3, HeLa, and A549 cells were cultured in DMEM medium containing 10% FBS and 100 IU/mL penicillin/streptomycin. DMEM contains 30 mg/L glycine and 42 mg/L L-serine; RPMI-1640 medium contains 10 mg/L glycine and 30 mg/L L-serine; and T-Medium contains 27 mg/L glycine and 37.8 mg/L L-serine. The cells were cultured in a 5% CO₂ humidified incubator at 37°C.

Cell viability assay

The live cell numbers were determined using the CellTiter-Glo® Luminescent Cell Viability Assay (Promega Corp, Fitchburg, WI, USA). This assay is based on quantitation of the adenosine triphosphate (ATP), an indicator of metabolically active cells, which is a well-established method for cell proliferation and cytotoxicity assays.^{15–17} To optimize the experimental conditions, we performed pilot experiments and determined that there was a linear relationship ($r^2 = 0.98$) between the luminescent signal and the number of cells, from 1,000 to 40,000 cells per well. Therefore, we plated 4,000 cells per well, so that the cell number was less than 40,000 cells per well after 72 hours in culture. The cells were plated in 100 µL complete culture medium with FBS in Costar® opaque-walled 96-well plates (Thermo Fisher Scientific Inc). After overnight incubation, the cells were treated with glyphosate or AMPA (Sigma-Aldrich Corp) at final concentrations of 0, 15, 25, or 50 mM for 72 hours. Both glyphosate and AMPA were used in their native forms in all the experiments, and they were dissolved in complete medium with FBS prior to use. Each treatment group had triplicate wells. Wells containing the same medium without cells were used to assess the background luminescence. The amount of 100 µL CellTiter-Glo® Reagent was added into each well according to the instructions. Luminescence was read using a FLUOstar OPTIMA (BMG Labtech GmbH, Ortenberg, Germany) microplate reader. Cell viability was calculated as (luminescence of the treatment group – background luminescence) ÷ (luminescence of the control group – background luminescence) × 100%. The data are presented as the mean and standard error of the mean (SEM) of three independent experiments.

Cell cycle analysis

C4-2B and PC-3 cells were plated in complete culture medium with FBS, into 60 mm dishes. After 16 hours, the cells were treated without or with AMPA at a final concentration of 50 mM for 24 hours. The cells were trypsinized, washed once with phosphate buffered saline (PBS), pelleted, and resuspended in 70% ice-cold ethanol and stored at –20°C until the cell cycle analysis. The fixed cells were stained in a solution containing 0.1% Triton™ X-100 (Sigma-Aldrich Corp), 0.2 mg/mL DNase-free RNase A, and 20 µg/mL propidium iodide for 30 min at room temperature in the dark. The percentages of cells at G1/G0, S, and G2/M phases were determined by flow cytometry analysis using DNA content frequency histogram deconvolution software (Becton, Dickinson and Company, Franklin Lakes, NJ, USA).

Cell apoptosis assay

C4-2B and PC-3 cells were plated in complete culture medium with FBS into 60 mm dishes. Sixteen hours later, the cells were treated without or with AMPA at a final concentration of 50 mM for 0, 24, 48, and 72 hours. The cells were trypsinized, washed once with PBS, pelleted and resuspended in annexin-binding buffer. The cells were stained with Annexin-V Fluorescein isothiocyanate (FITC) Conjugate (1:20 dilution; Life Technologies Corp) and propidium iodide (100 µg/mL) according to the manufacturers protocol, and the percentages of apoptotic cells were determined by flow cytometry analysis.^{18,19}

Western blot analysis

C4-2B cells were cultured in 60 mm dishes overnight. The cells were treated with AMPA at a final concentration of 50 mM for 0, 12, 24, 48, and 72 hours. Proteins were extracted from the treated cells in radioimmunoprecipitation assay (RIPA) lysis buffer (50 mM sodium fluoride, 0.5% Igepal® CA-630 [NP-40], 10 mM sodium phosphate, 150 mM sodium chloride, 25 mM Tris pH 8.0, 1 mM phenylmethylsulfonyl fluoride, 2 mM ethylenediaminetetraacetic acid [EDTA], 1.2 mM sodium vanadate) supplemented with protease inhibitor cocktail (Sigma-Aldrich Corp). An equal amount of proteins was subjected to 10% SDS-polyacrylamide gel electrophoresis and transferred to polyvinylidene difluoride membranes (Bio-Rad Laboratories, Hercules, CA, USA). The membranes were blocked with 5% nonfat dry milk in TBST buffer (25 mM Tris-HCl, 125 mM NaCl, 0.1% Tween 20) for 2 hours and probed with the indicated primary antibodies overnight and then IRDye®800CW- or IRDye®680-conjugated secondary antibodies (LI-COR Biosciences Inc, Lincoln,

NE, USA) for 1 hour. The results were visualized using an Odyssey® Infrared Imager (LI-COR Biosciences Inc). For loading control, the membranes were stripped and probed for glyceraldehyde-3-phosphate dehydrogenase (GAPDH). The antibodies used were as follows: rabbit anti-poly (adenosine diphosphate [ADP]-ribose) polymerase (PARP), rabbit anti-caspase 3, rabbit anti-caspase 9, and mouse anti-cyclin D3 antibodies, purchased from Cell Signaling Technology Inc (Danvers, MA, USA); mouse anti-p21 and goat anti-p53 antibodies, obtained from Santa Cruz Biotechnology Inc (Dallas, TX, USA); and mouse anti-GAPDH antibodies, ordered from EMD Millipore Corp (Billerica, MA, USA).

Statistical analysis

All experiments were repeated three times, and the results represent mean \pm SEM of three independent experiments. Statistical analysis was made using two-tailed Student's *t* test. A *P*-value < 0.05 was considered statistically significant.

Results

Glyphosate inhibits cell growth in cancer cell lines but not in normal cell lines

Glyphosate, at concentrations of 15, 25, and 50 mM, did not significantly decrease the cell viability in the RWPE-1 and pRNS-1-1 cell lines compared with the untreated control group ($P > 0.05$) (Figure 2A and B). Glyphosate, at concentrations of 15 and 25 mM, did not decrease the cell viability in the LNCaP cell line; however, it decreased 27% of the cell viability at a concentration of 50 mM ($P < 0.05$) (Figure 2C). Glyphosate, at concentrations of 15, 25, and 50 mM, significantly decreased the cell viability in the C4-2B and DU-145 cell lines ($P < 0.05$ or $P < 0.01$) (Figure 2D and E), with a 73.4% and 39.3% decrease at the dose of 50 mM, respectively. Glyphosate, at a concentration of 15 mM, did not decrease the cell viability in the PC-3 and SKOV-3 cell lines; however, it significantly decreased the cell viability at concentrations of 25 and 50 mM ($P < 0.05$ or $P < 0.01$) (Figure 2F and G), with a 36.9% and 28% decrease at the dose of 50 mM in the PC-3 and SKOV-3 cell lines, respectively. Glyphosate, at concentrations of 15, 25, and 50 mM, significantly decreased the cell viability in the OVCAR-3 cell line ($P < 0.05$ or $P < 0.01$) (Figure 2H), with a 58.8% decrease at the dose of 50 mM. However, at a concentration of 50 mM, glyphosate only decreased about 25% and 17% of the cell viability in the HeLa and A549 cell lines, respectively, though the decrease was statistically significant ($P < 0.05$) (Figure 2I and J). Based on the percentages of inhibition caused by different

concentrations of glyphosate, we estimated the half maximal (50%) inhibitory concentrations (IC_{50}) of glyphosate in the cell lines, using a linear regression model (Table 1).

AMPA inhibits cell growth in cancer cell lines but not in normal cell lines

AMPA, at concentrations of 15, 25, and 50 mM, did not significantly decrease the cell viability in the RWPE-1 and pRNS-1-1 cell lines ($P > 0.05$) (Figure 3A and B). In contrast, AMPA, at concentrations of 25 and 50 mM, significantly decreased the cell viability in the LNCaP, DU-145, SKOV-3, HeLa, and A549 cell lines ($P < 0.05$ or $P < 0.01$) (Figure 3C, E, G, I and J), while AMPA at concentrations of 15, 25, and 50 mM significantly decreased the cell viability in the C4-2B, PC-3, and OVCAR-3 cell lines ($P < 0.05$ or $P < 0.01$) (Figure 3D, F and H). The percentages of decrease in cell viability at 50 mM AMPA were 32% in LNCaP, 54.5% in C4-2B, 47% in DU-145, 41.7% in PC-3, 28.5% in SKOV-3, 33.6% in OVCAR-3, 25% in HeLa, and 31.4% in the A549 cell lines. Of note, we found that at a concentration of 100 mM, AMPA decreased the cell viability in the RWPE-1 and pRNS-1-1 cell lines by 59.5% and 57.6%, respectively. In contrast, this high concentration of AMPA decreased cell viability by 54% in LNCaP, 91% in C4-2B, 67% in DU-145, 85.1% in PC-3, 42% in SKOV-3, 79.9% in OVCAR-3, 50.6% in HeLa, and 53.1% in the A549 cell lines. The IC_{50} concentrations of AMPA in inhibition of the cell growth in the normal and cancer cell lines are shown in Table 1.

AMPA inhibits entry into the S phase of cell cycle and increases apoptosis

AMPA, at a concentration of 50 mM, significantly increased the number of C4-2B and PC-3 cells in the G1/G0 phase of cell cycle, compared with the control group ($P < 0.05$ or $P < 0.01$) (Figure 4A and B). In contrast, AMPA significantly decreased the number of C4-2B and PC-3 cells in the S phase of cell cycle ($P < 0.05$ or $P < 0.01$), whereas the number of cells in the G2/M phase was not affected (Figure 4A and B). In addition, AMPA, at a concentration of 50 mM, significantly increased apoptosis of C4-2B and PC-3 cells in a time-dependent manner ($P < 0.01$) (Figure 4C and D).

AMPA induces changes in expression levels of genes involved in cell cycle and apoptosis

AMPA, at a concentration of 50 mM, increased the levels of cleaved PARP in the C4-2B cells in a time-dependent

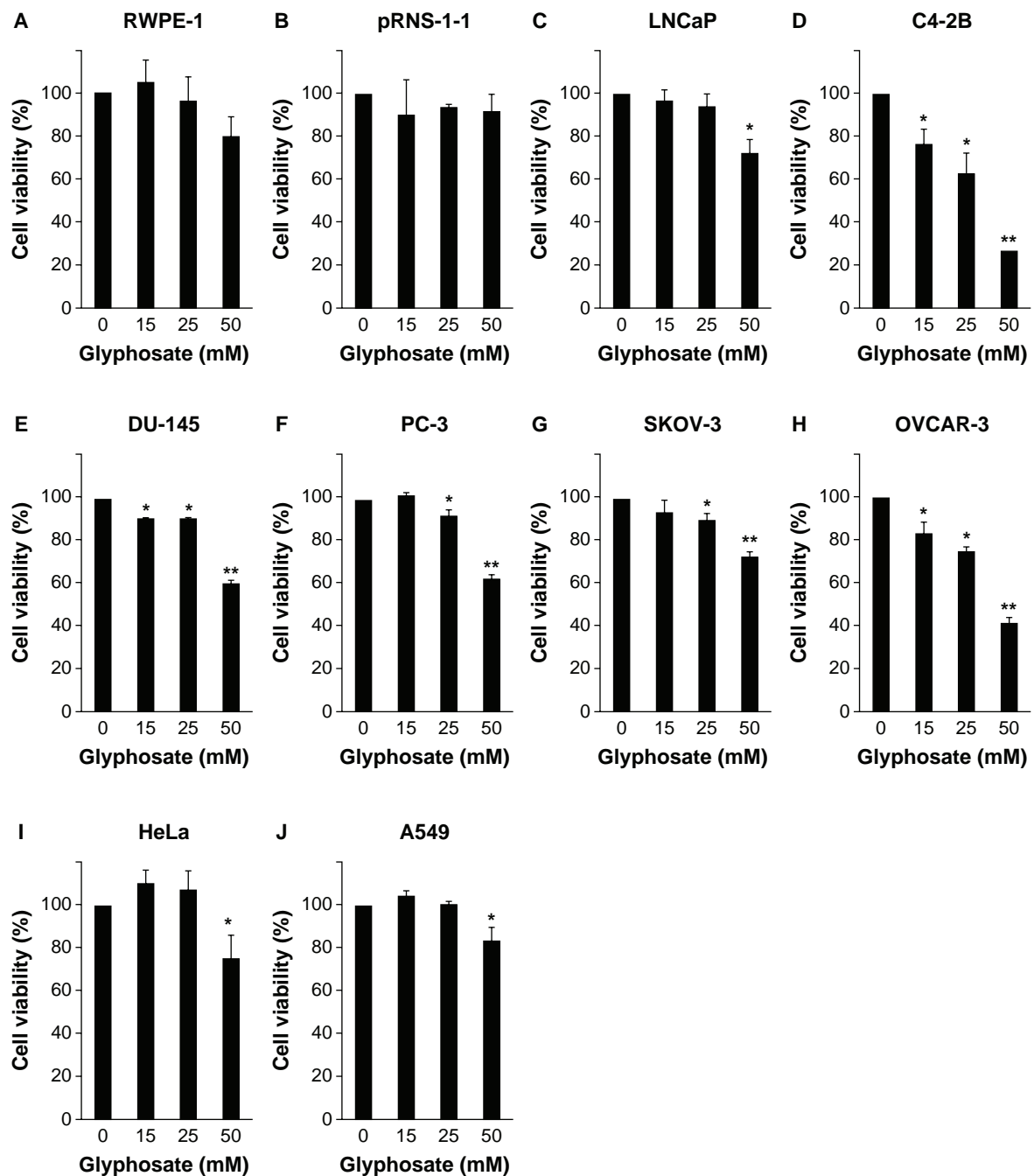


Figure 2 Glyphosate inhibits cell growth in cancer cell lines but not in normal cell lines.

Notes: (A–J) The cells were treated with 0, 15, 25, and 50 mM of glyphosate for 72 hours. Cell viability was determined using CellTiter-Glo® Luminescent Cell Viability Assay. Data represent the mean \pm SEM obtained from three independent experiments. * $P < 0.05$ and ** $P < 0.01$, compared with the untreated control group.

Abbreviation: SEM, standard error of the mean.

Table I Half maximal inhibitory concentrations (IC_{50}) of glyphosate and AMPA in inhibition of the cell growth in the normal and cancer cell lines

| Cell line | RWPE-I | pRNS-I-I | LNCaP | C4-2B | DU-145 | PC-3 | SKOV-3 | OVCAR-3 | HeLa | A549 |
|------------|--------|----------|-------|-------|--------|------|--------|---------|------|-------|
| Glyphosate | 109.1 | 372.8 | 90.4 | 34.2 | 63.9 | 63.2 | 89.0 | 42.7 | 89.4 | 136.7 |
| AMPA | 88.3 | 90.9 | 93.1 | 59.8 | 68.1 | 58.6 | 127.1 | 62.8 | 99.9 | 98.2 |

Note: Values are expressed in mM.

Abbreviation: AMPA, aminomethylphosphonic acid.

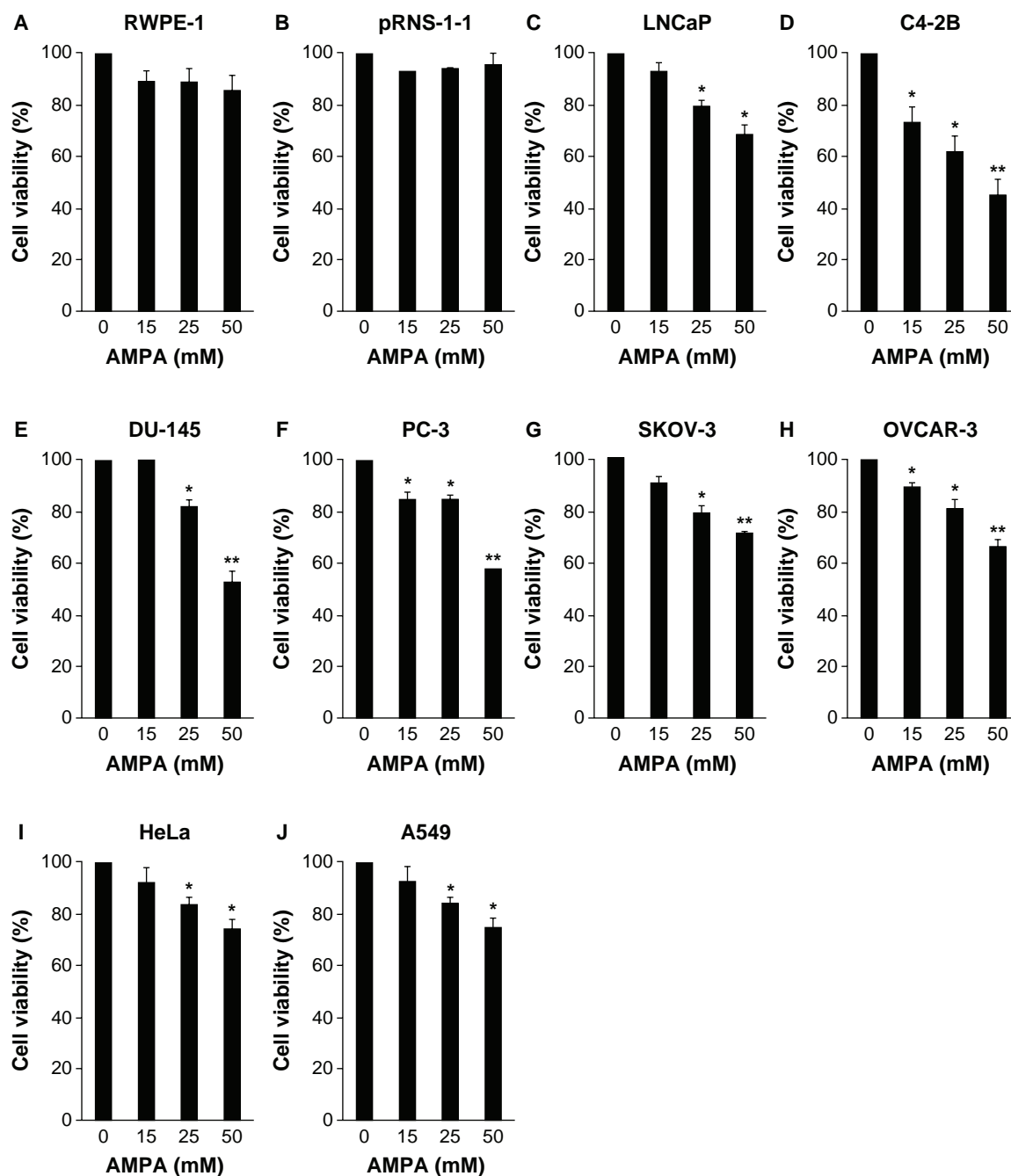


Figure 3 AMPA inhibits cell growth in cancer cell lines but not in normal cell lines.

Notes: (A–J) The cells were treated with 0, 15, 25, and 50 mM of AMPA for 72 hours. Cell viability was determined using CellTiter-Glo® Luminescent Cell Viability Assay. Data represent the mean \pm SEM obtained from three independent experiments. * $P < 0.05$ and ** $P < 0.01$, compared with the untreated control group.

Abbreviations: AMPA, aminomethylphosphonic acid; SEM, standard error of the mean.

manner (Figure 5A). AMPA transiently increased the levels of p53 and its downstream gene p21, at 12 hours after treatment (Figure 5B). It also decreased cyclin D3 protein levels, starting from 12 hours after treatment (Figure 5B). Further, AMPA increased the levels of procaspase 9, starting from 24 hours after treatment (Figure 5B). In contrast, AMPA decreased the levels of procaspase 3, starting from 24 hours after treatment (Figure 5B).

Discussion

A previous study identified glycine as being consumed by rapidly proliferating cancer cell lines. Among the 60 human cancer cell lines tested in the previous study, five were included in the present study, namely, DU-145, PC-3, SKOV-3, OVCAR-3, and A549. Previously, it was shown that cancer cell proliferation was impaired by knocking down the expression levels of *SHMT2* that is responsible

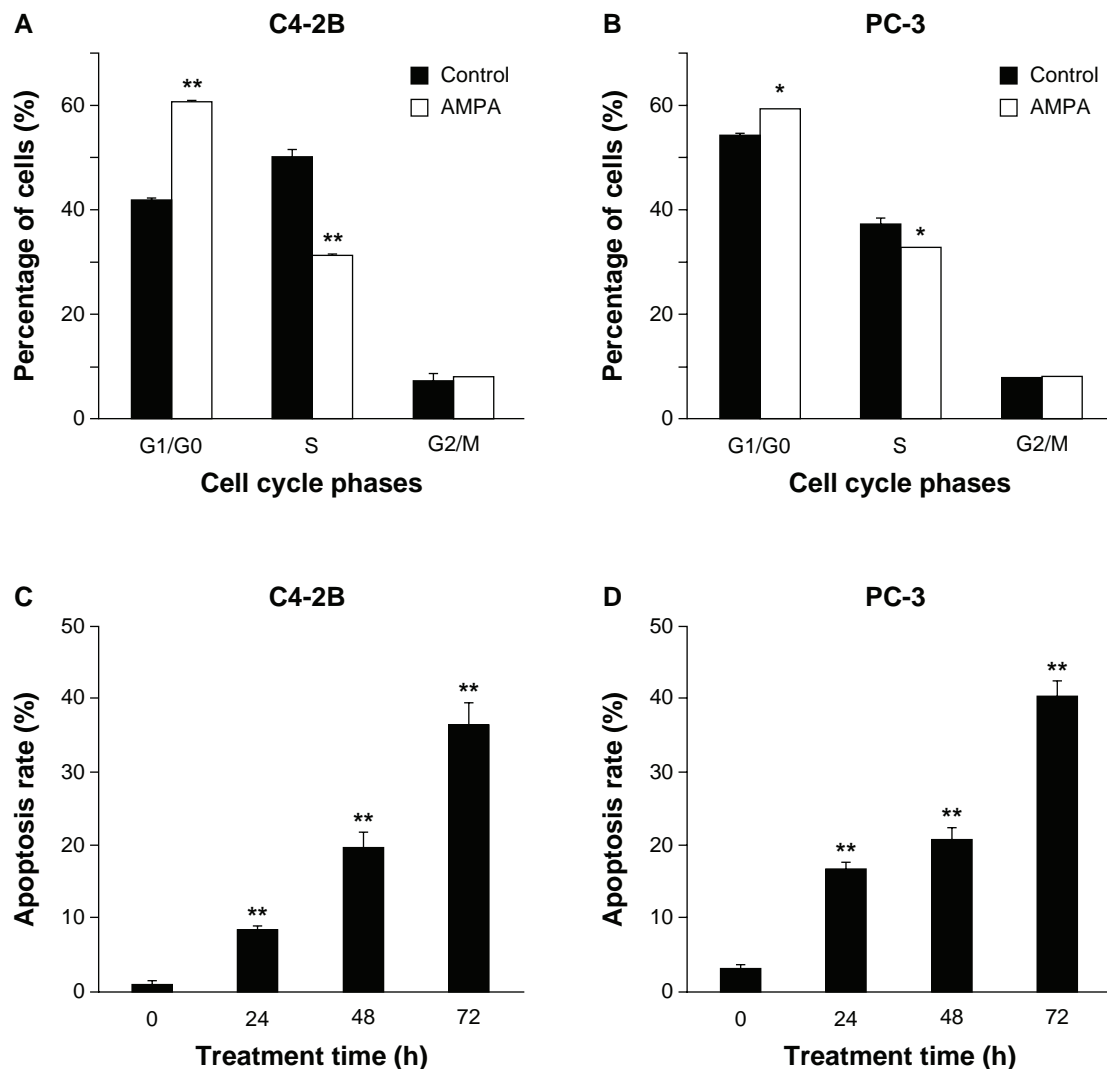


Figure 4 AMPA inhibits entry into the S phase of cell cycle and increases apoptosis.

Notes: C4-2B and PC-3 cells were treated with or without 50 mM AMPA for 24 hours (**A** and **B**) or 0, 24, 48, and 72 hours (h) (**C** and **D**). Percentages of the cells in G1/G0, S, and G2/M phases of cell cycle were determined using propidium iodide staining and flow cytometry analysis (**A** and **B**). Apoptosis rates were determined using Annexin-V FITC Conjugate and propidium iodide double staining and flow cytometry analysis (**C** and **D**). Data represent the mean \pm SEM obtained from three independent experiments. * $P < 0.05$ and ** $P < 0.01$, compared with the control group.

Abbreviations: AMPA, aminomethylphosphonic acid; FITC, Fluorescein isothiocyanate; SEM, standard error of the mean.

for intracellular glycine synthesis.⁵ Here we present data showing that glycine analogs, glyphosate and AMPA, inhibited cell growth in eight cancer cell lines, including four human prostate cancer cell lines (LNCaP, C4-2B, DU-145, and PC-3), two human ovarian cancer cell lines (SKOV-3 and OVCAR-3), one human cervical cancer cell line (HeLa), and one human lung cancer cell line (A549). In contrast, glyphosate and AMPA did not impair the growth of two immortalized human normal prostatic epithelial cell lines (RWPE-1 and pRNS-1-1) at concentrations up to 50 mM. These findings suggest that glyphosate and AMPA can differentially affect cancer cell growth but not normal cell growth at concentrations up to 50 mM. However, at a higher concentration of 100 mM, AMPA decreased cell viability of

the two normal cell lines, suggesting that potential adverse side effects may arise when the doses are too high. A safe therapeutic window may be limited to a drug concentration of between 50 mM to 100 mM. However, in clinical practice, it may be difficult to administer the drugs to reach this high concentration. Therefore, the use of glyphosate and AMPA in patients may be limited if the high IC_{50} concentrations are difficult to achieve in patients' blood. Nevertheless, glyphosate, particularly AMPA, may be a good lead compound for developing more potent inhibitors with low IC_{50} concentrations.

Among the human cancer cell lines, the castration-resistant prostate cancer cell lines (C4-2B, DU-145, and PC-3) and ovarian cancer cell line (OVCAR-3) appear to be

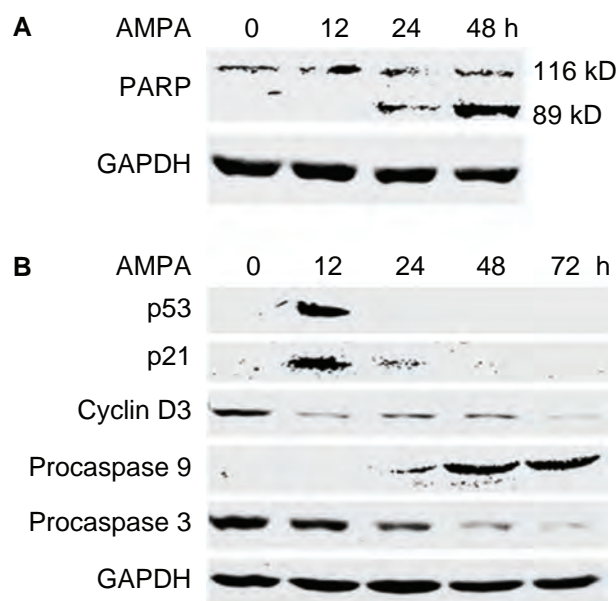


Figure 5 AMPA induces changes in expression levels of genes involved in cell cycle and apoptosis.

Notes: (A–B) C4-2B cells were treated with 50 mM AMPA for the indicated time. Western blot analysis was performed to determine the protein levels. For loading control, the blots were stripped and probed for GAPDH. For PARP, the 116-kD band is the full length, and the 89-kD band is the cleaved form.

Abbreviations: AMPA, aminomethylphosphonic acid; GAPDH, glyceraldehyde-3-phosphate dehydrogenase; h, hours; PARP, poly(ADP-ribose) polymerase; ADP, adenosine diphosphate.

more sensitive to glyphosate and AMPA than are the other human cancer cell lines. The IC_{50} concentrations varied from 34.2 to 68.1 mM among the four sensitive cancer cell lines (C4-2B, DU-145, PC-3, and OVCAR-3). In contrast, the IC_{50} concentrations were between 89 and 136.7 mM in other cancer cell lines, including LNCaP, SKOV-3, HeLa, and A549 (Table 1), suggesting that these four cell lines are resistant to glyphosate and AMPA. The differences in sensitivity may be caused by many factors that are not clearly understood because these cell lines are derived from different genetic backgrounds. The rate of cell proliferation may be one of the factors, as suggested by previous study.⁵ Indeed, the C4-2B cells were more sensitive to glyphosate and AMPA than LNCaP cells. Coincidentally, LNCaP cells grow slower than C4-2B cells, which are castration-resistant cells derived from the hormone-sensitive LNCaP cells.¹⁴ This observation indicates that glyphosate and AMPA are more effective in inhibiting growth of rapidly proliferating cancer cells.

Cell growth in a population of cells represents the net outcome of proliferation and apoptosis. Our data indicate that AMPA can arrest cancer cells in the G1/G0 phase of cell cycle, thus inhibiting entry into the S phase. On the other hand, AMPA can enhance apoptosis of cancer cells, as shown by the increased rates of annexin-V-positive

cells and increased levels of cleaved PARP, an indicator of apoptosis. Therefore, AMPA inhibits cancer cell growth through inhibition of cellular proliferation and promotion of apoptosis. The molecular mechanism may be that AMPA upregulates the p53 protein level, which subsequently increases p21 protein level. Activation of the p53-p21 pathway is known to cause G1-phase arrest and apoptosis in mammalian cells.^{20–22} AMPA downregulates the expression of cyclin D3, which may also contribute to the cell cycle arrest.²³ AMPA increases procaspase 9 levels and simultaneously decreases procaspase 3 levels, which may mediate apoptosis, as shown in a previous study.²⁴ However, how AMPA initiates these molecular changes and whether these changes apply to other cancer cell lines remain to be determined.

To our best knowledge, this is the first study showing that glycine analogs can inhibit proliferation and promote apoptosis of cancer cells but not normal cells, *in vitro* at concentrations up to 50 mM. Higher concentrations of the chemicals may affect normal cells, thus producing adverse side effects. These findings suggest that animal studies are warranted to assess the efficacy of glyphosate and AMPA in the treatment of tumors growing in animals and to test whether the effective inhibitory concentrations can be achieved in animal blood. If a positive outcome is obtained in preclinical animal study, it will be feasible to conduct human clinical trials because glyphosate and AMPA are of little toxicity to animals and humans.¹⁰ On the other hand, more potent inhibitors may be developed using glyphosate and AMPA as lead compounds. Based on our findings and the previous report,⁵ it appears promising to develop a new anticancer therapy targeting glycine metabolism.

Acknowledgments

This work was partly supported by a grant from the Department of Defense (PC121647), two grants from the National Institute of General Medical Sciences (P20GM103518) and the National Cancer Institute (R01CA174714) of the National Institutes of Health, the Developmental Fund of Tulane Cancer Center (TCC), and the Louisiana Cancer Research Consortium (LCRC) Fund (to ZY). Dr Zongbing You conceived the idea and designed the experiments. The content of this article is solely the responsibility of the authors and does not necessarily represent the official views of the National Institutes of Health. The TCC and LCRC FACS Core Facilities were used to conduct this study. Dr Qingli Li received a scholarship from the State Scholarship Fund via China Scholarship Council (CSC) for her training under Dr Zongbing You at Tulane University.

Disclosure

The authors report no conflicts of interest in this work.

References

- Nelson DL, Cox MM. 2008. *Principles of Biochemistry*. New York, NY: WH Freeman and Company; 2008.
- Kerr SJ. Competing methyltransferase systems. *J Biol Chem*. 1972;247(13):4248–4252.
- Porter DH, Cook RJ, Wagner C. Enzymatic properties of dimethylglycine dehydrogenase and sarcosine dehydrogenase from rat liver. *Arch Biochem Biophys*. 1985;243(2):396–407.
- Hahn RG. Dose-dependent half-life of glycine. *Urol Res*. 1993;21(4):289–291.
- Jain M, Nilsson R, Sharma S, et al. Metabolite profiling identifies a key role for glycine in rapid cancer cell proliferation. *Science*. 2012;336(6084):1040–1044.
- Garrow TA, Brenner AA, Whitehead VM, et al. Cloning of human cDNAs encoding mitochondrial and cytosolic serine hydroxymethyltransferases and chromosomal localization. *J Biol Chem*. 1993;268(16):11910–11916.
- Girgis S, Nasrallah IM, Suh JR, et al. Molecular cloning, characterization and alternative splicing of the human cytoplasmic serine hydroxymethyltransferase gene. *Gene*. 1998;210(2):315–324.
- Stover PJ, Chen LH, Suh JR, Stover DM, Keyomarsi K, Shane B. Molecular cloning, characterization, and regulation of the human mitochondrial serine hydroxymethyltransferase gene. *J Biol Chem*. 1997;272(3):1842–1848.
- Anderson DD, Stover PJ. SHMT1 and SHMT2 are functionally redundant in nuclear de novo thymidylate biosynthesis. *PLoS One*. 2009;4(6):e5839.
- World Health Organization (WHO). *Glyphosate and AMPA in Drinking-Water. Background Document for Development of WHO Guidelines for Drinking-Water Quality*. Geneva: WHO; 2005.
- World Health Organization (WHO). *IPCS, Environmental Health Criteria 159: Glyphosate*. Geneva: WHO; 1994.
- Williams GM, Kroes R, Munro IC. Safety evaluation and risk assessment of the herbicide Roundup and its active ingredient, glyphosate, for humans. *Regul Toxicol Pharmacol*. 2000;31(2 Pt 1):117–165.
- You Z, Dong Y, Kong X, Zhang Y, Vessella RL, Melamed J. Differential expression of IL-17RC isoforms in androgen-dependent and androgen-independent prostate cancers. *Neoplasia*. 2007;9(6):464–470.
- Thalmann GN, Sikes RA, Wu TT, et al. LNCaP progression model of human prostate cancer: androgen-independence and osseous metastasis. *Prostate*. 2000;44(2):91–103.
- Crouch SP, Kozlowski R, Slater KJ, Fletcher J. The use of ATP bioluminescence as a measure of cell proliferation and cytotoxicity. *J Immunol Methods*. 1993;160(1):81–88.
- Kangas L, Grönroos M, Nieminen AL. Bioluminescence of cellular ATP: a new method for evaluating cytotoxic agents in vitro. *Med Biol*. 1984;62(6):338–343.
- Elisia I, Popovich DG, Hu C, Kitts DD. Evaluation of viability assays for anthocyanins in cultured cells. *Phytochem Anal*. 2008;19(6):479–486.
- Vermes I, Haanen C, Steffens-Nakken H, Reutelingsperger C. A novel assay for apoptosis. Flow cytometric detection of phosphatidylserine expression on early apoptotic cells using fluorescein labelled Annexin V. *J Immunol Methods*. 1995;184(1):39–51.
- Mead RN, Ryu J, Liu S, et al. Supraphysiologic temperature enhances cytotoxic effects of bupivacaine on bovine articular chondrocytes in an in vitro study. *Arthroscopy*. 2012;28(3):397–404.
- He G, Siddik ZH, Huang Z, et al. Induction of p21 by p53 following DNA damage inhibits both Cdk4 and Cdk2 activities. *Oncogene*. 2005;24(18):2929–2943.
- el-Deiry WS, Harper JW, O'Connor PM, et al. WAF1/CIP1 is induced in p53-mediated G1 arrest and apoptosis. *Cancer Res*. 1994;54(5):1169–1174.
- el-Deiry WS, Tokino T, Velculescu VE, et al. WAF1, a potential mediator of p53 tumor suppression. *Cell*. 1993;75(4):817–825.
- Fimognari C, Nusse M, Berti F, Iori R, Cantelli-Forti G, Hrelia P. Cyclin D3 and p53 mediate sulforaphane-induced cell cycle delay and apoptosis in non-transformed human T lymphocytes. *Cell Mol Life Sci*. 2002;59(11):2004–2012.
- Sakai T, Liu L, Teng X, et al. Nucling recruits Apaf-1/pro-caspase-9 complex for the induction of stress-induced apoptosis. *J Biol Chem*. 2004;279(39):41131–41140.

Drug Design, Development and Therapy

Publish your work in this journal

Drug Design, Development and Therapy is an international, peer-reviewed open-access journal that spans the spectrum of drug design and development through to clinical applications. Clinical outcomes, patient safety, and programs for the development and effective, safe, and sustained use of medicines are a feature of the journal, which

Submit your manuscript here: <http://www.dovepress.com/drug-design-development-and-therapy-journal>

has also been accepted for indexing on PubMed Central. The manuscript management system is completely online and includes a very quick and fair peer-review system, which is all easy to use. Visit <http://www.dovepress.com/testimonials.php> to read real quotes from published authors.

Dovepress

Original Article

Methoxyacetic acid suppresses prostate cancer cell growth by inducing growth arrest and apoptosis

Keshab R Parajuli¹, Qiuyang Zhang¹, Sen Liu¹, Neil K Patel¹, Hua Lu^{2,3}, Shelya X Zeng^{2,3}, Guangdi Wang⁴, Changde Zhang⁴, Zongbing You^{1,3,5,6,7}

¹Department of Structural & Cellular Biology, Tulane University, New Orleans, LA, USA; ²Department of Biochemistry and Molecular Biology, Tulane University, New Orleans, LA, USA; ³Tulane Cancer Center and Louisiana Cancer Research Consortium, Tulane University, New Orleans, LA, USA; ⁴Department of Chemistry and RCMI Cancer Research Center, Xavier University of Louisiana, New Orleans, LA, USA; ⁵Department of Orthopaedic Surgery, Tulane University, New Orleans, LA, USA; ⁶Tulane Center for Stem Cell Research and Regenerative Medicine, Tulane University, New Orleans, LA, USA; ⁷Tulane Center for Aging, Tulane University, New Orleans, LA, USA

Received November 5, 2014; December 9, 2014; Epub December 25, 2014; Published December 31, 2014

Abstract: Methoxyacetic acid (MAA) is a primary metabolite of ester phthalates that are used in production of consumer products and pharmaceutical products. MAA causes embryo malformation and spermatocyte death through inhibition of histone deacetylases (HDACs). Little is known about MAA's effects on cancer cells. In this study, two immortalized human normal prostatic epithelial cell lines (RWPE-1 and pRNS-1-1) and four human prostate cancer cell lines (LNCaP, C4-2B, PC-3, and DU-145) were treated with MAA at different doses and for different time periods. Cell viability, apoptosis, and cell cycle analysis were performed using flow cytometry and chemical assays. Gene expression and binding to DNA were assessed using real-time PCR, Western blot, and chromatin immunoprecipitation analyses. We found that MAA dose-dependently inhibited prostate cancer cell growth through induction of apoptosis and cell cycle arrest at G1 phase. MAA-induced apoptosis was due to down-regulation of the anti-apoptotic gene baculoviral inhibitor of apoptosis protein repeat containing 2 (BIRC2, also named cIAP1), leading to activation of caspases 7 and 3 and turning on the downstream apoptotic events. MAA-induced cell cycle arrest (mainly G1 arrest) was due to up-regulation of p21 expression at the early time and down-regulation of cyclin-dependent kinase 4 (CDK4) and CDK2 expression at the late time. MAA up-regulated p21 expression through inhibition of HDAC activities, independently of p53/p63/p73. These findings demonstrate that MAA suppresses prostate cancer cell growth by inducing growth arrest and apoptosis, which suggests that MAA could be used as a potential therapeutic drug for prostate cancer.

Keywords: Prostate cancer, cell death, cell cycle, apoptosis, p21

Introduction

Methoxyacetic acid (MAA, linear chemical formula: $\text{CH}_3\text{OCH}_2\text{COOH}$) is a primary metabolite of ester phthalates widely used in the manufacture of household products (building materials, plastics, textiles, adhesives, paints, and deodorants), food and personal care products (agricultural adjuvants, pesticides, cosmetics, and perfumes), electronics (coatings, stabilizers, and surfactants), and pharmaceutical products (oral pill coatings, viscosity control agents, surfactants, and stabilizers) [1]. Over 18 billion pounds of ester phthalates are used globally each year. Ingestion, inhalation, intravenous injection, and dermal exposure of ester phthalates may lead to toxicities through their

metabolite MAA [1]. MAA is converted from ethylene glycol monomethyl ether (also called 2-methoxyethanol) by alcohol dehydrogenase. In a workplace with daily 2-methoxyethanol exposure of 4.5 $\mu\text{g}/\text{ml}$ (within the permissible exposure limit), urine MAA concentrations reached up to 0.6 millimoles/liter (mM) [2], which could be accumulated to higher concentrations due to the long elimination half-life of 77 hours [3]. Exposure to 2-methoxyethanol increases risks of spontaneous abortion and subfertility in women [4] and decreases sperm counts in men [5]. In pregnant mice, single i.v. injection of 250-325 mg/kg 2-methoxyethanol created peak plasma concentrations of 5-8 mM MAA, which led to embryo malformation and lethality [6].

MAA causes toxicities through multiple mechanisms. In normal human fibroblasts, MAA treatment induces production of radical oxygen species, resulting in DNA damage and loss of mitochondrial membrane potential [1]. MAA treatment down-regulates expression of estrogen receptor α (ER α) and estradiol-induced gene expression in human breast cancer cell line MCF-7 and mouse uterus [7]. In contrast, it has been reported that MAA exposure increases ER β expression in pachytene spermatocytes, which may be associated with MAA-induced apoptosis of pachytene spermatocytes in rats [8]. In rat seminiferous tubules, MAA treatment alters the expression of androgen receptor (AR) and androgen-binding protein (ABP) in a stage-specific manner. On one hand, MAA treatment up-regulates AR expression in the early and late stages, but down-regulates AR expression in the middle stage [9]; on the other hand, this same treatment down-regulates ABP expression in the late stage, but up-regulates ABP expression in the middle stage [9]. Spermatogenesis requires normal functions of AR [10, 11], ER α [12], and ER β [13] and their disruption leads to testicular degeneration after MAA exposure. In addition, MAA has been found to activate the tyrosine kinase – PI3K pathway and other pathways to enhance or antagonize androgen-induced gene expression [14-16]. Similarly, MAA can enhance the transcriptional activities of ER α and ER β by activating MAPK and inhibiting histone deacetylases (HDACs) [17]. MAA can inhibit HDAC1, HDAC2, and HDAC3, thus increasing the levels of acetylated histone H4, like the other well-known HDAC inhibitors such as trichostatin, valproic acid, and butyric acid [17]. In fact, it has been reported that MAA-induced hyperacetylation of histones H3 and H4 is associated with rapid spermatocyte death following MAA exposure [18].

These previous studies on MAA largely focused on its toxic effects on the reproductive system. Some HDAC inhibitors such as suberanilohydroxamic acid (SAHA) and romidepsin have been approved for the treatment of cutaneous T cell lymphoma, and panobinostat and valproic acid are being tested in the treatment of prostate cancer, breast cancer, cervical cancer, ovarian cancer, and lymphomas [19]. We speculated that MAA might also possess anti-cancer activity. In the present study, we tested this idea and found that MAA can indeed induce apoptosis and growth arrest of prostate cancer cells. MAA-induced apoptosis was highly asso-

ciated with decreased protein expression of baculoviral inhibitor of apoptosis protein repeat containing 2 (BIRC2, also named cIAP1), whereas MAA-caused G1 arrest was closely associated with induction of p21 level and reduction of cyclin-dependent kinase 4 (CDK4) and CDK2 levels. The MAA-induced p21 level was likely due to the inhibition of HDAC activities by this compound, leading to increased association of acetylated histone H3 and H4 with the specificity protein 1 (Sp1) binding sites-rich DNA element on the p21 promoter, independently of p53/p63/p73 proteins. Thus, these results suggest that MAA might possess a potential anti-cancer activity by inhibiting anti-apoptotic protein and inducing apoptosis as well as inducing cell growth arrest via induction of p21.

Materials and methods

Cell culture

The sources and cell culture conditions of two immortalized human normal prostatic epithelial cell lines (RWPE-1 and pRNS-1-1) and four human prostate cancer cell lines (LNCaP, C4-2B, PC-3, and DU-145) were described previously [20]. Cells were cultured in a 5% CO₂ humidified incubator at 37°C.

Cell viability assay

The number of live cells was determined using the CellTiter-Glo® Luminescent Cell Viability Assay (Promega Corp, Fitchburg, WI, USA) as described previously [20]. Cell viability was calculated as (luminescence of the treatment group – background luminescence) ÷ (luminescence of the control group – background luminescence) × 100%. The data are presented as the mean and standard error of the mean (SEM) of three independent experiments.

Detection of apoptotic nucleosomes

Cells were seeded on 12-well plates with 1 × 10⁵ cells/well in triplicate per group in the complete culture medium with FBS. After overnight incubation, cells were treated with 5 mM MAA for 24 hours (h); a control group was treated with PBS. Apoptotic nucleosomes were detected using Cell Death Detection ELISA kit (Roche Diagnostics Corporation, Indianapolis, IN, USA) according to the manufacturer's instructions [21]. Absorbance was measured at 405 nm (A405) with a reference wavelength at 490 nm (A490) using a plate reader (Bio-Tek U.S.,

Table 1. PCR primers

| Primer | | Sequence |
|-----------------|---------|----------------------------|
| p21 | Forward | 5'-ACCCATGCGGCAGCAA-3' |
| | Reverse | 5'-CGCCATTAGCGCATCACA-3' |
| GAPDH | Forward | 5'-TAAAGCAGCCCTGGTGACC-3' |
| | Reverse | 5'-CCACATCGCTCAGACACCAT-3' |
| Sp1-rich region | Forward | 5'-CAGCGCACCAACGCAGGCG-3' |
| | Reverse | 5'-CAGCTCCGGCTCCACAAGGA-3' |
| Adjacent region | Forward | 5'-GGTGTCTAGGTGCTCCAGGT-3' |
| | Reverse | 5'-GCACTCTCCAGGAGGACACA-3' |

Winooski, VT, USA). The amount of apoptotic nucleosomes was represented by A405-A490.

Cell cycle analysis

Cells were treated without or with 5 mM or 20 mM MAA for 24 h. The percentage of cells at G1/G0, S, and G2/M phases was determined by flow cytometry analysis as described previously [20].

Western blot analysis

Cells were treated without or with MAA at concentrations of 5 mM or 20 mM for 0, 12, 24, 48, and 72 h. Proteins were extracted for Western blot analysis as described previously [20]. Rabbit anti-caspase 7, rabbit anti-caspase 6, and rabbit anti-caspase 9 antibodies were purchased from Cell Signaling Technology (Danvers, MA, USA). Mouse anti-p53, mouse anti-p63, rabbit anti-p73, rabbit anti-caspase 10, mouse anti-caspase 8, rabbit anti-BIRC2, and rabbit anti-BIRC3 antibodies were obtained from Santa Cruz Biotechnology (Dallas, TX, USA). Mouse anti-GAPDH, mouse anti-caspase 3, and rabbit anti-cleaved poly (ADP-ribose) polymerase (PARP) antibodies were purchased from EMD Millipore Corp (Billerica, MA, USA). Rabbit anti-CDK2 and mouse anti-CDK4 antibodies were purchased from GeneTex, Inc., Irvine, CA, USA. Rabbit anti-cyclin D1 antibodies were bought from Abcam, Cambridge, MA, USA.

Reverse transcription (RT) and quantitative (q) PCR analysis

Cells were treated with 20 mM MAA for 0, 12, 24, 48, and 72 h. Total RNAs were extracted for RT and qPCR analysis as described previously [22]. Results were normalized against GAPDH levels using the formula ΔCt (Cycle threshold) = Ct of target gene – Ct of GAPDH. The mRNA

level of a control group was used as the baseline; therefore, $\Delta\Delta\text{Ct}$ was calculated using the formula $\Delta\Delta\text{Ct} = \Delta\text{Ct}$ of target gene – ΔCt of the baseline. The fold change of mRNA level was calculated as fold = $2^{-\Delta\Delta\text{Ct}}$. PCR primers used are shown in **Table 1**.

Chromatin immunoprecipitation (ChIP) assay

Cells were plated at a density of 2×10^6 cells per dish in four 100-mm dishes in each group and incubated overnight. Cells were treated without or with 20 mM MAA for 24 h and fixed in 1% formaldehyde for 10 minutes. ChIP assays were performed using Magna ChIP™ G Chromatin Immunoprecipitation Kit (EMD Millipore Corp, Billerica, MA, USA) according to the manufacturer's instructions. Briefly, 1 mL of 10x glycine was added to the cells to quench formaldehyde; after washing with ice-cold PBS containing protease inhibitor cocktail II, the cells were resuspended in 0.5 mL of SDS lysis buffer with protease inhibitor cocktail II; after centrifugation, cell pellets were resuspended in 0.5 mL nuclear lysis buffer; the lysates were sonicated for about 10-15 seconds on ice; after centrifugation, an aliquot of 5 microliter (μL) of the supernatant chromatin preparation was set aside as the Input fraction; then, 50 μL chromatin preparations were diluted with 450 μL ChIP dilution buffer and added with 5 μg of rabbit anti-acetyl-histone H3, rabbit anti-acetyl-histone H4 (EMD Millipore Corp), or rabbit IgG (Santa Cruz Biotechnology) for overnight incubation at 4°C; protein G magnetic beads (20 μL) were added for 1 h incubation; next, protein G magnetic bead complexes were separated with magnetic separator and washed with washing buffers; immune complex samples and inputs were eluted with 100 μL of ChIP elution buffer and digested with proteinase K at 62°C for 2 h; immunoprecipitated DNA samples and Inputs were purified with DNA purification spin column and analyzed by PCR with the products analyzed by 2% agarose/ethidium bromide gel electrophoresis. PCR primers used for ChIP assays are shown in **Table 1**.

Statistical analysis

Results from this study were presented as the mean \pm SEM. Statistical analysis was performed using two-tailed Student's *t* test. A *p*-value < 0.05 was considered statistically significant.

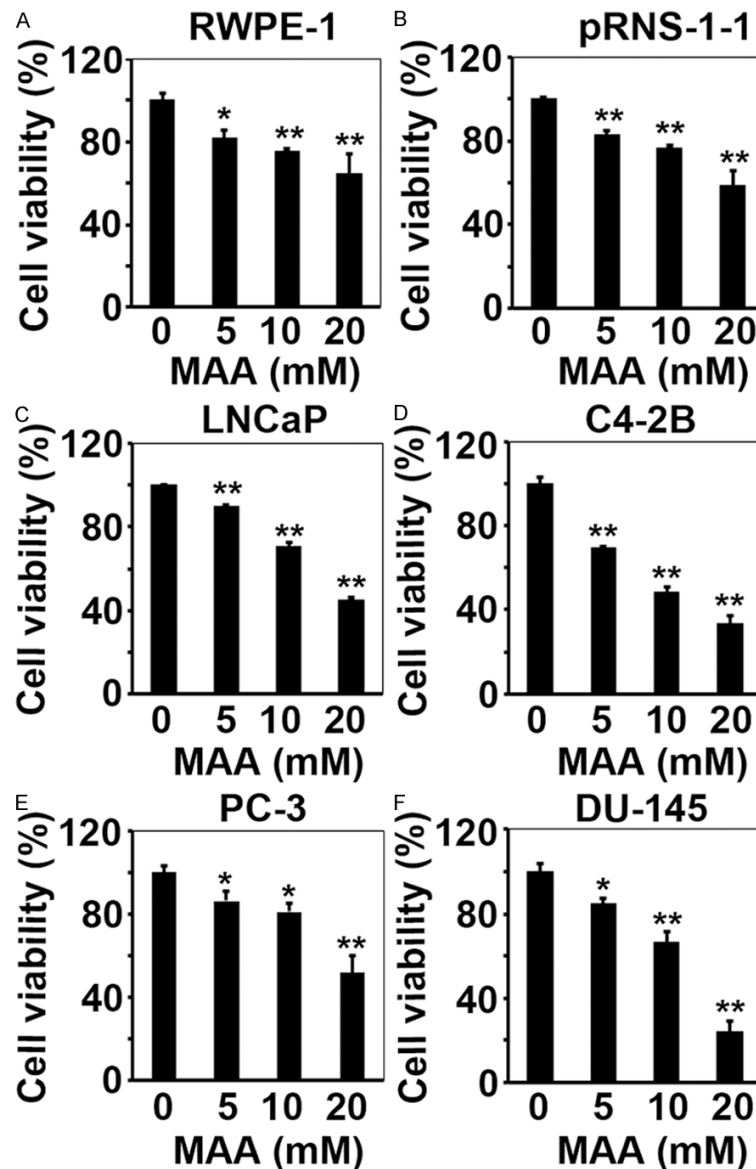


Figure 1. MAA inhibits prostate cancer cell growth. A-F: Normal prostatic epithelial cells and prostate cancer cells were plated in 96-well plates in triplicate per group and were treated with 0, 5, 10, and 20 mM MAA for 72 h. The live cell numbers were determined using the CellTiter-Glo® Luminescent Cell Viability Assay. The data are presented as the mean \pm SEM of three independent experiments. * $p < 0.05$; ** $p < 0.01$.

Results

MAA inhibits prostate cancer cell growth

To study the effects of MAA on prostate cancer cell growth, we treated two immortalized human normal prostatic epithelial cell lines RWPE-1 and pRNS-1-1 and four prostate cancer cell lines LNCaP, C4-2B, PC-3, and DU-145, with 5, 10, and 20 mM of MAA. We chose to start with 5 mM MAA because a previous study

showed that the IC_{50} was 5.6 mM for MAA to inhibit cell growth of human leukemia cell line HL60 [23]. We found that MAA inhibited cell growth in all of the six cell lines in a dose dependent fashion (Figure 1A-F). Interestingly, four prostate cancer cell lines (LNCaP, C4-2B, PC-3, and DU-145) were more sensitive to MAA than were two normal prostatic epithelial cell lines (RWPE-1 and pRNS-1-1), as the number of viable cells was decreased by approximately 50% to 75% in the four prostate cancer cell lines (Figure 1C-F), whereas it was only reduced by 40% in RWPE-1 and pRNS-1-1 cells, when these cell lines were individually treated with 20 mM MAA (Figure 1A, 1B).

MAA induces apoptosis of prostate cancer cells

To test if MAA induces apoptosis of prostate cancer cells, we measured apoptotic nucleosomes in untreated and MAA-treated cells. We found that 5mM MAA treatment for 24 h significantly increased the amounts of apoptotic nucleosomes in LNCaP, C4-2B, PC-3, and DU-145 cells, compared to the untreated control groups (Figure 2A-D, $p < 0.05$ or 0.01). Consistently, PARP cleavage in all four prostate cancer cell lines was induced by MAA in a dose- and time-

dependent manner (Figure 2E, 2F). Since PARP cleavage has been widely used as an indicator of apoptosis [24, 25], these results indicate that MAA induces apoptosis of four prostate cancer cell lines.

MAA blocks G1/S transition of prostate cancer cell cycle

To assess if MAA induces cell cycle arrest, we analyzed the percentages of cells in the G1

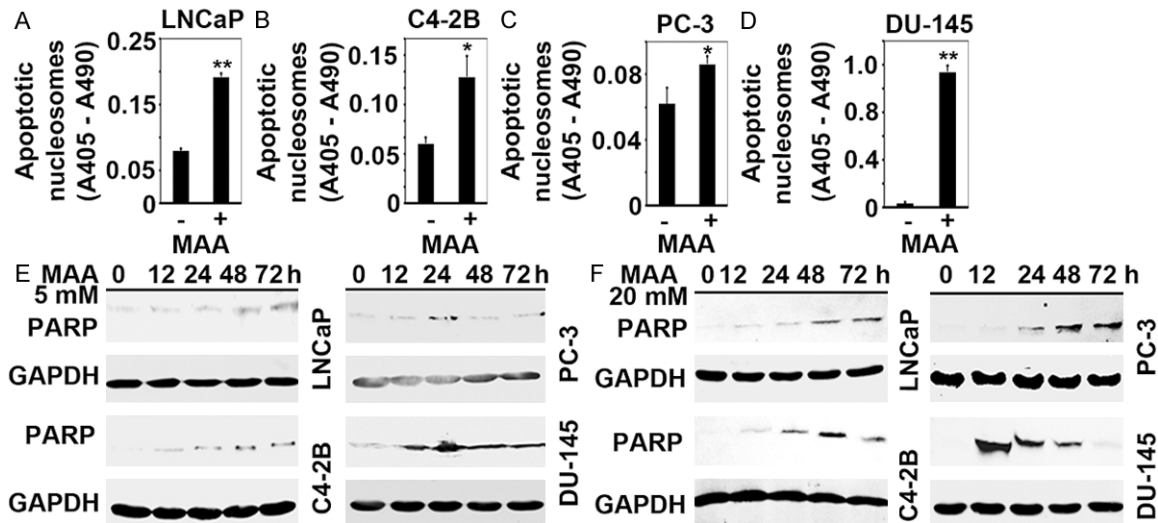


Figure 2. MAA induces apoptosis of prostate cancer cells. (A-D) Prostate cancer cells were plated in 12-well plates in triplicate per group and treated with 5 mM MAA for 24 h; the control group was treated with PBS. Apoptotic nucleosomes were detected using Cell Death Detection ELISA kit, which were calculated as absorbance at 405 nm (A405) – absorbance at 490 nm (A490). The data are presented as the mean \pm SEM of three independent experiments. * p < 0.05; ** p < 0.01. (E, F) Prostate cancer cells were treated with 5 mM (E) or 20 mM (F) MAA for up to 72 h. Protein extracts were used for Western blot analysis of cleaved PARP. For the loading control, the blots were probed for GAPDH.

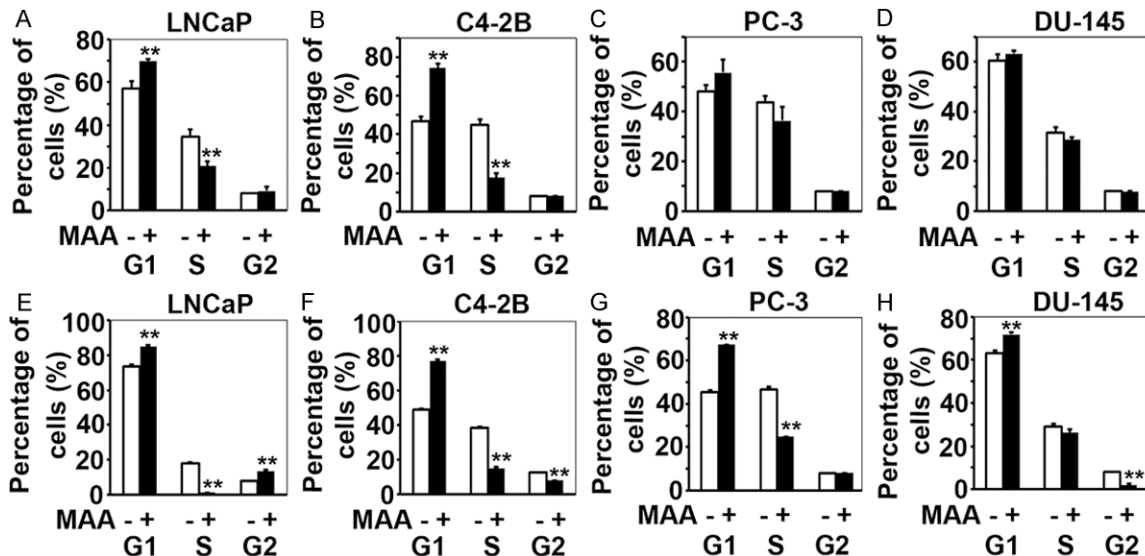


Figure 3. MAA blocks G1/S transition of prostate cancer cell cycle. (A-H) Prostate cancer cells were plated in 60-mm dishes in triplicate per group and treated with 5 mM (A-D) or 20 mM (E-H) MAA for 24 h; the control group was treated with PBS. The percentages of cells at G1 (and G0), S, and G2 (and M) phases were determined by flow cytometry analysis. The data are presented as the mean \pm SEM, n = 3. ** p < 0.01.

(and G0), S, and G2 (and M) phases of the cell cycle using flow cytometry analysis. We found that 5 mM MAA treatment significantly increased the percentage of LNCaP and C4-2B cells at the G1/G0 phase, but significantly decreased the percentage of cells at the S

phase (Figure 3A, 3B, p < 0.01). However, although some effects were found in PC-3 and DU-145 cells, the differences were not statistically significant at the low dosage of MAA (Figure 3C, 3D, p > 0.05). At a high dose such as 20 mM, MAA treatment significantly

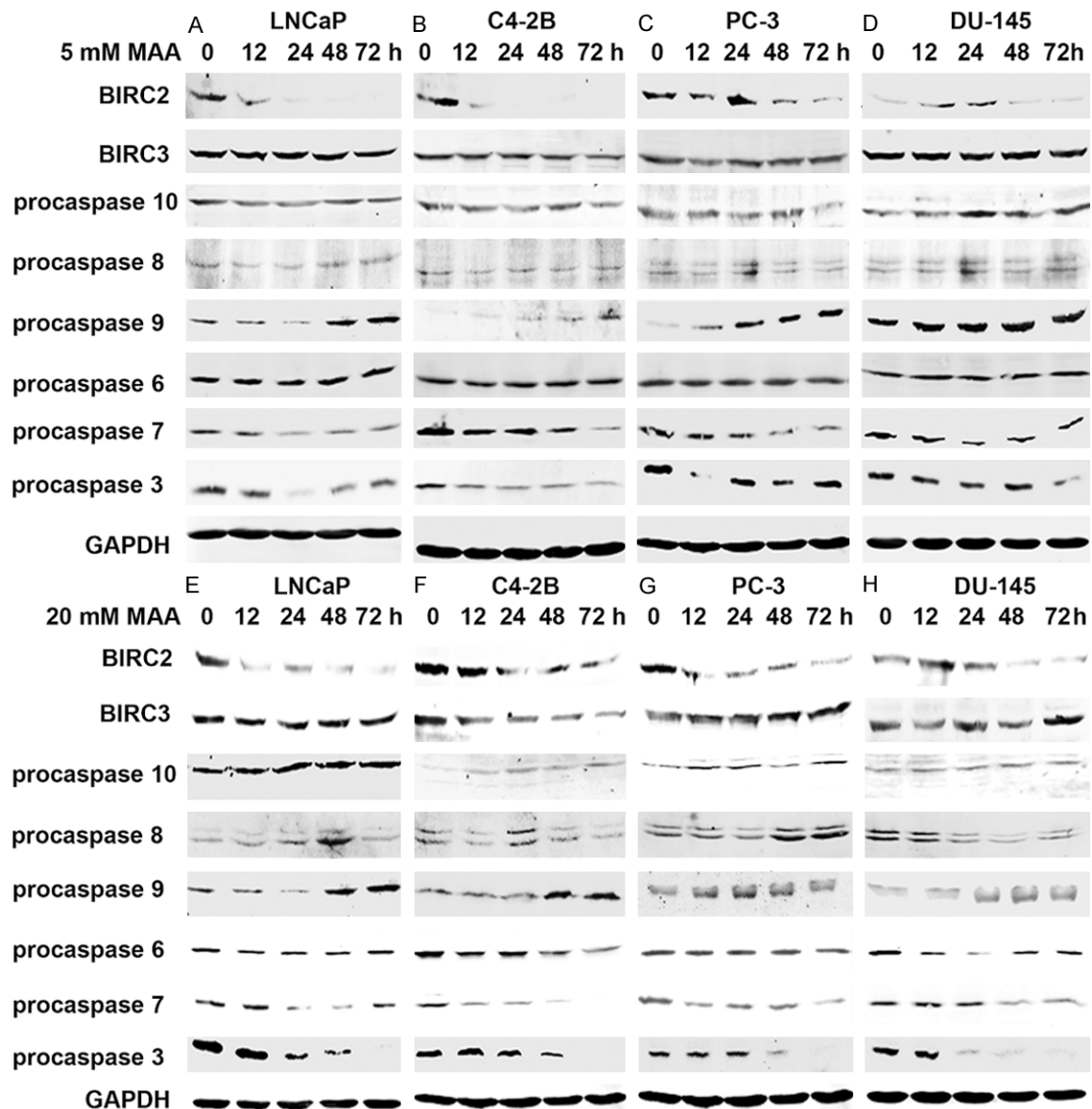


Figure 4. MAA decreases protein expression of BIRC2 and activates caspases 7 and 3. (A-H) Prostate cancer cells were treated with 5 mM (A-D) or 20 mM (E-H) MAA for up to 72 h. Protein extracts were used for Western blot analysis of the indicated proteins. For the loading control, the blots were probed for GAPDH.

increased the percentage of cells at the G1/G0 phase with the corresponding decrease of cells at the S phase in all four prostate cancer cell lines (Figure 3E-H). These results imply that MAA treatment blocks the G1/S transition, and thus inhibits cell proliferation.

MAA decreases protein expression of BIRC2 and activates caspases 7 and 3

To illustrate the mechanisms underlying MAA-induced apoptosis of prostate cancer cells, we examined the expression of a panel of anti-

apoptotic and pro-apoptotic genes, using Western blot analysis. Although there was not any detectable expression or any change upon MAA treatment for B-cell CLL/lymphoma 2 (BCL2), BCL2-associated X protein (BAX), BCL2-like 1 (BCL2L1), BCL2-associated agonist of cell death (BAD), BH3 interacting domain death agonist (BID), myeloid cell leukemia 1 (MCL1), and CASP8 and FADD-like apoptosis regulator (CFLAR) (data not shown), we found that MAA treatment decreased the protein level of BIRC2 in all four prostate cancer cell lines (Figure

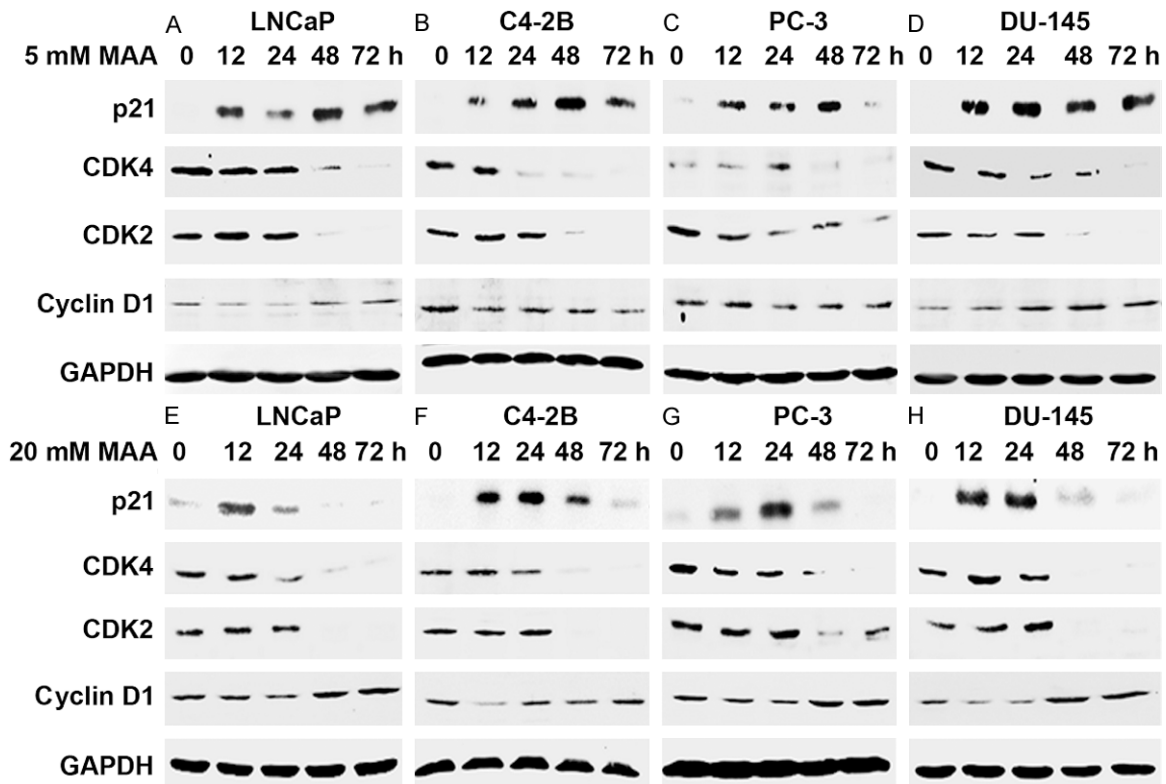


Figure 5. MAA induces p21 level but reduces CDK4 and CDK2 levels. (A-H) Prostate cancer cells were treated with 5 mM (A-D) or 20 mM (E-H) MAA for up to 72 h. Protein extracts were used for Western blot analysis of the indicated proteins. For the loading control, the blots were probed for GAPDH.

4A-H). This decrease was specific to BIRC2, as there were not any obvious changes in the protein levels of BIRC3, another member of the inhibitors of apoptosis protein (IAP) family [26]. It has been shown that proteasome-mediated and/or HTRA2 serine protease-mediated degradation of BIRC2 can relieve BIRC2's inhibitory function on caspases, thus activating caspases-mediated apoptosis [27, 28]. Therefore, we examined a panel of key caspases in both extrinsic and intrinsic apoptosis pathways. Caspases are endoproteases that are initially produced as inactive monomeric procaspases, which require dimerization and often cleavage for activation [29]. Among the apoptosis-relevant caspases, the level of procaspase 9 in all four prostate cancer cell lines was induced by MAA treatment at both 5 mM (**Figure 4A-D**) and 20 mM (**Figure 4E-H**), whereas little change of the level of procaspases 10, 8 and 6 was observed with the same treatment (**Figure 4A-H**). By contrast, the level of procaspases 7 and 3 was decreased by MAA treatment at both 5 mM (**Figure 4A-D**) and 20 mM (**Figure 4E-H**). Decrease of the procaspases indicates cleav-

age of the proenzymes and activation of caspases 7 and 3, two key executioner caspases [29].

MAA induces p21 level but reduces CDK4 and CDK2 levels

To determine which protein molecules might be responsible for MAA-induced G1 arrest, we first examined the levels of several cell cycle-regulated proteins during the G1/S transition. It has been shown that in the late G1 phase, the cyclin D-CDK4/6 kinase complex initiates phosphorylation of retinoblastoma protein (pRb), and this phosphorylation dissociates pRb from E2F transcription factors, thus allowing them to be functional and transactivate expression of the genes necessary for G1/S transition. This process is enhanced by the cyclin E-CDK2 complex, but inhibited by p21 [30]. We found that the level of p21 protein was increased as early as 12 h after cells were treated with 5 mM MAA (**Figure 5A-D**). However, surprisingly and interestingly, at 20 mM, MAA-induced p21 level reached a peak at 12 to 24 h, and then started

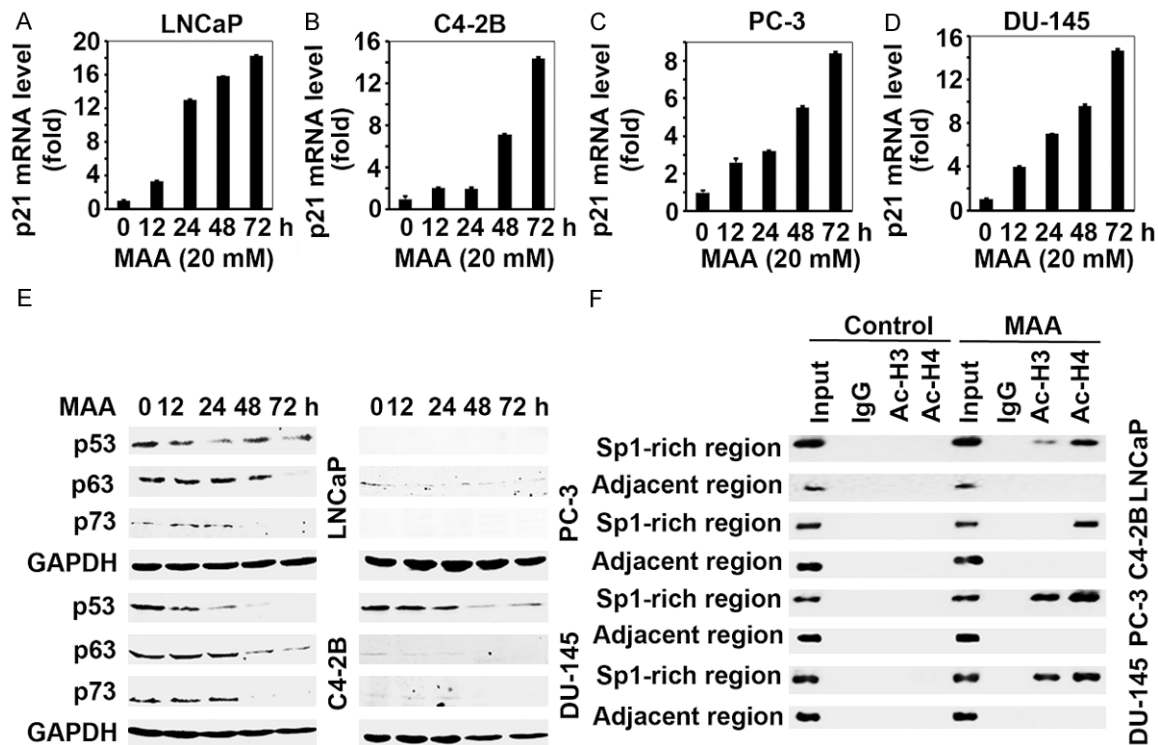


Figure 6. MAA enhances p21 transcription by inhibiting HDACs, independently of p53/p63/p73. A-D: Prostate cancer cells were treated with 20 mM MAA for up to 72 h. RNAs were analyzed with reverse transcription and quantitative PCR. Fold changes were calculated based on normalization to GAPDH levels and using the untreated control group as base line. The data are presented as the mean \pm SEM, $n = 3$. E: Prostate cancer cells were treated with 20 mM MAA for up to 72 h. Protein extracts were used for Western blot analysis of the indicated proteins. For the loading control, the blots were probed for GAPDH. F: Prostate cancer cells were treated with 20 mM MAA for 24 h and fixed in 1% formaldehyde. The chromatin preparations were immunoprecipitated with anti-acetyl-histone H3 (Ac-H3), anti-acetyl-histone H4 (Ac-H4), or control IgG, plus protein G magnetic beads. The purified DNAs were analyzed by PCR using primers specific for the Sp1 binding sites-rich region (Sp1-rich region) or the adjacent upstream region without Sp1 binding sites (Adjacent region). An aliquot of the chromatin preparations was used as Input control. PCR products were run on 2% agarose/ethidium bromide gel electrophoresis.

to drop down to the basal level from 48 h post treatment (**Figure 5E-H**). By contrast, CDK4 and CDK2 levels started to decrease in most of the four tested cell lines at 48 and 72 h after MAA treatment at 5 and 20 mM, whereas cyclin D1 levels were not dramatically altered after MAA treatment of all of the cell lines (**Figure 5A-H**). These results suggest that MAA may induce G1 arrest by increasing p21 level and decreasing the levels of CDK2 and CDK4.

MAA enhances p21 transcription by inhibiting HDACs

To further illustrate possible molecular mechanisms underlying p21 up-regulation by MAA, we first performed qPCR and found that MAA increased p21 mRNA levels as early as 12 h after its treatment at 20 mM, and p21 mRNA levels continued to rise over the 72 h treatment

period (**Figure 6A-D**). Since p21 transcription is often activated by the p53 family of genes [31, 32], we examined the levels of p53, p63, and p73 proteins. It is known that LNCaP and its derivative C4-2B cells harbor a wild-type TP53 gene, while DU-145 cells have a mutant TP53 gene, but PC-3 cells have a truncation mutation in the TP53 gene hence do not express p53 protein [33]. We found that none of p53, p63, and p73 protein expression was induced by MAA treatment; instead, they were decreased after 48 or 72 h in some cells, such as LNCaP, C4-2B and DU-145 (**Figure 6E**). Also, expression of p53 or p73 proteins was not detected in PC-3 cells, while a low level of p63 protein was present, but decreased during the treatment period (**Figure 6E**). Since it has been reported that p21 expression is repressed by HDAC1 and HDAC4 in a p53-independent mechanism

[34, 35], we examined whether MAA as an HDAC inhibitor could enhance binding of acetylated histone H3 and H4 to the Sp1 binding sites-rich region within the p21 promoter. We adopted the PCR primers spanning the Sp1 binding sites-rich region (abbreviated as Sp1-rich region) and the Sp1 binding sites-deficient adjacent region (abbreviated as adjacent region) used in a previous study [35]. We also used the same anti-acetylated histone H3 and H4 antibodies to perform ChIP analysis as previously described [34]. As shown in **Figure 6F**, MAA treatment increased binding of acetylated histone H3 and/or H4 to the Sp1-rich region of the p21 promoter, which was specific to this region as there was no increase in binding to the adjacent region (**Figure 6F**), suggesting that MAA might induce histone H3 and H4 acetylation at the p21 promoter region and thus open up the Sp1-binding DNA element to Sp1 that in turn activates the expression of p21 at the transcriptional level. Taken together, these results indicate that MAA induces p21 transcription by inhibiting HDAC activity and consequently leading to hyperacetylation of histone H3 and H4 and opening the promoter region of the p21 gene, in a p53 family independent manner.

Discussion

Prostate cancer, particularly castration-resistant prostate cancer, is lethal to the patients, as the currently available treatments can only extend patient's survival by 2.4 to 4.8 months [36]. Thus, new therapeutics are urgently needed for this type of malignancy. HDAC inhibitors can promote growth arrest, differentiation, and apoptosis of cancer cells, with minimal effects on normal tissues, thus HDAC inhibitors are emerging as promising anti-cancer drugs which possess tumor-selective cytotoxicity [37]. MAA has been demonstrated to be an HDAC inhibitor [17, 18], yet its anti-cancer potential has never been assessed. In the present study, we demonstrated that MAA suppressed the survival of four prostate cancer cell lines (LNCaP, C4-2B, PC-3, and DU-145) in a dose-dependent manner by inducing apoptosis and G1 arrest. Although MAA has been shown to cause apoptosis of spermatocytes (5), this cellular toxicity would be acceptable or minimal to most of the prostate cancer patients because the majority of the patients are 60 years or older who have passed their reproductive age [38]. MAA has been shown to be responsible for immunosup-

pression in rats, but it does not suppress humoral immunity in mice [39]. In humans, only a few cases were reported to have mild anemia and leukopenia in individuals exposed to ethylene glycol monomethyl ether [40]. Therefore, MAA is a promising chemical candidate for the treatment of prostate cancer.

MAA induces apoptosis of rat germ cells through release of mitochondrial cytochrome c, thus activating caspase 9 and caspase 3 [41]. Cytochrome c release from mitochondria is controlled by the antagonistic actions of pro-apoptotic and anti-apoptotic genes of the BCL2 family [42], which is true in rat germ cells [43]. However, we did not find any MAA-induced changes of BCL2, BAX, BCL2L1, BAD, BID, MCL1, and CFLAR in the four prostate cancer cell lines. Instead, we found that BIRC2 (also called cIAP1) protein expression was consistently decreased by MAA treatment in all four prostate cancer cell lines, which was specific to BIRC2 as BIRC3 (also called cIAP2) expression was not affected. BIRC2, like other IAP family proteins, has ubiquitin protein ligase (E3) activity [28]. BIRC2 binds to tumor necrosis factor receptor associated factor 2 (TRAF2) and becomes activated to initiate ubiquitination of receptor-interacting protein 1 (RIP1), subsequently inhibiting activation of caspase 8 [26]. However, we did not observe any MAA-induced activation of caspase 8 or other initiator caspases such as caspase 10, in the decrease of BIRC2 protein levels. On the other hand, we found activation of caspase 7 and caspase 3. Previously, it was found that although BIRC2 can bind to caspases 7 and 9, it is a weak inhibitor of caspases 9, 7, and 3 [44]. But later on, it was found that BIRC2 potentially inhibited activation of procaspase 3 by the cytochrome c-dependent apoptotic protease activating factor 1 (APAF1)-caspase 9 apoptosome complex [45]. This finding explains the observed activation of caspases 3 and 7 when MAA treatment decreased BIRC2 protein levels in our study. Of note, MAA treatment consistently increased the procaspase 9 protein level, though the mechanism of this action is not known. We and other investigators have previously noticed that some apoptosis-inducing chemicals can up-regulate procaspase 9 expression [20, 46]. Our speculation is that the increased procaspase 9 levels might be involved in activation of caspases 7 and 3, which awaits further verification.

Also, we showed that MAA causes G1 arrest in all of the four prostate cancer cell lines regardless of the status of p53. It is known that cyclin D-CDK4/6 complex phosphorylates pRb, leading to separation of pRb from E2F transcription factors, thus transactivating genes needed for the G1/S transition and S phase, including cyclin E. Then, activation of cyclin E-CDK2 complex further phosphorylates and completely releases pRb from interacting with E2Fs. However, association of p21 with cyclin D-CDK4/6 inhibits pRb phosphorylation and induces cell cycle arrest in G1 phase [30]. We found that MAA treatment induced up-regulation of p21 mRNA expression and protein expression. At the earlier time points, such as 12 and 24 h, p21 mRNA transcription could be responsible for the increase of its protein level by MAA. However, the protein level of p21 decreased after 24 h of MAA treatment at 20 mM (**Figure 5E-H**), which was inconsistent with the increase of its mRNA level (**Figure 6A-D**). The mechanism for this difference at later time points remains unclear, which is possibly caused by rapid degradation of p21 protein by caspase 3-mediated cleavage as shown in a previous study [47]. p21 is well known for its role in cell cycle arrest, yet p21 can also inhibit apoptosis by interacting with and inhibiting caspase 3 [48, 49]. On the other hand, active caspase 3 can cleave p21 protein, thus converting the cells from cell cycle arrest to apoptosis [47, 50]. This is consistent to our findings that procaspase 3 was dramatically cleaved hence activated at 48 to 72 h (**Figure 4E-H**), which then cleaved and degraded p21 protein (**Figure 5E-H**). Further, we found that at the high dose of 20 mM, MAA treatment also reduced the percentage of C4-2B and DU-145 cells in G2 phase (**Figure 3F, 3H**). This is possibly due to inhibition of cyclin A-CDK1/2 by p21, as it has been reported that p21 can induce G2 arrest [51], or due to loss of CDK2. On the other hand, we consistently found that 20 mM MAA treatment increased the percentage of LNCaP cells in G2 phase, but there were only few cells left in S phase (**Figure 3E**). We do not have a good explanation for this observation, which is unique only to LNCaP cell line at this 20 mM dose of MAA treatment. It is worthy notice that MAA-induced p21 up-regulation was independent of p53/p63/p73, as we did not find any induction of the p53 family proteins by MAA treatment, rather than seeing a slight decrease

of their expression (**Figure 6E**). Nevertheless, we found that MAA treatment increased binding of acetylated histone H3 and H4 to the Sp1 binding sites-rich region of p21 promoter, suggesting that MAA inhibits HDAC activities that repress p21 expression. Our findings are consistent with two previous studies showing that HDAC inhibitors up-regulate p21 expression through a Sp1-dependent, p53-independent mechanism [34, 35].

In addition, we also found that protein levels of CDK4 and CDK2, but not cyclin D1, were decreased by MAA treatment at 48 to 72 h. It has been demonstrated that CDK4 and CDK2 cooperate to phosphorylate pRb and drive G1/S transition, thus loss of both CDK4 and CDK2 leads to G1 arrest [52]. The timing of loss of CDK4 and CDK2 couples with reduction of p21 protein levels, particularly with 20 mM MAA treatment (**Figure 5E-H**), suggesting that in the absence of p21, loss of CDK4 and CDK2 becomes the main reason for G1 arrest. However, the mechanisms of how MAA treatment leads to loss of CDK4 and CDK2 are not clear, which requires further investigation.

In summary, the results as presented here demonstrate that MAA, as an HDAC inhibitor, can inhibit prostate cancer cell growth through induction of apoptosis and cell cycle arrest. MAA-induced apoptosis is likely due to down-regulation of the anti-apoptotic gene BIRC2, leading to activation of caspases 7 and 3 and turning on the downstream apoptotic events. MAA-induced G1 arrest is due to up-regulation of p21 expression at the early time and down-regulation of CDK4 and CDK2 expression at the late time post its treatment. MAA up-regulates p21 expression through inhibition of HDAC activities, independently of the p53 family members. Thus, our results strongly suggest that MAA could be developed into a potential therapy for prostate cancer.

Acknowledgements

The authors thank Mary Price from Tulane Cancer Center and Louisiana Cancer Research Consortium FACS Core for flow cytometry analysis. This work was supported in whole or in part by Department of Defense Health Program through the Prostate Cancer Research Program (W81XWH-14-1-0050, W81XWH-14-1-0149, and W81XWH-14-1-0458; the U.S. Army

Medical Research Acquisition Activity, 820 Chandler Street, Fort Detrick MD 21702-5014 is the awarding and administering acquisition office) and by National Institutes of Health (P20GM103518 and R01CA174714 to Z. Y.; 2G12MD007595 to G. W.). The content of this article is solely the responsibility of the authors and does not necessarily represent the official views of the National Institutes of Health or the Department of Defense.

Disclosure of conflicts of interest

The authors disclose no conflicts of interest.

Address correspondence to: Dr. Zongbing You, Department of Structural & Cellular Biology, Tulane University School of Medicine, 1430 Tulane Ave mailbox 8649, New Orleans, LA 70112, USA. Tel: 504-988-0467; Fax: 504-988-1687; E-mail: zyou@tulane.edu (Zongbing You); kparajuli55@gmail.com (Keshab R Parajuli)

References

- [1] Priyandoko D, Ishii T, Kaul SC and Wadhwa R. Ashwagandha leaf derived withanone protects normal human cells against the toxicity of methoxyacetic acid, a major industrial metabolite. *PLoS One* 2011; 6: e19552.
- [2] Shih TS, Liou SH, Chen CY and Smith TJ. Urinary 2-methoxy acetic acid accumulation in response to 2-methoxy ethanol exposure. *Arch Environ Health* 2001; 56: 20-25.
- [3] Groeseneken D, Veulemans H, Masschelein R and Van Vlem E. Experimental human exposure to ethylene glycol monomethyl ether. *Int Arch Occup Environ Health* 1989; 61: 243-247.
- [4] Correa A, Gray RH, Cohen R, Rothman N, Shah F, Seacat H and Corn M. Ethylene glycol ethers and risks of spontaneous abortion and subfertility. *Am J Epidemiol* 1996; 143: 707-717.
- [5] Welch LS, Schrader SM, Turner TW and Cullen MR. Effects of exposure to ethylene glycol ethers on shipyard painters: II. Male reproduction. *Am J Ind Med* 1988; 14: 509-526.
- [6] Terry KK, Elswick BA, Stedman DB and Welsch F. Developmental phase alters dosimetry-teratogenicity relationship for 2-methoxyethanol in CD-1 mice. *Teratology* 1994; 49: 218-227.
- [7] Henley DV, Mueller S and Korach KS. The short-chain fatty acid methoxyacetic acid disrupts endogenous estrogen receptor-alpha-mediated signaling. *Environ Health Perspect* 2009; 117: 1702-1706.
- [8] Tirado OM, Selva DM, Toran N, Suarez-Quian CA, Jansen M, McDonnell DP, Reventos J and Munell F. Increased expression of estrogen receptor beta in pachytene spermatocytes after short-term methoxyacetic acid administration. *J Androl* 2004; 25: 84-94.
- [9] Tirado OM, Martinez ED, Rodriguez OC, Danielsen M, Selva DM, Reventos J, Munell F and Suarez-Quian CA. Methoxyacetic acid dysregulation of androgen receptor and androgen-binding protein expression in adult rat testis. *Biol Reprod* 2003; 68: 1437-1446.
- [10] De Gendt K, Swinnen JV, Saunders PT, Schoonjans L, Dewerchin M, Devos A, Tan K, Atanassova N, Claessens F, Lecureuil C, Heyns W, Carmeliet P, Guillou F, Sharpe RM and Verhoeven G. A Sertoli cell-selective knockout of the androgen receptor causes spermatogenic arrest in meiosis. *Proc Natl Acad Sci U S A* 2004; 101: 1327-1332.
- [11] Roberts KP and Zirkin BR. Androgen regulation of spermatogenesis in the rat. *Ann N Y Acad Sci* 1991; 637: 90-106.
- [12] Abney TO. The potential roles of estrogens in regulating Leydig cell development and function: a review. *Steroids* 1999; 64: 610-617.
- [13] O'Donnell L, Robertson KM, Jones ME and Simpson ER. Estrogen and spermatogenesis. *Endocr Rev* 2001; 22: 289-318.
- [14] Bagchi G, Hurst CH and Waxman DJ. Interactions of methoxyacetic acid with androgen receptor. *Toxicol Appl Pharmacol* 2009; 238: 101-110.
- [15] Bagchi G, Zhang Y, Stanley KA and Waxman DJ. Complex modulation of androgen responsive gene expression by methoxyacetic acid. *Reprod Biol Endocrinol* 2011; 9: 42.
- [16] Bagchi G, Zhang Y and Waxman DJ. Impact of methoxyacetic acid on mouse Leydig cell gene expression. *Reprod Biol Endocrinol* 2010; 8: 65.
- [17] Jansen MS, Nagel SC, Miranda PJ, Lobenhofer EK, Afshari CA and McDonnell DP. Short-chain fatty acids enhance nuclear receptor activity through mitogen-activated protein kinase activation and histone deacetylase inhibition. *Proc Natl Acad Sci U S A* 2004; 101: 7199-7204.
- [18] Wade MG, Kawata A, Williams A and Yauk C. Methoxyacetic acid-induced spermatocyte death is associated with histone hyperacetylation in rats. *Biol Reprod* 2008; 78: 822-831.
- [19] Li X, Zhang J, Xie Y, Jiang Y, Yingjie Z and Xu W. Progress of HDAC inhibitor panobinostat in the treatment of cancer. *Curr Drug Targets* 2014; 15: 622-634.
- [20] Li Q, Lambrechts MJ, Zhang Q, Liu S, Ge D, Yin R, Xi M and You Z. Glyphosate and AMPA inhibit cancer cell growth through inhibiting intracellular glycine synthesis. *Drug Des Devel Ther* 2013; 7: 635-643.
- [21] You Z, Saims D, Chen S, Zhang Z, Guttridge DC, Guan KI, MacDougald OA, Brown AMC, Evan G,

- Kitajewski J and Wang CY. Wnt signaling promotes oncogenic transformation by inhibiting c-Myc-induced apoptosis. *J Cell Biol* 2002; 157: 429-440.
- [22] Ge D, Dauchy RT, Liu S, Zhang Q, Mao L, Dauchy EM, Blask DE, Hill SM, Rowan BG, Brainard GC, Hanifin JP, Cecil KS, Xiong Z, Myers L and You Z. Insulin and IGF1 enhance IL-17-induced chemokine expression through a GSK3B-dependent mechanism: a new target for melatonin's anti-inflammatory action. *J Pineal Res* 2013; 55: 377-387.
- [23] Takagi A, Yamada T, Hayashi K, Nakade Y, Kojima T, Takamatsu J, Shibata E, Ichihara G, Takeuchi Y and Murate T. Involvement of caspase 3 mediated apoptosis in hematopoietic cytotoxicity of metabolites of ethylene glycol monomethyl ether. *Ind Health* 2002; 40: 371-374.
- [24] You Z, Shi XB, DuRaine G, Haudenschild D, Tepper CG, Lo SH, Gandour-Edwards R, de Vere White RW and Reddi AH. Interleukin-17 receptor-like gene is a novel antiapoptotic gene highly expressed in androgen-independent prostate cancer. *Cancer Res* 2006; 66: 175-183.
- [25] Fang EF, Scheibye-Knudsen M, Brace LE, Kassahun H, SenGupta T, Nilsen H, Mitchell JR, Croteau DL and Bohr VA. Defective mitophagy in XPA via PARP-1 hyperactivation and NAD(+)/SIRT1 reduction. *Cell* 2014; 157: 882-896.
- [26] de Almagro MC and Vucic D. The inhibitor of apoptosis (IAP) proteins are critical regulators of signaling pathways and targets for anti-cancer therapy. *Exp Oncol* 2012; 34: 200-211.
- [27] Jin S, Kalkum M, Overholtzer M, Stoffel A, Chait BT and Levine AJ. cIAP1 and the serine protease HTRA2 are involved in a novel p53-dependent apoptosis pathway in mammals. *Genes Dev* 2003; 17: 359-367.
- [28] Yang Y, Fang S, Jensen JP, Weissman AM and Ashwell JD. Ubiquitin protein ligase activity of IAPs and their degradation in proteasomes in response to apoptotic stimuli. *Science* 2000; 288: 874-877.
- [29] McIlwain DR, Berger T and Mak TW. Caspase functions in cell death and disease. *Cold Spring Harb Perspect Biol* 2013; 5: a008656.
- [30] Jung YS, Qian Y and Chen X. Examination of the expanding pathways for the regulation of p21 expression and activity. *Cell Signal* 2010; 22: 1003-1012.
- [31] Lane D and Levine A. p53 Research: the past thirty years and the next thirty years. *Cold Spring Harb Perspect Biol* 2010; 2: a000893.
- [32] Riley T, Sontag E, Chen P and Levine A. Transcriptional control of human p53-regulated genes. *Nat Rev Mol Cell Biol* 2008; 9: 402-412.
- [33] Isaacs WB, Carter BS and Ewing CM. Wild-type p53 suppresses growth of human prostate cancer cells containing mutant p53 alleles. *Cancer Res* 1991; 51: 4716-4720.
- [34] Gui CY, Ngo L, Xu WS, Richon VM and Marks PA. Histone deacetylase (HDAC) inhibitor activation of p21WAF1 involves changes in promoter-associated proteins, including HDAC1. *Proc Natl Acad Sci U S A* 2004; 101: 1241-1246.
- [35] Mottet D, Pirotte S, Lamour V, Hagedorn M, Javerzat S, Bikfalvi A, Bellahcene A, Verdin E and Castronovo V. HDAC4 represses p21(WAF1/Cip1) expression in human cancer cells through a Sp1-dependent, p53-independent mechanism. *Oncogene* 2009; 28: 243-256.
- [36] Sartor O and Gillissen S. Treatment sequencing in metastatic castrate-resistant prostate cancer. *Asian J Androl* 2014; 16: 426-431.
- [37] Zhang L, Lei J, Shan Y, Yang H, Song M and Ma Y. Recent progress in the development of histone deacetylase inhibitors as anti-cancer agents. *Mini Rev Med Chem* 2013; 13: 1999-2013.
- [38] Siegel R, Ma J, Zou Z and Jemal A. Cancer statistics, 2014. *CA Cancer J Clin* 2014; 64: 9-29.
- [39] Riddle MM, Williams WC and Smialowicz RJ. Repeated high dose oral exposure or continuous subcutaneous infusion of 2-methoxyacetic acid does not suppress humoral immunity in the mouse. *Toxicology* 1996; 109: 67-74.
- [40] Larese F, Fiorito A and De Zotti R. The possible haematological effects of glycol monomethyl ether in a frame factory. *Br J Ind Med* 1992; 49: 131-133.
- [41] Rao AV and Shaha C. N-acetylcysteine prevents MAA induced male germ cell apoptosis: role of glutathione and cytochrome c. *FEBS Lett* 2002; 527: 133-137.
- [42] Yang J, Liu X, Bhalla K, Kim CN, Ibrado AM, Cai J, Peng TI, Jones DP and Wang X. Prevention of apoptosis by Bcl-2: release of cytochrome c from mitochondria blocked. *Science* 1997; 275: 1129-1132.
- [43] Yan W, Suominen J, Samson M, Jegou B and Toppari J. Involvement of Bcl-2 family proteins in germ cell apoptosis during testicular development in the rat and pro-survival effect of stem cell factor on germ cells in vitro. *Mol Cell Endocrinol* 2000; 165: 115-129.
- [44] Eckelman BP and Salvesen GS. The human anti-apoptotic proteins cIAP1 and cIAP2 bind but do not inhibit caspases. *J Biol Chem* 2006; 281: 3254-3260.
- [45] Burke SP, Smith L and Smith JB. cIAP1 cooperatively inhibits procaspase-3 activation by the caspase-9 apoptosome. *J Biol Chem* 2010; 285: 30061-30068.
- [46] Wong RP, Tsang WP, Chau PY, Co NN, Tsang TY and Kwok TT. p53-R273H gains new function in induction of drug resistance through down-regulation of procaspase-3. *Mol Cancer Ther* 2007; 6: 1054-1061.

- [47] Zhang Y, Fujita N and Tsuruo T. Caspase-mediated cleavage of p21Waf1/Cip1 converts cancer cells from growth arrest to undergoing apoptosis. *Oncogene* 1999; 18: 1131-1138.
- [48] Suzuki A, Kawano H, Hayashida M, Hayasaki Y, Tsutomi Y and Akahane K. Procaspase 3/p21 complex formation to resist fas-mediated cell death is initiated as a result of the phosphorylation of p21 by protein kinase A. *Cell Death Differ* 2000; 7: 721-728.
- [49] Suzuki A, Tsutomi Y, Miura M and Akahane K. Caspase 3 inactivation to suppress Fas-mediated apoptosis: identification of binding domain with p21 and ILP and inactivation machinery by p21. *Oncogene* 1999; 18: 1239-1244.
- [50] Jin YH, Yoo KJ, Lee YH and Lee SK. Caspase 3-mediated cleavage of p21WAF1/CIP1 associated with the cyclin A-cyclin-dependent kinase 2 complex is a prerequisite for apoptosis in SK-HEP-1 cells. *J Biol Chem* 2000; 275: 30256-30263.
- [51] Niculescu AB 3rd, Chen X, Smeets M, Hengst L, Prives C and Reed SI. Effects of p21(Cip1/Waf1) at both the G1/S and the G2/M cell cycle transitions: pRb is a critical determinant in blocking DNA replication and in preventing endoreduplication. *Mol Cell Biol* 1998; 18: 629-643.
- [52] Berthet C, Klarmann KD, Hilton MB, Suh HC, Keller JR, Kiyokawa H and Kaldis P. Combined loss of Cdk2 and Cdk4 results in embryonic lethality and Rb hypophosphorylation. *Dev Cell* 2006; 10: 563-573.

Article

Aminomethylphosphonic Acid and Methoxyacetic Acid Synergistically Induce Apoptosis in Prostate Cancer Cells

Keshab R. Parajuli¹, Qiuyang Zhang¹, Sen Liu¹, and Zongbing You^{1*}

¹Departments of Structural & Cellular Biology and Orthopaedic Surgery, Tulane Cancer Center and Louisiana Cancer Research Consortium, Tulane Center for Stem Cell Research and Regenerative Medicine, Tulane Center for Aging, Tulane University, New Orleans, Louisiana 70112, USA; E-Mails: kparajuli55@gmail.com (K.R.P.); qzhang3@tulane.edu (Q.Z.); senliu@yahoo.com (S.L.)

* Author to whom correspondence should be addressed; E-Mail: zyou@tulane.edu;

Tel.: +1-504-988-0467; Fax: +1-504-988-1687.

Academic Editor:

Received: / Accepted: / Published:

Abstract: Aminomethylphosphonic acid (AMPA) and its parent compound herbicide glyphosate are analogs to glycine, an amino acid, which has been reported to inhibit proliferation and promote apoptosis of cancer cells but not normal cells. Methoxyacetic acid (MAA) is the active metabolite of ester phthalates widely used in industrial as gelling, viscosity and stabilizer; its exposure is associated with developmental and reproductive toxicities in both rodents and humans. MAA has been reported to suppress prostate cancer cell growth by inducing growth arrest and apoptosis. However, it is unknown whether AMPA and MAA can synergistically suppress cancer cell growth. In this study, we found that AMPA and MAA inhibited cell growth in prostate cancer cell lines (LNCaP, C4-2B, PC-3, and DU-145) through induction of apoptosis and cell cycle arrest at G1 phase. Importantly, The AMPA-

induced apoptosis was synergistically increased with addition of MAA, which was due to down-regulation of the anti-apoptotic gene baculoviral inhibitor of apoptosis protein repeat containing 2 (BIRC2), leading to activation of caspases 7 and 3. These results demonstrate that combination of AMPA and MAA can promote apoptosis of prostate cancer cells, suggesting that they can be used as potential therapeutic drugs in the treatment of prostate cancer.

Keywords: Prostate cancer cells; cell death; apoptosis; AMPA; MAA

1. Introduction

Aminomethylphosphonic acid (AMPA, linear chemical formula: $\text{CH}_6\text{NO}_3\text{P}$) is the primary degradation product of glyphosate [N-(phosphonomethyl)glycine], which is a broad-spectrum systemic herbicide used to kill weeds, especially annual broadleaf weeds and grasses known to compete against commercial crops grown around the globe [1]. In the environment, glyphosate can be naturally converted into AMPA [2]. AMPA has no significant toxicity in acute, subchronic, and chronic animal studies, nor any genotoxicity, teratogenicity, or carcinogenicity [3,4]. When AMPA was administered via gavage at a dose of 6.7 mg/kg in rats, approximately 20% of AMPA was absorbed and 74% of the administered dose was excreted in the feces over a 5-day period of experimental observation. The absorbed AMPA was not bio-transformed and was excreted rapidly in the urine with approximately 65% of the absorbed dose eliminated in the urine within 12 hours (h) and essentially 100% excreted between 24 and 120 h. Only trace residues were detected in various organs including liver, kidney, and skeletal muscle 5 days after dosing [3,4]. AMPA and glyphosate are analogs to glycine. Glycine is not an essential amino acid to the human diet as it is biosynthesized in the body from the amino acid serine, which is in turn derived from 3-phosphoglycerate. Serine hydroxymethyltransferase (SHMT) can reversibly catalyze the conversion of serine to glycine and vice versa in mammalian cells. The main function of glycine is as a precursor to proteins. It is also a building block to numerous natural products. Recently, glycine was revealed to play a key role in rapid cancer cell proliferation [5]. In rapidly proliferating cancer cells, there is an increased reliance on glycine metabolism, a phenotype

that was not observed in rapidly proliferating non-transformed cells [5]. Glycine metabolism may therefore represent a metabolic vulnerability in rapidly proliferating cancer cells that may be targeted for therapeutic benefits. As analogs to glycine, glyphosate and AMPA were also found to inhibit proliferation and promote apoptosis in cancer cells but not in normal cells in our previous study [6]. However, higher concentrations of this chemical may affect normal cells and produce adverse side effects. One of the strategies to improve AMPA's inhibitory actions on cancer cells and reduce its side effects is to find a compound that can synergistically increase AMPA's efficacy, thus reducing its dosage.

Methoxyacetic acid (MAA) is the primary active metabolite of ester phthalates widely used in industry as gelling, viscosity and stabilizer reagents [7]. MAA exposure is associated with various developmental and reproductive toxicities in both rodents and humans, including neural toxicity, blood and immune disorders, limb degeneration and testicular toxicity [8-10]. The mechanisms of MAA-induced toxicities are multiple. MAA induces production of reactive oxygen species, resulting in DNA damage and loss of mitochondrial membrane potential in normal human fibroblasts [7]. MAA treatment alters the expression of androgen receptor (AR) and androgen-binding protein (ABP) in a stage-specific manner in rat seminiferous tubules [12]. MAA treatment down-regulates the expression of estrogen receptor α (ER α) and estradiol-induced gene expression in human breast cancer cell line MCF-7 and mouse uterus [11], but increases ER β expression by inducing apoptosis in pachytene spermatocytes in rats [12]. MAA has been found to activate the tyrosine kinase-PI3K pathway and other pathways to enhance or antagonize androgen-induced gene expression [9,10,13]. Similarly, MAA can activate MAPK and inhibit histone deacetylases (HDACs), increasing the levels of acetylated histone H4, like the other well-known HDAC inhibitors such as trichostatin, valproic acid, and butyric acid [14]. In fact, it has been reported that MAA-induced hyperacetylation of histone H3 and H4 is associated with rapid spermatocyte death [15]. Some HDAC inhibitors (suberanilohydroxamic acid and romidepsin) have been approved for the treatment of cutaneous T cell

lymphoma, while panobinostat and valproic acid are being tested in the treatment of prostate cancer, breast cancer, cervical cancer, ovarian cancer, and lymphomas [16]. We have previously shown that MAA can induce apoptosis and growth arrest of prostate cancer cells [17].

In the present study, we tested the effects of a combination of AMPA and MAA on two immortalized human normal prostatic epithelial cell lines (RWPE-1 and pRNS-1-1) and four human prostate cancer cell lines (LNCaP, C4-2B, PC-3, and DU-145). We found that the combination of AMPA and MAA significantly induced apoptosis and growth arrest of prostate cancer cells. The apoptosis induced by the combination of AMPA and MAA was highly associated with decreased protein expression of baculoviral inhibitor of apoptosis protein repeat containing 2 (BIRC2), whereas the G1 arrest caused by the combination of AMPA and MAA was closely associated with induction of p21 and reduction of cyclin D3. BIRC2 is also named cellular inhibitor of apoptosis protein (cIAP) 1 [18]. cIAP1 and cIAP2 have an N-terminal BIRC domain and a C-terminal ring domain that confers E3 ubiquitin ligase activity. cIAP2 also contain a caspase recruitment domain (CARD) which is involved in auto inhibition of their E3 ligase activity [19]. It is known that BIRC2 inhibits caspases 7 and 3 [20]. Therefore, decreased cIAP1 leads to activation of caspases 7 and 3 and thus inducing apoptosis. Our findings suggest that MAA can synergistically increase AMPA's anti-cancer activities by inhibiting anti-apoptotic protein and activating pro-apoptotic proteins.

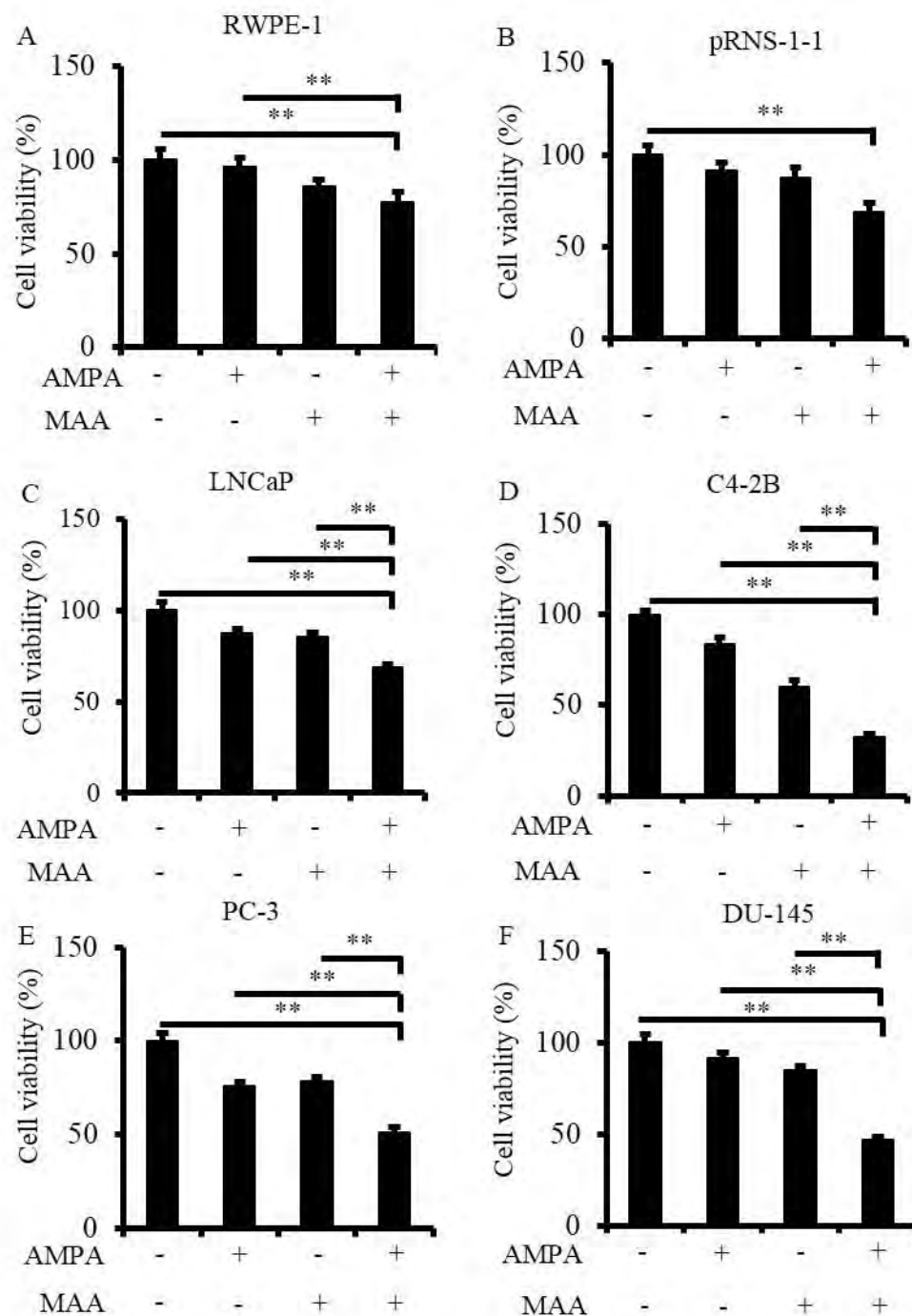
2. Results and Discussion

2.1. AMPA and MAA Combination Inhibits Prostate Cancer Cell Viability

Therapy for advanced prostate cancer centers on suppressing systemic androgens and blocking activation of the androgen receptor. However, nearly all patients develop castration-resistant prostate cancer (CRPC). The currently available treatments on CRPC can only extend patient's survival by 2.4 to 4.8 months [21]. Thus, new therapeutics is urgently needed for this type of malignancy. Based on our previous study, AMPA and MAA both have inhibitory effects on prostate cancer cells. In order to

enhance AMPA's efficacy and reducing its dosage, we investigated the effects of a combination of AMPA and MAA on the growth of prostate cancer cells. Our previous studies showed that 50 mM AMPA and 20 mM MAA can significantly inhibit the growth of prostate cancer cell individually [6,17]. In the present study we used 15 mM AMPA and 5 mM MAA to treat the two immortalized human normal prostatic epithelial cell lines (RWPE-1 and pRNS-1-1) and four prostate cancer cell lines (LNCaP, C4-2B, PC-3, and DU-145) alone or in combination. We found that the number of viable cells was decreased by approximately 9% to 24% or 15% to 40% in the four prostate cancer cells compared to 4% to 9% or 12% to 14% in normal prostatic epithelial cells, respectively, when treated with AMPA or MAA alone. However, the number of viable cell decreased by 32% to 68% in the four prostate cancer cells, compared to 22% and 31% in RWPE-1 and pRNS-1-1 cells when treated with the combination of AMPA and MAA (Figure 1A-F). Thus, MAA obviously has additive or synergistic effect with AMPA, especially on the rapidly proliferating prostate cancer cells, but less so on the normal prostatic cells. At these dosages, AMPA has little effect on normal prostatic cells. Although MAA has been reported to be a testicular toxicant in mammals [22,23], this toxicity would be acceptable to most of the prostate cancer patients, since the majority of the patients are old who have passed their reproductive age [15]. Therefore, AMPA and MAA combination appears to be a promising therapy in the treatment of prostate cancer.

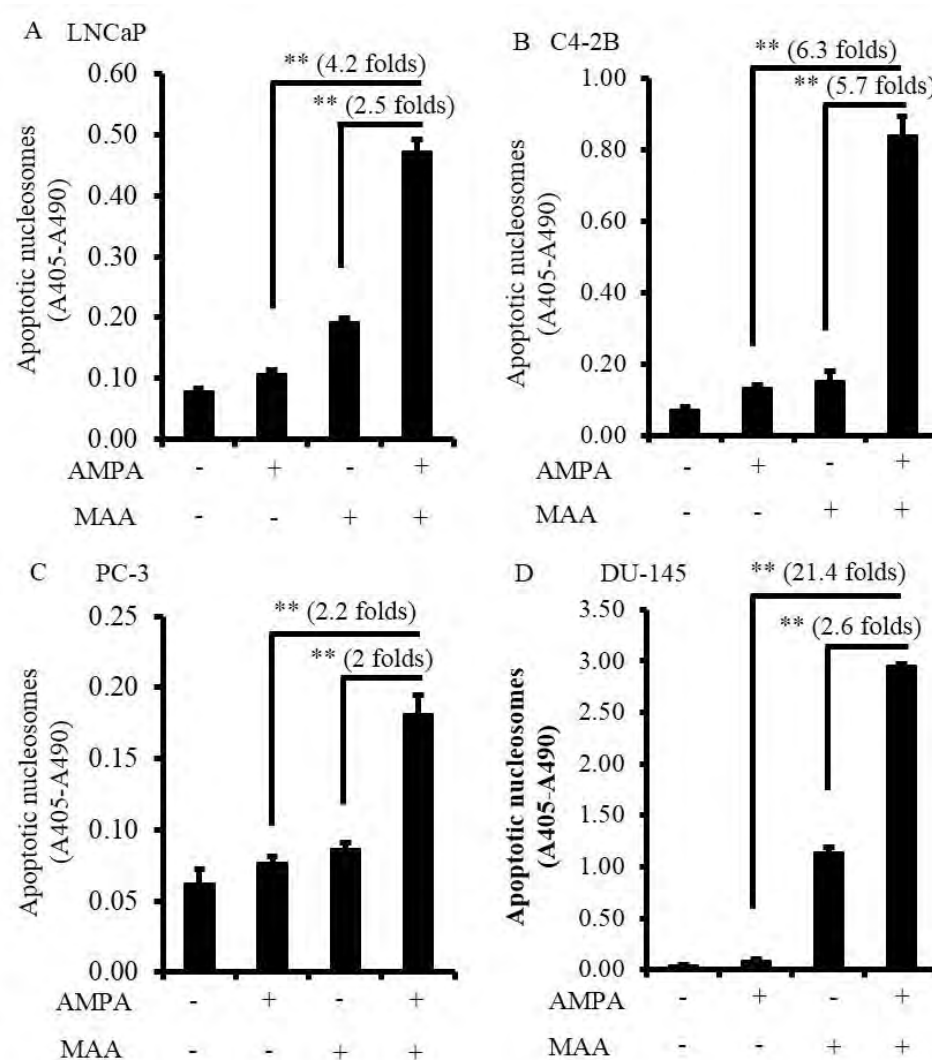
Figure 1. Combination of AMPA and MAA suppresses cancer cell viability. (A-F): Normal prostate epithelial cells and prostate cancer cells were plated in 96-well plates in triplicate per group and then treated with 15 mM AMPA, 5 mM MAA, and combination of both for 72 h. The viable cells were measured using the CellTiter-Glo® Luminescent Cell Viability Assay. The data are presented as the mean \pm SEM of three independent experiments (n=3). *p<0.05; **p<0.01.



2.2. Combination of AMPA and MAA Synergistically Induces Apoptosis in Prostate Cancer Cells

To know why the combination of AMPA and MAA can inhibit prostate cancer cell growth, we measured the apoptotic nucleosomes in the cells treated with 15 mM AMPA and 5 mM MAA, either alone or in combination for 24 h. Although the induced apoptotic nucleosomes were slightly increased when treated with AMPA or MAA alone compared to the non-treated cells, the combination of AMPA and MAA increased the apoptotic nucleosomes by 4.2 and 2.5 folds in LNCaP cells, by 6.3 and 5.7 folds in C4-2B cells, by 2.1 and 2 folds in PC3 cells, and by 21.4 and 2.6 folds in DU-145 cells, compared to the treatment with AMPA or MAA alone (Figure 2A-D). These results indicated that AMPA and MAA at low concentrations have a synergistic effect on prostate cancer cells.

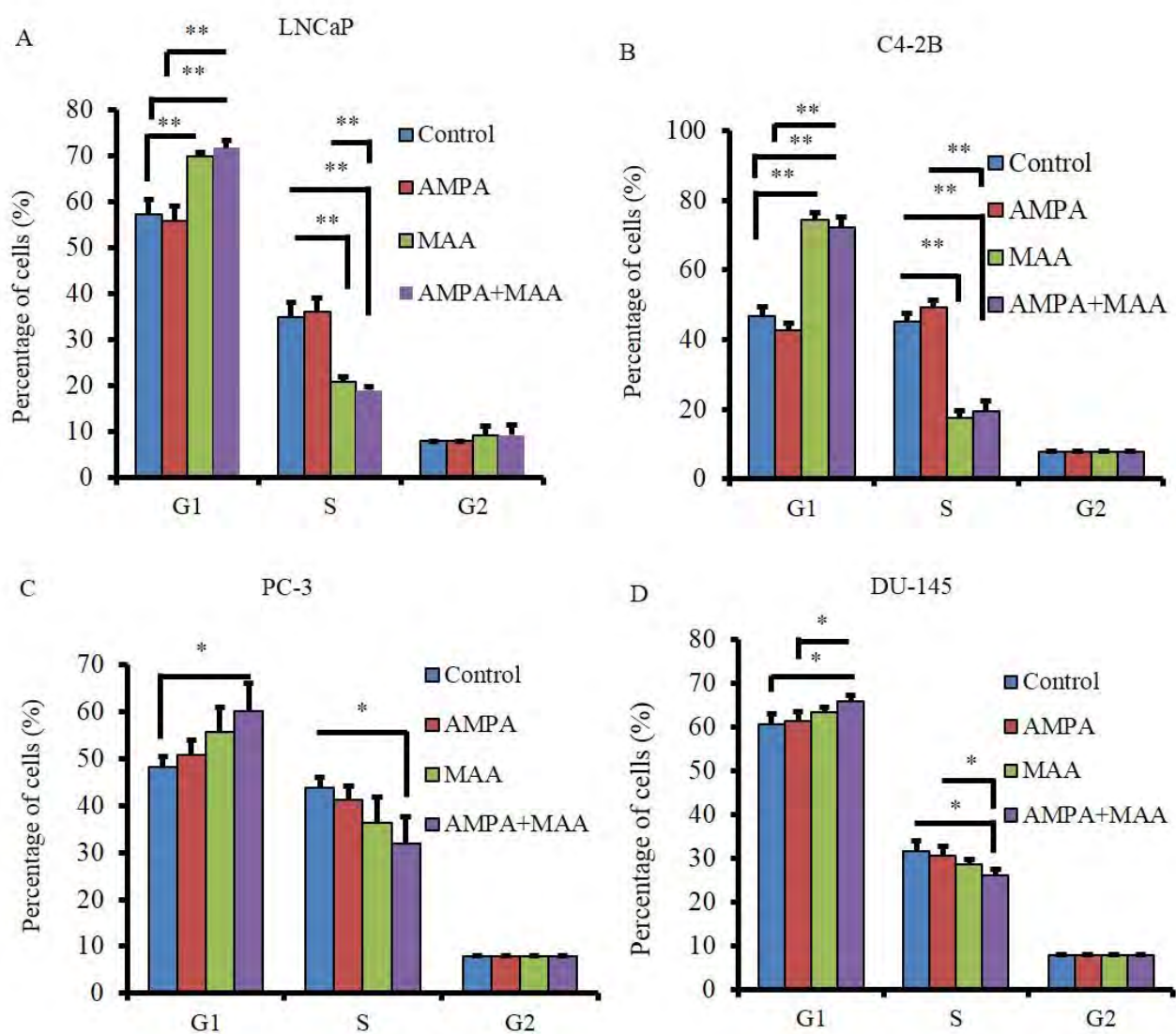
Figure 2. AMPA and MAA combination induces apoptosis in prostate cancer cells. **A-D:** Prostate cancer cells were plated in 12-well plates in triplicate per group and treated with 15 mM AMPA, 5 mM MAA, and combination of AMPA and MAA for 24 h. Apoptotic nucleosomes were measured using the Cell Death Detection ELISA kit. Apoptotic nucleosomes were calculated by absorbance at 405 nm (A405) - absorbance at 490 nm (A490). The data are presented as the mean \pm SEM of three independent experiments (n=3). *p<0.05; **p<0.01.



2.3. Combination of AMPA and MAA Blocks Entry of Cells from G1 to S Phase of Cell Cycle

To determine if the combination of AMPA and MAA induces cell cycle arrest, we treated four types of prostate cancer cells for 24 h and analyzed the percentage of cells in the G1 (and G0), S, and G2 (and M) phase of the cell cycle using flow cytometry analysis. We found that MAA alone increased the percentage of LNCaP and C4-2B cells at the G1/G0 phase and decreased the percentage of cells at S phase (Figure 3A and 3B, $p < 0.01$), whereas MAA alone did not have significant effects in PC-3 and DU-145 cells (Figure 3C and 3D, $p > 0.05$). However, the combination of AMPA and MAA significantly increased the percentage of PC-3 and DU-145 cells at the G1/G0 phase and decreased the percentage of cells at the S phase, whereas the number of cells in the G2/M phase was not affected (Figure 3C-D, $p < 0.05$). In addition, there were not any significant differences in all four cell lines when treated with AMPA alone (Figure 3A-D, $p > 0.05$). These results indicated that the combination of AMPA and MAA blocks the G1/S transition in PC-3 and DU-145 cell lines. Our previous study demonstrated that AMPA at 50 mM can arrest cancer cells in the G1/G0 phase of cell cycle, thus inhibiting entry into the S phase [6]. MAA has also been demonstrated to be a HDAC inhibitor [14,15], which suppresses the growth of four prostate cancer cell lines (LNCaP, C4-2B, PC-3, and DU-145) in a dose dependent manner by inducing apoptosis and G1 arrest.

Figure 3. AMPA and MAA blocks G1/S transition of prostate cancer cell cycle. (A-D): Prostate cancer cells were plated in 60-mm dishes in triplicate per group and treated with 15 mM AMPA, 5 mM MAA, alone or in combination for 24 h. The control groups was treated with PBS. The percentages of cells at G1 (and G₀), S and G2 (and M) phases were determined by flow cytometry analysis. The data are presented as the mean \pm SEM of three independent experiments (n=3). *p<0.05; **p<0.01.



2.4. AMPA and MAA Combination Induces Changes in Expression Levels of Genes Involved in Cell Cycle and Apoptosis

To study the genes involved in cell cycle arrest and apoptosis in prostate cancer cells treated with the combination of AMPA and MAA, we did Western blot analysis of the protein expression. We found that the combination treatment clearly increased the levels of cleaved poly (ADP-ribose) polymerase (PARP) in C4-2B, PC-3, and DU-145 cell lines in a time-dependent manner compared to the cells treated with AMPA or MAA alone (Figures 5, 6, 7), though there was no obvious increase in LNCaP cell line (Figure 4). PARP cleavage has been widely used as an indicator of apoptosis marker [24,25]. This finding confirmed that the combination of AMPA and MAA induced apoptosis in prostate cancer cells.

We found that the combination treatment clearly decreased the protein levels of BIRC2 in all four prostate cancer cell lines and decreased BIRC3 levels in C4-2B and DU-145 cells at late time points (48 and 72 h) (Figures 4-7). The protein level of BIRC2 was decreased more obviously than that of BIRC3, which is another member of the IAP family [26]. It has been shown that proteasome-mediated degradation of BIRC2 can relieve the inhibitory function of BIRC2 on caspases, thus activating caspase-mediated apoptosis [27,28]. We found that the combination of AMPA and MAA increased the levels of procaspase 9 starting from 24 h or 48 h in C4-2B, PC-3, and DU-145 cell lines (Figures 5-7). In contrast, the combination of AMPA and MAA decreased the levels of procaspases 7 and 3 at different time points (12, 24, 48, and 72 h) (Figures 4-7). The increases of procaspase 9 levels and simultaneously decreases of procaspase 3 levels induced by the combination of AMPA and MAA may mediate apoptosis as shown in a previous study [29]. The decrease of procaspase 3 indicated cleavage of the proenzyme and activation of caspase 3, which is a key executioner caspase [30]. The previous study demonstrated that MAA induces apoptosis of rat germ cells through release of mitochondrial cytochrome c, which further activating caspase 9 and 3 [31]. BIRC2 has also been reported to be able to bind to caspases 7 and 9, thus serving as a weak inhibitor of caspases 9, 7, and 3 [32]. Later on, it

was found that BIRC2 potently inhibited activation of procaspase 3 [33]. Thus, the decreased levels of procaspases 7 and 3 may be due to down-regulation of BIRC2.

We further checked the protein levels of p53 and its downstream gene p21. We found that the combination of AMPA and MAA obviously increased the levels of p21 at 12 h after treatment in LNCaP, C4-2B and DU-145 cells (Figures 4, 5, 7), and at a later time point in PC-3 cell (Figure 6). However, the levels of p53 protein were decreased slightly in the cells upon the combination treatment. Therefore, the induced expression of p21 in the cells under the combination treatment is independent of p53 protein level. This result is consistent with the previous study showing that MAA induces p21 transcription through inhibition of HDAC activities, in a p53 family-independent manner [17]. In addition, the protein levels of cyclin D3 were decreased in the cells under the combination treatment compared to the cells treated with AMPA or MAA alone (Figures 4-7). The down-regulated cyclin D3 may contribute to the cell cycle inhibition [32]. The combination of AMPA and MAA increased p21 and decreased protein level of cyclin D3, thus inducing G1 arrest.

Taken together, the combination of AMPA and MAA at low doses significantly induced apoptosis, and to a lesser extent, cell cycle arrest, in four prostate cancer cell lines in the present *in vitro* study. These findings suggest that a further *in vivo* study is warranted to test if the combined AMPA and MAA treatment may efficaciously inhibit prostate tumor growth in animals. Based on the present *in vitro* study, it appears that the combined AMPA and MAA treatment may be of potential in the treatment of prostate cancer.

Figure 4. AMPA and MAA induce changes in the expression levels of genes involved in cell cycle arrest and apoptosis. LNCaP cells were exposed to 15 mM AMPA, 5 mM MAA or a combination of both AMPA and MAA for different time periods. The protein extracts were analyzed by Western blot to detect the indicated proteins. Glyceraldehyde 3-phosphate dehydrogenase (GAPDH) was probed as the loading control.

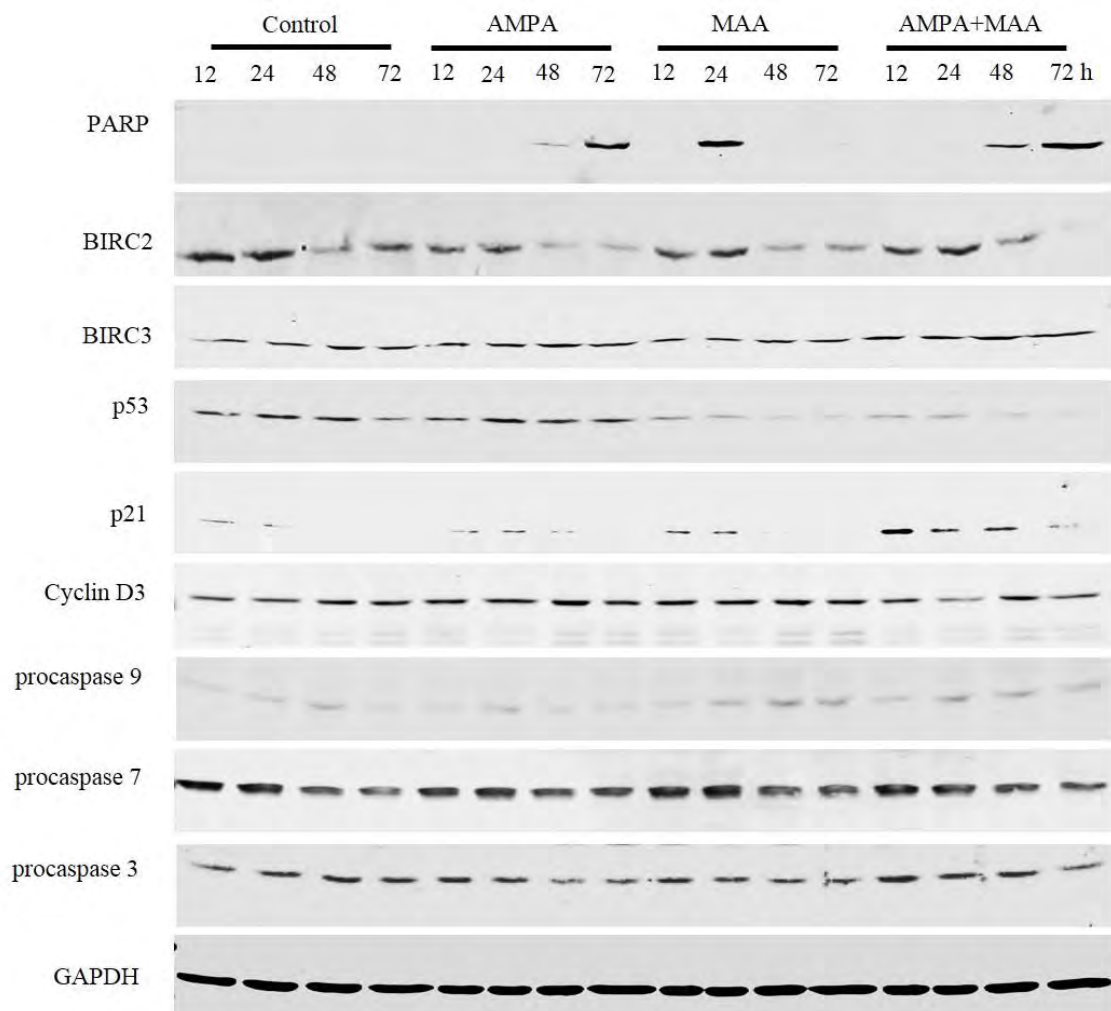


Figure 5. AMPA and MAA induce changes in the expression levels of genes involved in cell cycle arrest and apoptosis. C4-2B cells were exposed to 15 mM AMPA, 5 mM MAA or a combination of both AMPA and MAA for different time periods. The protein extracts were analyzed by Western blot to detect the indicated proteins. GAPDH was probed as the loading control.

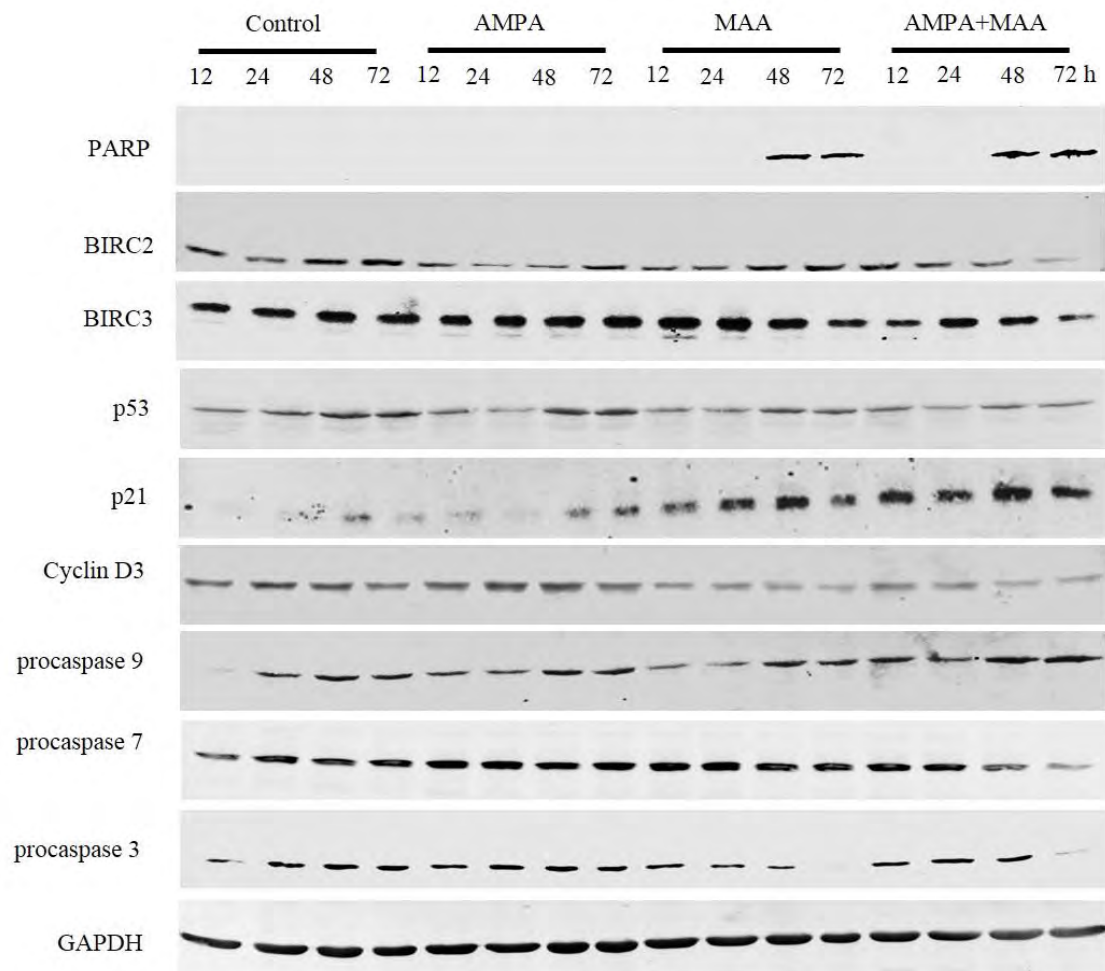
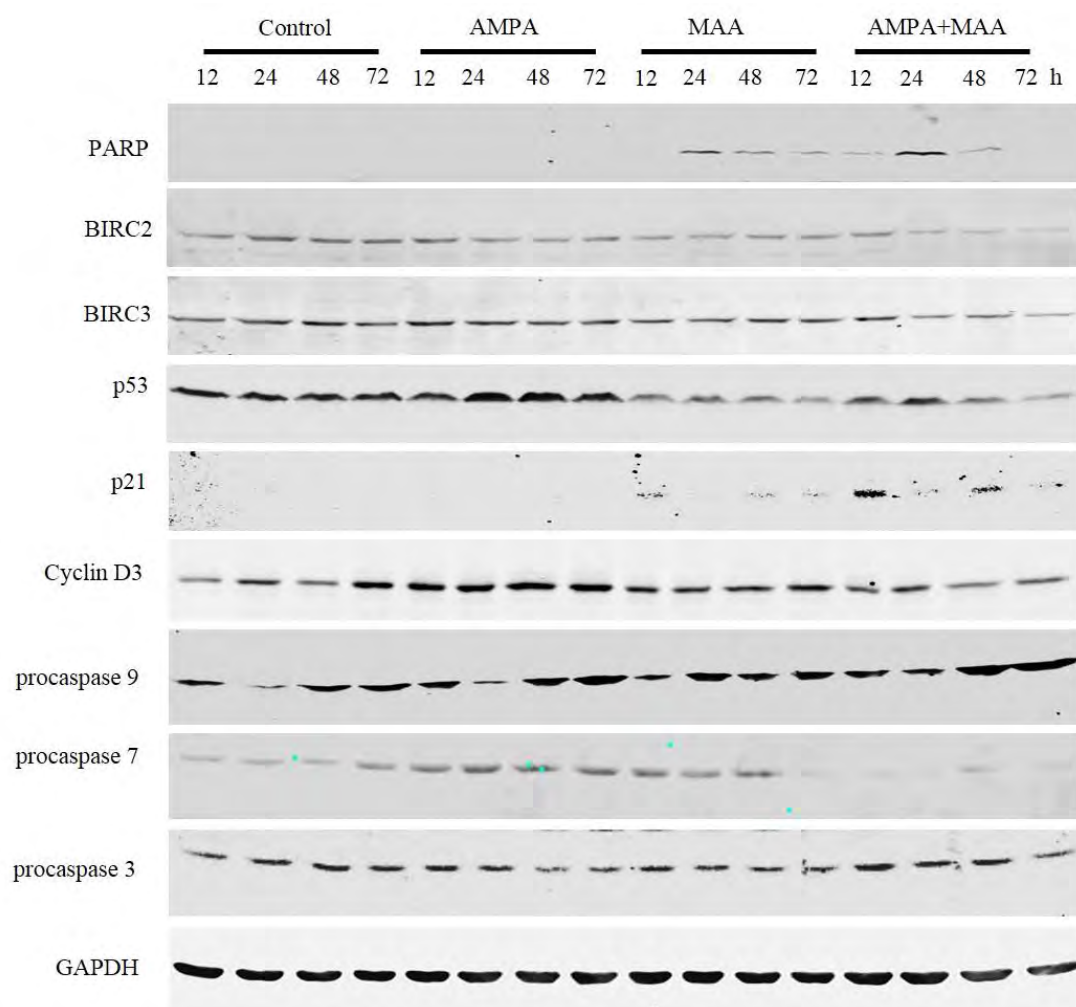


Figure 7. AMPA and MAA induce changes in the expression levels of genes involved in cell cycle arrest and apoptosis. DU-145 cells were exposed to 15 mM AMPA, 5 mM MAA or a combination of both AMPA and MAA for different time periods. The protein extracts were analyzed by Western blot to detect the indicated proteins. GAPDH was probed as the loading control.



3. Experimental Section

3.1. Cell Culture

The sources and cell culture conditions of two immortalized human normal prostatic epithelial cell lines (RWPE-1 and pRNS-1-1) and four human prostate cancer cell lines (LNCaP, C4-2B, PC-3, and DU-145) were described previously [6]. Cells were cultured in a 5% CO₂ humidified incubator at 37°C.

3.2. Cell Viability Assay

The number of live cells was determined using the CellTiter-Glo Luminescent Cell Viability Assay (Promega Corp, Fitchburg, WI, USA) as described previously [6]. Cell viability was calculated as (luminescence of the treatment group – background luminescence) ÷ (luminescence of the control group – background luminescence) × 100%. The data are presented as the mean and standard error of the mean (SEM) of three independent experiments.

3.3. Detection of Apoptotic Nucleosomes

Cells were seeded on 12-well plates with 1×10^5 cells/well in triplicate per group in the complete culture medium with fetal bovine serum (FBS). After overnight incubation, cells were treated with 15 mM AMPA, 5 mM MAA, and AMPA and MAA combination for 24 h; a control group was treated with phosphate-buffered saline (PBS). Apoptotic nucleosomes were detected using Cell Death Detection ELISA kit (Roche Diagnostics Corporation, Indianapolis, IN, USA) according to the manufacturer's instructions [34]. Absorbance was measured at 405 nm (A405) with a reference wavelength at 490 nm (A490) using a plate reader (Bio-Tek U.S., Winooski, VT, USA). The amount of apoptotic nucleosomes was represented by A405-A490.

3.4. Cell Cycle Analysis

Cells were treated without or with 15 mM AMPA or 5 mM MAA or AMPA, and MAA combination for 24 h. The percentage of cells at G1/G0, S, and G2/M phases were determined by flow cytometry analysis as described previously [6].

3.5. Western Blot Analysis

Cells were treated without or with 15 mM AMPA, 5 mM MAA, or AMPA and MAA combination for 0, 12, 24, 48, and 72 h. Proteins were extracted for Western blot analysis as described previously [6]. Rabbit anti-caspase 9, rabbit anti-caspase 7 and mouse anti-cyclin D3 antibodies were purchased from Cell Signaling Technology (Danvers, MA, USA). Mouse anti-p53, rabbit anti-BIRC2, and rabbit anti-BIRC3 antibodies were obtained from Santa Cruz Biotechnology (Dallas, TX, USA). Mouse anti-GAPDH, mouse anti-caspase 3, and rabbit anti-cleaved poly (ADP-ribose) polymerase (PARP) antibodies were purchased from EMD Millipore Corp (Billerica, MA, USA). Rabbit anti-p21 antibody was bought from Abcam, Cambridge, MA, USA.

3.6. Statistical Analysis

Results from this study were presented as the mean \pm SEM. Statistical analysis was performed using two-tailed Student's *t* test. A *p*-value < 0.05 was considered statistically significant.

4. Conclusions

The present study demonstrated that a combination of AMPA and MAA can inhibit prostate cancer cell growth through inducing apoptosis and cell cycle arrest. Induction of apoptosis may be due to down-regulation of BIRC2 (cIAP1), leading to activation of pro-apoptotic factors such as caspases 7 and 3. Induction of cell cycle arrest may be due to up-regulation of p21 expression at the early time and down-regulation of cyclin D3 expression at the late time. These findings suggest that AMPA and MAA combination may have potentials in the treatment of prostate cancer.

Acknowledgements

The authors thank Mary Price from Tulane Cancer Center and Louisiana Cancer Research Consortium FACS Core for flow cytometry analysis. This work was supported in whole or partially by Department of Defense Health Program through the Prostate Cancer Research Program (W81XWH-14-1-0050, W81XWH-14-1-0149, and W81XWH-14-1-0458; the U.S. Army Medical Research Acquisition Activity, 820 Chandler Street, Fort Detrick MD 21702-5014 is the awarding and administering acquisition office) and by National Institutes of Health (P20GM103518 and R01CA174714). The content of this article is solely the responsibility of the authors and does not necessarily represent the official views of the National Institutes of Health or the Department of Defense.

Author Contributions

K.R.P. designed the study, performed the experiment, analyzed and interpreted the data, and prepared the first draft of the manuscript. S.L. contributed to the design and statistical analysis. Q.Z. contributed to the design, data analysis, and revision of the manuscript. Z.Y. developed the concept of study, data analysis, and revision of the manuscript. All authors read and approved the final manuscript.

Conflicts of Interest

The authors declare no conflict of interests.

References

1. Kudzin, Z.H.; Gralak, D.K.; Drabowicz, J.; Luczak, J. Novel approach for the simultaneous analysis of glyphosate and its metabolites. *J Chromatogr A* **2002**, *947*, 129-141.
2. Vereecken, H. Mobility and leaching of glyphosate: A review. *Pest Manag Sci* **2005**, *61*, 1139-1151.

3. World Health Organization (WHO). Glyphosate and AMPA in drinking-water. Background document for development of WHO guidelines for drinking-water quality. Geneva: WHO; 2005.
4. Williams, G.M.; Kroes, R.; Munro, I.C. Safety evaluation and risk assessment of the herbicide roundup and its active ingredient, glyphosate, for humans. *Regul Toxicol Pharmacol* **2000**, *31*, 117-165.
5. Jain, M.; Nilsson, R.; Sharma, S.; Madhusudhan, N.; Kitami, T.; Souza, A.L.; Kafri, R.; Kirschner, M.W.; Clish, C.B.; Mootha, V.K. Metabolite profiling identifies a key role for glycine in rapid cancer cell proliferation. *Science* **2012**, *336*, 1040-1044.
6. Li, Q.; Lambrechts, M.J.; Zhang, Q.; Liu, S.; Ge, D.; Yin, R.; Xi, M.; You, Z. Glyphosate and ampa inhibit cancer cell growth through inhibiting intracellular glycine synthesis. *Drug Des Devel Ther* **2013**, *7*, 635-643.
7. Priyandoko, D.; Ishii, T.; Kaul, S.C.; Wadhwa, R. Ashwagandha leaf derived withanone protects normal human cells against the toxicity of methoxyacetic acid, a major industrial metabolite. *PLoS One* **2011**, *6*, e19552.
8. Li, L.H.; Wine, R.N.; Chapin, R.E. 2-methoxyacetic acid (maa)-induced spermatocyte apoptosis in human and rat testes: An in vitro comparison. *J Androl* **1996**, *17*, 538-549.
9. Bagchi, G.; Hurst, C.H.; Waxman, D.J. Interactions of methoxyacetic acid with androgen receptor. *Toxicol Appl Pharmacol* **2009**, *238*, 101-110.
10. Bagchi, G.; Zhang, Y.; Waxman, D.J. Impact of methoxyacetic acid on mouse leydig cell gene expression. *Reprod Biol Endocrinol* **2010**, *8*, 65.
11. Henley, D.V.; Mueller, S.; Korach, K.S. The short-chain fatty acid methoxyacetic acid disrupts endogenous estrogen receptor-alpha-mediated signaling. *Environ Health Perspect* **2009**, *117*, 1702-1706.

12. Tirado, O.M.; Selva, D.M.; Toràn, N.; Suárez-Quian, C.A.; Jansen, M.; McDonnell, D.P.; Reventós, J.; Munell, F. Increased expression of estrogen receptor beta in pachytene spermatocytes after short-term methoxyacetic acid administration. *J Androl* **2004**, *25*, 84-94.
13. Bagchi, G.; Zhang, Y.; Stanley, K.A.; Waxman, D.J. Complex modulation of androgen responsive gene expression by methoxyacetic acid. *Reprod Biol Endocrinol* **2011**, *9*, 42.
14. Jansen, M.S.; Nagel, S.C.; Miranda, P.J.; Lobenhofer, E.K.; Afshari, C.A.; McDonnell, D.P. Short-chain fatty acids enhance nuclear receptor activity through mitogen-activated protein kinase activation and histone deacetylase inhibition. *Proc Natl Acad Sci U S A* **2004**, *101*, 7199-7204.
15. Wade, M.G.; Kawata, A.; Williams, A.; Yauk, C. Methoxyacetic acid-induced spermatocyte death is associated with histone hyperacetylation in rats. *Biol Reprod* **2008**, *78*, 822-831.
16. Li, X.; Zhang, J.; Xie, Y.; Jiang, Y.; Yingjie, Z.; Xu, W. Progress of hdac inhibitor panobinostat in the treatment of cancer. *Curr Drug Targets* **2014**, *15*, 622-634.
17. Parajuli, K.R.; Zhang, Q.; Liu, S.; Patel, N.K.; Lu, H.; Zeng, S.X.; Wang, G.; Zhang, C.; You, Z. Methoxyacetic acid suppresses prostate cancer cell growth by inducing growth arrest and apoptosis. *Am J Clin Exp Urol* **2014**, *2*, 300-312.
18. Lorick, K.L.; Jensen, J.P.; Fang, S.; Ong, A.M.; Hatakeyama, S.; Weissman, A.M. Ring fingers mediate ubiquitin-conjugating enzyme (e2)-dependent ubiquitination. *Proc Natl Acad Sci U S A* **1999**, *96*, 11364-11369.
19. Lopez, J.; John, S.W.; Tenev, T.; Rautureau, G.J.; Hinds, M.G.; Francalanci, F.; Wilson, R.; Broemer, M.; Santoro, M.M.; Day, C.L., *et al.* Card-mediated autoinhibition of ciap1's e3 ligase activity suppresses cell proliferation and migration. *Mol Cell* **2011**, *42*, 569-583.
20. Huang, Y.; Park, Y.C.; Rich, R.L.; Segal, D.; Myszka, D.G.; Wu, H. Structural basis of caspase inhibition by xiap: Differential roles of the linker versus the bir domain. *Cell* **2001**, *104*, 781-790.

21. Sartor, O.; Gillessen, S. Treatment sequencing in metastatic castrate-resistant prostate cancer. *Asian J Androl* **2014**, *16*, 426-431.
22. Brinkworth, M.H.; Weinbauer, G.F.; Schlatt, S.; Nieschlag, E. Identification of male germ cells undergoing apoptosis in adult rats. *J Reprod Fertil* **1995**, *105*, 25-33.
23. Li, L.H.; Wine, R.N.; Miller, D.S.; Reece, J.M.; Smith, M.; Chapin, R.E. Protection against methoxyacetic-acid-induced spermatocyte apoptosis with calcium channel blockers in cultured rat seminiferous tubules: Possible mechanisms. *Toxicol Appl Pharmacol* **1997**, *144*, 105-119.
24. You, Z.; Shi, X.B.; DuRaine, G.; Haudenschild, D.; Tepper, C.G.; Lo, S.H.; Gandour-Edwards, R.; de Vere White, R.W.; Reddi, A.H. Interleukin-17 receptor-like gene is a novel antiapoptotic gene highly expressed in androgen-independent prostate cancer. *Cancer Res* **2006**, *66*, 175-183.
25. Fang, E.F.; Scheibye-Knudsen, M.; Brace, L.E.; Kassahun, H.; SenGupta, T.; Nilsen, H.; Mitchell, J.R.; Croteau, D.L.; Bohr, V.A. Defective mitophagy in xpa via parp-1 hyperactivation and nad(+)/sirt1 reduction. *Cell* **2014**, *157*, 882-896.
26. de Almagro, M.C.; Vucic, D. The inhibitor of apoptosis (iap) proteins are critical regulators of signaling pathways and targets for anti-cancer therapy. *Exp Oncol* **2012**, *34*, 200-211.
27. Jin, S.; Kalkum, M.; Overholtzer, M.; Stoffel, A.; Chait, B.T.; Levine, A.J. Ciap1 and the serine protease htra2 are involved in a novel p53-dependent apoptosis pathway in mammals. *Genes Dev* **2003**, *17*, 359-367.
28. Yang, Y.; Fang, S.; Jensen, J.P.; Weissman, A.M.; Ashwell, J.D. Ubiquitin protein ligase activity of iaps and their degradation in proteasomes in response to apoptotic stimuli. *Science* **2000**, *288*, 874-877.
29. Sakai, T.; Liu, L.; Teng, X.; Mukai-Sakai, R.; Shimada, H.; Kaji, R.; Mitani, T.; Matsumoto, M.; Toida, K.; Ishimura, K., *et al.* Nucling recruits apaf-1/pro-caspase-9 complex for the induction of stress-induced apoptosis. *J Biol Chem* **2004**, *279*, 41131-41140.
30. McIlwain, D.R.; Berger, T.; Mak, T.W. Caspase functions in cell death and disease. *Cold Spring Harb Perspect Biol* **2013**, *5*, a008656.

31. Rao, A.V.; Shaha, C. N-acetylcysteine prevents maa induced male germ cell apoptosis: Role of glutathione and cytochrome c. *FEBS Lett* **2002**, *527*, 133-137.
32. Eckelman, B.P.; Salvesen, G.S. The human anti-apoptotic proteins ciap1 and ciap2 bind but do not inhibit caspases. *J Biol Chem* **2006**, *281*, 3254-3260.
33. Burke, S.P.; Smith, L.; Smith, J.B. Ciap1 cooperatively inhibits procaspase-3 activation by the caspase-9 apoptosome. *J Biol Chem* **2010**, *285*, 30061-30068.
34. You, Z.; Saims, D.; Chen, S.; Zhang, Z.; Guttridge, D.C.; Guan, K.L.; MacDougald, O.A.; Brown, A.M.; Evan, G.; Kitajewski, J., *et al.* Wnt signaling promotes oncogenic transformation by inhibiting c-myc-induced apoptosis. *J Cell Biol* **2002**, *157*, 429-440.

Insulin and IGF1 enhance IL-17-induced chemokine expression through a GSK3B-dependent mechanism: a new target for melatonin's anti-inflammatory action

Abstract: Obesity is a chronic inflammation with increased serum levels of insulin, insulin-like growth factor 1 (IGF1), and interleukin-17 (IL-17). The objective of this study was to test a hypothesis that insulin and IGF1 enhance IL-17-induced expression of inflammatory chemokines/cytokines through a glycogen synthase kinase 3 β (GSK3B)-dependent mechanism, which can be inhibited by melatonin. We found that insulin/IGF1 and lithium chloride enhanced IL-17-induced expression of C-X-C motif ligand 1 (Cxcl1) and C-C motif ligand 20 (Ccl20) in the Gsk3b^{+/+}, but not in Gsk3b^{-/-} mouse embryonic fibroblast (MEF) cells. IL-17 induced higher levels of Cxcl1 and Ccl20 in the Gsk3b^{-/-} MEF cells, compared with the Gsk3b^{+/+} MEF cells. Insulin and IGF1 activated Akt to phosphorylate GSK3B at serine 9, thus inhibiting GSK3B activity. Melatonin inhibited Akt activation, thus decreasing P-GSK3B at serine 9 (i.e., increasing GSK3B activity) and subsequently inhibiting expression of Cxcl1 and Ccl20 that was induced either by IL-17 alone or by a combination of insulin and IL-17. Melatonin's inhibitory effects were only observed in the Gsk3b^{+/+}, but in not Gsk3b^{-/-} MEF cells. Melatonin also inhibited expression of Cxcl1, Ccl20, and Il-6 that was induced by a combination of insulin and IL-17 in the mouse prostatic tissues. Further, nighttime human blood, which contained high physiologic levels of melatonin, decreased expression of Cxcl1, Ccl20, and Il-6 in the PC3 human prostate cancer xenograft tumors. Our data support our hypothesis and suggest that melatonin may be used to dampen IL-17-mediated inflammation that is enhanced by the increased levels of insulin and IGF1 in obesity.

Dongxia Ge¹, Robert T. Dauchy¹, Sen Liu¹, Qiuyang Zhang¹, Lulu Mao¹, Erin M. Dauchy¹, David E. Blask^{1,2}, Steven M. Hill^{1,2}, Brian G. Rowan^{1,2,3}, George C. Brainard⁴, John P. Hanifin⁴, Kate S. Cecil⁴, Zhenggang Xiong⁵, Leann Myers⁶ and Zongbing You^{1,7,2,3,8}

¹Department of Structural & Cellular Biology, Tulane University Health Sciences Center, New Orleans, LA, USA; ²Tulane Cancer Center and Louisiana Cancer Research Consortium, Tulane University Health Sciences Center, New Orleans, LA, USA; ³Tulane Center for Stem Cell Research and Regenerative Medicine, Tulane University Health Sciences Center, New Orleans, LA, USA; ⁴Department of Neurology, Thomas Jefferson University, Philadelphia, PA, USA; ⁵Department of Pathology and Laboratory Medicine, Tulane University Health Sciences Center, New Orleans, LA, USA; ⁶Department of Biostatistics and Bioinformatics, School of Public Health and Tropical Medicine, Tulane University Health Sciences Center, New Orleans, LA, USA; ⁷Department of Orthopaedic Surgery, School of Medicine, Tulane University Health Sciences Center, New Orleans, LA, USA; ⁸Tulane Center for Aging, Tulane University Health Sciences Center, New Orleans, LA, USA

Key words: glycogen synthase kinase 3 β , inflammation, insulin, insulin-like growth factor 1, interleukin-17, melatonin, prostate cancer

Address reprint requests to Zongbing You, Department of Structural and Cellular Biology, Tulane University, 1430 Tulane Ave SL 49, New Orleans, LA 70112, USA.
E-mail: zyou@tulane.edu

Received May 20, 2013;

Accepted July 26, 2013.

Introduction

Melatonin (also known chemically as N-acetyl-5-methoxytryptamine) is an endogenous indolamine that is synthesized mainly by the pineal gland during the dark phase of circadian rhythm in mammals, including humans [1]. Melatonin acts through two G-protein-coupled melatonin receptors (MT1 and MT2) on the cytoplasmic membrane [2], a cytosolic melatonin receptor (MT3) [3], or directly as a free radical scavenger/antioxidant molecule [4]. Melatonin plays an important role in many physiological and pathological processes; thus, it has been tested in the treatments of a variety of diseases [5]. Among them, melatonin has been shown to improve the symptoms of inflammatory

bowel diseases. The anti-inflammatory actions of melatonin are mediated through multiple molecular mechanisms, including down-regulation of inducible nitric oxide synthase and cyclooxygenase, reduction in pro-inflammatory cytokines and chemokines (tumor necrosis factor- α (TNF- α), interferon- γ , interleukin-1 (IL-1), IL-6, IL-8, and IL-12), and increase in anti-inflammatory cytokines (IL-10 and IL-1 receptor antagonist; see a recent review [6]). We noted that TNF- α , IL-1, IL-6, and IL-8 are the downstream target genes of IL-17 [7], which led us to investigate melatonin's action on IL-17 signaling in the present study.

Interleukin-17 (including IL-17A, IL-17F, and IL-17A/F) binds to a heterodimer of IL-17RA/IL-17RC receptor complex, leading to recruitment of nuclear factor- κ B

(NF- κ B) activator 1 (Act1) through SEFIR (similar expression to fibroblast growth factor genes, IL-17 receptors, and Toll-IL-1R) domains that exist in IL-17RA, IL-17RC, and Act1 proteins [8–12]. Act1 is also named as connection of I κ B kinase and stress-activated protein kinase/Jun kinase (CIKS) [13]. Act1 is an E3 ubiquitin ligase that activates tumor necrosis factor receptor-associated factor 6 (TRAF6) through lysine-63-linked ubiquitination [14]. The polyubiquitinated TRAF6 activates transforming growth factor- β -activated kinase 1 (TAK1) and subsequently I κ B kinase (IKK) complex, leading to activation of NF- κ B pathway that induces transcription of a variety of cytokines, chemokines, and growth factors [13, 15–21]. While the IL-17-driven NF- κ B signaling pathway has been clearly defined, it is not quite clear how IL-17 activates the extracellular signal-regulated kinase 1/2 (ERK1/2), thus stabilizing the mRNAs of the IL-17 downstream target genes [22]. In addition, it has been demonstrated that IL-17 stabilizes downstream C-X-C motif ligand 1 (CXCL1) mRNA through an inducible kinase IKK1-dependent Act1-TRAF2-TRAF5 complex, which binds to splicing factor 2 (SF2, also named alternative splicing factor – ASF) and prevents SF2/ASF-mediated mRNA degradation [23, 24].

Insulin is a hormone produced by the β cells of the pancreas. Hyperinsulinemia occurs in obesity and type 2 diabetes mellitus with insulin resistance. Under the hyperinsulinemic status, insulin up-regulates the expression of growth hormone receptor in the liver, thus enhancing hepatic production of insulin-like growth factor 1 (IGF1) [25]. Insulin binds to insulin receptor (IR-A and IR-B), and IGF1 binds to IGF1 receptor (IGF1R). IGF1 can also bind to a heterodimer of IGF1R and IR-A (or IR-B). Ligand binding leads to autophosphorylation of the β subunit of IR or IGF1R, resulting in recruitment of insulin receptor substrates (IRS) 1 to IRS4 and other adaptor proteins. Consequently, phosphatidylinositol 3-kinase (PI3K)/Akt pathway and ERK1/2 pathway are activated [26]. One of the major substrates of Akt is glycogen synthase kinase 3 β (GSK3B). Insulin-stimulated Akt phosphorylates GSK3B at serine 9, thus inactivating GSK3B [27, 28]. A decrease in GSK3B activity leads to reduced phosphorylation of glycogen synthase; thus, glycogen synthase activity is increased, resulting in increased glycogen synthesis.

Glycogen synthase kinase 3 β is one of the two GSK3 isoforms (GSK3A and GSK3B) of serine/threonine protein kinases that are ubiquitously expressed in all cell types. GSK3B is constitutively active, and it phosphorylates more than 50 substrates [29]. Among these substrates, CAAT enhancer binding protein β (C/EBP β) is closely associated with IL-17 signaling. IL-17 induces expression of C/EBP β and C/EBP δ mRNA and protein [9, 20, 30]. C/EBP β and C/EBP δ transcription factors are essential for transcription of IL-17 downstream target genes such as IL-6 and 24p3/lipocalin 2 [31]. However, IL-17 also initiates a negative feedback mechanism by the activation of ERK1/2 to phosphorylate C/EBP β at threonine 188, followed by phosphorylation of C/EBP β at threonine 179 by GSK3B. Phosphorylation of C/EBP β inhibits expression of IL-17 downstream target genes, thus GSK3B

negatively regulates IL-17 signaling through phosphorylation of C/EBP β [32]. Indeed, inhibition of GSK3 activity by GSK3 inhibitor I can enhance IL-17-induced expression of IL-6, 24p3/lipocalin 2, CXCL5, C-C motif ligand 2 (CCL2), CCL7, and NF- κ B inhibitor zeta, whereas overexpression of GSK3B can inhibit IL-17-induced IL-6 promoter and 24p3 promoter activities in a mouse stromal ST2 cell line [32]. Therefore, GSK3B functions as an intrinsic negative regulator of IL-17-mediated inflammatory responses.

Approximately 35% of adult Americans are obese [33]. It is well known that obesity is associated with type 2 diabetes mellitus with increased serum levels of insulin and IGF1 and that obesity results in a chronic inflammatory state with increased serum levels of inflammatory mediators TNF α and IL-6 [34]. Recently, it has been found that serum and tissue levels of IL-17 are increased in obese mice [35, 36] and humans [37]. Given that insulin and IGF1 can inhibit GSK3B activity through PI3K/Akt pathway [27, 28], we hypothesized that insulin and IGF1 might enhance IL-17-induced expression of inflammatory chemokines/cytokines through a GSK3B-dependent mechanism, which can be inhibited by melatonin. In the current study, we tested this hypothesis. Our data demonstrated that insulin and IGF1 indeed enhanced IL-17-induced expression of CXCL1, CCL20, and IL-6 in the in vitro-cultured mouse embryonic fibroblast (MEF) cell lines and ex vivo-cultured mouse prostatic tissues, which was dependent on GSK3B. We also tested the postulate that melatonin, an endogenous indolamine molecule with anti-inflammatory actions [6], blocks the action of insulin and IGF1 through inhibition of Akt-mediated GSK3B phosphorylation.

Materials and methods

Cell and tissue culture

Mouse Gsk3b knockout (Gsk3b^{-/-}) and wild-type (Gsk3b^{+/+}) MEF cells were described previously [38]. Cells were maintained in Dulbecco's modified Eagle's medium (DMEM; Mediatech, Inc., Manassas, VA, USA) containing 10% fetal bovine serum (FBS; Mediatech, Inc.) and 100 IU/mL penicillin/streptomycin in a 37°C, 5% CO₂ humidified incubator. Six-week-old mice were euthanized by CO₂ asphyxiation. Mouse prostatic glands were dissected out, cut into cubes of approximately 1–2 mm³ in size, and washed three times with phosphate-buffered saline (PBS). The prostatic tissues were kept in 60-mm cell culture dishes in serum-free DMEM in the incubator and immediately treated with the reagents. The animal studies were approved by the Animal Care and Use Committee of Tulane University.

Treatment of cells and tissues

Cells were grown in 60-mm cell culture dishes to approximately 90% confluency and changed into serum-free DMEM for 16 hr prior to the treatments. The cells or mouse prostatic tissues were treated separately or in combination with 20 ng/mL recombinant mouse IL-17A (R&D Systems, Inc., Minneapolis, MN, USA), 10 nM

recombinant human insulin, 50 ng/mL recombinant human IGF1, 5 ng/mL TNF α , 10 nM melatonin, and/or 20 mM lithium chloride (LiCl; Sigma-Aldrich, St. Louis, MO, USA). Insulin, IGF1, melatonin, and LiCl were added 30 min prior to the addition of IL-17A in the combined treatments. At different time points as indicated, the cells or tissues were harvested for RNA or protein isolation.

Real-time quantitative reverse transcriptase PCR

After 2-hr treatment with IL-17A, the cells and tissues were collected in lysis buffer and homogenized with a 1-mL syringe connected to a 21-gauge needle. Total RNA was isolated according to the instructions of RNeasy Mini Kit (QIAGEN, Valencia, CA, USA) with on-membrane DNase I digestion to avoid genomic DNA contamination. cDNA was made from total RNA using iScriptTM cDNA Synthesis Kit (Bio-Rad Laboratories, Hercules, CA, USA). Mouse glyceraldehyde-3-phosphate dehydrogenase (GAPDH) primers were obtained from Applied Biosystems (Foster City, CA, USA). The PCR primers specific for each mouse gene are as follows: Cxcl1 forward (5'-CA CCAAACCGAAGTCATAG-3'), Cxcl1 reverse (5'-AAG CCAGCGTTCACCAGA-3'), Ccl20 forward (5'-AACTG GGTGAAAAGGGCTGT-3'), Ccl20 reverse (5'-GTCCAA TTCCATCCCAAAA-3'), Il-6 forward (5'-CTACCCCA ATTTCCAATGCT-3'), Il-6 reverse (5'-ACCACAGTGA GGAATGTCCA-3'). Real-time quantitative PCR (qRT-PCR) was performed in triplicates with an iQ5[®]iCycler and iQTM SYBR[®] Green Supermix (Bio-Rad Laboratories) following the recommended protocols. Results were normalized to GAPDH levels using the formula ΔC_t (Cycle threshold) = Ct of target gene - Ct of GAPDH. The mRNA level of the control group was used as the baseline; therefore, $\Delta\Delta C_t$ was calculated using the formula $\Delta\Delta C_t = \Delta C_t$ of target gene - ΔC_t of the baseline. The fold change of mRNA level was calculated as fold = $2^{-\Delta\Delta C_t}$.

Western blot analysis

Proteins were extracted from the treated cells in RIPA lysis buffer [50 mM sodium fluoride, 0.5% Igepal CA-630 (NP-40), 10 mM sodium phosphate, 150 mM sodium chloride, 25 mM Tris, pH 8.0, 1 mM phenylmethylsulfonyl fluoride, 2 mM ethylenediaminetetraacetic acid (EDTA), 1.2 mM sodium vanadate] supplemented with protease inhibitor cocktail (Sigma-Aldrich, St. Louis, MO, USA). Equal amount of proteins was subjected to 10% SDS-polyacrylamide gel electrophoresis and transferred to polyvinylidene difluoride membrane. The membranes were blocked with 5% nonfat dry milk in TBST buffer (25 mM Tris-HCl, 125 mM NaCl, 0.1% Tween 20) for 2 hr and probed with the indicated primary antibodies overnight and then IRDye[®] 800CW- or IRDye[®] 680RD-conjugated secondary antibodies (LI-COR Biosciences, Lincoln, NE, USA) for 1 hr. The results were visualized using an Odyssey Infrared Imager (LI-COR Biosciences). For loading control, the membranes were stripped and probed for unphosphorylated proteins and/or GAPDH. The antibodies used are as follows: rabbit anti-P-Akt (S473), rabbit

anti-Akt, rabbit anti-P-GSK3B (S9), rabbit anti-GSK3B, rabbit anti-P-GSK3A (S21), rabbit anti-GSK3A, rabbit anti-ERK1/2, rabbit anti-P-STAT3 (Y705), mouse anti-STAT3, rabbit anti-P-I κ B α , mouse anti-I κ B α , and rabbit anti-P-C/EBP β (human T235 and mouse T188) antibodies were purchased from Cell Signaling Technology (Danvers, MA, USA); mouse anti-P-ERK1/2, rabbit anti-C/EBP β , and rabbit anti-p65 antibodies were obtained from Santa Cruz Biotechnology (Santa Cruz, CA, USA); mouse anti-GAPDH antibodies were ordered from Millipore Corporation (MAB374, Billerica, MA, USA).

Tissue-isolated PC3 human prostate cancer xenografts

Fifteen xenograft tumor samples were obtained from our previous study [39]. Briefly, PC3 human prostate cancer xenografts were first grown subcutaneously in nude mice, then implanted in nude rats in a tissue-isolated manner, and finally perfused with human venous blood for 1 hr as previously described [40]. The blood was drawn from healthy male donors during the daytime, nighttime, and nighttime after 90 min of ocular, bright, white light exposure at 580 μ W/cm² (i.e., 2800 lux; so-called light-at-night). It has been previously determined that the physiological levels of melatonin were the lowest in the daytime (12:50 PM) blood (approximately 12–14 pg/mL), the highest in the nighttime (2:00 AM) blood (approximately 55–60 pg/mL), and intermediate in the nocturnal blood collected after ocular light exposure (approximately 28–29 pg/mL) [40]. The collection and use of human blood was approved by the Institutional Review Board at Thomas Jefferson University, and each donor signed a consent form. Three xenograft tumors per each type of blood were perfused in situ with the daytime blood, nighttime blood, light-at-night blood, nighttime blood supplemented with 1 nM of melatonin receptor antagonist S20928, or light-at-night blood supplemented with 500 pM of melatonin (Sigma-Aldrich, St. Louis, MO, USA). Approximately 100 mg of each tumor was frozen in liquid nitrogen and pulverized. Total RNA was isolated using RNeasy Mini Kit (QIAGEN) according to the instructions. Real-time quantitative PCR was performed as described above.

Statistical analysis

All experiments were repeated at least three times, and consistent results were obtained. The mRNA levels represent means \pm standard deviations of three independent experiments or three different tumor samples in the PC3 human prostate cancer xenograft study. The Student's *t*-test was used to analyze the quantitative data. *P*-value < 0.05 was considered statistically significant.

Results

As shown in Fig. 1A,B, we found that IL-17A alone, insulin alone, or IGF1 alone only slightly induced expression of Cxcl1 and Ccl20, two of the IL-17 downstream target genes, in the Gsk3b^{+/+} MEF cells. A combination of IL-17A and insulin (or IGF1), however, significantly

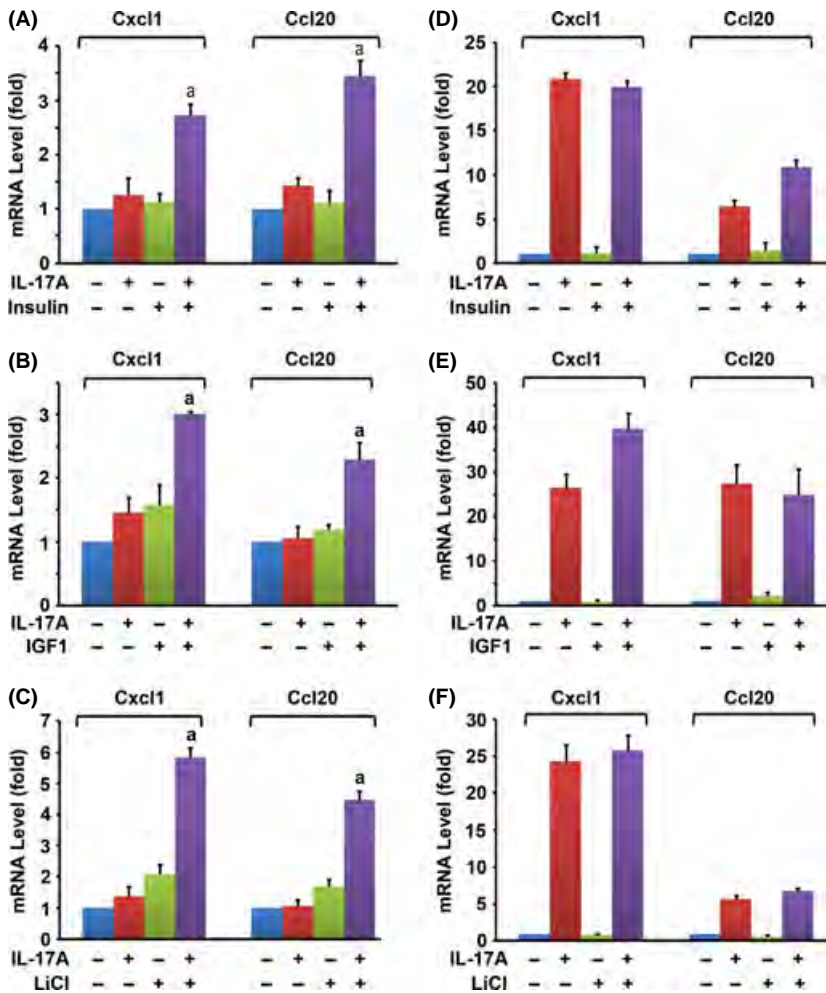


Fig. 1. Insulin, IGF1, and LiCl enhanced IL-17-induced chemokine expression in the Gsk3b^{+/+} mouse embryonic fibroblast (MEF) cells, but not in the Gsk3b^{-/-} MEF cells. (A–C) Gsk3b^{+/+} MEF cells. (D–F) Gsk3b^{-/-} MEF cells. Insulin (10 nM), IGF1 (50 ng/mL), or LiCl (20 mM) was added 30 min prior to the addition of IL-17A (20 ng/mL). Two hours after IL-17A treatment, the relative mRNA levels of Cxcl1 and Ccl20 were determined by qRT-PCR. The data are presented as mean \pm standard deviation of three experiments. ^a $P < 0.05$, compared with the IL-17A-alone group. When compared to the untreated control group, only the combined treatment groups showed $P < 0.05$ in panels (A–C); the IL-17A-alone groups and the combined treatment groups showed $P < 0.05$ in panels (D–F); the other treatment groups showed $P > 0.05$ in panels (A–F).

increased the mRNA levels of Cxcl1 and Ccl20 ($P < 0.05$; Fig. 1A,B). The classic GSK3 inhibitor LiCl also enhanced IL-17-induced gene expression (Fig. 1C). To determine whether GSK3B was involved, we performed the same experiments in the Gsk3b^{-/-} MEF cells. We found that in the absence of GSK3B, IL-17A alone induced more than 20-fold higher levels of Cxcl1 and more than five-fold higher levels of Ccl20 in the Gsk3b^{-/-} MEF cells, compared with the Gsk3b^{+/+} MEF cells (Fig. 1D–F versus A–C). When insulin, IGF1, or LiCl was combined with IL-17A, they did not further enhance IL-17-induced expression of Cxcl1 and Ccl20 in the Gsk3b^{-/-} MEF cells (Fig. 1D–F), suggesting that GSK3B is required to mediate the synergy between insulin/IGF1 and IL-17A.

We next assessed the signaling pathways activated by insulin and IGF1 in the Gsk3b^{-/-} and Gsk3b^{+/+} MEF cells. We found that insulin increased phosphorylated Akt (P-Akt at serine 473) from 0.5 to 4 hr in the Gsk3b^{-/-} MEF cells, whereas P-Akt levels were slightly lower in the Gsk3b^{+/+} MEF cells (Fig. 2A). This slight difference between the two cell lines was reflected in P-GSK3A (at serine 21) levels. Nevertheless, we confirmed that GSK3B protein was not expressed in the Gsk3b^{-/-} MEF cells, and P-GSK3B (at serine 9) was only increased by insulin in the Gsk3b^{+/+} MEF cells (Fig. 2A). We found that insulin

alone did not increase P-I κ B α levels in either the Gsk3b^{-/-} or the Gsk3b^{+/+} MEF cells. Although the basal levels of ERK1/2 and P-ERK1/2 were slightly higher in the Gsk3b^{+/+} MEF cells than in the Gsk3b^{-/-} MEF cells, insulin did not increase P-ERK1/2 levels in either cell line (Fig. 2A). We found that insulin only slightly increased P-STAT3 (Signal transducer and activator of transcription 3) levels from 1 to 4 hr in the Gsk3b^{+/+}, but not in the Gsk3b^{-/-} MEF cells (Fig. 2A). IGF1 increased P-Akt and P-GSK3A levels to the same magnitude in both Gsk3b^{-/-} and Gsk3b^{+/+} MEF cells, but only increased P-GSK3B levels in the Gsk3b^{+/+} MEF cells (Fig. 2B). IGF1 did not increase P-I κ B α , P-ERK1/2, or P-STAT3 levels in either Gsk3b^{-/-} or Gsk3b^{+/+} MEF cells (Fig. 2B). These findings suggest that insulin and IGF1 activate Akt pathway in both Gsk3b^{-/-} and Gsk3b^{+/+} MEF cells, which inactivates GSK3B through phosphorylation at serine 9 in the Gsk3b^{+/+} MEF cells.

Because we observed that IL-17A alone dramatically increased expression of Cxcl1 and Ccl20 in the Gsk3b^{-/-}, but not in the Gsk3b^{+/+} MEF cells, we investigated the differences in IL-17-activated NF- κ B and ERK1/2 pathways. We found that IL-17A dramatically increased the P-I κ B α levels at 0.5 to 1 hr in the Gsk3b^{-/-} MEF cells, whereas such an increase was absent in the Gsk3b^{+/+}

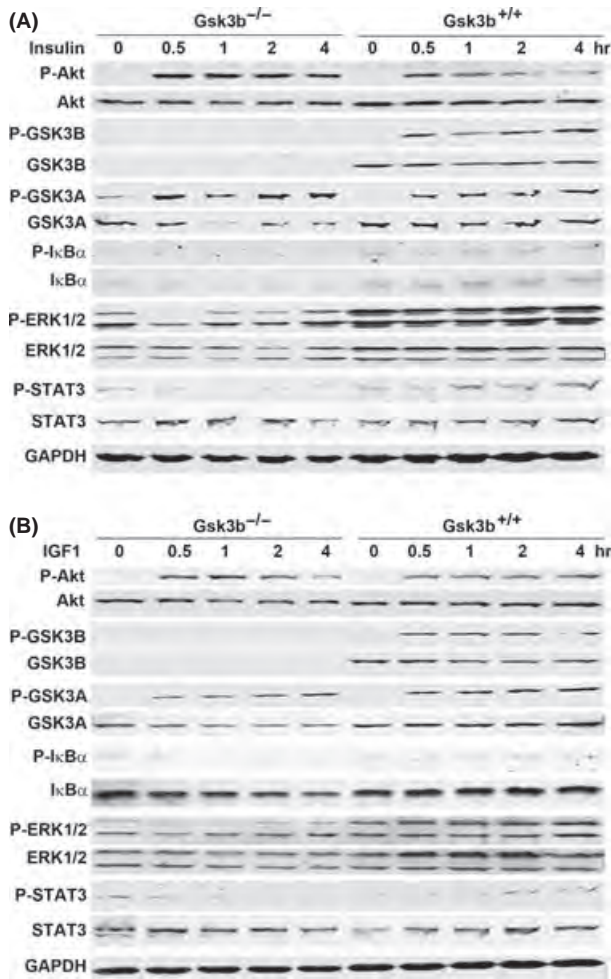


Fig. 2. Effects of insulin and IGF1 on intracellular signaling pathways. The Gsk3b^{-/-} and Gsk3b^{+/+} mouse embryonic fibroblast cells were treated with 10 nM insulin (A) or 50 ng/mL IGF1 (B) for the indicated time. The levels of phosphorylated and unphosphorylated proteins were determined by Western blot analysis. Equal loading of proteins was confirmed by reprobing the blot for GAPDH.

MEF cells (Fig. 3A). The increase in P-IκBα was accompanied by a decrease in IκBα, implicating that NF-κB is released from the NF-κB/IκBα complex and becomes activated. There were no any obvious changes in NF-κB p65 (RELA) levels after IL-17A treatment (Fig. 3A). On the other hand, there was not much difference in IL-17A-induced activation of P-ERK1/2 between the Gsk3b^{-/-} and Gsk3b^{+/+} MEF cells, except that there was a little higher level of P-ERK2 at 2 hr in the Gsk3b^{-/-} MEF cells than in the Gsk3b^{+/+} MEF cells (Fig. 3A). No increase in P-Akt levels was observed in either Gsk3b^{-/-} or Gsk3b^{+/+} MEF cells. These findings suggest that in the absence of GSK3B, IL-17A stimulates higher levels of NF-κB activation to transcribe the downstream genes. To examine whether the enhanced NF-κB activity is specific to IL-17 signaling, we treated the MEF cells with TNFα, a classic activator of NF-κB pathway. We found that TNFα induced similar time-dependent changes in P-IκBα and IκBα in both Gsk3b^{-/-} and Gsk3b^{+/+} MEF cells,

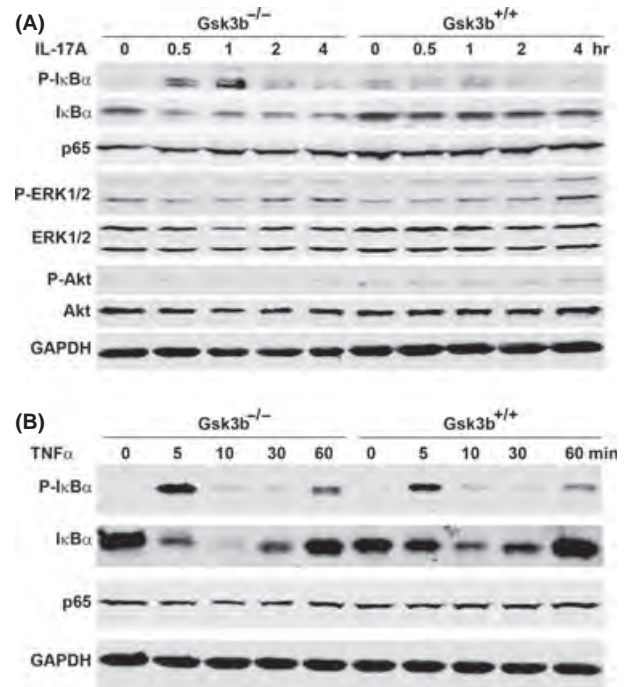


Fig. 3. Gsk3b knockout enhanced phosphorylation of IκBα induced by IL-17, but not by TNFα. The Gsk3b^{-/-} and Gsk3b^{+/+} mouse embryonic fibroblast cells were treated with 20 ng/mL IL-17A (A) or 5 ng/mL TNFα (B) for the indicated time. The levels of phosphorylated and unphosphorylated proteins were determined by Western blot analysis. Equal loading of proteins was confirmed by reprobing the blot for GAPDH.

without any changes in NF-κB p65 (RELA) levels (Fig. 3B). These findings suggest that GSK3B negatively regulates IL-17-induced phosphorylation of IκBα, but not TNFα-induced phosphorylation of IκBα.

Because phosphorylation of GSK3B at serine 9 inhibits GSK3B activity, melatonin can enhance GSK3B activity through decreasing P-GSK3B at serine 9. Having shown that GSK3B is a negative regulator of IL-17 signaling, we tested whether melatonin could inhibit IL-17-induced gene expression through enhancing GSK3B. We found that melatonin inhibited IL-17A-induced Cxcl1 expression in the Gsk3b^{+/+} MEF cells (Fig. 4A). Melatonin did not inhibit IL-17A-induced expression of Cxcl1 and Ccl20 in the Gsk3b^{-/-} MEF cells (Fig. 4B), suggesting that melatonin's action is mediated by GSK3B. Further, we found that although IL-17A did not activate Akt, melatonin reduced the basal levels of P-Akt and Akt, thus reduced the level of P-GSK3B at serine 9 in the Gsk3b^{+/+} MEF cells (Fig. 4C). The basal levels of P-STAT3 were not affected by melatonin (Fig. 4C), suggesting that melatonin's effect is specific to the Akt-GSK3B pathway.

Because insulin activates PI3K/Akt pathway to inhibit GSK3B activity and subsequently enhance IL-17-induced gene expression, we tested whether melatonin could antagonize insulin's action by inhibiting Akt activation. We found that melatonin indeed significantly reduced the mRNA levels of Cxcl1 and Ccl20 that were induced by a combination of insulin and IL-17A in the Gsk3b^{+/+} MEF cells ($P < 0.05$; Fig. 5A). Because melatonin did not

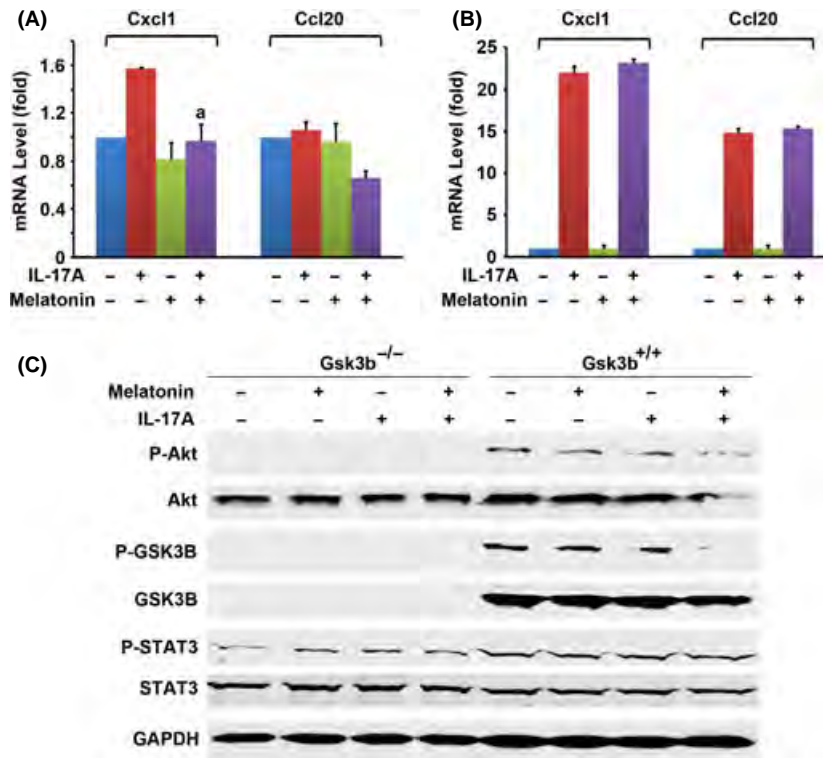


Fig. 4. Melatonin inhibited IL-17-induced chemokine expression in the Gsk3b^{+/+} mouse embryonic fibroblast (MEF) cells, but not in the Gsk3b^{-/-} MEF cells. (A) The Gsk3b^{+/+} MEF cells or (B) the Gsk3b^{-/-} MEF cells were treated with 10 nM melatonin 30 min prior to the addition of 20 ng/mL IL-17A. Two hours after IL-17A treatment, the relative mRNA levels of Cxcl1 and Ccl20 were determined by qRT-PCR. The data are presented as mean \pm standard deviation of three experiments. ^a $P < 0.05$, compared with the IL-17A-alone group. When compared to the untreated control group, the IL-17A-alone group in induction of Cxcl1 in panel A showed $P < 0.05$; the IL-17A-alone groups and the combined treatment groups in panel B showed $P < 0.05$; the other treatment groups showed $P > 0.05$ in panels A and B. (C) Effects of melatonin on intracellular signaling pathways: The Gsk3b^{-/-} and Gsk3b^{+/+} MEF cells were treated with 10 nM melatonin 30 min prior to the addition of 20 ng/mL IL-17A for 2 hr. The levels of phosphorylated and unphosphorylated proteins were determined by Western blot analysis. The loading of proteins was confirmed by reprobing the blot for GAPDH.

show any effects in the Gsk3b^{-/-} MEF cells (Fig. 5B), it suggests that melatonin's action is dependent on GSK3B. To rule out the possibility that 10 nM melatonin is not sufficient to inhibit IL-17A's effects in the Gsk3b^{-/-} MEF cells, we treated the cells with 500 nM of melatonin. We found that 500 nM of melatonin significantly inhibited induction of Cxcl1 and Ccl20 by insulin and IL-17A in the Gsk3b^{+/+} MEF cells ($P < 0.05$; Fig. 5C), but this high dose of melatonin still had no effects in the Gsk3b^{-/-} MEF cells (Fig. 5D). These findings further confirm that melatonin's action is GSK3B dependent.

We tested whether our findings obtained from the cultured MEF cell lines would be reproducible in mouse prostatic tissues. We harvested fresh mouse prostatic glandular tissues and treated them in the ex vivo cultures. We found that IL-17A alone significantly induced expression of Cxcl1, Ccl20, and Il-6 in the mouse prostatic tissues ($P < 0.05$, compared with the control group), and a combination of insulin and IL-17A induced expression of these genes to significantly higher levels ($P < 0.01$, compared with the IL-17A-alone group; Fig. 6A). Melatonin significantly reduced expression of these genes that was induced by insulin and IL-17A ($P < 0.01$, compared with the insulin + IL-17A group; Fig. 6A). These findings suggest that

insulin can enhance IL-17-induced gene expression in the mouse prostatic tissues, which can be antagonized by melatonin.

We found that the nighttime blood significantly reduced expression of Cxcl1, Ccl20, and Il-6 in the xenograft tumor tissues, compared with the tumor tissues perfused with the daytime blood ($P < 0.05$; Fig. 6B). On the other hand, the levels of gene expression in the tumor tissues perfused with the light-at-night blood were moderate compared with the daytime blood and nighttime blood groups (Fig. 6B). Because the blood contains many other factors that may regulate expression of the genes examined, we did two additional experiments to assess whether the observed changes in gene expression were dependent on melatonin. First, we added melatonin receptor antagonist S20928 to the nighttime blood. As expected, the addition of S20928 significantly increased the levels of gene expression ($P < 0.05$), compared with the nighttime blood group (Fig. 6B). Next, we added melatonin to the light-at-night blood. We found that the addition of melatonin significantly reduced expression of Cxcl1 and Ccl20 ($P < 0.05$), compared with the light-at-night blood-alone group (Fig. 6B). Collectively, these findings suggest that physiological levels of melatonin in the nighttime blood decrease

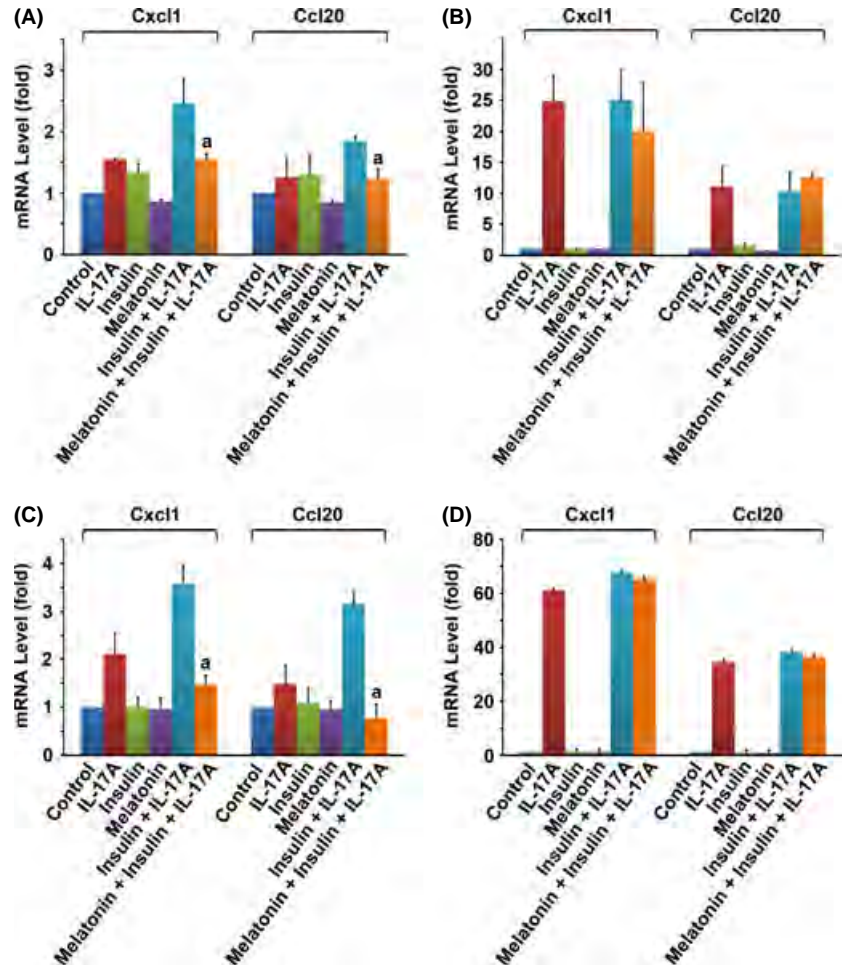


Fig. 5. Melatonin inhibited the synergy between insulin and IL-17 in induction of Cxcl1 and Ccl20 in the Gsk3b^{+/+} mouse embryonic fibroblast (MEF) cells, but not in the Gsk3b^{-/-} MEF cells. The Gsk3b^{+/+} MEF cells (A and C) or the Gsk3b^{-/-} MEF cells (B and D) were treated with melatonin (10 nM in A, B, 500 nM in C, D) and/or 10 nM insulin 30 min prior to the addition of IL-17A (20 ng/mL in A, B, 100 ng/mL in C, D). Two hours after IL-17A treatment, the relative mRNA levels of Cxcl1 and Ccl20 were determined by qRT-PCR. The data are presented as mean \pm standard deviation of three experiments. ^a $P < 0.05$, compared with the insulin + IL-17A group. When compared to the control group, the insulin + IL-17A groups in panels A and C showed $P < 0.05$; the IL-17A-alone group in induction of Cxcl1 in panel C showed $P < 0.05$; the IL-17A-alone groups, the insulin + IL-17A groups, and melatonin + insulin + IL-17A groups in panels B and D showed $P < 0.05$; the other treatment groups showed $P > 0.05$ in panels A–D.

expression of IL-17 downstream target genes in the tissue-isolated PC3 human prostate cancer xenografts.

Discussion

Melatonin has been shown to reduce mRNA levels of IL-6, IL-1 β , TNF- α , and matrix metalloproteinase-9 (MMP-9) in the rabbit liver infected with rabbit hemorrhagic disease viruses, thus attenuating inflammation and promoting liver regeneration [41]. Melatonin has also been demonstrated to reduce methamphetamine-induced overexpression of IL-6, IL-1 β , and TNF- α in microglial cell lines [42]. It is known that IL-17 cytokine induces expression of pro-inflammatory chemokines, cytokines, growth factors, and MMPs, including IL-6, IL-1 β , TNF- α , and MMP-9 [7, 43]. Therefore, we were prompted to investigate whether melatonin can regulate IL-17-induced expression of chemokines and cytokines.

IL-17 acts on the IL-17RA/IL-17RC receptor complex to recruit Act1 and then TRAF6, leading to activation of TAK1 and IKK kinases; thus, I κ B α is phosphorylated and degraded. Subsequently, NF- κ B is released from the NF- κ B/I κ B α complex and enters into the nucleus to initiate transcription of downstream target genes [44]. In addition, IL-17 activates ERK1/2 pathway and Act1-TRAF2-TRAF5-SF2/ASF complex to stabilize the mRNAs

of IL-17 downstream target genes [22–24]. Thus, IL-17 increases the expression levels of the downstream target genes through mechanisms of transcription and mRNA stabilization via distinct signaling pathways (Fig. 7).

In this study, we demonstrated that insulin and IGF1 enhance IL-17-induced expression of chemokines (Cxcl1 and Ccl20) and cytokine (IL-6). Insulin and IGF1 mainly act through the PI3K/Akt pathway to inhibit GSK3B activity by phosphorylation of GSK3B at serine 9, as it has been shown that phosphorylation of GSK3B at serine 9 decreases GSK3B enzyme activity [27, 28]. We also demonstrated that the cross talk between insulin/IGF1 and IL-17 signaling pathways is dependent on GSK3B. We provided three lines of evidence to support this concept: First, the synergy between insulin/IGF1 and IL-17 is only found in the Gsk3b wild-type MEF cells, which is abolished in the Gsk3b knockout MEF cells; second, the synergy between GSK3 inhibitor LiCl and IL-17 is only found in the Gsk3b wild-type MEF cells, which is also abolished in the Gsk3b knockout MEF cells; and third, melatonin, an activator of GSK3B activity, can only inhibit the synergistic action of insulin and IL-17 in the Gsk3b wild-type MEF cells, but not in the Gsk3b knockout MEF cells.

GSK3B has been shown to act as a negative regulator of IL-17 signaling in the previous study [32]. The mechanism of GSK3B's inhibitory action on IL-17 signaling has

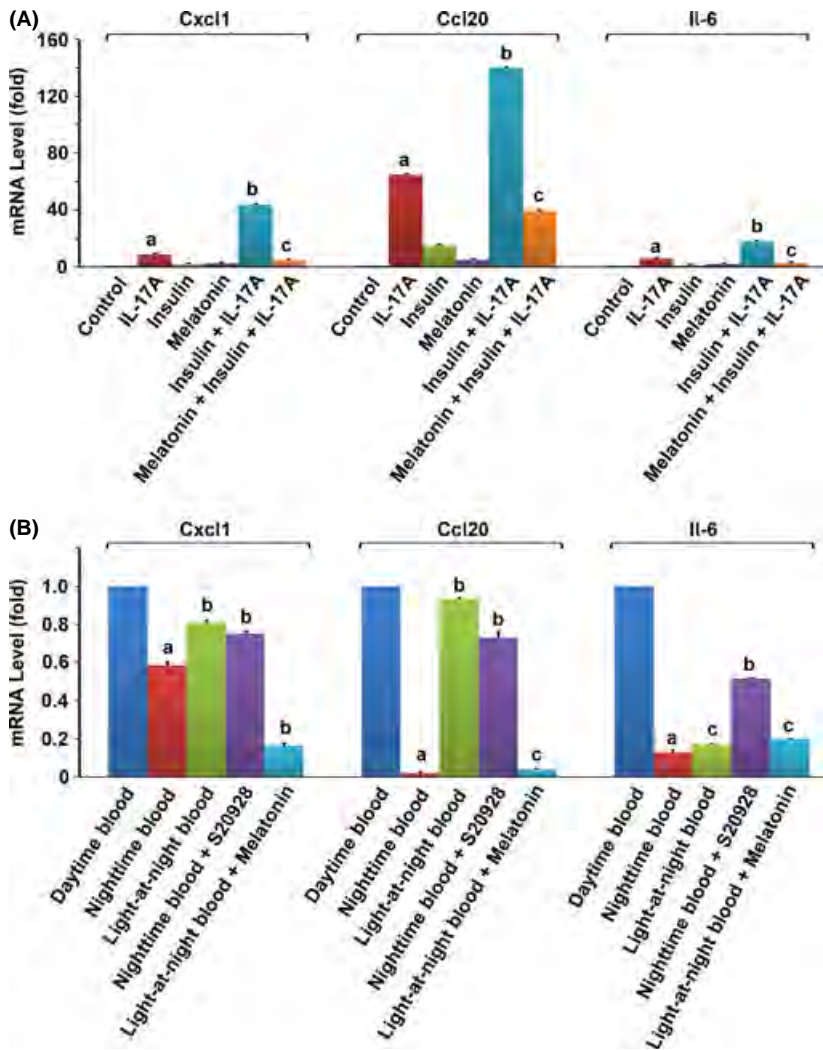


Fig. 6. Melatonin inhibited expression of IL-17 downstream target genes in mouse prostatic tissues and PC3 human prostate cancer xenograft tumors. (A) The ex vivo-cultured mouse prostatic tissues were treated with 10 nM insulin and/or 10 nM melatonin 30 min prior to the addition of 20 ng/mL IL-17A. Two hours after IL-17A treatment, the relative mRNA levels of Cxcl1, Ccl20, and Il-6 were determined by qRT-PCR. The data are presented as mean \pm standard deviation of three experiments. ^a $P < 0.05$, compared with the control group; ^b $P < 0.01$, compared with the IL-17A-alone group; ^c $P < 0.01$, compared with the insulin + IL-17A group. (B) The PC3 human prostate cancer xenograft tumors were perfused in situ with the daytime blood, nighttime blood, light-at-night blood, nighttime blood supplemented with 1 nM of melatonin receptor antagonist S20928, or light-at-night blood supplemented with 500 pM of melatonin, for 1 hr. The relative mRNA levels of Cxcl1, Ccl20, and Il-6 were determined by qRT-PCR. The data are presented as mean \pm standard deviation of three tumors. ^a $P < 0.05$, compared with the daytime blood group; ^b $P < 0.05$, compared with the nighttime blood group; ^c $P > 0.05$, compared with the nighttime blood group.

been proposed as that GSK3 β phosphorylates C/EBP β at threonine 179 after C/EBP β is phosphorylated at threonine 188 by ERK1/2; thereby, the phosphorylated C/EBP β inhibits the transcription function of the unphosphorylated C/EBP β [32] (Fig. 7). In addition, it is possible that GSK3 β may act on other unknown substrates to inhibit IL-17 signaling. For example, we demonstrated that Gsk3b knockout increases the levels of P-I κ B α induced by IL-17A (Fig. 3A), suggesting that GSK3 β may negatively regulate IL-17 signaling at the level of IKK or above in the signaling cascade (Fig. 7). Recently, it has been shown that GSK3 β phosphorylates C/EBP δ at threonine 156, leading to degradation of C/EBP δ , thus attenuating Toll-like receptor 4-induced inflammation-associated genes in macrophages and tumor cells [45]. Given that IL-17 induces expression of C/EBP δ [9, 20, 30] and C/EBP δ is essential for transcription of IL-17 downstream target genes such as IL-6 and 24p3/lipocalin 2 [31], it is intriguing to investigate whether the GSK3 β -C/EBP δ mechanism mediates GSK3 β 's inhibitory action in IL-17 signaling in future studies.

Two main implications of this study are identified. First, the synergy between insulin/IGF1 and IL-17 may

explain the chronic inflammatory status found in obesity. It is known that obese people have increased serum levels of insulin and IGF1 [34] and IL-17 [37]. Based on the current study, insulin and IGF1 can enhance IL-17-induced pro-inflammatory chemokines and cytokines; thus, the increased levels of insulin, IGF1, and IL-17 may act together to build up the chronic inflammatory status in obesity. This is consistent with the findings that many of the obesity-associated inflammatory cytokines/chemokines are IL-17 downstream target genes, including IL-6, IL-8, IL-1 β , TNF α , vascular endothelial growth factor, CCL2, and CCL5 [46]. Second, the synergy between insulin/IGF1 and IL-17 can be inhibited by melatonin. We found that melatonin at pharmacological concentrations (10–500 nM) inhibited chemokine expression induced by insulin and IL-17 in the cultured MEF cells and mouse prostatic tissues. We and other investigators have previously shown that human serum melatonin concentrations can reach 500 nM by oral administration of 80 mg melatonin or intravenous administration of 2 mg melatonin [47, 48]. Further, we found that melatonin at physiological concentrations inhibited chemokine expression in the tissue-isolated PC3 human prostate cancer

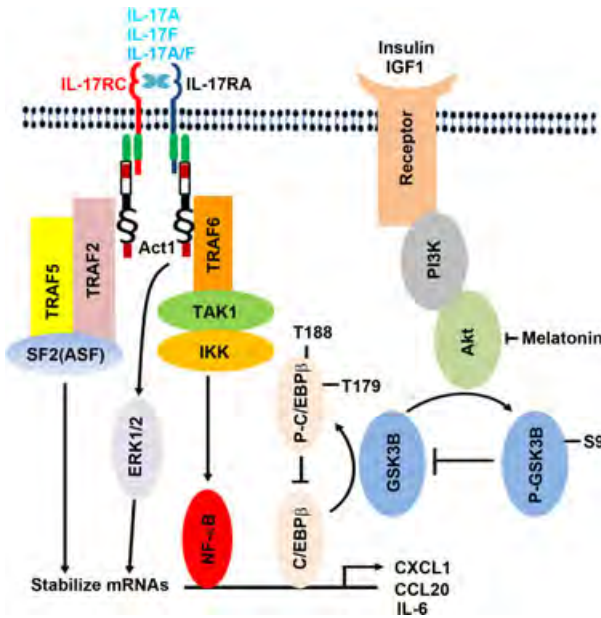


Fig. 7. Illustration of the proposed mechanisms underlying the cross talk between insulin/IGF1 and IL-17 signaling pathways. IL-17 acts on the IL-17RA/IL-17RC receptor complex to activate Act1-TRAF6-TAK1-IKK signaling cascade, thus activating NF- κ B and C/EBP β transcription factors for initiation of transcription of the downstream target genes. In addition, IL-17 activates ERK1/2 and Act1-TRAF2-TRAF5-SF2/ASF complex to stabilize mRNAs. Insulin and IGF1 activate PI3K/Akt pathway through their receptors; Akt phosphorylates GSK3B at serine 9 to inhibit GSK3B enzyme activity; GSK3B phosphorylates C/EBP β at threonine 179 after a priming phosphorylation at threonine 188 by ERK1/2, thus inhibiting C/EBP β 's transcription function. Therefore, insulin/IGF1 signaling is linked with IL-17 signaling by GSK3B and C/EBP β . Melatonin inhibits Akt activation, thus enhancing GSK3B activity and subsequently diminishing IL-17-induced gene expression by inhibiting C/EBP β function.

xenografts. The nighttime blood significantly reduced expression of Cxcl1, Ccl20, and Il-6 in the xenograft tumor tissues, compared with the tumor tissues perfused with the daytime blood. In contrast, the levels of gene expression in the tumor tissues perfused with the light-at-night blood were moderate compared with the daytime blood and nighttime blood groups. These findings are consistent with the blood levels of melatonin, that is, the lowest in the daytime blood, the highest in the nighttime blood, and intermediate in the light-at-night blood [40]. Of note, because we used the archived tumor samples, we were unable to retrospectively measure the levels of insulin and IL-17 in the blood samples that were used in perfusion of the tumors. Nevertheless, we speculate that the physiological levels of insulin and IL-17 might exist in the blood samples [49, 50]. To our best knowledge, this is the first time that melatonin is found to inhibit IL-17-mediated inflammation through enhancing GSK3B activity.

Obesity has been associated with many comorbidities, including type 2 diabetes and several cancers [34]. Light-at-night-induced suppression of melatonin production has been shown to contribute to obesity [51]. In a rabbit model

of high-fat-diet-induced obesity, intake of melatonin is associated with reduction in food consumption and weight gain, lowering of blood pressure and heart rate, and decrease in blood glucose and lipids [52]. In a rat model of high-calorie-diet-induced obesity, melatonin treatment reduces weight gain, visceral adiposity, and serum levels of insulin and triglycerides [53]. In male young Zucker diabetic fatty rats, melatonin reduces weight gain, serum triglyceride level, and low-density lipoprotein cholesterol, but increases high-density lipoprotein cholesterol [54]. Furthermore, melatonin significantly reduces the plasma levels of IL-6 and TNF- α in Zucker diabetic fatty rats [55], although it is not clear whether the reduction in IL-6 and TNF- α is mediated through inhibition of IL-17 signaling. Based on the findings in the present study and aforementioned previous studies, we speculate that melatonin is potentially able to dampen the inflammatory status in obesity. In conclusion, the present study has demonstrated that insulin and IGF1 enhance IL-17-induced expression of inflammatory chemokines/cytokines through a GSK3B-dependent mechanism, which can be inhibited by melatonin. The anti-inflammatory actions of melatonin may be utilized to treat obesity-associated chronic inflammation and comorbidities such as type 2 diabetes and cancer.

Acknowledgements

This work was partly supported by grants from the National Institute of General Medical Sciences (8P20GM103518-09) and the National Cancer Institute (R01CA174714) of the National Institutes of Health, a grant from Department of Defense (PC121647), the Developmental Fund of Tulane Cancer Center (TCC), and Louisiana Cancer Research Consortium (LCRC) Fund (to Z.Y.). This work was also supported by Grants for Laboratory Animal Science (GLAS) from the American Association for Laboratory Animal Science (to R.T.D. and D.E.B.) and in part by a Tulane University School of Medicine and LCRC Start-Up Grant (#631455) and NIH grant (1R21CA129875-01A1; to D.E.B.), and the Institute for Integrative Health (Baltimore, MD; to G.C.B.). The content is solely the responsibility of the authors and does not necessarily represent the official views of the National Institutes of Health. TCC and LCRC Core Facilities were used to conduct this study. The authors thank Dr. James R. Woodgett (Mount Sinai Hospital and the Samuel Lunenfeld Research Institute, Toronto, Ontario, Canada M5G 1X5) for providing the Gsk3b wild-type and knockout cell lines.

Author contributions

D Ge conducted the in vitro experiments and analyzed the data. RT Dauchy, L Mao, EM Dauchy, GC Brainard, JP Hanifin, KS Cecil, DE Blask, and SM Hill conceived and conducted the experiments on human xenograft tumors. S Liu, Q Zhang, BR Rowan, Z Xiong, and L Myers assisted in the design of experiments and analysis of data. Z You designed the experiments, analyzed the data, and prepared the manuscript. All authors contributed to the revision and approval of the article.

References

- REITER RJ. Pineal melatonin: cell biology of its synthesis and of its physiological interactions. *Endocr Rev* 1991; **12**:151–180.
- DUBOCOVICH ML, MARKOWSKA M. Functional MT1 and MT2 melatonin receptors in mammals. *Endocrine* 2005; **27**:101–110.
- NOSJEAN O, FERRO M, COGE F et al. Identification of the melatonin-binding site MT3 as the quinone reductase 2. *J Biol Chem* 2000; **275**:31311–31317.
- REITER RJ. Melatonin: lowering the high price of free radicals. *News Physiol Sci* 2000; **15**:246–250.
- SANCHEZ-BARCELO EJ, MEDIAVILLA MD, TAN DX et al. Clinical uses of melatonin: evaluation of human trials. *Curr Med Chem* 2010; **17**:2070–2095.
- MAURIZ JL, COLLADO PS, VENEROSO C et al. A review of the molecular aspects of melatonin's anti-inflammatory actions: recent insights and new perspectives. *J Pineal Res* 2013; **54**: 1–14.
- ONISHI RM, GAFFEN SL. Interleukin-17 and its target genes: mechanisms of interleukin-17 function in disease. *Immunology* 2010; **129**:311–321.
- NOVATCHKOVA M, LEIBBRANDT A, WERZOWA J et al. The STIR-domain superfamily in signal transduction, development and immunity. *Trends Biochem Sci* 2003; **28**:226–229.
- CHANG SH, PARK H, DONG C. Act1 adaptor protein is an immediate and essential signaling component of interleukin-17 receptor. *J Biol Chem* 2006; **281**:35603–35607.
- QIAN Y, LIU C, HARTUPEE J et al. The adaptor Act1 is required for interleukin 17-dependent signaling associated with autoimmune and inflammatory disease. *Nat Immunol* 2007; **8**:247–256.
- MAITRA A, SHEN F, HANEL W et al. Distinct functional motifs within the IL-17 receptor regulate signal transduction and target gene expression. *Proc Natl Acad Sci U S A* 2007; **104**:7506–7511.
- HO AW, SHEN F, CONTI HR et al. IL-17RC is required for immune signaling via an extended SEF/IL-17R signaling domain in the cytoplasmic tail. *J Immunol* 2010; **185**:1063–1070.
- LEONARDI A, CHARIOT A, CLAUDIO E et al. CIKS, a connection to Ikappa B kinase and stress-activated protein kinase. *Proc Natl Acad Sci U S A* 2000; **97**:10494–10499.
- LIU C, QIAN W, QIAN Y et al. Act1, a U-box E3 ubiquitin ligase for IL-17 signaling. *Sci Signal* 2009; **2**:ra63.
- YAO Z, FANSLAW WC, SELDIN MF et al. Herpesvirus Saimiri encodes a new cytokine, IL-17, which binds to a novel cytokine receptor. *Immunity* 1995; **3**:811–821.
- LI H, CHEN J, HUANG A et al. Cloning and characterization of IL-17B and IL-17C, two new members of the IL-17 cytokine family. *Proc Natl Acad Sci U S A* 2000; **97**:773–778.
- WANG C, DENG L, HONG M et al. TAK1 is a ubiquitin-dependent kinase of MKK and IKK. *Nature* 2001; **412**:346–351.
- KANAYAMA A, SETH RB, SUN L et al. TAB 2 and TAB 3 activate the NF-kappaB pathway through binding to polyubiquitin chains. *Mol Cell* 2004; **15**:535–548.
- ADHIKARI A, XU M, CHEN ZJ. Ubiquitin-mediated activation of TAK1 and IKK. *Oncogene* 2007; **26**:3214–3226.
- SHEN F, RUDDY MJ, PLAMONDON P et al. Cytokines link osteoblasts and inflammation: microarray analysis of interleukin-17- and TNF-alpha-induced genes in bone cells. *J Leukoc Biol* 2005; **77**:388–399.
- ZHU S, PAN W, SONG X et al. The microRNA miR-23b suppresses IL-17-associated autoimmune inflammation by targeting TAB 2, TAB 3 and IKK-alpha. *Nat Med* 2012; **18**:1077–1086.
- HATA K, ANDOH A, SHIMADA M et al. IL-17 stimulates inflammatory responses via NF-kappaB and MAP kinase pathways in human colonic myofibroblasts. *Am J Physiol Gastrointest Liver Physiol* 2002; **282**:G1035–G1044.
- BULEK K, LIU C, SWAIDANI S et al. The inducible kinase IKKi is required for IL-17-dependent signaling associated with neutrophilia and pulmonary inflammation. *Nat Immunol* 2011; **12**:844–852.
- SUN D, NOVOTNY M, BULEK K et al. Treatment with IL-17 prolongs the half-life of chemokine CXCL1 mRNA via the adaptor TRAF5 and the splicing-regulatory factor SF2 (ASF). *Nat Immunol* 2011; **12**:853–860.
- BAXTER RC, BRYSON JM, TURTLE JR. Somatogenic receptors of rat liver: regulation by insulin. *Endocrinology* 1980; **107**:1176–1181.
- GALLAGHER EJ, LEROITH D. The proliferating role of insulin and insulin-like growth factors in cancer. *Trends Endocrinol Metab* 2010; **21**:610–618.
- CROSS DA, ALESSI DR, VANDENHEEDE JR et al. The inhibition of glycogen synthase kinase-3 by insulin or insulin-like growth factor 1 in the rat skeletal muscle cell line L6 is blocked by wortmannin, but not by rapamycin: evidence that wortmannin blocks activation of the mitogen-activated protein kinase pathway in L6 cells between Ras and Raf. *Biochem J* 1994; **303**(Pt 1):21–26.
- CROSS DA, ALESSI DR, COHEN P et al. Inhibition of glycogen synthase kinase-3 by insulin mediated by protein kinase B. *Nature* 1995; **378**:785–789.
- CHIARA F, RASOLA A. GSK-3 and mitochondria in cancer cells. *Front Oncol* 2013; **3**:16.
- RUDDY MJ, WONG GC, LIU XK et al. Functional cooperation between interleukin-17 and tumor necrosis factor-alpha is mediated by CCAAT/enhancer-binding protein family members. *J Biol Chem* 2004; **279**:2559–2567.
- SHEN F, HU Z, GOSWAMI J et al. Identification of common transcriptional regulatory elements in interleukin-17 target genes. *J Biol Chem* 2006; **281**:24138–24148.
- SHEN F, LI N, GADE P et al. IL-17 receptor signaling inhibits C/EBPbeta by sequential phosphorylation of the regulatory 2 domain. *Sci Signal* 2009; **2**:ra8.
- FLEGAL KM, CARROLL MD, KIT BK et al. Prevalence of obesity and trends in the distribution of body mass index among US adults, 1999–2010. *JAMA* 2012; **307**:491–497.
- COHEN DH, LEROITH D. Obesity, type 2 diabetes, and cancer: the insulin and IGF connection. *Endocr Relat Cancer* 2012; **19**:F27–F45.
- WINER S, PALTZER G, CHAN Y et al. Obesity predisposes to Th17 bias. *Eur J Immunol* 2009; **39**:2629–2635.
- PINI M, FANTUZZI G. Enhanced production of IL-17A during zymosan-induced peritonitis in obese mice. *J Leukoc Biol* 2010; **87**:51–58.
- SUMARAC-DUMANOVIC M, STEVANOVIC D, LJUBIC A et al. Increased activity of interleukin-23/interleukin-17 proinflammatory axis in obese women. *Int J Obes (Lond)* 2009; **33**:151–156.
- HOEFELICH KP, LUO J, RUBIE EA et al. Requirement for glycogen synthase kinase-3beta in cell survival and NF-kappaB activation. *Nature* 2000; **406**:86–90.
- MAO L, DAUCHY RT, BLASK DE et al. Circadian gating of epithelial-to-mesenchymal transition in breast cancer cells via melatonin-regulation of GSK3beta. *Mol Endocrinol* 2012; **26**:1808–1820.

40. BLASK DE, BRAINARD GC, DAUCHY RT et al. Melatonin-depleted blood from premenopausal women exposed to light at night stimulates growth of human breast cancer xenografts in nude rats. *Cancer Res* 2005; **65**:11174–11184.
41. LALIENA A, SAN MIGUEL B, CRESPO I et al. Melatonin attenuates inflammation and promotes regeneration in rabbits with fulminant hepatitis of viral origin. *J Pineal Res* 2012; **53**:270–278.
42. TOCHARUS J, KHONTHUN C, CHONGTHAMMAKUN S et al. Melatonin attenuates methamphetamine-induced overexpression of pro-inflammatory cytokines in microglial cell lines. *J Pineal Res* 2010; **48**:347–352.
43. ZHANG Q, LIU S, GE D et al. Interleukin-17 promotes formation and growth of prostate adenocarcinoma in mouse models. *Cancer Res* 2012; **72**:2589–2599.
44. SONG X, QIAN Y. The activation and regulation of IL-17 receptor mediated signaling. *Cytokine* 2013; **62**:175–182.
45. BALAMURUGAN K, SHARAN S, KLARMANN KD et al. FBXW7- α attenuates inflammatory signalling by downregulating C/EBP δ and its target gene Tlr4. *Nat Commun* 2013; **4**:1662.
46. GILBERT CA, SLINGERLAND JM. Cytokines, obesity, and cancer: new insights on mechanisms linking obesity to cancer risk and progression. *Annu Rev Med* 2013; **64**:45–57.
47. DEMURO RL, NAFZIGER AN, BLASK DE et al. The absolute bioavailability of oral melatonin. *J Clin Pharmacol* 2000; **40**:781–784.
48. WALDHAUSER F, WALDHAUSER M, LIEBERMAN HR et al. Bioavailability of oral melatonin in humans. *Neuroendocrinology* 1984; **39**:307–313.
49. GARLEY M, JABLONSKA E, GRABOWSKA SZ et al. IL-17 family cytokines in neutrophils of patients with oral epithelial squamous cell carcinoma. *Neoplasma* 2009; **56**:96–100.
50. JAFARZADEH A, ESMAEELI-NADIMI A, NOUGH H et al. Serum levels of interleukin (IL)-13, IL-17 and IL-18 in patients with ischemic heart disease. *Anadolu Kardiyol Derg* 2009; **9**: 75–83.
51. REITER RJ, TAN DX, KORKMAZ A et al. Obesity and metabolic syndrome: association with chronodisruption, sleep deprivation, and melatonin suppression. *Ann Med* 2012; **44**:564–577.
52. HUSSEIN MR, AHMED OG, HASSAN AF et al. Intake of melatonin is associated with amelioration of physiological changes, both metabolic and morphological pathologies associated with obesity: an animal model. *Int J Exp Pathol* 2007; **88**:19–29.
53. NDUHIRABANDI F, DU TOIT EF, BLACKHURST D et al. Chronic melatonin consumption prevents obesity-related metabolic abnormalities and protects the heart against myocardial ischemia and reperfusion injury in a prediabetic model of diet-induced obesity. *J Pineal Res* 2011; **50**:171–182.
54. AGIL A, NAVARRO-ALARCON M, RUIZ R et al. Beneficial effects of melatonin on obesity and lipid profile in young Zucker diabetic fatty rats. *J Pineal Res* 2011; **50**:207–212.
55. AGIL A, REITER RJ, JIMENEZ-ARANDA A et al. Melatonin ameliorates low-grade inflammation and oxidative stress in young Zucker diabetic fatty rats. *J Pineal Res* 2013; **54**: 381–388.

Liposomal extended-release bupivacaine for postsurgical analgesia

Mark Lambrechts^{1,2}

Michael J O'Brien²

Felix H Savoie²

Zongbing You¹⁻³

¹Department of Structural and Cellular Biology, ²Department of Orthopaedic Surgery and Tulane Institute of Sports Medicine, ³Tulane Cancer Center, Louisiana Cancer Research Consortium, Tulane Center for Aging, Tulane Center for Stem Cell Research and Regenerative Medicine, Tulane University School of Medicine, New Orleans, Louisiana, USA

Abstract: When physicians consider which analgesia to use postsurgery, the primary goal is to relieve pain with minimal adverse side effects. Bupivacaine, a commonly used analgesic, has been formulated into an aqueous suspension of multivesicular liposomes that provide long-lasting analgesia for up to 72 hours, while avoiding the adverse side effects of opioids. The increased efficacy of liposomal extended-release bupivacaine, compared to bupivacaine hydrochloride, has promoted its usage in a variety of surgeries including hemorrhoidectomy, bunionectomy, inguinal hernia repair, total knee arthroplasty, and augmentation mammoplasty. However, like other bupivacaine formulations, the liposomal extended-release bupivacaine does have some side effects. In this brief review, we provide an update of the current knowledge in the use of bupivacaine for postsurgical analgesia.

Keywords: bupivacaine, liposome, analgesia, side effects, efficacy, patient satisfaction

Introduction

Postoperative pain management and minimal analgesic adverse side effects are critical factors in improving patient satisfaction.^{1,2} The systemic analgesic effects of opioids decrease pain in patients, but opioids are known to cause adverse side effects including nausea, dizziness, vomiting, urinary retention, constipation, pruritus, bradypnea, and sedation.^{3,4} These opioid-related symptoms often lead to a significant increase in total hospital cost and length of stay.⁵ Local analgesics have been utilized to avoid these side effects, but it is now known that they carry side effects of their own including but not limited to: chondrotoxicity, human tendon stem cell cytotoxicity, and intervertebral disk cytotoxicity. Furthermore, local analgesics have a short time of action, usually lasting less than 8 hours in adults.^{6,7} In order to prolong duration of action, catheters are inserted to the target site and connected to a local infusion pump, thereby analgesics are delivered to relieve pain with minimal adverse effects.^{8,9} However, the use of infusion pumps is often associated with tissue necrosis and wound infection.¹⁰ In order to provide long-lasting analgesia through single-dose administration, bupivacaine has been formulated with liposomes to create liposomal extended-release bupivacaine. One example of such a bupivacaine liposome injectable suspension is EXPAREL[®] (Pacira Pharmaceuticals, Inc., San Diego, CA, USA). EXPAREL[®] is an aqueous suspension of multivesicular liposomes (DepoFoam[®] drug delivery system; Pacira Pharmaceuticals, Inc.) containing bupivacaine at a concentration of 13.3 mg/mL. After injection of EXPAREL[®] into soft tissue, bupivacaine is released from the multivesicular liposomes over a period of time. In this review, we will update the clinical use of EXPAREL[®] and related analgesics.

Correspondence: Zongbing You
Department of Structural and Cellular
Biology, Tulane University School of
Medicine, 1430 Tulane Avenue SL-49,
New Orleans, LA 70112, USA
Tel +1 504 988 0467
Fax +1 504 988 1687
Email zyou@tulane.edu

Bupivacaine liposome injectable suspension

In 2006, Cocoran et al¹¹ conducted a survey of 135 academic anesthesiology departments and found that 55% of them preferred bupivacaine hydrochloride (HCl) as their local anesthetic of choice. Due to its novel design and slow release, EXPAREL[®] can produce local analgesia for up to 72 hours,¹² about ten times longer than bupivacaine HCl.¹³ EXPAREL[®] has greater upfront costs than bupivacaine HCl. The most recent wholesale acquisition cost for a vial of EXPAREL[®] 266 mg/20 mL is \$14.25 (pricing from December 1, 2011) compared to a 10 mL vial of 0.25% bupivacaine HCl costing \$0.291 (pricing from April 1, 2012; of note, the wholesale acquisition cost represents published catalog price and may not be the actual transaction cost price). The overall costs for patients using EXPAREL[®] are likely cheaper than for bupivacaine HCl in patients who need long-term analgesia due to decreased need for opioids.¹⁴ To our knowledge, no study has directly evaluated hospital cost or length of stay between EXPAREL[®] and bupivacaine HCl; however, it has been documented that the mean difference of cost and length of hospital stay between an EXPAREL[®]-based multimodal analgesia regimen (\$8,766 and 2.0 days) and an opioid-based regimen (\$11,850 and 4.9 days) was \$3,084 and 2.9 days in patients undergoing open colectomies.¹⁵

Bupivacaine blocks sodium channels during an action potential, thus inhibiting generation and conduction of nerve impulses initiated by painful stimuli.¹⁶ Chahar and Cummings¹⁷ described in detail the structure, pharmacodynamics, and pharmacokinetics of this new liposomal bupivacaine. The extended-release advantage of EXPAREL[®] has promoted its widespread use in surgical procedures such as hemorrhoidectomy, bunionectomy, inguinal hernia repair, total knee arthroplasty, augmentation mammoplasty, and colectomy.

Patient satisfaction and efficacy

Patients will have little tolerance of a drug that has numerous adverse effects, making this a necessary parameter in comparing drug choice. Baxter et al¹⁸ and Viscusi et al¹⁹ retrospectively reviewed ten randomized, double-blinded studies to determine total adverse events after administration of 66 mg to 532 mg EXPAREL[®] or 75 mg to 200 mg bupivacaine HCl. Adverse events (AEs) were classified as wound complications, wound healing times, and wound scarring. Local AEs, including erythema, drainage, edema, and induration, were noted over 36 days. Baxter et al found that the percent incidence of AEs was similar across both modes of analgesia.¹⁸ AEs occurred in 9%–20% of 823 patients who received EXPAREL[®] compared to 8%–19%

AEs in 446 patients who were treated with bupivacaine HCl. Furthermore, wound-healing and bone-healing at doses up to 532 mg EXPAREL[®] appeared similar to the bupivacaine HCl group. In contrast, Viscusi et al noted 62% of patients had AEs when they received EXPAREL[®], compared to 75% of patients who received bupivacaine HCl and 43% of the patients treated with placebo.¹⁹ Furthermore, serious AEs were noted in 2.7% of EXPAREL[®] users versus 5.4% of bupivacaine HCl users.

Dasta et al²⁰ examined the postsurgical use of EXPAREL[®] at doses ≤ 266 mg versus bupivacaine HCl at doses ≤ 200 mg. A total of nine double-blinded studies were pooled and analyzed from five surgical procedures including inguinal hernia repair, total knee arthroplasty, breast augmentation, hemorrhoidectomy, and bunionectomy. Patient outcomes were evaluated by cumulative pain intensity scores (area under the curve) based on a numerical rating scale throughout a period of 72 hours after surgery. The cumulative pain intensity score was found to be lower in patients using EXPAREL[®] than in patients using bupivacaine HCl (283 versus 329, $P = 0.039$). The median time until opioid rescue was 10 hours when using EXPAREL[®], compared to 3 hours when using bupivacaine HCl. Furthermore, opioid usage was decreased from 19 mg in the bupivacaine HCl group to 12 mg in the EXPAREL[®] group, suggesting a decrease in the opioid-related AEs.

By focusing on a dose of 266 mg EXPAREL[®] post hemorrhoidectomy, Haas et al²¹ found that the median time until opioid rescue was 19 hours, much longer than the 8 hours noted in the patients who received bupivacaine HCl ($P = 0.05$). AEs related to opioids were also found in 35% of the patients injected with bupivacaine HCl compared to only 4% of the patients injected with 266 mg EXPAREL[®].

Bramlett et al²² compared the efficacy and safety of 150 mg bupivacaine HCl with 1:200,000 epinephrine versus EXPAREL[®] at doses of 133 mg, 266 mg, 399 mg, and 532 mg, following total knee arthroplasty. The double-blinded study found that the cumulative pain intensity scores through 4 days postsurgery were 20.7, 19.5, 18.8, and 19.1, for using EXPAREL[®] at doses of 133 mg, 266 mg, 399 mg, and 532 mg, respectively, compared to a cumulative pain intensity score of 20.4 when using bupivacaine HCl at a dose of 150 mg. Smoot et al²³ conducted a randomized, double-blinded study on 136 patients who underwent submuscular augmentation mammoplasty and compared the pain and opioid usage after a single 600 mg dose of EXPAREL[®] and a single 200 mg dose of bupivacaine HCl. The mean cumulative pain scores (numerical rating scale with activity through 3 days) were 441.5 using EXPAREL[®] and 468.3

using bupivacaine HCl ($P = 0.3999$). EXPAREL[®] usage was associated with a significant decrease in opioids consumed during the first 24 hours ($P = 0.0211$) and 48 hours ($P = 0.0459$). Bergese et al²⁴ analyzed a pool of 823 patients, from ten randomized, double-blinded studies, who were injected via local wound infiltration sites with EXPAREL[®] (doses varied from 66 mg to 532 mg). Another group of 446 patients were injected with bupivacaine HCl at doses ranging from 75 mg to 200 mg, and 190 patients were included in a placebo group. The pain intensity scores were lower in the EXPAREL[®] group than in the placebo group in 16 of the 19 treatment arms analyzed ($P < 0.05$). In contrast, only five of the 17 treatment arms using bupivacaine HCl had a lower pain score than the placebo group ($P < 0.05$).

The efficacy of EXPAREL[®] was further supported by the mean time until opioid usage, consumption of opioids, and patient/care provider satisfaction with postsurgical analgesia. Golf et al²⁵ compared EXPAREL[®] to placebo in a randomized study of 193 patients who had undergone bunionectomy. Ninety-six patients were placed in the placebo group, while 97 patients were administered 120 mg of EXPAREL[®] through wound infiltration before closure. Over the first 24 hours and 36 hours, EXPAREL[®] significantly decreased pain compared to the placebo ($P = 0.0005$ and $P < 0.0229$, respectively). Patients also avoided opioid usage at a greater rate than placebo when injected with EXPAREL[®] (7.2% versus 1% of patients, $P < 0.0404$). The median time until first opioid usage was prolonged by EXPAREL[®] compared to placebo (7.2 hours versus 4.3 hours, $P < 0.0001$). Gorfine et al²⁶ conducted a double-blinded study with 186 patients, comparing EXPAREL[®] and placebo to assess postsurgical analgesia benefits. Pain intensity scores were lower in patients using EXPAREL[®] than in patients using placebo (141.8 versus 202.5, $P < 0.001$). The mean usage of opioids over the first 72 hours was 22.3 mg and 29.1 mg for EXPAREL[®] and placebo groups, respectively ($P < 0.0006$). The median time until first opioid usage was 14.3 hours and 1.2 hours for the EXPAREL[®] and placebo groups, respectively. Most importantly, 95% of patients in the EXPAREL[®] group were satisfied with their postsurgical analgesia, compared to 73% of patients in the placebo group ($P = 0.0007$). Based on the

mentioned studies, a comparison between EXPAREL[®] and bupivacaine HCl is summarized in Table 1.

Systemic toxicities

It is well documented that bupivacaine HCl can prolong QTc intervals (corrected intervals between the Q wave and T wave) and cause ventricular arrhythmias through potassium channel blockade.^{27–29} Borgeat et al³⁰ also noticed an increase in the PQ interval within 15 minutes of 5 mg/mL injection of bupivacaine. The prolongation continued for 1 hour, when the PQ interval shortened to near normal ranges. Furthermore, they reported no change in QRS, QT, or QTc intervals. However, current research suggests that EXPAREL[®] has a better cardiac safety profile compared to standard bupivacaine injections. Naseem et al³¹ conducted a study in healthy patients, evaluating their QTc intervals at doses of 300 mg, 450 mg, 600 mg, and 750 mg EXPAREL[®]. The alteration of QTc intervals by EXPAREL[®] was compared to changes caused by moxifloxacin. The authors found that moxifloxacin induced QTc prolongation of 12 seconds with a two-sided 95% confidence interval above 10 seconds. EXPAREL[®] at doses of 300 mg, 450 mg, 600 mg, and 750 mg caused the QTc interval to decrease by 2.24, 2.45, 3.6, and 7.67 milliseconds, respectively. Only the 600 mg dose fell short of the significance level of the two-sided 95% confidence interval. This study suggests that EXPAREL[®] reduces QTc intervals and may be a safer, long-lasting alternative to bupivacaine HCl.

Bupivacaine also carries significant risk of toxicity in the central nervous system if given in overdose or injected intravenously. Feldman et al³² found that the mean dosage to cause seizures in dogs after intravenous bupivacaine injection was as low as 8.6 mg/kg, leading to a mean duration of seizure of 307 seconds. Since substantial plasma concentrations of bupivacaine are required to cause toxicities in the central nervous system, it should be of minimal concern if the local anesthetic is properly administered.

Local toxicities

Intervertebral disk cell cytotoxicity, myocyte toxicity, chondrotoxicity, and granulomatous inflammation are potential localized side effects of EXPAREL[®] injection. The most

Table 1 Comparison between EXPAREL[®] and bupivacaine HCl

| Formulation | Costs | Pain intensity scores | Time until opioid rescue (h) | % adverse events |
|----------------------|---------------|--------------------------|------------------------------|--------------------------|
| EXPAREL [®] | \$14.25/20 mL | 283*, 441.5 [†] | 10*, 19 [#] | 9–20%*, 62% ^Δ |
| Bupivacaine HCl | \$0.291/10 mL | 329*, 468.3 [†] | 3*, 8 [#] | 8–19%*, 43% ^Δ |

Notes: *Baxter et al;¹⁸ ^ΔViscusi et al;¹⁹ [#]Dasta et al;²⁰ [†]Haas et al;²¹ [‡]Smoot et al.²³

Abbreviation: HCl, hydrochloride.

benign of these side effects is a small amount of granulomatous inflammation due to liposome degradation.^{10,33}

Chondrotoxicity appears to be a much more salient problem in intra-articular usage of EXPAREL®, like other local anesthetics, which is why Pacira Pharmaceuticals, Inc., does not recommend intra-articular use of EXPAREL®. While an intra-articular injection of 0.125% bupivacaine does not induce chondrocyte death, 0.25% bupivacaine is significantly chondrotoxic after 60 minutes exposure.³⁴ Alarming, Chu et al³⁵ reported that an intra-articular injection of 0.5% bupivacaine led to a 50% loss in chondrocyte density with no obvious cartilage loss. Chondrotoxicity has been investigated most extensively in the glenohumeral joint. Wiater et al³⁶ conducted a prospective level II cohort study analyzing 375 cases of arthroscopic shoulder surgeries to assess chondrolysis from intra-articular injections of bupivacaine and lidocaine. Survival analysis was implemented to assess chondrocyte death, and the strength of these results was computed as hazard ratios estimated from the Cox proportional hazard model. Both adjusted and unadjusted Cox proportional hazard models were used to account for the variability due to patient age and the date of surgery. Of the 375 surgeries, 49 patients suffered from chondrolysis, with half being identified within the first 18 months postsurgery. Each patient was known to have postsurgical intra-articular injection of bupivacaine or lidocaine ($P < 0.001$, Cox regression). No chondrolysis was found in patients who did not receive intra-articular injections of local anesthetics. In another study, Anderson et al³⁷ reported 18 individuals diagnosed with glenohumeral chondrolysis, all of them had received intra-articular injections of bupivacaine through an intra-articular pain pump catheter. No thermal energy was used as part of their operation. Decreased range of motion was also noted as a result of the surgeries. These studies caution against intra-articular injection of EXPAREL® or other local anesthetics. This precaution is further supported by a study of patients with damaged cartilage.³⁸ A recent in vitro study has shown that hyaluronan can prevent chondrocyte death caused by bupivacaine at supraphysiological temperatures.³⁹ However, whether coinjection of hyaluronan and bupivacaine intra-articularly may alleviate bupivacaine's chondrotoxicity awaits further evidence from in vivo studies.

It should be noted that the use of EXPAREL® has not been approved by the US Food and Drug Administration for spinal usage. To the best of our knowledge, no studies have been published in evaluating the use of EXPAREL® versus standard bupivacaine as a local anesthetic in spinal procedures. However, bupivacaine HCl is an anesthetic used in spinal procedures, and in vitro studies have shown that it is

toxic in a dose- and time-dependent manner. Doses as small as 0.25% bupivacaine induced nearly 100% cell death in the annulus pulposus and nucleus pulposus cells of intervertebral disks.^{40,41} These results have been supported by the results from an ex vivo mouse model in which bupivacaine reduced both cell viability and synthesis of matrix proteins.⁴² Coinjection of 1 mg triamcinolone with bupivacaine has been shown to have a protective effect on intervertebral disk cells.⁴³

Bupivacaine is also known to cause acute skeletal muscle degeneration with a slow but nearly maximal regeneration after 2 months.⁴⁴ A possible mechanism of myotoxicity is through induction of calcium release from the sarcoplasmic reticulum, while concurrently inhibiting calcium reuptake.⁴⁵ Although the muscle tissue is capable of regeneration after injection of bupivacaine at doses as high as 0.75%, late-stage scarring has been found. This damage is dose-dependent because injection of bupivacaine at doses $<0.38\%$ does not cause any long-term damage.⁴⁶ Although most studies typically focus on adults, myonecrosis may be even more pronounced in children due to oxidative mitochondrial changes.⁴⁷ Furthermore, the toxicity does not appear to be limited only to the muscle fibers. Haasters et al⁴⁸ has reported that 0.5% bupivacaine has cytotoxic effects on human tendon stem cell/progenitor cells, while morphine had no effect on apoptosis or decreased cell survival. Both erythropoietin⁴⁹ and N-acetylcysteine⁵⁰ may confer a protective action against bupivacaine-induced myocyte death.

Discussion

EXPAREL® has been found to be a more effective pain management treatment than standard bupivacaine in inguinal hernia repair, bunionectomy, hemorrhoidectomy, and breast augmentation surgery. There is a clear increase in efficacy in using EXPAREL® compared to using bupivacaine HCl, and no significant difference in AEs has been reported. Furthermore, EXPAREL® is likely to cost patients less money than bupivacaine HCl due to diminished opioids usage and shortened hospital stays. However, caution should be taken when performing the cost-benefit analysis of EXPAREL® injection as the main pain management therapy. Both intra-articular and spinal injections should be cautioned due to potential toxic effects and permanent damage to cartilage and intervertebral disk cells. Granulomatous inflammation and myonecrosis have not been found to cause permanent long-term damage at normal EXPAREL® dosages. Furthermore, cardiotoxicity does not appear to be significant compared to bupivacaine HCl. We conclude that EXPAREL® has potential value to decrease the length of hospital stay and increase patient satisfaction if used properly.

Acknowledgments

Dr Zongbing You was partly supported by a grant from the Department of Defense (PC121647), two grants from the National Institute of General Medical Sciences (P20GM103518) and the National Cancer Institute (R01CA174714) of the National Institutes of Health, the Developmental Fund of Tulane Cancer Center, and Louisiana Cancer Research Consortium Fund. The content is solely the responsibility of the authors and does not necessarily represent the official views of the National Institutes of Health. Dr Zongbing You, Dr Michael J O'Brien, and Dr Felix H Savoie received a research grant from DePuy Mitek, Raynham, MA, USA, for a different study, which had no role in the preparation and submission of this manuscript. Mr Mark Lambrechts was supported by a summer stipend from the DeBaKey Scholars Program of Tulane University School of Medicine.

Disclosure

The authors report no conflicts of interest in this work.

References

- Myles PS, Williams DL, Hendrata M, Anderson H, Weeks AM. Patient satisfaction after anaesthesia and surgery: results of a prospective survey of 10,811 patients. *Br J Anaesth*. 2000;84(1):6–10.
- Hanna MN, González-Fernández M, Barrett AD, Williams KA, Pronovost P. Does patient perception of pain control affect patient satisfaction across surgical units in a tertiary teaching hospital? *Am J Med Qual*. 2012;27(5):411–416.
- Benyamin R, Trescot AM, Datta S, et al. Opioid complications and side effects. *Pain Physician*. 2008;11(Suppl 2):105–120.
- Walder B, Schafer M, Henzi I, Tramèr MR. Efficacy and safety of patient-controlled opioid analgesia for acute postoperative pain. A quantitative systematic review. *Acta Anaesthesiol Scand*. 2001;45(7):795–804.
- Odera GM, Said Q, Evans RS, et al. Opioid-related adverse drug events in surgical hospitalizations: impact on costs and length of stay. *Ann Pharmacother*. 2007;41(3):400–406.
- Akhtar MI, Saleem M, Zaheer J. Wound infiltration with Bupivacaine versus Ketorolac for postoperative pain relief in minor to moderate surgeries. *J Pak Med Assoc*. 2009;59(6):385–388.
- Leone S, Di Cianni S, Casati A, Fanelli G. Pharmacology, toxicology, and clinical use of new long acting local anesthetics, ropivacaine and levobupivacaine. *Acta Biomed*. 2008;79(2):92–105.
- Tuominen M, Haasio J, Hekali R, Rosenberg PH. Continuous interscalene brachial plexus block: clinical efficacy, technical problems and bupivacaine plasma concentrations. *Acta Anaesthesiol Scand*. 1989;33(1):84–88.
- Klein SM, Grant SA, Greengrass RA, et al. Interscalene brachial plexus block with a continuous catheter insertion system and a disposable infusion pump. *Anesth Analg*. 2000;91(6):1473–1478.
- Brown SL, Morrison AE. Local anesthetic infusion pump systems adverse events reported to the Food and Drug Administration. *Anesthesiology*. 2004;100(5):1305–1307.
- Cocoran W, Butterworth J, Weller RS, et al. Local anesthetic-induced cardiac toxicity: a survey of contemporary practice strategies among academic anesthesiology departments. *Anesth Analg*. 2006;103(5):1322–1326.
- Richard BM, Newton P, Ott LR, et al. The safety of EXPAREL® (bupivacaine liposome injectable suspension) administered by peripheral nerve block in rabbits and dogs. *J Drug Deliv*. 2012;2012:962101.
- Marcaïne™ (bupivacaine HCl) [prescribing information]. Lake Forrest, IL: Hospira Inc; 2009.
- Drug pricing policy. San Francisco, CA: First Databank Inc; 2013. Available from: <http://www.fdbhealth.com/policies/drug-pricing-policy/>. Accessed July 19, 2013.
- Cohen SM. Extended pain relief trial utilizing infiltration of Exparel®, a long-acting multivesicular liposome formulation of bupivacaine: a Phase IV health economic trial in adult patients undergoing open colectomy. *J Pain Res*. 2012;5:567–572.
- Clarkson CW, Hondeghem LM. Mechanism for bupivacaine depression of cardiac conduction: fast block of sodium channels during the action potential with slow recovery from block during diastole. *Anesthesiology*. 1985;62(4):396–405.
- Chahar P, Cummings KC. Liposomal bupivacaine: a review of a new bupivacaine formulation. *J Pain Res*. 2012;5:257–264.
- Baxter R, Bramlett K, Onel E, Daniels S. Impact of local administration of liposome bupivacaine for postsurgical analgesia on wound healing: a review of data from ten prospective, controlled clinical studies. *Clin Ther*. 2013;35(3):312–320. e5.
- Viscusi ER, Sinatra R, Onel E, Ramamoorthy SL. The safety of liposome bupivacaine, a novel local analgesic formulation. *Clin J Pain*. Epub February 26, 2013.
- Dasta J, Ramamoorthy S, Patou G, Sinatra R. Bupivacaine liposome injectable suspension compared with bupivacaine HCl for the reduction of opioid burden in the postsurgical setting. *Curr Med Res Opin*. 2012;28(10):1609–1615.
- Haas E, Onel E, Miller H, Ragupathi M, White PF. A double-blind, randomized, active-controlled study for post-hemorrhoidectomy pain management with liposome bupivacaine, a novel local analgesic formulation. *Am Surg*. 2012;78(5):574–581.
- Bramlett K, Onel E, Viscusi ER, Jones K. A randomized, double-blind, dose-ranging study comparing wound infiltration of DepoFoam bupivacaine, an extended-release liposomal bupivacaine, to bupivacaine HCl for postsurgical analgesia in total knee arthroplasty. *Knee*. 2012;19(5):530–536.
- Smoot JD, Bergese SD, Onel E, Williams HT, Hedden W. The efficacy and safety of DepoFoam bupivacaine in patients undergoing bilateral, cosmetic, submuscular augmentation mammoplasty: a randomized, double-blind, active-control study. *Aesthet Surg J*. 2012;32(1):69–76.
- Bergese SD, Ramamoorthy S, Patou G, Bramlett K, Gorfine SR, Candiotti KA. Efficacy profile of liposome bupivacaine, a novel formulation of bupivacaine for postsurgical analgesia. *J Pain Res*. 2012;5:107–116.
- Golf M, Daniels SE, Onel E. A phase 3, randomized, placebo-controlled trial of DepoFoam® bupivacaine (extended-release bupivacaine local analgesic) in bunionectomy. *Adv Ther*. 2011;28(9):776–788.
- Gorfine SR, Onel E, Patou G, Krivokapic ZV. Bupivacaine extended-release liposome injection for prolonged postsurgical analgesia in patients undergoing hemorrhoidectomy: a multicenter, randomized, double-blind, placebo-controlled trial. *Dis Colon Rectum*. 2011;54(12):1552–1559.
- Gristwood RW. Cardiac and CNS toxicity of levobupivacaine: strengths of evidence for advantage over bupivacaine. *Drug Saf*. 2002;25(3):153–163.
- de La Coussaye JE, Bassoul BP, Albat B, et al. Succinylcholine does not worsen bupivacaine-induced cardiotoxicity in pentobarbital-anaesthetized dogs. *Can J Anaesth*. 1992;39(2):192–197.
- Huang YF, Pryor ME, Mather LE, Veering BT. Cardiovascular and central nervous system effects of intravenous levobupivacaine and bupivacaine in sheep. *Anesth Analg*. 1998;86(4):797–804.
- Borgeat A, Ekatodramis G, Blumenthal S. Interscalene brachial plexus anesthesia with ropivacaine 5 mg/mL and bupivacaine 5 mg/mL: effects on electrocardiogram. *Reg Anesth Pain Med*. 2004;29(6):557–563.
- Naseem A, Harada T, Wang D, et al. Bupivacaine extended release liposome injection does not prolong QTc interval in a thorough QT/QTc study in healthy volunteers. *J Clin Pharmacol*. 2012;52(9):1441–1447.

32. Feldman HS, Arthur GR, Covino BG. Comparative systemic toxicity of convulsant and supraconvulsant doses of intravenous ropivacaine, bupivacaine, and lidocaine in the conscious dog. *Anesth Analg*. 1989;69(6):794–801.
33. Richard BM, Ott LR, Haan D, et al. The safety and tolerability evaluation of DepoFoam bupivacaine (bupivacaine extended-release liposome injection) administered by incision wound infiltration in rabbits and dogs. *Expert Opin Investig Drugs*. 2011;20(10):1327–1341.
34. Chu CR, Izzo NJ, Coyle CH, Papas NE, Logar A. The in vitro effects of bupivacaine on articular chondrocytes. *J Bone Joint Surg Br*. 2008;90(6):814–820.
35. Chu CR, Coyle CH, Chu CT, et al. In vivo effects of single intra-articular injection of 0.5% bupivacaine on articular cartilage. *J Bone Joint Surg Am*. 2010;92(3):599–608.
36. Wiater BP, Neradilek MB, Polissar NL, Matsen FA. Risk factors for chondrolysis of the glenohumeral joint: a study of three hundred and seventy-five shoulder arthroscopic procedures in the practice of an individual community surgeon. *J Bone Joint Surg Am*. 2011;93(7):615–625.
37. Anderson SL, Buchko JZ, Taillon MR, Ernst MA. Chondrolysis of the glenohumeral joint after infusion of bupivacaine through an intra-articular pain pump catheter: a report of 18 cases. *Arthroscopy*. 2010;26(4):451–461.
38. Piper SL, Kramer JD, Kim HT, Feeley BT. Effects of local anesthetics on articular cartilage. *Am J Sports Med*. 2011;39(10):2245–2253.
39. Liu S, Zhang QS, Hester W, O'Brien MJ, Savoie FH, You Z. Hyaluronan protects bovine articular chondrocytes against cell death induced by bupivacaine at supraphysiologic temperatures. *Am J Sports Med*. 2012;40(6):1375–1383.
40. Lee H, Sowa G, Vo N, et al. Effect of bupivacaine on intervertebral disc cell viability. *Spine J*. 2010;10(2):159–166.
41. Quero L, Klawitter M, Nerlich AG, Leonardi M, Boos N, Wuertz K. Bupivacaine – the deadly friend of intervertebral disc cells? *Spine J*. 2011;11(1):46–53.
42. Wang D, Vo NV, Sowa GA, et al. Bupivacaine decreases cell viability and matrix protein synthesis in an intervertebral disc organ model system. *Spine J*. 2011;11(2):139–146.
43. Moon JH, Kuh SU, Park HS, et al. Triamcinolone decreases bupivacaine toxicity to intervertebral disc cell in vitro. *Spine J*. 2012;12(8):665–673.
44. Akbari MR, Amoli FA, Alhashemi LH, et al. Bupivacaine injection myotoxicity on extraocular muscles. A strabismus alternative treatment: extended histological changes induced in a rabbit model. *Binocul Vis Strabolog Q Simms Romano*. 2012;27(1):15–22.
45. Zink W, Graf BM, Sinner B, Martin E, Fink RH, Kunst G. Differential effects of bupivacaine on intracellular Ca²⁺ regulation: potential mechanisms of its myotoxicity. *Anesthesiology*. 2002;97(3):710–716.
46. Zhang C, Phamonvaechavan P, Rajan A, Poon DY, Topcu-Yilmaz P, Guyton DL. Concentration-dependent bupivacaine myotoxicity in rabbit extraocular muscle. *JAAPOS*. 2010;14(4):323–327.
47. Nouette-Gaulain K, Dadure C, Morau D, et al. Age-dependent bupivacaine-induced muscle toxicity during continuous peripheral nerve block in rats. *Anesthesiology*. 2009;111(5):1120–1127.
48. Haasters F, Polzer H, Prall WC, et al. Bupivacaine, ropivacaine, and morphine: comparison of toxicity on human hamstring-derived stem/progenitor cells. *Knee Surg Sports Traumatol Arthrosc*. 2011;19(12):2138–2144.
49. Nouette-Gaulain K, Bellance N, Prévost B, et al. Erythropoietin protects against local anesthetic myotoxicity during continuous regional analgesia. *Anesthesiology*. 2009;110(3):648–659.
50. Galbes O, Bourret A, Nouette-Gaulain K, et al. N-acetylcysteine protects against bupivacaine-induced myotoxicity caused by oxidative and sarcoplasmic reticulum stress in human skeletal myotubes. *Anesthesiology*. 2010;113(3):560–569.

Patient Preference and Adherence

Publish your work in this journal

Patient Preference and Adherence is an international, peer-reviewed, open access journal focusing on the growing importance of patient preference and adherence throughout the therapeutic continuum. Patient satisfaction, acceptability, quality of life, compliance, persistence and their role in developing new therapeutic modalities and compounds to

optimize clinical outcomes for existing disease states are major areas of interest. This journal has been accepted for indexing on PubMed Central. The manuscript management system is completely online and includes a very quick and fair peer-review system. Visit <http://www.dovepress.com/testimonials.php> to read real quotes from published authors.

Submit your manuscript here: <http://www.dovepress.com/patient-preference-and-adherence-journal>

Dovepress

Original Article

Open Access

Interleukin-17 Indirectly Promotes M2 Macrophage Differentiation through Stimulation of COX-2/PGE2 Pathway in the Cancer Cells

Qingli Li, MD, PhD^{1,2}
Lunxu Liu, MD, PhD³
Qiuyang Zhang, PhD¹
Sen Liu, MD¹
Dongxia Ge, MD, PhD¹
Zongbing You, MD, PhD¹

¹Departments of Structural and Cellular Biology and Orthopaedic Surgery, Tulane Cancer Center and Louisiana Cancer Research Consortium, Tulane Center for Stem Cell Research and Regenerative Medicine, and Tulane Center for Aging, Tulane University Health Sciences Center, New Orleans, LA, USA,

²Department of Obstetrics and Gynecology, West China Second University Hospital, Sichuan University, Chengdu,

³Department of Thoracic Surgery, West China Hospital, Sichuan University, Chengdu, China

Correspondence: Zongbing You, MD, PhD
Department of Structural and Cellular Biology,
Tulane University, 1430 Tulane Ave SL 49,
New Orleans, LA 70112, USA
Tel: 1-504-988-0467
Fax: 1-504-988-1687
E-mail: zyou@tulane.edu

Co-Correspondence: Lunxu Liu, MD, PhD
Department of Thoracic Surgery, West China
Hospital, Sichuan University, No. 37 Guoxue
Alley, Chengdu, Sichuan 610041, China
Tel: 86-13608236600
Fax: 86-28-85422494
E-mail: lunxu_liu@aliyun.com

Received July 27, 2013
Accepted September 11, 2013

Purpose

Interleukin-17 (IL-17) is a proinflammatory cytokine that plays important roles in inflammation, autoimmunity, and cancer. The purpose of this study was to determine if IL-17 indirectly regulates macrophage differentiation through up-regulation of cyclooxygenase-2 (COX-2) expression in the cancer cell lines.

Materials and Methods

Human cervical cancer HeLa, human lung cancer A549, and mouse prostate cancer Myc-CaP/CR cell lines were treated with recombinant IL-17; Western blot analysis, enzyme-linked immunosorbent assay, and quantitative real-time polymerase chain reaction analysis were utilized to examine the cellular responses.

Results

IL-17 up-regulated expression of COX-2 mRNA and protein in HeLa, A549, and Myc-CaP/CR cell lines. IL-17's effects were mediated through nuclear factor- κ B and ERK1/2 signaling pathways as the inhibitors of these pathways could inhibit IL-17-induced COX-2 expression. The conditional medium obtained from the cancer cells contained prostaglandin E2, the levels of which were increased by IL-17 treatment. When treated with the conditional medium, particularly with the IL-17-induced conditional medium, mouse RAW264.7 macrophages and human THP-1 monocytes expressed higher levels of IL-10 (a marker of M2 macrophages) than inducible nitric oxide synthase or tumor necrosis factor α (markers of M1 macrophages). In contrast, when RAW264.7 and THP-1 cells were treated directly with IL-17, expression of these marker genes was not markedly changed.

Conclusion

The results of this study suggest that IL-17 indirectly promotes M2 macrophage differentiation through stimulation of the COX-2/PGE2 pathway in the cancer cells, thus IL-17 plays an indirect role in regulating the tumor immune microenvironment.

Key words

Interleukin-17, Cyclooxygenase-2, Dinoprostone, Neoplasms, Macrophages, Tumor microenvironment

Introduction

Tumor microenvironment plays an important role in tumor growth and metastasis. Tumor microenvironment consists of tumor cells and stromal cells including fibroblasts,

endothelial cells, macrophages, dendritic cells, and lymphocytes, as well as these cells' products such as extracellular matrix, cytokines, chemokines, growth factors, enzymes, and cellular metabolites. Macrophages can influence tumor growth, angiogenesis, invasion, and metastasis by expressing growth factors, cytokines, chemokines, and enzymes. The

tumor-associated macrophages (TAMs) are a group of heterogeneous cells with a spectrum of diverse biological properties. The macrophages at the two ends of the spectrum are named M1 and M2 macrophages, mirroring the TH-1 and TH-2 nomenclature of T helper cells, respectively. Tumor necrosis factor α (TNF α), interferon- γ , lipopolysaccharides, and granulocyte-macrophage colony-stimulating factor are known to induce monocytes to differentiate into M1 macrophages. M1 macrophages express high levels of inducible nitric oxide synthase (iNOS), TNF α , interleukin (IL)-1 β , IL-6, IL-12, IL-18, IL-23, CXCL10, human leukocyte antigen-DR, and reactive oxygen and nitrogen intermediates. On the other hand, IL-4, IL-10, IL-13, IL-21, activin A, immune complexes, and glucocorticoids induce monocytes to become M2 macrophages [1]. M2 macrophages express high levels of IL-10, arginase I, IL-1 receptor antagonist, CD14, mannose receptor, galactose receptor, and CD163 antigen [1,2]. M1 macrophages inhibit tumor growth by producing effector molecules such as reactive oxygen intermediates, reactive nitrogen intermediates, and TNF α , whereas M2 macrophages promote tumor growth and metastasis by secretion of growth factors, vascular endothelial growth factor, matrix metalloproteinases, and immunosuppressive cytokines/chemokines [3]. The anti- or pro-tumor role of TAMs is determined by the balance between M1 and M2 macrophages [4]. We have previously reported that approximately 70% of TAMs are M2 macrophages and the remaining 30% are M1 macrophages in non-small cell lung cancers [5]. We have demonstrated that lung tumor tissues expressed significantly higher levels of IL-17 (also named IL-17A), cyclooxygenase-2 (COX-2), and prostaglandin E2 (PGE2) than normal lung tissues [6]. High levels of IL-17 in the lung cancer recruit monocytes/macrophages into the lung tumor microenvironment, and PGE2 induces them to differentiate into M2 macrophages [6]. However, it is not known if IL-17 also regulates the COX-2/PGE2 pathway in the cancer cells.

IL-17 binds to a heterodimer of IL-17 receptor A (IL-17RA) and IL-17 receptor C (IL-17RC). The activated receptor complex recruits nuclear factor- κ B (NF- κ B) activator 1 (Act1) through SEFIR (similar expression to fibroblast growth factor genes, IL-17 receptors and Toll-IL-1R) domains that exist in IL-17RA, IL-17RC, and Act1 proteins [7]. Act1 is an E3 ubiquitin ligase that activates tumor necrosis factor receptor-associated factor 6 (TRAF6) through lysine-63-linked ubiquitination [8]. Subsequently, the polyubiquitinated TRAF6 activates transforming growth factor- β -activated kinase 1 and I κ B kinase complex, resulting in activation of NF- κ B pathway that induces transcription of a variety of cytokines, chemokines and growth factors [7]. In addition, IL-17 activates the extracellular signal-regulated kinases 1 and 2 (ERK1/2) that stabilizes mRNAs of the IL-17 down-

stream target genes [9]. In this study, we found that IL-17 activated NF- κ B and ERK1/2 pathways to up-regulate expression of COX-2 mRNA and protein in HeLa, A549, and Myc-CaP/CR cancer cell lines. Subsequently, the cancer cells secreted more PGE2 that acted on monocytes to promote M2 macrophage differentiation.

Materials and Methods

1. Cell cultures

Human cervical cancer HeLa cell line, human lung cancer A549 cell line, human THP-1 monocytes (from acute monocytic leukemia), and mouse RAW264.7 macrophages (from a mouse tumor induced by Abelson murine leukemia virus) were purchased from the American Type Culture Collection (Manassas, VA). Mouse castration-resistant prostate cancer cell line Myc-CaP/CR was a gift from Dr. Leigh Ellis and Dr. Roberto Pili (Roswell Park Cancer Institute, Buffalo, NY) [10]. HeLa, A549, Myc-CaP/CR, and RAW264.7 cells were maintained in Dulbecco's modified Eagle's medium (Mediatech Inc., Manassas, VA) containing 10% fetal bovine serum (FBS; HyClone, Logan, UT) and 100 IU/mL penicillin/streptomycin. THP-1 cells were maintained in RPMI-1640 medium (HyClone) containing 10% FBS and 100 IU/mL penicillin/streptomycin. The cells were cultured in a 5% CO₂ humidified incubator at 37°C.

2. Real-time quantitative reverse transcriptase polymerase chain reaction (qRT-PCR)

After 15 hours of serum starvation, HeLa, A549, and Myc-CaP/CR cells were treated without or with 20 ng/mL recombinant IL-17A (R&D Systems Inc., Minneapolis, MN) for 2 hours. The cells were collected in lysis buffer and homogenized with a 1-mL syringe connected to a 21-gauge needle. Total RNA was isolated according to the instructions of RNeasy Mini Kit (Qiagen, Valencia, CA) with on-membrane DNase I digestion to avoid genomic DNA contamination. cDNA was made from total RNA using iScript cDNA Synthesis Kit (Bio-Rad Laboratories, Hercules, CA). Human and mouse glyceraldehyde-3-phosphate dehydrogenase (GAPDH) and COX-2 PCR primers were obtained from Eurofins MWG Operon (Huntsville, AL). Real-time quantitative PCR (qRT-PCR) was performed in triplicates with an iQ5 iCycler and iQ SYBR Green Supermix (Bio-Rad Laboratories) following the recommended protocols. Results were normalized to GAPDH levels using the formula $\Delta\Delta C_t$ (Cycle

threshold)=Ct of target gene–Ct of GAPDH. The mRNA level of the control group was used as the baseline, so $\Delta\Delta\text{Ct}$ was calculated using the formula $\Delta\Delta\text{Ct}=\Delta\text{Ct of target gene}-\Delta\text{Ct of the baseline}$. The fold change of mRNA level was calculated as $\text{fold}=2^{-\Delta\Delta\text{Ct}}$.

3. Induction of monocyte/macrophage differentiation

HeLa, A549, and Myc-CaP/CR cells were cultured in serum-free medium for 15 hours and then treated without or with 20 ng/mL IL-17A for 24 hours. The culture medium was centrifuged at $14,000 \times g$ for 10 minutes at 4°C. The supernatant from the untreated group was named conditional medium (CM) and the supernatant from the IL-17A-treated group was named IL-17A-induced CM. Approximately 2×10^6 THP-1 or RAW264.7 cells were cultured in serum-free medium in 60-mm dishes for 15 hours. The CM or IL-17A-induced CM from human HeLa or A549 cells was used to treat mouse RAW264.7 cells. Conversely, the CM or IL-17A-induced CM from mouse Myc-CaP/CR cells was used to treat human THP-1 cells. In this way, we could avoid cross-contamination of cancer cell mRNAs in qRT-PCR analysis of macrophage mRNAs because the PCR primers were species-specific. In addition, the control group was treated with serum-free medium without exposure to any cells and another group was treated with IL-17A in serum-free medium to assess the direct effects of IL-17A. After 3 hours of treatment, total RNA was isolated and qRT-PCR analysis was performed as described above. Human and mouse iNOS, TNF α , IL-10, arginase I, and GAPDH PCR primers were obtained from Eurofins MWG Operon.

4. Western blot analysis

To assess the effects of IL-17 on COX-2 protein expression, 2×10^6 cells were cultured in serum-free medium in 60-mm dishes for 15 hours. Then, the cells were treated without or with recombinant IL-17A (20 ng/mL) for 9, 12, and 24 hours. To assess the effects of IL-17 on NF- κ B and ERK1/2 pathways, 2×10^6 cells were cultured in serum-free medium in 60-mm dishes for 15 hours. Then, the cells were treated without or with recombinant IL-17A (20 ng/mL) for 5, 15, 60, and 180 minutes. To assess the effects of pharmacologic inhibitors on IL-17-induced COX-2 protein expression, 2×10^6 cells were cultured in serum-free medium in 60-mm dishes for 15 hours. Then, the cells were treated without or with 100 μ M NF- κ B inhibitor pyrrolidine dithiocarbamate (PDTC; Sigma-Aldrich, St. Louis, MO) or 10 μ M MEK inhibitor U0126 (Promega, Madison, WI), 30 minutes prior to addition of recombinant IL-17A (20 ng/mL) for 12 hours treatment. After the indicated time of treatment, proteins were extracted from

the treated cells in RIPA lysis buffer (50 mM sodium fluoride, 0.5% Igepal CA-630 [NP-40], 10 mM sodium phosphate, 150 mM sodium chloride, 25 mM Tris pH 8.0, 1 mM phenylmethylsulfonyl fluoride, 2 mM ethylenediaminetetraacetic acid [EDTA], 1.2 mM sodium vanadate) supplemented with protease inhibitor cocktail (Sigma-Aldrich). Equal amount of proteins was subjected to 10% sodium dodecyl sulfate-polyacrylamide gel electrophoresis and transferred to polyvinylidene difluoride membrane. The membranes were blocked with 5% nonfat dry milk in TBST buffer (25 mM Tris-HCl, 125 mM NaCl, 0.1% Tween 20) for 2 hours and probed with the indicated primary antibodies overnight and then IRDye 800CW- or IRDye 680RD-conjugated secondary antibodies (LI-COR Biosciences, Lincoln, NE) for 1 hour. The results were visualized by using an Odyssey Infrared Imager (LI-COR Biosciences). For loading control, the membranes were stripped and probed for unphosphorylated proteins and/or GAPDH. The antibodies used are as follows: mouse anti-COX-2 antibodies were obtained from Cayman Chemical (Ann Arbor, MI, USA); goat anti-COX-2 and mouse anti-P-ERK1/2 antibodies were obtained from Santa Cruz Biotechnology (Santa Cruz, CA); rabbit anti-ERK1/2, rabbit anti-P-I κ B α , and mouse anti-I κ B α antibodies were purchased from Cell Signaling Technology (Danvers, MA); mouse anti-GAPDH antibodies were ordered from Millipore Corporation (MAB374, Billerica, MA). Quantification of the Western blot signals was performed using the image analysis software of the Odyssey Infrared Imager system. The integrated density values of COX-2 signals were normalized by those of GAPDH. The ratio of COX-2/GAPDH indicates the relative level of COX-2 protein. The data represent the mean and standard deviation of three independent experiments.

5. Enzyme-linked immunosorbent assay of PGE2 levels

Approximately 2×10^6 cells of HeLa, A549, and Myc-CaP/CR cell lines were cultured in serum-free medium in 60-mm dishes for 15 hours. Then, the cells were treated without or with 20 ng/mL IL-17A for 24 hours. The culture medium was centrifuged at $14,000 \times g$ for 10 minutes at 4°C. The supernatant was collected and stored at –80°C until analysis. PGE2 levels were measured using a Prostaglandin E2 Enzyme Immunoassay Kit (Arbor Assays, Ann Arbor, MI) according to the manufacturer's instructions. Absorbance values were determined using a Bio-RAD Model 550 Microplate Reader. A standard curve was produced using a series of PGE2 concentrations from 31.25 to 1,000 pg/mL. The PGE2 level of each sample was obtained by plotting against the standard curve using Curve-Expert 1.4 software (<http://www.curveexpert.net>). The data represent the mean and standard deviation of three independent experiments.

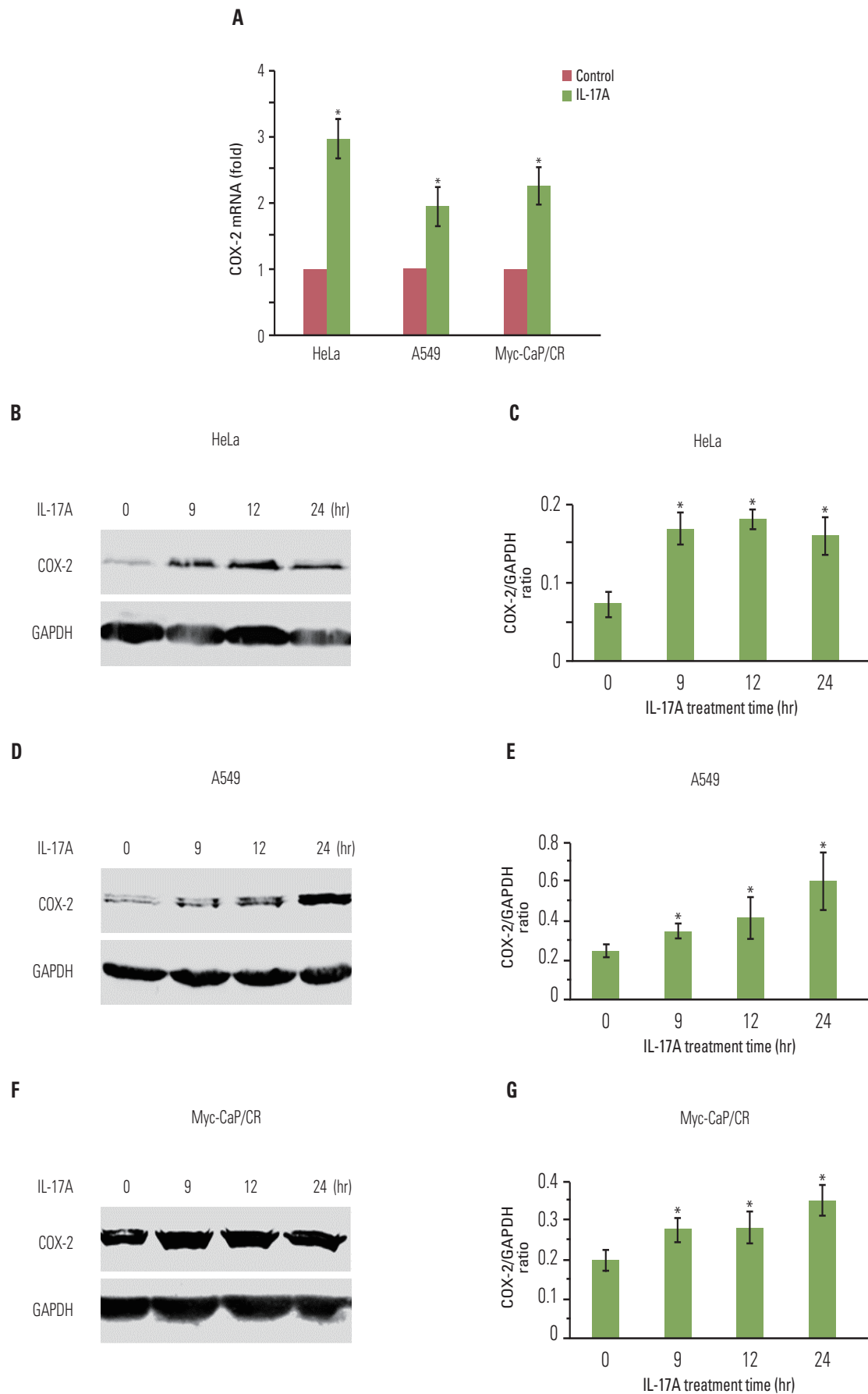


Fig. 1. Interleukin (IL)-17 up-regulates expression of cyclooxygenase-2 (COX-2) mRNA and protein in cancer cells. (A) The cancer cells were treated without or with 20 ng/mL IL-17A for 2 hours; COX-2 mRNA levels were determined by real-time quantitative reverse transcriptase polymerase chain reaction. (B, D, F) The cancer cells were treated with 20 ng/mL IL-17A; COX-2 protein levels were determined by Western blot analysis. (C, E, G) Quantification of Western blot signals in three independent experiments. The ratio represents COX-2 signal divided by glyceraldehyde 3-phosphate dehydrogenase (GAPDH) signal, where ratio=1 means that COX-2 signal is equal to GAPDH signal. Values are presented as the mean \pm standard deviation obtained from three independent experiments. * $p < 0.05$, compared to the control group.

6. Statistical analysis

All experiments were repeated three times and the results represent mean \pm standard deviation of three independent experiments. Statistical analysis was made using two-tailed Student's *t*-test. $p < 0.05$ was considered statistically significant.

Results

1. IL-17 up-regulates expression of COX-2 mRNA and protein in cancer cell lines

We have previously shown that IL-17 up-regulates expression of chemokines and cytokines in human cancer cell lines such as HeLa, HEC-1-B, and SKOV3 [11]. In this study, we found that IL-17 significantly up-regulated COX-2 mRNA expression in HeLa, A549, and Myc-CaP/CR cancer cell lines ($p < 0.05$) (Fig. 1A). IL-17 also significantly up-regulated COX-2 protein expression in HeLa cells ($p < 0.05$) (Fig. 1B and C), A549 cells ($p < 0.05$) (Fig. 1D and E), and Myc-CaP/CR cells ($p < 0.05$) (Fig. 1F and G).

2. IL-17 activates NF- κ B and/or ERK1/2 pathways in cancer cell lines

We found that IL-17A increased phosphorylated I κ B α (P-I κ B α) after 5, 60, and 180 minutes of IL-17A treatment in HeLa cells (Fig. 2A), suggesting that NF- κ B pathway was activated in the IL-17A-treated cells. In contrast, P-ERK1/2 was not increased by IL-17A treatment (Fig. 2A), suggesting that ERK1/2 pathway was not activated by IL-17A in this cancer cell line. Similarly, we found that IL-17A increased P-I κ B α after 15, 60, and 180 minutes of IL-17A treatment in A549 cells, however, P-ERK1/2 was not increased except a slight increase in P-ERK2 at 15 minutes (Fig. 2B), suggesting that NF- κ B pathway was also the main signaling pathway that was activated in the IL-17A-treated A549 cells while ERK1/2 signaling pathway was only slightly activated in this cell line.

In contrast, we found that IL-17A increased both P-I κ B α and P-ERK1/2 in Myc-CaP/CR cells (Fig. 2C), suggesting that both NF- κ B and ERK1/2 signaling pathways are activated in the IL-17A-treated Myc-CaP/CR cells. To determine if NF- κ B and ERK1/2 signaling pathways mediate IL-17's effects in regulation of COX-2 expression, we treated A549 and HeLa cells with an NF- κ B inhibitor PDTC or MEK inhibitor U0126 prior to IL-17A treatment. We found that U0126 dramatically and significantly inhibited IL-17A-induced COX-2 protein expression in A549 cells ($p < 0.05$) (Fig. 3A and C), whereas PDTC only slightly but significantly inhibited IL-17A-induced COX-2 protein expression in A549 cells ($p < 0.05$) (Fig. 3A and C). In HeLa cells, both U0126 and PDTC only slightly inhibited IL-17A-induced COX-2 protein expression, however, the inhibition was statistically significant ($p < 0.05$) (Fig. 3B and D). In Myc-CaP/CR cells, neither U0126 nor PDTC inhibited IL-17A-induced COX-2 protein expression (data not shown). These findings suggest that IL-17 indeed acts through NF- κ B and ERK1/2 signaling pathways in A549 and HeLa cells to regulate expression of downstream genes, which is consistent with our previous study [11].

3. IL-17 indirectly promotes M2 macrophage differentiation through induction of PGE2 synthesis

Since COX-2 is a critical enzyme for the production of PGE2 [12], we checked if IL-17 could induce PGE2 synthesis. We found that IL-17A significantly induced synthesis and secretion of PGE2 by HeLa, A549, and Myc-CaP/CR cancer cells ($p < 0.05$) (Fig. 4). Since we have previously demonstrated that PGE2 can induce RAW264.7 macrophages to express marker genes of M2 macrophages such as arginase I and IL-10 [6], we investigated if IL-17A-induced CM could show similar effects. We found that IL-17A-induced CM from HeLa cells significantly increased expression of iNOS, TNF α , IL-10, and arginase I, with the highest magnitude of induction seen in IL-10 ($p < 0.01$ or $p < 0.05$, compared to the IL-17A treatment group or CM treatment group, respectively) (Fig. 5A). The CM from HeLa cells also dramatically increased expression of iNOS, TNF α , and IL-10 (Fig. 5A), representing the effects of basal levels of PGE2 that was ex-

pressed in this cell line. In contrast, directly treating RAW264.7 macrophages with IL-17A did not dramatically increase expression of iNOS, TNF α , IL-10, or arginase I (Fig. 5A). Similar findings were obtained using the CM from A549 cells, again with the highest magnitude of induction seen in IL-10 (Fig. 5B). IL-17A-induced CM from Myc-CaP/CR cells significantly increased expression of TNF α and IL-10 in THP-1 monocytes ($p < 0.01$, compared to the IL-17A treat-

ment group) (Fig. 5C), and the CM from Myc-CaP/CR cells also dramatically increased expression of TNF α and IL-10, with IL-10 at a higher level than TNF α (Fig. 5C). However, there was no statistical significance between the treatments with the CM and IL-17A-induced CM (Fig. 5C). Consistently, directly treating THP-1 monocytes with IL-17A did not increase expression of iNOS, TNF α , IL-10, or arginase I (Fig. 5C).

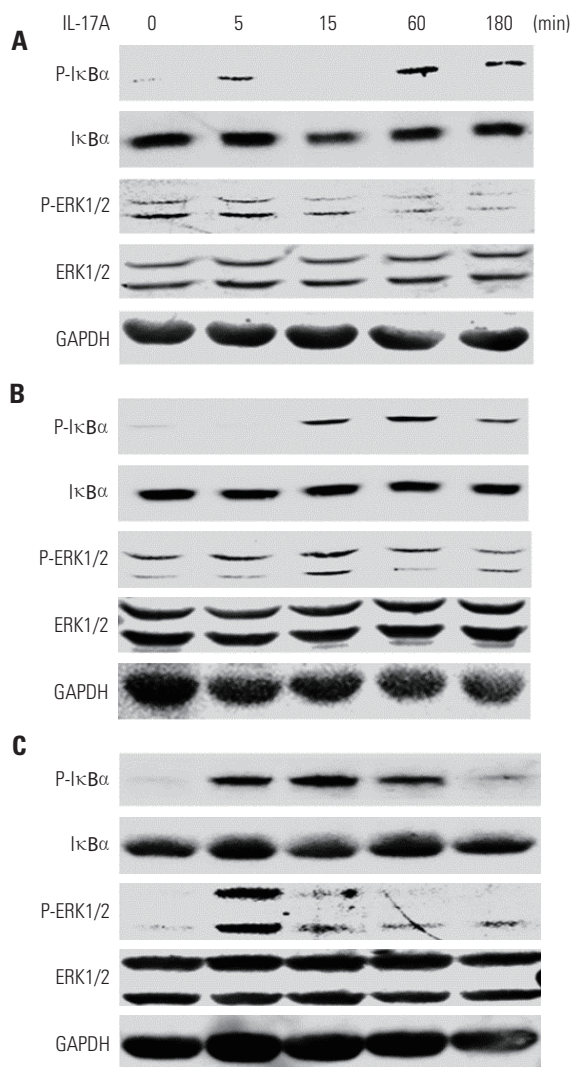


Fig. 2. Interleukin (IL)-17 activates nuclear factor- κ B and/or extracellular signal-regulated kinases 1 and 2 (ERK1/2) signaling pathways in cancer cells. HeLa cells (A), A549 cells (B), and Myc-CaP/CR cells (C) were treated without or with 20 ng/mL IL-17A; protein levels were determined by Western blot analysis. For protein loading control, the blots were stripped and reprobed for glyceraldehyde 3-phosphate dehydrogenase (GAPDH).

Discussion

Our previous study has demonstrated that IL-17 and PGE2 cooperatively contribute to creation of an M2-macrophage-dominant tumor microenvironment in lung cancer [6]. In the present study, our data showed that IL-17 up-regulated COX-2 expression through activation of NF- κ B and/or ERK1/2 signaling pathways in three cancer cell lines, namely, HeLa, A549, and Myc-CaP/CR. Subsequently, the increased COX-2 expression stimulated the synthesis and secretion of PGE2 by these cancer cells. Our findings demonstrated that the CM from these cancer cells contained PGE2. The CM induced expression of higher levels of IL-10 than iNOS or TNF α in the monocytes/macrophages, which was more obvious with the IL-17A-induced CM due to the higher levels of PGE2. It is worth pointing out that IL-17A may induce expression of other proteins besides PGE2, which may potentially affect macrophage differentiation. However, our previous study has demonstrated that PGE2 is the key heat-stable factor in inducing M2 macrophage differentiation [6]. Because IL-10 is a marker of M2 macrophages [1,2], it is likely that PGE2 in the CM induced M2 macrophage differentiation as we observed previously [6]. Yet, IL-17 did not show any direct effects on the monocytes/macrophages. These findings suggest that IL-17 may indirectly affect M2 macrophage differentiation through induction of PGE2 synthesis in the cancer cells. IL-17 levels are increased in many human cancers such as lung cancer [6] and prostate cancer [13]. Recently, it was reported that TH-17 cell number and IL-17 levels are increased in cervical cancers compared to normal cervical tissues [14]. It has previously been shown that IL-17 promotes growth of human xenograft cervical tumors through recruitment of macrophages to the tumor site [15]. We have previously demonstrated that IL-17, as a chemoattractant, can directly recruit monocytes/macrophages into the tumor microenvironment [6]. In this study, we demonstrated that IL-17 can indirectly induce M2 macrophage differentiation through stimulating cancer cells to secrete PGE2. Therefore, IL-17 appears to play an important role in creation of an M2-macrophage-dominant tumor microenvironment.

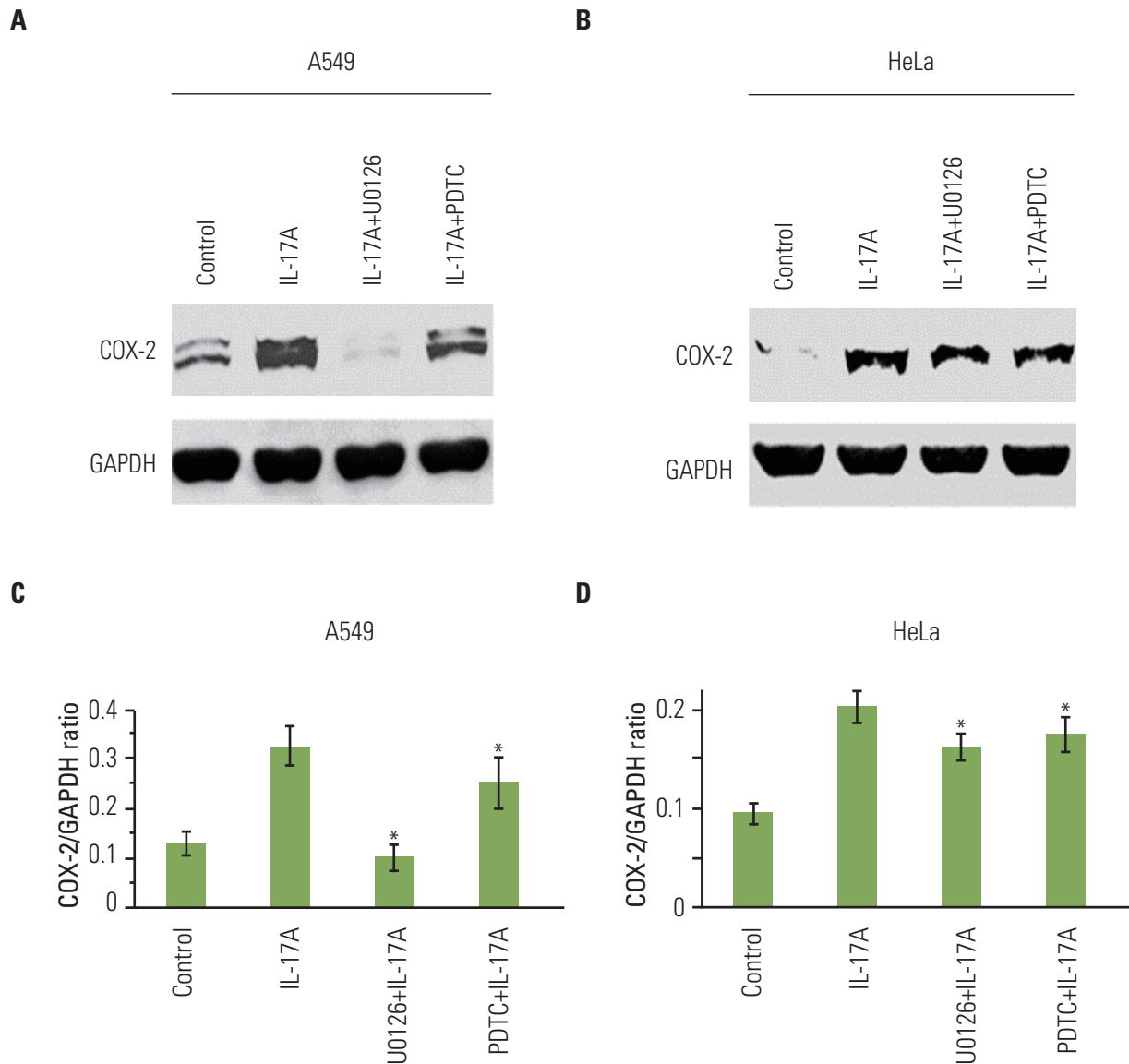


Fig. 3. U0126 and pyrrolidine dithiocarbamate (PDTC) inhibit interleukin (IL)-17-induced cyclooxygenase-2 (COX-2) protein expression in cancer cells. (A, B) The cancer cells were treated without or with 100 μ M nuclear factor- κ B (NF- κ B) inhibitor PDTC or 10 μ M MEK inhibitor U0126 for 30 minutes prior to addition of recombinant IL-17A (20 ng/mL) for 12 hours treatment. COX-2 protein expression was determined by Western blot analysis. (C, D) Quantification of Western blot signals in three independent experiments. GAPDH, glyceraldehyde-3-phosphate dehydrogenase. Values are presented as the mean \pm standard deviation obtained from three independent experiments. * p < 0.05, compared to the IL-17A treatment group.

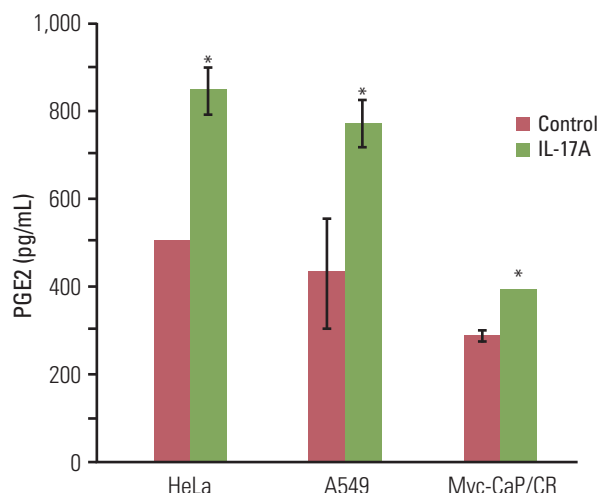


Fig. 4. Interleukin (IL)-17 induces prostaglandin E2 (PGE2) secretion in cancer cells. The cancer cells were serum starved for 15 hours and then treated without or with 20 ng/mL IL-17A for 24 hours; PGE2 levels were determined using an enzyme-linked immunosorbent assay kit. Values are presented as the mean \pm standard deviation obtained from three independent experiments. * $p < 0.05$, compared to the control group.

IL-17 has been shown to modulate tumor immune microenvironment by recruiting myeloid-derived suppressor cells (MDSCs) and inhibiting CD8⁺ T cell infiltration at the tumor sites, thus promoting tumor growth [16]. Both MDSCs and M2 macrophages suppress the activity of CD8⁺ T cells. Therefore, our study is consistent with this previous study in showing IL-17's role in creating an immunosuppressive tumor microenvironment. Recently, it was reported that IL-17 induces expression of granulocyte colony-stimulating factor that recruits MDSCs to the tumor microenvironment, thereby promoting tumor-resistance to anti-angiogenic therapy [17]. Another study found that blockade of IL-17 increases the cytotoxic activity of CD8⁺ T cells, and in contrast, eliminates MDSCs and regulatory T cells at tumor sites [18]. IL-17 has been shown to up-regulate expression of pro-survival genes, namely, myeloid cell leukemia sequence 1 (MCL1) and B-cell lymphoma 2 (Bcl-2)-related protein A1 (BCL2A1) in human dendritic cells, thus conferring chemoresistance to 11 chemotherapy agents [19]. High serum levels of IL-17 predict poor prognosis in non-small-cell lung cancer, hepatocellular carcinoma, gastric cancer, breast cancer, and colorectal cancer [20-24]. These recent findings highlight the important significance of IL-17's function in modulating tumor immune microenvironment.

Conclusion

IL-17 up-regulates COX-2 expression in HeLa, A549, and Myc-CaP/CR cancer cells and subsequently increases synthesis and secretion of PGE2 that induces M2 macrophage differentiation. Therefore, IL-17 indirectly promotes M2 macrophage differentiation through stimulation of the COX-2/PGE2 pathways in cancer cells, thus IL-17 plays an indirect role in regulating the tumor immune microenvironment.

Conflicts of Interest

Conflict of interest relevant to this article was not reported.

Acknowledgments

The authors thank Dr. Leigh Ellis and Dr. Roberto Pili (Roswell Park Cancer Institute, Buffalo, NY) for providing the Myc-CaP/CR cell line. This work was partly supported by two grants from the National Institute of General Medical Sciences (P20GM103518) and the National Cancer Institute (R01CA174714) of the National Institutes of Health, a grant from Department of Defense (PC121647), the Developmental Fund of Tulane Cancer Center (TCC), and Louisiana Cancer Research Consortium (LCRC) Fund (to Z.Y.). The content of this article is solely the responsibility of the authors and does not necessarily represent the official views of the National Institutes of Health. TCC and LCRC Core Facilities were used to conduct this study. This work was also partly supported by National Natural Science Foundation of China (NSFC 81172236: The mechanism of TAMs activation in lung cancer and a novel immunotherapy; 81372505: The role of IL-17 in formation and progression of primary lung cancer and the underlying molecular mechanisms) and Key Science and Technology Program of Sichuan Province, China (2009SZ0152 and 2011SZ0111) (to L.L.). Dr. Qingli Li received a scholarship from the State Scholarship Fund via China Scholarship Council (CSC) for her training under Dr. Zongbing You at Tulane University.

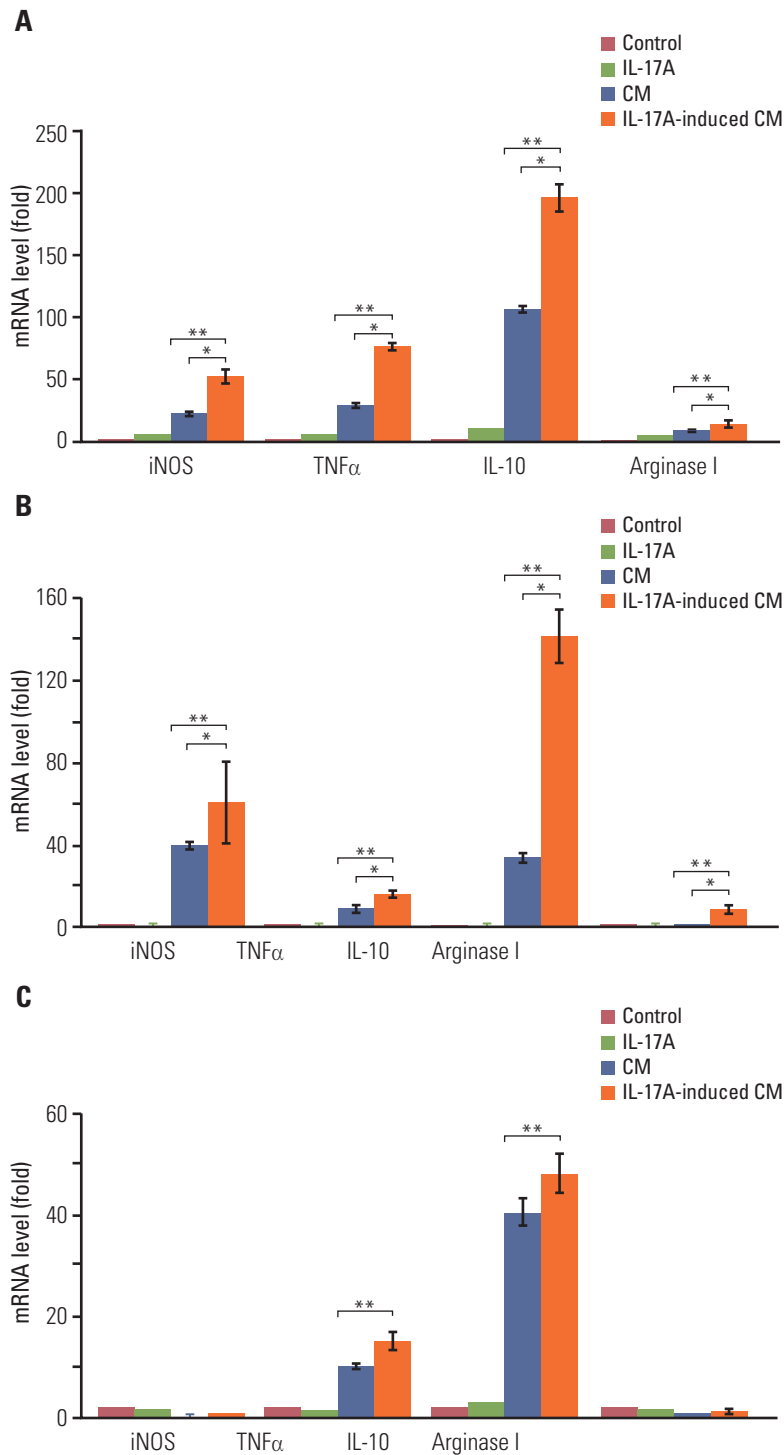


Fig. 5. Interleukin (IL)-17A-induced conditional medium increases expression of marker genes of M2 macrophages. The conditional medium (CM) or IL-17A-induced CM from human HeLa cancer cells (A) or human A549 cancer cells (B) was used to treat mouse RAW264.7 macrophages; the CM or IL-17A-induced CM from mouse Myc-CaP/CR cancer cells (C) was used to treat human THP-1 monocytes. The control group was treated with serum-free medium that had not been exposed to any cells. The IL-17A group was treated with 20 ng/mL IL-17A in serum-free medium. After 3 hours treatment, mRNA levels of the genes were determined by real-time quantitative reverse transcriptase polymerase chain reaction. Inducible nitric oxide synthase (iNOS) and tumor necrosis factor α (TNF α) are markers for M1 macrophages, and IL-10 and arginase I are markers for M2 macrophages. Values are presented as the mean \pm standard deviation obtained from three independent experiments. * p < 0.05 or ** p < 0.01, compared to the groups as indicated.

References

- Mantovani A, Sica A, Locati M. New vistas on macrophage differentiation and activation. *Eur J Immunol*. 2007;37:14-6.
- Gordon S. Alternative activation of macrophages. *Nat Rev Immunol*. 2003;3:23-35.
- Mantovani A, Sica A, Locati M. Macrophage polarization comes of age. *Immunity*. 2005;23:344-6.
- Mantovani A, Bottazzi B, Colotta F, Sozzani S, Ruco L. The origin and function of tumor-associated macrophages. *Immunol Today*. 1992;13:265-70.
- Ma J, Liu L, Che G, Yu N, Dai F, You Z. The M1 form of tumor-associated macrophages in non-small cell lung cancer is positively associated with survival time. *BMC Cancer*. 2010;10:112.
- Liu L, Ge D, Ma L, Mei J, Liu S, Zhang Q, et al. Interleukin-17 and prostaglandin E2 are involved in formation of an M2 macrophage-dominant microenvironment in lung cancer. *J Thorac Oncol*. 2012;7:1091-100.
- Onishi RM, Gaffen SL. Interleukin-17 and its target genes: mechanisms of interleukin-17 function in disease. *Immunology*. 2010;129:311-21.
- Liu C, Qian W, Qian Y, Giltiay NV, Lu Y, Swaidani S, et al. Act1, a U-box E3 ubiquitin ligase for IL-17 signaling. *Sci Signal*. 2009;2:ra63.
- Hata K, Andoh A, Shimada M, Fujino S, Bamba S, Araki Y, et al. IL-17 stimulates inflammatory responses via NF-kappaB and MAP kinase pathways in human colonic myofibroblasts. *Am J Physiol Gastrointest Liver Physiol*. 2002;282:G1035-44.
- Ellis L, Lehet K, Ramakrishnan S, Adelaiye R, Pili R. Development of a castrate resistant transplant tumor model of prostate cancer. *Prostate*. 2012;72:587-91.
- Lai T, Wang K, Hou Q, Zhang J, Yuan J, Yuan L, et al. Interleukin 17 induces up-regulation of chemokine and cytokine expression via activation of the nuclear factor kappaB and extracellular signal-regulated kinase 1/2 pathways in gynecologic cancer cell lines. *Int J Gynecol Cancer*. 2011;21:1533-9.
- Greenhough A, Smartt HJ, Moore AE, Roberts HR, Williams AC, Paraskeva C, et al. The COX-2/PGE2 pathway: key roles in the hallmarks of cancer and adaptation to the tumour microenvironment. *Carcinogenesis*. 2009;30:377-86.
- Steiner GE, Newman ME, Paikl D, Stix U, Memaran-Dagda N, Lee C, et al. Expression and function of pro-inflammatory interleukin IL-17 and IL-17 receptor in normal, benign hyperplastic, and malignant prostate. *Prostate*. 2003;56:171-82.
- Chen Z, Ding J, Pang N, Du R, Meng W, Zhu Y, et al. The Th17/Treg balance and the expression of related cytokines in Uyghur cervical cancer patients. *Diagn Pathol*. 2013;8:61.
- Tartour E, Fossiez F, Joyeux I, Galinha A, Gey A, Claret E, et al. Interleukin 17, a T-cell-derived cytokine, promotes tumorigenicity of human cervical tumors in nude mice. *Cancer Res*. 1999;59:3698-704.
- He D, Li H, Yusuf N, Elmets CA, Li J, Mountz JD, et al. IL-17 promotes tumor development through the induction of tumor promoting microenvironments at tumor sites and myeloid-derived suppressor cells. *J Immunol*. 2010;184:2281-8.
- Chung AS, Wu X, Zhuang G, Ngu H, Kasman I, Zhang J, et al. An interleukin-17-mediated paracrine network promotes tumor resistance to anti-angiogenic therapy. *Nat Med*. 2013;19:1114-23.
- Hayata K, Iwahashi M, Ojima T, Katsuda M, Iida T, Nakamori M, et al. Inhibition of IL-17A in tumor microenvironment augments cytotoxicity of tumor-infiltrating lymphocytes in tumor-bearing mice. *PLoS One*. 2013;8:e53131.
- Olsson Akefeldt S, Maisse C, Belot A, Mazzorana M, Salvatore G, Bissay N, et al. Chemoresistance of human monocyte-derived dendritic cells is regulated by IL-17A. *PLoS One*. 2013;8:e56865.
- Liao R, Sun J, Wu H, Yi Y, Wang JX, He HW, et al. High expression of IL-17 and IL-17RE associate with poor prognosis of hepatocellular carcinoma. *J Exp Clin Cancer Res*. 2013;32:3.
- Yamada Y, Saito H, Ikeguchi M. Prevalence and clinical relevance of Th17 cells in patients with gastric cancer. *J Surg Res*. 2012;178:685-91.
- Chen WC, Lai YH, Chen HY, Guo HR, Su IJ, Chen HH. Interleukin-17-producing cell infiltration in the breast cancer tumour microenvironment is a poor prognostic factor. *Histopathology*. 2013;63:225-33.
- Zhang GQ, Han F, Fang XZ, Ma XM. CD4+, IL17 and Foxp3 expression in different pTNM stages of operable non-small cell lung cancer and effects on disease prognosis. *Asian Pac J Cancer Prev*. 2012;13:3955-60.
- Liu J, Duan Y, Cheng X, Chen X, Xie W, Long H, et al. IL-17 is associated with poor prognosis and promotes angiogenesis via stimulating VEGF production of cancer cells in colorectal carcinoma. *Biochem Biophys Res Commun*. 2011;407:348-54.

Interleukin-17 Promotes Development of Castration-Resistant Prostate Cancer Potentially Through Creating an Immunotolerant and Pro-Angiogenic Tumor Microenvironment

Qiuyang Zhang,¹ Sen Liu,¹ Qingsong Zhang,^{1,2} Zhenggang Xiong,⁶ Alun R. Wang,⁶ Leann Myers,⁷ Jonathan Melamed,⁸ Wendell W. Tang,⁹ and Zongbing You^{1,2,3,4,5*}

¹Department of Structural & Cellular Biology, Tulane University, New Orleans, Louisiana

²Department of Orthopaedic Surgery, Tulane University, New Orleans, Louisiana

³Tulane Cancer Center and Louisiana Cancer Research Consortium, Tulane University, New Orleans, Louisiana

⁴Tulane Center for Stem Cell Research and Regenerative Medicine, Tulane University, New Orleans, Louisiana

⁵Tulane Center for Aging, Tulane University, New Orleans, Louisiana

⁶Department of Pathology and Laboratory Medicine, School of Medicine, Tulane University, New Orleans, Louisiana

⁷Department of Biostatistics and Bioinformatics, School of Public Health and Tropical Medicine, Tulane University, New Orleans, Louisiana

⁸Department of Pathology, New York University School of Medicine, New York, New York

⁹Department of Pathology, Ochsner Clinic Foundation, New Orleans, Louisiana

BACKGROUND. Interleukin-17 (IL-17) has been demonstrated to promote formation and growth of hormone-naïve prostate adenocarcinoma in mice. IL-17's role in development of castration-resistant prostate cancer is unknown. In the present study, we investigated IL-17's role in castration-resistant prostate cancer in a mouse model.

METHODS. IL-17 receptor C (IL-17RC) deficient mice were interbred with *Pten* conditional mutant mice to produce RC⁺ mice that maintained IL-17RC expression and RC[−] mice that were IL-17RC deficient. Male RC⁺ and RC[−] mice were *Pten*-null and were castrated at

Abbreviations: AR, androgen receptor; Bcl-2; B-cell, lymphoma 2; COX-2, cyclooxygenase-2; Cre, Cre recombinase; CRPC, castration-resistant prostate cancer; CXCL, C-X-C motif ligand; GU, genitourinary; Gr-1, granulocyte-differentiation antigen-1; H&E, hematoxylin and eosin; HER-2, human epidermal growth factor receptor 2; HIF, hypoxia inducible factor; IL, interleukin; IL-17RC, IL-17 receptor C; iNOS, inducible nitric oxide synthase; KO, knockout; MDSCs, myeloid-derived suppressor cells; MMP, matrix metalloproteinase; MTA1, metastasis associated 1; PIN, prostatic intraepithelial neoplasia; Pten, phosphatase and tensin homolog; Ras, rat sarcoma gene; SMA, smooth muscle actin; T_H17, T helper cells expressing IL-17; TMPRSS2-ERG, transmembrane protease, serine 2 - E-twenty six related gene; TUNEL, terminal deoxynucleotidyl transferase-mediated dUTP nick end labeling; UBE2C, ubiquitin-conjugating enzyme E2C; VEGF, vascular endothelial growth factor; YBX1, Y-box binding protein 1.

Grant sponsor: National Institute of General Medical Sciences; Grant number: P20GM103518; Grant sponsor: National Cancer Institute; Grant number: R01CA174714; Grant sponsor: Department of Defense; Grant numbers: PC121647; PC131448; Grant sponsor: The Developmental Fund of Tulane Cancer Center (TCC); Grant sponsor: Louisiana Cancer Research Consortium (LCRC) Fund.

The content of this article is solely the responsibility of the authors and does not necessarily represent the official views of the National Institutes of Health.

*Correspondence to: Zongbing You, Department of Structural & Cellular Biology, Tulane University School of Medicine, 1430 Tulane Ave SL 49, New Orleans, LA 70112. E-mail: zyou@tulane.edu

Received 27 January 2014; Accepted 5 March 2014

DOI 10.1002/pros.22805

Published online 1 April 2014 in Wiley Online Library

(wileyonlinelibrary.com).

16 weeks of age when invasive prostate cancer had already formed. At 30 weeks of age, all male mice were analyzed for the prostate phenotypes.

RESULTS. RC⁻ mice displayed prostates that were smaller than RC⁺ mice. Approximately 23% of prostatic glands in RC⁻ mice, in contrast to 65% of prostatic glands in RC⁺ mice, developed invasive adenocarcinomas. Compared to castrate RC⁺ mice, castrate RC⁻ mouse prostate had lower rates of cellular proliferation and higher rates of apoptosis as well as lower levels of MMP7, YBX1, MTA1, and UBE2C proteins. In addition, castrate RC⁻ mouse prostate had less angiogenesis, which was associated with decreased levels of COX-2 and VEGF. Moreover, castrate RC⁻ mouse prostate had fewer inflammatory cells including lymphocytes, myeloid-derived suppressor cells, and macrophages.

CONCLUSIONS. Taken together, our findings suggest that IL-17 promotes development of invasive prostate adenocarcinomas under castrate conditions, potentially through creating an immunotolerant and pro-angiogenic tumor microenvironment. *Prostate* 74:869–879, 2014.

© 2014 Wiley Periodicals, Inc.

KEY WORDS: prostate cancer; castration-resistant; interleukin-17; tumor immunology; tumor microenvironment

INTRODUCTION

Locally confined prostate cancer is treated by surgery or radiation. At the advanced stage when metastases occur, prostate cancer is treated with androgen deprivation therapy. However, Castration-induced regression of tumor is typically followed by re-growth with castrate levels of androgens, a status known as castration-resistant prostate cancer (CRPC) [1]. The mechanisms of how hormone-sensitive prostate cancer develops into CRPC remain to be defined. Alterations of androgen receptor (AR) signaling pathways, such as AR gene amplification, increase in AR expression, and AR gene mutations [2], may cause hypersensitivity of AR to low levels of both endocrine and intracrine androgens [3]. AR splicing variants may constitutively activate AR signaling in ligand-independent manners [4]. AR signaling may also be activated by growth factors in the absence of androgens [5]. Activation of HER-2/neu and Ras/mitogen-activated protein kinase pathways causes androgen-independent AR activities [6]. Transcriptional coactivators may lead to ligand-independent AR activation [7]. Focal neuroendocrine differentiation seems to be a common feature of prostate cancer. By secretion of a number of growth factor-like molecules (such as bombesin, calcitonin, and parathyroid hormone-related peptide), neuroendocrine cells can support the growth and progression of surrounding prostate cancer cells toward the castration-resistant state [8]. Androgen ablation up-regulates expression of the anti-apoptotic *Bcl-2* gene [9] and *clusterin* gene [10], whereas the pro-apoptotic *p53* gene is often mutated [11]. Decreased PTEN or increased Akt activities are linked to castration-resistant progression of prostate cancer [12,13]. Expression of TMPRSS2-ERG (transmembrane protease, serine 2-E26 related gene)

fusion protein [14,15] and some microRNAs [16,17] has also been associated with CRPC.

Interleukin-6 (IL-6) and IL-8 have been found to play a role in development of CRPC [18,19]. Both IL-6 and IL-8 are downstream targets of IL-17, a cytokine that is produced by T_H17 cells, $\gamma\delta$ T cells, and other immune cells [20]. IL-17 acts through a heterodimer of receptors IL-17RA and IL-17RC [21–23], thus, either *Il17ra* knock-out (KO) or *Il17rc* KO completely abolishes IL-17 signaling [24,25]. We have previously reported that IL-17RC protein expression as detected by the anti-IL-17RC intracellular domain antibodies is significantly increased in CRPC, compared to hormone-sensitive prostate cancer [26,27]. Recently, we cross-bred *Il17rc* KO (*Il17rc*^{-/-}) mice with *Pten* conditional KO mice (*Pten*^{L/L}; Cre⁺) and found that, in *Pten*-deficient context, *Il17rc* KO mice developed significantly smaller prostate tumors compared to *Il17rc* wild-type mice [28]. Our findings suggest that IL-17 promotes formation and growth of hormone-naïve prostate adenocarcinoma. However, it is unknown whether IL-17 plays any role in the development of CRPC. In the present study, we castrated the mice at 16 weeks of age and examined them at 30 weeks of age. We found that *Il17rc* KO mice developed significantly smaller prostates compared to *Il17rc* wild-type mice under castrate conditions.

MATERIALS AND METHODS

Mice

Animal protocol was approved by the Animal Care and Use Committee of Tulane University. The breeding strategy and genotyping protocols have been described previously, using *Pten*^{loxP/loxP} (*Pten*^{L/L}) mice, PB-Cre4 mice, and *Il17rc*^{-/-} mice [28]. Male RC⁺ (n = 9) and RC⁻ (n = 9) mice at 16 weeks of age were

castrated. This age was chosen because a majority of RC⁺ and RC⁻ mice had already developed invasive adenocarcinomas by this age [28,29]. The castration procedures were as the following: mice were anesthetized with 4% isoflurane; the skin over the scrotum was disinfected by 70% ethanol and Betadine solution; a 0.5-cm incision was made over the scrotum; the testes were exposed by pulling the adipose tissue; a hemostat was applied to curtail blood flow followed by silk ligation of blood vessels; the ductus deferentes were ligated and cut; the testes were excised; and the skin incision was closed with #5-0 nylon suture that was removed 7 days later. All instruments used were sterile. To alleviate pain, Carprofen (2 mg/kg) was injected subcutaneously at the end of surgical procedure and then every 12 hr up to 48 hr.

Histopathology

Mice were euthanized and weighed at 30 weeks of age. The genitourinary (GU) blocs were photographed, weighed with an empty bladder, and fixed *en bloc* as described previously [28,30]. Twenty-eight consecutive 4- μ m sections of each prostate were cut and four sections (from every seventh section) were stained with hematoxylin and eosin (H&E) for histopathologic assessment in a blinded fashion according to the Bar Harbor Classification [30]. The prostatic glands were assessed under low- and high-power magnifications, and approximately 27–94 prostatic glands in each prostate were counted, with a total of over 500 prostatic glands in nine mouse prostates per genotype. The number of inflammatory cells in the connective tissue space between the prostatic glands was counted in ten high-power fields ($\times 400$ magnification) of each dorsal prostatic lobe; the average number of inflammatory cells per high-power field in nine mouse prostates per genotype was compared.

Immunohistochemical and Terminal Deoxynucleotidyl Transferase-Mediated dUTP Nick End Labeling Staining

Immunohistochemical staining and double immunofluorescent staining were performed as described previously [28]. The antibodies used were: rabbit anti-p-Akt (1:100), mouse anti-PTEN (26H9, 1:50), rabbit anti-YB1 (D299, 1:50), and rabbit anti-MTA1 (D40D1, 1:25) from Cell Signaling Technology, Inc., Danvers, MA; rabbit anti-Ki-67 (1:100, EMD Millipore, Billerica, MA); rabbit anti-VEGF (A-20, sc-152, 1:200), goat anti-HIF-1 α (Y-15, sc-12542, 1:50), rabbit anti-NOS2 (iNOS, N-20, sc-651, 1:100), rabbit anti-Integrin α M (CD11b, H-61, sc-28664, 1:100), goat anti-Ly6C (P-12, sc-23080, 1:100), goat anti-Ly6G (Y-11, sc-103603, 1:100), goat anti-arginase I (V-20,

sc-18345, 1:100), and goat anti-COX-2 (C-20, sc-1745, 1:200) from Santa Cruz Biotechnology, Inc., Santa Cruz, CA; rabbit anti-CD31 (Ab28364, 1:50, Abcam, PLC., Cambridge, MA); rabbit anti-laminin (1:100, Sigma-Aldrich, St. Louis, MO); rabbit anti- α -smooth muscle actin (1:200, Pierce Biotechnology, Rockford, IL); goat anti-MMP7 (1:200, R&D systems, Minneapolis, MN); rabbit anti-UbcH10/UBE2C (1:200, Boston Biochem, Cambridge, MA); and Cy3-conjugated anti-goat IgG and DyLight 488-conjugated anti-rabbit IgG (Jackson ImmunoResearch Laboratories, Inc., West Grove, PA). Terminal deoxynucleotidyl transferase-mediated dUTP nick end labeling (TUNEL) staining was performed using TACS. XL[®] Blue Label *In Situ* Apoptosis Detection Kits (Trevigen, Inc., Gaithersburg, MD) according to the manufacturer's instructions [28]. To quantify Ki-67-positive and TUNEL-positive cells, three animals from each genotype group were randomly selected; three representative prostate sections from each animal were stained; approximately 200 cells per field of ten high-power fields ($\times 400$ magnification) of each prostate lobe were counted; and the percentages of positive cells were calculated as the number of positive cells divided by the total number of cells. The density of microvessels was evaluated by counting the CD31-positive microvessels in ten high-power fields per lobe; the average number of CD31-positive microvessels per high-power field in three random mouse prostates per genotype was compared. The myeloid-derived suppressor cells (MDSCs) were defined as CD11b/Gr-1 (CD11b/Ly6C and CD11b/Ly6G) double positive cells. The M1 and M2 macrophages were defined as iNOS-positive and arginase I-positive cells, respectively. The numbers of MDSCs, M1 macrophages, and M2 macrophages in the connective tissue space between the prostatic glands were counted in ten high-power fields ($\times 400$ magnification) in each dorsal prostatic lobe; the average numbers of MDSCs, M1 and M2 macrophages per high-power field in three random mouse prostates per genotype were compared.

Statistical Analysis

Comparisons of the GU-bloc weights were analyzed using Student's *t*-test. Kruskal–Wallis test was used to compare the incidences of normal, PIN and invasive adenocarcinoma. Student's *t*-test was used to analyze the remaining data.

RESULTS

Castrate RC⁻ Mice Developed Smaller Prostate Glands Than Castrate RC⁺ Mice

Previously, we found that there were no significant differences in the expression of *Il17rc* mRNA

and protein, GU-bloc weight, and histopathology between $Il17rc^{+/+};Pten^{L/L};Cre^{+}$ and $Il17rc^{+/-};Pten^{L/L};Cre^{+}$ mice [28]. Therefore, we put $Il17rc^{+/+};Pten^{L/L};Cre^{+}$ mice and $Il17rc^{+/-};Pten^{L/L};Cre^{+}$ mice into one group, named RC^{+} mice that expressed IL-17RC receptor. Likewise, $Il17rc^{-/-};Pten^{L/L};Cre^{+}$ mice were named RC^{-} mice that did not express IL-17RC receptor. Both RC^{+} and RC^{-} mice had *Pten* gene conditionally knocked out in the prostatic epithelium due to probasin promoter-driven Cre recombinase [28]. We reported that the GU blocs, including the prostatic glands, were clearly larger in the non-castrate (or intact) RC^{+} mice than in the intact RC^{-} mice at 30 weeks of age (Fig. 1A and B) [28]. In the present study, we found that the GU blocs also appeared larger in the castrate RC^{+} mice than in the castrate RC^{-} mice at 30 weeks of age (Fig. 1C and D). The average GU bloc weight was 946.3 mg in the intact RC^{+} mice compared to 644.7 mg in the intact RC^{-} mice ($P < 0.01$, Fig. 1E). Castration at 16 weeks of age significantly reduced the GU bloc weight at 30 weeks of age in both RC^{+} and RC^{-} mice to an average of 224.1 and 164.3 mg, respectively ($P < 0.01$, Fig. 1E). Yet, the GU bloc weight of castrate RC^{+} mice was still significantly heavier than that of castrate RC^{-} mice ($P < 0.05$, Fig. 1E).

Castrate RC^{-} Mice Developed Fewer Invasive Adenocarcinomas Than Castrate RC^{+} Mice

It has been reported that intact RC^{+} mice developed invasive adenocarcinomas, that is, the neoplastic cells have invaded through the basement membrane and into the stroma, at 30 weeks of age with 100% penetrance [28,29], whereas intact RC^{-} mice developed invasive adenocarcinomas in about 70% of prostates at 30 weeks of age [28]. In the castrate RC^{+} mice, we found that approximately 65% of prostatic glands presented with invasive adenocarcinomas (Fig. 2A), 33% of prostatic glands had prostatic intraepithelial neoplasia (PIN), and 2% of prostatic glands appeared "normal" as they presented with a single layer of luminal epithelial cells. In contrast, the castrate RC^{-} mice showed approximately 23% of prostatic glands with invasive adenocarcinomas, 64% of prostatic glands with PIN, and 12% of prostatic glands with normal epithelia (Fig. 2B). Under higher magnification, the invasive adenocarcinoma cells presented with atypical hyperchromatic nuclei and invaded into the surrounding stroma (Fig. 2C and D). The rate of invasive adenocarcinomas was 42% lower in RC^{-} mice than in RC^{+} mice ($P < 0.001$, Fig. 2E).

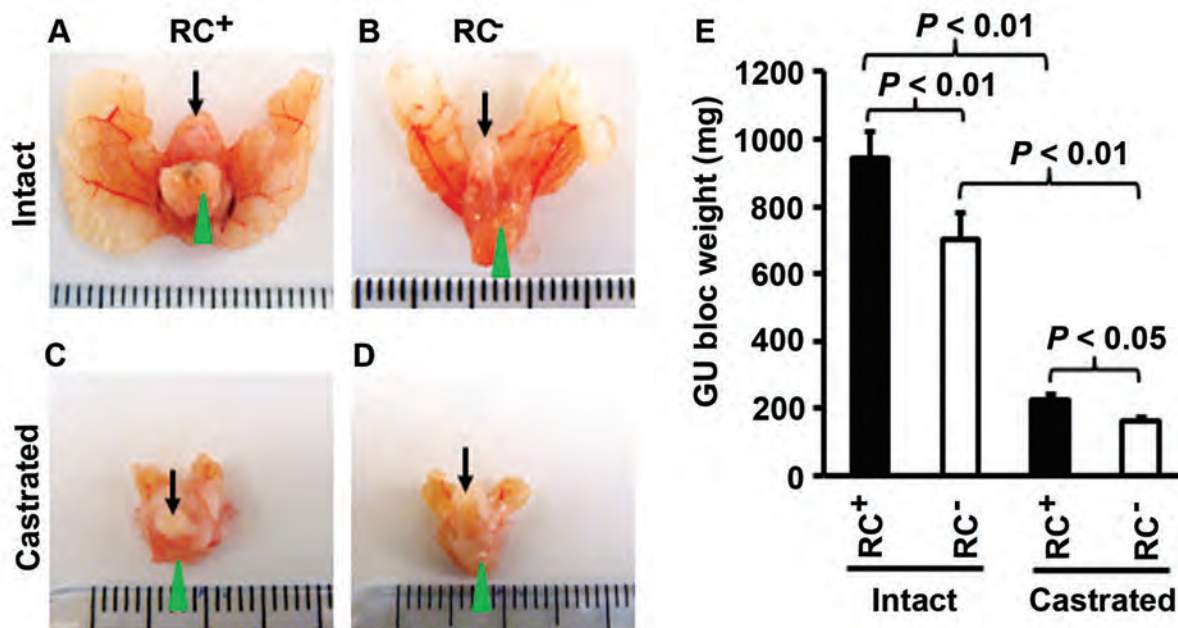


Fig. 1. Castrate RC^{-} mice developed smaller prostate glands than castrate RC^{+} mice. **A–D:** Representative photographs of the GU blocs; arrows indicate urinary bladders and arrowheads indicate the ventral prostatic lobes for orientation of the view. **E:** The GU bloc weights at 30 weeks of age; $n = 20$ for intact RC^{+} mice, $n = 12$ for intact RC^{-} mice, $n = 9$ for castrate RC^{+} mice, and $n = 9$ for castrate RC^{-} mice.

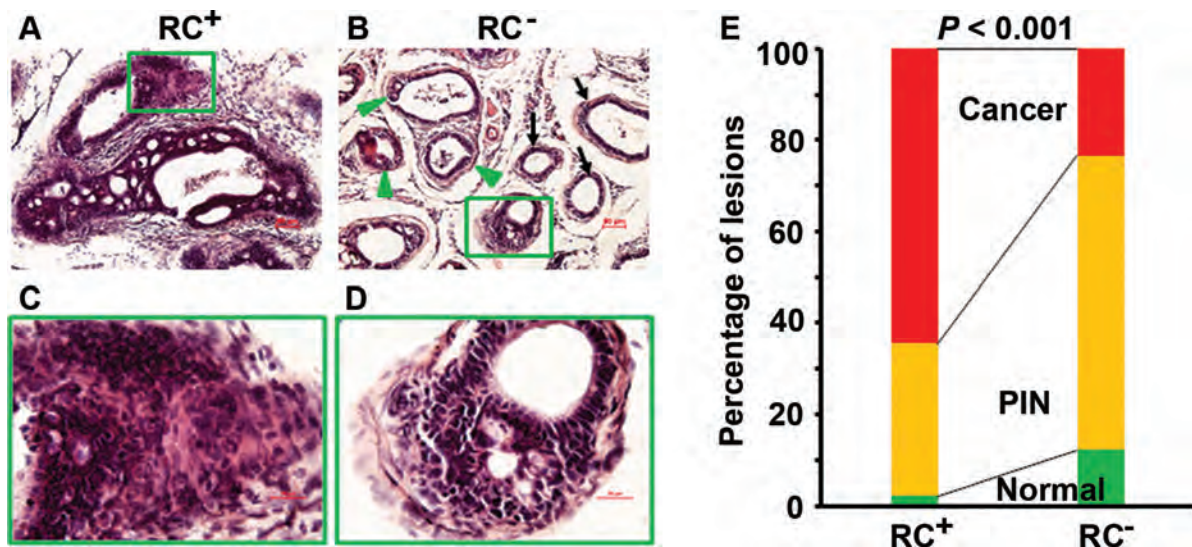


Fig. 2. Castrate RC^- mice developed fewer invasive adenocarcinomas than castrate RC^+ mice. **A–D:** Representatives of H&E-stained dorsal prostatic lobes; arrows indicate normal glands with a single layer of luminal epithelium, arrowheads indicate PIN lesions, and rectangular frames indicate invasive adenocarcinomas; original magnification, $\times 100$ for (A, B) and $\times 400$ for (C, D). **E:** Percentages of normal, PIN, and invasive cancer in dorsal, lateral, and ventral prostatic lobes.

To verify our diagnosis of invasive adenocarcinoma versus PIN based on H&E-stained tissue sections, consecutive sections were stained with H&E and immunohistochemically stained with anti-laminin or anti- α -smooth muscle actin (α -SMA) antibodies. As shown in Supplementary Figure S1A, invasive adenocarcinoma showed lack of staining or discontinuity of staining for laminin. In contrast, PIN lesion presented a continuous layer of laminin staining around the prostatic gland (Supplementary Fig. S1B). Similarly, α -SMA staining showed lack of continuity in invasive adenocarcinoma (Supplementary Fig. S1C), whereas a continuous layer of α -SMA staining was present in the PIN lesion and normal gland (Supplementary Fig. S1D).

Castrate RC^- Prostate Had Less Cellular Proliferation and More Apoptosis Than Castrate RC^+ Prostate

We found that RC^+ mouse prostate had clearly more Ki-67-positive neoplastic cells (Fig. 3A) than RC^- mouse prostate (Fig. 3B). The differences between RC^+ and RC^- mice were statistically significant in the dorsal prostatic lobes (DP), lateral prostatic lobes (LP), and ventral prostatic lobes (VP) ($P < 0.05$ or $P < 0.01$, Fig. 3C). On the other hand, the number of apoptotic cells as detected by TUNEL staining was fewer in the RC^+ mouse prostatic lobes (Fig. 3D) than in the RC^- mouse prostatic lobes (Fig. 3E), which was statistically significant ($P < 0.01$, Fig. 3F).

Castrate RC^- Prostate Decreased Expression of Invasion-Related Proteins

Previously, we reported that the intact RC^- mice expressed significantly less MMP7 in the prostate than the intact RC^+ mice, which partially explained the lower rate of invasive cancer in RC^- mice compared to RC^+ mice [28]. In the castrate mice, the level of MMP7 expression was also lower in the RC^- prostate than in the RC^+ prostate (Fig. 4A and B).

To search for other proteins that might contribute to the different incidence rates of invasive cancer in our animal models, we tested several candidates that were reportedly involved in prostate carcinogenesis. YBX1 (also known as YB-1) is a Y-box binding protein [31], which has been demonstrated to confer invasiveness to breast cancer cells [32]. YBX1 level is elevated in human PIN and invasive adenocarcinomas [33], similar to the pattern of MMP7 expression [28]. We found that YBX1 expression was clearly decreased in the castrate RC^- prostate compared to the castrate RC^+ prostate (Fig. 4C and D). Metastasis associated 1 (MTA1) was originally identified from rat mammary adenocarcinoma cell lines [34] and recently it has been associated with the invasiveness of human prostate cancer cells [35]. We found that MTA1 expression was discernibly decreased in the castrate RC^- prostate compared to the castrate RC^+ prostate (Fig. 4E and F). Ubiquitin-conjugating enzyme E2C (UBE2C, also called UBCH10) is needed for degradation of mitotic cyclins [36], which has been associated

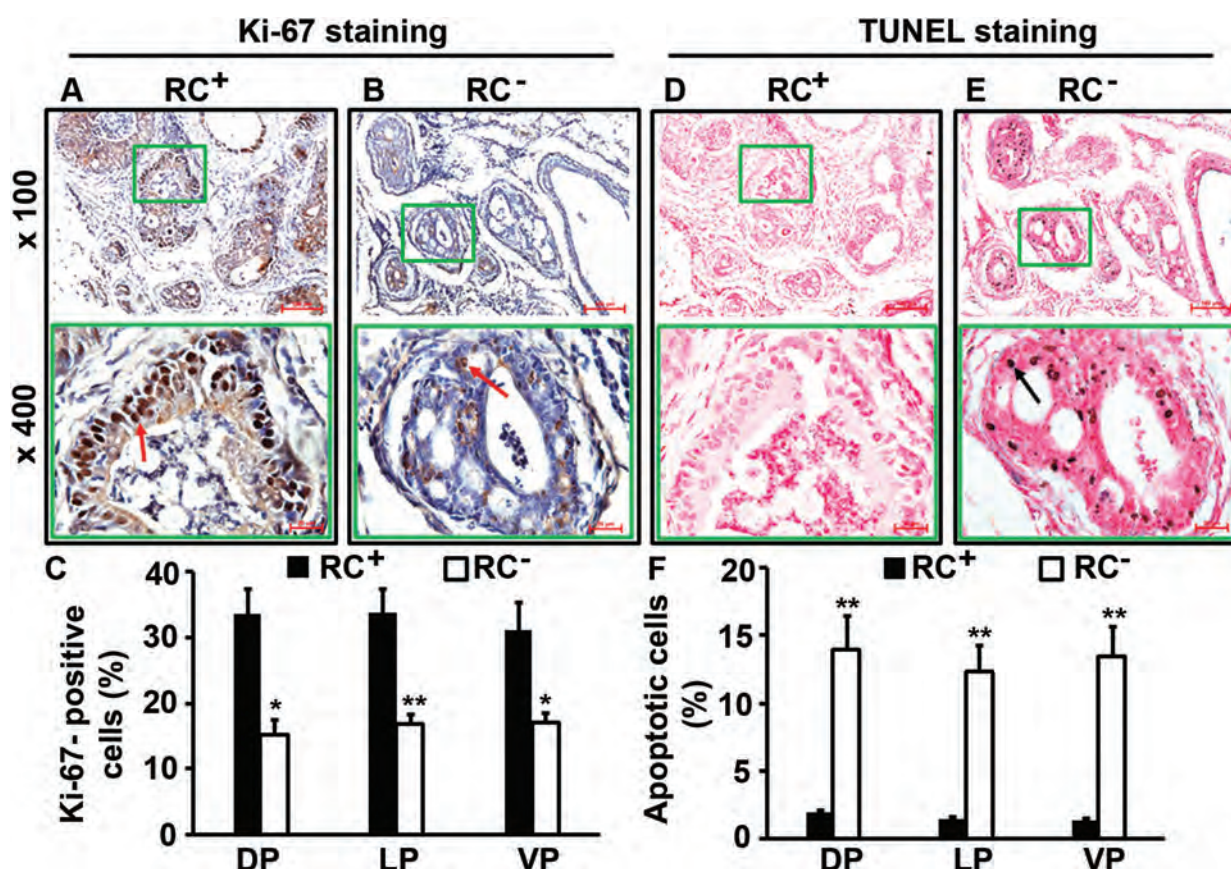


Fig. 3. Castrate RC⁻ prostate had less cellular proliferation and more apoptosis than castrate RC⁺ prostate. **A, B:** Ki-67 staining; arrows indicate the positive cells. **C:** Percentages of Ki-67-positive cells in dorsal (DP), lateral (LP), and ventral (VP) prostatic lobes; * $P < 0.05$ and ** $P < 0.01$. **D, E:** TUNEL staining; arrow indicates the positive cells. **F:** Percentages of apoptotic cells in prostatic lobes; ** $P < 0.01$.

with malignant transformation and aggressiveness of many tumors [37]. UBE2C level is undetectable in human normal prostate, low in hormone-sensitive prostate cancer and high in CRPC [38]. Again, we found that UBE2C level was obviously higher in the castrate RC⁺ prostate than the castrate RC⁻ prostate (Fig. 4G and H).

Castrate RC⁻ Prostate Had Less Angiogenesis Than Castrate RC⁺ Prostate

IL-17 has been found to be able to promote migration and cord formation of vascular endothelial cells through induction of a variety of proangiogenic factors [39], thus IL-17 may enhance in vivo lung cancer growth via promoting angiogenesis [40]. By immunohistochemical staining of CD31, we found that there were clearly more blood vessels in the castrate RC⁺ prostate than in the castrate RC⁻ prostate (Fig. 5A and B), which was statistically significant in the prostatic lobes examined ($P < 0.01$, Fig. 5C). We and other investigators have shown that IL-17 can

induce angiogenic CXC chemokines including CXCL1, CXCL5, and CXCL8 expression [28,40]. It has been reported that cyclooxygenase-2 (COX-2) is induced by IL-17 in keratinocytes [41]. In the present study, we found that COX-2 level was dramatically lower in RC⁻ prostate than RC⁺ prostate (Fig. 5D and E). We also found that hypoxia inducible factor 1- α (HIF1A) level was not discernibly different between RC⁺ and RC⁻ prostates (Fig. 5F and G). However, the level of vascular endothelial growth factor A (VEGFA) was clearly higher in RC⁺ prostate than RC⁻ prostate (Fig. 5H and I). It has been demonstrated that the COX-2-VEGF pathway is involved in gastric angiogenesis [42]. Our findings suggest that the COX-2-VEGF pathway plays a role in prostatic angiogenesis while HIF1A's role may be very limited.

Castrate RC⁻ Prostate Had Less Inflammatory Cell Infiltration Than Castrate RC⁺ Prostate

Previously, we reported that the inflammatory cell population was mainly composed of macrophages (or

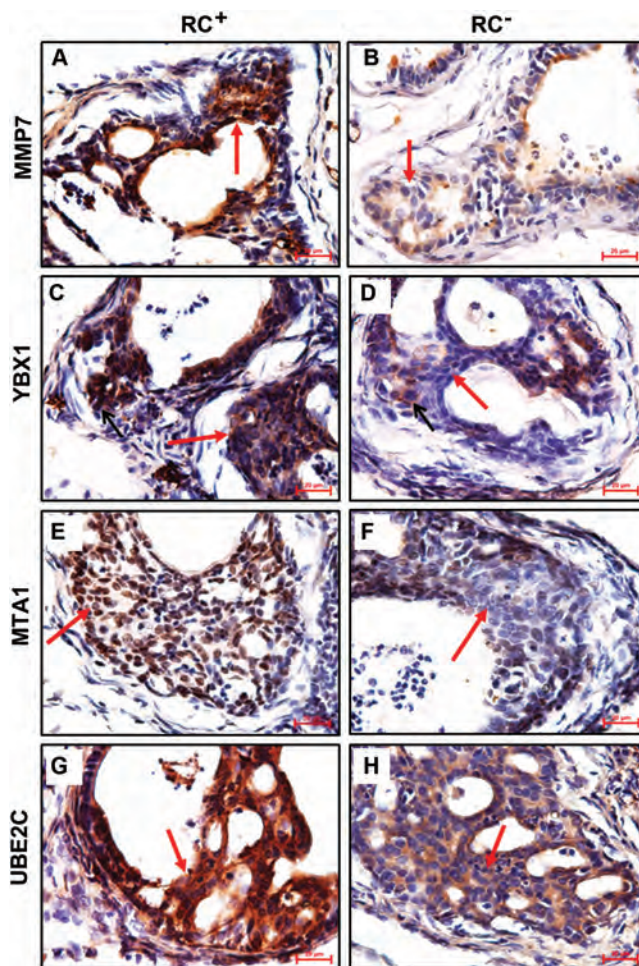


Fig. 4. Castrate RC^{-} prostate decreased expression of invasion-related proteins. **A–H:** Representatives of immunohistochemical staining; arrows indicate neoplastic cells; original magnification, $\times 400$.

myeloid cells) and lymphocytes in the intact mouse prostate and the number of inflammatory cells was significantly reduced in RC^{-} prostate compared to RC^{+} prostate [28]. In the castrate mouse prostate, the inflammatory cell population was mainly composed of lymphocytes (Fig. 6A). Consistent with our observation in the intact mice, we found that the number of inflammatory cells was much fewer in the castrate RC^{-} prostate than the castrate RC^{+} prostate (Fig. 6A and B), which was statistically significant ($P < 0.01$, Fig. 6C).

It has been shown that IL-17 induces infiltration of myeloid-derived suppressor cells (MDSCs) to promote prostate tumor growth [43]. MDSCs are considered as immature myeloid cells that are identified as CD11b/granulocyte-differentiation antigen-1 (Gr-1) double-positive cells. Gr-1 antigen consists of two epitopes recognized by anti-Ly6G (lymphocyte antigen 6 com-

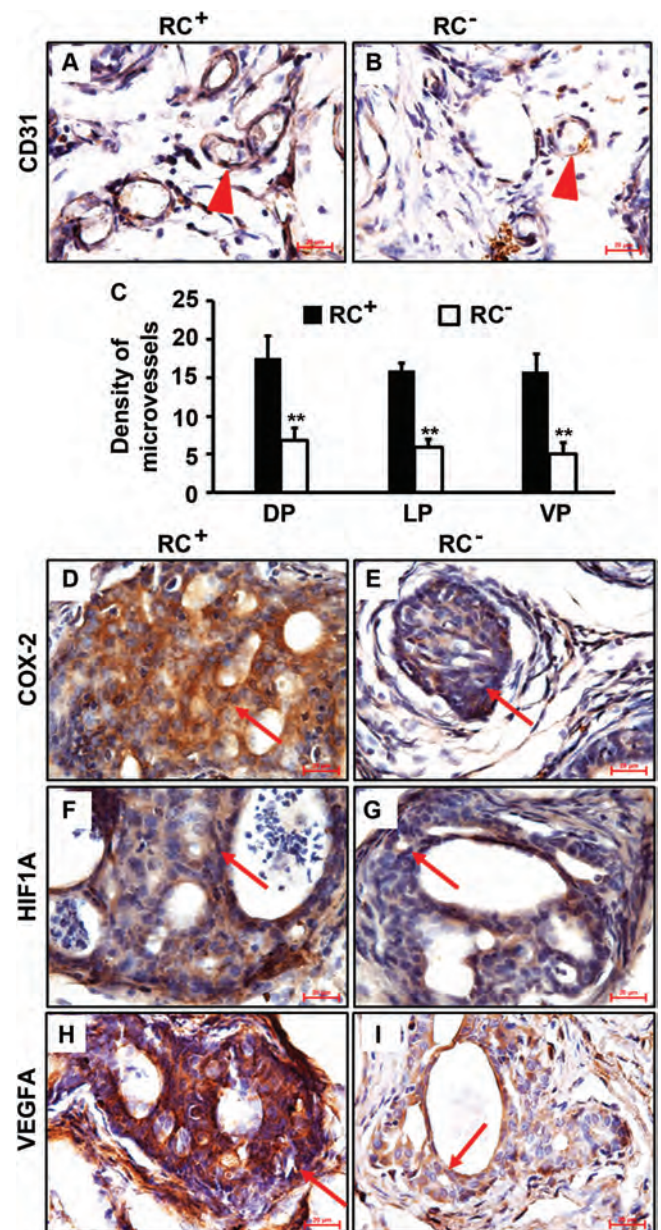


Fig. 5. Castrate RC^{-} prostate had less angiogenesis than castrate RC^{+} prostate. **A, B:** Representatives of CD31 staining; arrowheads indicate microvessels. **C:** Density of microvessels in prostatic lobes; $**P < 0.01$. **D–I:** Representatives of immunohistochemical staining; arrows indicate neoplastic cells; original magnification, $\times 400$.

plex, locus G) and anti-Ly6C (lymphocyte antigen 6 complex, locus C). Thus, MDSCs consist of two major subsets: cells with granulocytic phenotype marked by CD11b⁺/Ly6G⁺ and cells with monocytic phenotype marked by CD11b⁺/Ly6C⁺, both subsets having equal suppressive activities against T cell function [44]. Therefore, we examined the infiltration of the two MDSC subsets in mouse prostate. We found that the

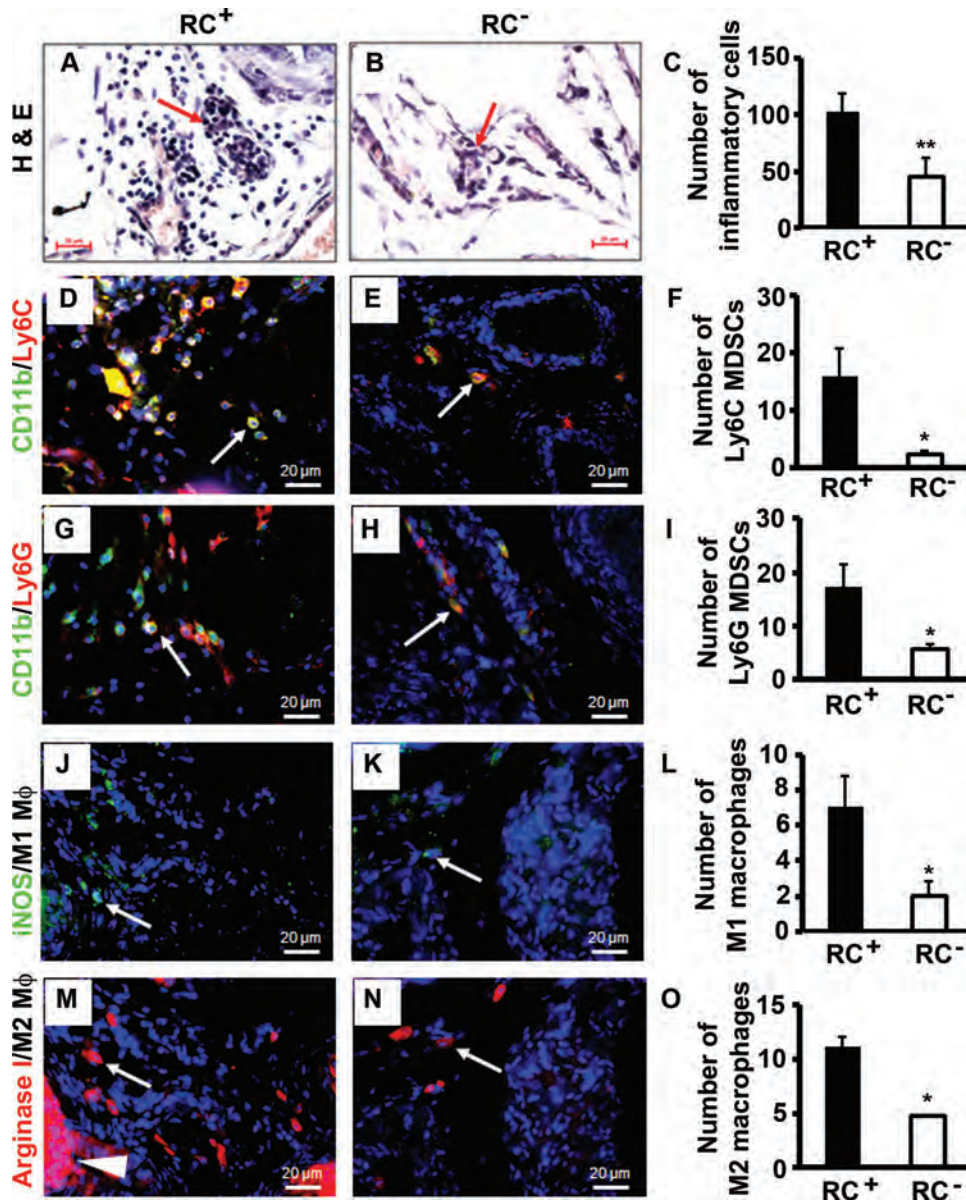


Fig. 6. Castrate RC⁻ prostate had less inflammatory cell infiltration than castrate RC⁺ prostate. **A, B:** H&E staining; arrows indicate lymphocytes. **C:** Number of inflammatory cells counted on H&E-stained sections. **D, E:** Double immunofluorescent staining of CD11b and Ly6C. **F:** Number of Ly6C MDSCs. **G, H:** Double immunofluorescent staining of CD11b and Ly6G. **I:** Number of Ly6G MDSCs. **J, K:** Immunofluorescent staining of iNOS-positive M1 macrophages. **L:** Number of M1 macrophages. **M, N:** Immunofluorescent staining of arginase I-positive M2 macrophages; arrowhead indicates positively stained prostatic epithelium. **O:** Number of M2 macrophages. Original magnification, $\times 400$; arrows indicate positive cells; * $P < 0.05$ and ** $P < 0.01$.

numbers of both MDSC subsets were significantly reduced in RC⁻ prostate compared to RC⁺ prostate ($P < 0.05$, Fig. 6D–I).

It has been reported that the inducible nitric oxide synthase (iNOS)-positive M1 macrophages and arginase I-positive M2 macrophages are present in the mouse prostate tumors, where M1 macrophages have anti-tumor functions while M2 macrophages have pro-tumor functions [45]. We found that there were slightly fewer M1 macrophages than M2 macrophages in both

RC⁺ and RC⁻ prostates (Fig. 6J–O). Yet, the numbers of M1 and M2 macrophages were significantly reduced in RC⁻ prostate compared to RC⁺ prostate (Fig. 6L and O).

DISCUSSION

We previously reported that *Il17rc* knockout inhibited formation and growth of hormone-naïve prostate adenocarcinoma in the *Pten* conditional knockout

mouse model [28]. In the present study, we used the same mouse model and castrated the animals at 16 weeks of age. Fourteen weeks after castration, we found that invasive adenocarcinomas were present in both RC⁺ and RC⁻ mouse prostates, albeit at different incidence rates. The GU bloc size, judged by the GU bloc weight, was significantly smaller in the castrate mice than the intact mice (Fig. 1). The remaining invasive adenocarcinomas in the castrate mice presumably are CRPC based on the direct evidence that cellular proliferation was still present 14 weeks after the absence of testicular androgens. Another line of indirect evidence is that UBE2C level was very high in the castrate RC⁺ mouse prostate as UBE2C was only expressed at high levels in CRPC [38].

The most significant phenotypic difference between the castrate RC⁺ and RC⁻ mice is the incidence rate of invasive adenocarcinomas. RC⁺ mice presented invasive adenocarcinomas in 65% of prostatic glands, in sharp contrast to 23% of prostatic glands in RC⁻ mice (Fig. 2E). These incidence rates are much lower than the rates in the non-castrate RC⁺ and RC⁻ mice (i.e., 100% and 70%, respectively) [28,29]. One possible reason is that the AR-positive prostatic epithelium undergoes increased apoptosis in response to castration. A 10-times increase of apoptotic cells in the *Pten*-null prostate cancer was found compared to the intact mouse prostate cancer, and the apoptotic rate was even higher in the prostate cancer than the normal epithelium 3 days post-castration [29]. Apoptosis may possibly lead to regression of some invasive adenocarcinomas and PIN lesions, resulting in a heterogeneous appearance of normal epithelium, PIN, and invasive adenocarcinomas.

There are several possible reasons to explain the different incidence rates of invasive adenocarcinomas between the castrate RC⁺ and RC⁻ mice. First, the cellular proliferation rate is higher in RC⁺ prostate than RC⁻ prostate while the apoptotic rate is lower in RC⁺ prostate than RC⁻ prostate. These differences confer an advantage to the tumor growth in RC⁺ mice over RC⁻ mice. Second, several proteins, namely, MMP7, YBX1, MTA1, and UBE2C, are expressed at higher levels in RC⁺ prostate than RC⁻ prostate. These proteins have been associated with the invasiveness and aggressiveness of human prostate cancer cells [28,32,33,35,38]. While we have demonstrated that MMP7 is a direct downstream target of IL-17 signaling pathway [28], it remains to be determined if YBX1, MTA1, and UBE2C are also IL-17 downstream targets. Third, angiogenesis is reduced in RC⁻ prostate compared to RC⁺ prostate. Angiogenesis is an integral hallmark of cancer and it has recently been associated with early neoplastic progression besides its well-known role in macroscopic tumors [46]. One mechanism by which IL-17 promotes

lung cancer growth is through induction of angiogenesis [40]. The reduced levels of COX-2 and VEGFA in RC⁻ prostate may be responsible for the decreased angiogenesis, as the COX-2-VEGF pathway has been associated with gastric angiogenesis [42]. COX-2 is an IL-17 downstream target in keratinocytes [41]. And last, inflammatory cell infiltration is reduced in RC⁻ prostate compared to RC⁺ prostate. The number of inflammatory cells appears to be more in the prostate of the castrate mice than the intact mice. It has been reported that androgen ablation increased infiltration of CD4⁺ T cells and macrophages in human prostate tumors [47]. The inflammatory cell population shifts from myeloid cells/lymphocytes in the intact mice to mainly lymphocytes in the castrate mice. This finding is in line with a recent report that castration elicits infiltration of T_H1 cells followed by predominantly T_H17 cells in rat prostate [48]. The subtypes of lymphocytes in our animal models are the subjects of our ongoing studies. Nevertheless, we have shown that the numbers of two major myeloid cell types, MDSCs and macrophages, are significantly reduced in RC⁻ mice compared to RC⁺ mice. We have recently demonstrated that IL-17 is a chemoattractant for monocytes/macrophages [49]. The reduced infiltration of MDSCs and macrophages may be caused by lack of IL-17RC receptor on these cells and/or indirectly by the decreased chemokine levels in the tumor microenvironment of RC⁻ mice. Since MDSCs and M2 macrophages are pro-tumor inflammatory cells, a decrease in their numbers may partially contribute to the phenotype of reduced incidence rate of invasive adenocarcinomas in RC⁻ mice.

In summary, the present study demonstrates that IL-17 promotes development of CRPC in the *Pten* conditional knockout mouse model. IL-17 may affect several hallmark capabilities of cancer, including sustaining proliferation, resisting cell death, activating invasion, inducing angiogenesis, and recruiting pro-tumor inflammatory cells [46]. These findings suggest that blocking IL-17 signaling through pharmacological interventions may have potentials in the prevention and treatment of CRPC.

CONCLUSIONS

IL-17 promotes development of invasive prostate adenocarcinomas in *Pten* conditional knockout mice under castrate conditions, potentially through creating an immunotolerant and pro-angiogenic tumor microenvironment.

ACKNOWLEDGMENTS

We thank Drs. Prescott L. Deininger, Asim B. Abdel-Mageed, Steven M. Hill, David E. Blask, Brian

G. Rowan, and Oliver Sartor (Tulane University) for their advices and comments on the manuscript. Tulane Cancer Center Core Facilities were used in this study. We thank Dr. Wenjun Ouyang and Genentech for providing the *Il17rc*^{-/-} mice and NCI MMHCC for providing the PB-Cre4 mice.

REFERENCES

- Harris WP, Mostaghel EA, Nelson PS, Montgomery B. Androgen deprivation therapy: Progress in understanding mechanisms of resistance and optimizing androgen depletion. *Nat Clin Pract Urol* 2009;6(2):76–85.
- Newmark JR, Hardy DO, Tonb DC, Carter BS, Epstein JI, Isaacs WB, Brown TR, Barrack ER. Androgen receptor gene mutations in human prostate cancer. *Proc Natl Acad Sci USA* 1992;89(14):6319–6323.
- Mohler JL, Gregory CW, Ford OH III, Kim D, Weaver CM, Petrusz P, Wilson EM, French FS. The androgen axis in recurrent prostate cancer. *Clin Cancer Res* 2004;10(2):440–448.
- Hu R, Dunn TA, Wei S, Isharwal S, Veltri RW, Humphreys E, Han M, Partin AW, Vessella RL, Isaacs WB, Bova GS, Luo J. Ligand-independent androgen receptor variants derived from splicing of cryptic exons signify hormone-refractory prostate cancer. *Cancer Res* 2009;69(1):16–22.
- Culig Z, Hobisch A, Cronauer MV, Radmayr C, Trapman J, Hittmair A, Bartsch G, Klocker H. Androgen receptor activation in prostatic tumor cell lines by insulin-like growth factor-I, keratinocyte growth factor, and epidermal growth factor. *Cancer Res* 1994;54(20):5474–5478.
- Craft N, Shostak Y, Carey M, Sawyers CL. A mechanism for hormone-independent prostate cancer through modulation of androgen receptor signaling by the HER-2/neu tyrosine kinase. *Nat Med* 1999;5(3):280–285.
- Debes JD, Schmidt LJ, Huang H, Tindall DJ. p300 mediates androgen-independent transactivation of the androgen receptor by interleukin 6. *Cancer Res* 2002;62(20):5632–5636.
- Jin RJ, Wang Y, Masumori N, Ishii K, Tsukamoto T, Shappell SB, Hayward SW, Kasper S, Matusik RJ. NE-10 neuroendocrine cancer promotes the LNCaP xenograft growth in castrated mice. *Cancer Res* 2004;64(15):5489–5495.
- McDonnell TJ, Troncoso P, Brisbay SM, Logothetis C, Chung LW, Hsieh JT, Tu SM, Campbell ML. Expression of the protooncogene bcl-2 in the prostate and its association with emergence of androgen-independent prostate cancer. *Cancer Res* 1992;52(24):6940–6944.
- July LV, Akbari M, Zellweger T, Jones EC, Goldenberg SL, Gleave ME. Clusterin expression is significantly enhanced in prostate cancer cells following androgen withdrawal therapy. *Prostate* 2002;50(3):179–188.
- Heidenberg HB, Bauer JJ, McLeod DG, Moul JW, Srivastava S. The role of the p53 tumor suppressor gene in prostate cancer: A possible biomarker? *Urology* 1996;48(6):971–979.
- Abate-Shen C, Banach-Petrosky WA, Sun X, Economides KD, Desai N, Gregg JP, Borowsky AD, Cardiff RD, Shen MM. Nkx3.1; Pten mutant mice develop invasive prostate adenocarcinoma and lymph node metastases. *Cancer Res* 2003;63(14):3886–3890.
- Graff JR, Konicek BW, McNulty AM, Wang Z, Houck K, Allen S, Paul JD, Hbaitu A, Goode RG, Sandusky GE, Vessella RL, Neubauer BL. Increased AKT activity contributes to prostate cancer progression by dramatically accelerating prostate tumor growth and diminishing p27Kip1 expression. *J Biol Chem* 2000;275(32):24500–24505.
- Cai C, Wang H, Xu Y, Chen S, Balk SP. Reactivation of androgen receptor-regulated TMPRSS2: ERG gene expression in castration-resistant prostate cancer. *Cancer Res* 2009;69(15):6027–6032.
- Tomkins SA, Rhodes DR, Perner S, Dhanasekaran SM, Mehra R, Sun XW, Varambally S, Cao X, Tchinda J, Kuefer R, Lee C, Montie JE, Shah RB, Pienta KJ, Rubin MA, Chinnaiyan AM. Recurrent fusion of TMPRSS2 and ETS transcription factor genes in prostate cancer. *Science* 2005;310(5748):644–648.
- Shi XB, Tepper CG, White RW. MicroRNAs and prostate cancer. *J Cell Mol Med* 2008;12(5A):1456–1465.
- Sun T, Wang Q, Balk S, Brown M, Lee GS, Kantoff P. The role of microRNA-221 and microRNA-222 in androgen-independent prostate cancer cell lines. *Cancer Res* 2009;69(8):3356–3363.
- Corcoran NM, Costello AJ. Interleukin-6: Minor player or starring role in the development of hormone-refractory prostate cancer? *BJU Int* 2003;91(6):545–553.
- Lee LF, Louie MC, Desai SJ, Yang J, Chen HW, Evans CP, Kung HJ. Interleukin-8 confers androgen-independent growth and migration of LNCaP: Differential effects of tyrosine kinases Src and FAK. *Oncogene* 2004;23(12):2197–2205.
- Onishi RM, Gaffen SL. Interleukin-17 and its target genes: Mechanisms of interleukin-17 function in disease. *Immunology* 2010;129(3):311–321.
- Toy D, Kugler D, Wolfson M, Vanden Bos T, Gurgel J, Derry J, Tocker J, Peschon J. Cutting edge: Interleukin 17 signals through a heteromeric receptor complex. *J Immunol* 2006;177(1):36–39.
- Haudenschild D, Moseley T, Rose L, Reddi AH. Soluble and transmembrane isoforms of novel interleukin-17 receptor-like protein by RNA splicing and expression in prostate cancer. *J Biol Chem* 2002;277(6):4309–4316.
- Ely LK, Fischer S, Garcia KC. Structural basis of receptor sharing by interleukin 17 cytokines. *Nat Immunol* 2009;10(12):1245–1251.
- Ye P, Rodriguez FH, Kanaly S, Stocking KL, Schurr J, Schwarzenberger P, Oliver P, Huang W, Zhang P, Zhang J, Shellito JE, Bagby GJ, Nelson S, Charrier K, Peschon JJ, Kolls JK. Requirement of interleukin 17 receptor signaling for lung CXCL chemokine and granulocyte colony-stimulating factor expression, neutrophil recruitment, and host defense. *J Exp Med* 2001;194(4):519–527.
- Hu Y, Ota N, Peng I, Refino CJ, Danilenko DM, Caplazi P, Ouyang W. IL-17RC is required for IL-17A- and IL-17F-dependent signaling and the pathogenesis of experimental autoimmune encephalomyelitis. *J Immunol* 2010;184(8):4307–4316.
- You Z, Dong Y, Kong X, Zhang Y, Vessella RL, Melamed J. Differential expression of IL-17RC isoforms in androgen-dependent and androgen-independent prostate cancers. *Neoplasia* 2007;9(6):464–470.
- You Z, Shi XB, DuRaine G, Haudenschild D, Tepper CG, Lo SH, Gandour-Edwards R, de Vere White RW, Reddi AH. Interleukin-17 receptor-like gene is a novel antiapoptotic gene highly expressed in androgen-independent prostate cancer. *Cancer Res* 2006;66(1):175–183.
- Zhang Q, Liu S, Ge D, Xue Y, Xiong Z, Abdel-Mageed AB, Myers L, Hill SM, Rowan BG, Sartor O, Melamed J, Chen Z, You Z. Interleukin-17 promotes formation and growth of prostate adenocarcinoma in mouse models. *Cancer Res* 2012;72(10):2589–2599.

29. Wang S, Gao J, Lei Q, Rozengurt N, Pritchard C, Jiao J, Thomas GV, Li G, Roy-Burman P, Nelson PS, Liu X, Wu H. Prostate-specific deletion of the murine Pten tumor suppressor gene leads to metastatic prostate cancer. *Cancer Cell* 2003;4(3):209–221.
30. Shappell SB, Thomas GV, Roberts RL, Herbert R, Ittmann MM, Rubin MA, Humphrey PA, Sundberg JP, Rozengurt N, Barrios R, Ward JM, Cardiff RD. Prostate pathology of genetically engineered mice: Definitions and classification. The consensus report from the Bar Harbor meeting of the Mouse Models of Human Cancer Consortium Prostate Pathology Committee. *Cancer Res* 2004;64(6):2270–2305.
31. Didier DK, Schiffenbauer J, Woulfe SL, Zacheis M, Schwartz BD. Characterization of the cDNA encoding a protein binding to the major histocompatibility complex class II Y box. *Proc Natl Acad Sci USA* 1988;85(19):7322–7326.
32. Lovett DH, Cheng S, Cape L, Pollock AS, Mertens PR. YB-1 alters MT1-MMP trafficking and stimulates MCF-7 breast tumor invasion and metastasis. *Biochem Biophys Res Commun* 2010;398(3):482–488.
33. Gimenez-Bonafe P, Fedoruk MN, Whitmore TG, Akbari M, Ralph JL, Ettinger S, Gleave ME, Nelson CC. YB-1 is upregulated during prostate cancer tumor progression and increases P-glycoprotein activity. *Prostate* 2004;59(3):337–349.
34. Toh Y, Pencil SD, Nicolson GL. A novel candidate metastasis-associated gene, mta1, differentially expressed in highly metastatic mammary adenocarcinoma cell lines. cDNA cloning, expression, and protein analyses. *J Biol Chem* 1994;269(37):22958–22963.
35. Kai L, Wang J, Ivanovic M, Chung YT, Laskin WB, Schulze-Hoepfner F, Mirochnik Y, Satcher RL Jr, Levenson AS. Targeting prostate cancer angiogenesis through metastasis-associated protein 1 (MTA1). *Prostate* 2011;71(3):268–280.
36. Townsley FM, Aristarkhov A, Beck S, Hershko A, Ruderman JV. Dominant-negative cyclin-selective ubiquitin carrier protein E2-C/UbcH10 blocks cells in metaphase. *Proc Natl Acad Sci USA* 1997;94(6):2362–2367.
37. Hao Z, Zhang H, Cowell J. Ubiquitin-conjugating enzyme UBE2C: Molecular biology, role in tumorigenesis, and potential as a biomarker. *Tumour Biol* 2012;33(3):723–730.
38. Wang Q, Li W, Zhang Y, Yuan X, Xu K, Yu J, Chen Z, Beroukhi R, Wang H, Lupien M, Wu T, Regan MM, Meyer CA, Carroll JS, Manrai AK, Janne OA, Balk SP, Mehra R, Han B, Chinnaiyan AM, Rubin MA, True L, Fiorentino M, Fiore C, Loda M, Kantoff PW, Liu XS, Brown M. Androgen receptor regulates a distinct transcription program in androgen-independent prostate cancer. *Cell* 2009;138(2):245–256.
39. Numasaki M, Fukushi J, Ono M, Narula SK, Zavodny PJ, Kudo T, Robbins PD, Tahara H, Lotze MT. Interleukin-17 promotes angiogenesis and tumor growth. *Blood* 2003;101(7):2620–2627.
40. Numasaki M, Watanabe M, Suzuki T, Takahashi H, Nakamura A, McAllister F, Hishinuma T, Goto J, Lotze MT, Kolls JK, Sasaki H. IL-17 enhances the net angiogenic activity and in vivo growth of human non-small cell lung cancer in SCID mice through promoting CXCR-2-dependent angiogenesis. *J Immunol* 2005;175(9):6177–6189.
41. Kanda N, Koike S, Watanabe S. IL-17 suppresses TNF-alpha-induced CCL27 production through induction of COX-2 in human keratinocytes. *J Allergy Clin Immunol* 2005;116(5):1144–1150.
42. Miura S, Tatsuguchi A, Wada K, Takeyama H, Shinji Y, Hiratsuka T, Futagami S, Miyake K, Gudis K, Mizokami Y, Matsuoaka T, Sakamoto C. Cyclooxygenase-2-regulated vascular endothelial growth factor release in gastric fibroblasts. *Am J Physiol Gastrointest Liver Physiol* 2004;287(2):G444–G451.
43. He D, Li H, Yusuf N, Elmets CA, Li J, Mountz JD, Xu H. IL-17 promotes tumor development through the induction of tumor promoting microenvironments at tumor sites and myeloid-derived suppressor cells. *J Immunol* 2010;184(5):2281–2288.
44. Youn JI, Nagaraj S, Collazo M, Gabrilovich DI. Subsets of myeloid-derived suppressor cells in tumor-bearing mice. *J Immunol* 2008;181(8):5791–5802.
45. Redente EF, Dwyer-Nield LD, Merrick DT, Raina K, Agarwal R, Pao W, Rice PL, Shroyer KR, Malkinson AM. Tumor progression stage and anatomical site regulate tumor-associated macrophage and bone marrow-derived monocyte polarization. *Am J Pathol* 2010;176(6):2972–2985.
46. Hanahan D, Weinberg RA. Hallmarks of cancer: The next generation. *Cell* 2011;144(5):646–674.
47. Mercader M, Bodner BK, Moser MT, Kwon PS, Park ES, Manecke RG, Ellis TM, Wojcik EM, Yang D, Flanigan RC, Waters WB, Kast WM, Kwon ED. T cell infiltration of the prostate induced by androgen withdrawal in patients with prostate cancer. *Proc Natl Acad Sci USA* 2001;98(25):14565–14570.
48. Morse MD, McNeel DG. T cells localized to the androgen-deprived prostate are T(H) 1 and T(H) 17 biased. *Prostate* 2012;72(11):1239–1247.
49. Liu L, Ge D, Ma L, Mei J, Liu S, Zhang Q, Ren F, Liao H, Pu Q, Wang T, You Z. Interleukin-17 and prostaglandin E2 are involved in formation of an M2 macrophage-dominant microenvironment in lung cancer. *J Thorac Oncol* 2012;7(7):1091–1100.

SUPPORTING INFORMATION

Additional supporting information may be found in the online version of this article at the publisher's website.

Article

Doublecortin May Play a Role in Defining Chondrocyte Phenotype

Dongxia Ge ^{1,†}, Qing-Song Zhang ^{1,2,†}, Jovanny Zabaleta ³, Qiuyang Zhang ¹, Sen Liu ¹,
Brendan Reiser ¹, Bruce A. Bunnell ⁴, Stephen E. Braun ⁴, Michael J. O'Brien ⁵,
Felix H. Savoie ⁵ and Zongbing You ^{1,5,*}

¹ Department of Structural and Cellular Biology, Tulane Cancer Center, Louisiana Cancer Research Consortium, Tulane Center for Aging and Tulane Center for Stem Cell Research and Regenerative Medicine, Tulane University Health Sciences Center, New Orleans, LA 70112, USA;

E-Mails: gedongx@gmail.com (D.G.); qingsong.chang@gmail.com (Q.-S.Z.);
qzhang3@tulane.edu (Q.Z.); senliu@yahoo.com (S.L.); brendan.reiser@gmail.com (B.R.)

² Department of Orthopaedic Surgery, Pu Ai Hospital of Tongji Medical College, Huazhong University of Science and Technology, Wuhan 430033, China

³ Department of Pediatrics and Stanley S. Scott Cancer Center, Louisiana State University Health Sciences Center, New Orleans, LA 70112, USA; E-Mail: jzabal@lsuhsc.edu

⁴ Department of Pharmacology, Tulane Center for Stem Cell Research and Regenerative Medicine and Division of Regenerative Medicine of Tulane National Primate Research Center, Tulane University Health Sciences Center, New Orleans, LA 70112, USA;
E-Mails: bbunnell@tulane.edu (B.A.B.); sbraun@tulane.edu (S.E.B.)

⁵ Department of Orthopaedic Surgery and Tulane Institute of Sports Medicine, Tulane University School of Medicine, New Orleans, LA 70112, USA;
E-Mails: michaelobrien76@gmail.com (M.J.O.); fsavoie@tulane.edu (F.H.S.)

[†] These authors contributed equally to this work.

* Author to whom correspondence should be addressed; E-Mail: zyou@tulane.edu;
Tel.: +1-504-988-0467; Fax: +1-504-988-1687.

Received: 17 February 2014; in revised form: 3 April 2014 / Accepted: 14 April 2014 /

Published: 22 April 2014

Abstract: Embryonic development of articular cartilage has not been well understood and the role of doublecortin (*DCX*) in determination of chondrocyte phenotype is unknown. Here, we use a *DCX* promoter-driven *eGFP* reporter mouse model to study the dynamic gene expression profiles in mouse embryonic handplates at E12.5 to E13.5 when the condensed mesenchymal cells differentiate into either endochondral chondrocytes or joint

interzone cells. Illumina microarray analysis identified a variety of genes that were expressed differentially in the different regions of mouse handplate. The unique expression patterns of many genes were revealed. *Cyt11* and *3110032G18RIK* were highly expressed in the proximal region of E12.5 handplate and the carpal region of E13.5 handplate, whereas *Olfr538*, *Kctd15*, and *Cited1* were highly expressed in the distal region of E12.5 and the metacarpal region of E13.5 handplates. There was an increasing gradient of *Hrc* expression in the proximal to distal direction in E13.5 handplate. Furthermore, when human DCX protein was expressed in human adipose stem cells, collagen II was decreased while aggrecan, matrilin 2, and *GDF5* were increased during the 14-day pellet culture. These findings suggest that *DCX* may play a role in defining chondrocyte phenotype.

Keywords: articular cartilage; chondrocytes; doublecortin; *DCX*

1. Introduction

Diseases of articular joints, such as osteoarthritis, cause pain and impaired mobility. It is estimated that 24.3 million American adults have osteoarthritis [1]. The current clinical treatments, other than total joint replacement, do not change the course of osteoarthritis. Regenerative medicine, including tissue engineering, offers exciting opportunities to restore functional articular cartilage. However, currently the tissue-engineered cartilages behave like physeal or endochondral cartilages that undergo premature hypertrophy, unlike the stable articular cartilage that lasts a lifetime [2]. The current tissue engineering of cartilage follows a paradigm of high-density cell culture such as pellet culture, micromass culture, or high-density culture in certain matrix scaffolds. This paradigm essentially mimics embryonic development of skeletal anlage (*i.e.*, endochondral cartilage), rather than articular cartilage. Although endochondral and articular cartilages are both hyaline cartilages, they differ significantly [3]. Embryonic development of articular cartilage has not been well understood. This lack of complete understanding of articular chondrocyte phenotype establishment is a problem for the field of articular cartilage tissue engineering/regeneration.

It is well recognized that the mechanism of regeneration recapitulates the mechanism of embryonic development [4,5]. Therefore, it is critical to understand the determinants of chondrocyte phenotype during embryonic chondrogenesis. In mouse embryonic limb buds, the mesenchymal cells appear homogeneous at embryonic stages of 9.5 to 11.5 days postcoitus (*i.e.*, E9.5 to E11.5). Mesenchymal condensation occurs in the limb buds at E12.5, without any signs of joint interzones—presumptive sites of articular joints [6]. At E13.5, joint interzones appear in the proximal to distal order [7], and the long bone anlagen intervening between the joint interzones become cartilaginous with endochondral chondrocytes residing within the anlagen [8]. Joint interzone can be recognized by postmortem histologic staining or LacZ staining in mice with *Gdf5-cre*-driven *LacZ* expression [8]. Recently, live imaging of joint interzones became possible when doublecortin reporter mice were developed [9]. Doublecortin (*DCX*) is a gene located on chromosome Xq22.3-Xq23, encoding a microtubule-binding protein that is expressed in migrating and differentiating neurons [10–12]. We originally found that *DCX* is expressed in human and mouse articular chondrocytes, but not in endochondral chondrocytes,

synovium, or cruciate ligaments [13]. Using two reporter mouse strains with *DCX* promoter-driven *LacZ* or enhanced green fluorescence protein (*eGFP*), we found that *DCX* is expressed in the mesenchymal cells in mouse embryonic limb buds, however, a population of mesenchymal cells maintain *DCX* expression when they differentiate into joint interzone cells and articular chondrocytes, whereas the other population of mesenchymal cells that differentiate into endochondral chondrocytes lose *DCX* expression [9]. The *DCX-EGFP* reporter mouse provides a unique tool to investigate the dynamic changes of chondrocyte phenotype *in vivo* or *ex vivo*.

2. Results and Discussion

2.1. The *DCX*-Positive Proximal and *DCX*-Negative Distal Regions of E12.5 Mouse Handplate Express Different Genes

Limbs develop in the proximal to distal order [7]. The regional differences are obvious morphologically. This study focused on mouse handplates at E12.5 to E13.5, because differentiation of the condensed mesenchymal cells into chondrocytes occurs during this period. Our previous study showed that the proximal region of E12.5 handplate expresses high levels of *DCX* as shown by eGFP signals, whereas the distal region is almost negative for eGFP signals except the faint signals in the digit rays [9]. Thus, we cut mouse handplates into proximal and distal regions based on eGFP signals under an epifluorescence microscope (Figure 1A). RNA was isolated from the proximal and distal tissues and Illumina microarray analysis was performed. Judging by a two-fold difference, we found that there were 34 genes with mRNA expression levels higher in the proximal region than the distal region, while there were 44 genes expressed at higher levels in the distal region than the proximal region (Tables 1 and S1). Many of these genes have never been studied in limb development. Delta-like 1 homolog (*Dlk1*, No. 1 in Table 1) was highly expressed in the proximal region of mouse handplate, where mesenchymal condensation occurs and chondrogenesis is ongoing. However, it has been shown that *Dlk1* inhibits *in vitro* chondrogenesis [14]. We speculate that the increased *Dlk1* level may be needed to antagonize other signals that drive chondrogenesis, so as chondrogenesis occurs in a controlled manner. Cytokine-like 1 (*Cytl1*, No. 3 in Table 1) was a gene highly expressed in the proximal region of mouse handplate. *Cytl1* is a secreted, cytokine-like factor that has chondrogenic effect via stimulation of sex determining region *Y-box 9* (*Sox9*) transcriptional activity [15]. The increased level of *Cytl1* in the proximal region possibly correlates with the earlier start of chondrogenesis in the proximal region than the distal region. However, a recent study showed that deletion of the *Cytl1* gene did not affect chondrogenesis or cartilage development [16]. In that study, *Cytl1*-null mice also showed normal endochondral ossification and long bone development. In addition, the ultrastructural features of matrix organization and chondrocyte morphology in articular cartilage were similar between wild-type and *Cytl1*-null mice. However, *Cytl1*-null mice were more sensitive to osteoarthritic (OA) cartilage destruction upon destabilization of the medial meniscus of mouse knee joints. Furthermore, the expression levels of *Cytl1* were markedly decreased in OA cartilage of humans and experimental mice. Therefore, the authors of that study concluded that, rather than regulating cartilage and bone development, *Cytl1* is required for the maintenance of cartilage homeostasis, and loss of *Cytl1* function is associated with experimental OA cartilage destruction in mice [16]. Another gene,

paired related homeobox 2 (*Prrx2*, No. 19 in Table 1), was highly expressed in the distal region compared to the proximal region. It has been reported that *Prrx2* is highly expressed in undifferentiated mesenchymal cells and its expression decreases when the mesenchymal cells differentiate into chondrocytes [17]. Given that chondrogenesis proceeds from the proximal region to the distal region, it makes sense that the distal region with more undifferentiated mesenchymal cells expresses higher levels of *Prrx2*. Therefore, our results, at least for *Cyt11* and *Prrx2*, are consistent with the published literature.

Figure 1. Illustration of dissection of mouse embryonic handplates. (a) the distal region (DCX-eGFP-negative); (b) the proximal region (DCX-eGFP-positive); (c) the metacarpal-phalange region (DCX-eGFP-positive); (d) the metacarpal region (DCX-eGFP-negative); (e) the carpal region (DCX-eGFP-positive). All photomicrographs were taken under an epifluorescence microscope with 6× (A); 1.3× (B) and (C); and 1× (D) original magnification.

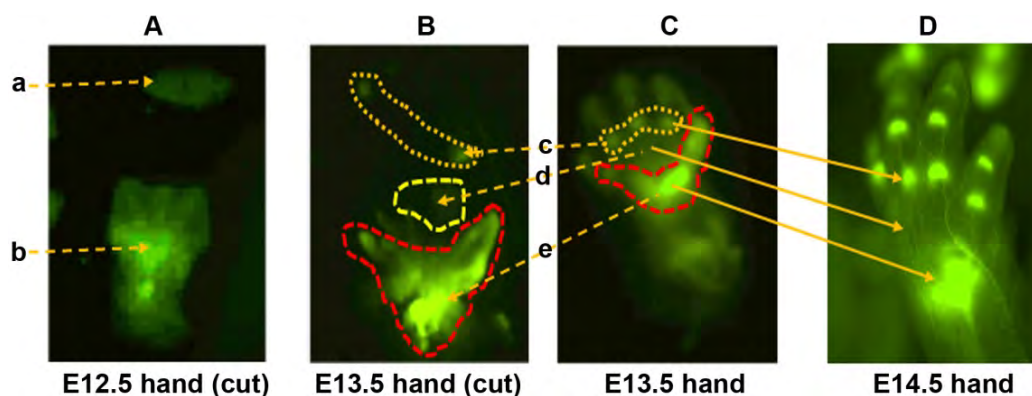


Table 1. Differential gene expression between the proximal and distal regions of E12.5 mouse handplate.

| No. | Gene ID | Gene Symbol | Proximal/Distal Ratio of Expression | Gene Name | Function |
|-----|---------|----------------|-------------------------------------|---|---|
| 1 | 13386 | <i>Dlk1</i> | 14.40 | <i>Delta-like 1 homolog (Drosophila)</i> | Inhibitory non-canonical protein ligand for the NOTCH1 receptor |
| 2 | 15464 | <i>Hrc</i> | 4.84 | <i>Histidine rich calcium binding protein</i> | Interactions with SERCA2 and triadin |
| 3 | 231162 | <i>Cyt11</i> | 4.53 | <i>Cytokine-like 1</i> | Cyt11-null mice show normal cartilage and bone development but exhibit augmented osteoarthritic cartilage destruction |
| 4 | 53412 | <i>Ppp1r3c</i> | 3.19 | <i>Protein phosphatase 1, regulatory (inhibitor) subunit 3C</i> | Activates glycogen synthase, reduces glycogen phosphorylase activity and limits glycogen breakdown |
| 5 | 16664 | <i>Krt14</i> | 3.15 | <i>Keratin 14</i> | Enhances the mechanical properties involved in resilience of keratin intermediate filaments |
| 6 | 74194 | <i>Rnd3</i> | 2.90 | <i>Rho family GTPase 3</i> | Binds GTP but lacks intrinsic GTPase activity |
| 7 | 12306 | <i>Anxa2</i> | 2.39 | <i>Annexin A2</i> | Calcium-regulated membrane-binding protein |
| 8 | 14314 | <i>Fstl</i> | 2.34 | <i>Follistatin-like 1</i> | May modulate the action of some growth factors on cell proliferation and differentiation |

Table 1. Cont.

| No. | Gene ID | Gene Symbol | Proximal/Distal Ratio of Expression | Gene Name | Function |
|-----|---------|----------------------|-------------------------------------|--|--|
| 9 | 21847 | <i>Klf10</i> | 2.32 | <i>Kruppel-like factor 10</i> | Inhibits cell growth |
| 10 | 16002 | <i>Igf2</i> | 2.31 | <i>Insulin-like growth factor 2</i> | Growth-promoting activity |
| 11 | 17709 | <i>Mt-co2</i> | 2.18 | <i>Cytochrome c oxidase subunit II</i> | Component of the respiratory chain |
| 12 | 73121 | <i>3110032G18RIK</i> | 2.05 | <i>Family with sequence similarity 101, member A</i> | Unknown |
| 13 | 15401 | <i>Hoxa4</i> | 0.49 | <i>Homeobox A4</i> | Sequence-specific transcription factor |
| 14 | 15117 | <i>Has2</i> | 0.48 | <i>Hyaluronan synthase 2</i> | Hyaluronan/hyaluronic acid (HA) synthesis |
| 15 | 77087 | <i>3010027A04RIK</i> | 0.44 | <i>Ankyrin repeat domain 11</i> | Bone development |
| 16 | 258201 | <i>Olf-538</i> | 0.43 | <i>Olfactory receptor 538</i> | Interact with odorant molecules in the nose |
| 17 | 233107 | <i>Kctd15</i> | 0.39 | <i>Potassium channel tetramerisation domain containing 15</i> | Unknown |
| 18 | 12705 | <i>Cited1</i> | 0.36 | <i>Cbp/p300-interacting transactivator with Glu/Asp-rich carboxy-terminal domain 1</i> | Transcriptional coactivator of the p300/CBP-mediated transcription complex |
| 19 | 20204 | <i>Prrx2</i> | 0.29 | <i>Paired related homeobox 2</i> | A developmental protein |

2.2. The DCX-Positive and DCX-Negative Regions of E13.5 Mouse Handplate Express Different Genes

At E13.5 in mouse handplate, the condensed mesenchymal cells already differentiate into endochondral chondrocytes or joint interzone cells. The joint interzones are clearly shown by expression of eGFP signals in the *DCX-EGFP* mice [9]. Based on the principle of proximal to distal development, the joint interzones in the carpal region develop first, followed by the joint interzones between the metacarpal bones and phalangeal bones, and then the joint interzones between the phalangeal bones. Due to the gel-like physical property and small size of mouse handplate at E13.5, it is very difficult to dissect out individual joint interzones and cartilaginous anlagen. Thus, we cut the mouse handplate into three regions, namely, the carpal region (containing *DCX*-positive joint interzones), metacarpal region (containing *DCX*-negative metacarpal cartilaginous anlagen), and metacarpal-phalange region (containing *DCX*-positive joint interzones between the metacarpal bones and phalangeal bones) (Figure 1B,C). These regions are so designated as we previously observed that they correspond to the aforementioned regions at E14.5 when hand morphogenesis becomes very clear (Figure 1D and reference [9]).

Microarray analysis showed that there were only four genes that were expressed at higher levels in the carpal region than the metacarpal region (Tables 2 and S2). One of these genes is *Cyt11* (No. 2 in Table 2). Since *Cyt11* has chondrogenic effect and its expression is high in articular chondrocytes [18], it is reasonably expected that *Cyt11* level should be higher in the joint interzones of the carpal region than the cartilaginous anlagen in the metacarpal region, which is consistent with the expression pattern

at E12.5. Microarray analysis also showed that there were 28 genes that were expressed at higher levels in the metacarpal region than the carpal region (Tables 2 and S2). Most of them have never been associated with chondrogenesis. *Frizzled homolog 10* (*Fzd10*, No. 8 in Table 2) is linked to Wnt signaling, and *Delta-like 2 homolog* (*Dlk2*, No. 10 in Table 2) inhibits NOTCH1 signaling. Both Wnt and NOTCH1 signaling pathways are known to play roles in chondrogenesis [19,20].

Table 2. Differential gene expression between the carpal and metacarpal regions of E13.5 mouse handplate.

| No. | Gene ID | Gene Name | Carpal/Metacarpal Ratio of Expression | Gene Name | Function |
|-----|---------|----------------------|---------------------------------------|--|--|
| 1 | 73121 | <i>3110032G18rik</i> | 4.55 | <i>Family with sequence similarity 101, member A</i> | A novel gene uniquely expressed in developing forebrain and midbrain, but its null mutant exhibits no obvious phenotype |
| 2 | 231162 | <i>Cytl1</i> | 3.54 | <i>Cytokine-like 1</i> | Cytl1-null mice show normal cartilage and bone development but exhibit augmented osteoarthritic cartilage destruction |
| 3 | 50781 | <i>Dkk3</i> | 3.26 | <i>Dickkopf homolog 3 (Xenopus laevis)</i> | Antagonizes canonical Wnt signaling |
| 4 | 77853 | <i>Msl2</i> | 2.17 | <i>Male-specific lethal 2 homolog (Drosophila)</i> | Promotes Mdm2-independent cytoplasmic localization of p53 |
| 5 | 17709 | <i>Mt-co2</i> | 0.46 | <i>Cytochrome c oxidase subunit II</i> | Component of the respiratory chain |
| 6 | 21804 | <i>Tgfb1III</i> | 0.46 | <i>Transforming growth factor beta 1 induced transcript 1</i> | A molecular adapter coordinating multiple protein-protein interactions |
| 7 | 233107 | <i>Kctd15</i> | 0.46 | <i>Potassium channel tetramerisation domain containing 15</i> | Unknown |
| 8 | 93897 | <i>Fzd10</i> | 0.45 | <i>Frizzled homolog 10 (Drosophila)</i> | Receptor for Wnt proteins |
| 9 | 258201 | <i>Olfir538</i> | 0.45 | <i>Olfactory receptor 538</i> | Interact with odorant molecules in the nose |
| 10 | 106565 | <i>Dlk2</i> | 0.42 | <i>Delta-like 2 homolog (Drosophila)</i> | Acts as inhibitory non-canonical protein ligands for the NOTCH1 receptor |
| 11 | 12705 | <i>Cited1</i> | 0.41 | <i>Cbp/p300-interacting transactivator with Glu/Asp-rich carboxy-terminal domain 1</i> | Transcriptional coactivator of the p300/CBP-mediated transcription complex |
| 12 | 15464 | <i>Hrc</i> | 0.32 | <i>Histidine rich calcium binding protein</i> | May play a key role in the regulation of SR Ca cycling through its direct interactions with SERCA2 and triadin |
| 13 | 54419 | <i>Cldn6</i> | 0.29 | <i>Claudin 6</i> | Plays a major role in tight junction-specific obliteration of the intercellular space, through calcium-independent cell-adhesion |
| 14 | 16664 | <i>Krt14</i> | 0.15 | <i>keratin 14</i> | The nonhelical tail domain is involved in promoting KRT5-KRT14 filaments to self-organize into large bundles |

Microarray analysis showed that there were six genes that were expressed at higher levels in the metacarpal region than the metacarpal-phalange region (Table 3). One of them is *Delta-like 1 homolog* (*Dlk1*, No. 1 in Table 3). *Dlk1* inhibits NOTCH signaling that inhibits chondrogenesis [20]. In contrast, there were 11 genes that were expressed at higher levels in the metacarpal-phalange region than the metacarpal region (Table 3). It appears that none of these genes has been studied in skeletal development.

Table 3. Differential gene expression between the metacarpal and metacarpal-phalange regions of E13.5 mouse handplate.

| No. | Gene ID | Gene Symbol | Metacarpal/Metacarpal-Phalange Ratio of Expression | Gene Name | Function |
|-----|---------|-----------------|--|--|--|
| 1 | 13386 | <i>Dlk1</i> | 2.64 | <i>Delta-like 1 homolog (Drosophila)</i> | Acts as inhibitory non-canonical protein ligand for the NOTCH1 receptor |
| 2 | 71706 | <i>Slc46a3</i> | 2.35 | <i>Solute carrier family 46, member 3</i> | Unknown |
| 3 | 11806 | <i>Apoa1</i> | 2.25 | <i>Apolipoprotein A-I</i> | Reverse transport of cholesterol from tissues to the liver for excretion |
| 4 | 54419 | <i>Cldn6</i> | 2.15 | <i>Claudin 6</i> | Role in tight junction-specific obliteration of the intercellular space, through calcium-independent cell-adhesion activity |
| 5 | 21804 | <i>Tgfb1l1</i> | 2.12 | <i>Transforming growth factor beta 1 induced transcript 1</i> | Functions as a molecular adapter coordinating multiple protein-protein interactions at the focal adhesion complex in nucleus |
| 6 | 12709 | <i>Ckb</i> | 2.06 | <i>Creatine kinase, brain</i> | Phospholipid biosynthesis |
| 7 | 11472 | <i>Actn2</i> | 0.48 | <i>Actinin alpha 2</i> | F-actin cross-linking protein which is thought to anchor actin to a variety of intracellular structures |
| 8 | 15464 | <i>Hrc</i> | 0.48 | <i>Histidine rich calcium binding protein</i> | Regulation of SR Ca cycling through its direct interactions with SERCA2 and triadin |
| 9 | 16876 | <i>Lhx9</i> | 0.46 | <i>LIM homeobox protein 9</i> | Gonadal development |
| 10 | 56360 | <i>Acot9</i> | 0.46 | <i>Acyl-CoA thioesterase 9</i> | Catalyze the hydrolysis of acyl-CoAs to the free fatty acid and coenzyme A |
| 11 | 72739 | <i>Zkscan3</i> | 0.46 | <i>Zinc finger with KRAB and SCAN domains 3</i> | Acts as a transcriptional regulator |
| 12 | 16704 | <i>Krtap8-2</i> | 0.45 | <i>Keratin associated protein 8-2</i> | Essential for the formation of a rigid and resistant hair shaft through their extensive disulfide bond cross-linking |
| 13 | 68895 | <i>Rasl11a</i> | 0.44 | <i>RAS-like, family 11, member A</i> | Regulator of rDNA transcription. Acts in cooperation UBF/UBTF and positively regulates RNA polymerase I transcription |
| 14 | 17883 | <i>Myh3</i> | 0.39 | <i>Myosin, heavy polypeptide 3, skeletal muscle, embryonic</i> | Mutations in this gene have been associated Freeman-Sheldon syndrome and Sheldon-Hall syndrome |

Table 3. Cont.

| No. | Gene ID | Gene Symbol | Metacarpal/Metacarpal-Phalange Ratio of Expression | Gene Name | Function |
|-----|---------|---------------|--|--|---|
| 15 | 17885 | <i>Myh8</i> | 0.38 | <i>Myosin, heavy polypeptide 8, skeletal muscle, perinatal</i> | Motor protein of muscle thick filaments |
| 16 | 19791 | <i>Rn18s</i> | 0.28 | <i>18S Ribosomal RNA</i> | A 45S rRNA, which serves as the precursor for the 18S, 5.8S and 28S rRNA, is transcribed from rDNA unit by RNA polymerase I |
| 17 | 226856 | <i>Lpgat1</i> | 0.26 | <i>Lysophosphatidylglycerol acyltransferase 1</i> | Recognizes various acyl-CoAs and LPGs as substrates but demonstrates a clear preference |

2.3. Dynamic Gene Expression Profiles between the DCX-Positive Proximal Region of E12.5 Mouse Handplate and the DCX-Positive Carpal or Metacarpal-Phalange Region of E13.5 Mouse Handplate

Microarray analysis found that there were 62 genes with expression levels higher in the proximal region of E12.5 mouse handplate than the carpal region of E13.5 mouse handplate (Tables 4 and S3). Among them, *Cyt11* (No. 1 in Table 4), Dickkopf homolog 3 (*Dkk3*, No. 3 in Table 4), and *Dkk1* (No. 6 in Table 4) are known for their roles in chondrogenesis. In contrast, there were 47 genes that were expressed at higher levels in the carpal region of E13.5 mouse handplate than the proximal region of E12.5 mouse handplate (Tables 4 and S3). Most of these genes are not known for their roles in chondrogenesis, except *Fzd10* (No. 15 in Table 4) that may play a role in chondrogenesis through Wnt signaling [19].

Table 4. Differential gene expression between the proximal region of E12.5 handplate and the carpal region of E13.5 mouse handplate.

| No. | Gene ID | Gene Symbol | E12.5 Proximal/E13.5 Carpal Ratio of Expression | Gene Name | Function |
|-----|---------|----------------------|---|--|--|
| 1 | 231162 | <i>Cyt11</i> | 18.15 | <i>Cytokine-like 1</i> | Cyt11-null mice show normal cartilage and bone development but exhibit augmented osteoarthritic cartilage destruction. |
| 2 | 73121 | <i>3110032G18rik</i> | 7.09 | <i>Family with sequence similarity 101, member A</i> | A novel gene uniquely expressed in developing forebrain and midbrain |
| 3 | 50781 | <i>Dkk3</i> | 6.15 | <i>Dickkopf homolog 3 (Xenopus laevis)</i> | Antagonizes canonical Wnt signaling |
| 4 | 19791 | <i>Rn18s</i> | 6.07 | <i>18S ribosomal RNA</i> | Encodes a 18S rRNA |
| 5 | 319480 | <i>Itga11</i> | 3.89 | <i>Integrin alpha 11</i> | Regulating Bone morphogenetic protein (BMP)-2 and transforming growth factor (TGF)-beta1 |

Table 4. Cont.

| E12.5 Proximal/E13.5 | | | | | |
|----------------------|-----------|-------------------|----------------------------|--|---|
| No. | Gene ID | Gene Symbol | Carpal Ratio of Expression | Gene Name | Function |
| 6 | 13386 | <i>Dlk1</i> | 2.93 | <i>Delta-like 1 homolog (Drosophila)</i> | Acts as inhibitory non-canonical protein ligand for the NOTCH1 receptor |
| 7 | 15401 | <i>Hoxa4</i> | 2.70 | <i>Homeobox A4</i> | Sequence-specific transcription factor |
| 8 | 20680 | <i>Sox7</i> | 2.29 | <i>SRY-box containing gene 7</i> | A member of the SOX (SRY-related HMG-box) family of transcription factors involved in regulation |
| 9 | 67586 | <i>D4bwg1540e</i> | 2.29 | <i>UBX domain protein 11</i> | May be involved in the reorganization of actin cytoskeleton mediated by RND1, RND2, and RND3 |
| 10 | 26433 | <i>Plod3</i> | 2.11 | <i>Procollagen-lysine, 2-oxoglutarate 5-dioxygenase 3</i> | Forms hydroxylysine residues in -Xaa-Lys-Gly- sequences in collagens |
| 11 | 100034361 | <i>Mfap1b</i> | 0.48 | <i>Microfibrillar-associated protein 1B</i> | Component of the elastin-associated microfibrils By similarity |
| 12 | 21371 | <i>Tbca</i> | 0.47 | <i>Tubulin cofactor A</i> | Tubulin-folding protein; involved in the early step of the tubulin folding pathway |
| 13 | 26941 | <i>Slc9a3r1</i> | 0.41 | <i>Solute carrier family 9 (sodium/hydrogen exchanger), member 3 regulator 1</i> | Scaffold protein that connects plasma membrane proteins with members of the ezrin/moesin/radixin |
| 14 | 12301 | <i>Cacybp</i> | 0.29 | <i>Calcyclin binding protein</i> | CacyBP/SIP interacts with tubulin in neuroblastoma NB2a cells and induces formation of globular tubulin assemblies. |
| 15 | 93897 | <i>Fzd10</i> | 0.25 | <i>Frizzled homolog 10 (Drosophila)</i> | Receptor for Wnt proteins. Most of frizzled receptors are coupled to the beta-catenin canonical signaling pathway |
| 16 | 18590 | <i>Pdgfa</i> | 0.24 | <i>Platelet derived growth factor, alpha</i> | Growth factor that plays an essential role in the regulation of embryonic development |
| 17 | 66643 | <i>Lix1</i> | 0.24 | <i>Limb expression 1 homolog (chicken)</i> | Unknown |
| 18 | 16664 | <i>Krt14</i> | 0.15 | <i>Keratin 14</i> | Involved in resilience of keratin intermediate filaments |

Microarray analysis also showed that there were 79 genes that were expressed at higher levels in the proximal region of E12.5 mouse handplate than the metacarpal-phalange region of E13.5 mouse handplate (Tables 5 and S4). These genes include *Cytl1* (No. 3 in Table 5) and *Dkk3* (No. 9 in Table 5) that are known to play roles in chondrogenesis. However, the other genes have rarely been studied in

chondrogenesis. On the other hand, there were 24 genes with expression levels higher in the metacarpal-phalange region of E13.5 mouse handplate than the proximal region of E12.5 mouse handplate (Tables 5 and S4). However, none of them has been studied in chondrogenesis.

Table 5. Differential gene expression between the proximal region of E12.5 handplate and the metacarpal-phalange region of E13.5 mouse handplate.

| No. | Gene ID | Gene Symbol | E12.5 Proximal/E13.5 Metacarpal-Phalange Ratio of Expression | Gene Name | Function |
|-----|-----------|----------------------|--|---|--|
| 1 | 19791 | <i>Rn18s</i> | 6.66 | <i>Rn18s 18S ribosomal RNA</i> | Encodes a 18S rRNA |
| 2 | 319480 | <i>Itga11</i> | 4.54 | <i>Integrin alpha 11</i> | Regulating Bone morphogenetic protein (BMP)-2 and transforming growth factor (TGF)-beta1 |
| 3 | 231162 | <i>Cyt11</i> | 4.09 | <i>Cytokine-like 1</i> | Cyt11-null mice show normal cartilage and bone development but exhibit augmented osteoarthritic cartilage destruction. |
| 4 | 72053 | <i>2010008E23Rik</i> | 3.93 | <i>Transmembrane and ubiquitin-like domain containing 2</i> | Unknown |
| 5 | 21804 | <i>Tgfb1i1</i> | 3.16 | <i>Transforming growth factor beta 1 induced transcript 1</i> | A molecular adapter coordinating multiple protein-protein interactions at the focal adhesion complex and in the nucleus |
| 6 | 108903 | <i>Tbcd</i> | 2.79 | <i>Tubulin-specific chaperone d</i> | Tubulin-folding protein |
| 7 | 67586 | <i>Ubxn11</i> | 2.3 | <i>UBX domain protein 11</i> | Reorganization of actin cytoskeleton member of the SOX |
| 8 | 20680 | <i>Sox7</i> | 2.24 | <i>SRY-box containing gene 7</i> | (SRY-related HMG-box) family of transcription factors |
| 9 | 50781 | <i>Dkk3</i> | 2.16 | <i>Dickkopf homolog 3 (Xenopus laevis)</i> | Inhibit Wnt regulated processes |
| 10 | 258201 | <i>Olf538</i> | 2.06 | <i>Olfactory receptor 538</i> | Olfactory receptors interact with odorant molecules in the nose |
| 11 | 100034361 | <i>Mfap1b</i> | 0.45 | <i>Microfibrillar-associated protein 1B</i> | Component of the elastin-associated microfibrils by similarity |
| 12 | 66643 | <i>Lix1</i> | 0.15 | <i>Limb expression 1 homolog (chicken)</i> | Little is known about LIX1, except that it is evolutionarily conserved and highly expressed in spinal cord motor neurons |

In a comparison analysis of the above microarray data, we found some patterns of gene expression that are worth discussion. First, *Cyt11* and *3110032G18RIK* (also called *Fam101a*, i.e., family with sequence similarity 101, member A) are consistently highly expressed in the *DCX*-positive proximal region of E12.5 mouse handplate and the *DCX*-positive carpal region of E13.5 mouse handplate, compared to the *DCX*-negative distal region of E12.5 mouse handplate and the *DCX*-negative metacarpal region of E13.5 mouse handplate (Figure 2A,B). On the opposite, Olfactory receptor 538 (*Olf538*), Potassium channel tetramerisation domain containing 15 (*Kctd15*), and Cbp/p300-interacting transactivator with Glu/Asp-rich carboxy-terminal domain 1 (*Cited1*) are expressed at higher levels in the *DCX*-negative distal region of E12.5 mouse handplate and the *DCX*-negative metacarpal region of E13.5 mouse handplate than the *DCX*-positive proximal region of E12.5 mouse handplate and the *DCX*-positive carpal region of E13.5 mouse handplate (Figure 2A,B). These genes show a consistent expression pattern in the proximal to distal direction through E12.5 to E13.5; Second, several genes present a reverse expression pattern, including *Hrc*, *Krt14*, and *Mt-co2*. These genes are expressed at higher levels in the *DCX*-positive proximal region than the *DCX*-negative distal region of E12.5 mouse handplate (Figure 2A), however, their levels are lower in the *DCX*-positive carpal region than the *DCX*-negative metacarpal region of E13.5 mouse handplate (Figure 2B). Interestingly, the level of *Hrc* is higher in the *DCX*-positive metacarpal-phalange region than the *DCX*-negative metacarpal region of E13.5 mouse handplate (Figure 2B). These findings suggest that at E13.5, *Hrc* gene displays an expression pattern with increasing levels along the proximal-distal axis. *Ras111a* gene also shows the similar pattern (Figure 2B); Third, *Claudin 6* (*Cldn6*) and *Transforming growth factor beta 1 induced transcript 1* (*Tgfb111*) genes are expressed at higher levels in the *DCX*-negative metacarpal region than the *DCX*-positive carpal region or metacarpal-phalange region of E13.5 mouse handplate (Figure 2B). Whether this expression pattern is linked to the difference between cartilaginous anlagen and joint interzone requires further investigation.

2.4. *DCX* Affects Expression of Genes Associated with Chondrocyte Phenotype

Our previous studies have demonstrated that *DCX* is expressed in the osteo-chondral mesenchymal precursor cells and its expression is maintained in joint interzone cells and articular chondrocytes [9,13]. Other investigators have also shown *DCX* expression in articular chondrocytes [21]. It has been recognized that the permanent cartilage (articular cartilage) expresses *DCX*, *growth differentiation factor 5* (*GDF5*), and versican, whereas the transient cartilage (skeletal anlagen or endochondral cartilage) expresses matrilin 1 [22]. However, the role of *DCX* in chondrogenesis has not been understood. Therefore, we studied whether consistent expression of low level of *DCX* in the mesenchymal stromal/stem cells (MSCs) would affect chondrocyte phenotype during chondrogenesis using a pellet culture model.

We constructed a lentiviral vector (HRST-*DCX-GP-eGFP*) to express human *DCX* in human adipose tissue-derived MSCs, also called adipose stem cells (ASCs). GP stands for glycine and proline within a consensus peptide sequence that automatically self-cleaves to separate *DCX* and eGFP proteins once *DCX-GP-eGFP* gene is translated based on a previous study [23]. As a control group, HRST-*eGFP* lentiviral vector was used. Human ASCs transduced with either HRST-*eGFP* or HRST-*DCX-GP-eGFP* lentiviruses were sorted out, based on eGFP expression (Figure 3A,B). *DCX* protein expression was

confirmed by Western blot analysis (Figure 3C). Of note, DCX protein size was approximately 40 KDa, similar to the endogenous DCX protein expressed in mouse brain tissues, which indicates that the DCX-GP-eGFP fusion protein was indeed cleaved into separate DCX and eGFP proteins. DCX protein expression level was much lower in the transduced ASCs than the mouse brain tissues, which is comparable to the physiologic levels where DCX expression level in the limbs is dramatically less than in the brain and spinal cord [9]. Human ASCs with eGFP or DCX-GP-eGFP expression were cultured in pellets with chondrogenic media for 14 days. We found that both groups of human ASCs produced pieces of cartilage-like tissues with similar appearance (Figure 3D,E). Western blot analysis showed that DCX protein was expressed in the cartilage-like tissues derived from HRST-DCX-GP-eGFP lentivirus-transduced ASCs, but not in the cartilage-like tissues derived from HRST-eGFP lentivirus-transduced ASCs (Figure 3F). We checked a series of genes that are known to be expressed in articular or endochondral chondrocytes. We found that expression of collagen II was significantly decreased in the DCX-expressing pellets, whereas expression of aggrecan, matrilin 2, and *GDF5* was significantly increased in the DCX-expressing pellets (Figure 3G, $p < 0.05$). Superficial zone protein (SZP) was not detectable in either group. Collagen I is expressed by human ASCs. Expression of collagen I is expected to be reduced in chondrogenesis, however, we only observed a slight decrease in collagen I expression (Figure 3G). We speculate that this may be caused by an incomplete change from fibroblastic to chondrocytic phenotypes. It is paradoxical to observe that collagen II was reduced by DCX expression. However, we previously found that collagen II is expressed at higher levels in endochondral cartilage than articular cartilage [3], which suggests that less collagen II expression implies more articular chondrocytic phenotype than endochondral chondrocytic phenotype. Matrilin 2 and *GDF5* are restricted to articular chondrocytes [22–25]. DCX expression was decreased by 44-fold when E11.5 mouse limb bud mesenchymal cells were cultured in micromasses from day 3 to day 15 [23]. It is noteworthy that, in monolayer culture of mouse embryonic stem cells, *GDF5* induced *DCX* expression on day four but its expression diminished over next eight days [26]. It is possible that *GDF5* and *DCX* provide reciprocal positive feedback in their expression, as both *GDF5* and *DCX* proteins are restricted to articular cartilage. The differences in collagen II, matrilin 2, and *GDF5* between the two groups indicate that the DCX-expressing cartilage-like tissues lean towards expressing more genes that are specific for articular cartilage. Matrilin 1 levels were quite variable during our experiments (Figure 3G). However, since matrilin 1 is specific for endochondral chondrocytes [25], its increased expression in the DCX-expressing cartilage-like tissues argues against the speculation that *DCX* drives ASCs towards articular chondrocyte differentiation. Therefore, it awaits further investigation to clarify what *DCX*'s role is in chondrogenesis.

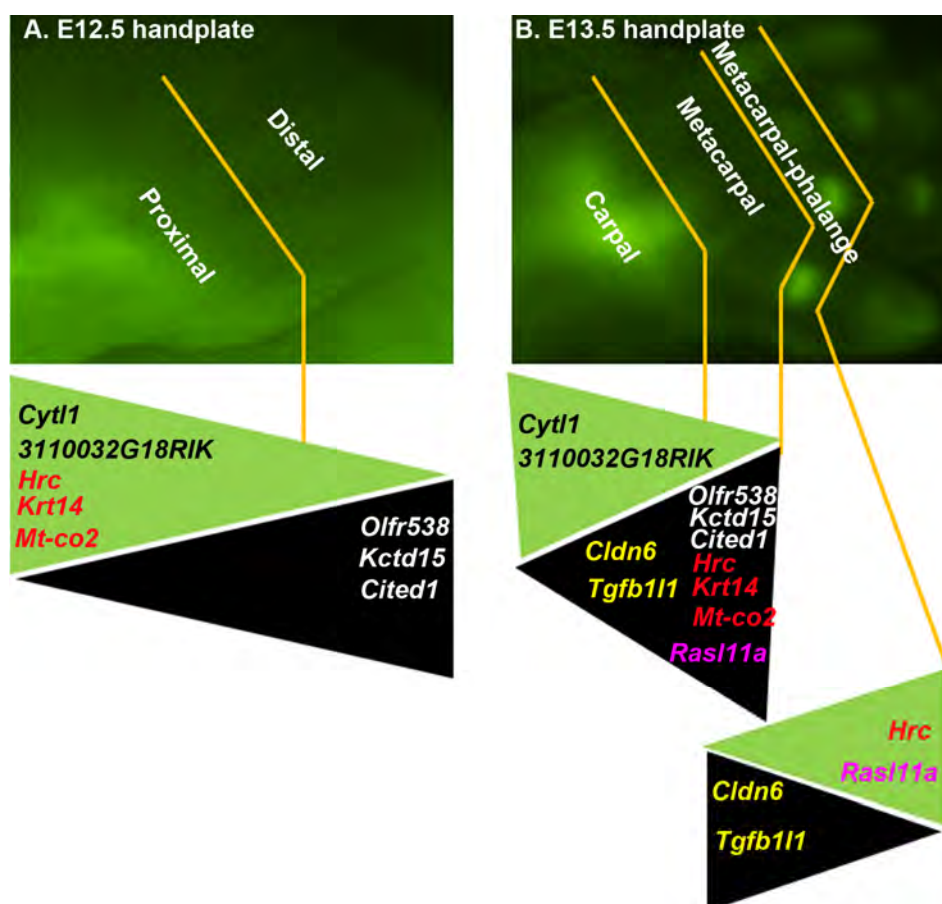
3. Experimental Section

3.1. Animals

Animal study was approved by the Institutional Animal Care and Use Committee of Tulane University (Protocol# 4040R, approved on 17 January 2011, valid through 16 January 2014). The *Dcx-EGFP* mice with a strain name of Tg (*Dcx-EGFP*) BJ224Gsat/Mmmh were obtained from the Mutant Mouse Regional Resource Center, University of Missouri, which were characterized previously [9]. Enhanced

green fluorescence protein (eGFP) was expressed in *Dcx*-expressing cells in these mice. E12.5 and E13.5 mouse embryos were obtained through timed pregnancies. Images of mouse handplates were taken with an epifluorescence microscope (Nikon AZ100) equipped with a digital camera (Nikon DS-Qi1Mc) and NIS-Elements Basic 3.0 software (Nikon Instruments Inc., Melville, NY, USA). The handplates were dissected into different regions under the epifluorescence microscope, using VANNAS microdissecting spring scissors (Roboz Surgical, Gaithersburg, MD, USA). Approximately 16 handplates from 8 embryos of a single pregnant mouse each at E12.5 and E13.5 were collected and pooled.

Figure 2. Comparison analysis of gene expression patterns between different regions. (A) E12.5 mouse handplate (original magnification, 6×); (B) E13.5 mouse handplate (original magnification, 1.3×). Selected genes are shown with their gene symbols color-coded and the ones with the same color are in comparison between the different regions. The genes are laid on colored triangles, the base of each triangle indicating higher levels of gene expression with the tip indicating lower levels of gene expression; green triangles indicate higher levels of gene expression in the DCX-eGFP-positive regions, whereas black triangles indicate higher levels of gene expression in the DCX-eGFP-negative regions.

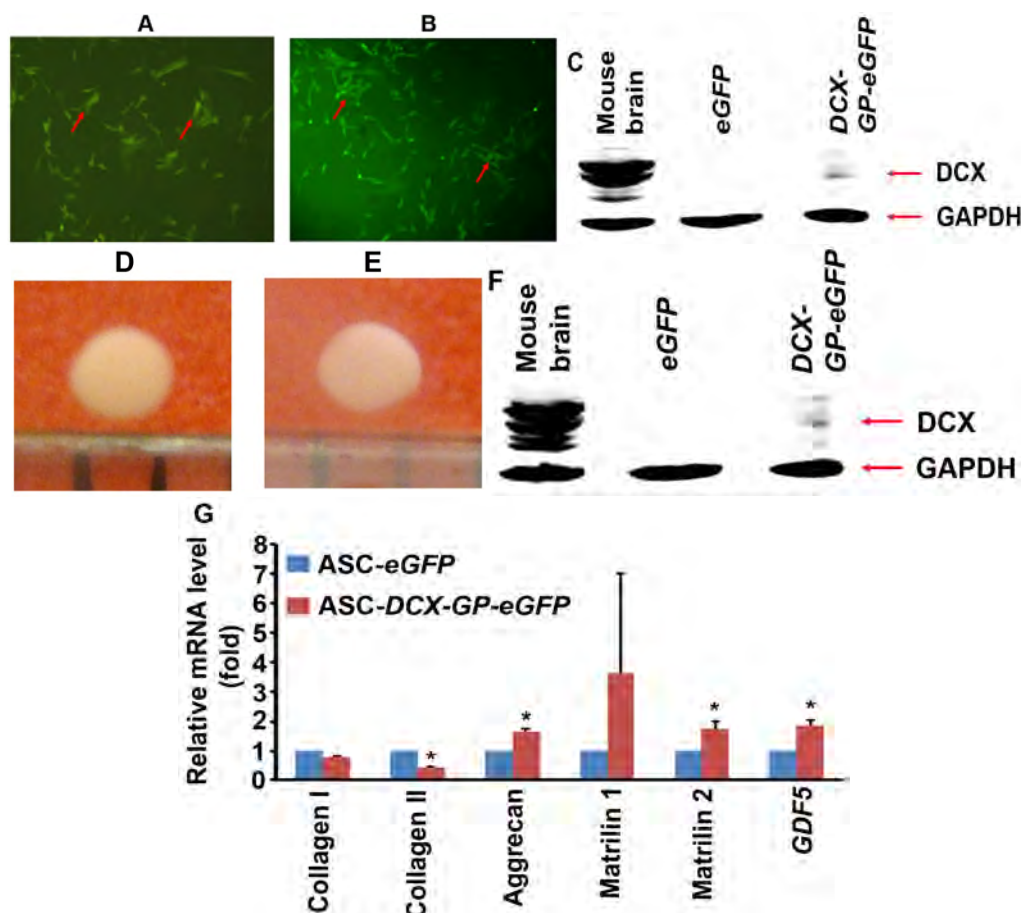


3.2. RNA Extraction and Microarray

The dissected mouse embryonic tissues were homogenized and total RNA was extracted using RNeasy Mini Kit (QIAGEN, Valencia, CA, USA) with DNase I digestion to avoid genomic DNA contamination. RNA was dissolved in DNase/RNase-free water, quantified by a NanoDrop instrument

(NanoDrop Products, part of Thermo Fisher Scientific, Wilmington, DE, USA) and set at a concentration of $\sim 1.0 \mu\text{g}/\mu\text{L}$. The quality of the RNA was confirmed by Agilent 2100 Bioanalyzer (Agilent Technologies, Palo Alto, CA, USA). Two hundred ng of RNA were used to make biotinylated cRNA using the Illumina TotalPrep RNA Amplification Kit (Ambion, Austin, TX, USA), and hybridized to the Illumina chips for 14 h at 58°C . After washing and staining, the arrays were scanned with the BeadArray Reader (Illumina Inc., San Diego, CA, USA) and analyzed with the GenomeStudio software (Illumina Inc.) as described previously [27]. All microarray analysis was done at the LCRC Genomics Facility in New Orleans, LA, USA.

Figure 3. The effects of *DCX* expression on chondrocyte differentiation of human ASCs in pellet cultures. (A) and (B) Human ASCs transduced with HRST-*eGFP* (A) and HRST-*DCX-GP-eGFP* (B) lentiviruses and sorted by flow cytometry; arrows indicate *eGFP*-positive cells; original magnification, $200\times$; (C) Western blot analysis of the sorted human ASCs; mouse brain serves as a positive control; (D) and (E) Representative photomicrographs of the cartilage-like tissues derived from HRST-*eGFP*-transduced ASCs (D) and HRST-*DCX-GP-eGFP*-transduced ASCs (E); (F) Western blot analysis of the proteins extracted from the cartilage-like tissues; (G) qRT-PCR analysis of gene expression in the cartilage-like tissues. Data represent mean \pm SD (error bars) of three independent experiments; the difference between the ASC-*eGFP* and ASC-*DCX-GP-eGFP* groups was statistically significant (* $p < 0.05$).



3.3. Microarray Data Analysis

After subtracting the background, the samples were normalized using the “cubic spline” algorithm assuming a similar distribution of transcript abundance in all the samples. Gene expression levels were compared to select only those genes with >2-fold differences (up or down-regulated) between the samples in comparison. All sequence data were assigned a gene ID corresponding to the Gene Symbol from the National Center for Biotechnology Information (NCBI) gene database [28]. These genes were then researched using both the NCBI database and the UniProt Protein Knowledgebase database [29] to annotate the corresponding protein function.

3.4. Cultures of Human Adipose Tissue-Derived Mesenchymal Stromal/Stem Cells

Human adipose tissue-derived mesenchymal stromal/stem cells (MSCs), also called adipose stem cells (ASCs), were collected at the Pennington Biomedical Research Center (Baton Rouge, LA, USA) with approval of the Institutional Review Board and all human participants provided written informed consent (PBRC #23040) as previously described [30,31]. The ASCs were provided to the researchers as de-identified materials. The ASCs were cultured in α -minimum essential medium (α -MEM, Mediatech Inc., Herndon, VA, USA) with 20% fetal bovine serum (FBS, Bio-West, Rosenberg, TX, USA) and 1% L-glutamine in a 37 °C, 5% CO₂ humidified incubator.

3.5. Transduction of Human ASCs

HRST-eGFP lentiviral expression vector was derived from the original pHR' CMV-lacZ vector [32], which expresses eGFP. Full-length human *DCX* cDNA was subcloned into HRST-eGFP vector through BamHI and XhoI sites, upstream to *eGFP*, thus, constructing HRST-*DCX-GP-eGFP* vector. GP stands for glycine and proline within a consensus peptide sequence that automatically self-cleaves to separate DCX and eGFP proteins once *DCX-GP-eGFP* gene was translated based on a previous study [33]. HRST-eGFP and HRST-*DCX-GP-eGFP* plasmids were individually packaged into replication-incompetent lentiviruses in 293T cells by co-transfection with packaging plasmids as described previously [34]. The packaging plasmids were pHDM-Hgpm2 (HIV gag-pol expression plasmid), pRC/CMV-Rev 1b (Accessory protein rev), pHDM-Tat 1b (Accessory protein tat), and pHDM.G (env, VSVG pseudotype). Human ASCs (within the first three passages following initial plating) were transduced with either HRST-eGFP or HRST-*DCX-GP-eGFP* lentiviruses for 16 h, and then thoroughly rinsed with phosphate-buffered saline (PBS) and cultured in complete medium. Forty-eight hours after transduction, the cells were harvested and eGFP-positive cells were sorted with a flow cytometry cell sorter (BD FACSAria, BD Biosciences, San Jose, CA, USA).

3.6. Pellet Culture

Approximately 200,000 eGFP⁺ or DCX-GP-eGFP⁺ ASCs were centrifuged in 15-mL conical polypropylene centrifuge tubes [13]. The cell pellets were cultured in chondrogenic media, that is, Dulbecco's modified Eagle's medium (DMEM) supplemented with 10 ng/mL BMP-7 (R&D Systems, Minneapolis, MN, USA), ITS solution (BD Biosciences, San Jose, CA, USA), 50 μ g/mL 2-phospho-L-ascorbic acid trisodium salt (Sigma-Aldrich, St. Louis, MO, USA), 100 μ g/mL sodium

pyruvate (Invitrogen, Carlsbad, CA, USA), 100 nM dexamethasone (Sigma-Aldrich), 0.1% bovine serum albumin (Sigma-Aldrich). The medium was replaced every 3 days during 14 days of pellet culture.

3.7. Real-Time Quantitative Reverse Transcriptase PCR (qRT-PCR)

Pellets were homogenized and total RNA was extracted using RNeasy Mini Kit (QIAGEN, Valencia, CA, USA) with DNase I digestion to avoid genomic DNA contamination. cDNA was made from total RNA using iScript™ cDNA Synthesis Kit (Bio-Rad Laboratories, Hercules, CA, USA). PCR primers for human collagen I, collagen II, aggrecan, superficial zone protein (SZP), matrilin 1, matrilin 2, *GDF5*, and glyceraldehyde-3-phosphate dehydrogenase (*GAPDH*) were obtained from Eurofins MWG Operon (Huntsville, AL, USA) (Table 6). qRT-PCR was done in triplicates with an iQ5® iCycler and iQ™ SYBR® Green Supermix (Bio-Rad Laboratories, Hercules, CA, USA) following the recommended protocols. Results were normalized to *GAPDH* levels using the formula ΔC_t (Cycle threshold) = C_t of target gene – C_t of *GAPDH*. The mRNA level of the ASCs transduced with HRST-eGFP lentiviruses was used as the baseline; therefore, $\Delta\Delta C_t$ was calculated using the formula $\Delta\Delta C_t = \Delta C_t$ of the target gene – ΔC_t of the baseline. The fold change of mRNA level was calculated as fold = $2^{-\Delta\Delta C_t}$ [35]. Three independent experiments were conducted and data represent mean \pm SD (error bars) of 3 independent experiments.

Table 6. Nucleotide sequences of each PCR primer pair.

| Gene | Primer | Nucleotide Sequence (5' to 3') |
|-------------------------|-----------|--------------------------------|
| Collagen I | sense | CACCAATCACCTGCGTACAGAA |
| | antisense | ACAGATCACGTCATCGCACAAC |
| Collagen II | sense | GGCAATAGCAGGTTACGTACA |
| | antisense | CGATAACAGTCTTGCCCCACTT |
| Aggrecan (core protein) | sense | AAGTATCATCAGTCCCAGAATCTAGCA |
| | antisense | CGTGGAATGCAGAGGTGGTT |
| SZP | sense | TTGCGCAATGGGACATTAGTT |
| | antisense | AGCTGGAGATGGTGGACTGAA |
| Matrilin 1 | sense | AGGGACTGCGTTTGCATTTTT |
| | antisense | TCAGTAAAGAAATTCACAGCACTCAGA |
| Matrilin 2 | sense | GACGGACGGGCTCAGGAT |
| | antisense | GATACCATTGGCCTTGGCTTTA |
| GDF5 | sense | ATTTGTGCCTGGTGACTTCC |
| | antisense | AGCCCTCTCCTCTTCTCTCC |
| GAPDH | sense | TAAAAGCAGCCCTGGTGACC |
| | antisense | CCACATCGCTCAGACACCAT |

3.8. Western Blot Analysis

Human ASCs (after flow cytometry sorting) and homogenates of the ASCs pellets were lysed with lysis buffer (50 mM sodium fluoride, 0.5% Igepal CA-630 (NP-40), 10 mM sodium phosphate, 150 mM sodium chloride, 25 mM Tris pH 8.0, 1 mM phenylmethylsulfonyl fluoride, 2 mM ethylenediaminetetraacetic acid (EDTA), 1.2 mM sodium vanadate) supplemented with protease

inhibitor cocktail (Sigma-Aldrich, St. Louis, MO, USA). Equal amount of proteins was subjected to 10% SDS-polyacrylamide gel electrophoresis and transferred to polyvinylidene difluoride membrane. Protein extract from mouse brain tissues was used as a positive control for DCX protein [36]. The membranes were blocked with 5% nonfat dry milk in TBST buffer (25 mM Tris-HCl, 125 mM NaCl, 0.1% Tween 20) for 2 h and incubated with goat anti-DCX antibodies (sc-8066, Santa Cruz Biotechnology, Santa Cruz, CA, USA) overnight and then IRDye[®]800CW-conjugated donkey anti-goat secondary antibodies (LI-COR Biosciences, Lincoln, NE, USA) for 1 h. The results were visualized by using an Odyssey Infrared Imager (LI-COR Biosciences, Lincoln, NE, USA). For loading control, the membranes were also probed for GAPDH using mouse anti-GAPDH antibodies (MAB374, Millipore Corporation, Billerica, MA, USA).

3.9. Statistical Analysis

Student's *t*-test (two-tailed) was used to analyze the qRT-PCR data and *p*-value <0.05 was considered statistically significant.

4. Conclusions

The present study used *DCX* promoter-driven *eGFP* expression as a guide to dissect different regions of E12.5 and E13.5 mouse embryonic handplates. Microarray analysis of gene expression profiles identified a variety of genes that were expressed differentially in the different regions of mouse handplate *in vivo*. The unique expression patterns of several genes, e.g., *Cyt11*, are intriguing targets for further investigation. The *in vitro* experiments showed that *DCX* affected expression of several genes associated with chondrocyte phenotype, such as collagen II, aggrecan, matrilin 2, and *GDF5*. These findings imply that *DCX* may play a role in driving differentiation of articular chondrocyte phenotype, which awaits future studies for further clarification.

Acknowledgments

This work was partially supported by a National Natural Science Foundation of China (NSFC#81201394: The mechanism of the effect and regulation from the dynamic expression of doublecortin on bone fracture healing, to Q.-S.Z). Z.Y. was partially supported by two grants from the National Institute of General Medical Sciences (P20GM103518) and the National Cancer Institute (R01CA174714) of the National Institutes of Health, four grants from Department of Defense (W81XWH-10-1-0937, W81XWH-14-1-0050, PC131448, and PC130118), the Developmental Fund of Tulane Cancer Center (TCC), Tulane University School of Medicine Pilot Fund, and Louisiana Cancer Research Consortium (LCRC) Fund. J.Z. was partially funded by the Louisiana Cancer Research Consortium and by a grant of the National Institute of General Medical Sciences (P20GM103501). S.E.B was partially funded by the base grant to the Tulane National Primate Research Center (2P51RR000164-52). The content of this article is solely the responsibility of the authors and does not necessarily represent the official views of the National Institutes of Health. TCC/LCRC Flow Cytometry Core Facility was used in this study.

Author Contributions

D.G. did the pellet culture and isolated RNA from mouse embryos; Q.-S.Z. participated in study design, animal husbandry, and manuscript preparation; J.Z. did Illumina microarray analysis; Q.Z. participated in animal husbandry and taking photos of mouse embryos; S.L. did Western blot analysis; B.R. annotated the microarray data; B.A.B. provided human ASCs and participated in study design; S.E.B. constructed the lentiviral vectors; M.J.O. and F.H.S. participated in study design; Z.Y. participated in study design, data analysis, and manuscript preparation. All authors contributed to manuscript preparation, agreed to be listed, and approved the submitted version of the manuscript.

Conflicts of Interest

The authors declare no conflict of interest.

References

1. Singh, G.; Miller, J.D.; Lee, F.H.; Pettitt, D.; Russell, M.W. Prevalence of cardiovascular disease risk factors among US adults with self-reported osteoarthritis: Data from the third national health and nutrition examination survey. *Am. J. Manag. Care* **2002**, *8*, S383–S391.
2. Tuan, R.S. Stemming cartilage degeneration: Adult mesenchymal stem cells as a cell source for articular cartilage tissue engineering. *Arthritis Rheumatol.* **2006**, *54*, 3075–3078.
3. Yamane, S.; Cheng, E.; You, Z.; Reddi, A.H. Gene expression profiling of mouse articular and growth plate cartilage. *Tissue Eng.* **2007**, *13*, 2163–2173.
4. Muneoka, K.; Bryant, S.V. Evidence that patterning mechanisms in developing and regenerating limbs are the same. *Nature* **1982**, *298*, 369–371.
5. Reddi, A.H. Cartilage-derived morphogenetic proteins and cartilage morphogenesis. *Microsc. Res. Tech.* **1998**, *43*, 131–136.
6. Martin, P. Tissue patterning in the developing mouse limb. *Int. J. Dev. Biol.* **1990**, *34*, 323–336.
7. Mitrovic, D. Development of the diarthrodial joints in the rat embryo. *Am. J. Anat.* **1978**, *151*, 475–485.
8. Koyama, E.; Shibukawa, Y.; Nagayama, M.; Sugito, H.; Young, B.; Yuasa, T.; Okabe, T.; Ochiai, T.; Kamiya, N.; Rountree, R.B.; *et al.* A distinct cohort of progenitor cells participates in synovial joint and articular cartilage formation during mouse limb skeletogenesis. *Dev. Biol.* **2008**, *316*, 62–73.
9. Zhang, Q.; Cigan, A.D.; Marrero, L.; Lopreore, C.; Liu, S.; Ge, D.; Savoie, F.H.; You, Z. Expression of doublecortin reveals articular chondrocyte lineage in mouse embryonic limbs. *Genesis* **2011**, *49*, 75–82.
10. Bai, J.; Ramos, R.L.; Ackman, J.B.; Thomas, A.M.; Lee, R.V.; LoTurco, J.J. RNAi reveals doublecortin is required for radial migration in rat neocortex. *Nat. Neurosci.* **2003**, *6*, 1277–1283.
11. Gleeson, J.G.; Allen, K.M.; Fox, J.W.; Lamperti, E.D.; Berkovic, S.; Scheffer, I.; Cooper, E.C.; Dobyns, W.B.; Minnerath, S.R.; Ross, M.E.; *et al.* Doublecortin, a brain-specific gene mutated in human X-linked lissencephaly and double cortex syndrome, encodes a putative signaling protein. *Cell* **1998**, *92*, 63–72.

12. Des Portes, V.; Francis, F.; Pinard, J.M.; Desguerre, I.; Moutard, M.L.; Snoeck, I.; Meiners, L.C.; Capron, F.; Cusmai, R.; Ricci, S.; *et al.* Doublecortin is the major gene causing X-linked subcortical laminar heterotopia (SCLH). *Hum. Mol. Genet.* **1998**, *7*, 1063–1070.
13. Zhang, Y.; Ryan, J.A.; di Cesare, P.E.; Liu, J.; Walsh, C.A.; You, Z. Doublecortin is expressed in articular chondrocytes. *Biochem. Biophys. Res. Commun.* **2007**, *363*, 694–700.
14. Chen, L.; Qanie, D.; Jafari, A.; Taipaleenmaki, H.; Jensen, C.H.; Saamanen, A.M.; Sanz, M.L.; Laborda, J.; Abdallah, B.M.; Kassem, M. Delta-like 1/fetal antigen-1 (Dlk1/FA1) is a novel regulator of chondrogenic cell differentiation via inhibition of the Akt kinase-dependent pathway. *J. Biol. Chem.* **2011**, *286*, 32140–32149.
15. Kim, J.S.; Ryoo, Z.Y.; Chun, J.S. Cytokine-like 1 (*Cytl1*) regulates the chondrogenesis of mesenchymal cells. *J. Biol. Chem.* **2007**, *282*, 29359–29367.
16. Jeon, J.; Oh, H.; Lee, G.; Ryu, J.H.; Rhee, J.; Kim, J.H.; Chung, K.H.; Song, W.K.; Chun, C.H.; Chun, J.S. Cytokine-like 1 knock-out mice (*Cytl1*^{−/−}) show normal cartilage and bone development but exhibit augmented osteoarthritic cartilage destruction. *J. Biol. Chem.* **2011**, *286*, 27206–27213.
17. Leussink, B.; Brouwer, A.; el Khattabi, M.; Poelmann, R.E.; Gittenberger-de Groot, A.C.; Meijlink, F. Expression patterns of the paired-related homeobox genes MHox/Prx1 and S8/Prx2 suggest roles in development of the heart and the forebrain. *Mech. Dev.* **1995**, *52*, 51–64.
18. Minogue, B.M.; Richardson, S.M.; Zeef, L.A.; Freemont, A.J.; Hoyland, J.A. Characterization of the human nucleus pulposus cell phenotype and evaluation of novel marker gene expression to define adult stem cell differentiation. *Arthritis Rheumatol.* **2010**, *62*, 3695–3705.
19. Liu, S.; Zhang, E.; Yang, M.; Lu, L. Overexpression of Wnt11 promotes chondrogenic differentiation of bone marrow-derived mesenchymal stem cells in synergism with TGF- β . *Mol. Cell. Biochem.* **2014**, *390*, 123–131.
20. Zanotti, S.; Canalis, E. Notch suppresses nuclear factor of activated T cells (NFAT) transactivation and Nfatc1 expression in chondrocytes. *Endocrinology* **2013**, *154*, 762–772.
21. Yamagami, T.; Molotkov, A.; Zhou, C.J. Canonical Wnt signaling activity during synovial joint development. *J. Mol. Histol.* **2009**, *40*, 311–316.
22. Pitsillides, A.A.; Beier, F. Cartilage biology in osteoarthritis—Lessons from developmental biology. *Nat. Rev. Rheumatol.* **2011**, *7*, 654–663.
23. James, C.G.; Appleton, C.T.; Ulici, V.; Underhill, T.M.; Beier, F. Microarray analyses of gene expression during chondrocyte differentiation identifies novel regulators of hypertrophy. *Mol. Biol. Cell.* **2005**, *16*, 5316–5333.
24. Klatt, A.R.; Paulsson, M.; Wagener, R. Expression of matrilins during maturation of mouse skeletal tissues. *Matrix Biol.* **2002**, *21*, 289–296.
25. Segat, D.; Frie, C.; Nitsche, P.D.; Klatt, A.R.; Piecha, D.; Korpos, E.; Deak, F.; Wagener, R.; Paulsson, M.; Smyth, N. Expression of matrilin-1, -2 and -3 in developing mouse limbs and heart. *Matrix Biol.* **2000**, *19*, 649–655.
26. Craft, A.M.; Ahmed, N.; Rockel, J.S.; Baht, G.S.; Alman, B.A.; Kandel, R.A.; Grigoriadis, A.E.; Keller, G.M. Specification of chondrocytes and cartilage tissues from embryonic stem cells. *Development* **2013**, *140*, 2597–2610.

27. Kim, S.H.; Sierra, R.A.; McGee, D.J.; Zabaleta, J. Transcriptional profiling of gastric epithelial cells infected with wild type or arginase-deficient *Helicobacter pylori*. *BMC Microbiol.* **2012**, *12*, 175.
28. National Center for Biotechnology Information (NCBI) Gene Database. Available online: <http://www.ncbi.nlm.nih.gov/> (accessed on 16 April 2014).
29. UniProt Protein Knowledgebase Database. Available online: <http://www.uniprot.org/> (accessed on 16 April 2014).
30. Yu, G.; Wu, X.; Dietrich, M.A.; Polk, P.; Scott, L.K.; Ptitsyn, A.A.; Gimble, J.M. Yield and characterization of subcutaneous human adipose-derived stem cells by flow cytometric and adipogenic mRNA analyzes. *Cytotherapy* **2010**, *12*, 538–546.
31. Strong, A.L.; Strong, T.A.; Rhodes, L.V.; Semon, J.A.; Zhang, X.; Shi, Z.; Zhang, S.; Gimble, J.M.; Burow, M.E.; Bunnell, B.A. Obesity associated alterations in the biology of adipose stem cells mediate enhanced tumorigenesis by estrogen dependent pathways. *Breast Cancer Res.* **2013**, *15*, R102.
32. Naldini, L.; Blomer, U.; Gallay, P.; Ory, D.; Mulligan, R.; Gage, F.H.; Verma, I.M.; Trono, D. *In vivo* gene delivery and stable transduction of nondividing cells by a lentiviral vector. *Science* **1996**, *272*, 263–267.
33. Szymczak, A.L.; Workman, C.J.; Wang, Y.; Vignali, K.M.; Dilioglou, S.; Vanin, E.F.; Vignali, D.A. Correction of multi-gene deficiency *in vivo* using a single ‘self-cleaving’ 2A peptide-based retroviral vector. *Nat. Biotechnol.* **2004**, *22*, 589–594.
34. Mostoslavsky, G.; Kotton, D.N.; Fabian, A.J.; Gray, J.T.; Lee, J.S.; Mulligan, R.C. Efficiency of transduction of highly purified murine hematopoietic stem cells by lentiviral and oncoretroviral vectors under conditions of minimal *in vitro* manipulation. *Mol. Ther.* **2005**, *11*, 932–940.
35. Ge, D.; Dauchy, R.T.; Liu, S.; Zhang, Q.; Mao, L.; Dauchy, E.M.; Blask, D.E.; Hill, S.M.; Rowan, B.G.; Brainard, G.C.; *et al.* Insulin and IGF1 enhance IL-17-induced chemokine expression through a GSK3B-dependent mechanism: a new target for melatonin’s anti-inflammatory action. *J. Pineal Res.* **2013**, *55*, 377–387.
36. Corbo, J.C.; Deuel, T.A.; Long, J.M.; LaPorte, P.; Tsai, E.; Wynshaw-Boris, A.; Walsh, C.A. Doublecortin is required in mice for lamination of the hippocampus but not the neocortex. *J. Neurosci.* **2002**, *22*, 7548–7557.

Promotion of lung tumor growth by interleukin-17

Beibei Xu,¹ James F. Guenther,¹ Derek A. Pociask,⁶ Yu Wang,¹ Jay K. Kolls,⁶ Zongbing You,⁴ Bysani Chandrasekar,⁵ Bin Shan,³ Deborah E. Sullivan,² and Gilbert F. Morris¹

¹Department of Pathology and Laboratory Medicine, Tulane University, New Orleans, Louisiana; ²Department of Microbiology, Tulane University, New Orleans, Louisiana; ³Department of Medicine-Pulmonary Section, Tulane University, New Orleans, Louisiana; ⁴Department of Structural and Cellular Biology, Tulane University, New Orleans, Louisiana; ⁵Heart and Vascular Institute, Tulane University, New Orleans, Louisiana; and ⁶Children's Hospital of Pittsburgh, University of Pittsburgh, Pittsburgh, Pennsylvania

Submitted 7 May 2014; accepted in final form 12 July 2014

Xu B, Guenther JF, Pociask DA, Wang Y, Kolls JK, You Z, Chandrasekar B, Shan B, Sullivan DE, Morris GF. Promotion of lung tumor growth by interleukin-17. *Am J Physiol Lung Cell Mol Physiol* 307: L497–L508, 2014. First published July 18, 2014; doi:10.1152/ajplung.00125.2014.—Recent findings demonstrate that inhaled cigarette smoke, the predominant lung carcinogen, elicits a T helper 17 (Th17) inflammatory phenotype. Interleukin-17A (IL-17), the hallmark cytokine of Th17 inflammation, displays pro- and anti-tumorigenic properties in a manner that varies according to tumor type and assay system. To investigate the role of IL-17 in lung tumor growth, we used an autochthonous tumor model (*K-Ras*^{LA1} mice) with lung delivery of a recombinant adenovirus that expresses IL-17A. Virus-mediated expression of IL-17A in *K-Ras*^{LA1} mice at 8–10 wk of age doubled lung tumor growth in 3 wk relative to littermates that received a green fluorescent protein-expressing control adenovirus. IL-17 induced matrix metalloproteinase-9 (MMP-9) expression in vivo and in vitro. In accord with this finding, selective and specific inhibitors of MMP-9 repressed the increased motility and invasiveness of IL-17-treated lung tumor cells in culture. Knockdown or mutation of p53 promoted the motility of murine lung tumor cells and abrogated the promigratory role of IL-17. Coexpression of siRNA-resistant wild-type, but not mutant, human p53 rescued both IL-17-mediated migration and MMP-9 mRNA induction in p53 knockdown lung tumor cells. IL-17 increased MMP-9 mRNA stability by reducing interaction with the mRNA destabilizing serine/arginine-rich splicing factor 1 (SRSF1). Taken together, our results indicate that IL-17 stimulates lung tumor growth and regulates MMP-9 mRNA levels in a p53- and SRSF1-dependent manner.

IL-17; MMP-9; p53; SRSF1; lung tumor growth

THE INTERLEUKIN-17 FAMILY consists of six members, IL-17A to IL-17F. Although the family members are structurally related, they originate from different cell types and have diverse biological functions (28). IL-17 family members bind to a family of IL-17 receptors (IL-17 receptor A to E) that form hetero- and homodimers with bound ligand to activate downstream signaling (14). Because these IL-17 receptor family members have different ligand-binding specificities and variable tissue distributions, the IL-17 cytokine family associates with multiple inflammatory responses. IL-17A, commonly called IL-17, is the first identified and by far the most well-studied IL-17 family member. T helper 17 (Th17) cells are the primary source of IL-17A and homologous family member IL-17F (56). In both humans and mice, IL-17A and IL-17F bind and activate a heterodimeric receptor formed by IL-17RA and IL-17RC (24, 30). IL-17RA is expressed ubiquitously,

whereas IL-17RC is mainly expressed in epithelial cells and fibroblasts (47).

Clinical findings with cancers of the stomach (78), prostate (59), colon (34), and lung (38) demonstrate that elevated levels of IL-17 correlate with a worse prognosis. However, in experimental models, the role of IL-17 in tumor growth depends on context. In many models, particularly in immunodeficient mice, IL-17 promotes tumorigenesis, and enhanced angiogenesis appears to account, in large part, for this protumorigenic effect (52). However, in immunocompetent mice, IL-17 impairs growth of tumor allografts by stimulating antitumor immunity (29, 42). A possible explanation for these disparate findings is that tumor graft models are inadequate in testing the effect of IL-17 in tumorigenesis. In autochthonous models of prostate and lung cancer in immunocompetent mice, IL-17 deficiency impairs tumor growth (3, 79). In an autochthonous model of pancreatic cancer, IL-17 overexpression accelerates tumorigenesis (44).

In lung cancer, dissection of the inflammatory response to lung carcinogens could be used to identify specific inflammatory mediators that promote lung tumor progression. In support of this view, lung inflammation induced by cigarette smoke accelerates progression of lung adenocarcinoma in mice (69). Since cigarette smoke elicits Th17 inflammation (4, 61), tumors arising in the lung must adapt to this inflammatory phenotype. This observation prompted us to determine the consequence of overexpression of IL-17A, the prototypical Th17 cytokine, on progression of mutant *K-Ras*-driven lung adenocarcinoma.

MATERIALS AND METHODS

Animal model. *K-Ras*^{LA1} mice in the C57BL/6 background were provided by Dr. Tyler Jacks through the National Cancer Institute Mouse Repository. Mice were maintained under pathogen-free conditions and experimental protocols were approved by the Tulane University Institutional Animal Care and Use Committee following guidelines of the Association for Assessment and Accreditation of Laboratory Animal Care.

Plasmids. Plasmids pCMV-p53-wt (60) and pCMV-p53-R175H express the wild-type human p53 and dominant negative R175H mutant human p53, respectively, from the CMV promoter. The pCMV-p53-R175H plasmid was constructed by digesting the SPC-p53-R175H plasmid (49) with *Bam*HI and adding *Eco*RI linkers after filling in the restricted DNA. After digestion with *Hind*III, the R175H mutant p53 cDNA was subcloned into the pCMV12S.FS plasmid (50) at the *Eco*RI-*Hind*III sites after removal of the EIA cDNA insert.

Adenovirus administration to mice and assessment of tumor progression. Lung tumor-bearing *K-Ras*^{LA1} mice 8–10 wk of age were anesthetized with isoflurane before being administered 1×10^8

Address for reprint requests and other correspondence: G. F. Morris, Dept. of Pathology and Laboratory Medicine, SL-79, Tulane Univ. Medical Center, 1430 Tulane Ave., New Orleans, LA 70112 (e-mail: gmmorris2@tulane.edu).

pfu IL-17-expressing recombinant adenovirus [AdV-IL-17 (58)] by oropharyngeal aspiration (32). Control *K-Ras^{LA1}* mice received an identical amount of GFP-expressing adenovirus [AdV-GFP (13)]. Three weeks after treatment the mice were euthanized and the lungs were inflated by perfusion with 10% formalin at 30 cm pressure for 20 min before removal. After overnight fixation, the number of lung tumors on the pleural surface was quantified without knowledge of the sample identity. Tissue sections prepared from paraffin-embedded lung tissue were stained with hematoxylin and eosin (H&E) before evaluation of tumor burden. The tumor burden [defined as the ratio of hyperplastic lesion area to total lung section area on H&E-stained sections (27)] was quantified with an Aperio ScanScope slide scanner.

Cell culture. mK-Ras-LE cells, a murine lung cancer epithelial cell line, were established from a lung tumor-bearing *K-Ras^{LA1}* mouse (35). The mK-Ras-LE cells form tumors in syngeneic mice and express the lung epithelial cell markers surfactant protein C and E-cadherin but fail to express Clara cell secretory protein or N-cadherin (data not shown). mK-Ras-R172H-LE cells were established from a lung tumor-bearing *K-Ras^{LA1}* mouse that was also heterozygous for a R172H knockin mutation of p53 (33). The line had been backcrossed to the C57BL/6 inbred strain for more than 10 generations before the cells were prepared. The mK-Ras-R172H-LE cells are positive for SPC and cytokeratin but negative for E-cadherin and slightly positive for vimentin (our unpublished observation). Both cell lines were cultured in RPMI medium with 10% FBS and 1% penicillin-streptomycin (complete medium) at 37°C with 5% CO₂ (35).

Immunohistochemistry. Immunohistochemistry was performed as described (17) with some modifications. Lung tissue sections were blocked in PBS with 3% BSA overnight at 4°C before incubation overnight at 4°C with the primary antibody against matrix metalloproteinase-9 (MMP-9; 1:200 dilution) (NBP1-57940; Novus Biologicals, Littleton, CO) diluted in PBS with 3% BSA. The negative control tissue sections were incubated with normal rabbit serum replacing the primary antibody diluted to the same concentration. After one washing with 3% BSA in PBS, the sections were incubated with biotin-conjugated donkey anti-rabbit secondary antibody (1:2,500 dilution) (711-065-152; Jackson ImmunoResearch Laboratories, West Grove, PA) for 1 h at room temperature. After three washes with 3% BSA in PBS, the sections were incubated with streptavidin-conjugated horseradish peroxidase (1:2,000 dilution) (016-030-084; Jackson ImmunoResearch Laboratories) in the same solution for 1 h at room temperature. Visualization with diaminobenzidine and counterstaining were as previously described (17).

Wound healing assay. Cells were seeded on 12-well plates with RPMI complete medium. When the cells reached about 80% confluence, the medium was replaced with serum-free RPMI followed by overnight incubation. Then a single artificial wound was made by scratching the center of the monolayer of cells with a 200- μ l pipet tip at time 0. After wounding, the cells were washed with PBS to remove detached cells and fresh serum-free RPMI was added containing increasing concentrations of mouse IL-17. During the postwounding period, images within the same area of the scratches were taken with a phase-contrast microscope. Ten measurements of wound width were taken for each scratch and were averaged. Percent of wound closure was calculated as the distance (μ m) the cells migrated relative to the initial scratch width. In some experiments, a selective inhibitor of MMP-9 or an antibody to MMP-9 was added simultaneously with IL-17. The MMP-9 selective inhibitor (MMP-9 Inhibitor I, CAS 1177749-58-4, Millipore, Billerica, MA) was added at the dose of 10 nM. The MMP-9 antibody (AB19016; Millipore) was added at the dose of 12 μ g/ml to inhibit MMP-9 and the same amount of rabbit IgG was used as the negative control. In the migration assay using cells infected with recombinant adenovirus expressing reversion-inducing-cysteine-rich protein with kazal motifs [AdV-RECK (63), a cellular repressor of metalloproteinases, including MMP-9 (2)], or AdV-GFP, cells were infected (MOI = 10) for 24 h before wounding and addition of IL-17. For the migration assays with p53 knockdown

experiments, cells growing in 1 ml RPMI containing 10% FBS in 24-well plate were transfected with 5 pm siRNA using Lipofectamine diluted in 50 μ l Opti-MEM according to the supplier's (Invitrogen) specifications. For the p53 knockdown-restoration experiments, cells growing in 1 ml RPMI containing 10% FBS in 24-well plate were transfected with 5 pm siRNA plus 150 ng pCMV-p53-wt plasmid or pCMV-p53-R175H plasmid using Lipofectamine diluted in 50 μ l Opti-MEM according to the supplier's (Invitrogen) specifications. The protocol for the wound healing assay in p53 knockdown or knockdown-restoration experiments was the same as in untransfected cells, except the treatment incubation time was 30 h. Silencer Select siRNAs specifically targeting mouse p53 (gene ID: s75472) and Silencer Select Negative Control no. 1 siRNA were purchased from Invitrogen.

Transwell migration assays. Cells at about 80% confluence were incubated overnight with serum-free RPMI. The next day, the cells were trypsinized and resuspended in serum-free RPMI before seeding 2.5×10^5 cells in 200 μ l in 24-well Transwell migration inserts (8- μ m pore, BD Biosciences, San Jose, CA). Serum-free RPMI with or without 10 ng/ml mouse IL-17 was added to the lower chamber. After 24 h, the cells on the upper surface of the insert were removed by scraping with cotton swabs and the cells that migrated to the lower surface were fixed and stained with the HEMA-3 staining kit (Thermo Fisher Scientific, Waltham, MA). After air drying, the inserts were mounted with Permount on glass slides. At least five random images were taken at $\times 200$ magnification under a light microscope. The number of migrated cells were quantified per image and averaged per well.

Transwell invasion assays. The invasion assays were performed with 24-well BD BioCoat Matrigel Invasion Chambers as described by the supplier (BD Biosciences). Briefly, cells were seeded in the inserts coated with growth factor reduced Matrigel at a density of 2.5×10^5 cells/well in 200 μ l serum-free RPMI. RPMI containing 0.5% FBS with or without 10 ng/ml mouse IL-17 was added to the lower chamber. After 48 h, the inserts were stained and photographed as described above and the number of cells that invaded through the Matrigel was quantified as described above.

RNA quantification. Total RNA was extracted from cultured cells or mouse lung tissue with TriPure Isolation Reagent (Roche Applied Science, Mannheim, Germany) and purified by use of the RNeasy Mini Kit (Qiagen, Valencia, CA), followed by TURBO DNase treatment (Invitrogen, Carlsbad, CA) as described by the supplier. RNA purity and concentration were measured using a NanoDrop Spectrophotometer (Thermo Scientific). First-strand cDNA was generated by reverse transcription using the iScript cDNA Synthesis Kit (Bio-Rad, Hercules, CA). Quantitative PCR of the MMP-9 and β -actin cDNAs was performed with primer sets (MMP-9 forward 5'-CAATCCTTG-CAATGTGGATG-3' and MMP-9 reverse 5'-TAAGGAAGGGGCC-CTGTAAT-3', β -actin forward 5'-TCTACGAGGGCTAT-CGTCTCC-3', β -actin reverse 5'-GGATGCCACAGGATT-CATAC-3') by use of iQ SYBR Green Supermix (Bio-Rad). PCR conditions were 95°C for 3 min, followed by 45 cycles at 95°C for 15 s, 60°C for 30 s, and 72°C for 15 s. After PCR, a melting curve validated the specificity of the amplification. Relative expression of the MMP-9 mRNA was normalized against the internal control mouse β -actin mRNA by the $2^{-\Delta\Delta C_t}$ method (39).

Cell viability assay. mK-Ras-LE cells were seeded into 96-well plates in RPMI complete medium for 24 h. Then the complete medium was removed and serum-free RPMI was added followed by incubation overnight. The next day the medium was replaced with serum-free RPMI with increasing concentrations of mouse IL-17. After 48 h, the cell viability was determined by using the MTT Cell Proliferation Assay kit (ATCC, Manassas, VA) according to the manufacturer's protocol.

Bronchoalveolar lavage. Bronchoalveolar lavage (BAL) was performed after intubation of mice with a 20-gauge 1.25-in. catheter secured in place with a suture (17). Mice were lavaged with 5×0.8 ml of ice-cold lavage buffer (0.137 M sodium chloride, 2.7 mM

potassium chloride, 12 mM phosphate buffer, 0.4 mM EDTA, pH 7.4). After removal of the cells from the first lavage by centrifugation at 1,500 g for 5 min, the samples were aliquoted and stored at -70°C . The cells from the first lavage were combined with lavages 2–5 and the collected cell pellet was resuspended in 500 μl of ice-cold lavage buffer. The total cell count was recorded by mixing 10 μl of the resuspended cells 1:1 with Trypan blue (MP Biomedicals, Solon, OH) and counted on a Bright-Line Hemacytometer. Then 5×10^4 cells were cytospun onto slides by using a Shandon Cytospin 3 at 600 RPM for 3 min. The slides were allowed to dry before staining with Hema 3 (Fisher Scientific, Pittsburgh, PA) followed by dehydration with xylene and mounting with Permount (Fisher Scientific). Differential cell counts were performed on 200 cells on randomly selected fields per sample by an investigator who was unaware sample identity. The first aliquot of BAL fluid was analyzed for IL-17 protein expression with a Mouse IL-17A ELISA kit (BioLegend, San Diego, CA) according to the manufacturer's instruction.

Gelatin zymography. MMP-9 levels in cell culture media or BAL fluid from mice was determined by gelatin zymography (55). The samples were loaded on a Novex 10% Zymogram (Gelatin) Gel (Invitrogen). The gel was run at constant voltage (~ 100 V) at 4°C until the bromophenol blue tracking marker reached the bottom. Then the gel was incubated in $1\times$ Zymogram Renaturing Buffer (2.5% Triton X-100 in water) for 30 min at room temperature with gentle agitation and subsequently incubated in $1\times$ Zymogram Developing Buffer (50 mM Tris, 5 mM CaCl_2 , 0.2 M NaCl) for another 30 min. The gel was incubated in fresh $1\times$ developing buffer overnight at 37°C for maximum sensitivity. Then the gel was stained with 0.5% Coomassie blue in methanol-acetic acid-water, 50:10:40, for 45 min and destained in the same solution without dye to detect the clear area of protease activity.

mRNA stability assay. mK-Ras-LE cells were pretreated in serum-free RPMI with or without 10 ng/ml IL-17 for 2 h. At *time 0* total RNA was prepared from the cells with Tripure (Roche) and RNeasy Mini Kit (Qiagen) as described above then the medium was replaced with fresh serum-free RPMI medium containing 10 $\mu\text{g}/\text{ml}$ actinomycin D (Sigma-Aldrich, St. Louis, MO) or the same concentration actinomycin D plus 10 ng/ml IL-17 for 8 h before preparation of total RNA. The abundance of mRNA for MMP-9, β -actin, CXCL-1, and CXCL-2 at *time 0* and 8 h was determined by quantitative RT-PCR (CXCL-1 forward 5'-GGGCGCCTATCGCCAAT-3', CXCL-1 reverse 5'-ACCTTCAAGCTCTGGA TGTCTTG-3'; CXCL-2 forward 5'-TGTCATGCTGAAGACCCTGCC-3', CXCL-2 reverse 5'-AACTTTTGGACCGCCC TTGAGA-3'). PCR conditions for CXCL-1 and CXCL-2 were 95°C for 3 min followed by 40 cycles at 95°C for 15 s, 60°C for 1 min.

siRNA transfection. Cells growing in 2 ml RPMI containing 10% FBS in a six-well plate were transfected with 30 pm siRNA by using Lipofectamine 2000 transfection reagent (Invitrogen) diluted in 500 μl of Opti-MEM I reduced-serum medium (Invitrogen) according to the manufacturer's recommendations. Silencer Select siRNAs specifically targeting serine/arginine-rich splicing factor 1 (SRSF1) (gene ID: s200965) and Silencer Select Negative Control no. 1 siRNA were purchased from Invitrogen. After 48 h, total cellular RNA was prepared and subjected to quantitative RT-PCR as described above.

RNA immunoprecipitation. RNA coimmunoprecipitation assays were performed as described previously with some modifications (19). mK-Ras-LE cells were incubated in serum-free RPMI medium overnight and treated with or without 10 ng/ml IL-17 for another 48 h. After treatment, 4×10^6 cells were harvested by trypsinization and fixed in PBS solution with 0.1% formalin for 15 min. The fixation procedure was quenched by incubating in 10 ml PBS with 0.25 M glycine (pH 7) for 5 min. Then the cells were washed with PBS and resuspended in 1 ml RIPA buffer (50 mM Tris-Cl pH 8, 150 mM NaCl, 1% Nonidet P-40, 0.5% sodium deoxycholate, 0.1% SDS) containing $1\times$ protease inhibitors (Roche), and sonicated (30% power, 12 s; 40% power, 12 s; 50% power, 5 s twice) with a Branson

Sonifier. After removal of insoluble material by centrifugation at 16,000 g for 15 min, 1 ml of each cell extract was incubated with 5 μg antibody to SRSF1 (Santa Cruz Biotechnology, Santa Cruz, CA) or the same volume of PBS for 1 h. Then 20 μl BSA preblocked protein A/G Plus-Agarose beads (Santa Cruz) were added and incubated on a rotating incubator overnight at 4°C . The next day, the agarose beads were collected by centrifugation at 3,000 g, 4°C for 5 min. After being washed three times with 1 ml RIPA buffer, the beads were resuspended in 200 μl elution buffer (50 mM Tris-Cl pH 7, 5 mM EDTA, 10 mM DTT, 1% SDS) and incubated at 70°C for 1 h to reverse formalin cross-linking. RNA was extracted from the eluate by using TriPure (Roche) reagent according to the manufacturer's protocol. cDNA was prepared as described above. The same volume of each cDNA product (1.5 out of 40 μl) was subjected to quantitative RT-PCR for measuring CXCL-2, β -actin, and MMP-9 mRNA levels as described above.

Statistical analysis. Data are presented as means \pm SE. Data were analyzed by using Student's *t*-test or Mann-Whitney test when appropriate with GraphPad Prism 5 software. *P* values lower than 0.05 were considered as statistically significant.

RESULTS

IL-17 overexpression increases lung tumor growth in *K-Ras^{LA1}* mice. To overexpress IL-17 in the lungs of mice we administered an IL-17A-expressing recombinant adenovirus (AdV-IL-17) to 8- to 10-wk-old wild-type mice by oropharyngeal aspiration. This route of delivery produces expression of the transduced gene in epithelial cells throughout the lung (17). For control purposes, an equivalent amount of AdV-GFP was delivered to littermates. One week after virus delivery, a 150-fold increase in IL-17 levels (Fig. 1A) and a corresponding fivefold increase in lung neutrophilia (Fig. 1B) were detected in the BAL fluid from mice treated with AdV-IL-17 compared with that of the AdV-GFP-treated control group.

To evaluate the effect of IL-17A on lung tumor growth, AdV-IL-17 or an equivalent amount of AdV-GFP was delivered to the lungs of tumor-bearing *K-Ras^{LA1}* mice at 8 to 10 wk of age. Three weeks after adenovirus treatment, the number of visible tumors on the pleural surface of AdV-IL-17-treated mice doubled relative to that in AdV-GFP-treated littermates (Fig. 2A). *K-Ras^{LA1}* littermates that did not receive adenovirus had a comparable number of tumors on the pleural surface relative to that of the AdV-GFP-treated control group. To confirm IL-17-mediated acceleration of lung tumor growth, we used a slide scanner to quantify tumor burden on H&E-stained lung tissue sections from the adenovirus-treated animals. Consistent with quantification of tumors on the pleural surface, tumor burden expressed as the ratio of tumor lesion area to total lung area in H&E-stained tissue sections (27) nearly doubled in *K-Ras^{LA1}* mice overexpressing IL-17 (AdV-IL-17) relative to the AdV-GFP control group (Fig. 2B). These data confirmed that IL-17 overexpression stimulated a rapid increase in lung tumor growth in vivo over a relatively brief 3-wk period. However, IL-17 failed to stimulate proliferation of serum-starved mutant K-Ras-expressing lung tumor cells [prepared from a *K-Ras^{LA1}* mouse (35)] in cell culture (Fig. 2C).

IL-17 enhances MMP-9 expression and lung tumor cell motility. IL-17 can stimulate expression of MMP-9 (1, 18, 36), and this may partially account for the selective stimulation of lung tumor growth in vivo. Consequently, we evaluated gelatinase activity in the BAL fluid from adenovirus-treated mice by zymography. One week after virus delivery, BAL fluid and

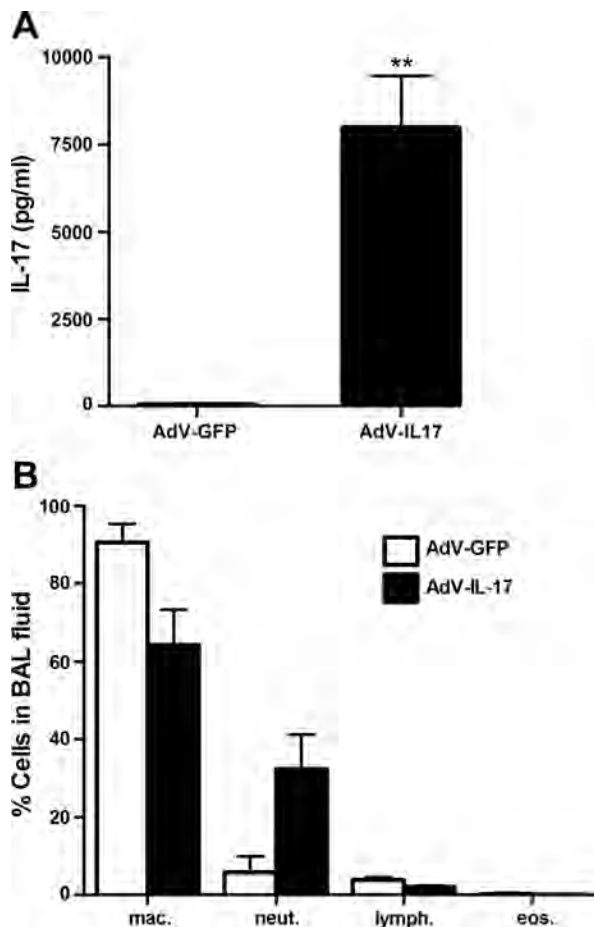


Fig. 1. Expression of IL-17 and lung neutrophilia in IL-17-expressing recombinant adenovirus (AdV-IL-17)-treated mice. **A**: AdV-IL-17 or an equivalent amount (1×10^8 pfu) of green fluorescent protein-expressing recombinant adenovirus (AdV-GFP) was delivered to C57BL/6 mice by oropharyngeal aspiration. One week posttreatment, bronchoalveolar lavage (BAL) was performed. The levels of IL-17 in the BAL fluid were determined by ELISA. Graph shows mean levels \pm SE IL-17 in the first 0.8 ml aliquot of BAL fluid (** $P < 0.01$ vs. AdV-GFP group, $n = 5$ per group). **B**: differential cell counts of BAL cells. Cytospin samples of the cells recovered by BAL were stained with Hema 3 (Fisher). Cells were visualized by microscopy, and 200 cells were counted from each sample. Graph shows percentage of the indicated cell type (means \pm SE) in the cells recovered from the BAL fluid from mice treated with AdV-IL-17 (solid bars) and AdV-GFP (open bars). $P = 0.07$, percentage neutrophils AdV-GFP vs. AdV-IL-17, $n = 5$ per group.

lung tissue were prepared from wild-type mice treated with AdV-IL-17 or AdV-GFP. Gelatin-zymography revealed a less than twofold increase in MMP-2 and approximately a 30-fold increase in MMP-9 in the BAL fluid from AdV-IL-17-treated mice relative to that from AdV-GFP-treated littermates (Fig. 3A). The increased amount of MMP-9 in the BAL fluid correlated with more than a twofold increase in MMP-9 mRNA in total lung RNA (Fig. 3B). Immunohistochemistry with tissue sections prepared from *K-Ras^{LA1}* mice 1 wk after AdV-IL-17 administration revealed expression of MMP-9 in a variety of lung cells including both tumor cells and immune cells infiltrating the tumor (Fig. 3C). These data are consistent with the possibility that induction of MMP-9 could at least partially account for lung tumor growth mediated by IL-17 overexpression. Since MMP-9 expression correlates with progression of lung adenocarcinoma in a number of studies (6, 7, 26, 43, 70,

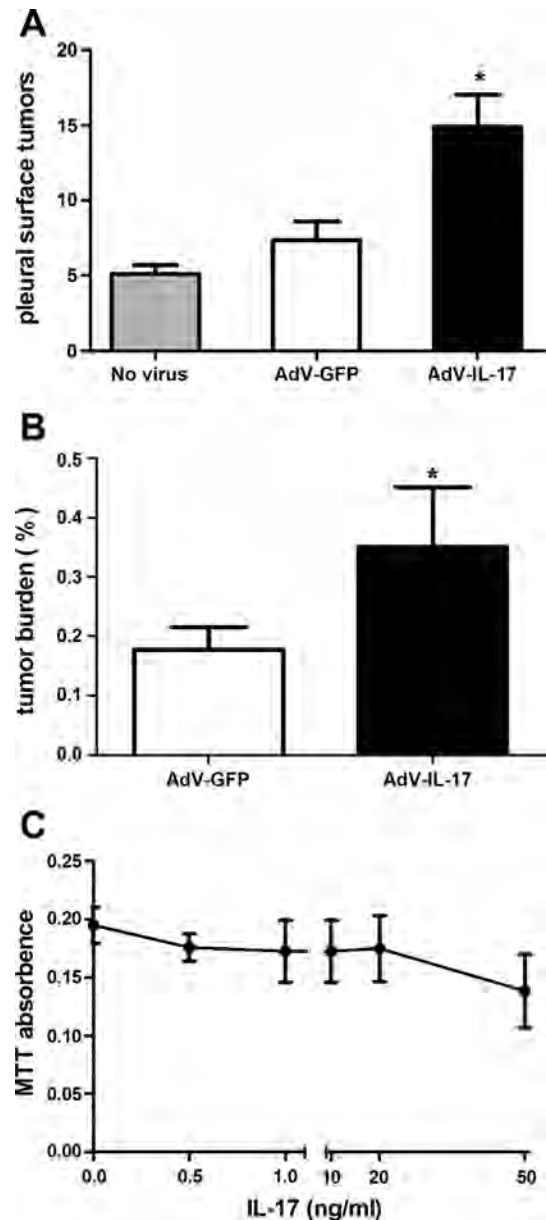


Fig. 2. Overexpression of IL-17 promotes lung tumor growth in *K-Ras^{LA1}* mice. **A**: quantification of tumor nodules on the lung pleural surfaces of *K-Ras^{LA1}* mice after AdV-IL-17 treatment. *K-Ras^{LA1}* mice at 8–10 wk received 1×10^8 pfu IL-17-expressing recombinant adenovirus (AdV-IL-17) ($n = 9$), green fluorescent protein expressing adenovirus (AdV-GFP) ($n = 6$), or no virus treatment ($n = 3$) by oropharyngeal aspiration. Three weeks after adenovirus treatment, the mice were evaluated for lung tumor nodules on the pleural surface. Graph shows the mean number (\pm SE) of tumor modules on the pleural surface of fixed lung tissue from *K-Ras^{LA1}* mice untreated (shaded bar, $n = 3$), or treated with control virus (AdV-GFP, open bar, $n = 6$), or treated with IL-17-expressing adenovirus (AdV-IL-17, solid bar, $n = 9$). * $P < 0.05$ AdV-IL-17 vs. AdV-GFP. **B**: evaluation of tumor burden. The area of hyperplastic lesions and total area of lung tissue examined was quantified on hematoxylin and eosin (H&E)-stained tissue sections from each mouse. Graph shows the mean lung tumor burden (\pm SE) as measured by the ratio (percent) of the tumor area vs. total area evaluated. Open bar represents the tumor burden of AdV-GFP treated *K-Ras^{LA1}* mice ($n = 6$) and solid bar represents the tumor burden of AdV-IL-17-treated littermates ($n = 9$). * $P < 0.05$ AdV-IL-17 vs. AdV-GFP. **C**: serum-starved mK-Ras-LE cells were treated with increasing concentrations of mouse IL-17 for 48 h. Relative cell number was assessed by MTT assay. The experiment was repeated twice in triplicate. Data shown are means \pm SE.

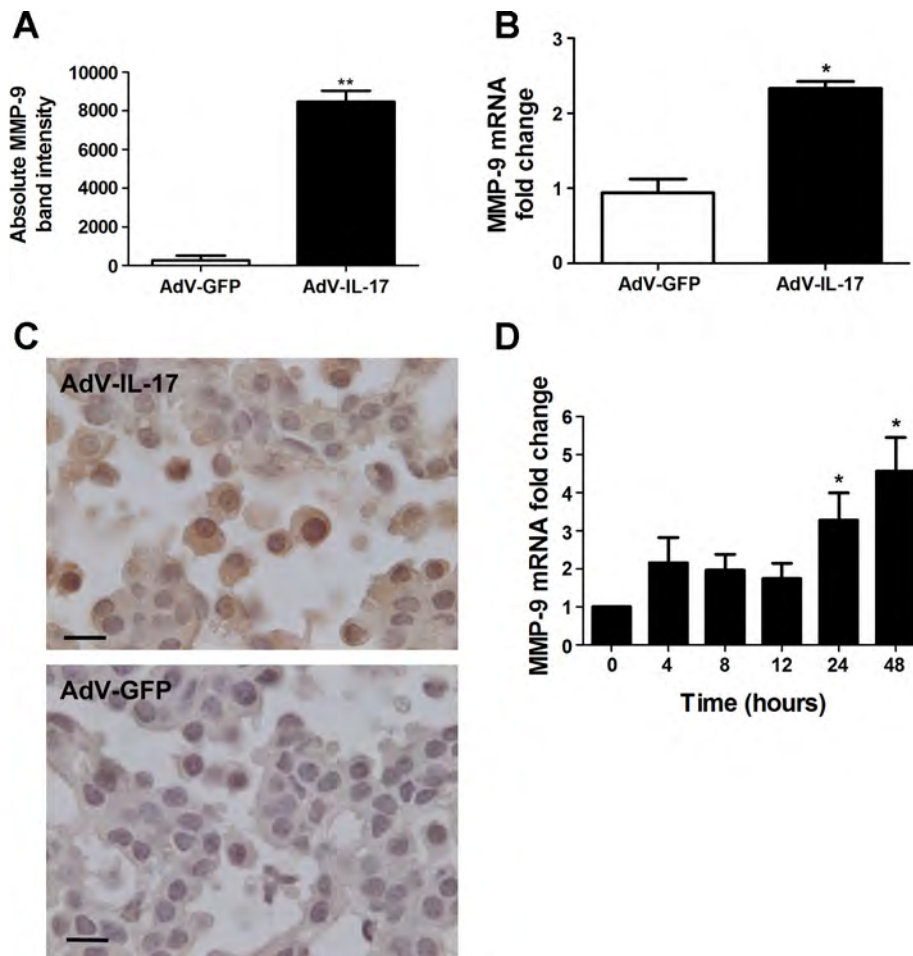


Fig. 3. Induction of MMP-9 by IL-17. **A**: wild-type mice were treated with 1×10^8 pfu AdV-IL-17 or AdV-GFP by oropharyngeal aspiration. One week after treatment, the mice were euthanized and evaluated for MMP-9 expression. Equal volumes of BAL fluid from AdV-IL-17- or AdV-GFP-treated mice were assessed by gelatin zymography for MMP activity ($n = 4$ per group). Bands corresponding to MMP-9 on the zymogram were quantified by densitometry. Graph shows the MMP-9 band intensity from the BAL fluid of AdV-GFP- (open bar) or AdV-IL-17-treated (solid bar) mice. Data shown are means \pm SE. ** $P < 0.01$ AdV-IL-17 vs. AdV-GFP. **B**: total lung RNA prepared from the mice in **A** was assessed by qRT-PCR for MMP-9 mRNA levels with β -actin mRNA as the internal control. Mice treated with AdV-IL-17 (solid bar) showed a 2.3-fold increase ($2^{-\Delta\Delta CT}$ method) in MMP-9 mRNA levels compared with AdV-GFP treated littermates (open bar). Data shown are means \pm SE; $n = 3$ per group. * $P < 0.05$ AdV-IL-17 vs. AdV-GFP. **C**: *K-Ras^{LAJ}* mice were treated with AdV-IL-17 as described above. One week post-exposure the lungs of the treated mice were fixed and paraffin embedded. Lung tissue sections were immunostained with an antibody to MMP-9 by the diaminobenzidine method. MMP-9-positive (brown) staining tumor and immune cells did not appear in the tumor area on an adjacent section stained with the negative control antibody. **D**: total RNA was prepared from mK-Ras-LE cells at increasing times after treatment with 10 ng/ml IL-17. Graph shows mean levels of MMP-9 mRNA relative to β -actin ($2^{-\Delta\Delta CT}$ method) at the indicated time after addition of IL-17 to the serum-starved cells. The bars represent means \pm SE ($n \geq 4$). * $P < 0.05$ relative to the 0 time point.

73, 74), we addressed the mechanism of MMP-9 activation by IL-17 in cell culture. Gelatin zymography of the cell culture medium from serum-starved mK-Ras-LE cells treated with IL-17 displayed a time- and concentration-dependent increase in MMP-9 (data not shown). In accord with these findings, IL-17 treatment increased MMP-9 mRNA levels more than fourfold relative to β -actin mRNA in mK-Ras-LE cells (Fig. 3E). Thus IL-17 enhanced expression of MMP-9 in murine lung tumor cells.

MMP-9 can increase cell motility and invasion (64). Therefore, we determined whether IL-17 could increase the motility and invasiveness of mK-Ras-LE cells. IL-17 promoted migration of mK-Ras-LE cells in a scratch-wound closure assay (Fig. 4A). In agreement with the concept that the enhanced motility and invasion of IL-17-treated mK-Ras-LE cells required MMP-9, a selective MMP-9 inhibitor prevented augmented migration mediated by IL-17 (Fig. 4B). In addition, enhanced invasion of IL-17-treated mK-Ras-LE cells through a Matrigel matrix in Transwell invasion assays was also repressed by the MMP-9 inhibitor (Fig. 4C). Although these results implicate MMP-9 in the enhanced motility and invasiveness of IL-17-treated mK-Ras-LE cells, the lack of inhibitor specificity precludes the conclusion that the enhanced motility is MMP-9 dependent. Two additional strategies were employed to further test role of MMP-9 in IL-17-mediated motility. In the first approach, mK-Ras-LE cells were infected with a recombinant adenovirus that expresses reversion-inducing-cysteine-rich

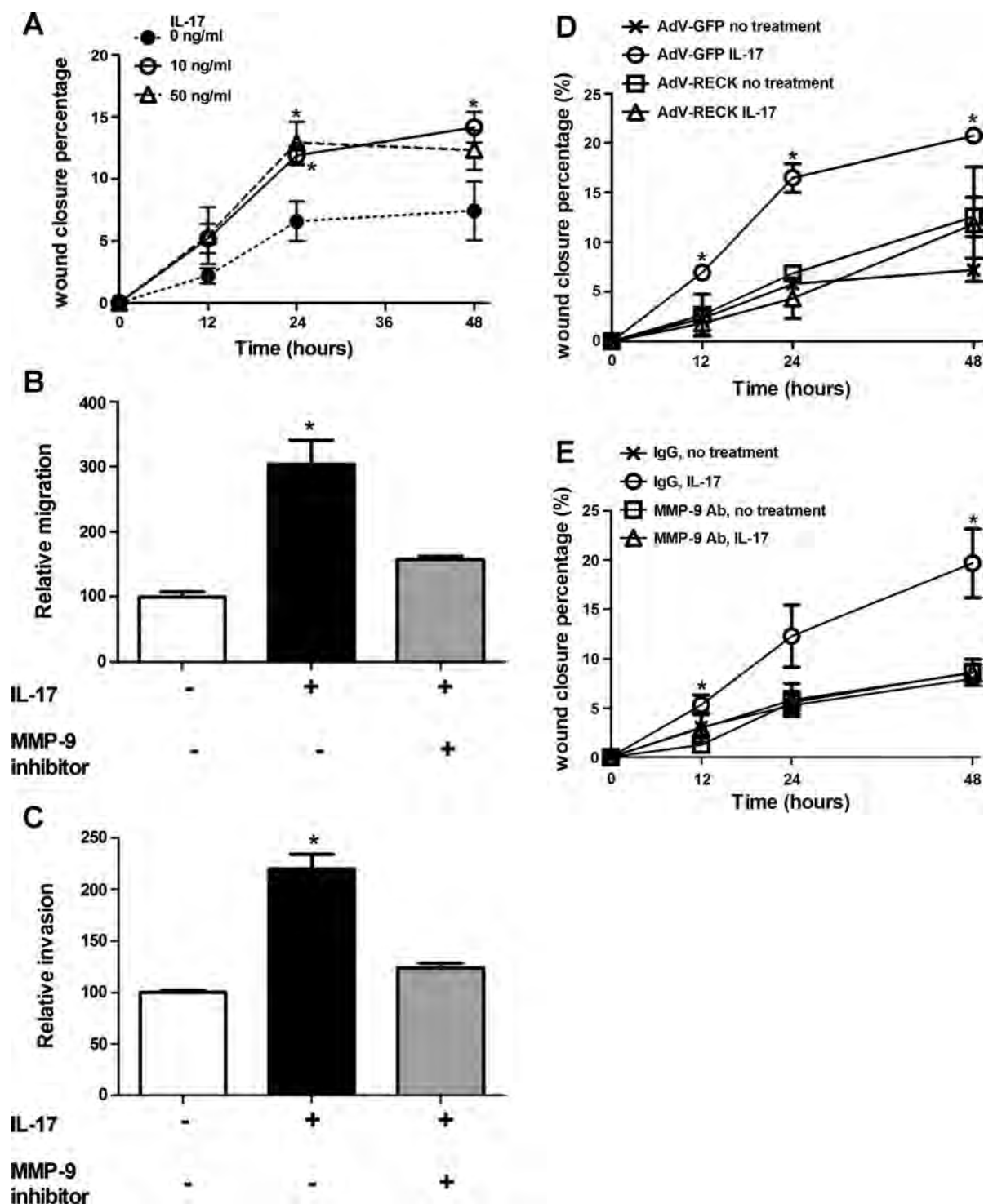
protein with kazal motifs [RECK, a cellular repressor of MMP-2, MMP-9, and MMP-14 (2, 54)] and the effect of IL-17 on the motility of the RECK-expressing cells was compared with that of IL-17-treated control cells infected with AdV-GFP. As expected, IL-17 increased wound closure of AdV-GFP-infected mK-Ras-LE cells. AdV-RECK infection increased RECK protein expression ~ 130 -fold compared with that in AdV-GFP infected mK-Ras-LE cells and significantly repressed the induction of motility mediated by IL-17 (Fig. 4D). Similarly, addition of an antibody that inhibits MMP-9 activity (15) also repressed the increased motility of IL-17-treated mK-Ras-LE cells (Fig. 4E). These data demonstrate that induction of lung tumor cell motility by IL-17 is MMP-9 dependent.

Knockdown or mutation of p53 abrogates promotion of lung tumor cell motility by IL-17. Lung tumors harboring mutations in both *K-Ras* and the p53 tumor suppressor protein grow more rapidly and metastasize more readily than lung tumors with mutations only in *K-Ras* (25, 33). To test the effect of p53 mutation on the response of lung tumor cells to IL-17, we determined the consequences of p53 knockdown in mK-Ras-LE cells upon promotion of migration by IL-17. Knockdown of p53 ($\sim 90\%$ knockdown efficiency confirmed by immunoblotting) enhanced migration of mK-Ras-LE cells and produced no additional effect on enhanced migration mediated by IL-17 (Fig. 5A). In contrast, mK-Ras-LE cells transfected with a mock siRNA migrated more slowly than the p53

siRNA-transfected counterparts and retained the response to IL-17. In accord with these findings, IL-17 increased MMP-9 mRNA levels in the mock siRNA-transfected cells, whereas p53 knockdown increased MMP-9 mRNA levels and IL-17 had no additional effect (Fig. 5B). Thus the effect of the p53 siRNA on migration and response to IL-17 correlated with a similar effect on MMP-9 expression. Restoration of p53 by cotransfection of the mouse p53 siRNA with a plasmid that expresses a siRNA resistant wild-type human p53 into mK-

Ras-LE cells repressed migration and restored the enhanced migratory response to IL-17 (Fig. 5C). Furthermore, restoration of wild-type p53 rescued IL-17-mediated induction of MMP-9 mRNA (Fig. 5D). These experiments demonstrated that IL-17-mediated induction of MMP-9 and migration is dependent on p53.

Although p53 deletion promotes tumor progression, most tumor-promoting mutations of p53 are missense mutations that lead to expression of a mutant protein (10). To address the



effects of mutant p53 upon lung tumor promotion by IL-17, we prepared a lung tumor cell line, mK-Ras-R172H-LE cells, from *K-Ras^{LA1}* mice that were also heterozygous knockin for the tumor promoting R172H mutation of p53 (33). Treatment of mK-Ras-R172H-LE cells with IL-17 had no effect on migration (Fig. 6A) or invasion (Fig. 6B) and IL-17 failed to increase MMP-9 mRNA levels in mK-Ras-R172H-LE cells (Fig. 6C). To confirm that IL-17 does not promote migration of mutant p53-expressing cells, we attempted a similar p53 rescue experiment like that shown in Fig. 5 with a mutant p53-expressing plasmid. mK-Ras-LE cells cotransfected with the mouse p53 siRNA and a plasmid that expresses a siRNA-resistant mutant human p53 R175H (equivalent to the mouse R172H mutant) failed to display enhanced migration upon IL-17 treatment (Fig. 6D). Taken together, these data suggest that IL-17 enhances migration of lung tumor cells through a MMP-9-dependent mechanism and that wild-type, but not mutant, p53 mediates the response to IL-17.

IL-17 upregulates MMP-9 expression via mRNA stabilization. A previous report demonstrated that IL-17 enhanced the stability of chemokine mRNAs (67). To test whether induction of MMP-9 by IL-17 also involved stabilization of MMP-9 mRNA, we treated mK-Ras-LE cells with IL-17 for 2 h before inhibiting transcription with 10 μ g/ml actinomycin D. The amount of β -actin mRNA remaining appeared similar in mK-Ras-LE cells in the presence and absence of IL-17 after 8 h of actinomycin D treatment (Fig. 7). Consistent with previous findings, IL-17 treatment increased CXCL-1 and CXCL-2 chemokine mRNA levels 8 h after inhibition of mRNA synthesis (Fig. 7). Similarly, IL-17 treatment also stabilized MMP-9 mRNA (Fig. 7). Chemokine mRNA stabilization by IL-17 requires the serine/arginine-rich splicing factor 1, SRSF1 (67). To determine whether SRSF1 altered the stability of MMP-9 mRNA, we transfected mK-Ras-LE cells with a siRNA that targeted SRSF1. After 48 h, Western blots showed ~80% knockdown efficiency of the SRSF1 protein in mK-Ras-LE cells (Fig. 8A). The SRSF1-targeting siRNA increased MMP-9 mRNA ~1.4-fold in transfected mK-Ras-LE cells relative to control cells transfected with scrambled siRNA (Fig. 8B). To demonstrate IL-17-regulated interaction between SRSF1 and MMP-9 mRNA, we performed RNA coimmuno-

precipitation assays followed by mRNA quantification by qRT-PCR. An antibody to SRSF1 coimmunoprecipitated approximately sevenfold more MMP-9 mRNA than the negative control from whole cell extracts of untreated serum-starved mK-Ras-LE cells (Fig. 8C). Treatment of the cells with IL-17 reduced the amount of MMP-9 mRNA that coimmunoprecipitated with the antibody to SRSF1 to levels approximating the negative control. Immunoblots confirmed that equal amounts of SRSF1 immunoprecipitated specifically with or without IL-17 treatment (Fig. 8C). Additional assays did not show an association between β -actin mRNA with SRSF1 in extracts from untreated or IL-17-treated cells (data not shown). Positive control experiments replicated previous findings (19), demonstrating an IL-17-dependent association between SRSF1 and CXCL-2 mRNA (Fig. 8D). These observations support the concept that IL-17 increased MMP-9 mRNA stability by reducing interaction with SRSF1. These data agree with our conclusion that IL-17 increases expression of MMP-9 in lung tumor cells via posttranscriptional stabilization of the MMP-9 mRNA by reducing interaction with SRSF1.

DISCUSSION

Our data show that IL-17A overexpression promotes rapid growth of mutant *K-Ras*-driven lung cancers. Coincident with stimulation of tumorigenesis *in vivo*, IL-17 stimulates the expression of MMP-9 in the lung and in lung epithelial cells in culture. Consistently, IL-17-treated mK-Ras-LE cells display enhanced migration and invasiveness that is MMP-9 dependent, as demonstrated by selective (pharmacological inhibitor and RECK overexpression) and specific (antibody) inhibition of MMP-9. A knockdown-restoration strategy demonstrated that IL-17-mediated migration and induction of MMP-9 depend on wild-type p53. In contrast, IL-17 does not enhance MMP-9 expression or consequent motility and invasion of mutant p53-expressing lung tumor cells. IL-17 increases MMP-9 mRNA stability. In accord with posttranscriptional regulation, siRNA-mediated knockdown of SRSF1 increases levels of MMP-9 mRNA. Moreover, MMP-9 mRNA binds to SRSF1 in a manner that is regulated by IL-17. We conclude that IL-17 enhances migration of wild-type p53-expressing lung tumor

Fig. 4. IL-17 promotes MMP-9-dependent migration and invasion of mK-ras-LE cells. **A:** confluent mK-Ras-LE cells in 24-well plates were serum-starved overnight, then a scratch wound was made at time 0 (0 h) and fresh serum-free medium or serum-free medium supplemented with 10 or 50 ng/ml IL-17 was added before returning the cells to the incubator. Cell motility was measured as the ratio of wound closure relative to initial wound width. Graph shows percentage of wound closure vs. time for cells incubated in 0 (●, dotted line), 10 (○, solid line) and 50 (△, dashed line) ng/ml IL-17. Data shown are means \pm SE ($n = 4$). * $P < 0.05$ vs. negative control group at the same time point. **B:** Transwell migration assays were performed with (solid and shaded bars) or without (open bar) 10 ng/ml IL-17 added to the bottom of the Transwells. The extent of migration is expressed as the number of cells on the underside of the Transwell in the treated group relative to the number of cells on the underside of the Transwell in the negative control group, which was normalized to 100. Enhanced migration mediated by IL-17 (solid bar) was reduced by the inhibitor of MMP-9 (shaded bar). Data shown are means \pm SE ($n = 4$). * $P < 0.05$ vs. negative control or IL-17 and MMP-9 inhibitor cotreatment. **C:** mK-Ras-LE cells were plated onto a Matrigel-coated porous membrane without serum. Transwell invasion assays were performed with (solid and shaded bars) or without (open bar) addition of 10 ng/ml IL-17 added to the bottom of the Transwells. The extent of invasion is expressed as the number of cells on the underside of the Transwell in the treated group relative to the number of cells on the underside of the Transwell in the negative control group, which was normalized to 100. Enhanced invasion mediated by IL-17 (solid bar) was reduced by the inhibitor of MMP-9 (shaded bar). Data shown are means \pm SE ($n = 4$). * $P < 0.05$ vs. negative control or IL-17 and MMP-9 inhibitor cotreatment. **D:** a migration assay was performed as described in A except the cells were infected at a MOI of 10 with recombinant adenovirus expressing reversion-inducing-cysteine-rich protein with kazal motifs (AdV-RECK) or AdV-GFP 24 h before wounding and addition of IL-17. Graph shows percentage wound closure at the indicated times in cells infected with AdV-GFP (×) or AdV-RECK (□) in the absence of IL-17 and in cells transfected with AdV-GFP (○) or AdV-RECK (△) in the presence of 10 ng/ml IL-17. Data shown are means \pm SE ($n = 3$). * $P < 0.05$ vs. negative control group at the same time point. **E:** a migration assay was performed as described in A except an MMP-9 antibody (12 μ g/ml, Millipore AB19016) was used to inhibit MMP-9. In place of the MMP-9 antibody, the same amount of rabbit IgG was used as the negative control. Graph shows percentage wound closure at the indicated times in cells treated with rabbit IgG (×) or MMP-9 antibody (□) in the absence of 10 ng/ml IL-17, and in cells treated with rabbit IgG (○) or MMP-9 antibody (△) in the presence of 10 ng/ml IL-17. Data shown are means \pm SE ($n = 3$). * $P < 0.05$ vs. negative control group at the same time point.

cells in a MMP-9-dependent manner that includes dissociation of the SRSF1-destabilizing factor from the MMP-9 mRNA.

IL-17A displays dichotomous roles in tumor progression. For example, it has been proposed that IL-17A enhances antitumor immunity in immunocompetent mice but increases tumor growth in the absence of an adaptive immune response (41), but this distinction is not so clear cut (40). Tumor type appears to be an important determinant of the prognostic significance of Th17 inflammation on clinical outcome (12). In addition, our data suggest that p53 status affects IL-17-mediated promotion of lung tumorigenesis. SRSF1 overexpression can induce p53 (11). Consequently, the ability of the activated

IL-17 receptor to sequester SRSF1 (67) may be related to the opposing effects of IL-17 and p53 in MMP-9 regulation shown here. Consistent with our findings, prior studies have identified a protumorigenic role for IL-17 in models of lung adenocarcinoma (3, 37, 38, 57). However, with one exception (3), these previous investigations did not examine the effects of IL-17A in an autochthonous lung tumor model and studies with tumor grafts have produced results that were often contradictory (40, 72). Our results agree with, and extend, previous findings demonstrating that Th17 inflammation accelerates lung tumorigenesis in an autochthonous model of mutant K-Ras-expressing lung cancer (3). However, the approach here differs by

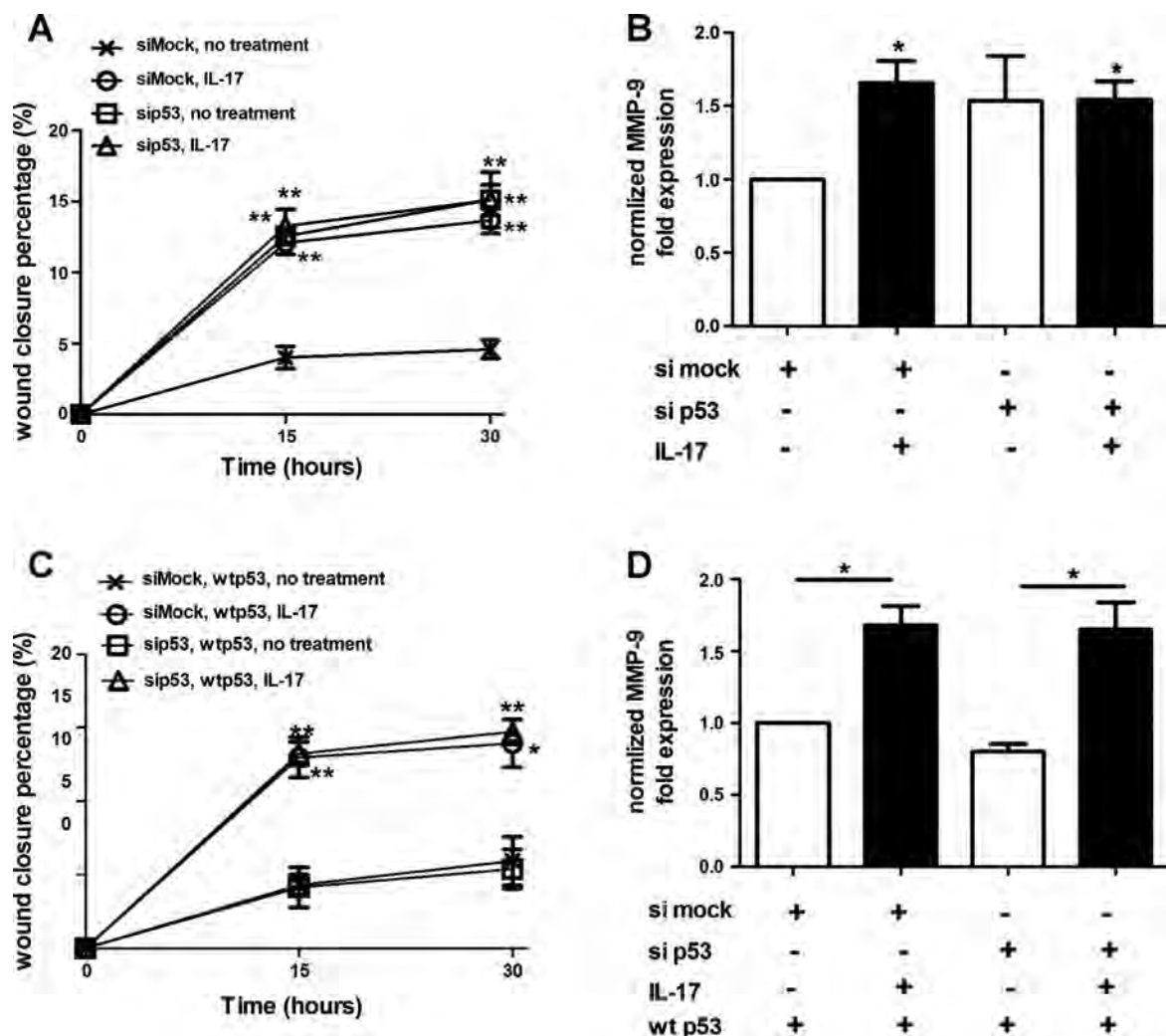


Fig. 5. IL-17 fails to enhance migration and MMP-9 expression in p53-knockdown lung tumor cells. A: knockdown of p53 prevents enhanced migration of IL-17-treated cells. mK-Ras-LE cells were transfected with a p53-targeting siRNA (sip53) or a non-targeting control siRNA (siMock) before growth to confluence. A scratch wound was made in the confluent cultures at time 0 (0 h) and fresh serum-free medium or serum-free medium supplemented with 10 ng/ml IL-17 was added before returning the cells to the incubator. At 15 and 30 h after the addition of IL-17, the percentage of wound closure was assessed for mock- (x) and p53-targeting (□) siRNA-transfected cells incubated without IL-17 or mock- (o) and p53-targeting (Δ) siRNA-transfected cells incubated with 10 ng/ml IL-17. Data shown are means \pm SE ($n = 4$). $^{*}P < 0.01$ vs. negative control at the same time point. B: RNA was prepared from the cells at the 30-h time point in A and levels of MMP-9 mRNA were determined by qRT-PCR. Graph shows the mean fold change (\pm SE) of MMP-9 mRNA levels relative to β -actin ($2^{-\Delta\Delta CT}$ method) with (solid bars) or without (open bars) IL-17. For normalization purposes, the MMP-9/ β -actin mRNA ratio in siMock-transfected, untreated cells was made equal to 1. $^{*}P < 0.05$ vs. negative control. C: restoration of wild-type p53 rescues enhanced motility mediated by IL-17. mK-Ras-LE cells were cotransfected with a p53-targeting siRNA (sip53) or a non-targeting control siRNA (siMock) with a plasmid (pCMV-p53-wt) that expresses wild-type human p53, which is siRNA resistant. Graph shows percentage wound closure at the indicated times after wild-type human p53 expression in cells transfected with mock siRNA (x) or p53 siRNA (□) in the absence of 10 ng/ml IL-17 and in cells transfected with mock siRNA (o) or p53 siRNA (Δ) in the presence of 10 ng/ml IL-17. Data shown are means \pm SE ($n = 4$). $^{*}P < 0.05$, $^{**}P < 0.01$ vs. negative control at the same time point. D: restoration of wild-type p53 rescues induction of MMP-9 mRNA by IL-17. Same as B, except the levels of MMP-9 mRNA at the 30-h time point from the cells in C were determined. $^{*}P < 0.05$.

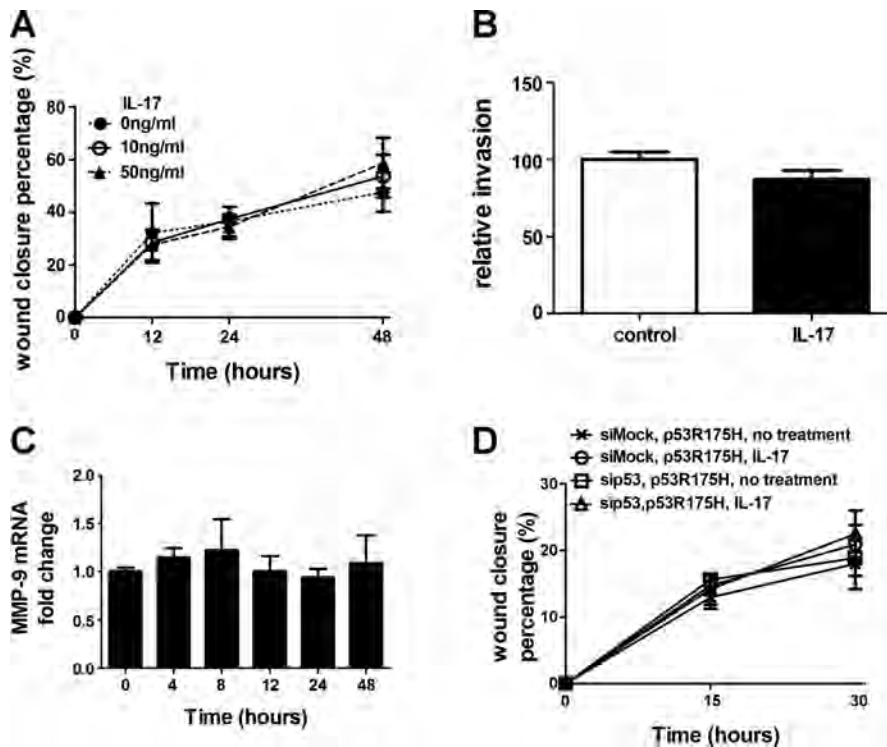


Fig. 6. Mutant p53 alters IL-17-mediated promotion of migration and induction of MMP-9. **A**: effect of IL-17 on migration of mutant p53-expressing cells. Same as Fig. 4A except confluent mK-Ras-R172H-LE cells were assessed for migration in serum-free medium (●, dotted line) or serum-free medium supplemented with 10 (○, solid line) or 50 (△, dashed line) ng/ml IL-17. Graph shows percentage of wound closure vs. time. Data shown are means \pm SE ($n = 4$). **B**: IL-17 does not promote invasion of mutant p53-expressing cells. Transwell migration assays (see Fig. 4B) were performed with mK-Ras-R172H-LE cells in serum-free media with (solid bar) or without (open bar) 10 ng/ml IL-17. Data shown are means \pm SE ($n = 4$). **C**: total RNA was prepared from mK-Ras-R172H-LE cells at increasing times after treatment with 10 ng/ml IL-17. Graph shows the mean level of MMP-9 mRNA relative to β -actin ($2^{-\Delta\Delta CT}$ method) at the indicated time after addition of IL-17 to the serum-starved cells. Data shown are means \pm SE ($n \geq 5$). **D**: same as Fig. 5C, except the cotransfected plasmid (pCMV-p53R175H) expressed the R175H mutant of human p53 in the K-Ras-LE cells with p53 knocked down. Graph shows percentage wound closure at the indicated times with mutant human p53 expression in cells transfected with mock siRNA (×) or p53 siRNA (□) in the absence IL-17 and in cells transfected with mock siRNA (○) or p53 siRNA (△) in the presence of 10 ng/ml IL-17. Data shown are means \pm SE ($n = 4$).

overexpressing IL-17 to identify the cytokine-tumor relationship rather than using IL-17-deficient mice, which lack the homeostatic functions of IL-17. Although IL-17 overexpression more accurately reflects the clinical scenario of lung inflammation than the use of genetically deficient mice, the epithelial source of IL-17 overexpression consequent to adenovirus infection does not model the Th17 cell source of IL-17 that occurs in the lung exposed to carcinogens. IL-17-mediated lung neutrophilia likely increases levels of neutrophil elastase, an established inducer of lung tumor growth (23). Indeed, IL-17 recruits Gr-1⁺-CD11b⁺ myeloid cells to the lung and their depletion suppresses growth of *K-Ras*-driven lung tumors (3).

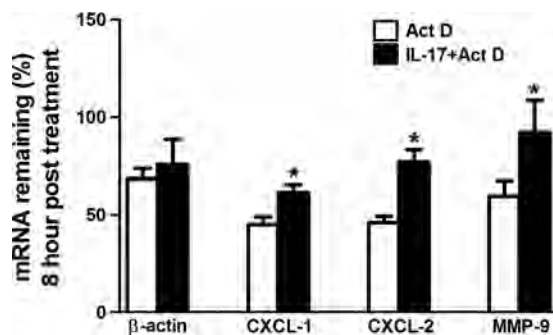


Fig. 7. IL-17 enhanced MMP-9 mRNA stability in mK-Ras-LE cells. Serum-starved mK-Ras-LE cells were untreated (open bars) or treated with 10 ng/ml IL-17 (solid bars) for 2 h. Then 10 μ g/ml actinomycin D (Act D) was added to both groups at time 0 and total RNA was prepared. Equal amounts of total RNA prepared at time 0 and 8 h from duplicate or triplicate samples were assessed for the target mRNAs (β -actin, CXCL-1, CXCL-2, and MMP-9) by qRT-PCR. Results are presented as percent of the indicated mRNA remaining relative to the amount at time 0. The mRNA levels before actinomycin D treatment were set to 1. Data shown are means \pm SE ($n \geq 4$). * $P < 0.05$ for IL-17 treated vs. untreated control.

Typically, lung tumors develop in the context of chronic inflammation associated with inhaled carcinogens, primarily cigarette smoke. Consistent with the approach here, cigarette smoke is a Th17 adjuvant (4, 61) and inflammation associated with cigarette smoke promotes progression of mutant *K-Ras*-driven lung tumors (69). Moreover, a bacterial pathogen promotes chronic Th17 lung inflammation and accelerates lung tumorigenesis in mutant *K-Ras*-expressing mice (3, 48). These observations are consistent with the dependence of mutant *K-Ras*-expressing lung tumors on signaling by the proinflammatory transcription factor nuclear factor- κ B [NF- κ B (45, 75)]. Enhanced tumor progression associated with inflammation occurs in other tumor types driven by mutant *K-Ras* (6, 16). In a model of pancreatic cancer, inflammation initiates an NF- κ B-dependent positive feedback loop that amplifies *K-Ras* activity (6). Moreover, tumors harboring mutant *K-Ras* develop in an inflammatory microenvironment fostered by the oncoprotein (44, 65, 68), and this selective pressure likely contributes to adaptation and escape from antitumor immunity.

High serum levels of MMP-9 (76) or immunohistochemical detection of MMP-9 in tumor specimens (80) are poor prognostic indicators in lung cancer. Moreover, increasing serum MMP-9 concentrations correlate with disease severity in chronic obstructive pulmonary disease, COPD (51), a disease that predisposes lung cancer (21). Chemokine-mediated release of MMP-9 stored in tertiary granules of neutrophils infiltrating the lung can exacerbate COPD (71) and lung cancer (22). Indeed, tumor-associated leukocytes appear to be a major source of MMP-9 during stimulation of tumor growth by AdV-IL-17 (Fig. 3C). Active MMP-9 can release growth factors, promote angiogenesis, accelerate tumor cell migration into surrounding normal tissue, and prepare the premetastatic niche (8, 20, 66, 77), which likely contributes to the association of MMP-9 expression with increasing lung tumor grade (46).

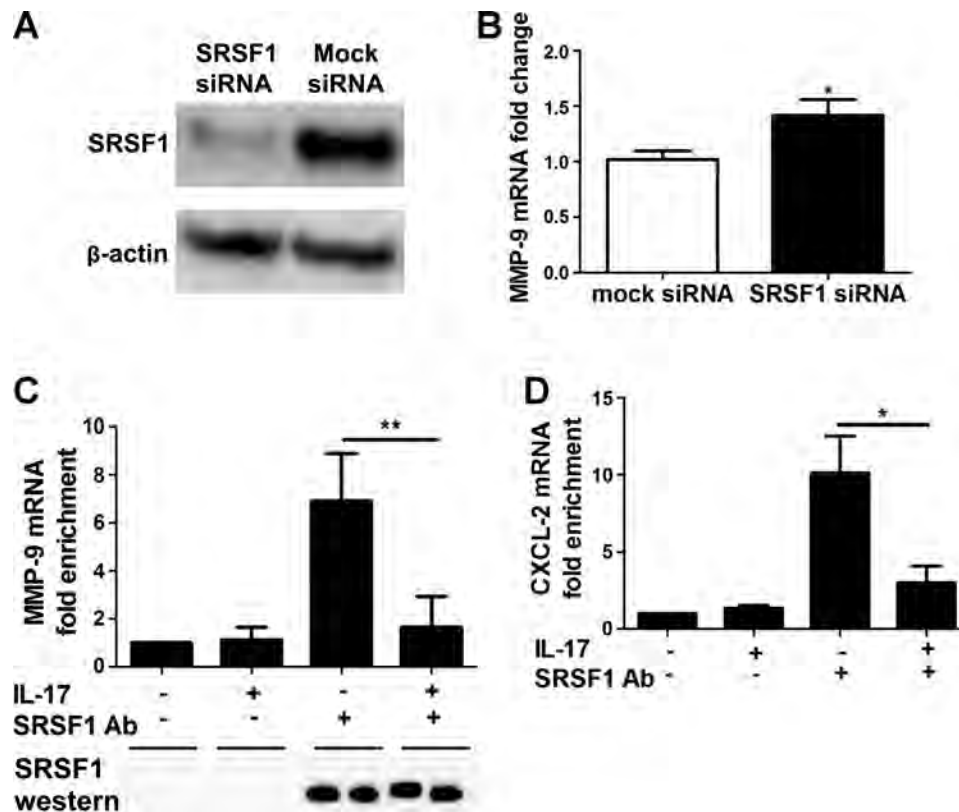


Fig. 8. IL-17 regulates MMP-9 mRNA levels via serine/arginine-rich splicing factor 1 (SRSF1). **A:** mK-Ras-LE cells were transfected with a scrambled siRNA or a siRNA targeted to SRSF1. After 48 h, cell lysates were prepared and subjected to Western blot. Western blots confirmed siRNA knockdown of SRSF1 compared with the level in cells transfected with a Mock siRNA. **B:** same as **A** except total RNA was analyzed for MMP-9 mRNA levels in mK-Ras-LE cells transfected with a siRNA targeting SRSF1. Reduction of SRSF1 with a siRNA increased the MMP-9 mRNA level 1.4-fold (solid bar) relative to that in cells transfected with the control siRNA (open bar). The levels of MMP-9 mRNA were determined by qRT-PCR ($2^{-\Delta\Delta CT}$ method) relative to β -actin mRNA. Results are means \pm SE of 3 independent experiments. * $P < 0.05$ vs. mock siRNA-transfected group. **C:** serum-starved mK-Ras-LE cells were treated with or without 10 ng/ml IL-17 for 48 h. The cells were briefly fixed with formalin prior to preparation of cell lysates as described in MATERIALS AND METHODS. Coimmunoprecipitated RNA was extracted from the protein A/G beads and cross-linking was reversed prior to conversion to cDNA. The amount of MMP-9 cDNA in each sample was quantified by real-time PCR. The results obtained with protein A/G beads alone with extracts from untreated cells were normalized to one. Data are presented as fold enrichment of MMP-9 mRNA compared with the negative control samples. Data shown are means \pm SE ($n = 4$). ** $P < 0.01$. Treatment of mK-Ras-LE cells with 10 ng/ml IL-17 reduced the amount of MMP-9 mRNA that could be selectively immunoprecipitated with an antibody to SRSF1 to near negative control levels. **Bottom:** immunoblotting showed that equal amounts of SRSF1 were immunoprecipitated from the extracts of IL-17-treated and untreated cells. **D:** same as **C**, except coimmunoprecipitation of CXCL-2 mRNA with an antibody to SRSF1 was assessed. Data are presented as fold enrichment of CXCL-2 mRNA compared with the negative control samples. Data are means \pm SE ($n = 4$). * $P < 0.05$.

Our data demonstrating MMP-9-dependent migration of lung epithelial cells agree with previous findings that addition of active MMP-9 accelerates migration of A549 cells (62) and that MMP-9 expression by alveolar type II cells is essential for wound healing (53). Knockdown or mutation of p53 increases lung tumor cell motility and abrogates IL-17-mediated induction of MMP-9. In addition, IL-17-mediated stabilization of MMP-9 mRNA by disruption of SRSF1 interaction coincides with previous findings demonstrating this mechanism of mRNA regulation for chemokine mRNAs (67).

Improving the survival rates in non-small cell lung cancer (NSCLC) will require the identification of novel therapeutic targets. Our data are consistent with the view that cigarette smoke promotes progression of NSCLC by inducing expression of IL-17. One mechanism that could account for enhanced proliferation in response to IL-17 is induction of MMP-9. Our data also suggest that, once p53 is inactivated by mutation, lung tumor promotion would be independent of IL-17. In NSCLC, serum MMP-9 levels potentially serve as a prognostic marker (31) and an indicator of response to chemotherapy (9). Although inhibitors of matrix

metalloproteinases have not improved survival in patients with NSCLC, clinical trial end points and the late stage of disease in study participants have complicated the interpretation of these findings (5). Toward a goal of personalized therapy, our results suggest that MMP-9 inhibition in lung tumors with high levels of IL-17 and wild-type p53 warrants reinvestigation.

GRANTS

This work was supported by National Institutes of Health Grant CA132603 (B. Shan, D. E. Sullivan, G. F. Morris) and by the Wetmore Foundation. B. Xu received fellowship support from the Foundation in Lung Pathobiology and Matching Funds from the Tulane Cancer Center. Z. You received grants from the National Institutes of Health (P20GM103518 and R01CA174714) and Department of Defense (PC121647, PC13448, and PC130118).

DISCLOSURES

J. Kolls is employed by Vitae and got grants from Amgen and Constellation Pharmaceuticals.

AUTHOR CONTRIBUTIONS

B.X., D.A.P., J.K.K., B.C., B.S., D.E.S., and G.F.M. conception and design of research; B.X., J.F.G., Y.W., B.S., D.E.S., and G.F.M. performed experi-

ments; B.X., B.S., D.E.S., and G.F.M. analyzed data; B.X., Z.Y., B.C., B.S., D.E.S., and G.F.M. interpreted results of experiments; B.X. and G.F.M. prepared figures; B.X. and G.F.M. drafted manuscript; B.X., D.A.P., B.S., D.E.S., and G.F.M. edited and revised manuscript; B.X., J.F.G., D.A.P., Y.W., J.K.K., Z.Y., B.C., B.S., D.E.S., and G.F.M. approved final version of manuscript.

REFERENCES

- Benevides L, Cardoso CR, Tiezzi DG, Marana HR, Andrade JM, Silva JS. Enrichment of regulatory T cells in invasive breast tumor correlates with the upregulation of IL-17A expression and invasiveness of the tumor. *Eur J Immunol* 43: 1518–1528, 2013.
- Chang CK, Hung WC, Chang HC. The Kazal motifs of RECK protein inhibit MMP-9 secretion and activity and reduce metastasis of lung cancer cells in vitro and in vivo. *J Cell Mol Med* 12: 2781–2789, 2008.
- Chang SH, Mirabolfathinejad SG, Katta H, Cumpian AM, Gong L, Caetano MS, Moghaddam SJ, Dong C. T helper 17 cells play a critical pathogenic role in lung cancer. *Proc Natl Acad Sci USA* 111: 5664–5669, 2014.
- Chen K, Pociask DA, McAleer JP, Chan YR, Alcorno JF, Kreindler JL, Keyser MR, Shapiro SD, Houghton AM, Kolls JK, Zheng M. IL-17RA is required for CCL2 expression, macrophage recruitment, and emphysema in response to cigarette smoke. *PLoS One* 6: e20333, 2011.
- Coussens LM, Fingleton B, Matrisian LM. Matrix metalloproteinase inhibitors and cancer: trials and tribulations. *Science* 295: 2387–2392, 2002.
- Daniluk J, Liu Y, Deng D, Chu J, Huang H, Gaiser S, Cruz-Monserrate Z, Wang H, Ji B, Logsdon CD. An NF-kappaB pathway-mediated positive feedback loop amplifies Ras activity to pathological levels in mice. *J Clin Invest* 122: 1519–1528, 2012.
- Diamant MJ, Peluffo GD, Stillitani I, Cerchietti LC, Navigante A, Ranuncolo SM, Klein SM. Inhibition of tumor progression and paraneoplastic syndrome development in a murine lung adenocarcinoma by medroxyprogesterone acetate and indomethacin. *Cancer Invest* 24: 126–131, 2006.
- Egeblad M, Werb Z. New functions for the matrix metalloproteinases in cancer progression. *Nat Rev Cancer* 2: 161–174, 2002.
- Ertan E, Soyuncu H, Yazar A, Ustuner Z, Tas F, Yasasever V. Matrix metalloproteinase-9 decreased after chemotherapy in patients with non-small cell lung cancer. *Tumori* 97: 286–289, 2011.
- Freed-Pastor WA, Prives C. Mutant p53: one name, many proteins. *Genes Dev* 26: 1268–1286, 2012.
- Fregoso OI, Das S, Akerman M, Krainer AR. Splicing-factor oncoprotein SRSF1 stabilizes p53 via RPL5 and induces cellular senescence. *Mol Cell* 50: 56–66, 2013.
- Fridman WH, Pages F, Sautes-Fridman C, Galon J. The immune contexture in human tumours: impact on clinical outcome. *Nat Rev Cancer* 12: 298–306, 2012.
- Friedlander PL, Delaune CL, Abadie JM, Toups M, LaCour J, Marrero L, Zhong Q, Kolls JK. Efficacy of CD40 ligand gene therapy in malignant mesothelioma. *Am J Respir Cell Mol Biol* 29: 321–330, 2003.
- Gaffen SL. Structure and signalling in the IL-17 receptor family. *Nat Rev Immunol* 9: 556–567, 2009.
- Gong Y, Hart E, Shchurin A, Hoover-Plow J. Inflammatory macrophage migration requires MMP-9 activation by plasminogen in mice. *J Clin Invest* 118: 3012–3024, 2008.
- Grivennikov SI, Wang K, Mucida D, Stewart CA, Schnabl B, Jauch D, Taniguchi K, Yu GY, Osterreicher CH, Hung KE, Datz C, Feng Y, Fearon ER, Oukka M, Tessarollo L, Coppola V, Yarovinsky F, Cheroutre H, Eckmann L, Trinchieri G, Karin M. Adenoma-linked barrier defects and microbial products drive IL-23/IL-17-mediated tumour growth. *Nature* 491: 254–258, 2012.
- Guenther JF, Cameron JE, Nguyen HT, Wang Y, Sullivan DE, Shan B, Lasky JA, Flemington EK, Morris GF. Modulation of lung inflammation by the Epstein-Barr virus protein Zta. *Am J Physiol Lung Cell Mol Physiol* 299: L771–L784, 2010.
- Hemdan NY. Anti-cancer vs. cancer-promoting effects of the interleukin-17-producing T helper cells. *Immunol Lett* 149: 123–133, 2013.
- Herjan T, Yao P, Qian W, Li X, Liu C, Bulek K, Sun D, Yang WP, Zhu J, He A, Carman JA, Erzurum SC, Lipshitz HD, Fox PL, Hamilton TA. HuR is required for IL-17-induced Act1-mediated CXCL1 and CXCL5 mRNA stabilization. *J Immunol* 191: 640–649, 2013.
- Hiratsuka S, Nakamura K, Iwai S, Murakami M, Itoh T, Kijima H, Shipley JM, Senior RM, Shibuya M. MMP9 induction by vascular endothelial growth factor receptor-1 is involved in lung-specific metastasis. *Cancer Cell* 2: 289–300, 2002.
- Houghton AM. Mechanistic links between COPD and lung cancer. *Nat Rev Cancer* 13: 233–245, 2013.
- Houghton AM. The paradox of tumor-associated neutrophils: fueling tumor growth with cytotoxic substances. *Cell Cycle* 9: 1732–1737, 2010.
- Houghton AM, Rzymkiewicz DM, Ji H, Gregory AD, Egea EE, Metz HE, Stolz DB, Land SR, Marconcini LA, Kliment CR, Jenkins KM, Beaulieu KA, Mouded M, Frank SJ, Wong KK, Shapiro SD. Neutrophil elastase-mediated degradation of IRS-1 accelerates lung tumor growth. *Nat Med* 16: 219–223, 2010.
- Hu Y, Ota N, Peng I, Refino CJ, Danilenko DM, Caplazi P, Ouyang W. IL-17RC is required for IL-17A- and IL-17F-dependent signaling and the pathogenesis of experimental autoimmune encephalomyelitis. *J Immunol* 184: 4307–4316, 2010.
- Jackson EL, Olive KP, Tuveson DA, Bronson R, Crowley D, Brown M, Jacks T. The differential effects of mutant p53 alleles on advanced murine lung cancer. *Cancer Res* 65: 10280–10288, 2005.
- Kao SJ, Su JL, Chen CK, Yu MC, Bai KJ, Chang JH, Bien MY, Yang SF, Chien MH. Osteonin inhibits the invasive ability of human lung adenocarcinoma cells via suppression of NF-kappaB-mediated matrix metalloproteinase-9 expression. *Toxicol Appl Pharmacol* 261: 105–115, 2012.
- Kasinski AL, Slack FJ. miRNA-34 prevents cancer initiation and progression in a therapeutically resistant K-ras and p53-induced mouse model of lung adenocarcinoma. *Cancer Res* 72: 5576–5587, 2012.
- Kolls JK, Linden A. Interleukin-17 family members and inflammation. *Immunity* 21: 467–476, 2004.
- Kryczek I, Wei S, Szeliga W, Vatan L, Zou W. Endogenous IL-17 contributes to reduced tumor growth and metastasis. *Blood* 114: 357–359, 2009.
- Kuestner RE, Taft DW, Haran A, Brandt CS, Brender T, Lum K, Harder B, Okada S, Ostrander CD, Kreindler JL, Aujla SJ, Reardon B, Moore M, Shea P, Schreckhise R, Bukowski TR, Presnell S, Guerra-Lewis P, Parrish-Novak J, Ellsworth JL, Jaspers S, Lewis KE, Appleby M, Kolls JK, Rixon M, West JW, Gao Z, Levin SD. Identification of the IL-17 receptor related molecule IL-17RC as the receptor for IL-17F. *J Immunol* 179: 5462–5473, 2007.
- Laack E, Kohler A, Kugler C, Dierlamm T, Knuffmann C, Vohwinkel G, Niestroy A, Dahmann N, Peters A, Berger J, Fiedler W, Hossfeld DK. Pretreatment serum levels of matrix metalloproteinase-9 and vascular endothelial growth factor in non-small-cell lung cancer. *Ann Oncol* 13: 1550–1557, 2002.
- Lakatos HF, Burgess HA, Thatcher TH, Redonnet MR, Hernady E, Williams JP, Sime PJ. Oropharyngeal aspiration of a silica suspension produces a superior model of silicosis in the mouse compared with intratracheal instillation. *Exp Lung Res* 32: 181–199, 2006.
- Lang GA, Iwakuma T, Suh YA, Liu G, Rao VA, Parant JM, Valentin-Vega YA, Terzian T, Caldwell LC, Strong LC, El-Naggar AK, Lozano G. Gain of function of a p53 hot spot mutation in a mouse model of Li-Fraumeni syndrome. *Cell* 119: 861–872, 2004.
- Le Gouvello S, Bastuji-Garin S, Aloulou N, Mansour H, Chaumette MT, Berrehar F, Seikour A, Charachon A, Karoui M, Leroy K, Farcet JP, Boshani I. High prevalence of Foxp3 and IL17 in MMR-proficient colorectal carcinomas. *Gut* 57: 772–779, 2008.
- Li C, Nguyen HT, Zhuang Y, Lin Y, Flemington EK, Guo W, Guenther J, Burrow ME, Morris GF, Sullivan D, Shan B. Post-transcriptional up-regulation of miR-21 by type I collagen. *Mol Carcinog* 50: 563–570, 2011.
- Li J, Lau GK, Chen L, Dong SS, Lan HY, Huang XR, Li Y, Luk JM, Yuan YF, Guan XY. Interleukin 17A promotes hepatocellular carcinoma metastasis via NF-kB induced matrix metalloproteinases 2 and 9 expression. *PLoS One* 6: e21816, 2011.
- Li Q, Han Y, Fei G, Guo Z, Ren T, Liu Z. IL-17 promoted metastasis of non-small-cell lung cancer cells. *Immunol Lett* 148: 144–150, 2012.
- Li Y, Cao ZY, Sun B, Wang GY, Fu Z, Liu YM, Kong QF, Wang JH, Zhang Y, Xu XY, Li HL. Effects of IL-17A on the occurrence of lung adenocarcinoma. *Cancer Biol Ther* 12: 610–616, 2011.
- Livak KJ, Schmittgen TD. Analysis of relative gene expression data using real-time quantitative PCR and the 2(-Delta Delta C(T)) Method. *Methods* 25: 402–408, 2001.
- Maniati E, Soper R, Hagemann T. Up for mischief? IL-17/Th17 in the tumour microenvironment. *Oncogene* 29: 5653–5662, 2010.
- Martin-Orozco N, Dong C. The IL-17/IL-23 axis of inflammation in cancer: friend or foe? *Curr Opin Investig Drugs* 10: 543–549, 2009.

42. Martin-Orozco N, Muranski P, Chung Y, Yang XO, Yamazaki T, Lu S, Hwu P, Restifo NP, Overwijk WW, Dong C. T helper 17 cells promote cytotoxic T cell activation in tumor immunity. *Immunity* 31: 787–798, 2009.
43. Martins SJ, Takagaki TY, Silva AG, Gallo CP, Silva FB, Capelozzi VL. Prognostic relevance of TTF-1 and MMP-9 expression in advanced lung adenocarcinoma. *Lung Cancer* 64: 105–109, 2009.
44. McAllister F, Bailey JM, Alsina J, Nirschl CJ, Sharma R, Fan H, Rattigan Y, Roeser JC, Lankapalli RH, Zhang H, Jaffee EM, Drake CG, Housseau F, Maitra A, Kolls JK, Sears CL, Pardoll DM, Leach SD. Oncogenic Kras activates a hematopoietic-to-epithelial IL-17 signaling axis in preinvasive pancreatic neoplasia. *Cancer Cell* 25: 621–637, 2014.
45. Meylan E, Dooley AL, Feldser DM, Shen L, Turk E, Ouyang C, Jacks T. Requirement for NF-kappaB signalling in a mouse model of lung adenocarcinoma. *Nature* 462: 104–107, 2009.
46. Minamoto H, Antonangelo L, da Silva AG, Gallo CP, de Andrade e Silva FB, Fenezelian S, Rodrigues OR, Jatene F, Saldiva P, Capelozzi VL. Tumour cell and stromal features in metastatic and non-metastatic non-small cell lung carcinomas. *Histopathology* 43: 427–443, 2003.
47. Miossec P, Kolls JK. Targeting IL-17 and TH17 cells in chronic inflammation. *Nat Rev Drug Discov* 11: 763–776, 2012.
48. Moghaddam SJ, Li H, Cho SN, Dishop MK, Wistuba II, Ji L, Kurie JM, Dickey BF, Demayo FJ. Promotion of lung carcinogenesis by chronic obstructive pulmonary disease-like airway inflammation in a K-ras-induced mouse model. *Am J Respir Cell Mol Biol* 40: 443–453, 2009.
49. Morris GF, Hoyle GW, Athas GB, Lei WH, Xu J, Morris CB, Friedman M. Lung-specific expression in mice of a dominant negative mutant form of the p53 tumor suppressor protein. *J La State Med Soc* 150: 179–185, 1998.
50. Morris GF, Labrie C, Mathews MB. Modulation of transcriptional activation of the proliferating cell nuclear antigen promoter by the adenovirus E1A 243-residue oncoprotein depends on proximal activators. *Mol Cell Biol* 14: 543–553, 1994.
51. Navratilova Z, Zatloukal J, Kriegova E, Kolek V, Petrek M. Simultaneous up-regulation of matrix metalloproteinases 1, 2, 3, 7, 8, 9 and tissue inhibitors of metalloproteinases 1, 4 in serum of patients with chronic obstructive pulmonary disease. *Respirology* 17: 1006–1012, 2012.
52. Numasaki M, Watanabe M, Suzuki T, Takahashi H, Nakamura A, McAllister F, Hishinuma T, Goto J, Lotze MT, Kolls JK, Sasaki H. IL-17 enhances the net angiogenic activity and in vivo growth of human non-small cell lung cancer in SCID mice through promoting CXCR-2-dependent angiogenesis. *J Immunol* 175: 6177–6189, 2005.
53. O’Kane CM, McKeown SW, Perkins GD, Bassford CR, Gao F, Thickett DR, McAuley DF. Salbutamol up-regulates matrix metalloproteinase-9 in the alveolar space in the acute respiratory distress syndrome. *Crit Care Med* 37: 2242–2249, 2009.
54. Oh J, Takahashi R, Kondo S, Mizoguchi A, Adachi E, Sasahara RM, Nishimura S, Imamura Y, Kitayama H, Alexander DB, Ide C, Horan TP, Arakawa T, Yoshida H, Nishikawa S, Itoh Y, Seiki M, Itoharu S, Takahashi C, Noda M. The membrane-anchored MMP inhibitor RECK is a key regulator of extracellular matrix integrity and angiogenesis. *Cell* 107: 789–800, 2001.
55. Okamoto T, Valacchi G, Gohil K, Akaike T, van der Vliet A. S-nitrosothiols inhibit cytokine-mediated induction of matrix metalloproteinase-9 in airway epithelial cells. *Am J Respir Cell Mol Biol* 27: 463–473, 2002.
56. Park H, Li Z, Yang XO, Chang SH, Nurieva R, Wang YH, Wang Y, Hood L, Zhu Z, Tian Q, Dong C. A distinct lineage of CD4 T cells regulates tissue inflammation by producing interleukin 17. *Nat Immunol* 6: 1133–1141, 2005.
57. Reppert S, Boross I, Koslowski M, Tureci O, Koch S, Lehr HA, Finotto S. A role for T-bet-mediated tumour immune surveillance in anti-IL-17A treatment of lung cancer. *Nat Commun* 2: 600, 2011.
58. Schwarzenberger P, La Russa V, Miller A, Ye P, Huang W, Zieske A, Nelson S, Bagby GJ, Stoltz D, Mynatt RL, Spriggs M, Kolls JK. IL-17 stimulates granulopoiesis in mice: use of an alternate, novel gene therapy-derived method for in vivo evaluation of cytokines. *J Immunol* 161: 6383–6389, 1998.
59. Sfanos KS, Bruno TC, Maris CH, Xu L, Thoburn CJ, DeMarzo AM, Meeker AK, Isaacs WB, Drake CG. Phenotypic analysis of prostate-infiltrating lymphocytes reveals TH17 and Treg skewing. *Clin Cancer Res* 14: 3254–3261, 2008.
60. Shan B, Morris GF. Binding sequence-dependent regulation of the human proliferating cell nuclear antigen promoter by p53. *Exp Cell Res* 305: 10–22, 2005.
61. Shan M, Yuan X, Song LZ, Roberts L, Zarinkamar N, Seryshev A, Zhang Y, Hilsenbeck S, Chang SH, Dong C, Corry DB, Kheradmand F. Cigarette smoke induction of osteopontin (SPP1) mediates TH17 inflammation in human and experimental emphysema. *Sci Transl Med* 4: 117ra119, 2012.
62. Shyamsundar M, McAuley DF, Ingram RJ, Gibson DS, O’Kane D, McKeown ST, Edwards A, Taggart C, Elborn JS, Calfee CS, Matthay MA, O’Kane CM. Keratinocyte growth-factor promotes epithelial survival and resolution in a human model of lung injury. *Am J Respir Crit Care Med* 189: 1520–1529, 2014.
63. Siddesha JM, Valente AJ, Sakamuri SS, Yoshida T, Gardner JD, Somanna N, Takahashi C, Noda M, Chandrasekar B. Angiotensin II stimulates cardiac fibroblast migration via the differential regulation of matrixins and RECK. *J Mol Cell Cardiol* 65: 9–18, 2013.
64. Sossey-Alaoui K, Ranalli TA, Li X, Bakin AV, Cowell JK. WAVE3 promotes cell motility and invasion through the regulation of MMP-1, MMP-3, and MMP-9 expression. *Exp Cell Res* 308: 135–145, 2005.
65. Sparmann A, Bar-Sagi D. Ras-induced interleukin-8 expression plays a critical role in tumor growth and angiogenesis. *Cancer Cell* 6: 447–458, 2004.
66. Stamenkovic I. Extracellular matrix remodelling: the role of matrix metalloproteinases. *J Pathol* 200: 448–464, 2003.
67. Sun D, Novotny M, Bulek K, Liu C, Li X, Hamilton T. Treatment with IL-17 prolongs the half-life of chemokine CXCL1 mRNA via the adaptor TRAF5 and the splicing-regulatory factor SF2 (ASF). *Nat Immunol* 12: 853–860, 2011.
68. Sunaga N, Imai H, Shimizu K, Shames DS, Kakegawa S, Girard L, Sato M, Kaira K, Ishizuka T, Gazdar AF, Minna JD, Mori M. Oncogenic KRAS-induced interleukin-8 overexpression promotes cell growth and migration and contributes to aggressive phenotypes of non-small cell lung cancer. *Int J Cancer* 130: 1733–1744, 2012.
69. Takahashi H, Ogata H, Nishigaki R, Broide DH, Karin M. Tobacco smoke promotes lung tumorigenesis by triggering IKKbeta- and JNK1-dependent inflammation. *Cancer Cell* 17: 89–97, 2010.
70. To Y, Dohi M, Matsumoto K, Tanaka R, Sato A, Nakagome K, Nakamura T, Yamamoto K. A two-way interaction between hepatocyte growth factor and interleukin-6 in tissue invasion of lung cancer cell line. *Am J Respir Cell Mol Biol* 27: 220–226, 2002.
71. Vlahos R, Wark PA, Anderson GP, Bozinovski S. Glucocorticosteroids differentially regulate MMP-9 and neutrophil elastase in COPD. *PLoS One* 7: e33277, 2012.
72. Wilke CM, Kryczek I, Wei S, Zhao E, Wu K, Wang G, Zou W. Th17 cells in cancer: help or hindrance? *Carcinogenesis* 32: 643–649, 2011.
73. Wu KC, Yang ST, Hsia TC, Yang JS, Chiou SM, Lu CC, Wu RS, Chung JG. Suppression of cell invasion and migration by propofol are involved in down-regulating matrix metalloproteinase-2 and p38 MAPK signaling in A549 human lung adenocarcinoma epithelial cells. *Anticancer Res* 32: 4833–4842, 2012.
74. Wu MH, Hong TM, Cheng HW, Pan SH, Liang YR, Hong HC, Chiang WF, Wong TY, Shieh DB, Shiau AL, Jin YT, Chen YL. Galectin-1-mediated tumor invasion and metastasis, up-regulated matrix metalloproteinase expression, and reorganized actin cytoskeletons. *Mol Cancer Res* 7: 311–318, 2009.
75. Xue W, Meylan E, Oliver TG, Feldser DM, Winslow MM, Bronson R, Jacks T. Response and resistance to NF-kappaB inhibitors in mouse models of lung adenocarcinoma. *Cancer Discov* 1: 236–247, 2011.
76. Ylisirnio S, Hoyhtya M, Turpeenniemi-Hujanen T. Serum matrix metalloproteinases -2, -9 and tissue inhibitors of metalloproteinases -1, -2 in lung cancer–TIMP-1 as a prognostic marker. *Anticancer Res* 20: 1311–1316, 2000.
77. Yu Q, Stamenkovic I. Localization of matrix metalloproteinase 9 to the cell surface provides a mechanism for CD44-mediated tumor invasion. *Genes Dev* 13: 35–48, 1999.
78. Zhang B, Rong G, Wei H, Zhang M, Bi J, Ma L, Xue X, Wei G, Liu X, Fang G. The prevalence of Th17 cells in patients with gastric cancer. *Biochem Biophys Res Commun* 374: 533–537, 2008.
79. Zhang Q, Liu S, Ge D, Xue Y, Xiong Z, Abdel-Mageed AB, Myers L, Hill SM, Rowan BG, Sartor O, Melamed J, Chen Z, You Z. Interleukin-17 promotes formation and growth of prostate adenocarcinoma in mouse models. *Cancer Res* 72: 2589–2599, 2012.
80. Zheng S, Chang Y, Hodges KB, Sun Y, Ma X, Xue Y, Williamson SR, Lopez-Beltran A, Montironi R, Cheng L. Expression of KISS1 and MMP-9 in non-small cell lung cancer and their relations to metastasis and survival. *Anticancer Res* 30: 713–718, 2010.

Interferon- γ and celecoxib inhibit lung-tumor growth through modulating M2/M1 macrophage ratio in the tumor microenvironment

Fuqiang Ren^{1,2,*}Mingyu Fan^{1,2,*}Jiandong Mei^{1,2}Yongqiang Wu³Chengwu Liu^{1,2}Qiang Pu^{1,2}Zongbing You⁴⁻⁹Lunxu Liu^{1,2}

¹Department of Thoracic Surgery, West China Hospital, ²Western China Collaborative Innovation Center for Early Diagnosis and Multidisciplinary Therapy of Lung Cancer,

³Regenerative Medicine Research Center, West China Hospital, Sichuan University, Chengdu, People's Republic of China; ⁴Department of Structural and Cellular Biology, ⁵Department of Orthopaedic Surgery, ⁶Tulane Cancer Center, ⁷Louisiana Cancer Research Consortium, ⁸Tulane Center for Stem Cell Research and Regenerative Medicine, ⁹Tulane Center for Aging, Tulane University Health Sciences Center, New Orleans, LA, USA

*These two authors contributed equally to this study

Correspondence: Zongbing You
Department of Structural and Cellular Biology, Tulane University, 1430 Tulane Avenue – SL49, New Orleans, LA 70112, USA

Tel +1 504 988 0467
Fax +1 504 988 1687
Email zyou@tulane.edu

Lunxu Liu
Department of Thoracic Surgery, West China Hospital, Sichuan University, 37 Guoxue Alley, Chengdu, Sichuan 610041, People's Republic of China
Tel +86 28 8542 2494
Fax +86 28 8542 2494
Email lunxu_liu@aliyun.com

Abstract: Tumor-associated macrophages play an important role in tumor growth and progression. These macrophages are heterogeneous with diverse functions, eg, M1 macrophages inhibit tumor growth, whereas M2 macrophages promote tumor growth. In this study, we found that IFN γ and/or celecoxib (cyclooxygenase-2 inhibitor) treatment consistently inhibited tumor growth in a mouse lung cancer model. IFN γ alone and celecoxib alone increased the percentage of M1 macrophages but decreased the percentage of M2 macrophages in the tumors, and thus the M2/M1 macrophage ratio was reduced to 1.1 and 1.7 by IFN γ alone and celecoxib alone, respectively, compared to the M2/M1 macrophage ratio of 4.4 in the control group. A combination of IFN γ and celecoxib treatment reduced the M2/M1 macrophage ratio to 0.8. Furthermore, IFN γ and/or celecoxib treatment decreased expression of matrix metalloproteinase (MMP)-2, MMP-9, and VEGF, as well as the density of microvessels in the tumors, compared to the control group. This study provides the proof of principle that IFN γ and/or celecoxib treatment may inhibit lung-tumor growth through modulating the M2/M1 macrophage ratio in the tumor microenvironment, suggesting that IFN γ and celecoxib have potential to be further optimized into a new anticancer therapy.

Keywords: tumor-associated macrophages, M1 macrophages, M2 macrophages, lung cancer, interferon- γ , celecoxib

Introduction

Globally, lung cancer is the most common cause of cancer-related deaths. Currently, surgical resection is the standard of care for most patients with nonmetastatic non-small-cell lung cancer. Other therapeutic approaches are needed to improve the survival of lung cancer patients. Cancer immunotherapy has reappeared as a powerful weapon against cancer recently,¹ since the US Food and Drug Administration approved Provenge® (sipuleucel-T) for the treatment of metastatic castration-resistant prostate cancer and Yervoy® (ipilimumab) for the treatment of metastatic melanoma.^{2,3} Inhibitors of PD-1, an immunosuppressive checkpoint protein, and its ligand PD-L1 and PD-L2, have shown promising results in the treatment of cancers, including lung cancer, in clinical trials.⁴ A Phase I clinical trial showed that anti-PD-1 antibody produced objective responses in approximately one in four to one in five patients with non-small-cell lung cancer, melanoma, or renal cell cancer; the adverse-event profile did not appear to preclude its use.⁵ Another Phase I clinical trial showed that anti-PD-L1 antibody induced objective response rates of 6%–17% and a stabilization of disease at rates of 12%–41% at 24 weeks in patients with advanced cancers, including non-small-cell lung cancer, melanoma, and renal cell cancer.⁶ Three patients sustained long-term partial or complete response 16 months to 3 years off therapy.⁷

The tumor microenvironment is critical for lung cancer growth and progression. The tumor microenvironment consists of tumor cells, fibroblasts, endothelial cells, and immune cells (including macrophages, dendritic cells, and lymphocytes), as well as these cells' products, such as extracellular matrix, cytokines, chemokines, growth factors, enzymes, and cellular metabolites.⁸ Macrophages influence tumor growth, angiogenesis, invasion, and metastasis through producing growth factors, cytokines, chemokines, and enzymes.⁹ The tumor-associated macrophages (TAMs) are heterogeneous, with diverse, and even opposite, biological properties, such as the so called M1 (classically activated) and M2 (alternatively activated) macrophages.¹⁰ IFN γ , lipopolysaccharides, TNF α , and GM-CSF induce monocytes to differentiate into M1 macrophages that express high levels of inducible nitric oxide synthase (iNOS), TNF α , IL-1 β , IL-6, IL-12, IL-18, IL-23, CXCL10, human leukocyte antigen DR, and reactive oxygen and nitrogen intermediates.^{10–14} IL-4, IL-10, IL-13, IL-21, activin A, immune complexes, and glucocorticoids are able to induce monocyte differentiation into M2 macrophages that express high levels of arginase (ARG)-1, IL-1RA, IL-10, CCL22, mannose receptor, galactose receptor, and CD163 antigen.^{10,15} M1 macrophages can inhibit tumor growth by producing effector molecules, such as reactive oxygen intermediates, reactive nitrogen intermediates, and TNF α , whereas M2 macrophages promote tumor growth and metastasis by secretion of growth factors, VEGF, matrix metalloproteinases (MMPs), and immunosuppressive cytokines/chemokines.¹¹ The ratio of M1 and M2 macrophages determines the net anti- or protumor effects of the TAM population in the tumor microenvironment.¹⁶ However, it is very common that M2 macrophages outnumber M1 macrophages in the tumors, so the TAMs provide a protumor microenvironment to support tumor progression.¹⁷

We previously found that about 70% of TAMs are M2 macrophages and the remaining 30% are M1 macrophages in human non-small-cell lung cancer.¹⁸ We have demonstrated that cyclooxygenase (COX)-2 is expressed at higher levels in human lung tumors than normal lung tissues, leading to increased prostaglandin E₂ (PGE₂) in lung tumors, which facilitates M2 macrophage differentiation.¹⁹ Given that IFN γ can induce M1 macrophage polarization,^{20,21} and celecoxib can inhibit COX-2 enzyme activity,²² we hypothesized that IFN γ and celecoxib might have a synergistic effect in reversing the M2/M1 macrophage ratio in the tumor microenvironment by promoting M1 macrophage differentiation and inhibiting M2 macrophage differentiation, thus inhibiting tumor growth. In the present study, we designed

an in vivo animal study to test this hypothesis. In addition, because zoledronic acid has been shown to deplete TAMs and inhibit tumor progression in a human liver cancer xenograft model,²³ we also tested if zoledronic acid could inhibit lung-tumor growth in a mouse lung cancer model in immunocompetent syngeneic mice. We found that IFN γ alone or celecoxib alone was able to significantly reduce the M2/M1 macrophage ratio in the tumors ($P < 0.01$), and thus significantly inhibited tumor growth ($P < 0.01$). However, although the combination of IFN γ and celecoxib further reduced the M2/M1 macrophage ratio, the combined treatment did not significantly inhibit tumor growth further, compared to the single-agent treatment. Furthermore, zoledronic acid alone did not show any consistent antitumor effects.

Materials and methods

Animal model

The animal study was approved by the Animal Care and Use Committee of West China Hospital, Sichuan University, Chengdu, People's Republic of China (PRC). The mouse Lewis lung carcinoma (LLC)-1 cell line was obtained from the American Type Culture Collection, Manassas, VA, USA. LLC1 was originally derived from C57BL/6 mouse LLC.²⁴ The cells were cultured in Dulbecco's Modified Eagle's Medium containing 10% fetal bovine serum (HyClone, Logan, UT, USA) and 100 IU/mL penicillin/streptomycin, in a 5% CO₂ humidified incubator at 37°C. A total of 115 8-week-old female C57BL/6 mice were purchased from the West China Laboratory Animal Center, Sichuan University, and were housed at this facility in a specific pathogen-free condition. The mice were used in two independent experiments. The first experiment used 75 mice ($n=15$ mice per group), and the second experiment used 40 mice ($n=8$ mice per group). In each experiment, 50 μ L (containing 1×10^6 cells) LLC1 cell suspension was mixed with 50 μ L of Matrigel® (BD Biosciences, San Jose, CA, USA), which was injected subcutaneously in the left axilla of each mouse, using a 20-gauge needle and 1 cc tuberculin syringe.

Experimental groups and treatment

One day after tumor-cell implantation, each mouse was randomly assigned to the following five groups ($n=15$ and $n=8$ per group, in the first and second independent experiments, respectively) and treated accordingly: a) treated with saline as a placebo control group; b) treated with recombinant human IFN γ (Shanghai Chemo Wanbang Biopharm, Shanghai, PRC), at a dose of 10,000 IU in 200 μ L saline by intraperitoneal injection once a day for 5 consecutive days,

then discontinued for 2 days, and followed by another 5 days (Figure 1A); c) treated with celecoxib (Pfizer China, Shanghai, PRC), at a dose of 60 mg/kg in 200 μ L saline, administered by gavage on every other day (Figure 1A); d) treated with a combination of IFN γ and celecoxib at the

same dose and schedule described earlier (Figure 1A); and e) treated with zoledronic acid (China National Medicines Guorui Pharmaceutical, Beijing, PRC), at a dose of 0.4 mg/kg in 100 μ L saline intraperitoneally twice a week (Figure 1A). Animal body weight was weighed on days 1, 4, 7, 10, and 14.

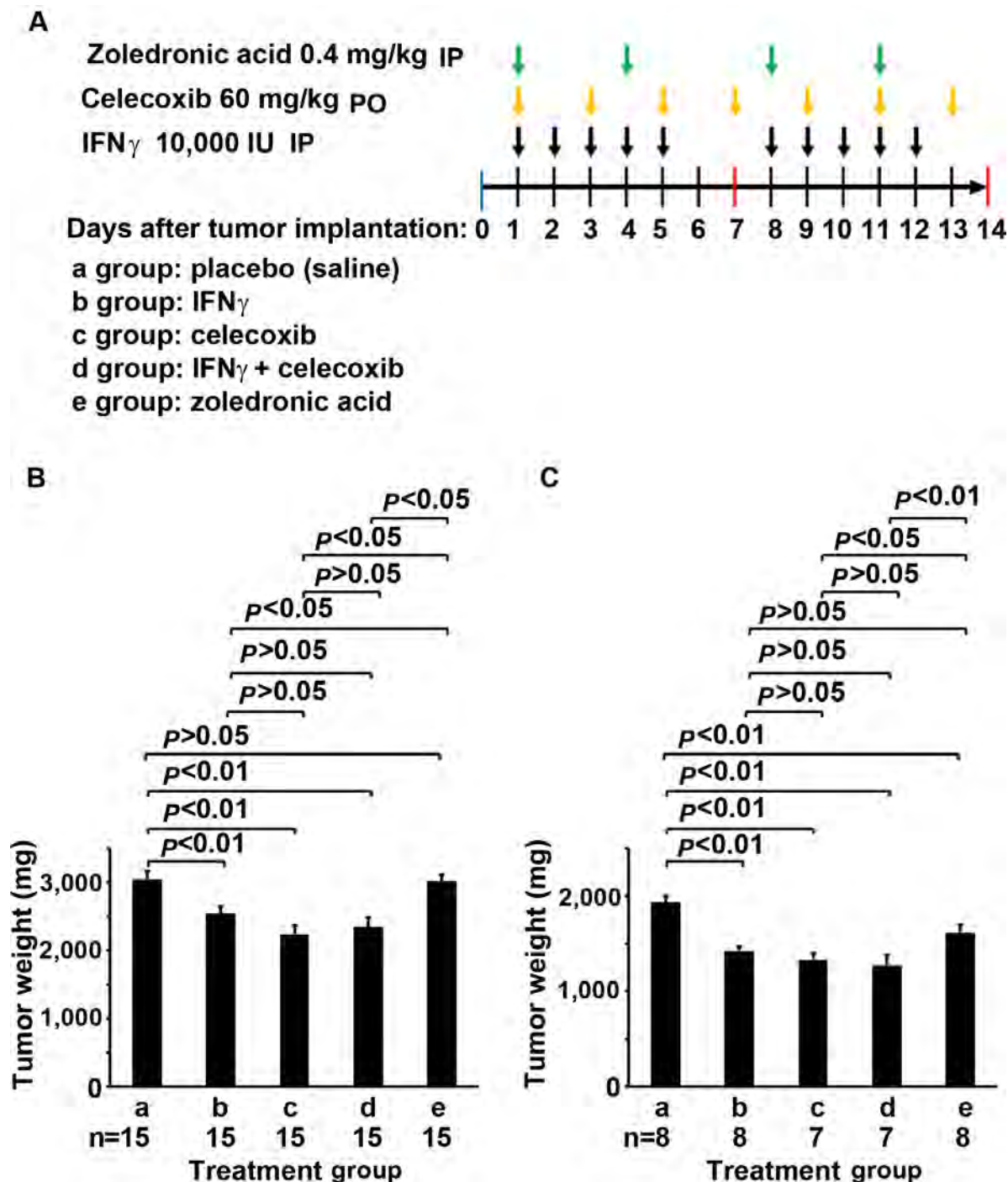


Figure 1 Experimental design and outcome.

Notes: (A) Mouse Lewis lung carcinoma LLC1 cells (1×10^6) mixed with Matrigel were injected subcutaneously in C57BL/6 mice on day 0. The mice were randomly assigned into five treatment groups (a–e). Treatment started on day 1, with the doses and schedules indicated by arrows along the time course. (B, C) The results (tumor weight) of the first and second experiments, respectively. Data represent means \pm SEM (error bars). The number of animals per group is indicated under each group.

Abbreviations: IP, intraperitoneally; PO, per os (by mouth); IU, international unit; SEM, standard error of the mean.

Animals were killed on day 14, when the largest tumors reached about 1.5 cm in diameter.

Histopathology

The subcutaneous tumors were dissected out en bloc and weighed for wet weight. In the first experiment, all tumor tissues were fixed with 10% formalin and embedded in paraffin. Five-micrometer sections were cut for histopathologic examination and immunohistochemical (IHC) staining. In the second experiment, approximately 10% of each tumor was fixed and paraffin-sectioned for histopathologic examination, and the rest was used for flow-cytometry analysis.

Immunohistochemical staining

IHC staining was performed as described previously.^{25,26} The primary antibodies used were: rabbit anti-MMP-2 (1:50 dilution), rabbit anti-MMP-9 (1:150 dilution), rabbit anti-VEGF (1:100 dilution), and rabbit anti-factor VIII (1:200). All primary antibodies were purchased from Beijing Biosynthesis Biotechnology (Beijing, PRC). Tissue sections previously stained positively were used as positive controls, while tissue sections with primary antibodies replaced by phosphate-buffered saline (PBS) served as negative controls. Streptavidin peroxidase-conjugated secondary antibodies (SP-9002) and a diaminobenzidine substrate kit were obtained from Zhongshan Golden Bridge Biotechnology (Beijing, PRC). The staining was performed according to the kit manufacturer's instructions. Sections were then counterstained with hematoxylin and mounted in an aqueous mounting medium. Positive cells showed brown particles on the cellular membrane and/or in the cytoplasm. The stained sections were evaluated in a blinded manner (ie, the examiner did not know which group the sections belonged to). Staining of MMP-2, MMP-9, and VEGF was graded in a two-score system according to a previous report.²⁷ The proportion score represented the estimated fraction of positive staining: 0=no staining, 1=1%–25%, 2=26%–50%, 3=51%–75%, 4=76%–100%. The intensity score represented the estimated average staining intensity of the positive staining: 0=no staining, 1=weak, 2=intermediate, 3=strong. The overall score of staining is the sum of the proportion score and the intensity score (range 0–7). The average score from five high-power fields (magnification 200×) represented the staining score of each tumor. The density of microvessels was assessed according to a previous study.²⁸ The number of factor VIII-positive microvessels was counted under five high-power fields (magnification 200×), and the average

number per high-power field represented the density of microvessels in each tumor. The data represent means \pm standard error of the mean of 15 tumors per group (n=15).

Flow-cytometry analysis

Fresh tumors were cut into approximately 1 mm³ pieces and digested with 0.5 mg/mL collagenase IV in Dulbecco's Modified Eagle's Medium at 37°C with shaking at 100 rounds per minute for 2 hours. The cells were filtered through a 70 μ m filter and subjected to red cell-lysis buffer. Then, the cells were fixed with 4% paraformaldehyde and permeabilized with 0.5% Triton X-100. After being washed twice with PBS, the cells were aliquoted into 1 \times 10⁶ cells in 100 μ L PBS in 1.5 mL microcentrifuge tubes for staining. To each test tube was added three antibodies conjugated with different fluorophores: rat antimouse CD68-phycoerythrin (PE) (1:100 dilution; BioLegend, San Diego, CA, USA), rat antimouse iNOS-Alexa Fluor[®] 488 (1:50 dilution; eBioscience, San Diego, CA, USA), and sheep antimouse arginase 1-allophycocyanin (APC) (1:50 dilution, R&D Systems, Minneapolis, MN, USA). As negative control, three isotype control antibodies were used: rat IgG_{2a}, κ -PE (1:100 dilution, BioLegend), rat IgG_{2a}, κ -Alexa Fluor 488 (1:50 dilution; eBioscience), and sheep IgG-APC (1:50 dilution; R&D Systems). The cells were stained for 1 hour at 4°C, with gentle shaking every 10 minutes. After being washed twice with PBS, the cells were suspended in 0.5 mL PBS and analyzed with Cytomics FC500 flow cytometry and its software (Beckman Coulter, Brea, CA, USA). Unstained and single antibody-stained samples were used to adjust color compensation and gating of the positively stained population. The CD68-PE-positive cells (macrophages) were gated first, from which population the iNOS-Alexa Fluor 488-positive cells (CD68⁺iNOS⁺ M1 macrophages) and ARG1-APC-positive cells (CD68⁺ARG1⁺ M2 macrophages) were gated. Data represent the means \pm standard error of the mean of seven or eight tumors (n=7 for groups c and d, in which one mouse each died due to injuries caused by gavage, and thus only seven mice per group survived to the end point; n=8 for groups a, b, and e, as originally planned).

Statistical analysis

Statistical analysis was carried out using the SPSS version 19.0 for Windows (SPSS, Chicago, IL, USA). Comparison among multiple groups was analyzed with analysis of variance. *P*-values <0.05 were considered statistically significant.

Results

IFN γ and celecoxib inhibit mouse lung-tumor growth

We implanted mouse LLC1 cells subcutaneously into syngeneic C57BL/6 mice. The mice were randomly assigned into five groups: a) treated with saline as the placebo control group, b) treated with IFN γ , c) treated with celecoxib (COX-2 inhibitor), d) treated with a combination of IFN γ and celecoxib, and e) treated with zoledronic acid that can kill macrophages (Figure 1A). In the first experiment, we found that IFN γ alone reduced tumor weight by 17% compared to the control group ($P < 0.01$, Figure 1B). Celecoxib alone reduced tumor weight by 27% compared to the control group ($P < 0.01$, Figure 1B). The combination of IFN γ and celecoxib reduced tumor weight by 23% compared to the control group ($P < 0.01$, Figure 1B). However, there was no statistically significant difference between the combined-treatment group and IFN γ -alone or the celecoxib-alone groups ($P > 0.05$, Figure 1B). Zoledronic acid did not significantly reduce tumor weight compared to the control group ($P > 0.05$, Figure 1B). In the second experiment, we found that IFN γ alone reduced tumor weight by 26% compared to the control group ($P < 0.01$, Figure 1C). Celecoxib alone reduced tumor weight by 31% compared to the control group ($P < 0.01$, Figure 1C). The combination of IFN γ and celecoxib reduced tumor weight by 34% compared to the control group ($P < 0.01$, Figure 1C). Like the first experiment, there was no statistically significant difference between the combined-treatment group and IFN γ -alone or celecoxib alone groups ($P > 0.05$, Figure 1C). Unlike the first experiment, zoledronic acid reduced tumor weight by 16% compared to the control group ($P < 0.01$, Figure 1C). Of note, we found that all animals gained body weight during the treatment, and there was no statistically significant difference among the five groups (data not shown).

IFN γ and celecoxib modulate the M2/M1 macrophage ratio in the tumors

We examined the percentage of macrophages in the cellular population of the tumors by staining with anti-CD68 antibodies and analyzing with flow cytometry. The CD68-positive macrophages were gated in window C of the histograms (Figure 2, A–E, left panels). From the CD68-positive population, iNOS-positive (CD68⁺iNOS⁺) cells and ARG1-positive (CD68⁺ARG1⁺) cells were separately gated out, representing M1 and M2 macrophages, respectively (Figure 2, A–E, right panels). Isotype antibody controls are shown in Figure 2F. We found that IFN γ or celecoxib alone did not change the

percentage of macrophages, while the combination of IFN γ and celecoxib increased the proportion of macrophages by approximately 11% ($P < 0.05$, Figure 2G). In contrast, zoledronic acid decreased the proportion of macrophages by approximately 30% ($P < 0.01$, Figure 2G). Both IFN γ alone and celecoxib alone increased the proportion of M1 macrophages by 116% compared to the control group ($P < 0.01$, Figure 2H). The combination of IFN γ and celecoxib increased the proportion of M1 macrophages by 158% compared to the control group ($P < 0.01$, Figure 2H), the increase of which was also significantly higher than IFN γ alone or celecoxib alone ($P < 0.01$). In contrast, zoledronic acid did not change the proportion of M1 macrophages ($P > 0.05$, Figure 2H). On the other hand, IFN γ decreased the proportion of M2 macrophages by 48% compared to the control group ($P < 0.01$, Figure 2I). Celecoxib decreased the proportion of M2 macrophages by 19% compared to the control group ($P < 0.01$, Figure 2I). The combination of IFN γ and celecoxib decreased the proportion of M2 macrophages by 52% compared to the control group ($P < 0.01$, Figure 2I), the decrease of which was significantly more than celecoxib alone ($P < 0.01$), but not significantly more than IFN γ alone ($P > 0.05$). In contrast, zoledronic acid did not change the proportion of M2 macrophages ($P > 0.05$, Figure 2I). Based on the proportions of M1 and M2 macrophages in the tumors (Figure 2, H and I), we calculated that the M2/M1 macrophage ratio in the control group was 4.4, whereas IFN γ reduced the M2/M1 macrophage ratio to 1.1. Celecoxib reduced the M2/M1 macrophage ratio to 1.7, and the combination of the IFN γ and celecoxib reduced the M2/M1 macrophage ratio to 0.8. In contrast, zoledronic acid slightly increased the M2/M1 macrophage ratio to 4.8.

IFN γ , celecoxib, and zoledronic acid decrease expression of MMP-2 and MMP-9

We did IHC staining of MMP-2 and MMP-9 in the tumor sections and quantified the staining using a two-score grading system.²⁷ We found that MMP-2 expression was significantly reduced by IFN γ alone, celecoxib alone, a combination of IFN γ and celecoxib, and zoledronic acid, compared to the control group (Figure 3, A–G, $P < 0.01$). However, there was no statistically significant difference among the four drug-treatment groups ($P > 0.05$). Similarly, we found that MMP-9 expression was significantly reduced by IFN γ alone, celecoxib alone, a combination of IFN γ and celecoxib, and zoledronic acid, compared to the control group (Figure 4, A–G, $P < 0.05$ and $P < 0.01$, respectively). Again, there was

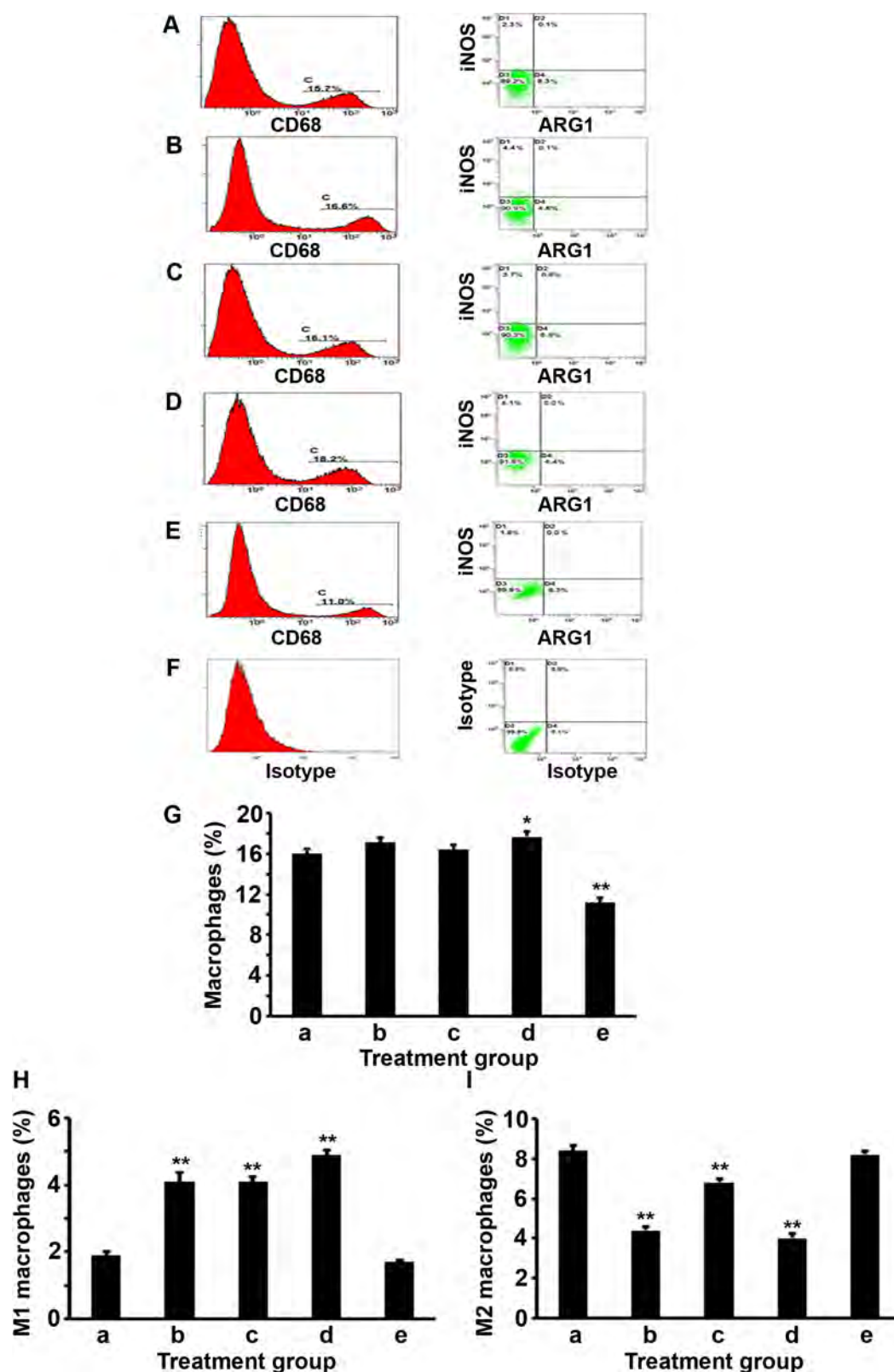


Figure 2 IFN γ and celecoxib modulate the M2/M1 macrophage ratio in the tumors.

Notes: (A–E) Representative gatings of flow-cytometry analysis of CD68⁺ macrophages (C in the histograms in the left panels), CD68⁺iNOS⁺ M1 macrophages (upper left window in the right panels), and CD68⁺ARG1⁺ M2 macrophages (lower right window in the right panels) from the mouse tumors. (A–E) Treatment groups a–e, ie, a, control; b, IFN γ ; c, celecoxib; d, IFN γ + celecoxib; and e, zoledronic acid. (F) Representative gatings of flow-cytometry analysis using isotype control antibodies. (G–I) Percentages of macrophages, M1 macrophages, and M2 macrophages, respectively. Data represent means \pm SEM (error bars). * $P < 0.05$; ** $P < 0.01$.

Abbreviations: iNOS, inducible nitric oxide synthase; SEM, standard error of the mean; ARG, arginase.

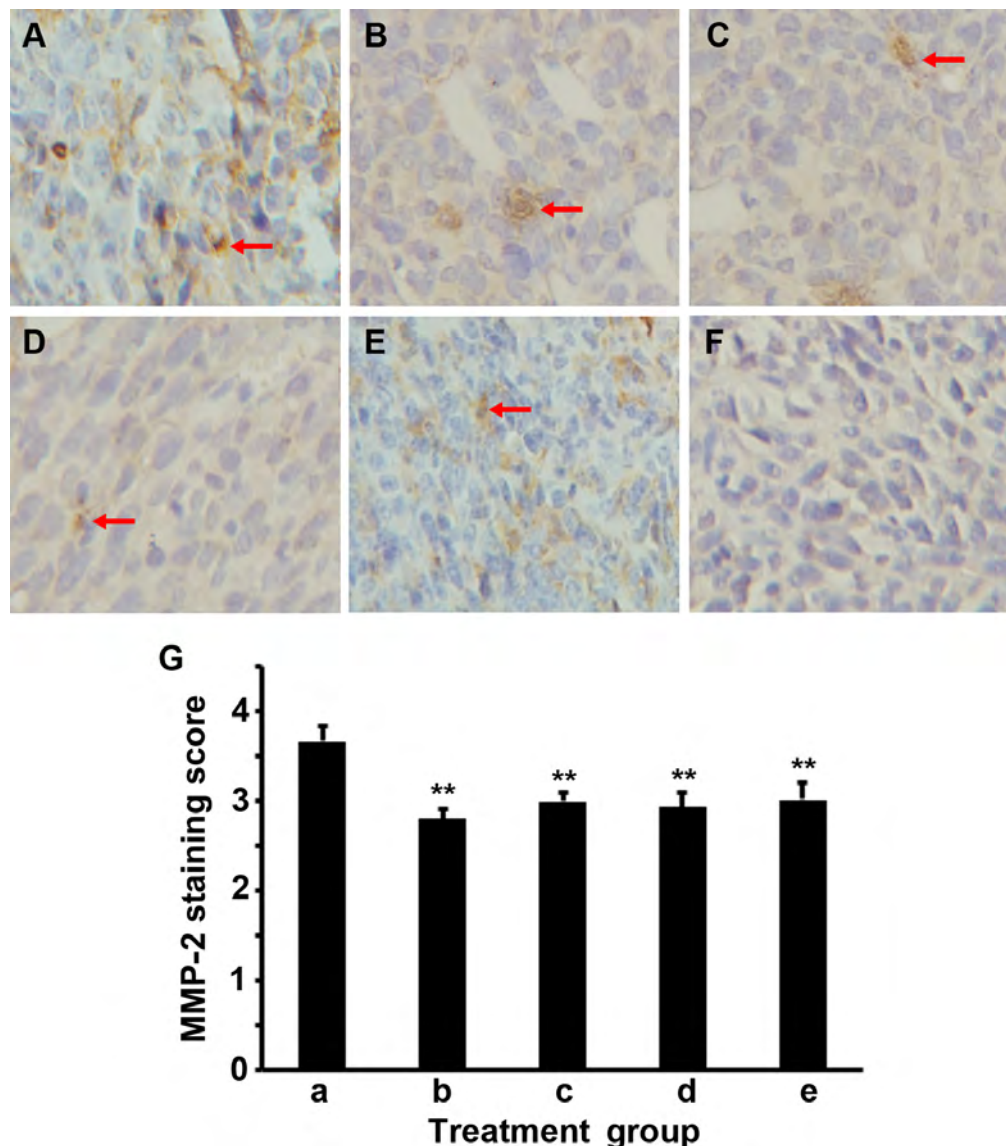


Figure 3 IFN γ , celecoxib, and zoledronic acid decrease expression of MMP-2.

Notes: (A–E) Representative immunohistochemical staining of MMP-2 in the mouse tumors from groups a–e, ie, a, control; b, IFN γ ; c, celecoxib; d, IFN γ + celecoxib; and e, zoledronic acid. Arrows indicate the positively stained cells. Original magnification 400 \times . (F) Negative control of staining. (G) Scores of immunohistochemical staining of MMP-2 in the mouse tumors. Data represent means \pm SEM (error bars; n=15 tumors per group). ** P <0.01.

Abbreviations: MMP, matrix metalloproteinase; SEM, standard error of the mean.

no statistically significant difference among the four drug-treatment groups (P >0.05).

IFN γ and celecoxib decrease VEGF expression and density of microvessels

We did IHC staining of VEGF in the tumor sections and quantified the staining using a two-score grading system.²⁷ We found that VEGF expression was significantly reduced by IFN γ alone, celecoxib alone, and a combination of IFN γ and celecoxib, compared to the control group (Figure 5, A–D, F, G; P <0.01). However, there was no statistically significant difference among these three drug-treatment groups

(P >0.05). In contrast, zoledronic acid did not significantly change the expression of VEGF (P >0.05, Figure 5, E–G). We assessed the density of microvessels in the tumors by factor VIII staining according to a previous study.²⁸ We found that IFN γ alone, celecoxib alone, and a combination of IFN γ and celecoxib significantly decreased the density of microvessels compared to the control group (Figure 6, A–D, F, G; P <0.05 and P <0.01, respectively). The density of microvessels was significantly lower in the combined-treatment group than the IFN γ -alone group (P <0.05), but not significantly different from the celecoxib-alone group (P >0.05). In contrast, zoledronic acid did not significantly

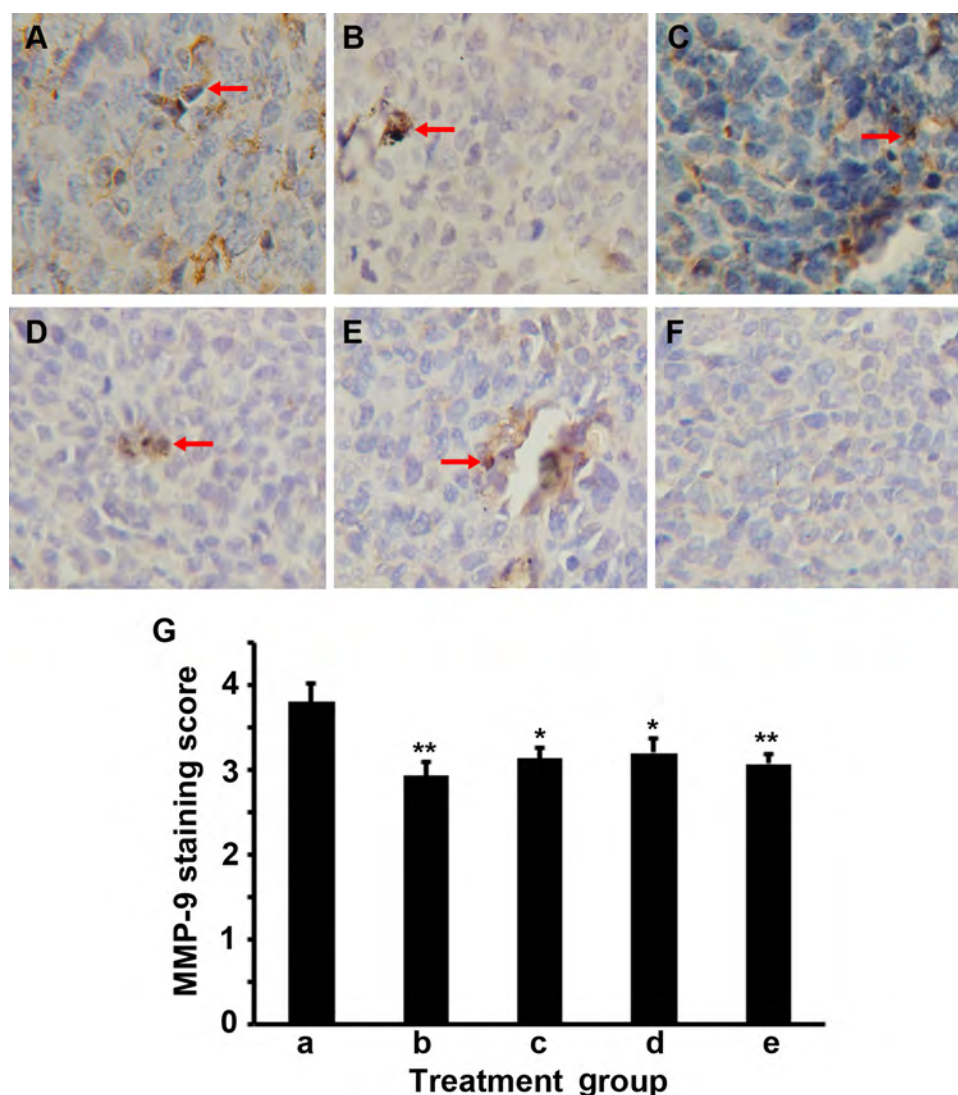


Figure 4 IFN γ , celecoxib, and zoledronic acid decrease expression of MMP-9.

Notes: (A–E) Representative immunohistochemical staining of MMP-9 in the mouse tumors from groups a–e, ie, a, control; b, IFN γ ; c, celecoxib; d, IFN γ + celecoxib; and e, zoledronic acid. Arrows indicate the positively stained cells. Original magnification 400 \times . (F) Negative control of staining. (G) Scores of immunohistochemical staining of MMP-9 in the mouse tumors. Data represent means \pm SEM (error bars; n=15 tumors per group). * P <0.05; ** P <0.01.

Abbreviations: MMP, matrix metalloproteinase; SEM, standard error of the mean.

change the density of microvessels in the tumors (P >0.05, Figure 6, E–G).

Discussion

In the lung-tumor microenvironment, M2 macrophages usually outnumber M1 macrophages, creating a protumor immune microenvironment. Other cancers also present an M2-dominant tumor microenvironment, including prostate cancer and ovarian cancer.^{29–31} Since M1 macrophages inhibit tumor growth while M2 macrophages promote tumor growth by expressing VEGF and MMPs,¹¹ it is intriguing to investigate if enhancing M1 macrophage differentiation and inhibiting M2 macrophage differentiation would affect tumor growth.

In the present study, we tested IFN γ , a well-known inducer of M1 macrophage differentiation,^{20,21} and celecoxib, a COX-2 inhibitor.²² We speculated that celecoxib could inhibit COX-2 and reduce PGE₂ production, thus inhibiting M2 macrophage differentiation, based on our previous study showing that PGE₂ facilitates M2 macrophage differentiation.¹⁹ We found that IFN γ and celecoxib, either used alone or in combination, consistently inhibited lung-tumor growth in two independent experiments. IFN γ or celecoxib alone did not change the percentage of total macrophages, but their combination slightly increased the percentage of total macrophages. What was remarkable was that both IFN γ alone and celecoxib alone significantly increased the

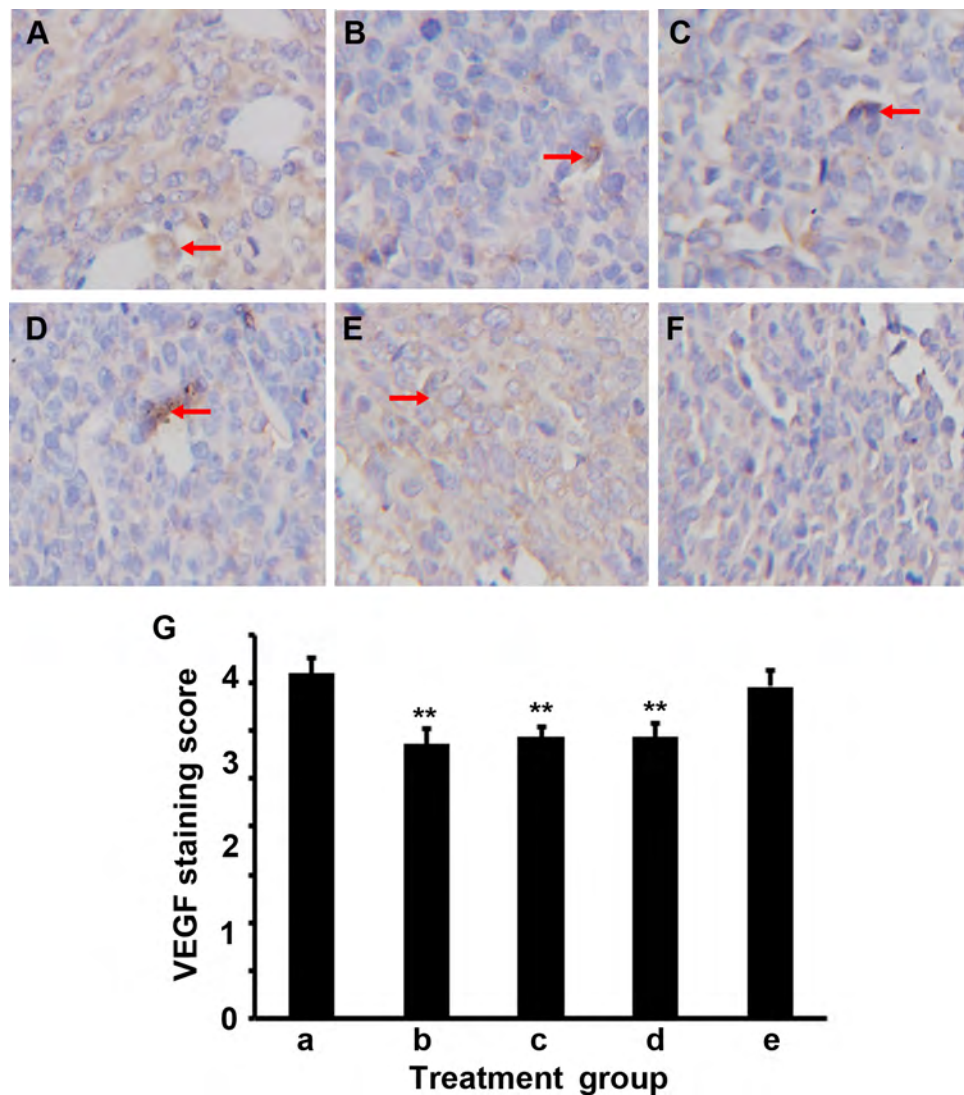


Figure 5 IFN γ and celecoxib decrease expression of VEGF.

Notes: (A–E) Representative immunohistochemical staining of VEGF in the mouse tumors from groups a–e, ie, a, control; b, IFN γ ; c, celecoxib; d, IFN γ + celecoxib; and e, zoledronic acid. Arrows indicate the positively stained cells. Original magnification 400 \times . (F) Negative control of staining. (G) Scores of immunohistochemical staining of VEGF in the mouse tumors. Data represent means \pm SEM (error bars; n=15 tumors per group). ** P <0.01.

Abbreviation: SEM, standard error of the mean.

percentage of M1 macrophages, but decreased the percentage of M2 macrophages in the tumors. Therefore, the M2/M1 macrophage ratio was reduced to 1.1 and 1.7 by IFN γ alone and celecoxib alone, respectively. In contrast, the M2/M1 macrophage ratio in the control group was 4.4, which is four times and 2.6 times of those in the IFN γ -alone and celecoxib-alone groups, respectively. These results suggest that IFN γ and celecoxib indeed can modulate the M2/M1 macrophage ratio in the lung-tumor microenvironment. However, we only observed a slight further reduction of the M2/M1 macrophage ratio to 0.8 by the combination of IFN γ and celecoxib. This is because the combined treatment did not reduce M2 macrophages further than IFN γ alone, although the combined treatment increased the M1 percentage significantly more

than IFN γ alone or celecoxib alone. Therefore, the synergy between IFN γ and celecoxib in modulating the M2/M1 macrophage ratio is not obvious, which is consistent with the lack of synergy in inhibition of tumor growth. Furthermore, IFN γ alone, celecoxib alone, and their combination reduced the expression of MMP-2, MMP-9, and VEGF to similar levels, which is another piece of evidence showing the lack of synergy between IFN γ and celecoxib. The density of microvessels in the tumors was also decreased by IFN γ alone, celecoxib alone, and their combination, except that the decrease with the combined treatment was significantly more than the IFN γ -alone treatment. Taken together, these results suggest that IFN γ alone or celecoxib alone can reduce the M2/M1 macrophage ratio in the tumor microenvironment,

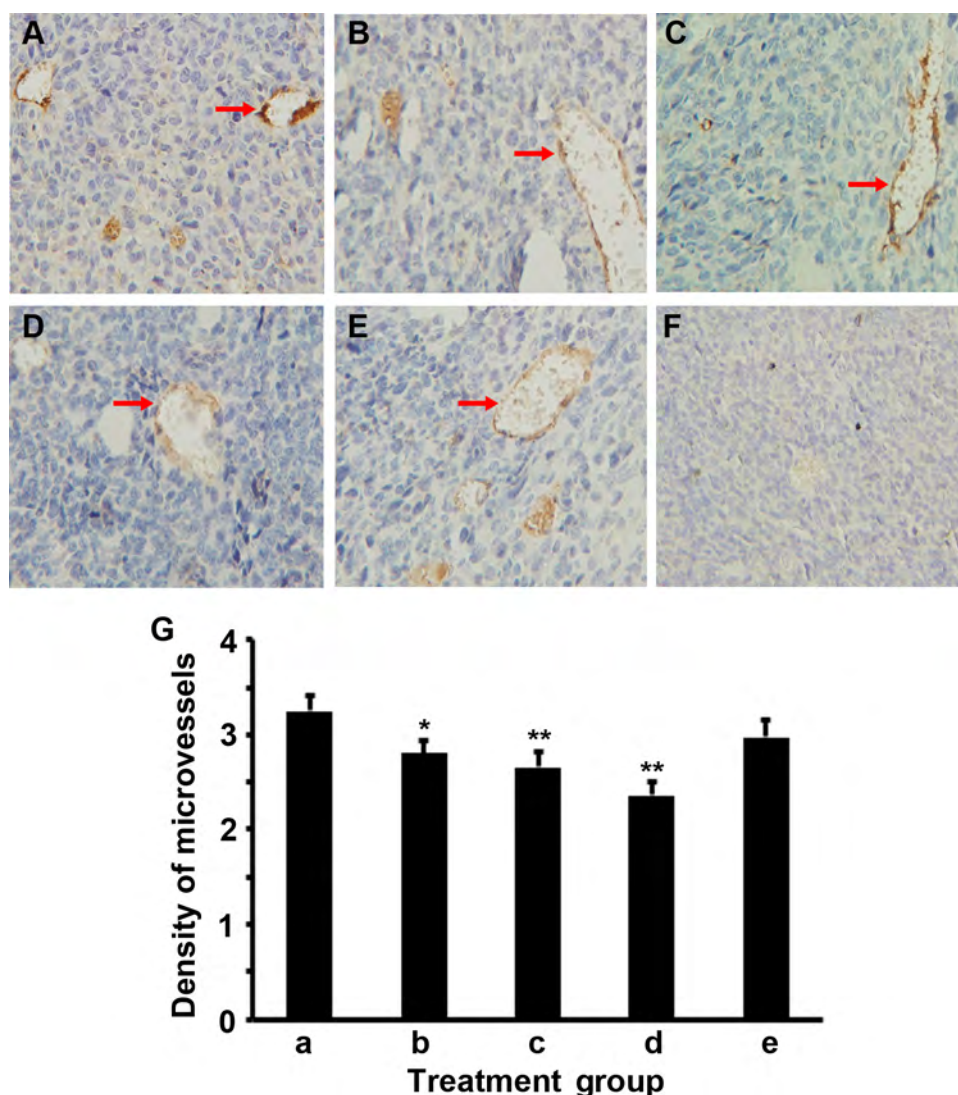


Figure 6 IFN γ and celecoxib decrease the density of microvessels in the tumors.

Notes: (A–E) Representative immunohistochemical staining of factor VIII to show the microvessels in the mouse tumors from groups a–e, ie, a, control; b, IFN γ ; c, celecoxib; d, IFN γ + celecoxib; and e, zoledronic acid. Arrows indicate the factor VIII-positive microvessels. Original magnification 200 \times . (F) Negative control of staining. (G) The density of microvessels in the mouse tumors. Data represent means \pm SEM (error bars; n=15 tumors per group). * P <0.05; ** P <0.01.

Abbreviation: SEM, standard error of the mean.

thus decreasing expression of MMP-2, MMP-9, and VEGF and associated angiogenesis, resulting in inhibition of mouse lung-tumor growth. IFN γ and celecoxib given at the current doses and schedules appear to have neither any synergy in modulating the M2/M1 macrophage ratio nor any synergy in inhibiting tumor growth.

It has been shown that TAM depletion reprograms the immunosuppressive tumor microenvironment and creates an antitumor immune microenvironment in breast cancer and liver cancer.^{23,32} TAMs may be a therapeutic target in other tumors, such as prostate cancer, renal cell carcinoma, and osteosarcoma.^{31,33,34} In addition, anti-EGFR antibody (cetuximab) may activate M2 macrophages, which might be the

reason that addition of cetuximab to bevacizumab plus chemotherapy showed a negative outcome.³⁵ This finding implies that anti-TAM approaches may have potential in combinatory therapies. In this study, we tested if TAM depletion by zoledronic acid could affect tumor growth in our mouse lung cancer model. We did not find any inhibition of tumor growth in the first experiment, but we did see a 16% decrease in the tumor weight in the second experiment. The percentage of total macrophages was decreased in both experiments. We speculate that the discrepancy between the two experiments may be due to the difference in tumor growth. On average, the tumors in the first experiment grew much bigger than the second experiment. Although we implanted the same

number of cells in both experiments, it could be that the cell viability and cellular growth status were not the same, so the live cell number was fewer in the second experiment than the first experiment. Therefore, inhibition of tumor growth was more obvious in the second experiment by IFN γ alone, celecoxib alone, and a combination of IFN γ and celecoxib, as well as zoledronic acid. Although zoledronic acid reduced expression of MMP-2 and MMP-9, it did not affect VEGF expression or the density of microvessels in the tumors. This may partially explain the fact that in small tumors, zoledronic acid may have some effects, but in large tumors where more angiogenesis occurs, zoledronic acid becomes ineffective in treating subcutaneous tumors. It is worth pointing out that zoledronic acid has only been approved for treating multiple myeloma and cancer bone metastasis, as well as other bone-related diseases.³⁶ Based on our study, we are not optimistic about zoledronic acid's effects on lung tumors other than bone metastasis.

One limitation of the present study is that only a single dosage of each drug was tested. The doses and administration schedules were chosen based on previous reports.^{37–39} It is reasonable to speculate that those doses may not necessarily be the optimal ones. Nevertheless, the positive results from the empirical doses used in this study are encouraging. Future studies are warranted to investigate the dose-dependent effects of IFN γ alone, celecoxib alone, and a combination of the optimal doses of IFN γ and celecoxib. The second limitation is that the treatments were given immediately after tumor inoculation. Any effects should be considered prophylactic in terms of preventing tumor growth, and the effects observed were minimal. The design of treatments after establishment of tumors and optimization to obtain more dramatic effects shall be considered in further studies. The third limitation of this study is that only CD68 in combination with iNOS and ARG1 were used for defining M1 and M2 macrophages, because the flow-cytometry instrument used was only able to show three colors. Ideally, a panel of six to eight markers (including F4/80) should be used. Finally, the association between macrophages and MMP-2, MMP-9, and VEGF is only suggestive, as other cells (tumor cells, fibroblasts, etc) may also express them.

In conclusion, this study provides the proof of principle that IFN γ and/or celecoxib treatment may inhibit lung-tumor growth through modulating the M2/M1 macrophage ratio in the tumor microenvironment, suggesting that IFN γ and celecoxib have potential to be further optimized in a new anticancer therapy.

Acknowledgments

This work was partially supported by the National Natural Science Foundation of China (NSFC 81172236 – The mechanism of TAMs activation in lung cancer and a novel immunotherapy; NSFC 81372505 – The role of IL-17 in formation and progression of primary lung cancer and the underlying molecular mechanisms) and the Key Science and Technology Program of Sichuan Province, People's Republic of China (2009SZ0152 and 2011SZ0111) to LL. ZY was partially supported by two grants from the National Institute of General Medical Sciences (P20GM103518) and the National Cancer Institute (R01CA174714) of the National Institutes of Health, three grants from Department of Defense Health Program through the Prostate Cancer Research Program (W81XWH-14-1-0050, W81XWH-14-1-0149, and PC130118; the US Army Medical Research Acquisition Activity, 820 Chandler Street, Fort Detrick, MD 21702-5014 is the awarding and administering acquisition office), the Developmental Fund of Tulane Cancer Center (TCC), and Louisiana Cancer Research Consortium (LCRC) Fund. The content of this article is solely the responsibility of the authors, and does not necessarily represent the official views of the National Institutes of Health or the Department of Defense.

Disclosure

The authors report no conflicts of interest in this work.

References

1. Ledford H. Cancer treatment: the killer within. *Nature*. 2014; 508(7494):24–26.
2. Kantoff PW, Higano CS, Shore ND, et al. Sipuleucel-T immunotherapy for castration-resistant prostate cancer. *N Engl J Med*. 2010;363(5): 411–422.
3. Hodi FS, O'Day SJ, McDermott DF, et al. Improved survival with ipilimumab in patients with metastatic melanoma. *N Engl J Med*. 2010;363(8):711–723.
4. Harvey RD. Immunologic and clinical effects of targeting of PD-1 in lung cancer. *Clin Pharmacol Ther*. 2014;96(2):214–223.
5. Topalian SL, Hodi FS, Brahmer JR, et al. Safety, activity, and immune correlates of anti-PD-1 antibody in cancer. *N Engl J Med*. 2012;366(26): 2443–2454.
6. Brahmer JR, Tykodi SS, Chow LQ, et al. Safety and activity of anti-PD-L1 antibody in patients with advanced cancer. *N Engl J Med*. 2012;366(26):2455–2465.
7. Lipson EJ, Sharfman WH, Drake CG, et al. Durable cancer regression off-treatment and effective reinduction therapy with an anti-PD-1 antibody. *Clin Cancer Res*. 2013;19(2):462–468.
8. Witz IP, Levy-Nissenbaum O. The tumor microenvironment in the post-PAGET era. *Cancer Lett*. 2006;242(1):1–10.
9. Lewis CE, Pollard JW. Distinct role of macrophages in different tumor microenvironments. *Cancer Res*. 2006;66(2):605–612.
10. Mantovani A, Sica A, Locati M. New vistas on macrophage differentiation and activation. *Eur J Immunol*. 2007;37(1):14–16.
11. Mantovani A, Sica A, Locati M. Macrophage polarization comes of age. *Immunity*. 2005;23(4):344–346.

12. Baj-Krzyworzeka M, Szatanek R, Weglarczyk K, Baran J, Zembala M. Tumor-derived microvesicles modulate biological activity of human monocytes. *Immunol Lett*. 2007;113(2):76–82.
13. Mantovani A, Sozzani S, Locati M, Allavena P, Sica A. Macrophage polarization: tumor-associated macrophages as a paradigm for polarized M2 mononuclear phagocytes. *Trends Immunol*. 2002;23(11):549–555.
14. Martinez FO, Sica A, Mantovani A, Locati M. Macrophage activation and polarization. *Front Biosci*. 2008;13:453–461.
15. Gordon S. Alternative activation of macrophages. *Nat Rev Immunol*. 2003;3(1):23–35.
16. Mantovani A, Bottazzi B, Colotta F, Sozzani S, Ruco L. The origin and function of tumor-associated macrophages. *Immunol Today*. 1992;13(7):265–270.
17. Galdiero MR, Garlanda C, Jaillon S, Marone G, Mantovani A. Tumor associated macrophages and neutrophils in tumor progression. *J Cell Physiol*. 2013;228(7):1404–1412.
18. Ma J, Liu L, Che G, Yu N, Dai F, You Z. The M1 form of tumor-associated macrophages in non-small cell lung cancer is positively associated with survival time. *BMC Cancer*. 2010;10:112.
19. Liu L, Ge D, Ma L, et al. Interleukin-17 and prostaglandin E2 are involved in formation of an M2 macrophage-dominant microenvironment in lung cancer. *J Thorac Oncol*. 2012;7(7):1091–1100.
20. Davis MJ, Tsang TM, Qiu Y, et al. Macrophage M1/M2 polarization dynamically adapts to changes in cytokine microenvironments in *Cryptococcus neoformans* infection. *MBio*. 2013;4(3):e00264–13.
21. Sica A, Mantovani A. Macrophage plasticity and polarization: in vivo veritas. *J Clin Invest*. 2012;122(3):787–795.
22. Zhang H, Li Z, Wang K. Combining sorafenib with celecoxib synergistically inhibits tumor growth of non-small cell lung cancer cells in vitro and in vivo. *Oncol Rep*. 2014;31(4):1954–1960.
23. Zhang W, Zhu XD, Sun HC, et al. Depletion of tumor-associated macrophages enhances the effect of sorafenib in metastatic liver cancer models by antimetastatic and antiangiogenic effects. *Clin Cancer Res*. 2010;16(13):3420–3430.
24. Bertram JS, Janik P. Establishment of a cloned line of Lewis lung carcinoma cells adapted to cell culture. *Cancer Lett*. 1980;11(1):63–73.
25. Zhang Q, Liu S, Ge D, et al. Interleukin-17 promotes formation and growth of prostate adenocarcinoma in mouse models. *Cancer Res*. 2012;72(10):2589–2599.
26. Dai F, Liu L, Che G, et al. The number and microlocalization of tumor-associated immune cells are associated with patient's survival time in non-small cell lung cancer. *BMC Cancer*. 2010;10:220.
27. Rahman MA, Dhar DK, Yamaguchi E, et al. Coexpression of inducible nitric oxide synthase and COX-2 in hepatocellular carcinoma and surrounding liver: possible involvement of COX-2 in the angiogenesis of hepatitis C virus-positive cases. *Clin Cancer Res*. 2001;7(5):1325–1332.
28. Weidner N. Current pathologic methods for measuring intratumoral microvessel density within breast carcinoma and other solid tumors. *Breast Cancer Res Treat*. 1995;36(2):169–180.
29. Redente EF, Dwyer-Nield LD, Merrick DT, et al. Tumor progression stage and anatomical site regulate tumor-associated macrophage and bone marrow-derived monocyte polarization. *Am J Pathol*. 2010;176(6):2972–2985.
30. Zhang M, He Y, Sun X, et al. A high M1/M2 ratio of tumor-associated macrophages is associated with extended survival in ovarian cancer patients. *J Ovarian Res*. 2014;7(1):19.
31. Lanciotti M, Masieri L, Raspollini MR, et al. The role of M1 and M2 macrophages in prostate cancer in relation to extracapsular tumor extension and biochemical recurrence after radical prostatectomy. *Biomed Res Int*. 2014;2014:486798.
32. DeNardo DG, Brennan DJ, Rexhepaj E, et al. Leukocyte complexity predicts breast cancer survival and functionally regulates responses to chemotherapy. *Cancer Discov*. 2011;1(1):54–67.
33. Santoni M, Massari F, Amantini C, et al. Emerging role of tumor-associated macrophages as therapeutic targets in patients with metastatic renal cell carcinoma. *Cancer Immunol Immunother*. 2013;62(12):1757–1768.
34. Pahl JH, Kwappenberg KM, Varypataki EM, et al. Macrophages inhibit human osteosarcoma cell growth after activation with the bacterial cell wall derivative liposomal muramyl tripeptide in combination with interferon- γ . *J Exp Clin Cancer Res*. 2014;33:27.
35. Pander J, Heusinkveld M, van der Straaten T, et al. Activation of tumor-promoting type 2 macrophages by EGFR-targeting antibody cetuximab. *Clin Cancer Res*. 2011;17(17):5668–5673.
36. Ibrahim A, Scher N, Williams G, et al. Approval summary for zoledronic acid for treatment of multiple myeloma and cancer bone metastases. *Clin Cancer Res*. 2003;9(7):2394–2399.
37. Senzaki M, Ishida S, Yada A, et al. CS-706, a novel cyclooxygenase-2 selective inhibitor, prolonged the survival of tumor-bearing mice when treated alone or in combination with anti-tumor chemotherapeutic agents. *Int J Cancer*. 2008;122(6):1384–1390.
38. Curmis F, Gasparri A, Sacchi A, Cattaneo A, Magni F, Corti A. Targeted delivery of IFN γ to tumor vessels uncouples antitumor from counter-regulatory mechanisms. *Cancer Res*. 2005;65(7):2906–2913.
39. Hung TT, Chan J, Russell PJ, Power CA. Zoledronic acid preserves bone structure and increases survival but does not limit tumour incidence in a prostate cancer bone metastasis model. *PLoS One*. 2011;6(5):e19389.

Drug Design, Development and Therapy

Publish your work in this journal

Drug Design, Development and Therapy is an international, peer-reviewed open-access journal that spans the spectrum of drug design and development through to clinical applications. Clinical outcomes, patient safety, and programs for the development and effective, safe, and sustained use of medicines are a feature of the journal, which

Submit your manuscript here: <http://www.dovepress.com/drug-design-development-and-therapy-journal>

Dovepress

has also been accepted for indexing on PubMed Central. The manuscript management system is completely online and includes a very quick and fair peer-review system, which is all easy to use. Visit <http://www.dovepress.com/testimonials.php> to read real quotes from published authors.



International Journal of Shoulder Surgery

Volume 8

Issue 3

Jul-Sep 2014

Contents

- ▶ Decreased scapular notching with lateralization and inferior baseplate placement in reverse shoulder arthroplasty with high humeral inclination
- ▶ Short stem shoulder replacement
- ▶ Long-term functional results and isokinetic strength evaluation after arthroscopic tenotomy of the long head of biceps tendon
- ▶ Comparison of the cheese-wiring effects among three sutures used in rotator cuff repair
- ▶ Noncomminuted lateral end clavicle fractures associated with coracoclavicular ligament disruption: Technical considerations for optimal anatomic fixation and stability
- ▶ Scapular spine stress fractures: To fix or not to fix, our experience in a patient with bilateral fractures and review of the literature



Comparison of the cheese-wiring effects among three sutures used in rotator cuff repair

Mark Lambrechts^{1,2}, Behrooz Nazari³, Arash Dini¹, Michael J. O'Brien¹, Wendell M. R. Heard¹, Felix H. Savoie¹, Zongbing You^{1,2,4}

ABSTRACT

Purpose: The goal of this study was to compare the cheese-wiring effects of three sutures with different coefficients of friction.

Materials and Methods: Sixteen human cadaveric shoulders were dissected to expose the distal supraspinatus and infraspinatus muscle tendons. Three sutures were stitched through the tendons: #2 Orthocord™ suture (reference #223114, DePuy Mitek, Inc., Raynham, MA), #2 ETHIBOND* EXCEL Suture, and #2 FiberWire® suture (FiberWire®, Arthrex, Naples, FL). The sutures were pulled by cyclic axial forces from 10 to 70 N at 1 Hz for 1000 cycles through a MTS machine. The cut-through distance on the tendon was measured with a digital caliper.

Results: The cut-through distance in the supraspinatus tendons (mean ± standard deviation, $n = 12$) were 2.9 ± 0.6 mm for #2 Orthocord™ suture, 3.2 ± 1.2 mm for #2 ETHIBOND* suture, and 4.2 ± 1.7 mm for #2 FiberWire® suture. The differences were statistically significant analyzing with analysis of variance ($P = 0.047$) and two-tailed Student's *t*-test, which showed significance between Orthocord™ and FiberWire® sutures ($P = 0.026$), but not significant between Orthocord™ and ETHIBOND* sutures ($P = 0.607$) or between ETHIBOND* and FiberWire® sutures ($P = 0.103$).

Conclusion: The cheese-wiring effect is less in the Orthocord™ suture than in the FiberWire® suture in human cadaveric supraspinatus tendons.

Clinical Relevance: Identification of sutures that cause high levels of tendon cheese-wiring after rotator cuff repair can lead to better suture selection.

Key words: Biomechanics, cadaver study, cheese-wiring, supraspinatus tendon, suture

INTRODUCTION

Rotator cuff tear is one of the most common injuries involving the shoulder. The tear most often involves the supraspinatus tendon. Without prompt treatment, the altered joint biomechanics can extend the tear to involve the infraspinatus tendon.^[1,2] Repair of these injuries is based on individual patients with few protocols established to determine whether the patient best fits for steroid injection, physical therapy, or surgical intervention. However, surgery is generally recommended for all symptomatic patients younger than 60 with a full-thickness rotator cuff tear.^[3] The expected outcome of surgery is a high

fixation strength, but many variables can affect the success of surgery including the patient's age, tendon health, smoking, time from tear to surgery, arthroscopic technique, suture location, and suture selection.^[4-7]

The choice of sutures has not been well studied. It has been reported that the suture location is a key factor in causing damage to the repaired tendons. Wieser *et al.*^[8] found the ideal placement to be located in the center of the tendon just medial to the rotator cable. This finding is in contrast to Wang *et al.*^[9] who found an ideal location of suture placement more medially at the muscle-tendon junction. Clearly, location of

Access this article online

Website:

www.internationalshoulderjournal.org

DOI:

10.4103/0973-6042.140115

Quick Response Code:



¹Department of Orthopaedic Surgery and Tulane Institute of Sports Medicine, Tulane University, School of Medicine, ²Department of Structural and Cellular Biology, Tulane University School of Medicine, ⁴Tulane Cancer Center, Louisiana Cancer Research Consortium, Tulane Center for Aging, Tulane Center for Stem Cell Research and Regenerative Medicine, Tulane University School of Medicine, New Orleans, LA 70112, USA, ³Department of Orthopaedics, Tabriz Emam Reza Hospital, Tabriz, Iran

Address for correspondence:

Prof. Zongbing You,
1430 Tulane Ave SL 49, New Orleans,
LA 70112, USA.
E-mail: zyou@tulane.edu

the placed sutures is important in minimizing postsurgical tendon damage, but the properties of the sutures should also be a consideration. Unfortunately, it is not easy to evaluate different sutures because different types of repair define surgical success differently. For example, rotator cuff repair requires suture stability under high load requirements, while flexor tendon repair requires minimal friction. Nevertheless, there are several well-recognized suture properties including the tensile strength, knot security, stiffness, and resistance to fraying.^[10-15]

Coefficient of friction is an inherent property of the suture, which has not been well investigated. Silva *et al.*^[6] found that #3-0 FiberWire® sutures (FiberWire®, Arthrex, Naples, FL) had a lower coefficient of friction (0.054) than #3-0 ETHIBOND® sutures (with a coefficient of friction of 0.076) (ETHIBOND® EXCEL, Ethicon, Somerville, NJ). We speculate that coefficient of friction may be an important factor in determining how easy the suture cuts through the tendon, that is, the cheese-wiring effect. Our hypothesis is that the sutures with lower coefficient of friction may be easier to cut-through the tendon than the sutures with higher coefficient of friction. The present study was conducted to test this hypothesis.

MATERIALS AND METHODS

This study was conducted using human cadaveric supraspinatus and infraspinatus muscle tendons. Eight pairs of unembalmed human shoulders ($n = 16$) were obtained from donors through the Bureau of Anatomical Services, Louisiana State Department of Health and Hospitals. The average age of the donors was 77.1 ± 9.8 years of age. The use of these deidentified specimens was determined as “not human subjects study” by Tulane University Institutional Review Board (Project no. 206610-1). The specimens were stored at -20°C and thawed at room temperature prior to use. Only grossly intact tendons without obvious damage were used for the study. Twelve supraspinatus tendons ($n = 12$) were dissected out and detached distally from the greater tubercle of the humerus. The supraspinatus muscles remained attached to the scapula and the subscapularis and infraspinatus muscles remained undisturbed during testing of the supraspinatus tendons. After testing on the supraspinatus tendons, the infraspinatus tendons were dissected out and detached distally, while the infraspinatus muscle remained attached to the scapula. Only 5 infraspinatus tendons ($n = 5$) were not damaged and were used for testing. The three types of sutures used in this study were #2 FiberWire® suture (reference #AR-7200, Arthrex, Inc., Naples, FL), #2 ETHIBOND® EXCEL suture (reference #X519, Ethicon, Inc., Somerville, NJ), and #2 Orthocord™ suture (reference #223114, DePuy Mitek, Inc., Raynham, MA). FiberWire® suture is constructed of a multi-strand, long chain ultra-high molecular weight polyethylene (UHMWPE) core with a braided jacket of polyester and UHMWPE. ETHIBOND® suture is composed of a braided polyester core coated with polybutylate. Orthocord™ suture is made with a braided polyethylene core coated with a copolymer of caprolactone and glycolide.

Biomechanical testing

We used a Bionix Servohydraulic Test System (MTS Systems Corporation, Eden Prairie, MN) for the mechanic tests. The scapula with the proximal attachment of supraspinatus (or infraspinatus) muscle was fixed to the sensor stage using a custom-made frame [Figure 1a]. A single pass-through suture loop was placed through the supraspinatus (or infraspinatus) tendon approximately 5 mm distal to the muscle-tendon junction [Figure 1b]. The other end of the suture loop was attached to the actuator [Figure 1a]. The specimen was kept moist at all times by spraying of phosphate buffered saline.

In our pilot study, two shoulders were used to determine the testing conditions. A force of 10 N was applied to preload the tendon and the suture for 1 min. No cutting through of the tendon was observed by any of the three sutures at 10 N loading. A mark line (start line) was made on the tendon with a marker pen. Then, a 10-50 N at 1 Hz for 1000 cycles of cyclic pulling load was applied to the suture. At the end of 1000 cycles, any cut-through of the tendon by the suture was recorded manually with a digital caliper [Figure 1c]. Then, the load was returned to 10 N for 1 min. Next, this step was repeated at 10-70 N at 1 Hz for 1000 cycles. Again, the cut-through distance was recorded. Finally, this step was repeated at 10-100 N at 1 Hz for 1000 cycles. However, at this load, all three sutures completely cut-through the tendon when the load was approximately 80-85 N. Therefore, we decided to test each suture by applying 10-70 N at 1 Hz for 1000 cycles.

Twelve supraspinatus muscle tendons were tested first, followed by testing five infraspinatus muscle tendons. The three sutures were tested on each tendon side-by-side, with approximately 5 mm inter-stitch distance. Each of the three sutures was stitched in an alternated order, so that the location of stitch

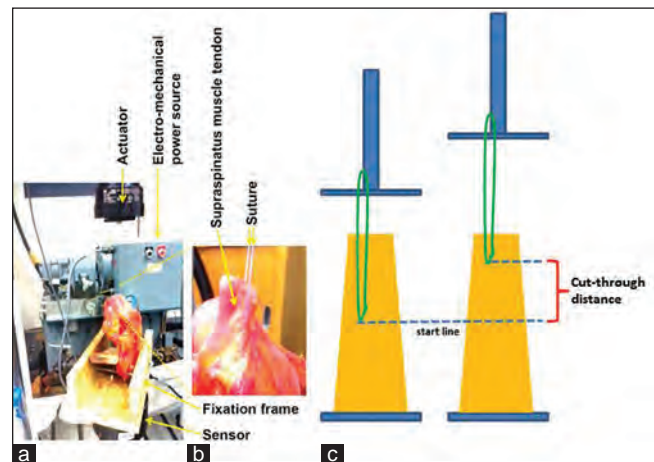


Figure 1: Illustration of how the mechanic testing was performed. (a) The specimen was fixed to the sensor of an MTS machine by a fixation frame; the suture was stitched through the supraspinatus muscle-tendon and connected to the actuator; and a computer (not shown) controlled the electro-mechanical power source to drive the actuator to provide uniaxial tensile force loading on the suture, and recorded the load and displacement through the testing time period. (b) A representative close-up picture showing the tendon and suture. (c) An illustration of how the cut-through in the tendon was recorded

and order of testing were equally assigned to each suture. For example, on tendon #1, Orthocord™ suture was tested first, followed by ETHIBOND* suture and then FiberWire® suture. On tendon #2, the order of testing was ETHIBOND*, FiberWire®, and Orthocord™. On tendon #3, the order of testing was FiberWire®, Orthocord™, and ETHIBOND*. On tendons #4-12, the alternating order was repeated. The three investigators (M.L., B.N., and A.D.) who performed the tests were blinded to the sources of the sutures during testing.

Measurement of the cut-through distance

After 1000 cycles of 10-70 N loading at 1 Hz were completed, the force was returned to 10 N. The cut-through distance [Figure 1c] was measured manually with a digital caliper. This cut-through distance is called displacement, which represents the cheese-wiring effect of the suture. The MTS machine also continuously recorded the axial displacement during the 1000 cycles, which was the change of distance between the sensor and actuator, including the cut-through distance and stretching of the muscle, tendon, and suture.

Statistical analysis

The displacement and axial displacement were shown as means and standard deviations. The data was analyzed with analysis of variance (ANOVA) software provided by GraphPad Prism (GraphPad Software, Inc., La Jolla, CA) and using two-tailed Student's *t*-test. The significance was set at $P < 0.05$.

RESULTS

We found that the axial displacement, as recorded by the MTS machine, was proportional to the cyclic load applied to each suture [Figure 2a-f]. In the tests of 12 supraspinatus tendons, the displacements (i.e., the cut-through distances on the tendons), as manually recorded with a digital caliper at the end of 1000 cycles of loading, were 2.9 ± 0.6 mm for #2 Orthocord™ suture, 3.2 ± 1.2 mm for #2 ETHIBOND* suture, and 4.2 ± 1.7 mm

for #2 FiberWire® suture. Statistical significance existed using ANOVA ($P = 0.047$) and comparing Orthocord™ to FiberWire® sutures ($P = 0.026$), however, the difference was not statistically significant between ETHIBOND* and FiberWire® sutures ($P = 0.103$) or between Orthocord™ and ETHIBOND* sutures ($P = 0.607$) [Figure 3a]. The axial displacements, as recorded by the MTS machine from cycle 1 to 1000, were not statistically different among the three sutures [$P > 0.05$, Figure 3b]. However, the axial displacement from cycle 100 to 1000, while not significant with ANOVA, was clearly longer in FiberWire® suture than in Orthocord™ or ETHIBOND* sutures [Figure 3c]. The difference was statistically significant between Orthocord™ and FiberWire® sutures ($P = 0.022$) and between ETHIBOND* and FiberWire® sutures ($P = 0.011$), but there was no statistical significance between Orthocord™ and ETHIBOND* sutures ($P = 0.510$) [Figure 3d].

In the tests of 5 infraspinatus tendons, the displacements (i.e., the cut-through distances on the tendons), as manually recorded with a digital caliper at the end of 1000 cycles of loading, were 6.7 ± 2.0 mm for #2 Orthocord™ suture and 6.1 ± 0.6 mm for #2 ETHIBOND* suture, which was not statistically significant [$P = 0.612$, Figure 4a]. In contrast, #2 FiberWire® suture completely cut-through the infraspinatus tendon, which was >15 mm from start line to the distal end of the tendon. The axial displacements, as recorded by the MTS machine from cycle 1 to 1000, were not statistically different between Orthocord™ and ETHIBOND* sutures [$P > 0.05$, Figure 4b-c].

DISCUSSION

This study found that #2 FiberWire® suture cuts through the supraspinatus tendon easier than #2 Orthocord™ suture under 1000 cycles of 10-70 N loading conditions. This finding was further supported by the tests with infraspinatus tendons, as #2 FiberWire® suture completely cut-through the tendon (>15 mm) whereas #2 Orthocord™ suture only cut-through <7 mm. Similarly, #2 ETHIBOND* suture only cut-through the infraspinatus tendons for approximately 6 mm. These findings suggest the #2 FiberWire® is more likely to cut-through the tendons than #2 Orthocord™ or ETHIBOND* suture. Although the difference is about 1 mm after 1000 cycles of loading at up to 70 N, the difference may be bigger at higher loads and/or more cycles.

It is worth pointing out that the overall axial displacements caused by the three sutures were of no difference [Figure 3b], which is contradictory to our manual measurement [Figure 3a]. We consider that this axial displacement, as recorded by the MTS machine, was the change of distance between the actuator and the sensor, including the cut-through by the suture and the stretched length of the muscle, tendon and suture. Thus, this axial displacement does not accurately reflect the cut-through by the suture at the beginning of the cyclic loading when the loading mainly stretched the muscle and tendon. This explanation is supported by our finding that the axial

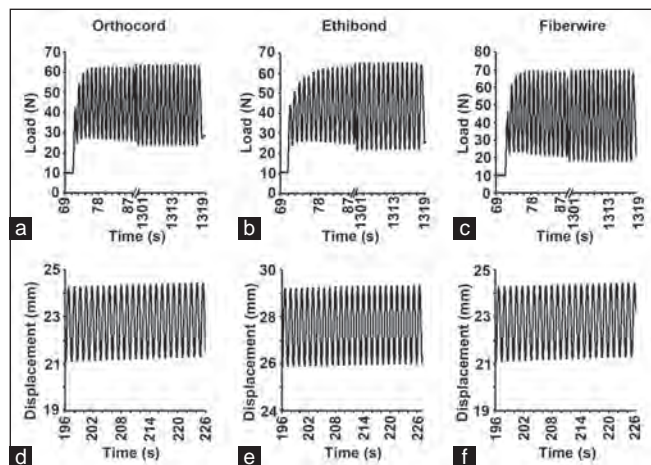


Figure 2: Representative recordings of uniaxial cyclic loading force over time (a-c) and axial displacement over time (d-f)

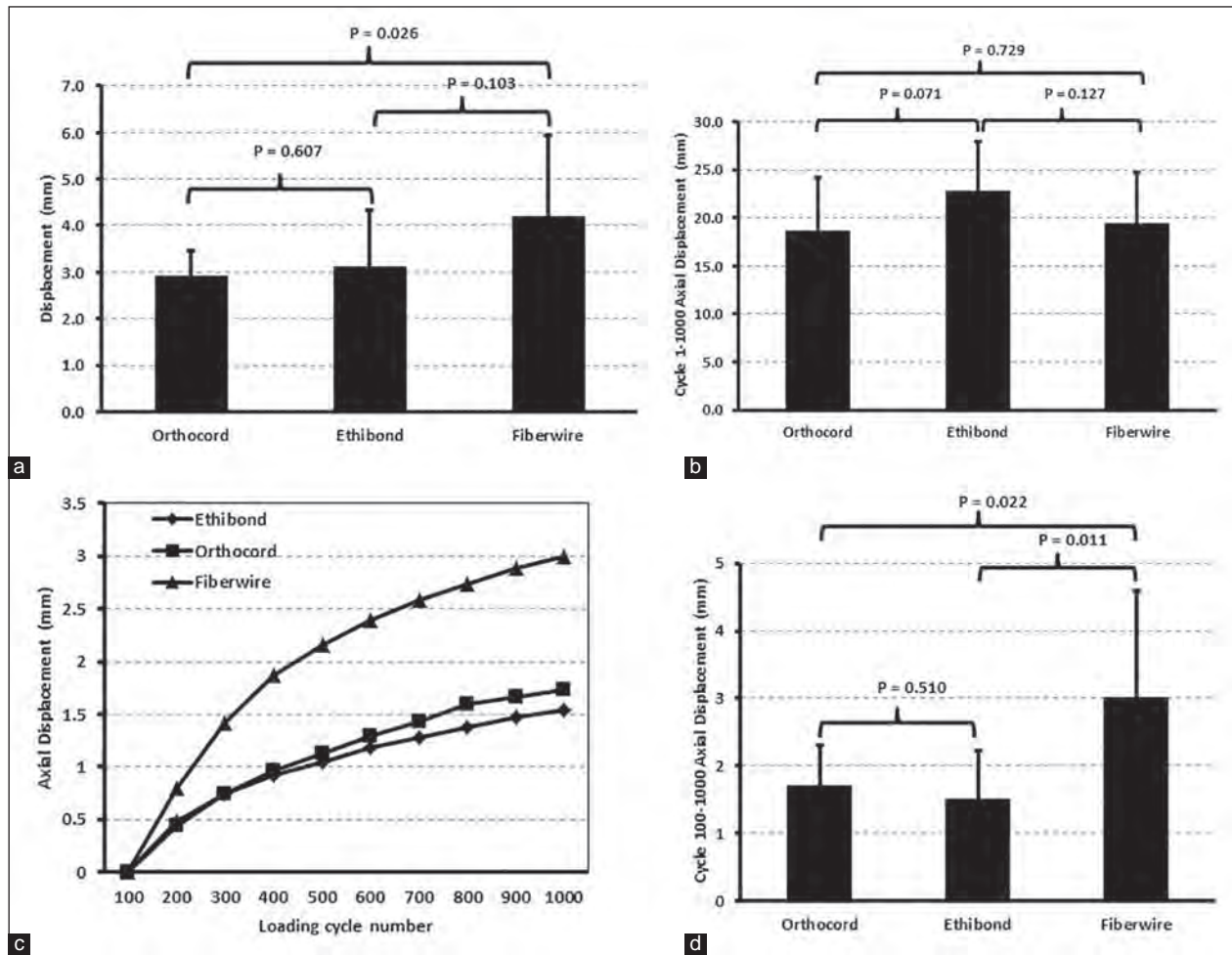


Figure 3: The displacements of sutures in the supraspinatus tendons recorded manually and automatically by the MTS machine. (a) The displacement (cut-through distance) of sutures measured manually with a digital caliper at the end of 1000 cycles of 10-70 N loading. (b) The overall axial displacements of sutures recorded by the MTS machine at the end of 1000 cycles of 10-70 N loading, which included the cut-through distance and the stretching of the muscle, tendon, and suture. (c) The axial displacements of sutures recorded by the MTS machine from 100 to 1000 cycles of 10-70 N loading. (d) The axial displacements of sutures at the end of 1000 cycles, recorded by the MTS machine from 100 to 1000 cycles of 10-70 N loading. The data represent means \pm standard deviations (error bars, $n = 12$)

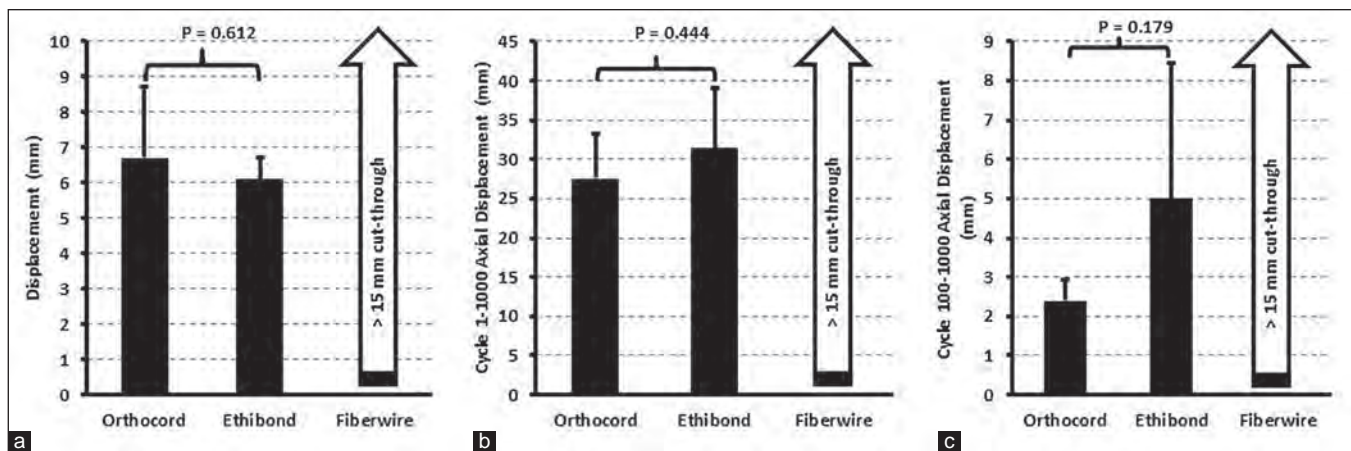


Figure 4: The displacements of sutures in the infraspinatus tendons recorded manually and automatically by the MTS machine. (a) The displacement (cut-through distance) of sutures measured manually with a digital caliper at the end of 1000 cycles of 10-70 N loading. (b) The overall axial displacements of sutures recorded by the MTS machine at the end of 1000 cycles of 10-70 N loading, which included the cut-through distance and the stretching of the muscle, tendon, and suture. (c) The axial displacements of sutures at the end of 1000 cycles, recorded by the MTS machine from 100 to 1000 cycles of 10-70 N loading. Of note, FiberWire® suture completely cut-through the infraspinatus tendons for a distance >15 mm. The data represent means \pm standard deviations (error bars, $n = 5$)

displacements from cycles 100 to 1000 [Figure 3c-d] were consistent to our manual measurement [Figure 3a], because at this late stage the axial displacement mainly reflects the cut-through after the muscle and tendon had already been stretched by the initial pulling loads.

We speculate that the observed differences in the cut-through (or cheese-wiring effect) are due to the different coefficients of friction of sutures. It has been reported that #3-0 FiberWire® suture had a lower coefficient of friction than #3-0 ETHIBOND® suture.^[16] This difference in friction may be caused by differences in material properties and the way how the strands are braided. FiberWire® suture is constructed of a multi-strand, long chain UHMWPE core with a braided jacket of polyester and UHMWPE. ETHIBOND® suture is composed of a braided polyester core coated with polybutylate. Orthocord™ suture is made with a braided polyethylene core coated with a copolymer of caprolactone and glycolide. Other physical properties of the sutures may also play a role. For example, it has been found that ETHIBOND® suture is considerably less stiff (13 ± 2 N/m) than FiberWire® suture (35 ± 6 N/m).^[12] This indicates that the stiffer FiberWire® suture may be more likely to cut-through the tendons.

This study has some limitations since it was a laboratory study using human cadaveric tendons. First, no healing occurred in the cadaveric specimens. In live patients, healing may occur between the physical loads, so as to mitigate the cheese-wiring effect. Second, only a single pass-through stitch was tested. This could be meaningful in clinical situations where this type of suture method is used to restore the continuity of broken tendons. However, this finding may not be applicable to other suture methods such as mattress or figure of eight sutures. Finally, only 10-70 N cyclic loading was tested. This was due to a limitation caused by the cadaveric tendon quality where a load of 80-85 N led to complete cut-through of the tendons. It is possible that higher loads may be applied to fresh (or live) tendons.

CONCLUSION

We found that #2 Orthocord™ and ETHIBOND® sutures cause less cheese-wiring effects than #2 FiberWire® suture in human cadaveric supraspinatus and infraspinatus tendons under 1000 cycles of 10-70 N cyclic pulling loads.

ACKNOWLEDGMENTS

The authors thank Eric Morales and Dr. Erich Richter (Department of Neurosurgery, Louisiana State University-New Orleans) and Rita Richardson and Donna Watkins (Department of Orthopaedic Surgery, Tulane University) for their laboratory assistance. Z. You was partially supported by two grants from the National Institute of General Medical Sciences (P20GM103518) and the National Cancer Institute (R01CA174714) of the National Institutes of Health, three grants from Department of Defense Health Program through the Prostate Cancer Research Program (W81XWH-14-1-0050, W81XWH-14-1-0149, and

PC130118; the U.S. Army Medical Research Acquisition Activity, 820 Chandler Street, Fort Detrick MD 21702-5014 is the awarding and administering acquisition office), the Developmental Fund of Tulane Cancer Center (TCC), and Louisiana Cancer Research Consortium (LCRC) Fund. The content of this article is solely the responsibility of the authors and does not necessarily represent the official views of the National Institutes of Health or the Department of Defense.

REFERENCES

1. Jerosch J, Müller T, Castro WH. The incidence of rotator cuff rupture. An anatomic study. *Acta Orthop Belg* 1991;57:124-9.
2. Lee TQ. Current biomechanical concepts for rotator cuff repair. *Clin Orthop Surg* 2013;5:89-97.
3. Williams GR Jr, Rockwood CA Jr, Bigliani LU, Iannotti JP, Stanwood W. Rotator cuff tears: Why do we repair them? *J Bone Joint Surg Am* 2004;86-A:2764-76.
4. Chung SW, Kim JY, Kim MH, Kim SH, Oh JH. Arthroscopic repair of massive rotator cuff tears: Outcome and analysis of factors associated with healing failure or poor postoperative function. *Am J Sports Med* 2013;41:1674-83.
5. Favard L, Bacle G, Berhouet J. Rotator cuff repair. *Joint Bone Spine* 2007;74:551-7.
6. Kukkonen J, Kauko T, Virolainen P, Äärämaa V. Smoking and operative treatment of rotator cuff tear. *Scand J Med Sci Sports* 2014;24:400-3.
7. Mukovozov I, Byun S, Farrokhhyar F, Wong I. Time to surgery in acute rotator cufftear: A systematic review. *Bone Joint Res* 2013;2:122-8.
8. Wieser K, Rahm S, Farshad M, Ek ET, Gerber C, Meyer DC. Stitch positioning influences the suture hold in supraspinatus tendon repair. *Knee Surg Sports Traumatol Arthrosc* 2013;21:1587-92.
9. Wang VM, Wang FC, McNickle AG, Friel NA, Yanke AB, Chubinskaya S, et al. Medial versus lateral supraspinatus tendon properties: Implications for double-row rotator cuff repair. *Am J Sports Med* 2010;38:2456-63.
10. Ilahi OA, Younas SA, Ho DM, Noble PC. Security of knots tied with ethibond, fiberwire, orthocord, or ultrabraid. *Am J Sports Med* 2008;36:2407-14.
11. Mahar AT, Moezzi DM, Serra-Hsu F, Pedowitz RA. Comparison and performance characteristics of 3 different knots when tied with 2 suture materials used for shoulder arthroscopy. *Arthroscopy* 2006;22:614.e1-2.
12. Najibi S, Banglmeier R, Matta J, Tannast M. Material properties of common suture materials in orthopaedic surgery. *Iowa Orthop J* 2010;30:84-8.
13. Swan KG Jr, Baldini T, McCarty EC. Arthroscopic suture material and knot type: An updated biomechanical analysis. *Am J Sports Med* 2009;37:1578-85.
14. Wright PB, Budoff JE, Yeh ML, Kelm ZS, Luo ZP. Strength of damaged suture: An *in vitro* study. *Arthroscopy* 2006;22:1270-1275.e3.
15. Wüst DM, Meyer DC, Favre P, Gerber C. Mechanical and handling properties of braided polyblend polyethylene sutures in comparison to braided polyester and monofilament polydioxanone sutures. *Arthroscopy* 2006;22:1146-53.
16. Silva JM, Zhao C, An KN, Zobitz ME, Amadio PC. Gliding resistance and strength of composite sutures in human flexor digitorum profundus tendon repair: An *in vitro* biomechanical study. *J Hand Surg Am* 2009;34:87-92.

Source of Support and Conflict of Interests: This work was partially supported by a grant provided by DePuy Mitek, Inc., to Tulane University (No. 551206, to Z.Y., F.H.S., and M.J.O.). F.H.S. is an unpaid consultant of DePuy Mitek, Inc., Smith & Nephew plc, and Rotation Medical and Biomet Sports Medicine, as well as a board member of the Arthroscopy Association of North America Education Foundation and of the Trustees for Arthroscopy.



AZD5363 inhibits inflammatory synergy between interleukin-17 and insulin/insulin-like growth factor 1

Chong Chen^{1,2}, Qiuyang Zhang^{1,2}, Sen Liu^{1,2}, Mark Lambrechts^{1,2}, Yine Qu^{1,2,3} and Zongbing You^{1,2*}

¹ Department of Structural and Cellular Biology, Tulane Cancer Center and Louisiana Cancer Research Consortium, Tulane Center for Stem Cell Research and Regenerative Medicine, Tulane Center for Aging, Tulane University School of Medicine, New Orleans, LA, USA

² Department of Orthopaedic Surgery, Tulane Cancer Center and Louisiana Cancer Research Consortium, Tulane Center for Stem Cell Research and Regenerative Medicine, Tulane Center for Aging, Tulane University School of Medicine, New Orleans, LA, USA

³ Department of Histology and Embryology, Hebei United University School of Basic Medicine, Tangshan, Hebei Province, China

Edited by:

Gyu Seog Choi, Kyungpook National University Medical Center, South Korea

Reviewed by:

Jennifer Wu, Medical University of South Carolina, USA
Chang-Deng Hu, Purdue University, USA

*Correspondence:

Zongbing You, Department of Structural and Cellular Biology, Tulane University School of Medicine, 1430 Tulane Avenue Mailbox 8649, New Orleans, LA 70112, USA
e-mail: zyou@tulane.edu

In the United States, one-third of population is affected by obesity and almost 29 million people are suffering from type 2 diabetes. Obese people have elevated serum levels of insulin, insulin-like growth factor 1 (IGF1), and interleukin-17 (IL-17). Insulin and IGF1 are known to enhance IL-17-induced expression of inflammatory cytokines and chemokines, which may contribute to the chronic inflammatory status observed in obese people. We have previously demonstrated that insulin/IGF1 signaling pathway crosstalks with IL-17-activated nuclear factor- κ B pathway through inhibiting glycogen synthase kinase 3 β (GSK3 β) activity. However, it is unclear whether GSK3 α also plays a role and whether this crosstalk can be manipulated by AZD5363, a novel pan-Akt inhibitor that has been shown to increase glycogen synthase kinase 3 activity through reducing phosphorylation of GSK3 α and GSK3 β . In this study, we investigated IL-17-induced expression of C-X-C motif ligand 1 (*Cxcl1*), C-C motif ligand 20 (*Ccl20*), and interleukin-6 (*Il-6*) in wild-type, GSK3 $\alpha^{-/-}$, and GSK3 $\beta^{-/-}$ mouse embryonic fibroblast cells as well as in mouse prostate tissues by real-time quantitative PCR. We examined the proteins involved in the signaling pathways by Western blot analysis. We found that insulin and IGF1 enhanced IL-17-induced expression of *Cxcl1*, *Ccl20*, and *Il-6*, which was associated with increased phosphorylation of GSK3 α and GSK3 β in the presence of insulin and IGF1. AZD5363 inhibited the synergy between IL-17 and insulin/IGF1 through reducing phosphorylation of GSK3 α and GSK3 β by inhibiting Akt function. These findings imply that the cooperative crosstalk of IL-17 and insulin/IGF1 in initiating inflammatory responses may be alleviated by AZD5363.

Keywords: IL-17, insulin, IGF1, inflammation, prostate cancer, obesity

INTRODUCTION

Interleukin-17 (IL-17 or IL-17A) is an inflammatory cytokine (1). It can activate nuclear factor- κ B (NF- κ B) activator 1 (Act1) through similar expression to fibroblast growth factor genes, IL-17 receptors, and Toll-IL-1R (SEFIR) domains, upon its binding to a heterodimer of IL-17RA/IL-17RC receptor complex (2–6). Act1, as an E3 ubiquitin ligase, activates tumor necrosis factor receptor-associated factor 6 (TRAF6) through lysine-63-linked

ubiquitination (7). The polyubiquitinated TRAF6 triggers transforming growth factor- β -activated kinase 1 (TAK1) and subsequently I κ B kinase (IKK) complex, which in turn leads to activation of NF- κ B pathway that induces transcription of a variety of cytokines, chemokines, and growth factor, e.g., C-X-C motif ligand 1 (*Cxcl1*) and IL-6 (8–10). Several studies have demonstrated that IL-17 stabilizes downstream *Cxcl1* mRNA through an inducible kinase IKKi-dependent Act1–TRAF2–TRAF5 complex, which ligands with splicing factor 2 [SF2, also named alternative splicing factor (ASF)] and prevents SF2/ASF-mediated mRNA degradation (11, 12).

Insulin is a hormone produced by the pancreas β cells, and its abnormal high concentration (hyperinsulinemia) may circulate in the body of people with obesity and type 2 diabetes mellitus with insulin resistance. Under hyperinsulinemic conditions, the liver produces insulin-like growth factor 1 (IGF1) (13). Two types of insulin receptors (IR-A and IR-B) can bind to either insulin or IGF1. IGF1 can also bind to a heterodimer of IR and IGF1 receptor (IGF1R). Upon binding with the receptors, insulin (or IGF1) leads to autophosphorylation of the β subunit of IR or IGF1R (14), which in turn recruits insulin receptor substrates-1 (IRS-1)

Abbreviations: Act1, NF- κ B activator 1; ASF, alternative splicing factor; CCL2, C-C motif ligand 2; Ccl20, C-C motif ligand 20; CCL7, C-C motif ligand 7; cDNA, complementary deoxyribonucleic acid; C/EBP β , CAAT enhancer binding protein β ; Cxcl1, C-X-C motif ligand 1; CXCL5, C-X-C motif ligand 5; DMEM, Dulbecco's modified eagle's medium; Gapdh, glyceraldehyde-3-phosphate dehydrogenase; GSK, glycogen synthase kinase; IGF1, insulin-like growth factor 1; IGF1R, insulin-like growth factor 1 receptor; IKK, I κ B kinase; IL-6, interleukin-6; IL-17, interleukin-17; IL-17R, interleukin-17 receptor; IR, insulin receptor; IRS, insulin receptor substrates; MEF, mouse embryonic fibroblast; mTORC2, mTor complex 2; NF- κ B, nuclear factor- κ B; PDK1, protein kinase 1; PH, pleckstrin homology; PI3K, phosphatidylinositol 3-kinase; SF2, splicing factor 2; SEFIR, similar expression to fibroblast growth factor genes, IL-17 receptors, and Toll-IL-1R; TAK1, transforming growth factor- β -activated kinase 1; TRAF6, tumor necrosis factor receptor-associated factor 6.

to IRS4, and then phosphatidylinositol 3-kinase (PI3K)/Akt pathway is activated (8). One of the major substrates of Akt is glycogen synthase kinase 3 β (GSK3 β) (8, 15). Previous studies have shown that insulin inactivates GSK3 β by inducing phosphorylation at serine 9 mainly via Akt signaling pathway (15, 16).

Glycogen synthase kinase 3 includes two type of isoforms GSK3 α and GSK3 β , which are ubiquitously expressed in all cells and capable of phosphorylating more than 50 substrates (17). One of the substrates, CAAT enhancer binding protein β (C/EBP β), is also induced by IL-17 (3, 9, 18). C/EBP β transcription factor is essential for transcription of IL-17 downstream target genes such as IL-6 and 24p3/lipocalin 2 (19). Phosphorylation of C/EBP β inhibits expression of IL-17 downstream target genes, thus GSK3 β negatively regulates IL-17 signaling through phosphorylation of C/EBP β (20). Indeed, inhibition of glycogen synthase kinase 3 (GSK3) activity by GSK3 inhibitor can enhance IL-17-induced expression of IL-6, 24p3/lipocalin 2, CXCL5, C-C motif ligand 2 (CCL2), CCL7, and NF- κ B inhibitor zeta, whereas, overexpression of GSK3 β can inhibit IL-17-induced IL-6 promoter and 24p3 promoter activities in a mouse stromal ST2 cell line (21). Therefore, GSK3 β functions as an intrinsic negative regulator of IL-17-mediated inflammatory responses (21). Our previous study has shown that GSK3 β inhibition by phosphorylation or gene knockout enhanced IL-17-induced expression of inflammatory cytokines and chemokines (8).

AZD5363 [(S)-4-amino-N-[1-(4-chlorophenyl)-3-hydroxypropyl]-1-(7H-pyrrolo [2, 3-d] pyrimidin-4-yl) piperidine-4-carboxamide] is a pan-Akt inhibitor that is currently being investigated in phase I clinical trials for cancer therapy (22, 23). Akt is a serine/threonine protein kinase, also known as protein kinase B (PKB), which regulates a variety of cellular process including cell proliferation, cell survival, and glucose and fatty acid metabolism (24–26). Because Akt signaling network is the key pro-tumor network in human cancers, it is a target in development of new therapies (27). The active form of Akt is phosphorylated Akt (P-Akt), which may occur at threonine 308 (Thr308) residue phosphorylated by 3-phosphoinositide dependent protein kinase 1 (PDK1), or at serine 473 (Ser 473) residue phosphorylated by mTor complex 2 (mTORC2) (28–30). Given that GSK3 is a downstream substrate of Akt, we hypothesized that inhibition of Akt by AZD5363 might inhibit the synergistic effects between IL-17 and insulin/IGF1. In this study, we tested this hypothesis.

MATERIALS AND METHODS

CELLS AND TISSUE CULTURE

Mouse embryonic fibroblast cells (wild-type, GSK3 $\alpha^{-/-}$, or GSK3 $\beta^{-/-}$ gene knockout) (31) were maintained in a 37°C, 5% CO₂ humidified incubator. All of these cell lines express IL-17 receptors A and C (data not shown). Dulbecco's Modified Eagle's Medium (DMEM; Mediatech, Inc., Manassas, VA, USA) with 10% fetal bovine serum (FBS; Mediatech, Inc.) and 1% penicillin/streptomycin was used as the growth medium. Mouse prostate tissues were dissected from 7 to 9-week-old male mice euthanized by CO₂ asphyxiation. The prostate tissues were washed three times with phosphate-buffered saline (PBS), cut into 1–2 mm³ cubes, and kept in 60-mm cell culture dishes in serum-free

DMEM in the incubator. The animal study was approved by the Animal Care and Use Committee of Tulane University.

TREATMENT OF CELLS AND TISSUES

Mouse embryonic fibroblast cells were seeded into 60-mm cell culture dishes with 0.5×10^6 cells/dish. After 24 h incubation, the cells were incubated with serum-free DMEM for 20 h, and then treated with IL-17 (R&D Systems, Inc., Minneapolis, MN, USA), insulin, IGF1 (Sigma Aldrich, Inc., St Louis, MO, USA), and/or AZD5363 (Selleck Chemicals, Inc., Houston, TX, USA). The harvested mouse prostate tissues immersed in serum-free DMEM were incubated for 20 h before any treatments. The treatment for cells and tissues included: (1) control with vehicle; (2) AZD5363 at 2 μ M for 3 h; (3) insulin at 50 ng/ml for 2.5 h; (4) IGF1 at 50 ng/ml for 2.5 h; (5) IL-17 at 20 ng/ml for 2 h; (6) insulin + IL-17 at the same doses but adding insulin 0.5 h before addition of IL-17; (7) IGF1 + IL-17 at the same doses but adding IGF1 0.5 h before addition of IL-17; (8) AZD5363 + Insulin + IL-17 at the same doses but adding AZD5363 1 h and insulin 0.5 h before addition of IL-17; and (9) AZD5363 + IGF1 + IL-17 at the same doses but adding AZD5363 1 h and IGF1 0.5 h before addition of IL-17.

REAL-TIME QUANTITATIVE REVERSE TRANSCRIPTASE PCR

Following treatments, mouse embryonic fibroblast (MEF) cells or mouse prostate tissues were collected in lysis buffer. Mouse prostate tissues were homogenized with Fisher Scientific™ Model 505 sonic dismembrator. Total RNAs of MEF cells or mouse prostate tissues were isolated by using RNeasy Kit (QIAGEN, Valencia, CA, USA) according to the manufacturer's instructions. Genomic DNA contamination of each sample was avoided by using DNase I digestion. RNA was reversed to cDNA by using iScript™ cDNA synthesis kit (Bio-rad Laboratories, Hercules, CA, USA). Mouse glyceraldehyde-3-phosphate dehydrogenase (*Gapdh*), *Cxcl1*, *Ccl20*, and *Il-6* primers were obtained from Eurofins (Huntsville, AL, USA). The PCR primers specific for each gene were as follows: *Cxcl1* forward: 5'-CACCCAAACCGAAGTCATAG-3', reverse: 5'-AAGCCAGCGTT CACAGA-3'; *Ccl20* forward: 5'-AACTGGGTGAAAAGGGCT GT-3', reverse: 5'-GTCCAATTCCATCCCCAAAAA-3'; *Il-6* forward: 5'-CTACCCCAATTTCCAATGCT-3', reverse: 5'-ACCACAG TGAGGAATGTCCA-3'; *Gapdh* forward: 5'-TGCACCACCAAC TGCTTAG-3', reverse: 5'-GGATGCAGGGATGATGTTC-3'. Quantitative real-time PCR (qRT-PCR) was conducted using iQ5® iCycler and iQ™ SYBR Green Supermix (Bio-Rad Laboratories) following the manufacturer's protocols. The result of each group was normalized to its own *Gapdh* level by using the formula Δ Ct (Cycle threshold) = Ct of target gene – Ct of *Gapdh*. The fold change of mRNA level of each treatment group was calculated as: $\Delta\Delta$ Ct = Δ Ct of target gene in the treatment group – Δ Ct of target gene in control group, and fold change = $2^{-\Delta\Delta$ Ct}.

WESTERN BLOT ANALYSIS

Following the treatment of cells or tissues, proteins were extracted by using RIPA lysis buffer, which contains 50 mM sodium fluoride, 0.5% Igepal CA-630 (NP-40), 10 mM sodium phosphate, 150 mM sodium chloride, 25 mM Tris (pH 8.0), 1 mM phenylmethylsulfonyl fluoride, 2 mM ethylenediaminetetraacetic

acid (EDTA), and 1.2 mM sodium vanadate. Protein concentration was assessed by using Bio-Rad Protein Assay Dye Reagent Concentrate (Bio-Rad Laboratories, Hercules, CA, USA) and BioTek ELx800 microplate reader (BioTek, Winooski, VT, USA). Eighty microgram of protein of each group was loaded to 10% SDS-polyacrylamide gel electrophoresis and transferred to polyvinylidene difluoride membrane. Membrane blocking was done using 5% non-fat dry milk in TBST buffer (25 mM Tris-HCl, 125 mM sodium chloride, and 0.1% Tween 20). Primary antibody was incubated with the membrane at 4°C overnight. The membrane was washed three times with TBST, and incubated with IRDye® 800CW- or IRDye® 680RD-conjugated secondary antibodies (LI-COR Biosciences, Lincoln, NE, USA) at room temperature for 1 h. The membrane was scanned by Odyssey Infrared Imager (LI-COR Biosciences) for visualization. The antibodies used included: rabbit anti-P-Akt (S473), rabbit anti-Akt, rabbit anti-P-GSK3 α (S21), rabbit anti-GSK3 α , rabbit anti-P-GSK3 β (S9), and rabbit anti-GSK3 β antibodies were purchased from Cell Signaling Technology, Danvers, MA, USA. Mouse anti-GAPDH antibody was purchased from Millipore, Billerica, MA, USA.

STATISTICAL ANALYSIS

The data were presented as mean \pm SD of triplicate experiments ($n = 3$). Statistical significance was determined by one-way ANOVA and Tukey's tests. All of the analyses were performed using GraphPad Prism® 5.0 (GraphPad Software, La Jolla, CA, USA).

RESULTS

In the wild-type MEF cells, insulin or IGF1 alone treatment led to increased levels of P-Akt, P-GSK3 α , and P-GSK3 β (Figures 1A,B). When AZD5363 treatment was added, the levels of P-Akt were further increased. On the contrary, AZD5363 treatment reduced the levels of P-GSK3 α and P-GSK3 β (Figures 1A,B). In the GSK3 α ^{-/-} MEF cells (Figures 1C,D) and GSK3 β ^{-/-} MEF cells (Figures 1E,F), insulin or IGF1 alone treatment increased the levels of P-Akt, and subsequently the levels of P-GSK3 β and P-GSK3 α in GSK3 α ^{-/-} and GSK3 β ^{-/-} MEF cells, respectively. AZD5363 treatment led to a further increase of P-Akt compared to insulin or IGF1 alone treatment in both GSK3 α ^{-/-} and GSK3 β ^{-/-} MEF cells. However, AZD5363 treatment reduced the levels of P-GSK3 β and P-GSK3 α in GSK3 α ^{-/-} and GSK3 β ^{-/-} MEF cells, respectively, in comparison to insulin or IGF1 alone treatment.

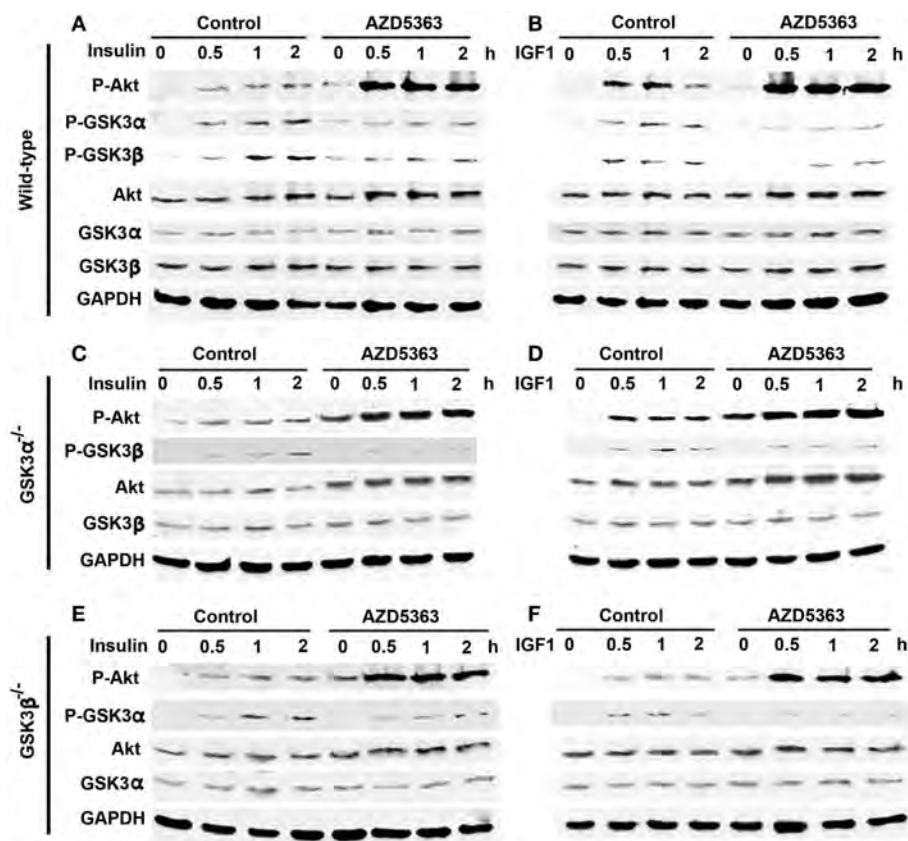
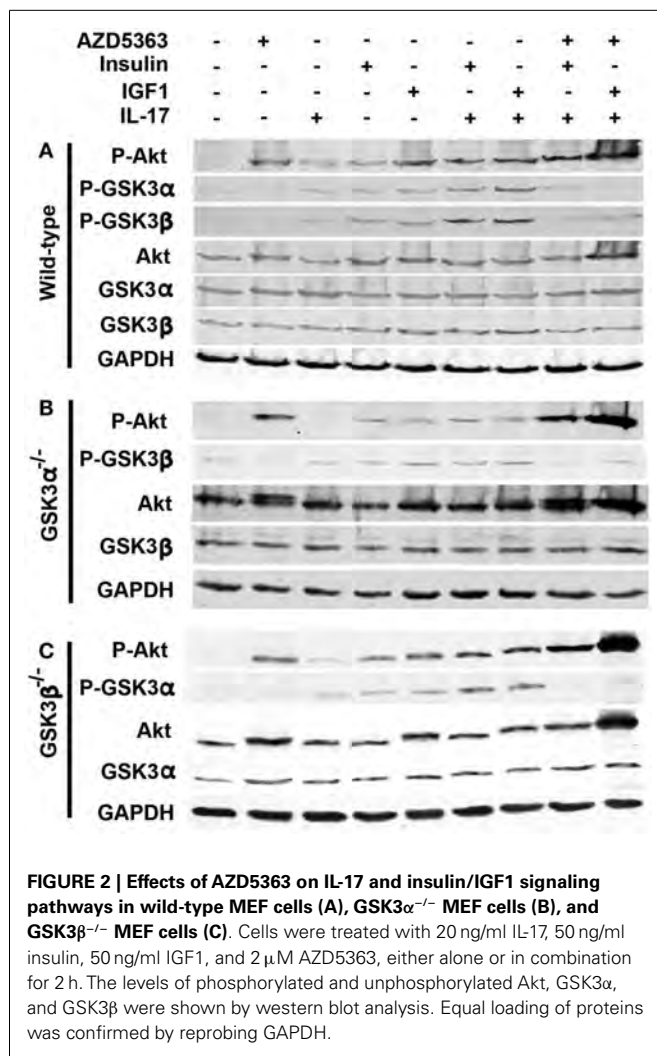


FIGURE 1 | Effects of AZD5363 on insulin/IGF1 signaling pathways. (A) Effects of insulin with or without AZD5363 on wild-type MEF cells; **(B)** Effects of IGF1 with or without AZD5363 on wild-type MEF cells; **(C)** Effects of insulin with or without AZD5363 on GSK3 α ^{-/-} MEF cells; **(D)** Effects of IGF1 with or without AZD5363 on GSK3 α ^{-/-} MEF cells; **(E)** Effects of insulin with or without

AZD5363 on GSK3 β ^{-/-} MEF cells; **(F)** Effects of IGF1 with or without AZD5363 on GSK3 β ^{-/-} MEF cells. The concentrations of insulin and IGF1 were 50 ng/ml and the concentration of AZD5363 was 2 μ M. The levels of phosphorylated and unphosphorylated Akt, GSK3 α , and GSK3 β were shown by western blot analysis. Equal loading of proteins was confirmed by reprobing GAPDH.



As shown in **Figure 2A**, IL-17, insulin or IGF1 alone treatment only slightly increased the levels of P-Akt, P-GSK3α, and P-GSK3β in wild-type MEF cells, compared to control group. A combination of insulin and IL-17, or IGF1 and IL-17, further increased the levels of P-Akt, P-GSK3α, and P-GSK3β. When AZD5363 treatment was added to the combined treatment groups, the levels of P-GSK3α and P-GSK3β were dramatically reduced, though the levels of P-Akt were further increased. In GSK3α^{-/-} and GSK3β^{-/-} MEF cells, similar changes were observed, except that only GSK3β (**Figure 2B**) or GSK3α (**Figure 2C**) was present due to knockout of the other GSK3 isoform.

Because AZD5363 treatment decreased the levels of P-GSK3α and P-GSK3β that might affect IL-17-induced gene expression (8), we checked the mRNA levels of *Cxcl1* and *Ccl20* in wild-type, GSK3α^{-/-} and GSK3β^{-/-} MEF cells after the treatment as described above. In the wild-type MEF cells, IL-17 or insulin alone treatment increased *Cxcl1* mRNA levels by 2.0 ± 0.4 or 1.6 ± 0.8 -fold, compared to control group (**Figure 3A**). *Cxcl1* mRNA level was increased by 4.6 ± 0.6 -fold in the insulin and IL-17 combined treatment group, which was statistically significant compared to

insulin or IL-17 alone treatment group ($p < 0.05$). Addition of AZD5363 to this combined treatment group reduced *Cxcl1* mRNA level to 1.8 ± 0.1 -fold, which was significantly less than the insulin and IL-17 combined treatment group (**Figure 3A**, $p < 0.05$). Similarly, *Ccl20* mRNA levels were increased by 2.0 ± 0.5 and 1.6 ± 0.3 -fold in IL-17 or insulin alone treated group, respectively. A combination of insulin and IL-17 treatment increased *Ccl20* mRNA level by 3.0 ± 0.8 -fold, which was significantly higher than either IL-17 or insulin alone treatment. In contrast, addition of AZD5363 to the combined treatment reduced *Ccl20* mRNA level almost to the basal level of 1.1 ± 0.3 -fold, which was significantly lower than the insulin and IL-17 combined treatment group (**Figure 3A**, $p < 0.05$). As shown in **Figure 3B**, IGF1 and IL-17 also synergistically induced *Cxcl1* and *Ccl20* mRNA expression, which was inhibited by addition of AZD5363. In GSK3α^{-/-} (**Figures 3C,D**) and GSK3β^{-/-} (**Figures 3E,F**) MEF cells, IL-17 alone treatment dramatically increased the levels of *Cxcl1* and *Ccl20* mRNA. In contrast to wild-type MEF cells, combination of insulin or IGF1 with IL-17 did not further increase levels of *Cxcl1* and *Ccl20* mRNA, compared to IL-17 alone treatment (**Figures 3C–F**). Furthermore, addition of AZD5363 to the combined treatment did not reduce the elevated mRNA levels of *Cxcl1* or *Ccl20* (**Figures 3C–F**).

In order to assess if our findings in the studies of cell lines are relevant to the *in vivo* organ tissues, we did similar experiments using *ex vivo* cultured mouse prostate tissues. As shown in **Figure 4A**, increased levels of P-Akt, P-GSK3α, and P-GSK3β were observed in mouse prostate tissues treated with insulin alone, IGF1 alone, a combination of insulin and IL-17, and a combination of IGF1 and IL-17, compared to the control group. However, addition of AZD5363 to the combined treatment groups reduced the levels of P-GSK3α and P-GSK3β, compared to the combined treatment groups. The changes in the signaling proteins were associated with the changes in the mRNA levels of *Cxcl1*, *Ccl20*, and *Il-6*. As shown in **Figure 4B**, a combination of insulin and IL-17 treatment significantly increased the mRNA levels of *Cxcl1*, *Ccl20*, and *Il-6*, compared to insulin or IL-17 alone treatment ($p < 0.05$). Similarly, a combination of IGF1 and IL-17 treatment showed the same effects (**Figure 4C**). However, when AZD5363 was added to the combined treatment groups, the induction of mRNA levels of *Cxcl1*, *Ccl20*, and *Il-6* was significantly reduced, compared to the combined treatment groups without AZD5363 (**Figures 4B,C**).

DISCUSSION

Inflammation has been shown to be a driving force behind a variety of cancer types (32–34). IL-17 is an inflammatory cytokine that stimulates leukocytes, fibroblasts, epithelial cells, and endothelial cells to release inflammatory signals that can further fire up inflammation (1). We have previously demonstrated that IL-17 promotes formation and growth of prostate cancer in a mouse model (35, 36). Recently, we showed that insulin and IGF1 enhance IL-17-induced expression of inflammatory cytokines and chemokines (8). The crosstalk between insulin/IGF1 signaling pathway and IL-17 signaling pathway is mediated by GSK3β, as GSK3β knockout blocks the crosstalk. In the present study, we found that GSK3α

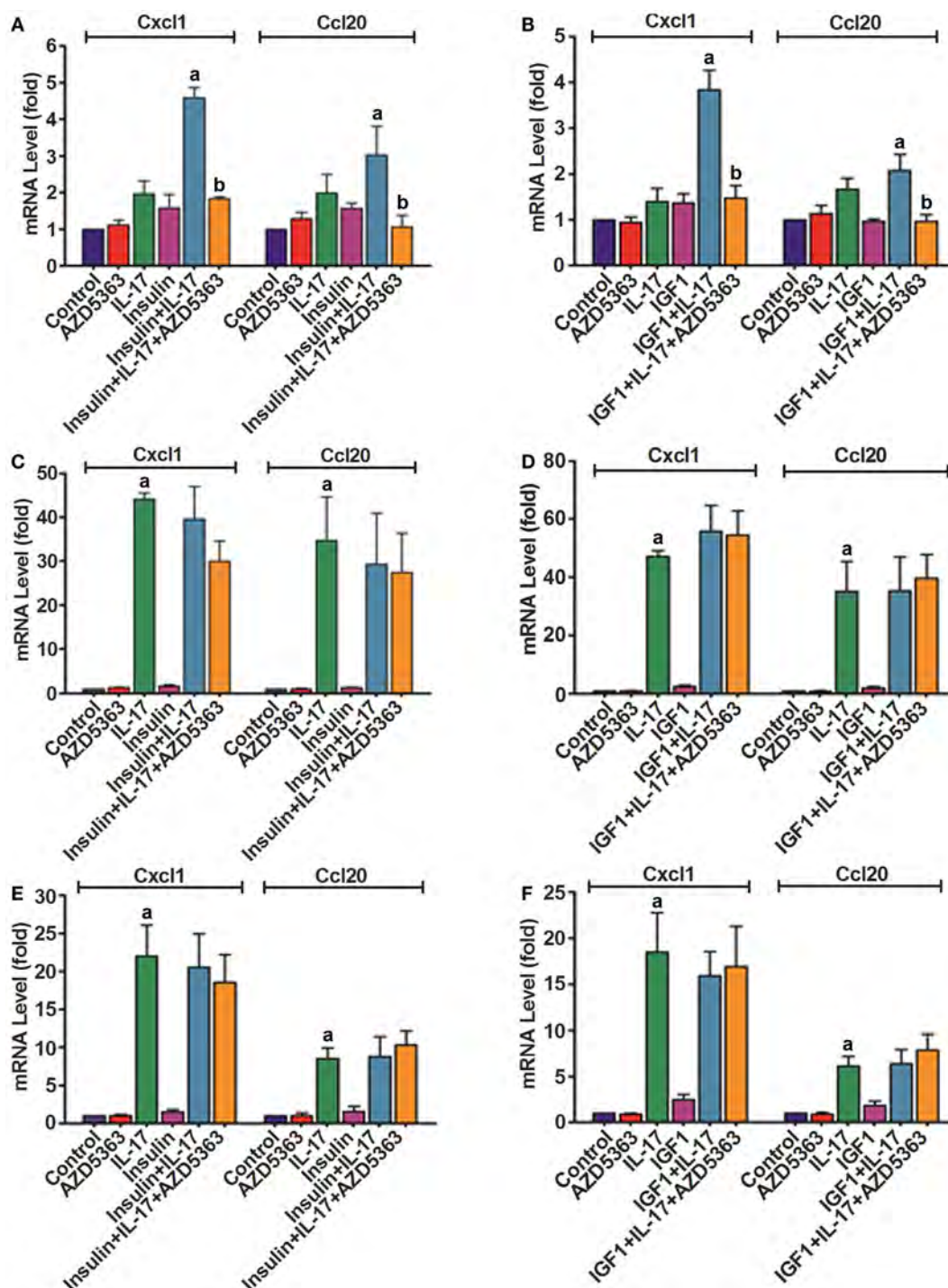


FIGURE 3 | Expression of *Cxcl1* and *Ccl20* mRNAs in wild-type MEF cells (A,B), GSK3 $\alpha^{-/-}$ MEF cells (C,D), and GSK3 $\beta^{-/-}$ MEF cells (E,F). Cells were treated with 20 ng/ml IL-17, 50 ng/ml insulin, 50 ng/ml IGF1, and 2 μ M AZD5363, either alone or in combination for 2 h. The levels of *Cxcl1* and *Ccl20*

mRNAs were determined using real-time PCR. Data represent mean \pm SD of triplicate experiments ($n=3$). a, $p < 0.05$ Compared to IL-17 alone or insulin/IGF1 alone; b, $p < 0.05$ compared to the combination of IL-17 and insulin or IGF1.

knockout also blocks the crosstalk between insulin/IGF1 and IL-17 pathways. In fact, knockout of either GSK3 α or GSK3 β appears to relieve the repressive function of GSK3 on IL-17-induced gene

expression, as IL-17 can induce gene expression to the levels significantly higher than in the wild-type MEFs where IL-17 can usually induce gene expression to very modest levels. These findings

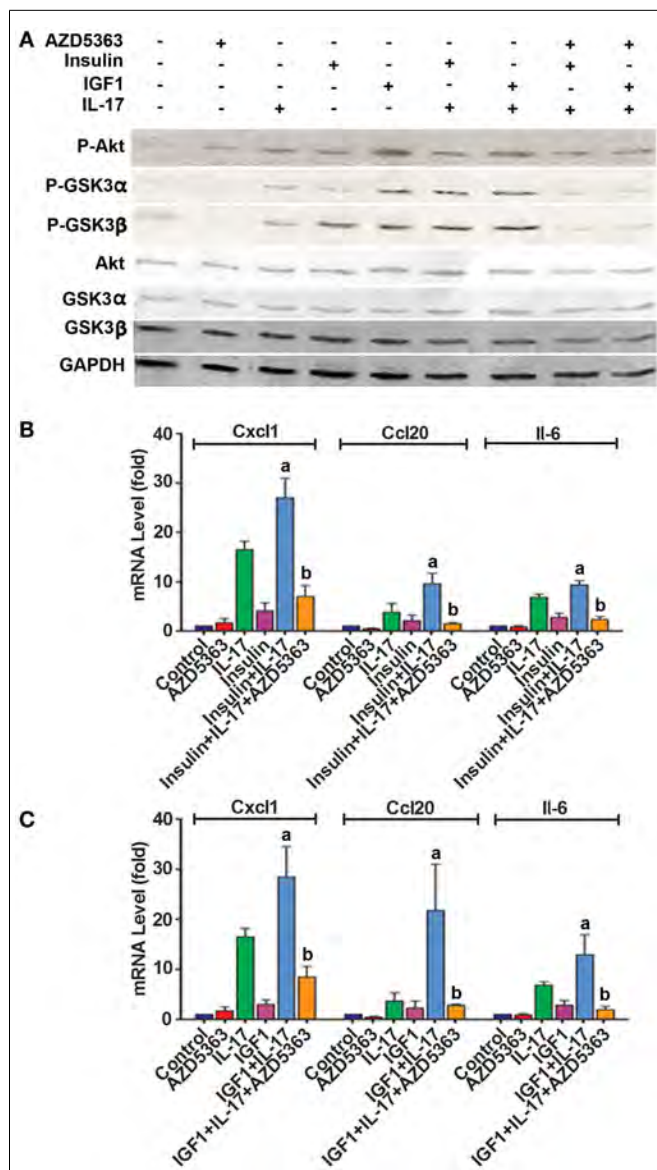
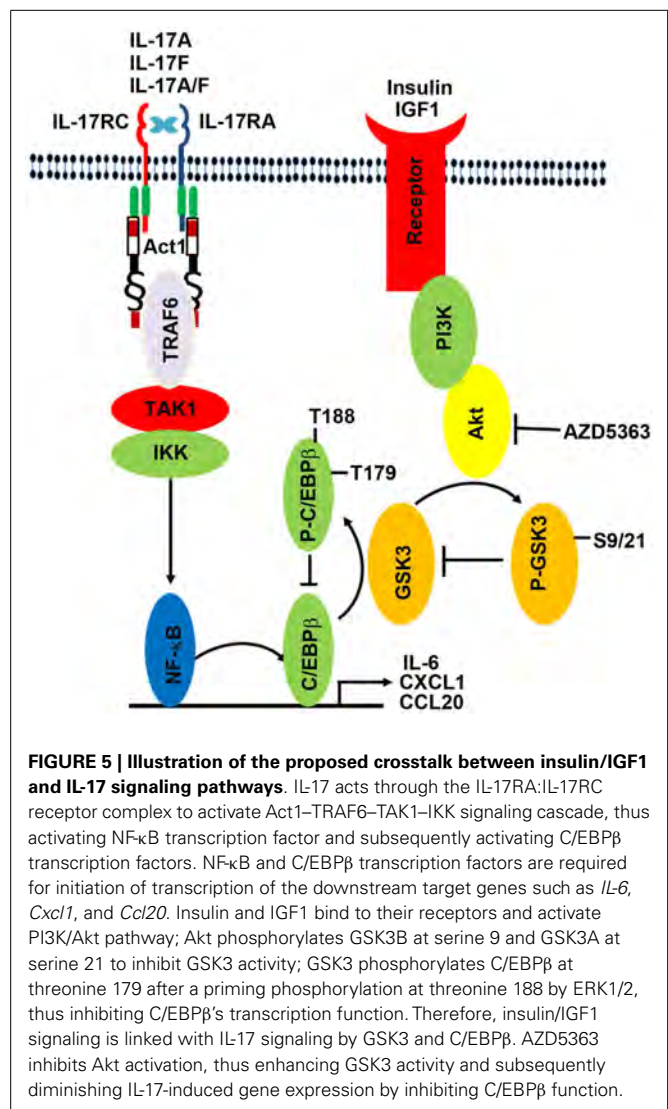


FIGURE 4 | Effects of AZD5363 on IL-17 and insulin/IGF1 signaling pathways and expression of *Cxcl1* and *Ccl20* mRNAs in mouse prostate tissues. Mouse prostate tissues were cultured *ex vivo* and treated with 20 ng/ml IL-17, 50 ng/ml insulin, 50 ng/ml IGF1, and 2 μ M AZD5363, either alone or in combination for 2 h. **(A)** The levels of phosphorylated and unphosphorylated Akt, GSK3 α and GSK3 β were shown by western blot analysis. Equal loading of proteins was confirmed by reprobing GAPDH. **(B,C)** The levels of *Cxcl1* and *Ccl20* mRNAs were determined using real-time PCR. Data represent mean \pm SD of triplicate experiments ($n=3$). a, $p < 0.05$ Compared to IL-17 alone or insulin/IGF1 alone; b, $p < 0.05$ compared to the combination of IL-17 and insulin or IGF1.

suggest that both GSK3 α and GSK3 β isoforms are required to be present, in order to repress IL-17-induced gene expression. Lithium chloride is an inhibitor to both GSK3 α and GSK3 β isoforms, which has been shown to increase IL-17-induced gene expression in two previous studies (8, 20). The exact molecular mechanisms underlying the crosstalk are yet to be determined,



though a previous study suggested that it might be phosphorylation of C/EBP β by GSK3, which inhibits the transcription function of C/EBP β (21). As shown in **Figure 5**, IL-17 acts through the IL-17RA:IL-17RC receptor complex to activate Act1-TRAF6-TAK1-IKK signaling cascade, thus activating NF- κ B transcription factor and subsequently activating C/EBP β transcription factors. NF- κ B and C/EBP β transcription factors are required for initiation of transcription of the downstream target genes such as *IL-6*, *Cxcl1*, and *Ccl20*. Insulin and IGF1 bind to their receptors and activate PI3K/Akt pathway; Akt phosphorylates GSK3 β at serine 9 and GSK3 α at serine 21 to inhibit GSK3 activity; GSK3 phosphorylates C/EBP β at threonine 179 after a priming phosphorylation at threonine 188 by ERK1/2, thus inhibiting C/EBP β 's transcription function. Therefore, insulin/IGF1 signaling is linked with IL-17 signaling by GSK3 and C/EBP β . AZD5363 inhibits Akt activation, thus enhancing GSK3 activity and subsequently diminishing IL-17-induced gene expression by inhibiting C/EBP β function.

Manipulation of the crosstalk between insulin/IGF1 and IL-17 is potentially significant in obese population. It has been reported

that serum and tissue levels of IL-17 are increased in obese mice (37, 38) and humans (39). Interestingly, serum levels of insulin and IGF1 are also increased in obese population, which together with IL-17, may be the underlying cause of the chronic inflammatory state with increased serum levels of inflammatory mediators TNF α and IL-6 (8, 40). Obesity has been associated with increased risks of breast cancer, endometrial cancer, esophageal adenocarcinoma, pancreas cancer, colorectal cancer, renal cancer, thyroid cancer, gallbladder cancer, and prostate cancer (41–49). Chronic inflammation in obesity is suspected as one of the possible mechanisms underlying the increased cancer risk. In our previous study, we found that melatonin can block the crosstalk between insulin/IGF1 and IL-17 through inhibition of Akt function (8). In the present study, we found that AZD5363, a pan-Akt inhibitor, can do the same. AZD5363 reduced phosphorylation of GSK3 α at serine 21 and GSK3 β at serine 9, thus increasing the enzyme activities of GSK3 α and GSK3 β , and subsequently represses IL-17-induced gene expression. Preclinical studies have shown that AZD5363 may be effective in inhibiting tumor growth (27), yet it remains to be determined whether AZD5363 may alter the inflammatory microenvironment in the tumors and how this contributes to the anti-tumor function of AZD5363.

Interestingly, we observed that AZD5363, a pan-Akt inhibitor, increased the P-Akt levels in wild-type, GSK3 $\alpha^{-/-}$ and GSK3 $\beta^{-/-}$ MEF cells. In general, phosphorylated Akt is the activated form of Akt (30). However, it has been reported that several Akt inhibitors elevate the levels of P-Akt. The mechanism behind this may be that suppression of S6K (p70S6K) activity stabilizes IRS-1 and increases IRS-1 adapter protein levels, which in turn induces Akt activity (50–54). Another possible cause of the hyperphosphorylation is that the Akt inhibitor sensitizes the pleckstrin homology (PH) domain to bind basal levels of PIP3 to facilitate membrane localization and induce conformational change of Akt to become more susceptible to kinase phosphorylation or less susceptible to phosphatase dephosphorylation (55). Of note, the increase of P-Akt and total Akt was less obvious in the mouse prostate tissues, compared to the MEFs upon AZD5363 treatment. We speculate that this might be due to that the prostate glandular tissues responded differently from the MEFs. But the exact reason is not clear.

In summary, this study indicates that insulin and IGF1 can enhance IL-17-induced inflammatory responses through suppression of GSK3 function by phosphorylation of GSK3 α and GSK3 β . AZD5363 inhibits Akt function and thus inhibits the synergy between IL-17 and insulin/IGF1 through enhancing GSK3 function by reducing phosphorylation of GSK3 α and GSK3 β . These findings imply that the cooperative crosstalk of IL-17 and insulin/IGF1 in initiating inflammatory responses may be alleviated by AZD5363.

AUTHOR CONTRIBUTIONS

Chong Chen performed the experiments, analyzed the data, and prepared the manuscript. Qiuyang Zhang, Mark Lambrechts, Sen Liu, and Yine Qu participated in the experiments and analysis of data. Zongbing You conceived and designed the work, analyzed the data, and prepared the manuscript. All authors critically

revised the manuscript, approved the final version, and agreed to be accountable for all aspects of the manuscript.

ACKNOWLEDGMENTS

The authors thank Dr. James R. Woodgett (Mount Sinai Hospital and the Samuel Lunenfeld Research Institute, Toronto, ON, Canada M5G1X5) for providing the wild-type, GSK3 $\alpha^{-/-}$, and GSK3 $\beta^{-/-}$ MEF cells. The core facilities of Tulane Cancer Center and Louisiana Cancer Research Consortium were used in this study. This work was supported in whole or in part by National Institutes of Health (P20GM103518 and R01CA174714), by Department of Defense Health Program through the Prostate Cancer Research Program (W81XWH-14-1-0050, W81XWH-14-1-0149, and W81XWH-14-1-0458; the U.S. Army Medical Research Acquisition Activity, 820 Chandler Street, Fort Detrick MD 21702-5014 is the awarding and administering acquisition office), and by the Developmental Fund of Tulane Cancer Center (TCC) and Louisiana Cancer Research Consortium (LCRC) Fund. The content of this article is solely the responsibility of the authors and does not necessarily represent the official views of the National Institutes of Health or the Department of Defense.

REFERENCES

- Kolls JK, Linden A. Interleukin-17 family members and inflammation. *Immunity* (2004) **21**(4):467–76. doi:10.1016/j.immuni.2004.08.018
- Novatchkova M, Leibbrandt A, Werzowa J, Neubuser A, Eisenhaber F. The STIR-domain superfamily in signal transduction, development and immunity. *Trends Biochem Sci* (2003) **28**(5):226–9. doi:10.1016/S0968-0004(03)00067-7
- Chang SH, Park H, Dong C. Act1 adaptor protein is an immediate and essential signaling component of interleukin-17 receptor. *J Biol Chem* (2006) **281**(47):35603–7. doi:10.1074/jbc.C600256200
- Qian Y, Liu C, Hartupree J, Altuntas CZ, Gulen MF, Jane-Wit D, et al. The adaptor Act1 is required for interleukin 17-dependent signaling associated with autoimmune and inflammatory disease. *Nat Immunol* (2007) **8**(3):247–56. doi:10.1038/ni1439
- Maitra A, Shen F, Hanel W, Mossman K, Tocker J, Swart D, et al. Distinct functional motifs within the IL-17 receptor regulate signal transduction and target gene expression. *Proc Natl Acad Sci U S A* (2007) **104**(18):7506–11. doi:10.1073/pnas.0611589104
- Ho AW, Shen F, Conti HR, Patel N, Childs EE, Peterson AC, et al. IL-17RC is required for immune signaling via an extended SEF/IL-17R signaling domain in the cytoplasmic tail. *J Immunol* (2010) **185**(2):1063–70. doi:10.4049/jimmunol.0903739
- Liu C, Qian W, Qian Y, Giltaiy NV, Lu Y, Swaidani S, et al. Act1, a U-box E3 ubiquitin ligase for IL-17 signaling. *Sci Signal* (2009) **2**(92):ra63. doi:10.1126/scisignal.2000382
- Ge D, Dauchy RT, Liu S, Zhang Q, Mao L, Dauchy EM, et al. Insulin and IGF1 enhance IL-17-induced chemokine expression through a GSK3B-dependent mechanism: a new target for melatonin's anti-inflammatory action. *J Pineal Res* (2013) **55**(4):377–87. doi:10.1111/jpi.12084
- Zhu S, Pan W, Song X, Liu Y, Shao X, Tang Y, et al. The microRNA miR-23b suppresses IL-17-associated autoimmune inflammation by targeting TAB2, TAB3 and IKK- α . *Nat Med* (2012) **18**(7):1077–86. doi:10.1038/nm.2815
- Hwang SY, Kim JY, Kim KW, Park MK, Moon Y, Kim WU, et al. IL-17 induces production of IL-6 and IL-8 in rheumatoid arthritis synovial fibroblasts via NF- κ B- and PI3-kinase/Akt-dependent pathways. *Arthritis Res Ther* (2004) **6**(2):R120–8. doi:10.1186/ar1038
- Bulek K, Liu C, Swaidani S, Wang L, Page RC, Gulen MF, et al. The inducible kinase IKKi is required for IL-17-dependent signaling associated with neutrophilia and pulmonary inflammation. *Nat Immunol* (2011) **12**(9):844–52. doi:10.1038/ni.2080
- Sun D, Novotny M, Bulek K, Liu C, Li X, Hamilton T. Treatment with IL-17 prolongs the half-life of chemokine CXCL1 mRNA via the adaptor TRAF5 and

- the splicing-regulatory factor SF2 (ASF). *Nat Immunol* (2011) **12**(9):853–60. doi:10.1038/ni.2081
13. Baxter RC, Bryson JM, Turtle JR. Somatogenic receptors of rat liver: regulation by insulin. *Endocrinology* (1980) **107**(4):1176–81. doi:10.1210/endo-107-4-1176
 14. Gallagher EJ, LeRoith D. The proliferating role of insulin and insulin-like growth factors in cancer. *Trends Endocrinol Metab* (2010) **21**(10):610–8. doi:10.1016/j.tem.2010.06.007
 15. Cross DA, Alessi DR, Cohen P, Andjelkovich M, Hemmings BA. Inhibition of glycogen synthase kinase-3 by insulin mediated by protein kinase B. *Nature* (1995) **378**(6559):785–9. doi:10.1038/378785a0
 16. Cross DA, Alessi DR, Vandenheede JR, McDowell HE, Hundal HS, Cohen P. The inhibition of glycogen synthase kinase-3 by insulin or insulin-like growth factor 1 in the rat skeletal muscle cell line L6 is blocked by wortmannin, but not by rapamycin: evidence that wortmannin blocks activation of the mitogen-activated protein kinase pathway in L6 cells between Ras and Raf. *Biochem J* (1994) **303**(Pt 1):21–6.
 17. Chiara F, Rasola A. GSK-3 and mitochondria in cancer cells. *Front Oncol* (2013) **3**:16. doi:10.3389/fonc.2013.00016
 18. Ruddy MJ, Wong GC, Liu XK, Yamamoto H, Kasayama S, Kirkwood KL, et al. Functional cooperation between interleukin-17 and tumor necrosis factor- α is mediated by CCAAT/enhancer-binding protein family members. *J Biol Chem* (2004) **279**(4):2559–67. doi:10.1074/jbc.M308809200
 19. Shen F, Hu Z, Goswami J, Gaffen SL. Identification of common transcriptional regulatory elements in interleukin-17 target genes. *J Biol Chem* (2006) **281**(34):24138–48. doi:10.1074/jbc.M604597200
 20. Shen F, Li N, Gade P, Kalvakolanu DV, Weibley T, Doble B, et al. IL-17 receptor signaling inhibits C/EBP β by sequential phosphorylation of the regulatory 2 domain. *Sci Signal* (2009) **2**(59):ra8. doi:10.1126/scisignal.2000066
 21. Demarchi F, Bertoli C, Sandy P, Schneider C. Glycogen synthase kinase-3 β regulates NF- κ B/p105 stability. *J Biol Chem* (2003) **278**(41):39583–90. doi:10.1074/jbc.M305676200
 22. Toren P, Kim S, Cordonnier T, Crafter C, Davies BR, Fazli L, et al. Combination AZD5363 with enzalutamide significantly delays enzalutamide-resistant prostate cancer in preclinical models. *Eur Urol* (2014). doi:10.1016/j.eururo.2014.08.006
 23. Lamoureux F, Thomas C, Crafter C, Kumano M, Zhang F, Davies BR, et al. Blocked autophagy using lysosomotropic agents sensitizes resistant prostate tumor cells to the novel Akt inhibitor AZD5363. *Clin Cancer Res* (2013) **19**(4):833–44. doi:10.1158/1078-0432.CCR-12-3114
 24. Yung HW, Charnock-Jones DS, Burton GJ. Regulation of AKT phosphorylation at Ser473 and Thr308 by endoplasmic reticulum stress modulates substrate specificity in a severity dependent manner. *PLoS One* (2011) **6**(3):e17894. doi:10.1371/journal.pone.0017894
 25. Altomare DA, Testa JR. Perturbations of the AKT signaling pathway in human cancer. *Oncogene* (2005) **24**(50):7455–64. doi:10.1038/sj.onc.1209085
 26. Bellacosa A, Kumar CC, Di Cristofano A, Testa JR. Activation of AKT kinases in cancer: implications for therapeutic targeting. *Adv Cancer Res* (2005) **94**:29–86. doi:10.1016/S0065-230X(05)94002-5
 27. Davies BR, Greenwood H, Dudley P, Crafter C, Yu DH, Zhang J, et al. Preclinical pharmacology of AZD5363, an inhibitor of AKT: pharmacodynamics, antitumor activity, and correlation of monotherapy activity with genetic background. *Mol Cancer Ther* (2012) **11**(4):873–87. doi:10.1158/1535-7163.MCT-11-0824-T
 28. Alessi DR, Andjelkovic M, Caudwell B, Cron P, Morrice N, Cohen P, et al. Mechanism of activation of protein kinase B by insulin and IGF-1. *EMBO J* (1996) **15**(23):6541–51.
 29. Alessi DR, James SR, Downes CP, Holmes AB, Gaffney PR, Reese CB, et al. Characterization of a 3-phosphoinositide-dependent protein kinase which phosphorylates and activates protein kinase B α . *Curr Biol* (1997) **7**(4):261–9. doi:10.1016/S0960-9822(06)00122-9
 30. Sarbassov DD, Guertin DA, Ali SM, Sabatini DM. Phosphorylation and regulation of Akt/PKB by the rictor-mTOR complex. *Science* (2005) **307**(5712):1098–101. doi:10.1126/science.1106148
 31. Hoeflich KP, Luo J, Rubie EA, Tsao MS, Jin O, Woodgett JR. Requirement for glycogen synthase kinase-3 β in cell survival and NF- κ B activation. *Nature* (2000) **406**(6791):86–90. doi:10.1038/35017574
 32. Chen C, Khismatullin DB. Lipopolysaccharide induces the interactions of breast cancer and endothelial cells via activated monocytes. *Cancer Lett* (2014) **345**(1):75–84. doi:10.1016/j.canlet.2013.11.022
 33. Couzin-Frankel J. Inflammation bares a dark side. *Science* (2010) **330**(6011):1621. doi:10.1126/science.330.6011.1621
 34. Coussens LM, Werb Z. Inflammation and cancer. *Nature* (2002) **420**(6917):860–7. doi:10.1038/nature01322
 35. Zhang Q, Liu S, Ge D, Xue Y, Xiong Z, Abdel-Mageed AB, et al. Interleukin-17 promotes formation and growth of prostate adenocarcinoma in mouse models. *Cancer Res* (2012) **72**(10):2589–99. doi:10.1158/0008-5472.CAN-11-3795
 36. Zhang Q, Liu S, Xiong Z, Wang AR, Myers L, Melamed J, et al. Interleukin-17 promotes development of castration-resistant prostate cancer potentially through creating an immunotolerant and pro-angiogenic tumor microenvironment. *Prostate* (2014) **74**(8):869–79. doi:10.1002/pros.22805
 37. Winer S, Paltser G, Chan Y, Tsui H, Engleman E, Winer D, et al. Obesity predisposes to Th17 bias. *Eur J Immunol* (2009) **39**(9):2629–35. doi:10.1002/eji.200838893
 38. Pini M, Fantuzzi G. Enhanced production of IL-17A during zymosan-induced peritonitis in obese mice. *J Leukoc Biol* (2010) **87**(1):51–8. doi:10.1189/jlb.0309188
 39. Sumarac-Dumanovic M, Stevanovic D, Ljubic A, Jorga J, Simic M, Stamenkovic-Pejkovic D, et al. Increased activity of interleukin-23/interleukin-17 proinflammatory axis in obese women. *Int J Obes (Lond)* (2009) **33**(1):151–6. doi:10.1038/ijo.2008.216
 40. Cohen DH, LeRoith D. Obesity, type 2 diabetes, and cancer: the insulin and IGF connection. *Endocr Relat Cancer* (2012) **19**(5):F27–45. doi:10.1530/ERC-11-0374
 41. Stephenson GD, Rose DP. Breast cancer and obesity: an update. *Nutr Cancer* (2003) **45**(1):1–16. doi:10.1207/S15327914NC4501_1
 42. Kaaks R, Lukanova A, Kurzer MS. Obesity, endogenous hormones, and endometrial cancer risk: a synthetic review. *Cancer Epidemiol Biomarkers Prev* (2002) **11**(12):1531–43.
 43. Chen Q, Zhuang H, Liu Y. The association between obesity factor and esophageal cancer. *J Gastrointest Oncol* (2012) **3**(3):226–31. doi:10.3978/j.issn.2078-6891.2012.026
 44. Bracci PM. Obesity and pancreatic cancer: overview of epidemiologic evidence and biologic mechanisms. *Mol Carcinog* (2012) **51**(1):53–63. doi:10.1002/mc.20778
 45. Moghaddam AA, Woodward M, Huxley R. Obesity and risk of colorectal cancer: a meta-analysis of 31 studies with 70,000 events. *Cancer Epidemiol Biomarkers Prev* (2007) **16**(12):2533–47. doi:10.1158/1055-9965.EPI-07-0708
 46. Chow WH, Gridley G, Fraumeni JF Jr, Jarvholm B. Obesity, hypertension, and the risk of kidney cancer in men. *N Engl J Med* (2000) **343**(18):1305–11. doi:10.1056/NEJM200011023431804
 47. Kitahara CM, Platz EA, Freeman LE, Hsing AW, Linet MS, Park Y, et al. Obesity and thyroid cancer risk among U.S. men and women: a pooled analysis of five prospective studies. *Cancer Epidemiol Biomarkers Prev* (2011) **20**(3):464–72. doi:10.1158/1055-9965.EPI-10-1220
 48. Larsson SC, Wolk A. Obesity and the risk of gallbladder cancer: a meta-analysis. *Br J Cancer* (2007) **96**(9):1457–61. doi:10.1038/sj.bjc.6603703
 49. Amling CL, Riffenburgh RH, Sun L, Moul JW, Lance RS, Kusuda L, et al. Pathologic variables and recurrence rates as related to obesity and race in men with prostate cancer undergoing radical prostatectomy. *J Clin Oncol* (2004) **22**(3):439–45. doi:10.1200/JCO.2004.03.132
 50. Shah OJ, Wang Z, Hunter T. Inappropriate activation of the TSC/Rheb/mTOR/S6K cassette induces IRS1/2 depletion, insulin resistance, and cell survival deficiencies. *Curr Biol* (2004) **14**(18):1650–6. doi:10.1016/j.cub.2004.08.026
 51. Manning BD, Logsdon MN, Lipovsky AI, Abbott D, Kwiatkowski DJ, Cantley LC. Feedback inhibition of Akt signaling limits the growth of tumors lacking Tsc2. *Genes Dev* (2005) **19**(15):1773–8. doi:10.1101/gad.1314605
 52. Um SH, Frigerio F, Watanabe M, Picard F, Joaquin M, Sticker M, et al. Absence of S6K1 protects against age- and diet-induced obesity while enhancing insulin sensitivity. *Nature* (2004) **431**(7005):200–5. doi:10.1038/nature02866
 53. Harrington LS, Findlay GM, Gray A, Tolkacheva T, Wigfield S, Rebholz H, et al. The TSC1-2 tumor suppressor controls insulin-PI3K signaling via regulation of IRS proteins. *J Cell Biol* (2004) **166**(2):213–23. doi:10.1083/jcb.200403069
 54. O'Reilly KE, Rojo F, She QB, Solit D, Mills GB, Smith D, et al. mTOR inhibition induces upstream receptor tyrosine kinase signaling and activates Akt. *Cancer Res* (2006) **66**(3):1500–8. doi:10.1158/0008-5472.CAN-05-2925

55. Okuzumi T, Fiedler D, Zhang C, Gray DC, Aizenstein B, Hoffman R, et al. Inhibitor hijacking of Akt activation. *Nat Chem Biol* (2009) 5(7):484–93. doi:10.1038/nchembio.183

Conflict of Interest Statement: The authors declare that the research was conducted in the absence of any commercial or financial relationships that could be construed as a potential conflict of interest.

Received: 22 September 2014; paper pending published: 04 November 2014; accepted: 17 November 2014; published online: 01 December 2014.

Citation: Chen C, Zhang Q, Liu S, Lambrechts M, Qu Y and You Z (2014) AZD5363 inhibits inflammatory synergy between interleukin-17 and insulin/insulin-like growth factor 1. *Front. Oncol.* 4:343. doi: 10.3389/fonc.2014.00343

This article was submitted to *Surgical Oncology*, a section of the journal *Frontiers in Oncology*.

Copyright © 2014 Chen, Zhang, Liu, Lambrechts, Qu and You. This is an open-access article distributed under the terms of the Creative Commons Attribution License (CC BY). The use, distribution or reproduction in other forums is permitted, provided the original author(s) or licensor are credited and that the original publication in this journal is cited, in accordance with accepted academic practice. No use, distribution or reproduction is permitted which does not comply with these terms.

IL-17 and Insulin/IGF1 Enhance Adhesion of Prostate Cancer Cells to Vascular Endothelial Cells Through CD44-VCAM-1 Interaction

Chong Chen,¹ Qiuyang Zhang,¹ Sen Liu,¹ Keshab R. Parajuli,¹ Yine Qu,^{1,2} Jiandong Mei,^{1,3} Zhiquan Chen,^{1,4} Hui Zhang,^{1,5} Damir B. Khismatullin,^{6,7} and Zongbing You^{1,6,8,9,10*}

¹Department of Structural and Cellular Biology, Tulane University, New Orleans, Louisiana

²Department of Histology and Embryology, Hebei United University School of Basic Medicine, Tangshan, Hebei Province, China

³Department of Thoracic Surgery, West China Hospital/West China School of Medicine, Sichuan University, Chengdu, China

⁴Department of Cardiothoracic Surgery, the Affiliated Hospital of Hebei United University, Tangshan, Hebei Province, China

⁵Department of Gynecology, the Affiliated Hospital of Taishan Medical College, Taian City, Shandong Province, China

⁶Tulane Cancer Center, Louisiana Cancer Research Consortium, Tulane University, New Orleans, Louisiana

⁷Department of Biomedical Engineering, Tulane University, New Orleans, Louisiana

⁸Department of Orthopaedic Surgery, Tulane University, New Orleans, Louisiana

⁹Tulane Center for Stem Cell Research Regenerative Medicine, Tulane University, New Orleans, Louisiana

¹⁰Tulane Center for Aging, Tulane University, New Orleans, Louisiana

BACKGROUND. Extravasation is a critical step in cancer metastasis, in which adhesion of intravascular cancer cells to the vascular endothelial cells is controlled by cell surface adhesion molecules. The role of interleukin-17 (IL-17), insulin, and insulin-like growth factor 1 (IGF1) in adhesion of prostate cancer cells to the vascular endothelial cells is unknown, which is the subject of the present study.

METHODS. Human umbilical vein endothelial cells (HUVECs) and human prostate cancer cell lines (PC-3, DU-145, LNCaP, and C4-2B) were analyzed for expression of vascular cell adhesion molecule 1 (VCAM-1), integrins, and cluster of differentiation 44 (CD44) using flow cytometry and Western blot analysis. The effects of IL-17, insulin, and IGF1 on VCAM-1 expression and adhesion of prostate cancer cells to HUVECs were examined. The interaction of VCAM-1 and CD44 was assessed using immunoprecipitation assays.

Grant sponsor: National Institute of General Medical Sciences; Grant number: P20GM103518; Grant sponsor: National Cancer Institute; Grant number: R01CA174714; Grant sponsor: Department of Defense; Grant numbers: W81XWH-14-1-0050; W81XWH-14-1-0149; W81XWH-14-1-0458; Grant sponsor: The Developmental Fund of Tulane Cancer Center (TCC); Grant sponsor: Louisiana Cancer Research Consortium (LCRC) Fund.

The content of this article is solely the responsibility of the authors and does not necessarily represent the official views of the National Institutes of Health or the Department of Defense.

*Correspondence to: Zongbing You, Department of Structural and Cellular Biology, Tulane University School of Medicine, 1430 Tulane Ave mailbox 8649, New Orleans, LA 70112.

E-mail: zyou@tulane.edu

Received 24 November 2014; Accepted 6 January 2015

DOI 10.1002/pros.22971

Published online 14 February 2015 in Wiley Online Library
(wileyonlinelibrary.com).

RESULTS. Insulin and IGF1 acted with IL-17 to increase VCAM-1 expression in HUVECs. PC-3, DU-145, LNCaP, and C4-2B cells expressed $\beta 1$ integrin but not $\alpha 4$ integrin. CD44 was expressed by PC-3 and DU-145 cells but not by LNCaP or C4-2B cells. When HUVECs were treated with IL-17, insulin or IGF1, particularly with a combination of IL-17 and insulin (or IGF1), adhesion of PC-3 and DU-145 cells to HUVECs was significantly increased. In contrast, adhesion of LNCaP and C4-2B cells to HUVECs was not affected by treatment of HUVECs with IL-17 and/or insulin/IGF1. CD44 expressed in PC-3 cells physically bound to VCAM-1 expressed in HUVECs.

CONCLUSIONS. CD44-VCAM-1 interaction mediates the adhesion between prostate cancer cells and HUVECs. IL-17 and insulin/IGF1 enhance adhesion of prostate cancer cells to vascular endothelial cells through increasing VCAM-1 expression in the vascular endothelial cells. These findings suggest that IL-17 may act with insulin/IGF1 to promote prostate cancer metastasis. *Prostate* 75:883–895, 2015. © 2015 Wiley Periodicals, Inc.

KEY WORDS: prostate cancer metastasis; IL-17; insulin; IGF1; VCAM-1

INTRODUCTION

More than 90% of deaths from cancer are caused by the metastases instead of the primary tumors [1]. Cancer metastasis is a process in which the secondary tumor sites are formed at locations distant to the primary site, including steps of stromal invasion and intravasation at the primary site, circulation in blood and lymph vessels, and extravasation and tumor formation at the distant site [2]. The number of cancer cells entering the systemic circulation (i.e., intravasation) daily can reach up to 4×10^6 per gram of primary tumor [3]. With a large number of cancer cells circulating intravascularly, the interactions between cancer cells and vascular endothelial cells play a key role in hematogenous cancer metastases to the distant sites of the body [4]. Several previous studies have shown that inflammatory cytokines cause adhesion of cancer cells to the activated vascular endothelium through inducing expression of adhesion molecules on the endothelium [5–7]. Colorectal cancer cells were observed to adhere to the vascular endothelium through binding to vascular cell adhesion molecule 1 (VCAM-1) in the presence of E-selectin [8]. It has been shown that cancer cells with expression of integrin $\alpha_4\beta_1$ (also called very late antigen-4, VLA-4) favorably attached to bone marrow stromal cells that constitutively expressed VCAM-1, leading to bone metastasis [9]. Therefore, understanding the molecular mechanisms underlying the interactions between cancer cells and vascular endothelial cells is vital to our understanding of cancer cells extravasation during cancer metastasis.

Interleukin-17 (IL-17 or IL-17A) is an inflammatory cytokine [10]. When it binds to a heterodimer of IL-17RA/IL-17RC receptor complex, IL-17 is able to activate nuclear factor- κ B (NF- κ B) activator 1 (Act1) through SEFIR (similar expression to fibroblast growth factor genes, IL-17 receptors, and Toll-IL-1R)

domains [11–15]. Activation of Act1 triggers lysine-63-linked ubiquitination of tumor necrosis factor receptor-associated factor 6 (TRAF6), leading to activation of transforming growth factor- β -activated kinase 1 (TAK1) and I κ B kinase (IKK) complex, and finally resulting in activation of NF- κ B pathway that induces transcription of a variety of cytokines, chemokines, and growth factor [16–19]. We have previously demonstrated that IL-17 promotes development of hormone-dependent and castration-resistant prostate cancer in mouse prostates [20,21]. However, the role of IL-17 in development of metastatic tumors has not been determined.

Insulin is a hormone produced by pancreas β cells. The abnormal high concentration of insulin (hyperinsulinemia) may circulate in the body of people with obesity and type 2 diabetes mellitus with insulin resistance. Insulin-like growth factor 1 (IGF1) is produced by liver when stimulated by insulin [22]. Two types of insulin receptors (IR-A and IR-B) can bind to either insulin or IGF1. The receptors of IGF1 also include a heterodimer of IR and IGF1 receptor (IGF1R). Both insulin and IGF1 have been found to induce VCAM-1 expression in the vascular endothelial cells [23,24]. IL-17 can also increase expression of adhesion molecules, including intercellular adhesion molecule-1 (ICAM-1), VCAM-1 and E-selectin in the endothelial cells [25,26]. It has been shown that insulin can augment tumor necrosis factor- α (TNF- α)-induced expression of VCAM-1 in the endothelial cells [27]. We have previously demonstrated that insulin and IGF1 can enhance IL-17-induced chemokine expression [17]. Therefore, we conducted the present study to investigate if insulin and IGF1 can enhance IL-17-induced VCAM-1 expression in human umbilical vein endothelial cells (HUVECs), and hence boost adhesion of prostate cancer cells to HUVECs.

MATERIALS AND METHODS

Cell Culture

Human umbilical vein endothelial cells (HUVECs) were obtained from Life Technologies (Grand Island, NY) and cultured in Medium 200 with Low Serum Growth Supplement and Gentamicin/Amphotericin B (Life Technologies). HUVECs of passages 5–9 were used in the experiments. Human prostate cancer cell lines PC-3, DU-145, and LNCaP were purchased from the American Type Culture Collection (Manassas, VA) and C4-2B cell line was a gift from Dr. Leland WK Chung (Cedars-Sinai Medical Center, Los Angeles, CA). PC-3 and DU-145 cells were cultured in Dulbecco's Modified Eagle's Medium (DMEM; Mediatech, Inc., Manassas, VA) with 10% fetal bovine serum (FBS; Mediatech, Inc.) and 1% penicillin/streptomycin. C4-2B cells were cultured in Roswell Park Memorial Institute (RPMI)-1640 medium (Thermo Fisher Scientific, Inc., Waltham, MA) with 10% FBS and 1% penicillin/streptomycin. LNCaP cells were cultured in T-medium (Life Technologies) with 5% FBS and 1% penicillin/streptomycin. The cells were cultured in a 5% CO₂ humidified incubator at 37°C.

Western Blot Analysis

Proteins of HUVECs, PC-3, DU-145, LNCaP, and C4-2B cells were extracted using RIPA lysis buffer, which contains 50 mM sodium fluoride, 0.5% Igepal CA-630 (NP-40), 10 mM sodium phosphate, 150 mM sodium chloride, 25 mM Tris (pH 8.0), 1 mM phenylmethylsulfonyl fluoride, 2 mM ethylenediaminetetraacetic acid (EDTA), and 1.2 mM sodium vanadate. The concentration of protein was measured using Bio-Rad protein Assay Dye Reagent Concentrate (Bio-Rad Laboratories, Hercules, CA) and BioTek ELx800 microplate reader (BioTek, Winooski, VT). Approximately 80 µg of protein was loaded to 10% SDS-polyacrylamide gel electrophoresis and transferred to polyvinylidene difluoride membrane. 5% nonfat dry milk in TBST buffer (25 mM Tris-HCl, 125 mM sodium chloride and 0.1% Tween 20) was used to block the membrane. The membrane was incubated with primary antibodies at 4°C overnight, and then incubated with IRDye[®] 800CW- or IRDye[®] 680RD-conjugated secondary antibodies (LI-COR Biosciences, Lincoln, NE) at room temperature for 1 hr. The results were scanned with an Odyssey Infrared Imager (LI-COR Biosciences). For loading control, the membrane was re-probed for glyceraldehyde 3-phosphate dehydrogenase (GAPDH). The antibodies used included: rabbit anti-VCAM-1 and mouse anti-CD44 antibodies (Cell Signaling Technology, Danvers, MA), and mouse anti-GAPDH antibodies (Millipore, Billerica, MA).

Static Adhesion Assays

Approximately 1×10^5 HUVECs were seeded in each well of the 96-well plates. Two days later when the cells reached about 95% confluence, they were treated with 20 ng/ml recombinant human IL-17 (R&D Systems, Inc., Minneapolis, MN), 50 ng/ml recombinant human insulin, or 50 ng/ml recombinant human IGF1 (Sigma Aldrich, Inc., St. Louis, MO), or a combination of IL-17 and insulin (or IGF1), for 24 hr. Prostate cancer cells were stained with 0.8 µM calcein AM (Life Technologies) for 15 min at 37°C and then washed three times with complete medium, thus the stained live prostate cancer cells gave rise to intense green fluorescence. Next, prostate cancer cells (0.5×10^5 cells in 100-µl complete medium) were added onto HUVECs in the 96-well plates and incubated for 15 min at 37°C. After incubation, each well was gently washed three times with phosphate-buffered saline (PBS) to remove non-adherent prostate cancer cells. The adherent prostate cancer cells were visualized and photomicrographs were taken using an inverted fluorescence microscope with a digital camera (LEICA DMIRB, Leica Microsystems Inc., Buffalo Grove, IL). The fluorescence intensity (representing the number of adherent prostate cancer cells) was measured with a microplate reader (FLUOstar Optima, BMG Labtech, Cary, NC) at excitation/emission wavelengths of 495 nm/520 nm.

Flow Cytometry Analysis and Fluorescence-Activated Cell Sorting (FACS)

HUVECs, PC-3, DU-145, LNCaP, and C4-2B cells were grown to confluence in 100-mm tissue culture dishes and harvested using an Enzyme-Free PBS-based Cell Dissociation Buffer (Life Technologies). Approximately 1×10^6 cells were suspended in 100-µl FACS buffer (2% bovine serum albumin and 0.1% sodium azide in PBS). Fluorescein isothiocyanate (FITC)-conjugated mouse IgG1 (as isotype control) and mouse anti-human VCAM-1 antibodies (Ancell, Bayport, MN) were added to HUVECs separately. Phycoerythrin (PE)-conjugated mouse IgG1 (as isotype control), mouse anti-human β1 integrin and α4 integrin antibodies (Ancell), and mouse anti-human CD44 antibodies (Cell Signaling Technology) were added to PC-3, DU-145, LNCaP, and C4-2B cells separately. The cells were incubated with the antibodies (1:50 dilution) on ice for 45 min, followed by washing with FACS buffer twice. Flow cytometry analysis was conducted using a BD LSR II analyzer and FACS was conducted using BD FACSAria (BD Biosciences, San Jose, CA).

Immunoprecipitation (IP)

HUVECs were grown to 100% confluence in 100-mm dishes and then treated with 20 ng/ml IL-17 and 50 ng/ml IGF1 for 24 hr or treated with PBS as control. Approximately 3×10^6 PC-3 or LNCaP cells were plated onto the confluent HUVECs for 30 min at 37°C. Non-adherent cancer cells were washed off with PBS. Next, HUVECs and adherent cancer cells were lysed in RIPA buffer. In a parallel set of groups, HUVECs and adherent cancer cells were first fixed with 2% formaldehyde at room temperature for 10 min according to a previous study [28], in order to preserve the binding of molecules between HUVECs and adherent cancer cells. After quenching with ice-cold 1.25 M glycine, HUVECs and adherent cancer cells were lysed in RIPA buffer. Mouse anti-CD44 antibodies (1 μ g) or mouse isotype IgG control antibodies (1 μ g) were added to the protein extract and incubated at 4°C for 1 hr. Then, 10 μ l of protein A Sepharose™ CL-4B beads (GE Healthcare, Waukesha, WI) was added for incubation at 4°C overnight. After three washes with PBS, the immunoprecipitated protein was released from the beads by boiling and analyzed for VCAM-1 and CD44 using Western blot analysis.

Statistical Analysis

The results were presented as mean \pm standard deviation (SD) of three independent experiments ($n=3$). Two-way analysis of variance (ANOVA) and one-way ANOVA and Tukey's test were used to determine the statistical significance using GraphPad Prism® 5.0 (Graphpad Software, La Jolla, CA). $P < 0.05$ was considered as statistically significant.

RESULTS

Insulin and IGF1 Enhance IL-17-Induced VCAM-1 Expression

When treated with IL-17, insulin, or IGF1 alone for 24 hr, VCAM-1 expression was only slightly increased in HUVECs (Fig. 1A), however, a combination of IL-17 and insulin (or IGF1) dramatically increased VCAM-1 expression (Fig. 1A). Expression of ICAM-1 and E-selectin was not affected (data not shown). Induction of VCAM-1 expression in HUVECs by IL-17 or the combination of IL-17 and insulin/IGF1 reached a peak level at 24 hr (Fig. 1B). Extension of the treatment time to 48 hr did not further increase the levels of VCAM-1 expression (data not shown). Flow cytometry analysis showed that the combination of IL-17 and insulin/IGF1 increased VCAM-1 expression on the surfaces of HUVECs to the levels higher than IL-17 or insulin/IGF1 alone (Fig. 1C and D).

Prostate Cancer Cells Differentially Express Integrins and CD44

The conventional ligand of VCAM-1 is very late antigen-4 (VLA-4), which is made up by $\alpha 4$ and $\beta 1$ integrins. Flow cytometry analysis showed that PC-3, DU-145, LNCaP, and C4-2B cells expressed $\beta 1$ integrin, but not $\alpha 4$ integrin (Fig. 2A). This finding indicates that there is no intact VLA-4 ligand in PC-3, DU-145, LNCaP, and C4-2B cells to bind to VCAM-1 expressed in HUVECs. PC-3, DU-145, LNCaP, and C4-2B cells did not express VCAM-1, nor did HUVECs express CD44 (data not shown). Since it has been reported that CD44 can physically interact with VCAM-1 [29], we assessed CD44 expression in the prostate cancer cells. Flow cytometry analysis showed that more than 95% of PC-3 and DU-145 cells expressed high levels of CD44 on the cell surfaces (Fig. 2B), whereas LNCaP and C4-2B cells did not express CD44 at any detectable levels (Fig. 2B). Western blot analysis confirmed the results from flow cytometry analysis (Fig. 2C).

Combination of IL-17 and Insulin/IGF1 Treatment Enhances Adhesion of PC-3 and DU-145 Cells to HUVECs

In assays of static adhesion within 15 min of time, few PC-3 cells adhered to the untreated HUVECs (Fig. 3A and B, the control group). When HUVECs were treated with insulin, IGF1, and IL-17 alone for 24 hr prior to addition of PC-3 cells, there were slightly more PC-3 cells adhered to HUVECs, which was statistically insignificant (Fig. 3A). In contrast, when HUVECs were treated with a combination of IL-17 and insulin/IGF1 for 24 hr prior to addition of PC-3 cells, the number of PC-3 cells adhered to HUVECs was significantly increased compared to the control group or any group treated with IL-17 or insulin/IGF1 alone (Fig. 3A and B, $P < 0.05$). Similarly, the combination of IL-17 and insulin/IGF1 also significantly increased the adhesion of DU-145 cells to HUVECs (Fig. 3C and D, $P < 0.05$). In contrast, when HUVECs were treated with IL-17, insulin, and IGF1, either alone or in combination, there was no increase in adhesion between LNCaP cells and HUVECs (Fig. 3E and F) or between C4-2B cells and HUVECs (Fig. 3G and H).

CD44-VCAM-1 Interaction Mediates the Adhesion Between Prostate Cancer Cells and HUVECs

DU-145 cells were sorted into CD44^{bright} and CD44^{dim} populations using FACS (Fig. 4A). When HUVECs were treated with the combination of IL-17

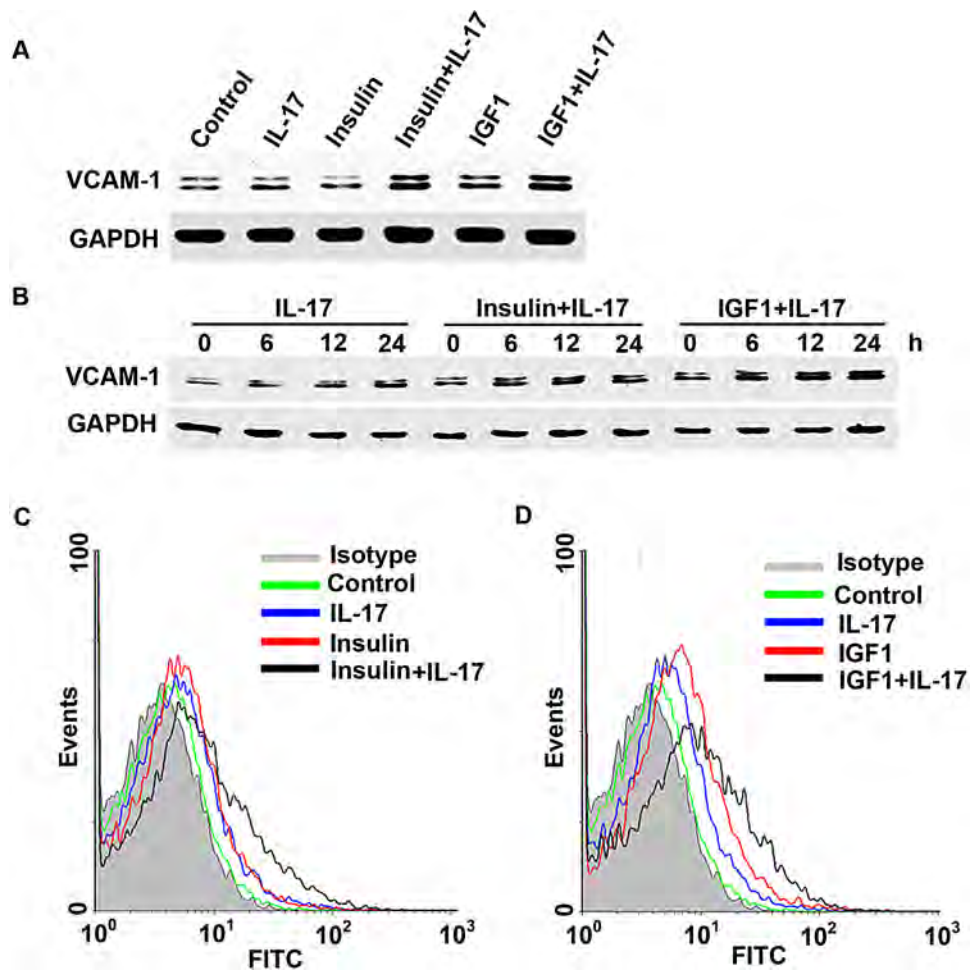


Fig. 1. VCAM-1 expression in HUVECs was induced by IL-17 and insulin/IGF1. **A:** Western blot analysis of VCAM-1 expression in HUVECs treated with IL-17, insulin, and IGF1, alone or in combination, for 24 hr. **B:** Western blot analysis of VCAM-1 expression in HUVECs treated with IL-17, insulin, and IGF1, alone or in combination, for 6, 12, and 24 hr. **C** and **D:** Flow cytometry analysis of VCAM-1 surface expression in HUVECs treated with IL-17, insulin, and IGF1, alone or in combination, for 24 hr.

and insulin/IGF1, there were significantly more CD44^{bright} DU-145 cells adhered to HUVECs, compared to the unsorted DU-145 cells (Fig. 4B). However, the adhesion of CD44^{dim} DU-145 cells to HUVECs was not increased by IL-17 and/or insulin/IGF1 treatment (Fig. 4B). Western blot analysis confirmed that CD44^{bright} DU-145 cells expressed higher levels of CD44 than the unsorted DU-145 cells, whereas CD44^{dim} DU-145 cells expressed little CD44 (Fig. 4C). Similarly, PC-3 cells were sorted into CD44^{bright} and CD44^{dim} populations using FACS (Fig. 5A). When HUVECs were treated with the combination of IL-17 and insulin/IGF1, there were significantly more CD44^{bright} PC-3 cells adhered to HUVECs, compared to the HUVECs treated with IL-17 or insulin/IGF1 alone (Fig. 5B). However, there was no statistical difference between CD44^{bright} and the unsorted PC-3 cells. In contrast, the adhesion of

CD44^{dim} PC-3 cells to HUVECs was not increased by IL-17 and/or insulin/IGF1 treatment (Fig. 5B). Since the adhesion between prostate cancer cells and HUVECs appeared to be dependent on expression of CD44 that has been shown to physically interact with VCAM-1 [29], we checked if CD44 binds to VCAM-1 when prostate cancer PC-3 cells adhered to HUVECs. We used three different negative controls: first, HUVECs alone control; as HUVECs expressed VCAM-1 but no CD44, anti-CD44 IP did not pull down VCAM-1 or CD44 (Fig. 6, lane 1); second, addition of LNCaP cells to HUVECs; as LNCaP cells expressed no CD44, anti-CD44 IP did not pull down VCAM-1 or CD44 (Fig. 6, lane 2); and third, IP with isotype IgG; as the non-specific IgG did not pull down CD44, VCAM-1 was not pulled down, either (Fig. 6, lanes 7–10). We initially used anti-CD44 antibodies to immunoprecipitate the CD44-VCAM-1

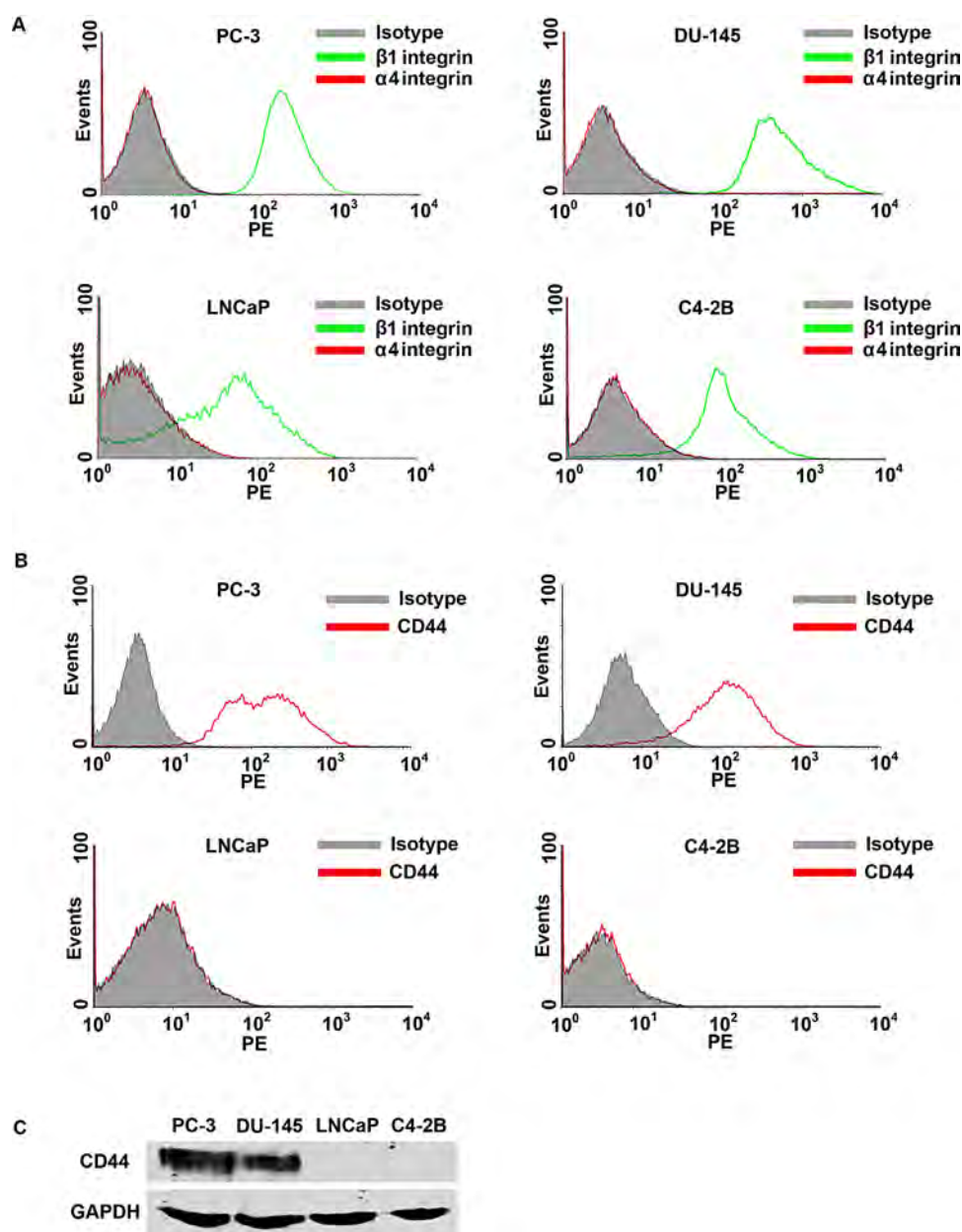


Fig. 2. Expression of adhesion molecules in prostate cancer cells. **A** and **B**: Flow cytometry analysis of α_4 integrin, β_1 integrin, and CD44 expression in PC-3, DU-145, LNCaP, and C4-2B cells. **C**: Western blot analysis of CD44 expression in PC-3, DU-145, LNCaP, and C4-2B cells. Equal loading of proteins was confirmed by re-probing GAPDH.

complex when PC-3 cells were added onto HUVECs that were not treated (control group) or treated with IL-17 and IGF1 to increase VCAM-1 expression, without fixation using 2% formaldehyde. To our surprise, we did not pull down any VCAM-1 in either the control group or the IL-17 and IGF1 treated group, though CD44 was pulled down (Fig. 6, lanes 3–4). We suspected that the CD44-VCAM-1 interaction might be transient or weak, hence could not remain stable during the protein extraction procedure. Therefore, we adopted a previously reported technique to

cross-link the protein interaction using 2% formaldehyde [28]. We found that anti-CD44 antibodies pulled down VCAM-1 in both the control and IL-17/IGF1 treated groups (Fig. 6, lanes 5–6). The amount of VCAM-1 protein pulled down was consistent to the levels of expression (Fig. 1A).

DISCUSSION

It has been reported that IL-17 can activate NF- κ B pathway [19], which is responsible for synthesis of

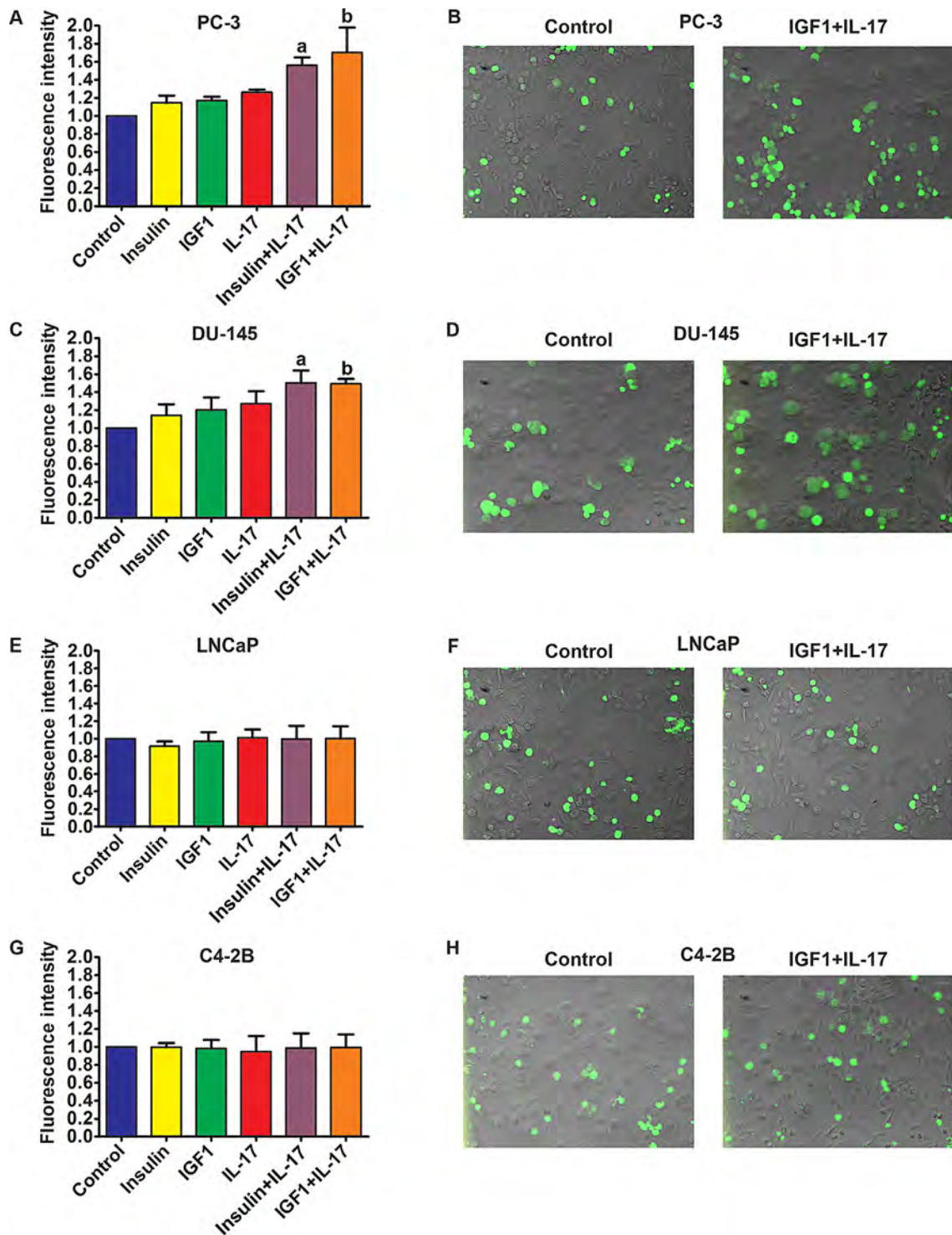


Fig. 3. Adhesion of prostate cancer cells to HUVECs. **A, C, E, and G:** Quantification of green fluorescence-labelled prostate cancer cells adhered to HUVECs within 15 min. HUVECs were treated with IL-17, insulin, and IGF1, alone or in combination, for 24 hr prior to addition of prostate cancer cells. Fluorescence intensity was proportional to the number of prostate cancer cells adhered to HUVECs. The fluorescence intensity of the control group was arbitrarily designated as "1," so the other groups were normalized with a formula: the fluorescence intensity of the treated group = the recorded fluorescence intensity of the treated group ÷ the recorded fluorescence intensity of the control group. Data represent means \pm standard deviations of three independent experiments ($n = 3$). **a,** $P < 0.05$ compared to the control, insulin alone and IL-17 alone treatment groups; **b,** $P < 0.05$ compared to the control, IGF1 alone and IL-17 alone treatment groups. **B, D, F, and H:** representative photomicrographs of the adhered prostate cancer cells labelled with green fluorescence. HUVECs were not labelled and laid in the background beneath the green cells.

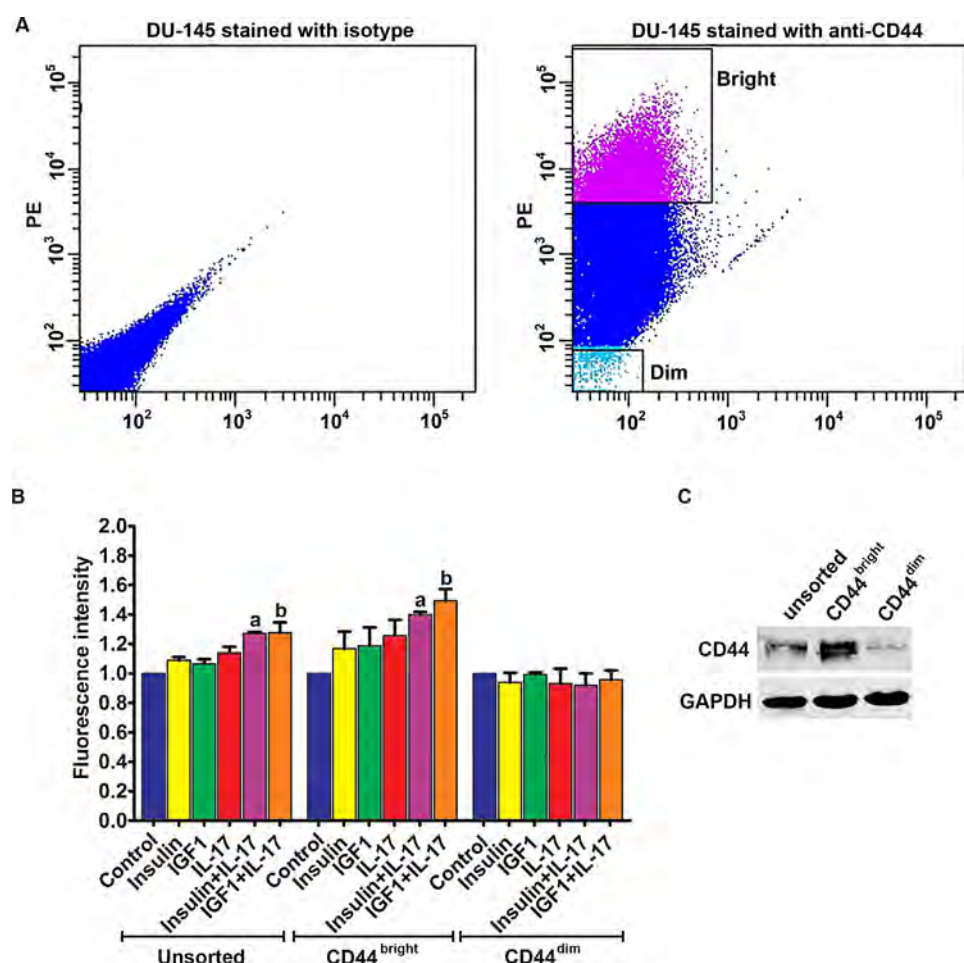


Fig. 4. Adhesion of the unsorted, CD44^{bright}, and CD44^{dim} DU-145 cells to HUVECs. **A:** Left panel, flow cytometry analysis of DU-145 cells stained with isotype control IgG; right panel, a representative dot plot shows how CD44^{bright} and CD44^{dim} DU-145 cells were sorted using FACS. **B:** Quantification of green fluorescence-labelled prostate cancer cells adhered to HUVECs within 15 min. HUVECs were treated with IL-17, insulin, and IGF1, alone or in combination, for 24 hr prior to addition of prostate cancer cells. Fluorescence intensity was proportional to the number of prostate cancer cells adhered to HUVECs. The fluorescence intensity of the control group was arbitrarily designated as "1," so the other groups were normalized with a formula: the fluorescence intensity of the treated group = the recorded fluorescence intensity of the treated group ÷ the recorded fluorescence intensity of the control group. Data represent means ± standard deviations of three independent experiments (n = 3). In the unsorted DU-145 cells panel, a indicates $P < 0.05$ compared to the control, insulin alone and IL-17 alone treatment groups; b indicates $P < 0.05$ compared to the control, IGF1 alone and IL-17 alone treatment groups. In the CD44^{bright} DU-145 cells panel, a and b indicate $P < 0.05$ compared to the corresponding single treatment and combined treatment groups within the CD44^{bright} DU-145 cells panel, and between the CD44^{bright} DU-145 cells panel and the unsorted DU-145 cells panel, as well as between the CD44^{bright} DU-145 cells panel and the CD44^{dim} DU-145 cells panel. **C:** Western blot analysis of CD44 expression in the unsorted, CD44^{bright}, and CD44^{dim} DU-145 cells. Equal loading of proteins was confirmed by re-probing GAPDH.

VCAM-1 in the vascular endothelial cells [30]. In the present study, we showed that insulin and IGF1 were able to enhance IL-17-induced VCAM-1 expression in HUVECs. Of note, VCAM-1 is a glycoprotein with two different splice isoforms, namely, VCAM-1a (full-length with Mr ~ 90–95 kDa) and VCAM-1b (lacking exon 5 with Mr ~ 80–83 kDa) [31]. We observed that IL-17 single treatment slightly increased VCAM-1b but not VCAM-1a, while insulin single treatment slightly decreased VCAM-1a but slightly

increased VCAM-1b, yet the combination of IL-17 and insulin treatment dramatically increased both VCAM-1a and VCAM-1b (Fig. 1A). The exact molecular mechanism that caused the different effects of IL-17 or insulin single treatment is not clear. Our previous study has demonstrated that insulin and IGF1 are able to enhance IL-17-induced expression of proinflammatory chemokines and cytokines [17]. We have shown that the underlying mechanism involves inhibition of glycogen synthase kinase 3 β (GSK3B) by

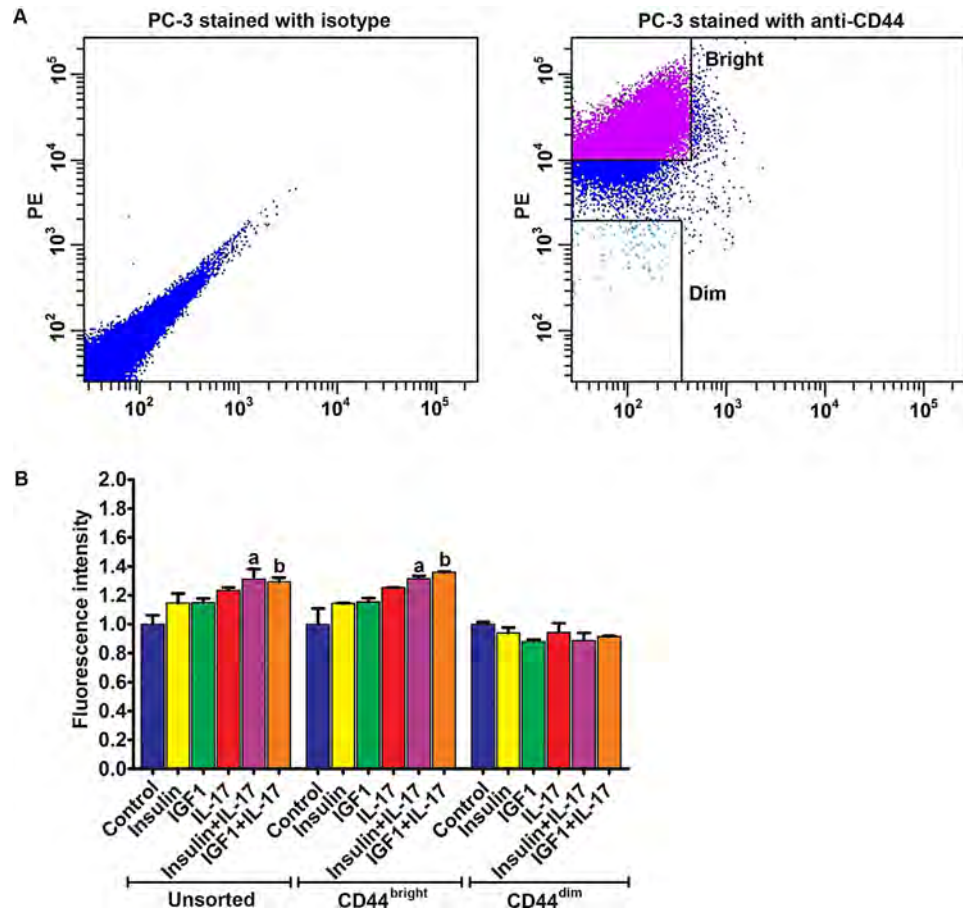


Fig. 5. Adhesion of the unsorted, CD44^{bright}, and CD44^{dim} PC-3 cells to HUVECs. **A:** Left panel, flow cytometry analysis of PC-3 cells stained with isotype control IgG; right panel, a representative dot plot shows how CD44^{bright} and CD44^{dim} PC-3 cells were sorted using FACS. **B:** Quantification of green fluorescence-labelled prostate cancer cells adhered to HUVECs within 15 min. HUVECs were treated with IL-17, insulin, and IGF1, alone or in combination, for 24 hr prior to addition of prostate cancer cells. Fluorescence intensity was proportional to the number of prostate cancer cells adhered to HUVECs. The fluorescence intensity of the control group was arbitrarily designated as "1," so the other groups were normalized with a formula: the fluorescence intensity of the treated group = the recorded fluorescence intensity of the treated group ÷ the recorded fluorescence intensity of the control group. Data represent means ± standard deviations of three independent experiments (n = 3). In the unsorted PC-3 cells panel, a indicates $P < 0.05$ compared to the control, insulin alone and IL-17 alone treatment groups; b indicates $P < 0.05$ compared to the control, IGF1 alone and IL-17 alone treatment groups. In the CD44^{bright} PC-3 cells panel, a and b indicate $P < 0.05$ compared to the corresponding single treatment and combined treatment groups within the CD44^{bright} PC-3 cells panel, and between the CD44^{bright} PC-3 cells panel and the CD44^{dim} PC-3 cells panel.

Akt. Akt is activated by insulin and IGF1 through their receptor-activated phosphatidylinositol 3-kinase (PI3K). GSK3B phosphorylates CAAT enhancer binding protein β (C/EBP β) and inhibits C/EBP β 's transcriptional function that is responsible for IL-17-induced gene expression [17,32]. Insulin and IGF1 can activate PI3K/Akt to phosphorylate GSK3B at serine 9 and inhibit GSK3B activity, and consequently increase C/EBP β function to enhance IL-17-induced gene expression. Recently, we have demonstrated that insulin and IGF1 can also activate PI3K/Akt to phosphorylate GSK3A at serine 21 and inhibit GSK3A activity, and consequently

enhance IL-17-induced gene expression [33]. We believe this mechanism may also be true for the enhanced expression of VCAM-1 in HUVECs treated with IL-17 and insulin/IGF1. IL-17 alone did not dramatically increase VCAM-1 expression to enhance adhesion because GSK3 negatively inhibits IL-17 signaling as demonstrated by previous studies [17,33,34]. In the presence of IGF1 or insulin, GSK3 function is inhibited by PI3K/Akt activated by IGF1 or insulin [17,33], thus VCAM-1 expression and subsequent adhesion are enhanced by IL-17. We have shown that the synergy between IL-17 and insulin/IGF1 can be blocked by melatonin that inhibits

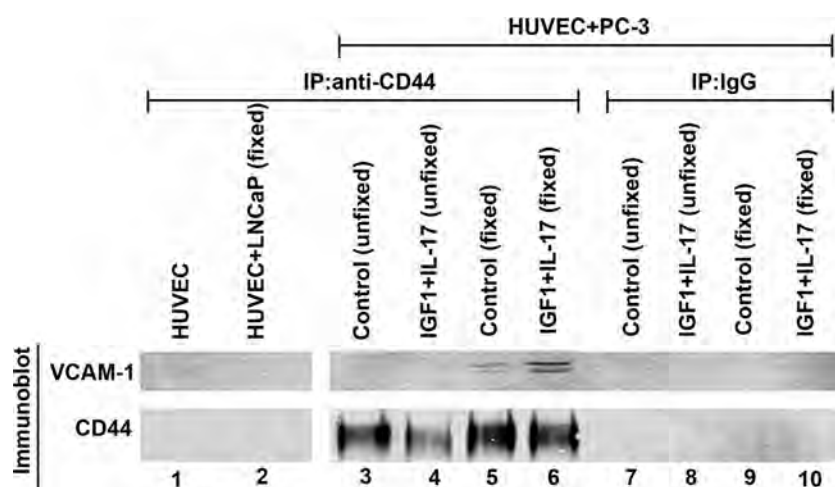


Fig. 6. CD44 expressed in prostate cancer cells binds to VCAM-1 expressed in HUVECs. Proteins were extracted from HUVECs alone and HUVECs with addition of LNCaP or PC-3 cells with or without cross-linking using 2% formaldehyde fixation. Immunoprecipitation (IP) was performed using isotype control mouse IgG or mouse anti-CD44 antibodies. Immunoblot (Western blot) was performed using anti-VCAM-1 or anti-CD44 antibodies. Where indicated (including the HUVEC + LNCaP group), HUVECs were treated with IL-17 and IGF1 for 24 hr. Unfixed, adherent PC-3 cells and HUVECs were harvested for protein extraction without fixation. Fixed, adherent PC-3 cells and HUVECs were harvested for protein extraction after fixation with 2% formaldehyde for 10 min.

Akt [17] or by a new pan-Akt inhibitor AZD5363 [33]. Therefore, it is potentially possible to use melatonin or AZD5363 to manipulate the cross-talk between IL-17 and insulin/IGF1 signaling pathways for preventive and therapeutic purposes.

VCAM-1 expression on the surface of endothelial cells contributes to leukocyte capture via binding to VLA-4 ($\alpha_4\beta_1$ integrin) expressed on the surface of leukocytes [35,36]. In the present study, we showed that the static adhesion of PC-3 and DU-145 cells to HUVECs was increased when HUVECs were treated with IL-17 and insulin/IGF1, which may be due to increased expression of VCAM-1 on the treated HUVECs. However, PC-3 and DU-145 cells did not express VLA-4, indicating that these prostate cancer cells cannot adhere to the endothelial cells through VLA-4-VCAM-1 interaction. It has been reported that VCAM-1 may bind to CD44 [4,29]. Therefore, we checked CD44 expression in the prostate cancer cells. We found that PC-3 and DU-145 cells expressed CD44 on their surface, whereas LNCaP and C4-2B cells did not express CD44. CD44 is a cell surface adhesion molecule and its main ligand is hyaluronic acid (HA) [37]. However, HA expression on HUVECs is usually not induced by inflammatory cytokines such as tumor necrosis factor- α (TNF- α), IL-1 β , lipopolysaccharide, or interferon γ [38]. Thus, CD44-HA interaction may not be able to explain the increased adhesion of PC-3 and DU-145 cells to HUVECs. P-selectin, L-selectin, and E-selectin have been reported to bind to CD44 and facilitate capture of colon cancer cells and leukocytes on the vascular

endothelial cells [39,40]. However, we did not detect any E-selectin expression in the HUVECs used in our study, thus E-selectin is unlikely to play any role in the adhesion of prostate cancer cells to HUVECs. We believe that the adhesion of prostate cancer cells to HUVECs is mediated through CD44-VCAM-1 interaction, based on the following evidence: first, only prostate cancer cells that express CD44 (PC-3 and DU-145 cells) adhered to HUVECs, particularly when VCAM-1 expression was enhanced by the treatment with IL-17 and insulin/IGF1, whereas the prostate cancer cells that do not express CD44 (LNCaP and C4-2B cells) did not adhere to HUVECs even after the treatment with IL-17 and insulin/IGF1; second, the sorted CD44^{dim} populations of PC-3 and DU-145 cells no longer adhered to HUVECs, due to reduced or lack of CD44 expression; and third, CD44 expressed in PC-3 cells physically bound to VCAM-1 expressed in HUVECs under the static adhesion condition.

It is of significance to identify CD44-VCAM-1 interaction that mediates adhesion of prostate cancer cells to the vascular endothelial cells, as CD44 is usually expressed in the stem cell-like prostate and breast cancer cells that circulate intravascularly and eventually metastasize to distant organs [41–44]. Thus, prostate cancer stem cells may adhere to the vascular endothelium through CD44-VCAM-1 interaction. Previously, Draffin et al. have shown that CD44 is able to facilitate the adherence of metastatic prostate and breast cancer cells to bone marrow endothelial cells via binding to HA [45]. When CD44 expression was down-regulated by miR34-a, prostate

cancer regeneration and metastasis was inhibited [46]. In the present study, we provided evidence to support that CD44-VCAM-1 interaction may also contribute to the adhesion of prostate cancer cells to the vascular endothelium. Of particular interest, the adhesion is enhanced by IL-17 and insulin/IGF1 due to increased VCAM-1 expression in the vascular endothelial cells. This may be relevant to the increased risks of metastasis and mortality in obese men with prostate cancer. It has been found that obese men have a 3.6-fold increase in risk of prostate cancer metastasis and a 2.6-fold increased risk of prostate cancer-specific mortality, compared to prostate cancer patients with normal body mass index [47]. Another recent study found that overweight and obese men were threefold and fivefold more likely to develop metastases than normal weight men [48]. It is well known that obese people have increased serum levels of insulin and IGF1 [49] as well as IL-17 [50]. Thus, we speculate that, due to increased levels of IL-17 and insulin/IGF1, VCAM-1 expression is increased in the vascular endothelial cells in obese men with prostate cancer, which facilitates adhesion of the stem cell-like circulating tumor cells through CD44-VCAM-1 interaction and subsequently promotes extravasation and metastasis of prostate cancer. Further studies are required to validate this speculation.

CONCLUSIONS

CD44-VCAM-1 interaction mediates the adhesion between prostate cancer cells and HUVECs. IL-17 and insulin/IGF1 enhance adhesion of prostate cancer cells to vascular endothelial cells through increasing VCAM-1 expression in the vascular endothelial cells. These findings suggest that IL-17 may act with insulin/IGF1 to promote prostate cancer metastasis.

ACKNOWLEDGMENTS

The authors thank Mary Price from Tulane Cancer Center and Louisiana Cancer Research Consortium FACS Core for flow cytometry analysis. Jiandong Mei is a visiting scholar at Tulane University School of Medicine sponsored by the China Scholarship Council (201406240145).

REFERENCES

- Entschladen F, Drell TL, Lang K, Joseph J, Zaenker KS. Tumour-cell migration, invasion, and metastasis: Navigation by neurotransmitters. *Lancet Oncol* 2004;5(4):254–258.
- Orr FW, Wang HH, Lafrenie RM, Scherbarth S, Nance DM. Interactions between cancer cells and the endothelium in metastasis. *J Pathol* 2000;190(3):310–329.
- Wong SY, Hynes RO. Lymphatic or hematogenous dissemination: How does a metastatic tumor cell decide. *Cell Cycle* 2006;5(8):812–817.
- Miles FL, Pruitt FL, van Golen KL, Cooper CR. Stepping out of the flow: Capillary extravasation in cancer metastasis. *Clin Exp Metastasis* 2008;25(4):305–324.
- Fidler IJ. The pathogenesis of cancer metastasis: The 'seed and soil' hypothesis revisited. *Nat Rev Cancer* 2003;3(6):453–458.
- Scherbarth S, Orr FW. Intravital videomicroscopic evidence for regulation of metastasis by the hepatic microvasculature: Effects of interleukin-1 α on metastasis and the location of B16F1 melanoma cell arrest. *Cancer Res* 1997;57(18):4105–4110.
- Huh SJ, Liang S, Sharma A, Dong C, Robertson GP. Transiently entrapped circulating tumor cells interact with neutrophils to facilitate lung metastasis development. *Cancer Res* 2010;70(14):6071–6082.
- Auguste P, Fallavollita L, Wang N, Burnier J, Bikfalvi A, Brodt P. The host inflammatory response promotes liver metastasis by increasing tumor cell arrest and extravasation. *Am J Pathol* 2007;170(5):1781–1792.
- Matsuura N, Puzon-McLaughlin W, Irie A, Morikawa Y, Kakudo K, Takada Y. Induction of experimental bone metastasis in mice by transfection of integrin $\alpha 4 \beta 1$ into tumor cells. *Am J Pathol* 1996;148(1):55–61.
- Kolls JK, Linden A. Interleukin-17 family members and inflammation. *Immunity* 2004;21(4):467–476.
- Novatchkova M, Leibbrandt A, Werzowa J, Neubuser A, Eisenhaber F. The STIR-domain superfamily in signal transduction, development and immunity. *Trends Biochem Sci* 2003;28(5):226–229.
- Chang SH, Park H, Dong C. Act1 adaptor protein is an immediate and essential signaling component of interleukin-17 receptor. *J Biol Chem* 2006;281(47):35603–35607.
- Qian Y, Liu C, Hartup J, Altuntas CZ, Gulen MF, Jane-Wit D, Xiao J, Lu Y, Giltaiy N, Liu J, Kordula T, Zhang QW, Vallance B, Swaidani S, Aronica M, Tuohy VK, Hamilton T, Li X. The adaptor Act1 is required for interleukin 17-dependent signaling associated with autoimmune and inflammatory disease. *Nat Immunol* 2007;8(3):247–256.
- Maitra A, Shen F, Hanel W, Mossman K, Tocker J, Swart D, Gaffen SL. Distinct functional motifs within the IL-17 receptor regulate signal transduction and target gene expression. *Proc Natl Acad Sci U S A* 2007;104(18):7506–7511.
- Ho AW, Shen F, Conti HR, Patel N, Childs EE, Peterson AC, Hernandez-Santos N, Kolls JK, Kane LP, Ouyang W, Gaffen SL. IL-17RC is required for immune signaling via an extended SEF/IL-17R signaling domain in the cytoplasmic tail. *J Immunol* 2010;185(2):1063–1070.
- Liu C, Qian W, Qian Y, Giltaiy NV, Lu Y, Swaidani S, Misra S, Deng L, Chen ZJ, Li X. Act1, a U-box E3 ubiquitin ligase for IL-17 signaling. *Sci Signal* 2009;2(92):63.
- Ge D, Dauchy RT, Liu S, Zhang Q, Mao L, Dauchy EM, Blask DE, Hill SM, Rowan BG, Brainard GC, Hanifin JP, Cecil KS, Xiong Z, Myers L, You Z. Insulin and IGF1 enhance IL-17-induced chemokine expression through a GSK3 β -dependent mechanism: a new target for melatonin's anti-inflammatory action. *J Pineal Res* 2013;55(4):377–387.
- Zhu S, Pan W, Song X, Liu Y, Shao X, Tang Y, Liang D, He D, Wang H, Liu W, Shi Y, Harley JB, Shen N, Qian Y. The microRNA miR-23b suppresses IL-17-associated autoimmune

- inflammation by targeting TAB2, TAB3 and IKK- α . *Nat Med* 2012;18(7):1077–1086.
19. Hwang SY, Kim JY, Kim KW, Park MK, Moon Y, Kim WU, Kim HY. IL-17 induces production of IL-6 and IL-8 in rheumatoid arthritis synovial fibroblasts via NF- κ B- and PI3-kinase/Akt-dependent pathways. *Arthritis Res Ther* 2004;6(2):R120–R128.
 20. Zhang Q, Liu S, Ge D, Xue Y, Xiong Z, Abdel-Mageed AB, Myers L, Hill SM, Rowan BG, Sartor O, Melamed J, Chen Z, You Z. Interleukin-17 promotes formation and growth of prostate adenocarcinoma in mouse models. *Cancer Res* 2012;72(10):2589–2599.
 21. Zhang Q, Liu S, Xiong Z, Wang AR, Myers L, Melamed J, Tang WW, You Z. Interleukin-17 promotes development of castration-resistant prostate cancer potentially through creating an immunotolerant and pro-angiogenic tumor microenvironment. *Prostate* 2014;74(8):869–879.
 22. Baxter RC, Bryson JM, Turtle JR. Somatogenic receptors of rat liver: regulation by insulin. *Endocrinology* 1980;107(4):1176–1181.
 23. Madonna R, Pandolfi A, Massaro M, Consoli A, De Caterina R. Insulin enhances vascular cell adhesion molecule-1 expression in human cultured endothelial cells through a pro-atherogenic pathway mediated by p38 mitogen-activated protein-kinase. *Diabetologia* 2004;47(3):532–536.
 24. Balaram SK, Agrawal DK, Allen RT, Kuszyński CA, Edwards JD. Cell adhesion molecules and insulin-like growth factor-1 in vascular disease. *J Vasc Surg* 1997;25(5):866–876.
 25. Roussel L, Houle F, Chan C, Yao Y, Berube J, Olivenstein R, Martin JG, Huot J, Hamid Q, Ferri L, Rousseau S. IL-17 promotes p38 MAPK-dependent endothelial activation enhancing neutrophil recruitment to sites of inflammation. *J Immunol* 2010;184(8):4531–4537.
 26. Xing X, Yang J, Yang X, Wei Y, Zhu L, Gao D, Li M. IL-17A induces endothelial inflammation in systemic sclerosis via the ERK signaling pathway. *PLoS ONE* 2013;8(12):e85032.
 27. Mackesy DZ, Goalstone ML. Insulin augments tumor necrosis factor- α stimulated expression of vascular cell adhesion molecule-1 in vascular endothelial cells. *J Inflamm (Lond)* 2011;8:34.
 28. Klockenbusch C, Kast J. Optimization of formaldehyde cross-linking for protein interaction analysis of non-tagged integrin β 1. *J Biomed Biotechnol* 2010;2010:927585.
 29. Wang PC, Weng CC, Hou YS, Jian SF, Fang KT, Hou MF, Cheng KH. Activation of VCAM-1 and its associated molecule CD44 leads to increased malignant potential of breast cancer cells. *Int J Mol Sci* 2014;15(3):3560–3579.
 30. Chen CC, Rosenbloom CL, Anderson DC, Manning AM. Selective inhibition of E-selectin, vascular cell adhesion molecule-1, and intercellular adhesion molecule-1 expression by inhibitors of I κ B- α phosphorylation. *J Immunol* 1995;155(7):3538–3545.
 31. Montes-Sanchez D, Ventura JL, Mitre I, Frias S, Michan L, Espejel-Nunez A, Vadillo-Ortega F, Zentella A. Glycosylated VCAM-1 isoforms revealed in 2D western blots of HUVECs treated with tumoral soluble factors of breast cancer cells. *BMC Chem Biol* 2009;9:7.
 32. Ruddy MJ, Wong GC, Liu XK, Yamamoto H, Kasayama S, Kirkwood KL, Gaffen SL. Functional cooperation between interleukin-17 and tumor necrosis factor- α is mediated by CCAAT/enhancer-binding protein family members. *J Biol Chem* 2004;279(4):2559–2567.
 33. Chen C, Zhang Q, Liu S, Lambrechts M, Qu Y, You Z. AZD5363 Inhibits Inflammatory Synergy between Interleukin-17 and Insulin/Insulin-Like Growth Factor 1. *Front Oncol* 2014;4:343.
 34. Shen F, Li N, Gade P, Kalvakolanu DV, Weibley T, Doble B, Woodgett JR, Wood TD, Gaffen SL. IL-17 receptor signaling inhibits C/EBP β by sequential phosphorylation of the regulatory 2 domain. *Sci Signal* 2009;2(59):ra8.
 35. Galkina E, Ley K. Immune and inflammatory mechanisms of atherosclerosis. *Annu Rev Immunol* 2009;27:165–197.
 36. Alon R, Kassner PD, Carr MW, Finger EB, Hemler ME, Springer TA. The integrin VLA-4 supports tethering and rolling in flow on VCAM-1. *J Cell Biol* 1995;128(6):1243–1253.
 37. Goodison S, Urquidí V, Tarín D. CD44 cell adhesion molecules. *Mol Pathol* 1999;52(4):189–196.
 38. Mohamadzadeh M, DeGrendele H, Arizpe H, Estess P, Siegelman M. Proinflammatory stimuli regulate endothelial hyaluronan expression and CD44/HA-dependent primary adhesion. *J Clin Invest* 1998;101(1):97–108.
 39. Thomas SN, Zhu F, Schnaar RL, Alves CS, Konstantopoulos K. Carcinoembryonic antigen and CD44 variant isoforms cooperate to mediate colon carcinoma cell adhesion to E- and L-selectin in shear flow. *J Biol Chem* 2008;283(23):15647–15655.
 40. Dimitroff CJ, Lee JY, Rafii S, Fuhlbrigge RC, Sackstein R. CD44 is a major E-selectin ligand on human hematopoietic progenitor cells. *J Cell Biol* 2001;153(6):1277–1286.
 41. Al-Hajj M, Wicha MS, Benito-Hernandez A, Morrison SJ, Clarke MF. Prospective identification of tumorigenic breast cancer cells. *Proc Natl Acad Sci U S A* 2003;100(7):3983–3988.
 42. Collins AT, Berry PA, Hyde C, Stower MJ, Maitland NJ. Prospective identification of tumorigenic prostate cancer stem cells. *Cancer Res* 2005;65(23):10946–10951.
 43. Patrawala L, Calhoun T, Schneider-Broussard R, Li H, Bhatia B, Tang S, Reilly JG, Chandra D, Zhou J, Claypool K, Coghlan L, Tang DG. Highly purified CD44⁺ prostate cancer cells from xenograft human tumors are enriched in tumorigenic and metastatic progenitor cells. *Oncogene* 2006;25(12):1696–1708.
 44. Hurt EM, Kawasaki BT, Klarmann GJ, Thomas SB, Farrar WL. CD44⁺ CD24[−] prostate cells are early cancer progenitor/stem cells that provide a model for patients with poor prognosis. *Br J Cancer* 2008;98(4):756–765.
 45. Draffin JE, McFarlane S, Hill A, Johnston PG, Waugh DJ. CD44 potentiates the adherence of metastatic prostate and breast cancer cells to bone marrow endothelial cells. *Cancer Res* 2004;64(16):5702–5711.
 46. Liu C, Kelnar K, Liu B, Chen X, Calhoun-Davis T, Li H, Patrawala L, Yan H, Jeter C, Honorio S, Wiggins JF, Bader AG, Fagin R, Brown D, Tang DG. The microRNA miR-34a inhibits prostate cancer stem cells and metastasis by directly repressing CD44. *Nat Med* 2011;17(2):211–215.
 47. Gong Z, Agalliu I, Lin DW, Stanford JL, Kristal AR. Obesity is associated with increased risks of prostate cancer metastasis and death after initial cancer diagnosis in middle-aged men. *Cancer* 2007;109(6):1192–1202.
 48. Keto CJ, Aronson WJ, Terris MK, Presti JC, Kane CJ, Amling CL, Freedland SJ. Obesity is associated with castration-resistant disease and metastasis in men treated with androgen deprivation.

tion therapy after radical prostatectomy: Results from the SEARCH database. *BJU Int* 2012;110(4):492–498.

49. Cohen DH, LeRoith D. Obesity, type 2 diabetes, and cancer: The insulin and IGF connection. *Endocr Relat Cancer* 2012;19(5): F27–F45.
50. Sumarac-Dumanovic M, Stevanovic D, Ljubic A, Jorga J, Simic M, Stamenkovic-Pejkovic D, Starcevic V, Trajkovic V, Micic D. Increased activity of interleukin-23/interleukin-17 proinflammatory axis in obese women. *Int J Obes (Lond)* 2009;33(1): 151–156.



This information is current as
of April 23, 2015.

Estradiol Inhibits Th17 Cell Differentiation through Inhibition of *ROR γ T* Transcription by Recruiting the ER α /REA Complex to Estrogen Response Elements of the *ROR γ T* Promoter

Rong-Yi Chen, Yi-Ming Fan, Qiuyang Zhang, Sen Liu,
Qingli Li, Guo-Lin Ke, Chen Li and Zongbing You

J Immunol 2015; 194:4019-4028; Prepublished online 13
March 2015;

doi: 10.4049/jimmunol.1400806

<http://www.jimmunol.org/content/194/8/4019>

**Supplementary
Material** <http://www.jimmunol.org/content/suppl/2015/03/13/jimmunol.1400806.DCSupplemental.html>

References This article **cites 58 articles**, 26 of which you can access for free at:
<http://www.jimmunol.org/content/194/8/4019.full#ref-list-1>

Subscriptions Information about subscribing to *The Journal of Immunology* is online at:
<http://jimmunol.org/subscriptions>

Permissions Submit copyright permission requests at:
<http://www.aai.org/ji/copyright.html>

Email Alerts Receive free email-alerts when new articles cite this article. Sign up at:
<http://jimmunol.org/cgi/alerts/etoc>

Estradiol Inhibits Th17 Cell Differentiation through Inhibition of *ROR γ T* Transcription by Recruiting the ER α /REA Complex to Estrogen Response Elements of the *ROR γ T* Promoter

Rong-Yi Chen,^{*,†,1} Yi-Ming Fan,^{*,1} Qiuyang Zhang,[†] Sen Liu,[†] Qingli Li,^{†,‡}
Guo-Lin Ke,^{*} Chen Li,^{*} and Zongbing You^{†,§,¶,||,#}

The symptoms of vaginal candidiasis exacerbate in the second half of the menstrual cycle in premenopausal women when the serum estradiol level is elevated. Estradiol has been shown to inhibit Th17 differentiation and production of antifungal IL-17 cytokines. However, little is known about the mechanisms. In the present study, we used mouse splenocytes and found that estradiol inhibited Th17 differentiation through downregulation of *Ror γ t* mRNA and protein expression. Estradiol activated estrogen receptor (ER) α to recruit repressor of estrogen receptor activity (REA) and form the ER α /REA complex. This complex bound to three estrogen response element (ERE) half-sites on the *Ror γ t* promoter region to suppress *Ror γ t* expression. Estradiol induced *Rea* mRNA and protein expression in mouse splenocytes. Using *Rea* small interfering RNA to knock down *Rea* expression enhanced *Ror γ t* expression and Th17 differentiation. Alternatively, histone deacetylase 1 and 2 bound to the three ERE half-sites, independent of estradiol. Histone deacetylase inhibitor MS-275 dose- and time-dependently increased *Ror γ t* expression and subsequently enhanced Th17 differentiation. In 15 healthy premenopausal women, high serum estradiol levels are correlated with low *ROR γ T* mRNA levels and high *REA* mRNA levels in the vaginal lavage. These results demonstrate that estradiol upregulates *REA* expression and recruits *REA* via ER α to the EREs on the *ROR γ T* promoter region, thus inhibiting *ROR γ T* expression and Th17 differentiation. This study suggests that the estradiol/ER α /REA axis may be a feasible target in the management of recurrent vaginal candidiasis. *The Journal of Immunology*, 2015, 194: 4019–4028.

Naive CD4⁺ T cells differentiate into several effector subsets with distinct functions, including Th1, Th2, Th17, and regulatory T cells (Tregs) (1). Th17 differentiation has been intensively studied, yet the underlying molecular mechanisms have not been fully understood. Naive CD4⁺ T cells are induced to differentiate into Th17 cells by a combination of TGF- β and IL-6 (2–4), TGF- β and IL-1 β (5, 6), or TGF- β and IL-21 (7). IL-23 was originally found to stimulate IL-17 expression (8); however, later studies found that IL-23 is responsible for the survival and expansion of Th17 cells (2–4). Blockade of Th1 and/or Th2 differentiation (via anti-IFN- γ and/or anti-IL-4 Abs) can enhance Th17 differentiation (9, 10). The converging point of actions by these cytokines is a thymus-specific isoform of the retinoid acid receptor-related orphan receptor C (*RORC* or *ROR γ*), also called *ROR γ T* (11). *ROR γ T* is the key transcription factor that orchestrates Th17 differentiation and transcription of IL-17A and IL-17F (12).

Another related orphan nuclear receptor ROR α plays a partially redundant role with *ROR γ T* in promoting Th17 differentiation, and double deficiencies in *ROR α* and *ROR γ T* globally impair Th17 generation and completely protect mice against experimental autoimmune encephalomyelitis (13). T cell-specific deficiency of *STAT3* impairs Th17 differentiation through decreasing *ROR γ T* expression and increasing expression of T-bet, a transcription factor responsible for Th1 differentiation, and Foxp3, a transcription factor responsible for Treg differentiation (14, 15). Recently, it has been shown that Th17 differentiation is regulated by a network of transcription factors, including *ROR γ T*, *STAT3*, *BATF*, IFN regulatory factor 4, c-Maf, and EP300 (16). The members of the regulatory network for Th17 differentiation are still expanding (17).

Th17 cells secrete IL-17A, IL-17F, IL-17A/F, IL-22, IL-21, and other cytokines and chemokines, which play important roles in host defense, autoimmunity, inflammation, and tumorigenesis (18, 19).

^{*}Department of Dermatology, Affiliated Hospital of Guangdong Medical College, Zhanjiang, Guangdong 524001, China; [†]Department of Structural and Cellular Biology, Tulane University Health Sciences Center, New Orleans, LA 70112; and [‡]Department of Obstetrics and Gynecology, West China Second University Hospital, Sichuan University, Chengdu, Sichuan 610041, China; [§]Department of Orthopaedic Surgery, Tulane University Health Sciences Center, New Orleans, LA 70112; [¶]Tulane Cancer Center and Louisiana Cancer Research Consortium, Tulane University Health Sciences Center, New Orleans, LA 70112; ^{||}Tulane Center for Aging, Tulane University Health Sciences Center, New Orleans, LA 70112; and [#]Tulane Center for Stem Cell Research and Regenerative Medicine, Tulane University Health Sciences Center, New Orleans, LA 70112

¹R.-Y.C. and Y.-M.F. contributed equally to this work.

Received for publication March 28, 2014. Accepted for publication February 9, 2015.

This work was supported by National Natural Science Foundation of China Grant 81171512 (to Y.-M. F.) and by Affiliated Hospital of Guangdong Medical College Matching Fund 1100/B010002 (to R.-Y.C.). Z.Y. was partially supported by National Institute of General Medical Sciences Grant P20GM103518 and National Cancer Institute Grant R01CA174714 of the National Institutes of Health, Department of Defense Grants W81XWH-14-1-0050, W81XWH-14-1-0149, and W81XWH-14-1-0458, the Developmental Fund of Tulane Cancer Center, and by Louisiana Cancer

Research Consortium funds. The content of this article is solely the responsibility of the authors and does not necessarily represent the official views of the National Institutes of Health or Department of Defense.

Address correspondence and reprint requests to Dr. Zongbing You or Dr. Yi-Ming Fan, Department of Structural and Cellular Biology, Tulane University School of Medicine, 1430 Tulane Avenue, Mailbox 8649, New Orleans, LA 70112 (Z.Y.) or Department of Dermatology, Affiliated Hospital of Guangdong Medical College, Zhanjiang, Guangdong 524001, China (Y.-M.F.). E-mail addresses: zyou@tulane.edu (Z.Y.) or ymfan1963@163.com (Y.-M.F.)

The online version of this article contains supplemental material.

Abbreviations used in this article: ChIP, chromatin immunoprecipitation; Ct, cycle threshold; E2, 17 β -estradiol; ER, estrogen receptor; ERE, estrogen response element; HDAC, histone deacetylase; MAA, methoxyacetic acid; qPCR, quantitative PCR; qRT-PCR, real-time quantitative RT-PCR; REA, repressor of estrogen receptor activity; ROR α , retinoid acid receptor-related orphan receptor α ; ROR γ T, thymus-specific isoform of retinoid acid receptor-related orphan receptor C; siRNA, small interfering RNA; Treg, regulatory T cell.

Copyright © 2015 by The American Association of Immunologists, Inc. 0022-1767/15/\$25.00

IL-17-deficient mice are susceptible to bacterial infections (20–23) and oral candidiasis caused by the commensal fungus *Candida albicans* (24, 25). In humans, autosomal recessive deficiency in *IL-17RA* and autosomal-dominant deficiency of *IL-17F* lead to chronic mucocutaneous candidiasis disease, characterized by infections of the skin, nails, and oral and genital mucosae with *C. albicans* (26). IL-17 can recruit neutrophils and monocytes (27–30). IL-17 acts on neutrophils to enhance production of reactive oxygen species, which mediate killing of fungi (31). On the one hand, candida mannan of *C. albicans* may induce host IL-17 production to trigger antifungal activity (32–34). On the other hand, candidal 5-hydroxytryptophan metabolites inhibit host IL-17 production (35). When a balance is achieved, commensalism between *C. albicans* and the host is established. However, in many physiologic and pathologic conditions, the balance is interrupted, resulting in candidiasis.

In premenopausal women, serum estradiol level is at a high peak around ovulation, which slightly decreases after ovulation, but elevates to a low peak at the midluteal phase, and then returns to the basal level during menses (36). Coincidentally, colonization of *C. albicans* generally rises in the second half of the menstrual cycle when serum estradiol level is elevated, which is accompanied with exacerbated symptoms in patients with vaginal candidiasis (37). Therefore, we hypothesized that there might be a link between vaginal candidiasis and estradiol level. One clue for this link came from a recent report that estradiol deficiency increased Th17 cell population and serum IL-17 levels in ovariectomized mice, which could be prevented by administration of exogenous estradiol (38). The purified CD4⁺ T cells expressed higher mRNA levels of *Roryt*, *Rora*, and *Stat3* in the ovariectomized mice, compared with the sham control mice. In contrast, *Foxp3* mRNA levels were lower in ovariectomized mice than in sham mice. Administration of exogenous estradiol to ovariectomized mice decreased *Roryt* expression but increased *Foxp3* expression in CD4⁺ T cells (38). These findings suggest that estradiol inhibits Th17 differentiation through downregulation of transcription factors, particularly *RORγT*. Another study further found that estrogen receptor (ER)α signaling in T cells inhibited Th1 and Th17 differentiation, as conditional knockout of *ERα* in T cells abolished estradiol-mediated experimental autoimmune encephalomyelitis protection (39). However, the mechanisms of how estradiol regulates *RORγT* expression are not known. In the present study, we report that estradiol acts on ERα to recruit repressor of ER activity (REA); binding of the ERα/REA complex to the estrogen response elements (EREs) of the *RORγT* promoter region suppresses *RORγT* expression, thus inhibiting Th17 differentiation.

Materials and Methods

Animals

Animal protocol was approved by the Animal Care and Use Committee of Tulane University, which was in compliance with the U.S. Department of Health and Human Services *Guide for the Care and Use of Laboratory Animals*. Six- to 8-wk-old mice of C57BL/6J or 129S4/SvJae**BALB/c* genetic background were used. Our preliminary experiments found that the results were similar using either male or female mice of either genetic background, and thus this study was conducted with the pooled splenocytes from both male and female mice of the two genetic backgrounds.

Reagents

17β-Estradiol (Tocris Bioscience) was dissolved as 50 mmol/l stock solutions in ethanol. Histone deacetylase (HDAC) inhibitor MS-275 (C₂₁H₂₀N₄O₃, Chemical Abstracts Service no. 209783-80-2, Sigma-Aldrich) was dissolved as 2.66 mmol/l stock solutions in DMSO. Cytokines (mouse IL-6, IL-23, and TGF-β1) and Abs (anti-mouse CD3e, CD28, IL-4, and IFN-γ) for Th17 polarization of mouse naive T cells (CD4⁺CD62L⁺) were purchased from BioLegend. A mouse CD4⁺CD62L⁺ T cell isolation kit II, MidiMACS separator, and columns were purchased from Miltenyi Biotec.

Isolation of naive T cells from mouse splenocytes

Lymphocyte suspension was prepared from fresh mouse spleens by gently grinding the spleens between two glass slides. The lymphocyte suspension was filtered through 70-μm cell strainers (BD Biosciences) to make a single-lymphocyte suspension. This lymphocyte suspension was further filtered through 30-μm pre-separation filters (Miltenyi Biotec). Then, CD4⁺CD62L⁺ naive T cells were isolated using a mouse CD4⁺CD62L⁺ T cell isolation kit II and MidiMACS separator, following the manufacturer's instructions. The collected cells were stained with anti-CD4-FITC and anti-CD62L-allophycocyanin Abs (Miltenyi Biotec) and analyzed with flow cytometry, which showed that the isolated lymphocytes were ≥92% positive for both CD4 and CD62L that were considered as naive T cells (40).

Th17 polarization

Cell culture dishes (60 × 15 mm in size) were first coated with anti-mouse CD3e (2 μg/ml) at 37°C for 2 h. After removing the Ab solution, the dishes were gently washed twice with PBS. Naive T cells at 2 × 10⁶/ml were plated in the coated dishes in RPMI 1640 medium (phenol red-free, Invitrogen) containing 2 mM glutamine and 10% FBS (charcoal/dextran treated, catalog no. SH30068.03, HyClone Laboratories) in the presence of Th17 polarization medium consisting of anti-mouse CD28 (5 μg/ml), IL-6 (50 ng/ml), TGF-β1 (1 ng/ml), IL-23 (5 ng/ml), anti-mouse IL-4 (10 μg/ml), and anti-mouse IFN-γ (10 μg/ml). Where indicated, the cells were simultaneously treated without or with 1 nmol/l 17β-estradiol (E2), or with MS-275 at doses of 2.66, 26.6, and 266 nmol/l, or with methoxyacetic acid (MAA, an HDAC inhibitor; Sigma-Aldrich) at 2 mmol/l. Three days after the treatment, the cells were harvested for analysis.

Real-time quantitative RT-PCR

Total RNA was isolated according to the instructions of an RNeasy Mini Kit (Qiagen) with on-membrane DNase I digestion to avoid genomic DNA contamination. cDNA was made from total RNA using an iScript cDNA synthesis kit (Bio-Rad Laboratories). The PCR primer sequences are shown in Table I. Real-time quantitative RT-PCR (qRT-PCR) was performed in triplicates with an iQ5 iCycler and iQ SYBR Green Supermix (Bio-Rad Laboratories) following the recommended protocols. Results were normalized to *Gapdh* levels using the formula $\Delta\text{cycle threshold (Ct)} = \text{Ct of target gene} - \text{Ct of Gapdh}$. The mRNA level of the control group (without Th17 polarization) was used as the baseline; therefore, $\Delta\Delta\text{Ct}$ was calculated using the formula $\Delta\Delta\text{Ct} = \Delta\text{Ct of target gene} - \Delta\text{Ct of the baseline}$. The fold change of mRNA level was calculated as $\text{fold} = 2^{-\Delta\Delta\text{Ct}}$.

Flow cytometry analysis

The differentiated splenocytes were fixed with fixation buffer and stained with a mouse Th17/Treg phenotyping kit (BD Pharmingen) containing Abs against mouse CD4 conjugated with PerCP-Cy5.5, mouse IL-17A conjugated with PE, and mouse Foxp3 conjugated with Alexa Fluor 647. The staining procedures were performed according to the manufacturer's instructions. Approximately 10,000 cells were analyzed using BD FACSCanto II flow cytometry (BD Biosciences). The control cells were stained with isotype Abs conjugated with fluorophores and served as the control staining group to set up the gating. The Th17 population was defined as CD4⁺IL-17A⁺ and the Treg population was defined as CD4⁺Foxp3⁺.

Western blot analysis

Proteins were extracted from the treated cells in RIPA lysis buffer (50 mM sodium fluoride, 0.5% Igepal CA-630 [Nonidet P-40], 10 mM sodium phosphate, 150 mM sodium chloride, 25 mM Tris [pH 8.0], 1 mM PMSF, 2 mM EDTA, 1.2 mM sodium vanadate) supplemented with protease inhibitor mixture (Sigma-Aldrich). An equal amount of proteins was subjected to 10% SDS-PAGE and transferred to polyvinylidene difluoride membranes. The membranes were blocked with 5% BSA in TBST buffer (25 mM Tris-HCl, 125 mM NaCl, 0.1% Tween 20) for 2 h and probed with the indicated primary Abs overnight and then IRDye 800CW- or IRDye 680-conjugated secondary Abs (LI-COR Biosciences) for 1 h. The results were visualized by using an Odyssey infrared imager (LI-COR Biosciences). For loading control, the membranes were stripped and probed for GAPDH. The Abs used are as follows: anti-*RORγT* (1:250 dilution, catalog no. 14-6988, eBioscience), anti-REA (1:500 dilution, catalog no. 07-234, Millipore), anti-STAT3 (1:1000 dilution, catalog no. 9139, Cell Signaling Technology), and anti-GAPDH (1:10,000 dilution, catalog no. MAB374, Millipore).

Coimmunoprecipitation

Mouse splenocytes were isolated by density gradient centrifugation with Ficoll-Paque Premium (GE Healthcare Life Sciences) following the manufacturer's instructions. The splenocytes were treated with or without 1 nmol/l E2 in RPMI 1640 medium for 45 min. Protein was extracted from the treated cells with RIPA buffer and divided into 500- μ l aliquots (each containing ~500 μ g protein). One microgram of the following Abs was added to the protein aliquots: chromatin immunoprecipitation (ChIP)-validated anti-ER α (catalog no. 17-603, Millipore), anti-REA, anti-HDAC1 (catalog no. 3601-100, BioVision), anti-HDAC2 (catalog no. 3602-100, BioVision), and normal rabbit IgG (catalog no. SC-2027, Santa Cruz Biotechnology) as negative control. After 1 h incubation at 4°C, 20 μ l 50% protein G agarose bead slurry was added for overnight incubation at 4°C. The beads were washed three times with PBS and boiled in 20 μ l SDS protein loading buffer. Then, the protein supernatants were subjected to 10% SDS-PAGE and analyzed as described in Western blot analysis.

ChIP

Mouse splenocytes were treated with or without 1 nmol/l E2 in RPMI 1640 medium for 45 min. A ChIP assay was performed using an EZ-Magna ChIP G chromatin immunoprecipitation kit (catalog no. 17-409, Millipore) following the manufacturer's instructions. Briefly, the cells were cross-linked with 1% formaldehyde. After stopping the cross-linking reaction with 10 \times glycine solution, the cells were lysed and the lysates were sonicated to shear DNAs into 200- to 1000-bp fragments. Fifty microliters chromatin extract of each sample was added to 450 μ l dilution buffer. Five microliters of the mixture was aliquoted as "input" and the rest was added with 1 μ g Ab and 20 μ l protein G magnetic beads for overnight incubation with rotation at 4°C. The protein G magnetic beads were washed four times on the Magna GriP rack (Millipore). Then, the beads were digested with proteinase K in 100 μ l ChIP elution buffer at 62°C for 2 h. Finally, DNA was purified for 32 cycles of PCR analysis and the products were run on 2% agarose gel electrophoresis and stained with ethidium bromide. Alternatively, quantitative PCR (qPCR) was performed using the purified DNA. Results were normalized to DNA inputs using the formula Δ Ct (cycle threshold) = Ct of DNA from immunoprecipitate (IP) – Ct of DNA input. The Δ Ct of IgG IP was used as the baseline; therefore, $\Delta\Delta$ Ct was calculated using the formula $\Delta\Delta$ Ct = Δ Ct of anti-ER α IP – Δ Ct of IgG IP.

The fold change of ChIP results was calculated as fold = $2^{-\Delta\Delta$ Ct}. The PCR and qPCR primer sequences are shown in Table I.

Small interfering RNA transfection

Pre-designed SMARTpool Accell mouse Phb2 small interfering RNA (siRNA, catalog no. E-040938-00-0020, product of GE Healthcare/Dharmacon, Lafayette, CO; purchased from Thermo Scientific) was used to target *Rea* (also named prohibitin 2, *Phb2*). An Accell nontargeting siRNA pool (catalog no. D-001910-10-20, product of GE Healthcare/Dharmacon; purchased from Thermo Scientific; contained four siRNAs that were designed with no homology to known human, mouse, or rat genes) was used as negative control. One μ mol/l targeting or nontargeting siRNA was added to naive T cells for a 3-d incubation using Accell siRNA delivery media (Thermo Scientific) following the manufacturer's instructions. Then, the transfected cells were used in Th17 polarization as described above, followed by qRT-PCR and Western blot analysis.

Analysis of human specimens

This human subject study was approved by the Institutional Review Board of the Affiliated Hospital of Guangdong Medical College. The procedures to obtain human specimens were in accordance with the *Ethical Principles for Medical Research Involving Human Subjects* as formulated in the World Medical Association Declaration of Helsinki (revised in 2008). Twenty-one healthy female volunteers (age 29–39 y) were recruited during their routine physical examination at the Affiliated Hospital of Guangdong Medical College. Informed consent was signed by each volunteer. The inclusion criteria were: 1) married; 2) with regular menstruation; 3) with normal vulva, vagina, and uterus on physical examination; and 4) with normal vaginal discharge under microscopic examination. The exclusion criteria were: 1) pregnant; 2) autoimmune diseases; 3) use of steroid hormones; 4) vaginal sexual intercourse, use of vaginal cream or vaginal suppositories, or vaginal lavage within 1 wk; 5) diabetes mellitus; 6) abnormal liver or renal function; or 7) systemic or local inflammatory diseases. Two milliliters vaginal lavage and 4 ml venous blood were collected from each volunteer. For vaginal lavage, 2 ml saline was used to rinse the vagina three times and finally collected at the posterior vaginal fornix. The vaginal lavage from six women was used to count the number of epithelial and

Table I. Nucleotide sequences of each PCR primer pair

| Species | Gene | Primer | Nucleotide Sequence (5' to 3') |
|------------------|--------------------------------|-----------|--------------------------------|
| Mouse qRT-PCR | <i>Il17a</i> | Sense | CAGGGAGAGCTTCATCTGTGT |
| | | Antisense | GCTGAGCTTTGAGGGATGAT |
| | <i>Il17f</i> | Sense | CCCAGGAAGACATACTTAGAAGAAA |
| | | Antisense | CAACAGTAGCAAAGACTTGACCA |
| | <i>Rorc (Roryt)</i> | Sense | GCTGAGGAAGTGGGAAAGTC |
| | | Antisense | GAAAGCAGGAGCAATGGAAGT |
| | <i>Rora</i> | Sense | TCACCTCTCTGCTTGTCTTG |
| | | Antisense | GCTTCTTCCCCTACTGTTCTCT |
| | <i>Stat3</i> | Sense | AGGAATCGGCTATATTGCTGGT |
| | | Antisense | CACCTTGGATTGAGAGTCAAGAC |
| | <i>Foxp3</i> | Sense | GCAAGAGCTCTTGTCCATTGA |
| | | Antisense | CACCAGGAAAGACAGCAACC |
| | <i>Gapdh</i> | Sense | TGCACCACCAACTGCTTAG |
| | | Antisense | GGATGCAGGGATGATGTTC |
| ChIP PCR | <i>Roryt primer 1</i> | Sense | ATCCCTCCAGTGGATCTGA |
| | | Antisense | GCCTTTGGAAACAAGACTGC |
| | <i>Roryt primer 2</i> | Sense | GTGCATACCCCTCAGCACCTT |
| | | Antisense | CTGTGGCTAGTGACAGGAG |
| ChIP qPCR | <i>Roryt primer 1</i> | Sense | GAGCTGAATCATTTCCCAACA |
| | | Antisense | GCCTTTGGAAACAAGACTGTC |
| | <i>Roryt primer 2</i> | Sense | GGTTGCCCAACATCTGT |
| | | Antisense | AGCTCAGGGAGGAGGGAT |
| Human qRT-PCR | <i>RORγT</i> | Sense | GTAACGCGGCCTACTCCTG |
| | | Antisense | GTCTTGACCACTGGTTCTGT |
| | <i>REA</i> | Sense | AGGGTAAGAAATGAGCCTAGTCACC |
| | | Antisense | GGTAGGGCTGTGCTGGACC |
| | <i>GAPDH</i> | Sense | TGCACCACCAACTGCTTAGC |
| | | Antisense | GGCATGGACTGTGGTCATGAG |

inflammatory cells after standard Giemsa stain, using a hematometer. The vaginal lavage from 15 women was centrifuged and the cell pellet was used for qRT-PCR analysis of *ROR γ T* and *REA* mRNA levels. The case with the lowest levels was used as the baseline, and the relative mRNA levels of other cases were calculated as described above. The PCR primer sequences are shown in Table I. Serum levels of estradiol were measured in the clinical laboratory using the routine chemiluminescent assay (Access estradiol reagent, catalog no. 33540, Beckman Coulter).

Statistical analysis

All bar graphs are presented as mean \pm SEM of three independent experiments ($n = 3$). One-way ANOVA was used to analyze the quantitative data. Pearson's correlation analysis was used to evaluate the correlations between the serum estradiol levels and vaginal *ROR γ T* or *REA* mRNA levels in human specimens. A p value <0.05 was considered statistically significant.

Results

Estradiol inhibits Th17 differentiation through downregulation of *Ror γ T* expression

Using a well-established protocol of Th17 differentiation (2–4) and qRT-PCR analysis (see primers in Table I), we found that naive T cells were induced to express *Il17a* and *Il17f* mRNAs, starting from 24 h with a peak at 72 h after induction with the Th17 polarization medium (Fig. 1A, 1B). Expression of both *Il17a* and *Il17f* was almost completely inhibited by addition of

1 nmol/l E2, a physiological concentration of E2 (41) (Fig. 1A, 1B). The key transcription factors *Ror γ T* and *Rora* mRNAs were induced by the Th17 polarization medium, starting from 24 h with a peak at 48 h (Fig. 1C, 1D). Addition of 1 nmol/l E2 to the Th17 polarization medium significantly downregulated *Ror γ T* and *Rora* mRNA levels (Fig. 1C, 1D, $p < 0.05$). In contrast, induction of *Stat3* mRNA expression by the Th17 polarization medium was not affected by addition of 1 nmol/l E2 (Fig. 1E). *Foxp3* mRNA expression was transiently induced by the Th17 polarization medium at 48 h, which was slightly enhanced by addition of 1 nmol/l E2 (Fig. 1F). We checked the protein expression of the transcription factors. We found that ROR γ T protein level was dramatically decreased by E2, whereas STAT3 protein level was not obviously affected by E2 (Fig. 1G). Furthermore, Th17 polarization increased Th17 cells to 8.5% of the assessed population, compared with 1.1% in the control treatment group, whereas E2 treatment group only had 3.2% Th17 cells (Fig. 2A–D). Alternatively, Th17 polarization slightly increased Tregs to 1.6%, compared with 0.5% in the control treatment group; however, E2 treatment further increased Tregs to 8.6% (Fig. 2E–H). These findings are consistent with the previous studies showing that estradiol binds to ER α and inhibits Th17 differentiation (38, 39).

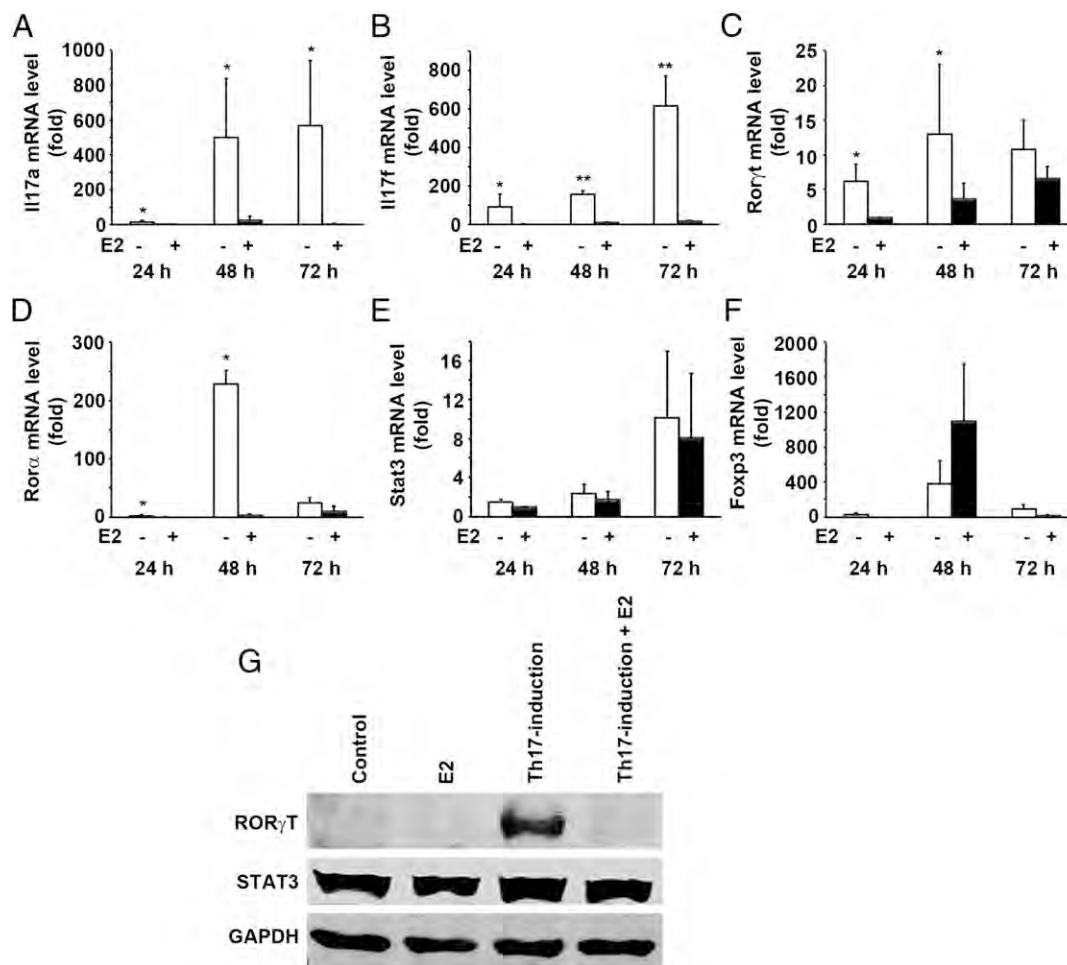


FIGURE 1. Estradiol inhibits Th17 differentiation through downregulation of *Ror γ T* expression. CD4⁺CD62L⁺ naive T cells from mouse spleens were cultured in 2 μ g/ml anti-CD3e-coated dishes with 5 μ g/ml anti-CD28, 50 ng/ml IL-6, 1 ng/ml TGF- β 1, 5 ng/ml IL-23, 10 μ g/ml anti-IL-4, and 10 μ g/ml anti-IFN- γ , with or without 1 nmol/l E2. After 24, 48, and 72 h of differentiation, mRNA levels were measured by qRT-PCR. Data are means \pm SEM ($n = 3$) of three independent experiments, with triplicates in each experimental group. * $p < 0.05$, ** $p < 0.01$ compared with the corresponding E2-treated groups as determined by ANOVA. (A–F) mRNA levels of *Il17a*, *Il17f*, *Ror γ T*, *Rora*, *Stat3*, and *Foxp3*. (G) Protein level was analyzed by Western blot analysis, as shown in representative blots from one of three independent experiments. The membranes were probed for GAPDH as a loading control.

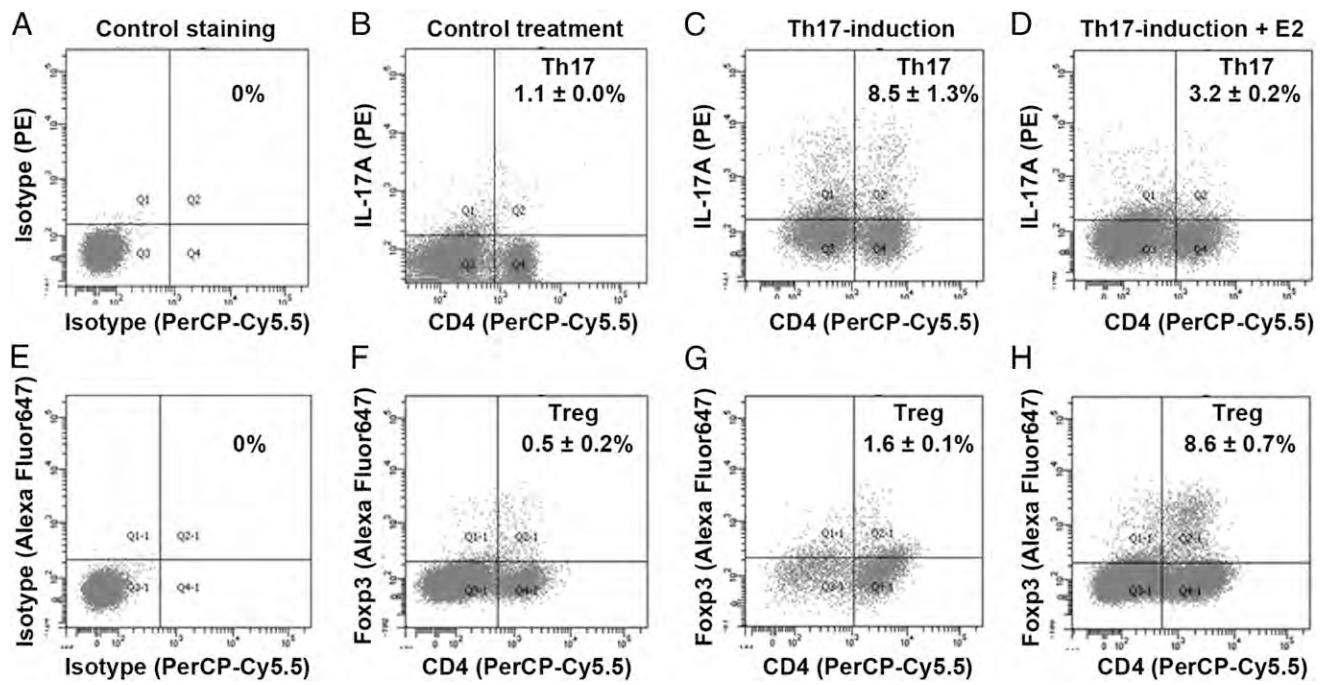


FIGURE 2. Estradiol reduces Th17 cells but increases Tregs. CD4⁺CD62L⁺ naive T cells from mouse spleens were cultured in 2 μ g/ml anti-CD3e-coated dishes with 5 μ g/ml anti-CD28, 50 ng/ml IL-6, 1 ng/ml TGF- β 1, 5 ng/ml IL-23, 10 μ g/ml anti-IL-4, and 10 μ g/ml anti-IFN- γ , with or without 1 nmol/l E2. After 3 d of differentiation, the cells were double stained for CD4⁺IL-17A⁺ Th17 and CD4⁺Foxp3⁺ Tregs using flow cytometry analysis. (A–H) Representative dot plots of two sets of independent flow cytometry analyses.

Mouse Ror γ t gene promoter region contains three ERE half-sites

Estradiol acts through ER α and ER β . Because ER α has been shown to be responsible for inhibition of Th17 differentiation (39), our study focused on ER α . ER α is known to bind to the ERE sites of the promoter regions of the ER α target genes. The essential ERE is a 13-bp inverted repeat with the consensus sequence 5'-GGTCAnnnTGACC-3' (42). Under certain conditions (such as when accompanied with another cofactor), ER α may also bind to the sequence with half of the 13-bp, so-called ERE half-site (43). We used the Transcription Element Search System (University of Pennsylvania) and analyzed a 2-kb (–1994 to +151) promoter re-

gion of mouse *Ror γ t* gene (NC_00069.6). We found that there were three ERE half-sites located at 799 (named ERE1), 1618 (named ERE2), and 1653 bp (named ERE3) upstream to the *Ror γ t* transcription start site (Supplemental Fig. 1). We designed two PCR primer sets to perform ChIP assays to determine whether ER α indeed binds to the ERE half-sites. Because ERE2 and ERE3 are only 31 bp apart and it is difficult to separate them in ChIP assays, they were covered by one PCR primer pair (Supplemental Fig. 1). We found that anti-ER α Ab did not pull down ERE1 in the absence of E2, but pulled down ERE1 in the presence of E2 (Fig. 3A, 3C). Similarly, anti-ER α Ab did not pull down ERE2/3 in the absence of E2, but pulled down ERE2/3 in the presence of E2 (Fig. 3B, 3D).

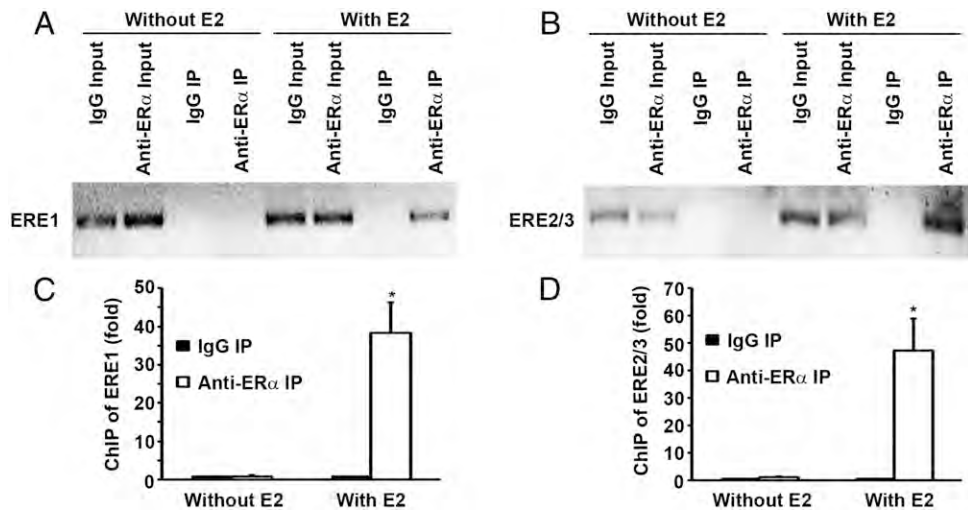


FIGURE 3. ER α binds to the three ERE half-sites (ERE1, ERE2, and ERE3) of mouse *Ror γ t* gene promoter region. (A and B) Results of ChIP assays performed on mouse splenocytes treated with or without 1 nmol/l E2 for 45 min. Chromatin was immunoprecipitated (IP) with normal rabbit IgG or anti-ER α ; PCR products were visualized on agarose gel stained with ethidium bromide. One representative of three independent experiments is shown. (C and D) Results of ChIP assays were measured by qPCR. Data are means \pm SEM (n = 3) of three independent experiments. * p < 0.01 compared with the corresponding IgG IP groups as determined by ANOVA.

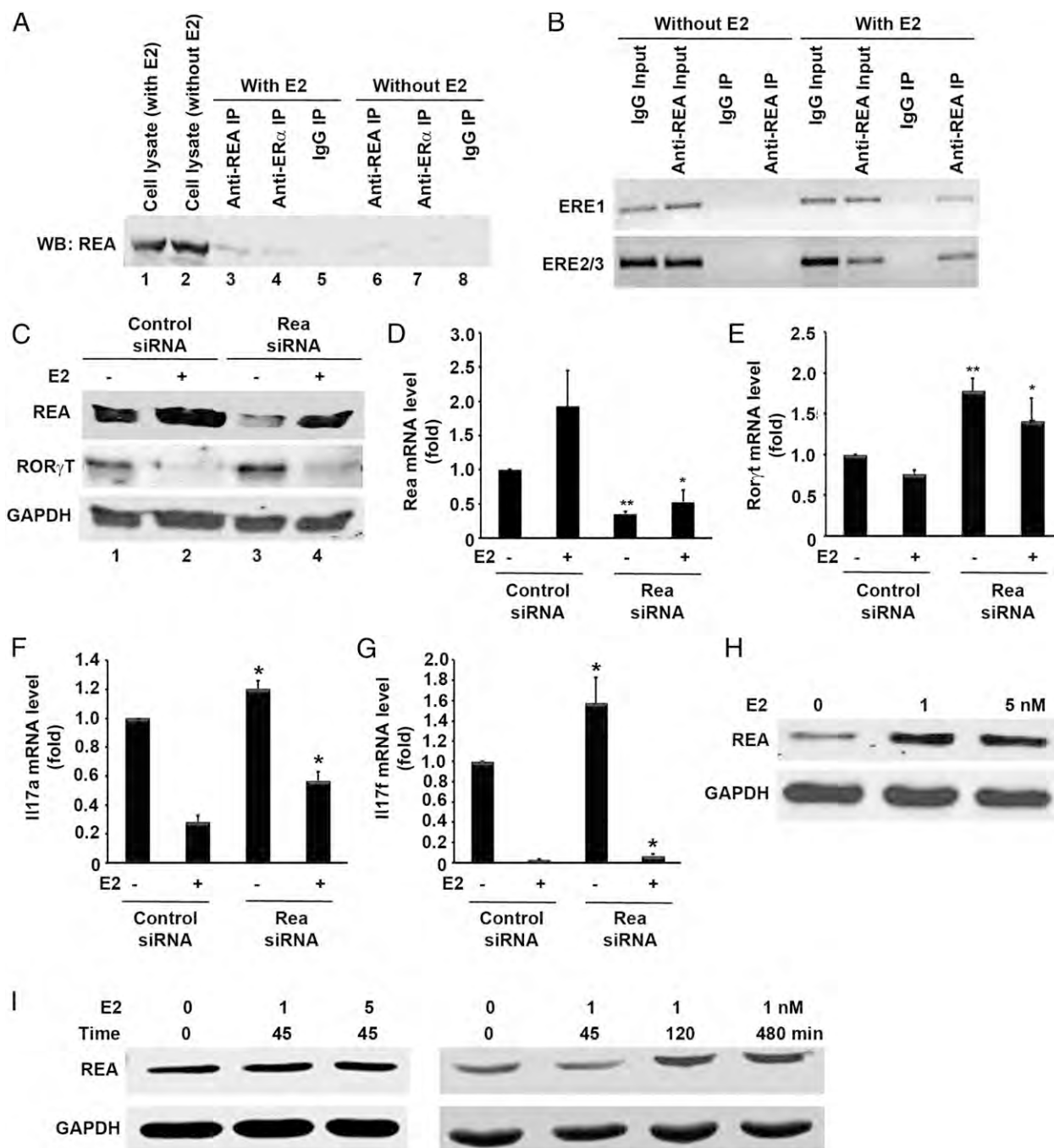


FIGURE 4. Estradiol activates ER α to recruit REA to inhibit *Ror γ t* expression. **(A)** Results of coimmunoprecipitation assays performed on mouse splenocytes treated with or without 1 nmol/l E2 for 45 min. Protein was immunoprecipitated (IP) with normal rabbit IgG, anti-ER α , or anti-REA and analyzed by Western blot (WB) analysis. One representative of three independent experiments is shown. **(B)** Results of ChIP assays performed on mouse splenocytes treated with or without 1 nmol/l E2 for 45 min. One representative of three independent experiments is shown. **(C–G)** Mouse naive T cells were transfected with 1 μ mol/l control or *Rea* siRNA for 3 d, followed by Th17 polarization for 3 d with or without 1 nmol/l E2. Protein level was analyzed by Western blot analysis, as shown in representative blots from one of three independent experiments (C); mRNA levels were measured by qRT-PCR (D–G), shown as mean \pm SEM ($n = 3$) of three independent experiments, with triplicates in each experimental group. * $p < 0.05$, ** $p < 0.01$ compared with the corresponding control siRNA-treated groups as determined by ANOVA. **(H and I)** Mouse splenocytes were treated with 0, 1, and 5 nmol/l E2 for 24 h (H) or 45, 120, or 480 min (I). Protein level was analyzed by Western blot analysis and one representative of three independent experiments is shown.

ER α recruits REA to inhibit *Ror γ t* expression

Because we found that E2 inhibited *Ror γ t* expression, we examined protein expression of several known corepressors of ER α in mouse splenocytes, including REA, nuclear receptor corepressor, silencing mediator of retinoid and thyroid hormone receptors, metastasis-associated 1, HDAC1, and HDAC2 (44). We found that only REA, HDAC1, and HDAC2 proteins were readily detectable

in mouse splenocytes using Western blot analysis. Using coimmunoprecipitation assays, we found that anti-ER α Ab did not pull down REA in the absence of E2 (Fig. 4A, lane 7). In contrast, anti-ER α Ab pulled down REA in the presence of E2 (Fig. 4A, lane 4). Using ChIP assays, we found that anti-REA Ab did not pull down either ERE1 or ERE2/3 in the absence of E2, whereas it pulled down both ERE1 and ERE2/3 in the presence of E2 (Fig. 4B). To

determine whether REA regulates *Roryt* expression, we used a prevalidated commercial *Rea* siRNA to knock down REA protein expression in the absence of E2 (Fig. 4C, compare lanes 1 and 3) and in the presence of E2 (Fig. 4C, compare lanes 2 and 4). We found that a decrease of REA levels was accompanied with an increase of ROR γ T protein levels (Fig. 4C, compare lanes 1 versus 3 and lanes 2 versus 4). We found that *Rea* siRNA decreased *Rea* mRNA levels in the absence and presence of E2 (Fig. 4D), which was accompanied with an increase in *Roryt* mRNA levels (Fig. 4E). Subsequently, we found that *Il17a* and *Il17f* mRNA levels were also increased by *Rea* siRNA in both the

absence and presence of E2, compared with the corresponding control siRNA groups (Fig. 4F, 4G). Because we observed that estradiol treatment increased *Rea* mRNA and protein levels in the presence of the control and *Rea* siRNAs (Fig. 4C, 4D), we examined the effects of estradiol on mouse splenocytes in the absence of any siRNAs to rule out any effects caused by the siRNAs. We found that REA protein expression was increased by E2 at 1 and 5 nmol/l after 24 h treatment (Fig. 4H). However, the levels of REA protein were not affected by E2 treatment at doses of either 1 or 5 nmol/l for 45 min; instead, REA expression was increased after 2 h treatment with 1 nmol/l E2 (Fig. 4I).

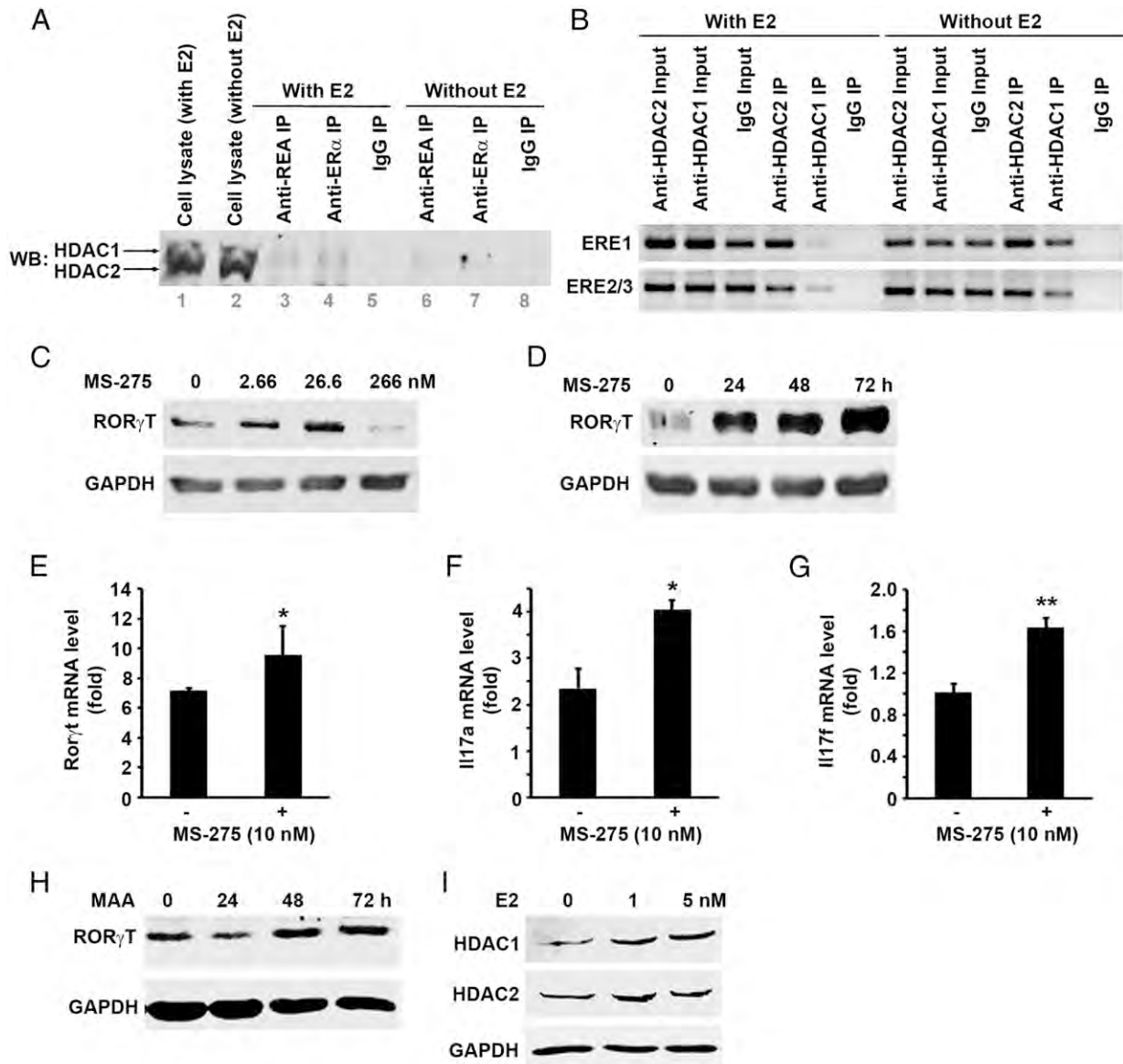


FIGURE 5. HDAC1 and HDAC2 constitutively bind to the EREs of *Roryt* promoter region and inhibit *Roryt* expression. **(A)** Results of coimmunoprecipitation assays performed on mouse splenocytes treated with or without 1 nmol/l E2 for 45 min. Protein was immunoprecipitated (IP) with normal rabbit IgG, anti-ER α , or anti-REA and analyzed by Western blot (WB) analysis. One representative of three independent experiments is shown. **(B)** Results of ChIP assays performed on mouse splenocytes treated with or without 1 nmol/l E2 for 45 min. One representative of three independent experiments is shown. **(C)** Mouse naive T cells were cultured in Th17 polarization medium in the presence of 0, 2.66, 26.6, and 266 nmol/l MS-275 for 24 h. Protein level was analyzed by Western blot analysis, and one of three independent experiments is shown. **(D)** Mouse naive T cells were cultured in Th17 polarization medium in the presence of 10 nmol/l MS-275 for 0, 24, 48, and 72 h. Protein level was analyzed by Western blot analysis and one of three independent experiments is shown. **(E–G)** Mouse naive T cells were cultured in Th17 polarization medium with or without 10 nmol/l MS-275 for 72 h. The mRNA levels were measured by qRT-PCR, shown as mean \pm SEM ($n = 3$) of three independent experiments, with triplicates in each experimental group. * $p < 0.05$, ** $p < 0.01$ as determined by ANOVA, compared with the corresponding groups without MS-275 treatment. **(H and I)** Mouse splenocytes were treated with 2 mM MAA for 0, 24, 48, and 72 h (H), or with 0, 1, and 5 nmol/l E2 for 24 h (I). Protein level was analyzed by Western blot analysis and one of three independent experiments is shown.

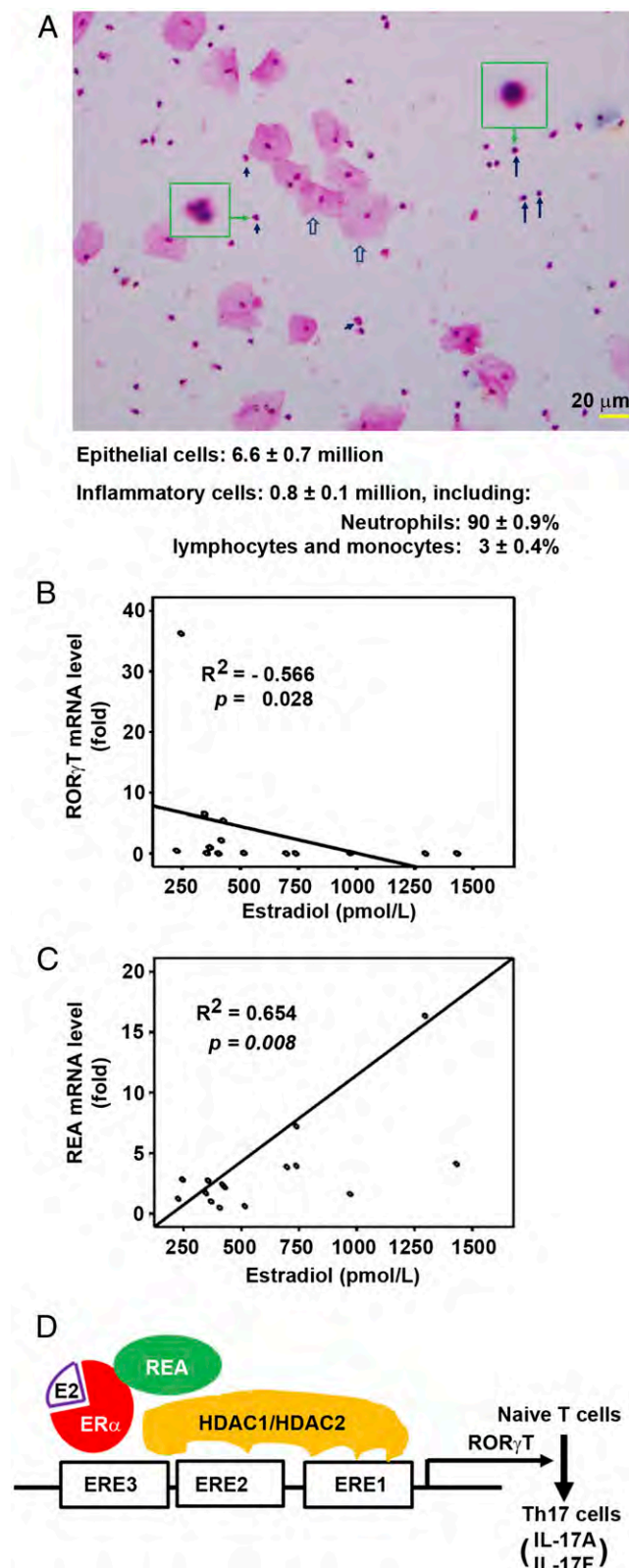


FIGURE 6. Human serum estradiol levels are correlated with *REA* and *RORγT* mRNA levels in the vaginal lavage. **(A)** Vaginal lavage from six healthy women was examined for the number of epithelial cells (open arrows) and inflammatory cells including neutrophils with segmented or banded nuclei (arrowheads) and lymphocytes/monocytes (arrows). The cells were stained with Giemsa stain. Original magnification $\times 250$; the cells in the green boxes were enlarged 8-fold to show the morphology of the indicated cells. **(B and C)** Fifteen healthy women were examined for their serum E2 levels using routine chemiluminescent assays and *RORγT*

HDAC1 and HDAC2 constitutively bind to the *EREs* of *Rorγt* promoter region and inhibit *Rorγt* expression

HDAC1 and *HDAC2* have been shown to interact with *REA* in transcriptional repression (45). Using coimmunoprecipitation assays, we found that in the absence of *E2*, neither anti-*REA* or anti-*ERα* Abs pulled down *HDAC1* or *HDAC2* (Fig. 5A, lanes 6 and 7). In the presence of *E2*, both anti-*REA* and anti-*ERα* Abs pulled down a faint band corresponding to *HDAC1* (Fig. 5A, lanes 3 and 4). Using ChIP assays, we found that both anti-*HDAC1* and anti-*HDAC2* Abs pulled down *ERE1* and *ERE2/3* in the absence and presence of *E2* (Fig. 5B). We then tested whether *HDAC* inhibitor *MS-275* (46) could affect *RORγT* protein expression in mouse splenocytes. We found that *MS-275* increased *RORγT* protein expression at 2.66 and 26.6 nmol/l, whereas it decreased *RORγT* protein expression at 266 nmol/l after 24 h treatment (Fig. 5C). A low dose (10 nmol/l) of *MS-275* increased *RORγT* protein expression furthermore after 48 and 72 h treatment (Fig. 5D). *MS-275* also significantly increased *Rorγt* mRNA levels (Fig. 5E, $p < 0.05$). Additionally, *MS-275* significantly increased *Il17a* and *Il17f* mRNA levels (Fig. 5F, 5G, $p < 0.05$ or 0.01 , respectively). *MAA* is an *HDAC* inhibitor that inhibits *HDAC1*, *HDAC2*, and *HDAC3* (47, 48). *RORγT* protein expression was also increased by treatment with 2 mM *MAA* after 48 and 72 h treatment (Fig. 5H). Additionally, *E2* also slightly increased expression of *HDAC1* and *HDAC2* proteins after 24 h treatment (Fig. 5I).

Human serum estradiol levels are correlated with REA and RORγT mRNA levels in the vaginal lavage

To determine whether the effects of estradiol on Th17 differentiation in the culture dishes are relevant to human physiologic conditions, we collected vaginal lavage from 21 healthy women. In each vaginal lavage of six healthy women, there were 6.6 ± 0.7 (mean \pm SEM, $n = 6$) million epithelial cells and 0.8 ± 0.1 million inflammatory cells (Fig. 6A). Among the inflammatory cells, $90 \pm 0.9\%$ of them were neutrophils and $3 \pm 0.4\%$ of them were lymphocytes and monocytes (Fig. 6A). We measured the serum estradiol levels and *RORγT* and *REA* mRNA levels in the vaginal lavage in 15 healthy women. We found that the serum estradiol levels were inversely correlated with *RORγT* mRNA levels (Fig. 6B, $p < 0.05$). In contrast, the serum estradiol levels were positively correlated with *REA* mRNA levels (Fig. 6C, $p < 0.01$).

Discussion

Although estradiol has been shown to inhibit *RORγT* expression in an *ERα*-dependent manner (38, 39), little is known about how *E2/ERα* act to inhibit *RORγT* expression. In this study, we demonstrate that *E2* inhibits *RORγT* expression through recruitment of *ERα/REA* complex to the three *ERE* half-sites on the *RORγT* promoter region. *ERα* only binds to *ERE1* and *ERE2/3* in the presence of *E2* (Fig. 3A, 3B). *ERα* only forms a complex with *REA* in the presence of *E2* (Fig. 4A), and *REA* only binds to *ERE1* and *ERE2/3* in the presence of *E2* (Fig. 4B). These results suggest that the *E2*-induced *ERα/REA* complex binds to the *EREs*

and *REA* mRNA levels in the vaginal lavage using qRT-PCR. Scatter plots show the correlations between serum E2 levels and *RORγT* (or *REA*) mRNA levels using Pearson's correlation analysis. **(D)** Proposed model of how *E2* inhibits Th17 differentiation. *E2*-induced *ERα/REA* complex binds to the *EREs* of the *RORγT* promoter region and suppresses *RORγT* transcription, resulting in decreased *RORγT* protein level and inhibition of Th17 differentiation and expression of IL-17A and IL-17F. *HDAC1* and *HDAC2* constitutively bind to the *RORγT* promoter region and inhibit *RORγT* transcription, independent of *E2/ERα*.

of the *RORγT* promoter region and suppresses *RORγT* transcription, resulting in decreased *RORγT* protein level and inhibition of Th17 differentiation as evidenced by reduced numbers of Th17 cells (Fig. 2C, 2D) and decreased expression of IL-17A and IL-17F (summarized in Fig. 6D). REA selectively represses the transcriptional activity of the ER, but not other steroid and non-steroid nuclear receptors (49–52). ERα–REA interaction is required for E2-mediated repression of B cell translocation gene 2 (53). We found that E2 upregulates *Rea* mRNA and protein expression (Fig. 4C, 4D, 4H, 4I). Knockdown of *Rea* expression by *Rea* siRNA can increase *Rorγt* expression and subsequently increase *Il17a* and *Il17f* expression. However, because E2 upregulates *Rea* expression, *Rea* siRNA is less effective in reducing REA levels in the presence of E2, compared with in the absence of E2 (Fig. 4C, 4E). Nevertheless, to our knowledge, this is the first study showing that E2 upregulates REA expression, in addition to inducing ERα/REA complex formation. Of note, in the control siRNA group, E2 treatment dramatically increased *Rea* and decreased *Il17* expression, but less so in reducing *Rorγt* mRNA expression (Fig. 4E), although *RORγT* protein level was dramatically decreased (Fig. 4C, lanes 1 versus 2). We are not sure about what caused the difference between *Rorγt* mRNA and protein levels.

Alternatively, we found that HDAC1 and HDAC2 bind to ERE1 and ERE2/3 in the presence and absence of E2 (Fig. 5B), which suggests that HDAC1 and HDAC2 constitutively bind to the *RORγT* promoter region, independent of estradiol. However, we did observe that at least HDAC1 forms a weak interaction with ERα and REA in the presence of E2 (Fig. 5A, lanes 3 and 4). A previous report showed that REA interacts with HDAC1 and HDAC2 in a ligand-independent manner using GST fusion proteins (45). We cannot rule out the possibility that E2 is required to translocate ERα/REA to the proximity of HDAC1/2 in the nucleus, thereby they may form a corepressor complex in inhibition of *RORγT* expression (Fig. 6D). This becomes more likely as expression of HDAC1 and HDAC2 is increased by E2 after 24 h treatment (Fig. 5I). We found that an HDAC inhibitor MS-275 upregulates *RORγT* expression in a dose- and time-dependent manner (Fig. 5C, 5D). MS-275 selectively inhibits HDAC1, HDAC2, and HDAC3 (46, 54, 55). We found that at low doses (up to 26.6 nmol/l), MS-275 upregulates *RORγT* expression; however, at a high dose (266 nmol/l), MS-275 decreases *RORγT* expression (Fig. 5C), which may be due to MS-275's toxicities, as we observed obvious lymphocyte death at this high dose (data not shown). MAA also inhibits HDAC1, HDAC2, and HDAC3 (47, 48), and thus MAA also increased *RORγT* expression, although at a later time point compared with MS-275 (Fig. 5H versus Fig. 5D). Our findings suggest that HDAC inhibitors may promote Th17 differentiation through enhancing *RORγT* expression, which warrants further investigation to test whether this is valid in animals.

The clinical relevance of this study is demonstrated by the correlation of serum estradiol levels and *RORγT* and *Rea* mRNA levels in the vaginal lavage of 15 healthy women. We found that high levels of serum estradiol are correlated with low levels of *RORγT* mRNA but with high levels of *Rea* mRNA (Fig. 6B, 6C). These human in vivo data are consistent with our in vitro results showing that E2 upregulates *Rea* to inhibit *Rorγt* transcription. Whether this mechanism is true in humans requires further investigation in human clinical trials using pharmacologic manipulations of E2 levels and/or REA levels. Serum E2 levels in premenopausal women fluctuate with elevated levels in the second half of the regular menstrual cycle (36). Given the findings from this study, it is reasonably to speculate that the elevated E2 levels inhibit *RORγT* transcription, thus inhibiting Th17 differentiation. Indeed, we observed that serum E2 levels were inversely corre-

lated with vaginal *IL-17A* mRNA levels ($R^2 = -0.377$), but the correlation was not statistically significant ($p = 0.166$), which may be due to the small number of specimens. Other investigators have shown that across the menstrual cycle in healthy reproductive-aged women, serum E2 levels are inversely associated with the urine levels of IL-1β, IL-6, and IL-8 (56), which are IL-17 downstream target genes. Clinically, the symptoms of vaginal candidiasis are often exacerbated in the second half of the menstrual cycle when colonization of *C. albicans* rises (37), which may be related to the decrease in Th17 differentiation and reduction of IL-17 levels, as IL-17 has important antifungal activities (32–34). Whereas our present study focused on estradiol, other studies have demonstrated that progesterone may also inhibit Th17 differentiation (57, 58). Given that progesterone levels are also elevated in the second half of the menstrual cycle (36), we think that the elevated serum levels of E2 and progesterone may be responsible for the inhibition of Th17 differentiation and exacerbation of vaginal candidiasis in the second half of the menstrual cycle.

In conclusion, the present study demonstrates that estradiol acts on ERα to recruit REA and form ERα/REA complex; binding of the ERα/REA complex to the EREs of the *RORγT* promoter region suppresses *RORγT* expression, thus inhibiting Th17 differentiation. Additionally, HDAC1 and HDAC2 constitutively bind to the *RORγT* promoter region and suppress *RORγT* expression.

Acknowledgments

This study used the core facilities of Tulane Cancer Center and Louisiana Cancer Research Consortium. We thank the clinical laboratory of the Affiliated Hospital of Guangdong Medical College for assistance in counting the cells in the vaginal lavage.

Disclosures

The authors have no financial conflicts of interest.

References

- Ouyang, W., J. K. Kolls, and Y. Zheng. 2008. The biological functions of T helper 17 cell effector cytokines in inflammation. *Immunity* 28: 454–467.
- Veldhoen, M., R. J. Hocking, C. J. Atkins, R. M. Locksley, and B. Stockinger. 2006. TGFβ in the context of an inflammatory cytokine milieu supports de novo differentiation of IL-17-producing T cells. *Immunity* 24: 179–189.
- Mangan, P. R., L. E. Harrington, D. B. O'Quinn, W. S. Helms, D. C. Bullard, C. O. Elson, R. D. Hatton, S. M. Wahl, T. R. Schoeb, and C. T. Weaver. 2006. Transforming growth factor-β induces development of the T_H17 lineage. *Nature* 441: 231–234.
- Betelli, E., Y. Carrier, W. Gao, T. Korn, T. B. Strom, M. Oukka, H. L. Weiner, and V. K. Kuchroo. 2006. Reciprocal developmental pathways for the generation of pathogenic effector T_H17 and regulatory T cells. *Nature* 441: 235–238.
- Acosta-Rodriguez, E. V., G. Napolitani, A. Lanzavecchia, and F. Sallusto. 2007. Interleukins 1β and 6 but not transforming growth factor-β are essential for the differentiation of interleukin 17-producing human T helper cells. *Nat. Immunol.* 8: 942–949.
- Chung, Y., S. H. Chang, G. J. Martinez, X. O. Yang, R. Nurieva, H. S. Kang, L. Ma, S. S. Watowich, A. M. Jetten, Q. Tian, and C. Dong. 2009. Critical regulation of early Th17 cell differentiation by interleukin-1 signaling. *Immunity* 30: 576–587.
- Korn, T., E. Bettelli, W. Gao, A. Awasthi, A. Jäger, T. B. Strom, M. Oukka, and V. K. Kuchroo. 2007. IL-21 initiates an alternative pathway to induce proinflammatory T_H17 cells. *Nature* 448: 484–487.
- Aggarwal, S., N. Ghilardi, M. H. Xie, F. J. de Sauvage, and A. L. Gurney. 2003. Interleukin-23 promotes a distinct CD4 T cell activation state characterized by the production of interleukin-17. *J. Biol. Chem.* 278: 1910–1914.
- Park, H., Z. Li, X. O. Yang, S. H. Chang, R. Nurieva, Y. H. Wang, Y. Wang, L. Hood, Z. Zhu, Q. Tian, and C. Dong. 2005. A distinct lineage of CD4 T cells regulates tissue inflammation by producing interleukin 17. *Nat. Immunol.* 6: 1133–1141.
- Harrington, L. E., R. D. Hatton, P. R. Mangan, H. Turner, T. L. Murphy, K. M. Murphy, and C. T. Weaver. 2005. Interleukin 17-producing CD4⁺ effector T cells develop via a lineage distinct from the T helper type 1 and 2 lineages. *Nat. Immunol.* 6: 1123–1132.
- Villey, I., R. de Chasseval, and J. P. de Villartay. 1999. RORγT, a thymus-specific isoform of the orphan nuclear receptor RORγ/TOR, is up-regulated by signaling through the pre-T cell receptor and binds to the TEA promoter. *Eur. J. Immunol.* 29: 4072–4080.

^{*-1705}
g tgcataccct cagcaccttg ggggcactct ggaaaagcca caagcatGGT CAttaagtta
^{ERE3 *-1653}
 Primer 2F
^{ERE2 *-1618}
 atagtgacaa tctcatcaga ggaGGTCACc tctactcttc catcacatac tcattgggtg
 cccaccaatc tgtcccact acaaaagcca tctgtggcct tctgtccca gcatccctcc
 tccctgagct tggggctcca tctcctggg gggggctcgga gctgcttggc tcagcataat
 cctgatcagc ctcctgtgca ctagccacag.....
 Primer 2R ^{*-1435}
^{*-822} Primer 1F ^{ERE1 *-799}
atccctcc agtggatctg aGGTCActct acctggccat aagtccttac tcaaccattc
 actactgtgt gatcttgagc aggttactta atctctctgt gtctcacctt cctgtcttt
 ggaatggtag ttatcacata aagtatttta tggggattat gaagtcaca cagagctgaa
 tcattcccaa cactgaatta agcactgctg ctaagaggat gaagatggta gtgtcactat
 ctgtgtccca gactagcagt ctgtttcca aaggc
 Primer 1R ^{*-550}

Supplementary Figure 1. Mouse Roryt gene promoter region contains 3 ERE half-sites (ERE1, ERE2, and ERE3) identified in mouse Roryt promoter region by the Transcription Element Search System (University of Pennsylvania) as shown in upper cases in the nucleotide sequence (reference#: NC_00069.6). The numbers indicate how many bp upstream to the Roryt transcription start site. The ChIP PCR primer sequences are underlined.

2014 SBUR Fall Symposium, Nov 13-16, 2014, Dallas, TX.

Methoxyacetic Acid Inhibits Prostate Cancer Cell Growth

Keshab R. Parajuli, Qiuyang Zhang, Sen Liu, Neil K. Patel, and Zongbing You

Departments of Structural & Cellular Biology and Orthopaedic Surgery, Tulane Cancer Center and Louisiana Cancer Research Consortium, Tulane Center for Stem Cell Research and Regenerative Medicine, and Tulane Center for Aging, Tulane University School of Medicine, New Orleans, Louisiana 70112

Background: Methoxyacetic acid (MAA) is a primary metabolite of ester phthalates that are used in production of consumer and pharmaceutical products. Environmental exposure to MAA causes embryo abnormalities in pregnant women and spermatocyte death in men through inhibition of histone deacetylases (HDACs). MAA's effects on solid tumors have never been investigated. The objective of this in-vitro study was to determine MAA's effects on prostate cancer cells.

Methods: Two immortalized human normal prostatic epithelial cell lines (RWPE-1 and pRNS-1-1) and four human prostate cancer cell lines (LNCaP, C4-2B, PC-3, and DU-145) were examined for their cell viability, apoptosis, cell cycle arrest, and gene expression after treatment with MAA at different concentrations and time points, using flow cytometry, Western blot, real-time PCR, and chromatin immunoprecipitation analyses.

Results: MAA time- and dose-dependently inhibited prostate cancer cell growth through induction of apoptosis and cell cycle arrest at G1 phase. Prostate cancer cell lines were more sensitive to MAA than normal prostatic epithelial cell lines. MAA-induced apoptosis was due to down-regulation of the anti-apoptotic gene baculoviral inhibitor of apoptosis protein repeat containing 2 (BIRC2, also named cIAP1), leading to activation of caspases 7 and 3, thus triggering off the downstream apoptotic events. MAA-induced cell cycle arrest (mainly G1 arrest) was due to up-regulation of p21 expression at the early time and down-regulation of cyclin-dependent kinase 4 (CDK4) and CDK2 expression at the late time. MAA up-regulates p21 expression through inhibition of HDAC activities, independent of p53/p63/p73.

Conclusions: These results suggest that MAA may be a potential therapeutic drug for the treatment of prostate cancer.

METHOXYACETIC ACID SUPPRESSES PROSTATE CANCER CELL GROWTH BY INDUCING GROWTH ARREST AND APOPTOSIS

Parajuli KR*, Jhang Q*, Liu S*, Patel NK*, You Z*

*Department of Structural & Cellular Biology, Tulane University, New Orleans, LA.

Methoxyacetic acid (MAA) is a primary metabolite of ester phthalates that are used in production of consumer products and pharmaceutical products. MAA causes embryo malformation and spermatocyte death through inhibition of histone deacetylases (HDACs). Little is known about MAA's effects on cancer cells. In this study, two immortalized human normal prostatic epithelial cells (RWPE-1 and pRNS-1-1) and four human prostate cancer cell lines (LNCaP, C4-2B, PC3, and DU-145) were treated with at different doses (5, 10, and 20 mM) and for different time periods (12, 24, 48, and 72 hours). Cell viability, apoptosis, and cell cycle analysis were performed using flow cytometry and chemical assays. Gene expression and binding to DNA were assessed using real-time PCR, Western blot, and chromatin immunoprecipitation analyses. Here we report that MAA can dose-dependently inhibit prostate cancer cell growth through induction of apoptosis and cell cycle arrest at G1 phase. MAA-induced apoptosis is due to down-regulation of the anti-apoptotic gene baculoviral inhibitor of apoptosis protein repeat containing 2 (BIRC2, also named cIAP1), leading to activation of caspases 7 and 3, thus triggering off the downstream apoptotic events. MAA-induced cell cycle arrest (mainly G1 arrest) is due to up-regulation of p21 expression at the early time and down-regulation of cyclin-dependent kinase 4 (CDK4) and CDK2 expression at the late time. MAA up-regulates p21 expression through inhibition of HDAC activities, independent of p53/p63/p73. These results suggest that MAA may be a potential therapeutic drug for the treatment of prostate cancer.

This work was supported by Department of Defense Health Program and National Institutes of Health.

2015 Metabolism and Cancer, American Association of Cancer Research, June 7-10, 2015, Hyatt Regency Bellevue, Bellevue, WA.

Aminomethylphosphonic acid inhibits human prostate xenograft tumor growth through interfering glycine synthesis in the cancer cells.

Keshab R. Parajuli, Qiuyang Zhang, Sen Liu, and Zongbing You

Rapidly proliferating cancer cells consume more glycine than rapidly proliferating normal cells, which offers an opportunity to target glycine metabolism in the cancer cells while avoiding causing severe side effects in the normal cells. Two-thirds of glycine consumed is synthesized intracellularly, e.g., through conversion of serine into glycine by serine hydroxymethyltransferase (SHMT). Aminomethylphosphonic acid (AMPA, $C_3H_3NO_5P$) is an analog to glycine, which inhibits SHMT enzyme activity, thus blocking conversion of serine into glycine. Our previous in-vitro studies have shown that AMPA inhibited cell growth in six cancer cell lines (including four human prostate cancer cell lines PC-3, DU-145, LNCaP, and C4-2B), while had little effects on two human normal immortalized prostatic epithelial cell lines (RWPE-1 and pRNS-1-1). The purpose of the present study was to determine if AMPA could inhibit PC-3 xenograft tumor growth in nude mice. PC-3-LacZ-luc cells (stably expressing LacZ and luciferase for staining and in-vivo imaging) were first implanted subcutaneously to form tumors. Then, the tumors were cut into 2-mm pieces and surgically implanted orthotopically in the prostates of 39 six-week-old athymic nude male mice that were castrated during the same surgery. One week later, the prostate tumor sizes were measured using D-luciferin and IVIS® Lumina XRMS imaging system (PerkinElmer, Inc.). The animals were randomized into three treatment groups: 1) saline as control (n = 14); 2) 400 mg/kg/day of AMPA (n = 10); and 3) 800 mg/kg/day of AMPA (n = 15). The treatment was administrated intraperitoneally once a day until animal death. Animal body weight measurement and in-vivo imaging were performed once every 5 to 7 days. Upon animal death, tumors were harvested and weighed. Pathologic examination, immunohistochemical staining, and Western blot analyses were performed using the tumors. We found that the tumor size rapidly increased in the control group, whereas the tumor size increased only slightly in the two AMPA-treated groups ($p < 0.05$). Animal survival time was significantly longer in the AMPA-treated groups than the control group ($p < 0.05$) and the high-dose group had slightly longer survival time than the low-dose group ($p = 0.087$). The average final tumor weight was significantly less in the high-dose group than the control group ($p < 0.05$). The levels of cellular inhibitor of apoptosis protein 1 (C-IAP1) and cyclin D1 were dramatically reduced in the tumors from the two AMPA-treated groups compared to the control group. We also observed that the two AMPA-treated groups had much less intra-abdominal metastases compared to the control group. Further in-vitro studies found that AMPA inhibited migration and invasion of PC-3 cells using Transwell assays. In conclusion, we found that AMPA inhibits human prostate xenograft tumor growth through inducing apoptosis and inhibiting cellular proliferation, which suggests that AMPA may be developed into a new treatment for prostate cancer.